RAIL VEHICLES IN CROSSWINDS: ANALYSIS OF STEADY AND UNSTEADY AERODYNAMIC EFFECTS THROUGH STATIC AND MOVING MODEL TESTS

by

FRANCESCO DORIGATTI

A thesis submitted to
the University of Birmingham
for the degree of
DOCTOR OF PHILOSOPHY

School of Civil Engineering
University of Birmingham
March 2013

Abstract

The author of this thesis presents the results of an experimental investigation of scale-model trains in crosswinds, undertaken in order to assess steady and unsteady aerodynamic effects of the vehicle movement simulation. A 1:25 scale-model train was tested in the University of Birmingham's TRAIN (Transient Railway Aerodynamic Investigation) rig facility. A crosswind generator was designed and constructed to enable static and moving model experiments in the presence of crosswinds in this facility. An on-board pressure measuring system comprising a series of miniaturised pressure transducers and a bespoke stand-alone data logger were developed. Finally, static and moving model experiments were carried out investigating a scale-model of the Class 390 Pendolino train, on a nominal flat ground infrastructure scenario whilst subjected to a crosswind at 30° yaw angle.

The test facility, measuring equipment and experimental methodology that were developed led to a more realistic underbody flow simulation and to a reduced margin of experimental uncertainty with respect to previous moving model tests. Furthermore, they enabled detailed surface pressure data to be measured, which are suitable for CFD benchmarking.

The simulation of the vehicle movement causes slightly greater magnitudes of the mean (i.e. time average) pressure coefficient on the train nose, but it does not produce significant variations of the overall mean aerodynamic load coefficients compared to the static test results. The correlation between the pressure fluctuations occurring along the vehicle varies from static to moving model tests, thus suggesting that a difference might arise in the overall peak aerodynamic load coefficients measured in the two test conditions. Accordingly, this research supports the reliability of wind tunnel tests on static vehicles for investigating steady aerodynamic coefficients but suggests that their use in the analysis of train unsteady aerodynamics is not entirely satisfactory.

Acknowledgements

Table of Contents

List of Figures

Chapter 7

List of Tables

Chapter 6

Chapter 7

Glossary

Onset wind	Wind impinging on the train described with respect to an absolute reference system fixed with respect to the ground. In this thesis this refers both to the natural wind at full-scale and to the wind at model-scale, as simulated by the TRAIN rig crosswind generator
Streamwise direction	Direction of the mean (i.e., time averaged) onset wind. In this thesis, when referred to the wind simulated by the crosswind generator, it is defined as the horizontal direction perpendicular to the track
Streamwise wind velocity ( )	Component of the onset wind velocity directed according to the streamwise direction (sign convention in figure 4.10)
Lateral wind velocity ( )	Component of the onset wind velocity directed horizontal and parallel to the track (sign convention in figure 4.10)
Vertical wind velocity ( )	Component of the onset wind velocity directed vertically (sign convention in figure 4.10)
Relative wind	Wind impinging on the train as seen by an observer positioned on the moving vehicle (both at full-scale and at model-scale)
Relative wind velocity ( )	Horizontal component of the relative wind given by the vector combination of the onset wind horizontal components with the train speed
Spanwise direction	It refers to the span of the crosswind generator and defines the horizontal direction parallel to the track
Spanwise position	Position along the track within the span of the crosswind generator. It refers either to the train or to the measurement instruments
Spanwise average	Spatial average calculated by averaging the local values of a physical quantity in the spanwise direction (within the crosswind generator).
Double-average	Average of a physical quantity calculated both in time and space. Based on a time history recorded at a single spanwise position, it is calculated according to procedure in sections 5.2.1 and 5.2.2.
Corrected double-average	Double-average of a physical quantity corrected in order to take into account the streamwise gradient of such a quantity inside the crosswind generator (calculation procedure provided in sections 5.2.1 and 5.2.2).

List of Notations

Principal Symbols

Train reference area (vehicle nominal side area)

Standard track gauge (1.435 m at full-scale)

Aerodynamic load coefficient (= , , ,)

Mean aerodynamic load coefficient (= , , ,)

Peak-over-mean aerodynamic load coefficient (= , , ,)

Peak-over-peak aerodynamic load coefficient (= , , ,)

Aerodynamic load coefficient per unit length on loop (j) (= , , ,)

Mean aerodynamic load coefficient per unit length on loop (j) (= , , ,)

Peak-over-mean aerodynamic load coefficient per unit length on loop (j) (= , , ,)

Peak-over-peak aerodynamic load coefficient per unit length on loop (j) (= , , ,)

Pressure coefficient relating to the pressure tap (i) on loop (j)

Mean pressure coefficient relating to the pressure tap (i) on loop (j)

Ensemble average Pressure coefficient relating to the pressure tap (i) on loop (j)

Bias limit

Random uncertainty

Total experimental uncertainty

Aerodynamic side force

Aerodynamic lift force

Frequency

Normalised frequency ——

Gust factor (peak to mean reference velocity ratio)

Train reference height (nominal vehicle height)

Turbulence intensity ($\eta =$ u v w)

Spanwise-to-local ratio ($\eta =$ U, P_{ST}; $\zeta =$ ST, MOV)

Length of the train's leading car

Crosswind generator total span along the track

Length of the stripe j (on the discretized train model)

Turbulence length scale ($\eta =$ u v w; $\xi =$ X Y Z)

Aerodynamic rolling moment about the -axis

Aerodynamic rolling moment about the leeward rail

Streamwise gradient ($\eta = U, P_{ST}; \zeta = ST, MOV$)

Instantaneous surface pressure at the pressure tap (i) on loop (j)

Barometric pressure (in still air)

Wind static pressure

Wind static differential pressure (-   )

Double-average wind static differential pressure

Double-average wind static differential pressure corrected according to the streamwise gradient

Mean wind static differential pressure

Dynamic pressure –

Total number of moving model test runs to calculate the ensemble averages time series (R = 15)

Reynolds number

Critical Reynolds number

Power spectral density ($\eta = u\ v\ w$)

Spanwise coordinate along the track (origin at the CWG entry, positive according to the direction of travel)

Spanwise coordinate along the track (origin at the CWG midspan, positive opposite to the direction of travel)

Nominal normalised spanwise position of the train within the CWG (=   ).

Turbulence time scales ($\eta = u\ v\ w$)

Time (discrete) synchronised with the onboard data acquisition system

Nominal normalised discrete time relating to the train travelling within the CWG (= 0.0001)

Instantaneous streamwise wind velocity

Mean (time average) streamwise wind velocity

Double-average (spanwise & time average) of the streamwise wind velocity

Double-average of the streamwise wind velocity corrected according to the streamwise gradient

Streamwise wind velocity fluctuations

Instantaneous wind velocity

Reference wind velocity

Wind velocity relative to the train

Double-average of the relative wind velocity corrected according to the streamwise gradient

Train speed

zero pressure offset (pressure transducer)

Lateral wind velocity fluctuations

Mean lateral wind velocity

Vertical wind velocity fluctuations

Mean vertical wind velocity

Train reference system

x,y,z   Onset wind reference system

Distance between the loop of taps (j) and the nose of the train

Reference height for the crosswind measurements (3 m full-scale equivalent)

Principal Greek Symbols

☐   Wind angle

Moving to static tests reference velocity ratio

Air dynamic viscosity

☐   Yaw angle

Length scaling factor

Time scaling factor

Velocity scaling factor

Air density

Autocorrelation coefficient of the time series $\eta(t)$

Cross-correlation coefficient of the time series $\eta(t)$ *and* $\xi(t)$

Time delayed cross-correlation coefficient of the time series $\eta(t)$ *and* $\xi(t+\tau)$

Standard deviation ($\eta = u, v, w$)

Principal Subscripts

CW	Trim (of time series) relating to the train travelling within the CWG
I	Index of the individual facets of the discretised train geometry (numeration in figure 5. 12)
i	Index of the individual pressure tap on each loop (numeration in figure 4.27)
j	Index of the loops of pressure tap (numeration in figure 4.26) corresponding also to the index of the stripes of the discretised train geometry (figure 5.11)
k	Index of the on-board pressure transducer
Loc	Local measurement
r	Moving model test single-run ordinal number

rel	Relative (to the train)
ref	Reference
SW	Spanwise average
tr	Train

Principal Abbreviations

ABL	Atmospheric boundary layer
AFG	Approximate flat ground (ground scenario)
CFD	Computational fluid dynamics
CP	Reference Cobra probe
CWG	Crosswind generator
FG	Flat ground (ground scenario)
FS	Full-scale
GRP	Glass reinforced plastic (fibreglass)
HPP / LPP	High / low pressure port (of differential pressure transducers)
HWP	Horizontal wind profile
ID / OD	Inner / outer diameter
LD	Onboard light-beam detector
LES	Large eddy simulation
RANS	Reynolds-averaged Navier-Stokes
LD1 / LD2	Trackside light-beam detectors
LS1 / LS2	Trackside light sources
MOV	Moving (model tests)
MS	Model-scale
PCWG	Previously (existing) crosswind generator
PS	Reference Pitot-static tube
SD1 / SD2	Trackside vehicle speed detectors
ST	Static (model tests)
STBR	Single track ballast and rail (ground scenario)
TFI	Turbulent Flow Instrumentation Ltd.
TRAIN (rig)	Transient Railway Aerodynamic Investigation (rig)
VWP	Vertical wind profile

Chapter 1

Introduction

1.1   Outline of studies

This thesis is formed of a collection of several pieces of work undertaken by the author as part of his PhD studies. The principal research consisted of an experimental investigation of the crosswind effects on rail vehicles. The details and results of this work form the main content of this thesis. A preliminary version of these results has been published in a conference paper (included in appendix I) which has been presented at the Seventh International Colloquium on Bluff Body Aerodynamics and Applications (BBAA7). Complementary to the main research was the design and construction of a crosswind generator for the TRAIN rig facility (where the experiments were carried out), the details of which are reported in appendix A. Finally, a separate piece of work consisted of the assessment of the crosswind stability of high-sided road vehicles over long-span bridges. Wind tunnel experimental data were analysed by the author as part of a collaborative project between the University of Birmingham, Politecnico di Milano and ARUP, and the work has been presented in a paper (included in appendix I) which has been published in the Journal of Wind Engineering and Industrial Aerodynamics.

1.2   Research background

A train travelling through a natural crosswind is surrounded by a complex flow field, which leads to a series of steady and unsteady aerodynamic forces and moments. These aerodynamic loads may induce significant changes in the vehicle dynamic behaviour, in comparison to a no-crosswind condition, and can cause issues relating to train stability (Gawthorpe, 1994; Diedrichs, 2005). Among

these issues, the most severe scenario is vehicle overturning, which may happen in the presence of strong crosswinds and poses a significant risk to the passengers' safety (Baker et al., 2009).

To minimise the risk of wind-induced railway accidents, dedicated analyses are currently prescribed as part of the rolling stock homologation process by the European and national standards (EC, 2008; CEN, 2010; RSSB, 2009a). These analyses evaluate the combination of the inertial and aerodynamic loads acting on a train (sometimes including the dynamics of its suspension system) and identify the crosswind speed that may cause it to overturn. By comparing this speed with pre-determined limiting values it is possible to assess the safe operation of the vehicle.

Currently different limiting wind speeds are adopted by different standards (CEN, 2010; RSSB, 2009a). Furthermore, various methods can be applied for carrying out the vehicle stability analysis (Cheli et al., 2007; Ding et al., 2008; Baker, 2010a). However, all such methods share a formulation of the aerodynamic loads that embeds the information concerning the vehicle aerodynamic characteristics into a series of non-dimensional coefficients.

These non-dimensional aerodynamic coefficients are provided to the vehicle stability analysis as an external input and, in principle, can be obtained through three different techniques of investigation: via scale-model tests, via full-scale measurements or by performing computational fluid dynamic (CFD) simulations (Baker et al., 2009; Sterling et al., 2010). Among these, wind tunnel tests on static scale-models offer the best compromise between the effectiveness (in terms of both cost and time) and the accuracy of the aerodynamic investigation (Baker and Humphreys, 1996). Hence, they represent the current standard and, as such, are prescribed within the rolling stock homologation process (EC, 2008; CEN, 2010; RSSB, 2009a).

Wind tunnel tests on static, scale-model trains, avoid the technical complexity and the vulnerability to uncontrollable environmental conditions inherent in full-scale measurements (Baker et al, 2004; Quinn et al.,2007). In addition, they are perceived currently to deliver a better accuracy than CFD,

whose full validation has not yet been achieved (Baker et al., 2009). Furthermore, since they do not involve any vehicle movement representation, these tests are suitable for conventional wind tunnel facilities (Gawthorpe, 1994; Sanquer et al., 2004; Baker et al., 2009; Baker and Sterling, 2009; Rocchi et al., 2009) using the methodology normally applied for testing civil engineering structures (Barlow et al., 1999; Holmes, 2007). As such, they enable comprehensive vehicle aerodynamic characterisations to be obtained in a relatively short time-frame and at reasonable cost.

In such tests, the orientation of the scale-models with respect to the streamwise wind direction can be changed in order to replicate the variety of yaw angles (i.e., the angles between the relative incident wind and the direction of travel) typically experienced by a real train when in operation. However, since the vehicle movement is not recreated, the simulation is not entirely realistic. In particular, in wind tunnel tests on static trains, the following approximations must be accepted:

- Since the wind direction with respect to the train coincides with the wind direction with respect to the ground, to properly replicate the former an incorrect representation has to be accepted for the latter.

- There is no possibility of reproducing the '*skewed wind profile*' originally seen by a moving train (Diedrichs, 2005). This implies an incorrect simulation of both the intensity and direction of the local wind velocity impinging on the train (at distances from the ground that are different from the reference height), whose effects are enhanced in the presence of an embankment scenario (Suzuky et al., 2003; Schober et al., 2010; Cheli et al., 2008; Cheli et al., 2011a).

- Unless dedicated (active) turbulence generating systems are employed (Cooper, 1991), there is a mismatch between the simulated incident turbulence and the actual turbulence perceived by a real train moving through a natural crosswind (Cooper, 1984).

Thus, in a static test, the flow field surrounding the train is likely to differ from that associated with a moving train. Consequently, it can also be hypothesised that the non-dimensional aerodynamic load

coefficients obtained through a static test might contain systematic approximations due to this unrealistic representation of the flow field.

To verify such a hypothesis, and to assess the magnitude of these systematic approximations (if any), a number of previous studies have compared the aerodynamic load coefficients obtained with static and moving model experiments (Cooper, 1981; Baker, 1986; Howell, 1986; Humphreys, 1995; Muggiasca, 2002). Furthermore, similar analyses have been performed recently based on CFD simulations (Hemida and Baker, 2010; Cheli et al., 2011a). Current knowledge is limited, however, due to a series of issues related to these past investigations. There have been numerous technical and practical difficulties inherent in moving model tests, which led to difficult interpretation and to a lack of agreement in the previous experimental results. Furthermore, because of a lack of detailed surface pressure data from moving model tests, no evaluation has been performed so far regarding the effect of the vehicle movement simulation on the surface pressure distribution on the train. Finally, only qualitative indications can currently be drawn from CFD, for which the challenge of reaching a full validation is enhanced by a lack of moving model experimental data suitable for benchmarking.

1.3 Research aim and objectives

The main aim of this research was to assess the impact of the method of vehicle movement simulation on the accuracy of the non-dimensional coefficients that express the aerodynamic behaviour of trains in crosswinds.

To accomplish this aim, an experimental investigation on a 1:25 scale-model train was undertaken in the Transient Railway Aerodynamic Investigation (TRAIN) rig, a test facility owned by University of Birmingham. The following detailed research objectives were set relating to the investigation:

1. Explore the performance of the original crosswind generator (CWG) of the TRAIN rig and, when this was found to be inadequate for this research, design and install a new CWG.

2. Develop an on-board stand-alone pressure measuring system for measuring the surface pressure distribution on the train during both static and moving model tests.

3. Develop a test methodology for undertaking TRAIN rig moving model experiments in crosswinds, i.e., design an experimental setup comprising of both trackside and on-board measurements and upgrade the standard TRAIN rig test procedure to include the operation of the CWG and of the on-board pressure measuring system.

4. Undertake a series of static model experiments in crosswinds, measuring the train surface pressure distribution.

5. Undertake a series of moving model experiments in crosswinds, measuring the train surface pressure distribution.

6. Compare the results from static and moving model experiments in order to assess the influence of the vehicle movement simulation on the steady and unsteady aerodynamic behaviour of the train.

7. Deliver a set of moving (and static) test experimental data of the train surface pressure distribution for CFD benchmarking.

It should be noted that part of this research was undertaken by the author in the context of the AeroTRAIN project, Aerodynamics: Total Regulatory Acceptance for the Interoperable Network (within work package 3.4 (ERA, 2009)). AeroTRAIN was a collaborative project - medium-scale - focused research project supported by the European 7th Framework Programme, contract number: 233985 (UNIFE, 2009-2010).

1.4   Structure of the thesis

The content of the remainder of the thesis is organised as follows:

- In chapter 2, the author reviews the crosswind effects on rail vehicles. Moving from the examination of past wind-induced railway accidents, he examines the characteristics and the analytical formulation relating to the natural winds near the ground and the aerodynamic behaviour of a train when subjected to such winds. Furthermore, presenting an overview of the methods of analysis currently undertaken for assessing the train stability in crosswinds, he outlines the primary role played by the non-dimensional coefficients, which capture the information concerning the train aerodynamics.

- Chapter 3 is used to analyse the different techniques of investigation through which such non-dimensional aerodynamic coefficients can be obtained. Considering experiments on scale-model vehicles in crosswinds, a comparison between static and moving model tests is presented that highlights the advantages and disadvantages related to such approaches. Reviewing past moving model test campaigns, the writer outlines the major challenges involved in reproducing the vehicle movement. Furthermore, evaluating the results from previous (experimental and numerical) studies that undertook a comparison between static and moving model train simulations, he highlights the lack of agreement that is the motivation for the present research.

- Chapter 4 defines the case study that was analysed in this research. It describes the test facility, train model and measuring instrumentation that were employed in the test campaign. Furthermore, it provides details of the experimental methodology that was adopted for the static and moving model tests.

- Chapter 5 illustrates the data reduction methods that were developed in order to process the raw data and to calculate the non-dimensional coefficients for both the surface pressure and the aerodynamic loads on the train. In addition, it includes the uncertainty analysis that was carried out for assessing the accuracy of the present investigation.

- Chapter 6 presents and discusses the results of the mean (i.e., time averaged) non-dimensional coefficients for the pressure distribution and the aerodynamic loads. It analyses both static and moving model experiments and then, by comparison, it assesses the impact of the modelling of the vehicle movement on such coefficients.

- Chapter 7 reports and discusses the results concerning the unsteady aerodynamics. Analyses of the non-dimensional peak normalised coefficients and of the correlation between the pressure fluctuations occurring along the train are presented. In both cases, the effect of the vehicle movement simulation is assessed through a comparison between static and moving model test results.

- Chapter 8 summarises the main outcomes of the research and provides recommendations for further developments.

Chapter 2

Crosswind effects on rail vehicle dynamic behaviour

2.1   Introduction

Chapter 2 examines the main characteristics of rail vehicle aerodynamics in the presence of crosswinds. Firstly, to clarify the relevant effects that a crosswind can have on the train stability, section 2.2 illustrates the major types of wind-induced railway accidents reported in several surveys. Following that, section 2.3 describes the analytical approach taken for natural winds in proximity of the ground, while section 2.4 examines the characteristics of the flow around a train in crosswinds and introduces the formulation of the steady and unsteady aerodynamic loads. The variety of analyses that are currently undertaken for assessing the train stability is presented in section 2.5. Finally, section 2.6 outlines the primary role that non-dimensional vehicle aerodynamic coefficients play in such an assessment.

2.2   Wind-induced railway accidents

Stability issues and, hence, serious accidents can be caused by the action of a natural wind on a travelling train. The extreme scenario where the train overturns occurs when the contribution of the aerodynamic rolling moment (with respect to the leeward rail) generated by a side wind is large enough to overcome the restoring moment associated with the train weight. In addition, crosswinds can cause further problems, such as dewirement of the pantograph due to excessive wind-induced lateral deflection of the vehicle (Gawthorpe, 1994). Finally, even in the presence of moderate winds, a compromised level of travel comfort can occur where the turbulence of the relative wind excites the natural frequencies of the suspension system (Cooper, 1984).

A number of surveys have documented the occurrence of wind-induced train accidents. They were part of different studies concerned either with the assessment of the crosswind effects on railway traffic (Gawthorpe 1994; Johnson 1996; Ushijima, 2006; Baker et al., 2009) or with the review of the vehicle stability methods of analysis (Diedrichs, 2005). In addition, accidents that took place in recent years have been reported in the press (The Japan Times, 2008; BBC, 2007) and through the publication of investigation reports commissioned by national safety authorities (ATSB, 2008; ATSB, 2010).

Derailed or overturned trains have been reported since the end the 19th century in Europe (in the UK, Ireland, Belgium, Switzerland, Austria and Italy) and in China, Japan, Australia, New Zealand, Canada and the United States. Involving passenger and freight trains, these accidents took place in a variety of situations: along railway lines characterised by different track gauges (standard or narrow), on tangent or curved track sections and on different infrastructure elements (relatively flat and open areas, embankments, bridges and viaducts). Wide ranges of data have been registered for the train speed (approximately between 10 and 100 km/h) and wind velocity (from 30 to 50 m/s) associated with these accidents.

The analysis of the historical statistics outlines that wind-related railway accidents still represent a risk factor in modern railways. In light of the injuries and fatalities reported in the past (especially if passengers trains were involved) the safety implications become clear. Furthermore, the introduction of lightweight coaches and the progressive raising of the operating speed contribute to potentially increased risk (Matschke et al., 2000). Consequently, to minimise and possibly prevent the occurrence of future accidents, the assessment of train stability under the effect of a crosswind is currently prescribed by a number of standards (EC, 2008; CEN, 2010; RSSB, 2009a).

2.3   Natural winds near the ground

In order to assess wind-induced forces it is necessary first to understand the main characteristics of the natural winds to which real trains are exposed. The friction developing between a mass of moving air and the ground, in the lower layers of the Earth's atmosphere induces the formation of the so-called Atmospheric Boundary Layer (ABL). This ABL is characterised by a turbulent flow with a horizontal mean wind speed that increases with height above the ground and can present different vertical mean wind profiles and turbulence levels, depending on the topography.

The conventional wind engineering approach (Dyrbye and Hansen, 1999; Holmes, 2007; ESDU, 1974) models the velocity field associated with natural winds through the superposition of a mean flow and a series of turbulent fluctuations. The following main assumptions are normally made:

- the flow is stationary within a sufficiently long time interval;

- the mean wind velocity depends only on the height above the ground;

- over small heights, the direction of the mean wind does not change.

For the purpose of the present work, these assumptions are accepted and the reference frame specified in figure 2.1 is adopted in order to have the   -axis aligned to the mean wind direction.
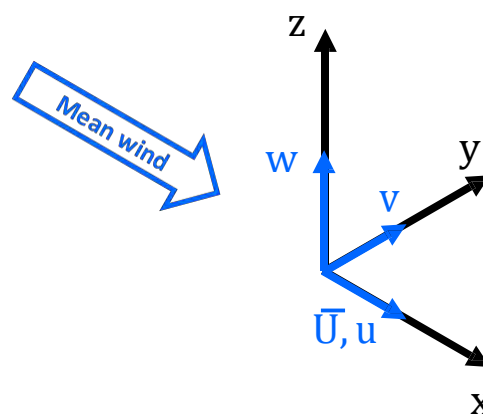
Figure 2.1 Reference system of the atmospheric (onset) wind

Accordingly, the instantaneous wind velocity vector at a generic time and relative to a height above the ground can be expressed as:

$$\mathbf{V}(x,y,z,t) = \bar{U}(z)\mathbf{i} + \lfloor u(x,y,z,t)\mathbf{i} + v(x,y,z,t)\mathbf{j} + w(x,y,z,t)\mathbf{k} \rceil \qquad (2.1)$$

where , and are the unit vectors relating to the , and axes, respectively, which form the reference system for the onset wind, is the longitudinal (horizontal) mean wind velocity component and , and are the components of the turbulent velocity fluctuations according to the axe , and , respectively. Based on the aforementioned assumptions, in equation (2.1) the mean wind speed depends only on the height. Conversely, turbulent velocity fluctuations depend both on the time and on the position in three dimensional space and are treated as stationary stochastic variables with zero mean.

The characteristics of the atmospheric turbulence are described by three different parameters:

- turbulence intensity;
- length (and time) scales of turbulence;
- power spectral density of the turbulent flow velocity components.

Mean wind velocity

A logarithmic profile defined according to equation (2.2) is conventionally suggested (for < 200 m according to Dyrbye and Hansen (1999), or for < 30 m according to the ESDU (Engineering Sciences Data Unit) 82026 (2002)) in order to approximate the variations of the mean wind velocity with respect to the height.

$$\bar{U}(z) = 2.5u^* ln\left(\frac{z}{z_0}\right) \qquad (2.2)$$

In equation (2.2) is the friction velocity and indicates the roughness length, which depends on the surface roughness and thus varies according to the typology of the area under investigation (e.g., open sea, rural area, urban area). Detailed definitions and typical values for both and are provided in the ESDU 82026 (2002).

Turbulence intensity

By definition, the turbulence intensity is given by the standard deviation ( ) of the relevant component of the fluctuating velocity divided by the mean wind speed (ESDU, 1974). If the assumption of a horizontally homogeneous flow is made, and individual standard deviations thus depend only on the height (Dyrbye and Hansen, 1999), the turbulence intensities relating to each of the three velocity components are defined as:

$$I_u(z) = \frac{\sigma_u(z)}{\overline{U}(z)} \tag{2.3a}$$

$$I_v(z) = \frac{\sigma_v(z)}{\overline{U}(z)} \tag{2.3b}$$

$$I_w(z) = \frac{\sigma_w(z)}{\overline{U}(z)} \tag{2.3c}$$

Length scales of turbulence

The ESDU 74030 (1974) introduces the nine length scales   given in (2.4), where   =   and   =   , in order to provide an indication concerning the average dimensions of the turbulent structures that characterise a natural wind.

$$\begin{matrix} L_{ux} & L_{uy} & L_{uz} \\ L_{vx} & L_{vy} & L_{vz} \\ L_{wx} & L_{wy} & L_{wz} \end{matrix} \tag{2.4}$$

With consideration of each Cartesian axis (i.e.,   , respectively), the turbulence length scales relative to any of the three velocity components are defined as:

$$L_{\eta x} = \int_0^\infty \rho_\eta (x' - x) d(x' - x) \tag{2.5a}$$

$$L_{\eta y} = \int_0^\infty \rho_\eta (y' - y) d(y' - y) \tag{2.5b}$$

$$L_{\eta z} = \int_0^\infty \rho_\eta (z' - z) d(z' - z) \tag{2.5c}$$

where   ,   and   are the cross-correlation coefficients (relative to the generic velocity component) given by:

$$\rho_\eta \left(x' - x \right) = \frac{\overline{\eta \left(x, y, z, t \right) \cdot \eta \left(x', y, z, t \right)}}{\sigma_\eta \left(x, y, z, t \right) \cdot \sigma_\eta \left(x', y, z, t \right)}$$
(2.6a)

$$\rho_\eta \left(y' - y \right) = \frac{\overline{\eta \left(x, y, z, t \right) \cdot \eta \left(x, y', z, t \right)}}{\sigma_\eta \left(x, y, z, t \right) \cdot \sigma_\eta \left(x, y', z, t \right)}$$
(2.6b)

$$\rho_\eta \left(z' - z \right) = \frac{\overline{\eta \left(x, y, z, t \right) \cdot \eta \left(x, y, z', t \right)}}{\sigma_\eta \left(x, y, z, t \right) \cdot \sigma_\eta \left(x, y, z', t \right)}$$
(2.6c)

In equations (2.6), an overbar is used for denoting a time average over a time interval that should be long enough to support the initial hypothesis of stationary flow.

In addition to the length scales, the ESDU 74030 (1974) introduces also three time scales in order to quantify the typical duration of a wind gust induced by the transit of vortex on fixed position in space. They are defined as:

$$T_u = \int_0^\infty \rho_u \left(\tau \right) d\tau$$
(2.7a)

$$T_v = \int_0^\infty \rho_v \left(\tau \right) d\tau$$
(2.7b)

$$T_w = \int_0^\infty \rho_w \left(\tau \right) d\tau$$
(2.7c)

In equation (2.7),   ,   and   are the autocorrelation coefficients expressed in function of the lag . Each of them, indicated generically as   , is given by:

$$\rho_\eta \left(\tau \right) = \frac{\overline{\eta \left(t \right) \cdot \eta \left(t + \tau \right)}}{\sigma_\eta^2}$$
(2.8)

where, again, an overbar indicates the time average over a sufficiently long time interval.

If Taylor's hypothesis of 'frozen vortices' (ESDU, 1974) is assumed, it follows that:

$$L_{\eta x} = T_\eta \cdot \bar{U} \quad \text{(with } \eta = u, v, w\text{)}$$
(2.9)

Power spectral density

The power spectral density   can be calculated from a time series, relative to any of the three velocity components, recorded through a single point measurement. Such a quantity expresses the distribution over the frequency range of the velocity fluctuations and is usually presented in the normalised form given by (ESDU, 1974, Dyrbye and Hansen, 1999; Holmes, 2007):

$$\frac{S_\eta\left(z, f\right) \cdot f}{\sigma_\eta^2\left(z\right)}$$

(2.10)

where the dependence of   on the height ( ) only is consistent with the assumption of horizontally homogenous flow. Different standards currently adopt different formulations in order to express the power spectral density of an atmospheric wind (ESDU, 2001; CEN, 2005). One of these, normally employed in relation to railway aerodynamic applications (Cooper, 1984; Baker, 2010a; CEN, 2010), has been proposed by Von Karman. Reported in equations (2.11) and illustrated in figure 2.2, it expresses the normalised power spectral densities in function of a normalised frequency given by

=   .

$$\frac{S_u\left(z, f\right) \cdot f}{\sigma_u^2\left(z\right)} = \frac{4 f_N}{\left(1 + 70.8 f_N^2\right)^{5/6}}$$

(2.11a)

$$\frac{S_v\left(z, f\right) \cdot f}{\sigma_v^2\left(z\right)} = \frac{4 f_N \cdot \left(1 + 755.2 f_N^2\right)}{\left(1 + 283.2 f_N^2\right)^{11/6}}$$

(2.11b)

$$\frac{S_w\left(z, f\right) \cdot f}{\sigma_w^2\left(z\right)} = \frac{4 f_N \cdot \left(1 + 755.2 f_N^2\right)}{\left(1 + 283.2 f_N^2\right)^{11/6}}$$

(2.11c)
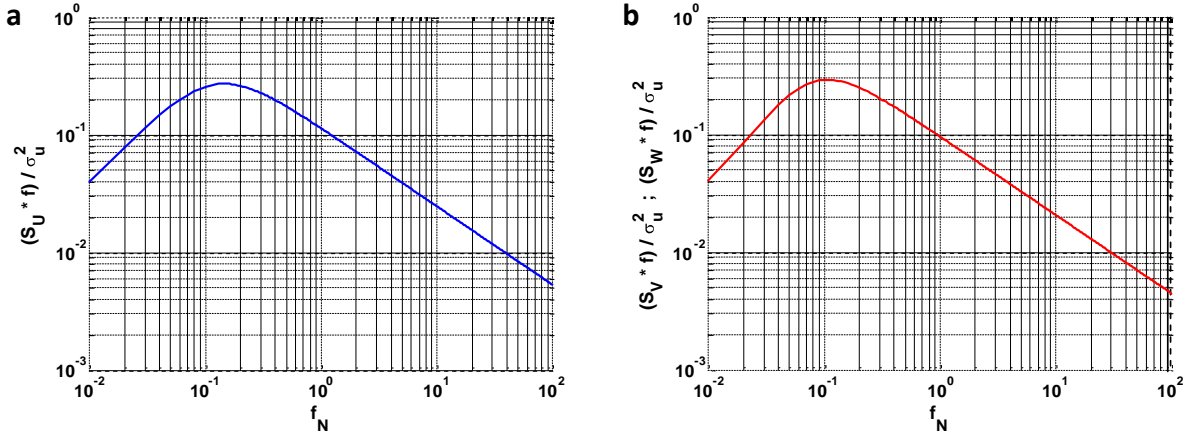
Figure 2.2 Von Karman wind spectra. a) longitudinal velocity component b) vertical and lateral velocity components

2.3.1 Natural crosswind relative to a moving vehicle

As illustrated in figure 2.3, when a vehicle travels through a natural wind blowing from the side, the wind velocity that it actually perceives (is given by the vector combination of the onset wind velocity and the train speed (with bold letters indicating vector entities).
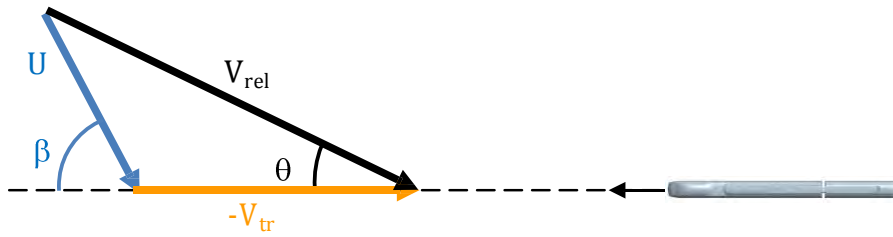
Figure 2.3 Vector diagram of the wind velocity relative to a moving vehicle

Accordingly, the magnitude of the relative wind velocity and its orientation with respect to the direction of travel (i.e. the yaw angle) can be expressed as follows:

$$V_{rel}^2 = U^2 + V_{tr}^2 + U V_{tr} \cos(\beta) \tag{2.12}$$

$$\theta = \arctan\left(\frac{U \sin(\beta)}{V_{rel} + U \cos(\beta)} \right) \tag{2.13}$$

It can be seen in equations (2.12) and (2.13), that both and depend not only on the magnitude of the train speed and of the onset wind velocity, but also on the orientation of the latter with respect to the travel direction (indicated by the wind angle).

Mean wind profile relative to a moving vehicle
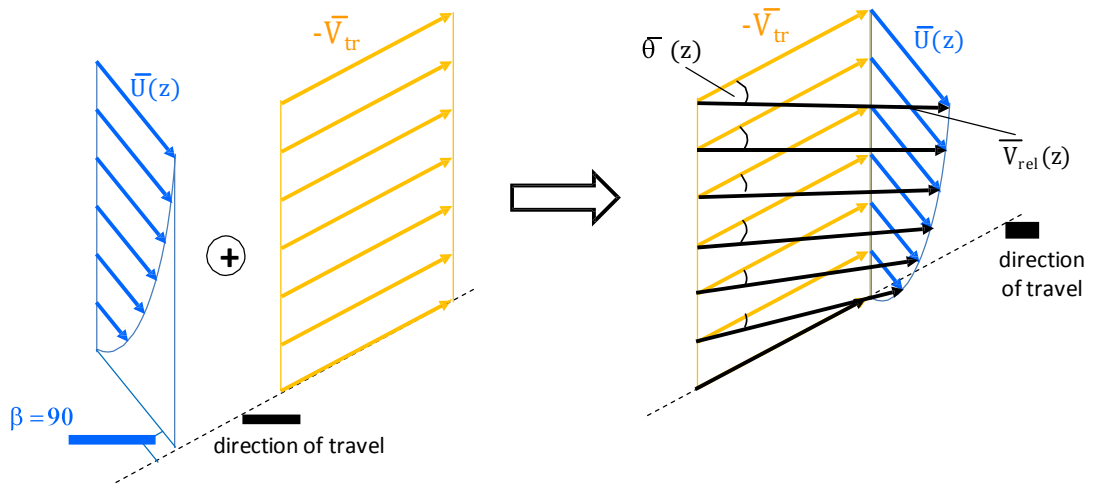
Figure 2.4 Skewed wind profile relative to a moving vehicle

Since a typical ABL wind profile is characterised by a mean wind velocity   increasing with height, the vector combination with the train speed produces a mean relative velocity   that is 'skewed' (figure 2.4). Accordingly, the rate of change of both   and   (i.e. the mean yaw angle) with respect to the vertical coordinate depends on the ratio between the onset wind velocity and the vehicle speed.

Figure 2.5 illustrates an example reported by Baker (2010b) where the variation with height of such quantities is given as a function of increasing vehicle speeds. It can be observed that the higher the vehicle speed, the more uniform are the vertical profiles of both the mean velocity relative to the train (normalised with respect to its values at   =3 m) and the mean yaw angle.
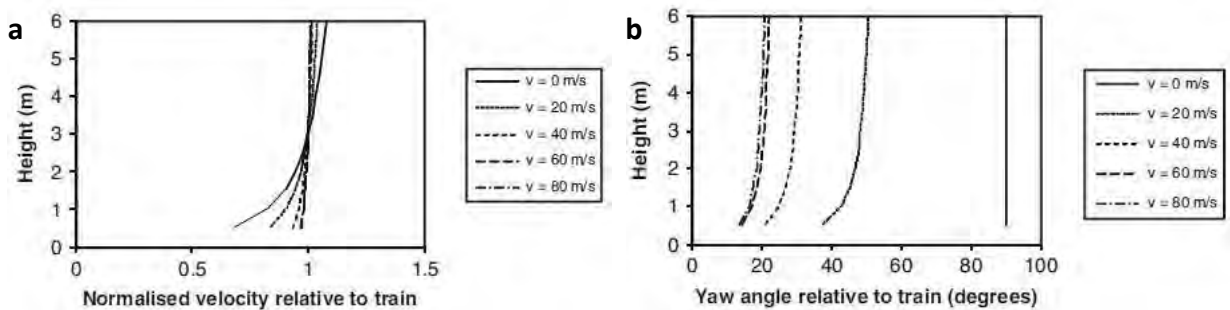
Figure 2.5 Vertical profile of the mean wind relative to a moving vehicle (= 20 m/s at 3 m height, □=90° and   = 0.03 m (Baker, 2010b)). a) Normalised relative wind velocity b) Yaw angle

Atmospheric turbulence relative to a moving vehicle

As the mean wind speed, so the turbulent velocity fluctuations perceived by a moving vehicle are different from those seen by a stationary observer. Following Baker (2010b), the turbulence intensity relative to a moving vehicle can be expressed through the definition given in equations (2.3) once the relative mean wind velocity   is taken as the reference (to replace   . Accordingly, the vertical profile of turbulence changes depending both on the onset wind velocity and on the vehicle speed. Figure 2.6 illustrates such a variation with consideration of the same example in figure 2.5 and using the onset turbulence profile suggested in the ESDU 85020 (2001).
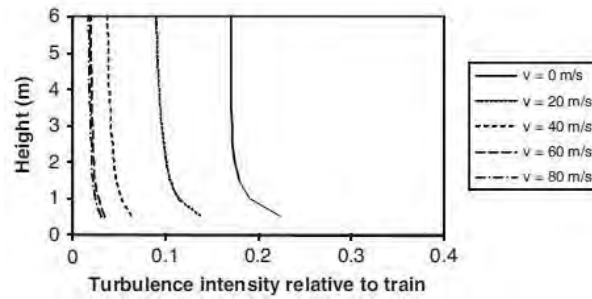
Figure 2.6 Vertical profile of turbulence relative to a moving vehicle (= 20 m/s at 3 m height, and   = 0.03 m (Baker, 2010b))

Cooper (1984) provides a theory which outlines how the turbulence length scales and power spectral density relative to a moving vehicle can be expressed knowing the turbulence, magnitude and direction of the onset (mean) wind and the train speed.

Assuming Taylor's *'frozen vortices'* hypothesis, Cooper introduces the ratio   :

$$c_u = \left[\frac{V_{tr}}{V_{rel}} \cos(\beta) + \frac{\bar{U}}{V_{rel}} \right]^2 \tag{2.14}$$

and suggests that the turbulence length scale   seen by a moving vehicle is given by:

$$L_u = L_{ux} \left[c_u + 2 \left(\frac{L_{uy}}{L_{ux}} \right)^2 \cdot (1 - c_u) \right]^{1/2} \tag{2.15}$$

Furthermore, assuming a Von Karman spectrum for the onset wind turbulence and introducing a non-dimensional frequency normalised with respect to the relative mean wind (i.e., $f_N^* = \frac{f L_u}{V_{rel}}$), Cooper's theory expresses the spectral density of the longitudinal velocity component seen by a moving vehicle as:

$$S_u(f) = \left[\frac{\frac{4\sigma_u^2 L_V}{\underline{V}_{rel}}}{\left(1 + 70.8 f_N^{*2}\right)^{5/6}} \right] \cdot \left[c_u + \left(1 - c_u\right) \frac{0.5 + 94.4 f_N^{*2}}{1 + 70.8 f_N} \right] \tag{2.16}$$

2.3.2   Effect of the infrastructure scenario

Local changes in either the terrain roughness or the topography can lead to modifications of the conventional ABL wind characteristics described above (ESDU, 2002). Of particular interest in relation to the wind susceptibility of railway traffic is the case of an embankment, which is quite common in current railway networks. Embankments cause a local increment of the wind velocity downstream of the crest, where the railway tracks are normally positioned, thus increasing aerodynamic loads on a transiting train.

To clarify the local wind velocity variations, Baker (1985) carried out full-scale and wind tunnel experiments examining typical railway embankments. This work supported the reliability of the method stated by the ESDU 82026 (ESDU, 2002) for predicting the mean wind velocity speed-up. Furthermore, investigating a variety of onset wind directions, it found that only the velocity component perpendicular to the track is accelerated through the embankment slope. This led to specify a dependence of the velocity speed-up not only on the embankment geometry, but also on the onset wind direction and, in light of the difficulties related to simulating the train movement (chapter 3), it makes this scenario particularly challenging for railway aerodynamic investigations.

2.4 Crosswind aerodynamic loads

2.4.1 Flow around rail vehicles

Numerous studies have been undertaken in order to investigate the characteristics of the flow field developing around a train in the presence of a crosswind. Originally, these were based on experimental measurements (Mair and Stewart, 1985; Copley, 1987; Chiu and Squire, 1992) and led to the development of theoretical models for reproducing and predicting the observed flow behaviour (Chiu, 1991). More recently, CFD (computational fluid dynamics) simulations have been performed (Diedrichs, 2003; Hemida and Krajnovic, 2009a; Diedrichs, 2010). The results from many of these studies are collected in a number of reviews and, regardless of the specific vehicle geometries that were examined, they show a good agreement in the flow pattern developing around a train (Baker, 1991a; Schetz, 2001; Baker et al., 2009; Baker, 2010b).

a **b**
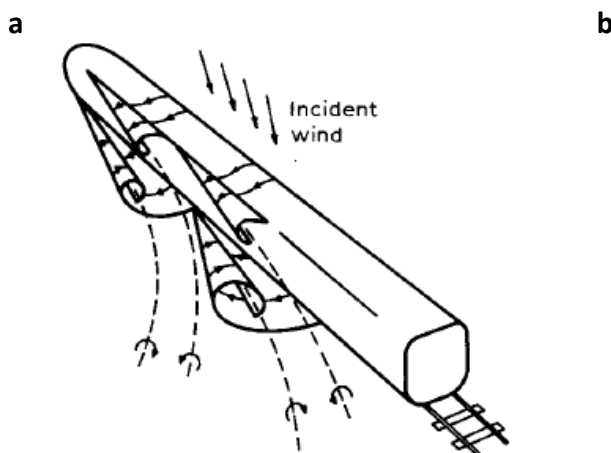
Figure 2.7 Flow around a train a) Idealised train model at low yaw angles (Copley, 1987) b) Wind tunnel flow visualisation at 90° yaw angle (Bocciolone et al., 2008)

Considering streamlined smooth-edged rail vehicles, two different flow regimes have been identified that depend on the yaw angle. For yaw angles between 0° and ~40-50°, the aerodynamic behaviour of a train's leading car appears similar to that of a slender body in proximity to the ground. As illustrated in figure 2.7a, it presents a series of vortices forming on the roof and ground corner of the leeward side that roll up moving from the nose to the tail and progressively detach from the vehicle surface. Conversely, at yaw angles from 60°-70□ up to 90□ the flow pattern resembles that around

smooth-edged bluff body (like a circular cylinder) and, as such, is characterised by a large wake and,

a

2.4 Crosswind aerodynamic loads

possibly, by the onset of vortex shedding (figure 2.7b). Within this conceptual framework, the yaw angle range from 40°-50° to 60°-70° is considered to be a transition interval, where an unstable flow tends to switch between the two conditions described above.

2.4.2 Aerodynamic loads on rail vehicles

As a result of the flow pattern surrounding a train in a crosswind, a specific surface pressure distribution and, in turn, a series of steady and unsteady aerodynamic forces and moments develop. According to the general approach adopted in wind engineering (Simiu and Scanlan, 1996; Dyrbye and Hansen, 1999; Holmes, 2007) and following the analysis of Baker (1991a) of ground vehicles, the surface pressure distribution can be expressed using a non-dimensional pressure coefficient defined as:

$$C_P = \frac{P - P_0}{\frac{1}{2} \rho V_{ref}^2} \tag{2.17}$$

where   is the actual pressure at any point on the train surface,   is the reference pressure,   is the air density and   is the magnitude of the reference velocity (defined below).
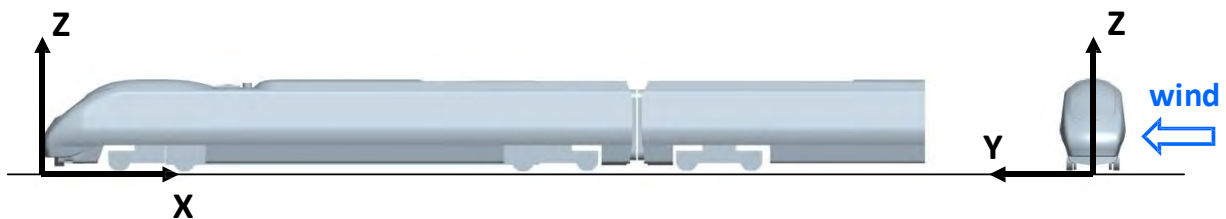
Figure 2.8 Train reference system

In terms of aerodynamic loads acting on a train, three forces (   ) and three moments (   ) can be defined with respect to the generic axis   of the Cartesian reference system adopted in this research (figure 2.8). They are given by:

$$F_\xi = \frac{1}{2} C_\xi \rho A_{ref} V_{ref}^2 \quad (\text{with } \xi = X, Y, Z) \tag{2.18}$$

The onset wind velocity involved in the determination of   is conventionally referred to as that of

$$M_\xi = \frac{1}{2} \, C_{M_\xi} \, \rho \, A_{ref} \, L_{ref} \, V_{ref}^2 \quad (\text{with } \xi = X, Y, Z) \tag{2.19}$$

where   and   are the body reference area and reference dimension, while   and

represent the non-dimensional coefficients defined for each component of the forces and moments,

respectively. These coefficients can be obtained by integration of the aforementioned   (section

5.3).

The lateral and vertical forces, together with the rolling moment, are the components of the

aerodynamic loads normally investigated as part of the analysis of wind-induced overturning risk

(Baker et al., 2009; RSSB, 2009a; 2009b). Given the reference frame in figure 2.8 and following from

equations (2.18) and (2.19), they are given by:

$$F_Y = \frac{1}{2} C_Y \, \rho \, A_{ref} V_{rel}^2 \tag{2.20a}$$

$$F_Z = \frac{1}{2} C_Z \rho \, A_{ref} V_{rel}^2 \tag{2.20b}$$

$$M_X = \frac{1}{2} \, C_{M_X} \, \rho \, A_{ref} H_{ref} V_{rel}^2 \tag{2.20c}$$

$$M_{X,lee} = \frac{1}{2} \, C_{M_{X,lee}} \, \rho \, A_{ref} H_{ref} V_{rel}^2 \tag{2.20d}$$

where   and   are the side and lift forces, respectively,   is the rolling moment about the   -axis

(defined positive following the 'right-hand screw' rule) and   is the rolling moment about the

leeward rail (following the same sign convention as   ).   and   are the reference values for

the area and height, respectively.

In order to account for the train movement, the reference velocity is normally taken as the velocity

of the wind relative to the moving vehicle defined in equation (2.12):

$$V_{ref} = V_{rel} \tag{2.21}$$

the undisturbed flow, i.e., the flow at a distance sufficiently upstream of the vehicle so as not to be affected by the presence of the vehicle itself. In the present work, the reference onset wind velocity is associated with a reference height above the ground (   ) of 3 m at full-scale. This reflects the convention adopted for numerous railways applications (RSSB, 2009a; Baker et al., 2004; Sterling et al., 2009). Furthermore, consistent with previous studies (Baker et al., 2004),   and   are assumed as the nominal side area and nominal height, respectively, of one coach of the train under investigation.

Following an approach similar to that undertaken for the wind velocity, the generic aerodynamic force   can be expressed as

$$F_\xi\left(t\right) = \overline{F}_\xi + F_\xi{}'\left(t\right) \tag{2.22}$$

where   is the *mean force* that represents the steady (i.e., time averaged) contribution due to the mean wind, while   is the *time-varying force*, which expresses the unsteady fluctuations of the aerodynamic loads. The same approach can be applied to each of the aerodynamic moments   .

2.4.2.1 *Steady aerodynamic loads*

The steady aerodynamic forces and moments on a rail vehicle follow from equations (2.22) and are defined by Baker (1991a) as:

$$\overline{F}_Y\left(\theta\right) = \frac{1}{2}\overline{C}_Y\left(\theta\right)\rho A_{ref}\overline{V}_{rel}^2 \tag{2.23a}$$

$$\overline{F}_Z\left(\theta\right) = \frac{1}{2}\overline{C}_Z\left(\theta\right)\rho A_{ref}\overline{V}_{rel}^2 \tag{2.23b}$$

$$\overline{M}_X\left(\theta\right) = \frac{1}{2}\overline{C}_{M_X}\left(\theta\right)\rho A_{ref}H_{ref}\overline{V}_{rel}^2 \tag{2.23c}$$

$$\overline{M}_{X,lee}\left(\theta\right) = \frac{1}{2}\overline{C}_{M_{X,lee}}\left(\theta\right)\rho A_{ref}H_{ref}\overline{V}_{rel}^2 \tag{2.23d}$$

where an overbar is adopted to indicate a time averaged mean.

The nondimensional velocity coefficients in the equation (2.23) contain conventionally the reference to that of concerning the aerodynamic behaviour of the vehicle. They depend primarily on the vehicle geometry and on the nominal yaw angle (defined by the combination of the velocity vectors at the reference height above the ground). Baker (1991a) discusses their dependence also on the turbulence characteristics of the onset wind, on the Reynolds number (see section 3.4.1) and, as specifically investigated in the present work, on the simulation of the vehicle movement. In addition, an effect of the infrastructure scenario is outlined in a number of studies (see section 3.3.3). This is because local variations in the onset wind speed (induced by the ground topology in proximity to the train) are not accounted for by the reference wind speed defined above.

In section 2.5 the writer discusses the role of the mean coefficients within train stability analysis, while chapter 3 presents the techniques currently applied for their investigation. In general, once the mean aerodynamic loads acting on the train are known (from measurements or computations), as well as the corresponding reference wind velocity, the mean coefficients relating to a generic yaw angle are obtained as:

$$\overline{C}_Y\left(\theta\right)=\frac{\overline{F}_Y\left(\theta\right)}{\frac{1}{2}\rho A_{ref}\overline{V}_{rel}^2} \tag{2.24a}$$

$$\overline{C}_Z\left(\theta\right)=\frac{\overline{F}_Z\left(\theta\right)}{\frac{1}{2}\rho A_{ref}\overline{V}_{rel}^2} \tag{2.24b}$$

$$\overline{C}_{M_X}\left(\theta\right)=\frac{\overline{M}_X\left(\theta\right)}{\frac{1}{2}\rho A_{ref}H_{ref}V_{rel}^2} \tag{2.24c}$$

$$\overline{C}_{M_{X,lee}}\left(\theta\right)=\frac{\overline{M}_{X,lee}\left(\theta\right)}{\frac{1}{2}\rho A_{ref}H_{ref}\overline{V}_{rel}^2} \tag{2.24d}$$

2.4.2.2 Unsteady aerodynamic loads

An approach commonly adopted for treating unsteady aerodynamic loads on trains relies on the *'Quasi-Steady'* theory (Holmes, 2007; Baker, 1991b). It is inferred that the fluctuations of the aerodynamic forces are entirely due to the variations in the intensity of the reference velocity that

the main concern of the analysis, Baker (1991b) identified three different domains of study:

2007). Following the formulation proposed by Baker (2010a), a generic aerodynamic force can be written as:

$$F_\xi\left(t\right) = \overline{F}_\xi + F_\xi{}'\left(t\right) = \frac{1}{2}\overline{C}_\xi \rho A_{ref}\left(\overline{V}_{ref} + V'{}_{ref}\left(t\right)\right)^2 \tag{2.25}$$

Substituting the expression for the mean force into equation (2.25) and assuming that the fluctuations of the reference velocity (   ) are significantly smaller than the mean value   , the unsteady contribution can be expressed as:

$$F_\xi{}'\left(t\right) = \overline{C}_\xi \rho A_{ref}\overline{V}_{ref}V'{}_{ref}\left(t\right) \tag{2.26}$$

Two main assumptions are inherent in the *Quasi-Steady* theory:

- Since the unsteady forces are entirely ascribed to buffeting, the contributions of vehicle-induced turbulent fluctuations are assumed to be negligible.

- Since the load fluctuations follow the velocity variations with no attenuation or lag, it is assumed that the turbulence in the incident wind is fully correlated along the vehicle.

The first assumption can be accepted as reasonable in the majority of cases (even if particular care should be paid in the case of the lift force at high yaw angles, when vortex shedding can occur (Sterling et al., 2009)). Conversely, a full correlation of the relative wind turbulence along the vehicle is a realistic assumption only if the turbulence length scale perceived by the train is greater than the car length (Baker, 1991b). In practice, however, such a condition is not necessarily verified. It depends not only on the ratio between the onset wind turbulence scale and the typical length of a railway coach, but also on the train speed (section 2.3.1). In light of this, it is acknowledged that the *Quasi-Steady* theory could lead to conservative estimations of the aerodynamic loads.

To refine the indications obtained through such a theory, a number of specific approaches have been developed for treating the unsteady loads on rail vehicles. As in control engineering, depending on

are, in turn, caused by the onset wind turbulence, i.e., the so-called buffeting contribution (Holmes,

amplitude, *frequency* and *time*.

Amplitude Domain

The *amplitude domain* is mainly concerned with the assessment of the train overturning risk. In this

regard, reporting the research of Cooper (1979) and Surrey *et al.* (1988), Baker (1991c) suggested

that a wind gust with a duration of between 1 and 3 s might be sufficient to overturn a train. Hence,

it is believed that the '*extreme*' aerodynamic loads that may occur within such a time interval

(referred as *peak loads*), rather than the 'long-term' mean forces and moments, play a key role in

determining the accident risk.

If the *Quasi-Steady* theory is applied, the *peak* aerodynamic loads can be obtained via equations

(2.23) from the mean load coefficients and the 1 s (or 3 s) extreme reference velocity (instead of the

long-term mean velocity). Alternatively, to overcome the approximation inherent in this approach, a

series of non-dimensional peak load coefficients has been defined as (Baker, 1991b):

$$\hat{C}_Y\left(\theta\right) = \frac{\hat{I}_Y\left(\theta\right)}{\frac{1}{2}\rho A_{ref}\hat{V}_{rel}^2} \tag{2.27a}$$

$$\hat{C}_Z\left(\theta\right) = \frac{\hat{I}_Z\left(\theta\right)}{\frac{1}{2}\rho A_{ref}\hat{V}_{rel}^2} \tag{2.27b}$$

$$\hat{C}_{M_X}\left(\theta\right) = \frac{\hat{M}_X\left(\theta\right)}{\frac{1}{2}\rho A_{ref}H_{ref}\hat{V}_{rel}^2} \tag{2.27c}$$

$$\hat{C}_{M_{X,lee}}\left(\theta\right) = \frac{\hat{M}_{X,lee}\left(\theta\right)}{\frac{1}{2}\rho A_{ref}H_{ref}\hat{V}_{rel}^2} \tag{2.27d}$$

where   and   indicate the 1 s (or 3 s) extreme values of the generic forces and moments, while

is the extreme value of the velocity relative to the train. Such quantities can be calculated from

the time series of the aerodynamic loads and the wind velocity, respectively, through an extreme

value analysis. Different methods can be used for carrying out such analysis, with those of Gumbel or

Lieblein (Cook, 1985) often employed for railway aerodynamics studies (Baker, 1991b; RSSB, 2009b).

where   , the correction factor, is termed the '(*aerodynamic) admittance function'*. As the peak coefficients over the corresponding mean coefficients (i.e.,   ). Accordingly, as discussed by Baker and Humphreys (1996), a *Quasi-Steady* behaviour of the aerodynamic loads implies that such peak normalised coefficients are equal to 1. Values larger than 1 either suggest the presence of turbulent fluctuations induced by the wind-vehicle interaction (for example, vortex shedding), or they can be ascribed to the turbulent fluctuations both in the velocity components and in the yaw angle (Baker et al., 2004; Baker, 2010a). Peak normalised coefficients lower than 1, instead, denote a lack of correlation in the relative wind velocity and, in turn, in the force fluctuations, along the length of the vehicle.

Frequency Domain

The analyses carried out for the *frequency domain* deal either with wind-induced vehicle suspension excitations (Cooper, 1984), or with the overall assessment of the train crosswind stability (Cheli et al., 2007). In the *frequency domain*, the following formulation for the *Quasi-Steady* theory can be obtained rearranging equation (2.25) and then performing the Fourier transform (Baker, 1991b):

$$S_F(f) = 4 \left(\frac{\overline{F}}{\overline{U}} \right)^2 S_u(f) \tag{2.28}$$

where f indicates the frequency, while   and   are the power spectral densities of the generic aerodynamic force and of the wind velocity fluctuations, respectively.

To account for the non-perfect correlation of the wind velocity fluctuations along the vehicle, a correction factor can be included in the previous formulation leading to the so-called '*Quasi-Steady corrected*' theory:

$$S_F(f) = 4 \left(\frac{\overline{F}}{\overline{U}} \right)^2 S_u(f) \left| X_F(f) \right|^2 \tag{2.29}$$

To ease interpretation in relation to the *Quasi-Steady* theory, Baker (1991b) suggested to normalise outlined in equation (2.29) such a quantity varies with respect to the frequency. In addition, studies initially undertaken by Cooper (1984), later developed by Baker (1991b) and by Baker and Humphreys (1996), outlined further dependences on the vehicle geometry, the wind turbulence characteristics, the onset wind direction and, finally, the yaw angle.

Time Domain

The *time domain* considers the vehicle stability analysis. Numerical models, incorporating the aerodynamic forces, simulate the vehicle dynamics and wheel-rail interaction and, given the onset wind characteristics, provide an indication of the train stability. As such, they are normally employed within the accident risk assessment.

In the *time domain*, the formulation of the *Quasi-Steady* theory is given by equation (2.26). Consistent with the *frequency domain* approach, a correction factor is introduced accounting for the non-perfect correlation of turbulence along the vehicle (Baker 1991b). The corresponding *Quasi-Steady corrected* formulation is given by:

$$F'(t) = \overline{C}_F \rho A \overline{V}_{rel} \int_0^\infty h_F(\tau) V'_{ref}(t-\tau) d\tau \tag{2.30}$$

where , the correction factor, is the *aerodynamic weighting function* associated with the generic aerodynamic load . and are related via:

$$h_F(\tau) = \int_0^\infty |X_F(f)| e^{2\pi f \tau i} df \tag{2.31}$$

2.5.1 TSI and EN standard

The EU method for assessing the crosswind stability of Class 1 high-speed trains is stated in the Technical Specification for Interoperability (TSI) HS-TSI-RST (EC, 2008) in conjunction with the European Standard EN 14067-6 (CEN, 2010). This method performs a comparison between the Characteristic Wind Curve (CWC), which describes the critical wind conditions for wheel unloading of the most vulnerable car of the train and the corresponding Characteristic Reference Wind Curves (CRWC) specified in the TSI (EC, 2008). If the CWC is equal to or higher than the CRWC then the train is acceptable in crosswind stability terms.
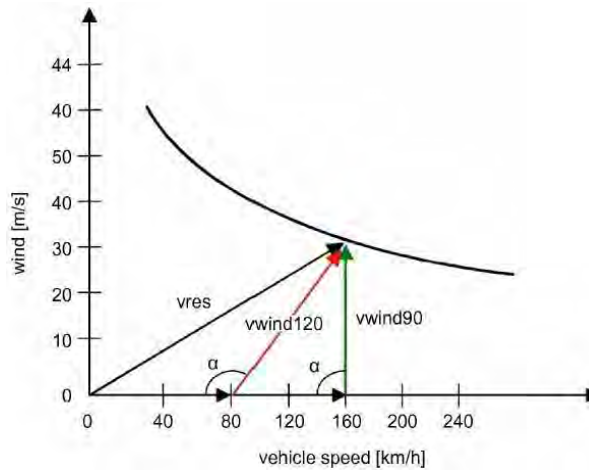
Figure 2.9 Generic Characteristic Wind Curve (CWC) (EC, 2008)

As illustrated in figure 2.9, the CWC relates train speed and onset wind velocity. For a given value of the former, each point of the curve represents '*the maximum natural wind speed that the train can withstand before a characteristic limit for wheel unloading is exceeded' (CEN, 2010),* i.e., before 90% wheel unloading occurs on any bogie. When calculating the CWC, a numerical simulation that reproduces the train behaviour under the effect of a crosswind is carried out in the *time domain*. In this simulation, inertial and dynamic characteristics of the vehicle are modelled using a multi-body simulation (MBS) method and the wind-induced aerodynamic loads are introduced as external inputs. These loads are normally expressed through the following *Quasi-Steady* formulation:

2.5 – Assessment of the crosswind stability

$$F_\xi(t) = \frac{1}{2} \bar{C}_\xi(\theta(t)) \rho A_{ref} V_{rel}^2(t)$$ (2.32a)

$$M_\xi(t) = \frac{1}{2} \bar{C}_{M_\xi}(\theta(t)) \rho A_{ref} H_{ref} V_{rel}^2(t)$$ (2.32b)

where   =   and, according to the conventions in figure 2.3, it is:

$$V_{rel} = \sqrt{\left[V_{tr} + \bar{U}(t)\cos\beta\right]^2 + \left[\bar{U}(t)\sin\beta\right]^2}$$ (2.33)

$$\theta(t) = \arctan\left[\frac{\bar{U}(t)\sin\beta}{V_{tr} + \bar{U}(t)\cos\beta}\right]$$ (2.34)

For a given combination of train speed and wind direction, the forces and moments depend on the non-dimensional mean aerodynamic load coefficients and on the wind velocity. Wind tunnel tests on static scale-models, carried out in a low-turbulence wind simulation, are prescribed for obtaining the load coefficients (as discussed in chapter 3). For the onset wind velocity, the so-called '*Chinese hat*' wind scenario is adopted. This is a time-invariant gust wind profile whose spatial distribution has been defined to approximate a turbulent natural wind in the proximity of a local maximum (CEN, 2010). Such an onset wind scenario is identified by a maximum wind velocity and corresponds to a deterministic time series (of the type shown in figure 2.10). In combination with the vehicle speed, this onset wind scenario produces a time history of the wind relative to the train that, substituted into equations (2.32), leads to the aerodynamic forces that are the input into the vehicle dynamic simulation.
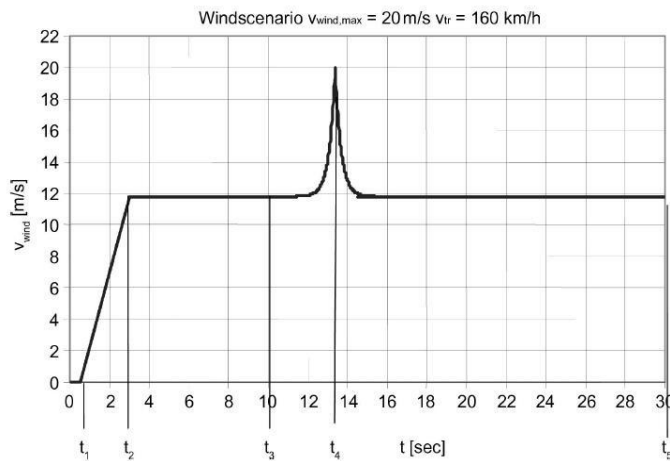
Figure 2.10 Generic Chinese hat wind scenario (EC, 2008)

(by iteration) as the input onset wind velocity that produces a 90% wheel unloading. The TSI prescribes the CWC to be calculated for a set of pre-determined lateral accelerations and wind directions both on a flat ground and on a 6 m high embankment. The EN 14067-6, instead, considers only a ballast and rail scenario.

2.5.2 UK standard

In the UK, the method used to evaluate the stability of trains in crosswinds is defined by the national standard GM/RT 2142 (RSSB, 2009a) in combination with the code of practice GC/RC 5521 (RSSB, 2001) and the recommendations in GM/RC 2542 (RSSB, 2009b). The prescribed assessment relies on the calculation of the '*intrinsic roll-over wind speed'.* According to GM/RT 2142, this is '*that wind speed which is just sufficient to cause 100% unloading of the wheels on the windward side of the vehicle, when the vehicle is running in its tare condition at its maximum design operating speed on straight track'.*

In order to calculate such a quantity, the train is modelled using a two-dimensional (three-mass) schematisation. Instability occurs when:

$$M_{over} = M_R \tag{2.35}$$

where   and   denote the restoring and overturning moments, respectively, both referred to the leeward rail. The former is determined taking into account the vehicle mass and the displacements allowed by the suspension system. The latter, when a train travels on a straight track, coincides with the aerodynamic moment given by:

$$M_{over} = M_{X,lee}\left(\theta\right) = \frac{1}{2}\, C_{M_{X,lee}}\left(\theta\right) \rho A_{ref} H_{ref} V_{rel}^2 \tag{2.36}$$

Furthermore, to extend the analysis to the case of a train on a curve,   may also include the overturning contribution of the uncompensated lateral acceleration.

For a specified combination of (maximum) train speed and wind direction, the relative wind velocity identified in equation (2.36) can be expressed as a function of the onset wind velocity (from equations (2.12-2.13)). Accordingly, the intrinsic roll-over wind speed can be obtained from equation (2.35).

Once this has been determined, the safe operation of the train can be assessed according to two different criteria:

- For a train travelling on a straight track, or curving within conventional cant deficiencies, the intrinsic roll-over wind speed is required to be higher than the minimum stated in GM/RT 2142 (RSSB, 2009a).

- For operation above conventional cant deficiencies (e.g., for tilting trains), a probabilistic assessment is carried out evaluating the intrinsic roll-over wind speed with respect to the 3 s gust wind speed expected on the track section under investigation. This process enables determination of an enhanced permissible train speed such that the risk of wind-induced accident is within a range of acceptability stated in GC/RC 5521 (RSSB, 2001).

Different types of non-dimensional coefficient can be employed in equation (2.36) (RSSB, 2009b). For a train travelling on a straight track, or curving at conventional cant deficiencies, the use of a mean coefficient is accepted (either extrapolated from reference data or obtained through wind tunnel tests on static scale-models subjected to low-turbulence crosswinds). For a titling train operating above conventional cant deficiencies, to improve the accuracy of the estimation, the use of peak aerodynamic coefficients (obtained through wind tunnel tests on static scale-models subjected to an ABL wind simulation) is recommended .

2.5.3 Further investigation methods

In addition to the analyses described above, a number of further techniques have been developed for assessing the train crosswind stability. Most of these techniques use numerical models based on MBS for reproducing the vehicle dynamics and introduce the aerodynamic loads as external inputs.

conventional *Quasi-Steady corrected* theory, Baker has also considered a first order expansion for the

the simulations provided for natural winds.

Cheli et al. (2007) have expressed the aerodynamic loads through a *Quasi-Steady corrected* formulation and adopted a stochastic approach in order to simulate (numerically) a time and space-varying onset wind (rather than a deterministic *Chinese hat* scenario). This method takes into consideration the mean velocity profile, turbulence intensity and length scales of a natural wind and enables the calculation of time histories of the relative wind as seen by the train travelling along the track. Furthermore, the piece of information concerning the correlation of the aerodynamic load fluctuation along the train is included by using the admittance function (in addition to the mean load coefficients). This is employed to compute a 'corrected absolute wind speed' in the *frequency domain* that, once transformed into the *time domain*, allows the calculation of the 'corrected' overall aerodynamic loads on the train.

Ding et al. (2008) and Baker et al. (2008) have undertaken similar stability analyses using a wind simulation varying in time and space and adopting a *Quasi-Steady corrected* formulation for the aerodynamic loads. In this case, however, forces and moments have been expressed directly in the *time domain* using the mean load coefficients in combination with a set of weighting functions.

Both of the previous techniques provide a refined simulation with respect to the TSI methodology. As a drawback, however, they require additional inputs to enable the use of the *Quasi-Steady corrected* formulation. Furthermore, they become computationally intensive because they employ numerical simulations of time and space varying wind distributions.

To address the latter issue, Baker (2010a) has proposed to examine a train in one fixed position and to calculate the time histories of the turbulent wind relative to such a train by applying the theory of Cooper (section 2.3.1). Expressing the aerodynamic loads in the *time domain* (though aerodynamic mean load coefficients and weighting functions), as a further development with respect to the

However, they differ from the TSI methodology either in the aerodynamic loads formulation, or in fluctuations not only of the relative wind velocity magnitude, but also of the yaw angle.

2.6   Closing remarks

The review of previous wind-induced railway accidents confirms that the action of side winds poses a significant risk for the safe operation of modern trains. The examination of the physical phenomena related to the wind-vehicle interaction outlines the complexity inherent in the assessment of train stability in crosswinds. This stability depends on a number of aspects, such as: the dynamic and aerodynamic characteristics of the vehicle, the actual train operating speed, the infrastructure scenario and, finally, the strength, direction and turbulence level of the onset wind. The complexity of the stability analysis, thus, comes from the need to evaluate accurately as many as possible of these aspects.

To address this challenge a variety of methods are currently in use, which offer balance between the accuracy of the analysis and the resources demanded. Different techniques can be used for modelling both the vehicle dynamics and the onset wind characteristics, as well as different formulations of the aerodynamic loads can be employed. However, in every method examined, the information concerning the wind-vehicle interaction is introduced by a series of non-dimensional coefficients. Hence, the crucial role of these coefficients becomes clear and the importance of the correct selection and accuracy in their estimation is apparent to increase the overall reliability of the train stability analysis.

Aerodynamic investigation of rail vehicles in crosswinds

3.1   Introduction

Chapter 3 reviews the different approaches through which non-dimensional aerodynamic coefficients of a rail vehicle can be obtained. The various techniques currently adopted are presented in section 3.2, while section 3.3 examines the challenges involved in recreating the train movement and compares moving and static vehicle representations. Section 3.4 analyses major aspects related to undertaking scale-model experiments (which represent the current standard method) with both static and moving trains. Previous studies concerned with assessing the effect of the vehicle movement simulation on the train aerodynamics are illustrated and compared in Section 3.5. Based on those, finally, section 3.6 discusses the main challenges and the improvements achievable through the present research.

3.2   Techniques of investigation

Three major approaches are currently adopted to estimate the (steady and unsteady) aerodynamic load coefficients of a given train: full-scale measurements, scale-model experiments and CFD (computational fluid dynamics) simulations. Of these, experiments on scale-models currently represent the most widely used option as they are perceived to offer the best compromise between time (and cost) effectiveness of the test methodology and accuracy of the results.

Full-scale measurements require the availability of a properly instrumented (real) train and of a test site. Furthermore, they are inevitably subject to uncontrollable environmental conditions (Baker et al., 2004; Quinn et al., 2007). As such, they become both expensive and time-consuming (Baker et al.,

2002).

CFD simulations are perceived by the industry as particularly promising. They ensure a level of accuracy proportional to the computational cost. Therefore, the development of computational resources envisages an increasing use of the most accurate techniques (e.g. LES) without leading to excessive processing times (Baker et al., 2009; Hemida and Krajnovic, 2009a). However, since CFD simulations are still under validation in comparison with experimental results (ERA, 2009), currently they are not accepted to provide vehicle aerodynamic coefficients within the rolling stock homologation process (EC, 2008; CEN, 2010; RSSB, 2009b).

As discussed in the following section 3.4.1, scale-model experiments inevitably lead to a degree of approximation because of their intrinsic inability to entirely fulfil the Reynolds similitude criteria (Gawthorpe, 1994). Therefore, particular care is needed both in the set up and in the interpretation of their results. Nevertheless, their suitability for use with conventional environmental wind tunnels enables the simulation of different incident flow characteristics, from low-turbulence to ABL representations, as well as the employment of various measurement techniques (section 3.4.2). In addition, if a propulsion system and sufficient space is available, both static and moving model experiments can be carried out.

3.3 Scale-model vehicle movement simulation

As discussed in section 2.3.1, a real operating train is typically subjected to a relative wind determined by the combination of the onset (natural) crosswind and the vehicle speed. Hence, a moving vehicle simulation should ideally be performed in order to carry out reliable aerodynamic measurements. However, this involves a series of practical challenges and, therefore, simpler investigations based on a static vehicle representation are typically undertaken.

3.3.1 Moving vehicles

A moving vehicle experiment at reduced scale consists of a model train propelled across a test section where a transverse airflow simulation is provided. In these experiments, so as for real trains operating at full-scale, the relative wind is determined by the vector sum of the wind and vehicle speed (figure 3.1a) and, therefore, a range of yaw angles can be investigated by varying either of such velocities.
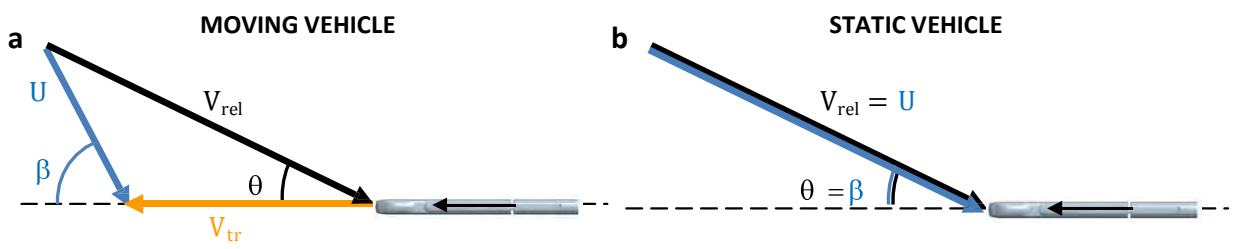
Figure 3.1 Velocity triangle: moving vs static vehicle simulation

To enable this type of test, a facility is required that can provide both the scale train movement and the crosswind simulation. In addition, a measurement and data logging system is needed, capable of capturing the aerodynamic loads acting on the scale-model vehicle whilst in motion. Finally, the implementation of a specific test procedure and data processing method is necessary (sections 3.4 and 3.5). However, these requirements pose a series of non-conventional demands with respect to the current environmental wind tunnel best-practice (mainly associated with scale-model tests on civil engineering structures). Consequently, previous moving scale-model tests have encountered numerous technical difficulties, making them rather expensive and time-consuming (Cooper, 1981; Baker, 1986; Howell, 1986; Humphreys, 1995; Baker, 2002; Muggiasca, 2002).

In CFD simulations it is also possible to reproduce a moving train subjected to a lateral wind. However, an accurate representation of a moving vehicle requires the use of specific techniques for meshing and solving such problems, thus increasing both the computational costs and the processing times involved. Furthermore, in light of the current limited availability of experimental data for benchmarking, moving model CFD simulations are particularly challenging to validate (Cheli et al., 2011a).

figure 3.2, there is necessarily a mismatch in the vertical profiles of the magnitude of the relative

When a static train representation is adopted, the vehicle is not moving and the relative wind coincides with the onset wind (figure 3.1b). Consequently, since the yaw angle is determined by the direction of the onset wind to the track, its effect is investigated by changing the relative orientation between the vehicle and the oncoming flow.

Static tests on scale-models are typically undertaken in conventional environmental wind tunnels and follow a procedure similar to that used for experiments on civil engineering structures. The train model is statically mounted in the testing chamber (possibly on a turntable) where, given the constant direction of the simulated flow, it is progressively rotated about the vertical axis to investigate the required yaw angle range.

A static vehicle simulation can be performed using CFD by properly setting the boundary conditions. In this context, to investigate a yaw angle range, either the vehicle can be rotated whilst the inlet velocity boundary conditions remain fixed or, vice versa, the latter can be changed whilst keeping a permanent vehicle model orientation (Diedrichs, 2003).

3.3.3 Moving vs. static vehicles

According to the definitions discussed in section 2.4.2.1, the non-dimensional mean aerodynamic coefficients depend on the vehicle geometry and on the reference yaw angle (i.e., the yaw angle determined by the velocity vector combination at the reference height above the ground, typically 3 m at full-scale). Hence, a static test typically aims to ensure a good aerodynamic representation of an actual travelling train by appropriately replicating such a yaw angle. However, a static test is inherently incapable of reproducing the actual skewed wind profile seen by a moving train (figure 2.4 in section 2.3.1). Consequently, by neglecting the vehicle movement, the actual yaw angle perceived by a travelling train can be correctly replicated only at one (reference) height and, as illustrated by

3.3.2 Static vehicles

mean wind velocity, as well as of the yaw angle.
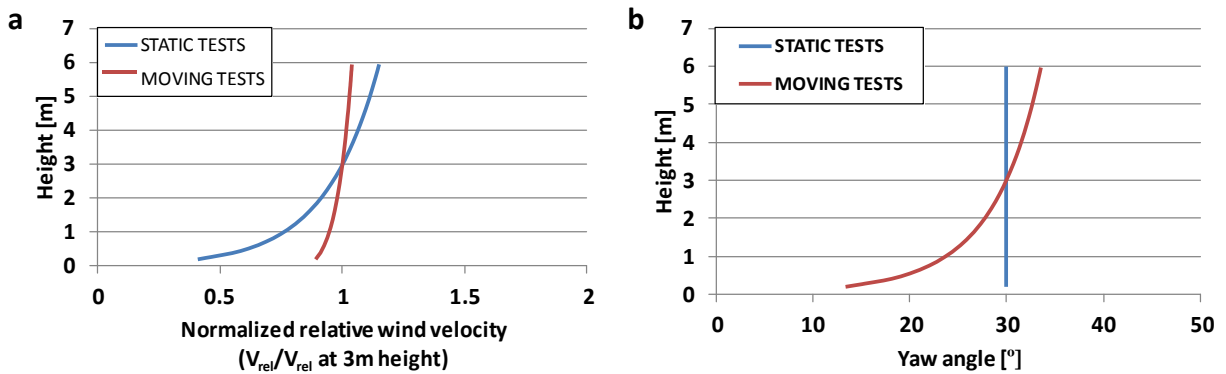
Figure 3.2 Relative wind vertical profile (reference height: = 3 m; Nominal yaw angle: 30°). a) Normalised magnitude of the relative wind velocity b) Yaw angle

In light of the above considerations, it is expected that static tests are incapable of providing a realistic simulation of the flow around the train, particularly near the ground (Hemida and Baker, 2010). Hence, it can be hypothesised that a systematic approximation might affect the aerodynamic load coefficients obtained through static model experiments (Howell, 1986; Baker, 1986; Baker and Humphreys, 1996).

Particular concern arises concerning the relevance of this approximation if a train is tested on an embankment (Cheli et al., 2011a). In this scenario, the direction of the onset wind contributes to the speed-up of the velocity downstream of the crest (ESDU, 2002; Baker, 1985). In a static test, however, such a direction cannot be correctly simulated because the embankment has to be rotated by the same angle as the train in order to match the yaw angle. This leads to an unrealistic replication of the local wind profile acting on the train, whose impact on the aerodynamic load coefficients measured during such static tests is still a matter of discussion (Suzuky et al., 2003; Cheli et al., 2008; Schober et al., 2008).

Experiments on static scale-model vehicles are the type of tests currently prescribed in the railway standards (EC, 2008; CEN, 2010; RSSB, 2009b) and, as such, performed in the vast majority of the

this study   is the wind velocity relative to the train, taken at the reference height, while   is

would ensure a better representation of the real condition, it would entail a higher level of technical

complexity and greater resources. On the other hand, as discussed above, static model experiments

have the significant advantage of being suitable for conventional wind tunnels and standard test

procedures. Furthermore, it is assumed that the limitations inherent in a static vehicle representation

lead to small errors affecting the non-dimensional aerodynamic coefficients although, as discussed in

section 3.5.3, such an assumption is still under debate.

3.4   Scale-model experiments

3.4.1   Reynolds number similitude

The similitude theory provides the theoretical background that supports the capability of scale-

model experiments to simulate correctly a real physical phenomenon (Barlow et al., 1999; Baron,

2001). It states the modelling requirements to enable the non-dimensional coefficients obtained

through scale-model tests to predict the full-scale behaviour.

Specifically concerned with investigating the non-dimensional aerodynamic coefficients, scale-model

experiments on trains in crosswinds commonly employ '*rigid models*' (which do not scale down the

vehicle mass or the dynamic characteristics of the suspension system). Accordingly, they have as the

primary criterion of similarity the Reynolds number similitude and, in some cases, may consider also

the Mach and Jensen numbers (Dyrbye and Hansen, 1999).

Commonly described as the ratio between the inertial loads and the viscous forces (Dyrbye and

Hansen, 1999), the Reynolds number is defined as:

$$\text{Re} = \frac{\rho V_{ref} H_{ref}}{\mu} \tag{3.1}$$

where   and   are the density and viscosity of the fluid, respectively,   is the reference velocity

and   is the reference dimension. As common for railway applications (e.g., Gawthorpe, 1994), in

investigations. On the one hand, whilst it may be acknowledged that the use of moving vehicles

the nominal height of the vehicle.

Similitude states that the Reynolds numbers at full-scale (FS) and model-scale (MS) are equal. Accordingly, for scale-model tests performed in air at ambient conditions, it leads to the condition below.

$$\left(V_{ref}H_{ref}\right)_{MS} = \left(V_{ref}H_{ref}\right)_{FS} \tag{3.2}$$

To fulfil the Reynolds similitude, it follows from equation (3.2) that the reference wind velocity at model-scale should increase proportionally to the reduction of the model dimensions. However, practical limitations prevent this constraint from being satisfied in light of the typically adopted geometrical scaling factors of between 1:7 and 1:100, according to Baker et al. (2009). The required wind speed would be excessive both for conventional wind tunnel capabilities and because it would lead to unrealistic compressibility effects. The Mach number should remain < 0.3 (CEN, 2010). Furthermore, considering moving model experiments, the vehicle speed would need to be similarly scaled. Consequently, since the actual relative wind velocity achieved at model-scale is normally lower than what required by equation (3.2), the model-scale Reynolds number is also lower than at full-scale where, for rail vehicles, it is estimated to be in the range 8 to 10×10^6 (Baker et al., 2009).

To address this issue, an approach based on a relaxation of the Reynolds similitude assumes that a scale-model test can properly represent a full-scale condition as long as its Reynolds number (although smaller than at full-scale) exceeds a threshold called the '*critical Reynolds number*' (   ). Such an approach is currently accepted widely and enables the employment of scale-model tests for predicting the aerodynamic behaviour at full-scale of rail vehicles, as well as of civil engineering structures.

This approach was originally developed through general studies on bluff bodies (Simiu and Scanlan, 1996; Holmes, 2007) and dedicated investigations support its validity for rail vehicles (e.g. Cooper,

scale-model vehicle statically tested in a conventional wind tunnel, can normally ensure a better

number has a significant dependence on multiple factors, the identification of a general reference

value is not straightforward.

For bluff bodies, while $= 2 \times 10^5$ to 5×10^5 is indicated for smooth-edged shapes, lower values are

advised for objects with sharp-edges bodies presenting a relatively high surface roughness and also

in the presence of turbulent onset flows (Dyrbye and Hansen, 1999; Simiu and Scanlan, 1996). For rail

vehicles, $= 2 \times 10^5$ - 2.5×10^5 is specified in the current railway standards (EC, 2008; CEN, 2010;

RSSB, 2009b). Supported by experimental evidence (Cooper, 1981; Copley, 1987), this value refers to

smooth-edged trains in low-turbulence flows at 90° yaw angle. However, a reduction of such a

threshold has been outlined for sharp-edged vehicle shapes (e.g., container freight trains

(Gawthorpe, 1994)), for models with rough surface finishing (Cheli et al., 2011b) and in the presence

of turbulent onset wind simulations, with $= 6 \times 10^4$ suggested by Baker (1986) for a smooth-edged

vehicle. In addition, indications of $< 2 \times 10^5$ were found when yaw angles between 0 and 30° were

investigated (Bocciolone et al., 2008; Cheli et al., 2011b).

3.4.2 Measurement techniques

Non-dimensional aerodynamic coefficients can be obtained from combined measurements of the

crosswind (and train) speed and of the aerodynamic loads acting on a vehicle. Two approaches are

currently adopted for detecting the aerodynamic loads acting on a scale-model vehicle:

- measuring the overall aerodynamic forces and moments;

- measuring the pressure distribution on the vehicle surface and integrate it to obtain the overall

  loads.

If '*direct*' load measurements are carried out, the accuracy of the non-dimensional coefficients

depends on the experimental arrangement and on the instrumentation performance. When pressure

measurements are undertaken, the total number of pressure taps and the model discretisation also

play a significant role. A *direct* measurement, such as the use of a force balance in conjunction with a

1981; Copley, 1987; Gawthorpe, 1994; Bocciolone et al., 2008). However, since the *critical Reynolds*

accuracy. For this reason, it is prescribed by the railway standards (CEN, 2010; RSSB, 2009b).

However, pressure measurements provide additional information concerning the distribution of the

crosswind loads along and around the vehicle, which supports a deeper understanding of the

phenomenon and enables accurate CFD validation (Sterling et al., 2010).

3.4.2.1 Measurements of forces and moments

Non-integrated balances

A 'non-integrated balance' is a dynamometric system that is not fully accommodated inside the

vehicle model. Systems of this type normally consist of a '6-component external force balance'

positioned under the model and anchored to the ground. The model is connected to such a balance

through dedicated supports (figure 3.3a) and suspended a small distance above the ground to ensure

that the entire load is detected. The dynamometric system that forms the balance is typically

accommodated below the floor level (or splitter plate), or hidden inside the simulated infrastructure

scenario (figure 3.3b). The use of this type of balance represents the standard for wind tunnel tests

on static scale-model vehicle (EC, 2008; CEN, 2010; RSSB, 2009b). However, it is not particularly

suitable for moving model experiments, for which a rare example of use is provided by Li et al. (2011)

(section 3.4.3.1).
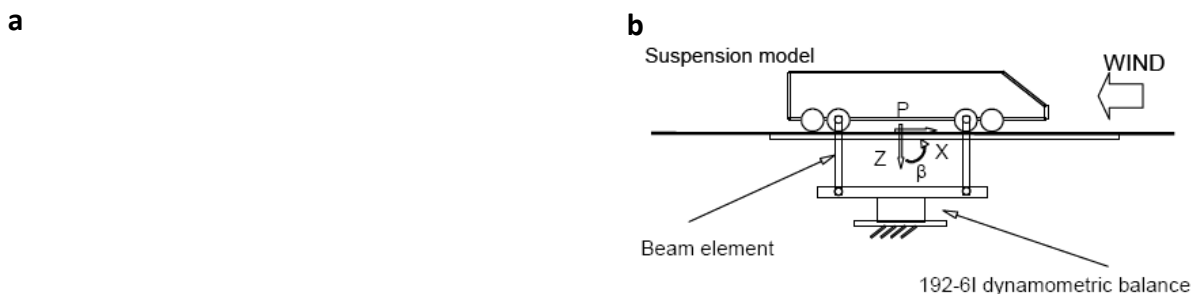
Figure 3.3 Non-integrated 6-component external force balances a) Sanquer et al. (2004) b) Cheli et al. (2008)

A second version of non-integrated balance consists of a '6-component internal force balance' (figure

3.4). Anchored to the ground by a vehicle-supporting frame analogous to that of an external balance,

For moving model tests on trains, Cooper (1981) employed an on-board balance consisting of 5 load model. Internal balances are used in static model tests when in the presence of infrastructure scenarios like bridges (Dorigatti et al., 2012), viaducts and embankments (Suzuky et al., 2003). Furthermore, they have been adopted for past moving model tests using the arrangement illustrated in figure 3.7c (section 3.4.3.1).
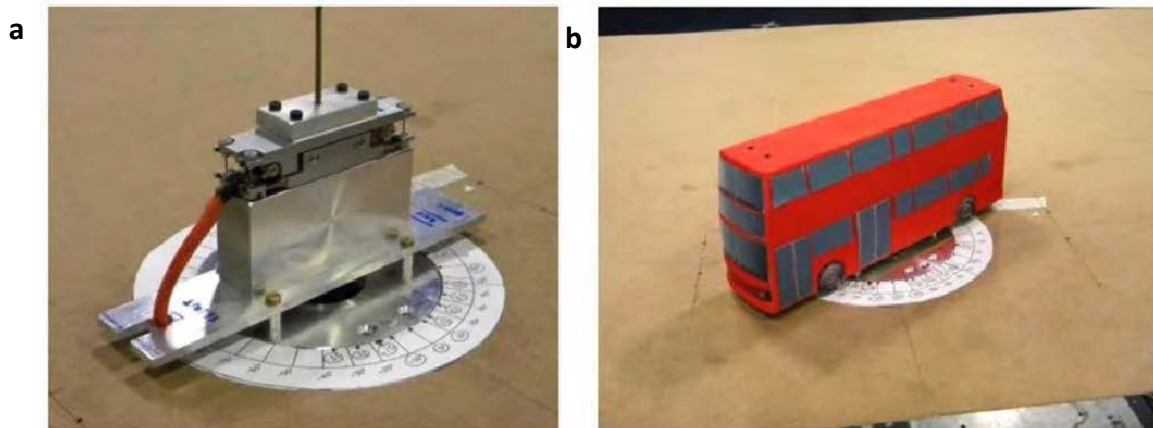
Figure 3.4 Non-integrated 6-component internal force balance (Dorigatti et al., 2012)

On-board balances

An *on-board balance* is, by definition, entirely accommodated inside the scale-model vehicle and makes no connection with anything external. Since such a system does not require any supporting frame that anchors to the model to the ground, it is suited to moving model experiments and causes minimum flow interference. Nevertheless, it entails an increased technical complexity and may have limited flexibility of use (in combination with different models) because it requires that the components are miniaturised and customised.

Yoshida et al. (1977) developed an early version of an on-board balance based on the use of 'wire strain-gauges' integrated into the internal chassis of a road vehicle scale-model. Once calibrated, this system enabled moving model tests but, due to the involvement of a permanent wiring between the scale-model and a trackside data acquisition device, it was not stand-alone. The maximum sampling frequency was 10 Hz but a low-pass filter at 4 Hz was applied to remove *mechanical noise* interference (section 3.5).

it differs from the latter because it has the dynamometric system accommodated inside the scale-cells integrated in the two wheel-sets of a 1:5 scale-model vehicle. This system enabled detection of five components of the load (except the drag force) and, by taking advantage of the large scale, did not require miniaturised components.

An alternative on-board balance was developed by Bocciolone et al. (2008) to measure all 6-components of the aerodynamic load on a scale-model train during moving model tests. Designed as an integral part of the model, this balance comprised seven miniaturised load cells connected to two horizontal plates as per figure 3.5. The 'lower plate' was mounted onto the model wheel-sets through a suspension system (thus avoiding any connection to the ground). The *'upper plate'* supported the external shell of the vehicle model and, as such, transferred loads from the latter to the load cells. Once calibrated, the accuracy of this system was comparable to that of an external balance (for static applications). However, when employed in moving tests it revealed a significant sensitivity to the vibrations induced by track irregularities.
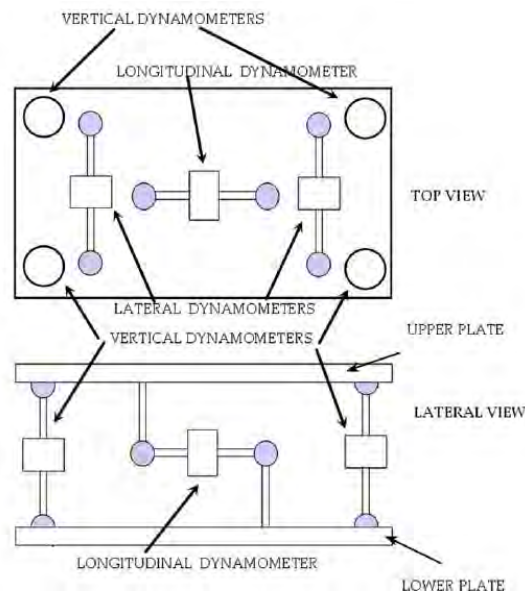
Figure 3.5 On-board force balance (Bocciolone et al., 2008)

When overall aerodynamic loads are obtained through discrete integration of the surface pressure

Non-integrated pressure measuring systems

'Non-integrated pressure measuring systems' require a scale-model equipped with a number of pressure taps (figure 3.6) and comprise a tubing system and a pressure scanner remotely positioned with respect to the model (which prevents their use in moving model experiments). They are of common use in wind tunnel investigations (Barlow et al., 1999; Holmes, 2007) and, as such, are currently adopted for static tests on scale-model trains (Sanquer et al., 2004; Rocchi et al., 2009; Baker and Sterling, 2009).

Figure 3.6 Pressure taps on a TGV-DUPLEX 1:15 scale-model (Sanquer et al., 2004)

Different types of pressure scanners can be employed in such systems. The transducers and pneumatic circuit are selected and designed, respectively, to ensure an appropriate frequency response to resolve unsteady pressure fluctuations (Coleman, 1990; Sanquer et al., 2004; Holmes, 2007). Furthermore, a set of transducers are normally employed to monitor multiple taps simultaneously, since as many pressure taps as possible should be monitored in order to maximise the accuracy of the integrated pressure. For rail vehicles, the typical numbers of taps on a single coach are between 100 and 600 (Sanquer et al., 2004; Baker and Sterling, 2009; Cheli et al., 2011a), depending on the characteristics and dimensions of the scale-model. How many of them can be monitored simultaneously depends on the pressure scanner.

distribution, in principle, an approximation is involved because the contribution of skin friction to forces and moments is not evaluated. The results of Sanquer et al. (2004), however, suggest only minor impact of such an approximation in crosswind studies on rail vehicles.

On-board pressure measuring system

An 'on-board pressure measuring system' relies on miniaturised pressure transducers instead of using a conventional pressure scanner positioned remotely. Tubing system and transducers are accommodated inside a pressure-tapped scale-model and, therefore, any external link is avoided. This arrangement not only enables moving model tests but is also expected to reduce the sensitivity to track-induced vibrations outlined by previous studies that employed on-board force balances (section 3.5). However, the reduced space typically available inside a scale-model, as well as the performance of on-board data loggers (if used), could limit the maximum number of pressure transducers that can be monitored simultaneously (chapter 4).

A limited number of on-board pressure measuring systems have been developed in the past. One that comprised five miniaturised transducers was implemented by Chadwick et al. (2000) for carrying out moving model tests on '*simple* [road] *vehicle shapes*'. A second, operated in combination with an on-board data logging system, was employed by researchers at the University of Birmingham to enable wind tunnel pressure measurements on auto-rotating '*sheet-type debris'* (Martinez-Vazquez et al., 2009).

3.4.3 Integration of crosswind and vehicle movement simulations

One of the major challenges involved in moving model tests relates to the need to develop a (non-conventional) test facility that ensures a crosswind simulation in conjunction with the representation of the vehicle-ground relative motion.

Alternatively, Cooper (1981) investigated a 1:5 scale-model train travelling on a test-track in the field ensures a moving ground simulation underneath a statically mounted vehicle. This technique is widely employed in the automotive industry for wind tunnel tests on road vehicles subjected to head-wind (Cogotti, 2008). However, its application to crosswind experiments becomes inconvenient because it would require changing the orientation of the rolling floor and, therefore, lead to excessive technical complexity (Gawthorpe, 1994).

Hence, the approach undertaken in the past involved a vehicle movement simulation and, in turn, demanded the availability of a propulsion system that could fulfil the requirements specified in table 3.1.

- Provide model acceleration and deceleration
- Maintain an approximately constant vehicle speed along the track portion invested by the crosswind
- Enable a range of different vehicle speeds for test cases flexibility
- Maximise the top vehicle speed to enable high Re to be achieved (according to the crosswind velocity)
- Limit the peak acceleration and deceleration (during the launch and braking phases, respectively) to preserve the integrity of the model and of the on-board instrumentation
- Ensure a good level of vehicle speed repeatability between successive runs (to ensure run-to-run consistency)
- Minimise the single-run operating time (i.e. set-up + firing) to ease multiple-run sessions
- Maximise the track smoothness to reduce the vehicle mechanical vibrations and thus ease data processing
- Prevent any major vehicle geometry alteration
- Minimise any flow interference around the vehicle, especially in the underbody region
- Enable simulation of multiple ground scenarios (embankment in particular)
- In cases of wind tunnel integrated systems, respect the dimensional constraints that might be imposed by the size of the building hosting the facility

Table 3.1 Main requirements of a scale vehicle propulsion system

In the past, two different strategies were applied in order to combine vehicle movement and crosswind simulations:

- integrate a propulsion system into an existing wind tunnel;

- use a moving model rig (i.e., a facility designed for moving model experiments) equipped with a crosswind generator.

In principle, one approach to accomplish this requirement relies on using a '*rolling floor*', which whilst subjected to a natural wind.

3.4.3.1   Propulsion systems integrated into wind tunnels

Mechanical propulsion systems

One example of mechanical propulsion system integrated in a wind tunnel is illustrated in figure 3.7. Constructed by British Rail Research and first employed at the Cranfield Institute of Technology wind tunnel (Baker, 1986), this system was later transferred to the University of Nottingham wind tunnel and developed further (Humphreys, 1995). It comprised of an I-shape "Hepco" guideway 16 m long supported by a series of concrete blocks and positioned underneath the floor of the wind tunnel perpendicular to the mean wind direction. A so-called '*firing carriage'* (i.e., the '*live trolley*' specified in figure 3.7c) was moving along such a guideway under the action of four elastic ropes. Vehicle speeds of 5 to 20 m/s were achievable and, in the upgraded version of the system, an automatic re-firing system was available (Humphreys, 1995). The scale-model vehicle was equipped with an internal strain-gauge balance and this was connected to the *firing carriage* by a series of vertical bolts. Since such bolts were crossing the ground level, a slot in the floor underneath the vehicle had to be provided across the entire span of the wind tunnel testing chamber (figure 3.7c).

a

b   c

Figure 3.7 British Rail Research mechanical propulsion system a) Baker (1986) b) Gawthorpe (1994) c) Humphreys (1995)

cause an unrealistic simulation of the underbody flow and this placed a question on the reliability of the non-dimensional aerodynamic load coefficients that were measured. Furthermore, during each moving model test run, the roughness and irregularities in the alignment of the guideway caused vibration on the *firing carriage* and, in turn, on the scale-model vehicle. Detected by the force balance, these vibrations led to a series of spurious fluctuations in the recorded time histories (i.e., *'mechanical noise'*) that interfered with the identification of the aerodynamic contribution to forces and moments. To mitigate this interference, test methodologies based on series of 25 to 50 runs were adopted, despite this approach being relatively time-consuming (Baker, 1986; Humphreys, 1995).

Mechanical propulsion systems similar to that in figure 3.7 were used in further moving model experiments undertaken by Baker (2002) on a DB Inter-Regio 1:50 scale train and in a number of studies on road vehicles (e.g., Cairns, 1994; Macklin et al., 1996). The *mechanical noise* interference described above was reported in all of these cases.

A slight variation of such a design is represented by the system developed by Li et al. (2011) at the XNJD-3 wind tunnel, in China (figure 3.8). In this system, a set of *'sliding devices'* travel along an 18 m long guideway dragged by a pulling rope driven by a servo-motor. The guideway is supported above the vehicle model, to which the sliding devices are connected by a series of vertical joints. A non-integrated external force balance mounted on one of the joints provides force measurements. This propulsion system enables 1:45 scale-model vehicles to travel at a maximum speed of 10 m/s. Not comprising any equipment positioned underneath the model, this design eases experiments involving infrastructure scenarios like bridges and viaducts and prevents underbody flow interference. However, unrealistic distortions in the flow field are caused by the vertical joints that support the scale-model vehicle from above.

In the
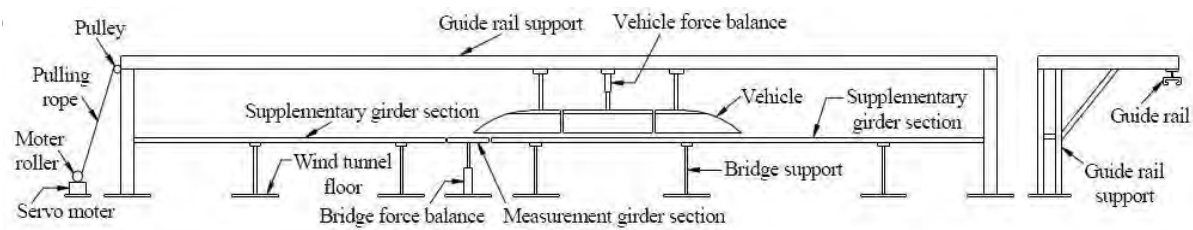
Figure 3.8 Mechanical propulsion system at the XNJD-3 wind tunnel (Li et al., 2011)

Gravity launching ramp

The gravity launching ramp in figure 3.9 was used in the (~14 m wide) environmental test chamber at the Politecnico di Milano Wind Tunnel (PMWT), in Italy (Muggiasca, 2002; Bocciolone et al., 2008). Such a ramp accelerated a 1:20 scale-model train to approximately 4 m/s projecting it into a straight track portion 4.5 m long. The entire system comprising of the ramp and the straight track was supported by a wooden structure and was placed on the wind tunnel turntable to ease testing of different wind angles. Force measurements were carried out using the on-board balance described in section 3.4.2.2.

The use of this gravity launching ramp in combination with an on-board balance minimised flow interferences around the vehicle and enabled tests on a variety of ground simulations and for a range of wind angles. However, the limited vehicle speed led to relatively low Reynolds numbers. Furthermore, *mechanical noise* interference induced by track-induced vibrations affected the performance of the on-board force measuring system (section 3.5).

Figure 3.9 Gravity launching ramp (Bocciolone et al., 2008)

A moving model rig facility independent from a wind tunnel was developed by Howell (1986) to carry out moving model tests on ~1:20 scale-models of Maglev trains. This facility consisted of a mechanical propulsion system, the design of which was similar to that used by Baker and Humphreys (described above), and of a series of centrifugal blowers that provided a (crude) crosswind simulation.

The simulated crosswind was turbulent, perpendicular to the track and had a mean wind velocity of ~4 m/s. The propulsion system consisted of a 24 m long guideway positioned below the ground level and a *firing carriage* moving along such a guideway under the action of pre-tensioned elastic cords. Different from the system of Baker and Humphreys, the guideway was positioned downwind of the track centreline and the scale-model vehicle was supported by L-shaped bars attached to its leeward side (figure 3.10). At the price of flow interference downstream of the vehicle, this arrangement enabled tests of multiple track configurations and ensured a realistic representation of the underbody flow.
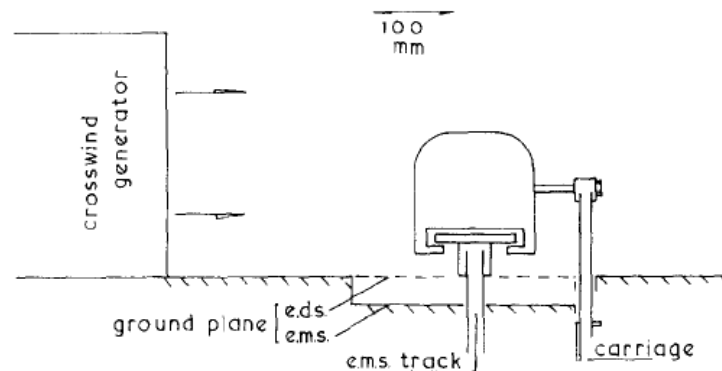
Figure 3.10 Moving model rig and crosswind generator (Howell, 1986)

A second example of moving model rig is the facility at the Simulation Centre of Aerodynamic Research in Transportation (SCART), in Germany (SCART, 2012). It employs a hydro-pneumatic propulsion system that projects 1:20 to 1:100 scale-model vehicles along a 60 m long track at a maximum speed of ~100 m/s. The vehicles travel along the track on their own wheels and, therefore, neither an additional guideway nor a model supporting system is required. The crosswind simulation

consists of an open jet perpendicular to the track generated by a closed-loop wind tunnel. Maximum wind speed is ~25 m/s. Based on the specifications available, this facility minimises the flow interferences around the vehicle and enables tests at high Reynolds numbers. To measure the wind-induced aerodynamic loads an on-board measuring system appears to be required.

The TRAIN rig used for the present research is a further example of a moving model rig equipped with a crosswind generator. The details of this facility are described in full in section 4.3. In summary, it consists of three parallel tracks 150 m long and has a mechanical propulsion system capable of catapulting 1:25 scale vehicles at a maximum speed of ~75 m/s. A crosswind generator provides a turbulent crosswind perpendicular to the direction of travel within a portion of track 6.35 m long. The mean wind speed is ~12 m/s. An on-board stand-alone measuring system is currently employed for measuring the pressure distribution on the train surface (section 4.5.1).

3.5   Review of previous investigations on moving model trains

As stated in section 3.3.3, the standard technique of investigation for train aerodynamics is represented by wind tunnel measurements on scale vehicles tested in static conditions. Nevertheless, a number of experimental (and CFD) studies on moving model (road and rail) vehicles were undertaken in the past for different purposes. Some of them analysed the transient aerodynamic loads on a vehicle entering a gust (Yoshida et al., 1977; Chadwick et al., 2000; Hemida and Krajnovic, 2009b). Others addressed the design of wind barriers (Baker, 2002). In addition, a number of them investigated the effect of the vehicle movement simulation by comparing a static and moving vehicle representation. Consistent with the purposes of the present research, this review focuses on this latter type of studies that involved rail vehicles.

3.5.1   Scale-model experiments

Table 3.2 summarises the main details of the past model experiments discussed in this section.

Source	Facility	Propulsion system	crosswind characteristics	Train model (geom. scale)	Measuring system	Test procedure	Yaw angle	Ground sim.	Re (estimate)
Cooper (1981)	Natural wind (at a FS site)	full-scale (pushing) van	Natural turbulent wind	APT (1:5)	On-board FB (5)	SR	~ 15-90°	EMB (h=1m)	~ 1x10^6
Howell (1986)	MMR + CWG	M	Turbulent wind (crude simulation)	Mag-Lev vehicle (~1:20)	Non-integrated internal FB (2)	SR (Won–Woff)	~ 0-15°	FG + EMST	~ 2x10^5
Baker (1986)	EWT + PS	M	ABL simulation (approximate)	APT (1:50)	Non-integrated internal FB (5)	MR (25)	~ 20-90°	FG + EMB	~ 6-10x10^4
Humphreys (1995) Humphreys and Baker (1996)	EWT + PS	M	ABL simulation (approximate)	railway container (1:45)	Non-integrated internal FB (5)	MR (50-100)	~ 25-70°	FG	~ 4x10^4
Muggiasca (2002) Bocciolone et al (2008)	EWT + PS	GLR	Low turbulence	ETR 480 (1:20)	On-board FB (6)	MR (N/A)	~ 15-50°	V	~ 4-6x10^4

Table 3.2 Principal past moving model experiments on rail vehicles. Abbreviations: EWT: environmental wind tunnel; MMR: moving model rig; PS: propulsion system; M: mechanical propulsion system; GLR: gravity-launching ramp; FB (·): force balance (measured load components); SR: single run; Won-Woff: Wind-on wind-off runs; MR (·): multiple runs (runs N° for ensemble averages); FG: flat ground; EMB: embankment; V: viaduct; EMST: electromagnetic suspension track

The campaign of Cooper (1981) comprised of '*hybrid*' experiments, between the (classic) full-scale and model-scale tests. It employed a 1:5 scale-model of an Advanced Passenger Train (APT) and included both static wind tunnel tests (on a flat ground simulation) and '*outdoor*' moving model experiments. During the latter, the same scale-model used for the wind tunnel tests was propelled on a test-track 950 m long using a van equipped with a push rod. Since this test-track was in the field (on the top of a 1 m high embankment), the scale-model was exposed to the action of natural (rather than simulated) winds. Force measurements were undertaken using the on-board balance described in section 3.4.5.1. Steady and unsteady train aerodynamics were analysed over a 15-90° yaw angle range and a comparison between static and moving model tests was arranged considering the mean coefficients of side and lift force, and of the rolling moment.

In this campaign, although there was a slight mismatch between the scaling ratio of the train model and the full-scale ABL profile, the use of an aerodynamic excitation provided by natural winds ensured a good representation of the conditions experienced by an operating train, in reality. The turbulent nature of the onset wind enabled investigation of both steady and unsteady aerodynamic coefficients. Furthermore, the large geometrical scale led to Reynolds numbers of ~1×10^{6}, higher than in any other past moving model test. However, these advantages were achieved at the price of a remarkable demand of resources. In addition, there was a discrepancy between the flat ground simulation of the wind tunnel static tests and the 1 m high embankment of the moving model tests. Also, only an approximate simulation of the natural wind profile was achieved in the wind tunnel. Finally, the uncontrollability of natural winds led to a significant scatter in the moving model test results and, consequently, to relatively large experimental uncertainties. These were estimated as 10% (random) and 5% (systematic) of the mean coefficients, at yaw angles lower than 40°.

Considering the estimated uncertainty and the discrepancy in the ground simulation between static and moving model tests, the results of Cooper indicated no significant effect associated to the simulation of the vehicle movement.

Howell (1986) performed moving model tests on a ~1:20 scale Maglev prototype train considering two different infrastructure scenarios: a flat ground and an electromagnetic suspension track. He used the moving model rig facility and the crosswind generator described in section 3.4.3.2. Force measurements were obtained using a strain-gauge internal non-integrated balance capable of monitoring simultaneously two force components. To deal with *mechanical noise* generated by track-induced vibrations, '*wind-off*' runs were carried out in still air and the relative time series were subtracted from those recorded during '*wind-on*' runs. Transient and steady train aerodynamics were investigated at yaw angles less than 15° and a comparison was arranged with wind tunnel static tests carried out on the same train models.

The mean force coefficients obtained tended to be higher in static conditions for both side and lift forces. Their variations between static and moving model tests increased with the yaw angle and were larger in the presence of a modelled electromagnetic suspension track scenario (rather than on a conventional flat ground). The use of a ~1:20 scale led to Reynolds numbers of ~$2x10^5$ and a realistic underbody flow simulation was performed. However, the vehicle supporting system caused flow interference on the leeward side (section 3.4.3.2) and a rather crude crosswind simulation with a low mean wind speed was provided by the crosswind generator employed.

The moving model tests of Baker (1986) were carried out in the wind tunnel at the Cranfield Institute of Technology using the mechanical propulsion system described in section 3.4.3.1. A 1:50 scale-model of the APT train (the same train studied by Cooper (1981)) was investigated whilst subjected to an approximate ABL simulation, at yaw angles between 20° and 90°, both on a flat ground and on an embankment. In addition, static tests on the same scale-model were undertaken in the same conditions. Transient and steady aerodynamic loads were measured using the 5-component internal non-integrated balance illustrated in figure 3.7 (section 3.4.2.1). In light of the short duration of the time series relating to the train travelling across the wind tunnel, a test procedure based on ensembles of 25 runs was adopted to account properly for the run-to-run data variability. In addition,

this test procedure eased the removal of the *mechanical noise* from the signals detected by the on-board force balance: seen the random nature of such a noise, spurious forces fluctuations relating to different runs were progressively cancelled out within the ensemble averaging process.

The analysis of the aerodynamic loads on the train's leading car when entering into the wind tunnel testing chamber indicated a transition lasting 1.5 times the length of such a car (in agreement with the observations of Howell (1986)). A comparison between static and moving model tests showed higher mean side force coefficients in the static case. For the mean lift force coefficients, by contrast, static and moving tests values were '*fairly similar*'. However, difficulties arose in the interpretation of these results for two main reasons: an unrealistic underbody flow representation caused by the supporting system and by the slot in the ground underneath the model; a residual *mechanical noise* interference that had not been removed by the ensemble average process.

Further moving model tests were undertaken by Humphreys in the University of Nottingham wind tunnel (Humphreys, 1995; Baker and Humphreys, 1996). The propulsion system used by Baker (1986) was upgraded to enable automatic re-firing and was employed in conjunction with the original internal balance. A train formed by an array of three sharp-edged railway containers at 1:45 scale was tested on a flat ground scenario, both in static and moving conditions, in the presence of an approximate ABL wind simulation. Aerodynamic loads were measured on the central container of such an array and mean and peak coefficients of side and lift forces were investigated at yaw angles between 25° and 70°.

A good agreement was found between static and moving model test results at yaw angles larger than 50°. For yaw angles lower than 50°, the vehicle movement simulation caused an increment of both mean coefficients and peak normalised (i.e., peak / mean) coefficients. Any difference observed between static and moving test results, however, was smaller than the experimental uncertainties (Baker and Humphreys, 1996). For static tests, the measurement repeatability for mean and peak normalised coefficients was estimated as 3% and 9%, respectively. For moving model tests,

repeatability of mean coefficients remained 3%, while for peak normalised coefficients it rose to approximately 13%. Such estimations were obtained from the standard deviation of the *mechanical noise,* assuming a normal distribution and considering a 68% confidence level.

With respect to the tests of Baker (1986), in this case the partial automation of the propulsion system enabled a series of 50 (rather than 25) runs to be carried out in a relatively short time-frame. Enlarging the size of the ensembles, this reduced the *mechanical noise* interference on the estimated mean coefficients and, therefore, led to smaller uncertainties. However, since the peak normalised coefficients were calculated by processing the time series from different runs individually, increasing the ensemble size did not lead to a reduction in the *mechanical noise* interference. Hence, the associated uncertainty remained large. Furthermore, doubts about the reliability of the load aerodynamic coefficients estimations were posed relating to the unrealistic underbody flow representation already outlined by Baker (1986).

Further moving model experiments were undertaken by Muggiasca (2002), and later reported by Bocciolone et al. (2008), in the Politecnico di Milano wind tunnel. A 1:20 scale-model of an ETR480 train was investigated whilst running on a viaduct and subject to a low-turbulence crosswind at 15° to 50° yaw angle. The gravity launching ramp illustrated in figure 3.9 (section 3.4.3.1) provided vehicle movement and aerodynamic loads were measured using the on-board balance described in section 3.4.2.1. Static and moving model test results were compared relating to side and lift force mean coefficients for both the first and second car of the train.

A substantial agreement between static and moving model test was found for all the examined coefficients. However, the accuracy of the results was limited due to technical challenges involved in the experimental arrangement. Even if a good simulation of the underbody flow was provided, track irregularities created relatively high *mechanical noise* in the signals detected by the on-board balance. Furthermore, although different wind angles could be simulated, the maximum vehicle speed of ~4 m/s led to relatively low Reynolds numbers (of 4 to 6×10^{4}).

Comparison

The results of the past experimental campaigns reported in table 3.2 can be compared to assess the effect of the vehicle movement simulation on the measurements of the mean aerodynamic coefficients.

Cooper (1981) and Bocciolone et al. (2008) found an agreement between static and moving model tests for both the side and lift force mean coefficients, while some differences emerged in the other studies. Such differences, however, varied from one investigation to the others. Howell (1986) found larger side and lift force mean coefficients when obtained through static tests. Baker (1986) confirmed a larger mean side force coefficient from static tests, but found no significant differences between moving and static experiments for the lift force mean coefficient. The results from Humphreys (1995) were partially consistent with those of Cooper (1981) and of Bocciolone et al. (2008). Since the variations observed between the best-estimate values of static and moving model test mean coefficients fell within the margin of uncertainty, in a conservative approach they indicated no significant differences. Nevertheless, if such variations were evaluated, at low yaw angles a moving vehicle was characterised by higher mean coefficients, particularly for the lift force. In light of the relatively large experimental uncertainties, these results did not entirely exclude the possibility that the vehicle movement simulation might have a significant effect. An increment of the mean load coefficients, however, was opposite to that indicated by Howell and by Baker.

What emerges from the studies above is a lack of agreement on the aerodynamic effect of the vehicle movement simulation. Such a broad range of conflicting indications poses the question as to whether or not a sufficient level of accuracy was reached in past moving model experiments to address properly the problem under investigation. This doubt is consistent with the relatively wide margins of uncertainty estimated by Cooper (1981) and by Baker and Humphreys (1996) and caused by the numerous practical and technical difficulties that were reported.

3.5.2 CFD simulations

Table 3.3 specifies details of two CFD studies that specifically analysed the aerodynamic effect of the rail vehicle movement simulation.

Source	Turbulence model	Vehicle movement simulation	crosswind characteristics	Train model (scale)	Yaw angle	Ground scenario	Re (estimated)
Hemida and Baker (2010)	LES	Moving ground	Low-turbulence	Freight wagon (1:20)	90°	FG	~3×10^5
Cheli et al. (2011)	RANS	Moving vehicle	Low-turbulence	ETR 500 (1:15)	0-30°	STRB + EMB	~2.5×10^5

Table 3.3 Principal past CFD simulations involving a vehicle-ground relative movement representation

Hemida and Baker (2010) carried out Large Eddy Simulations (LES) on a 1:20 scale-model of a (sharp-edged) freight wagon, for a flat ground scenario. This train was subjected to a low-turbulence onset wind at a wind angle larger than 90° and the effect of the vehicle movement was recreated by adopting a moving ground boundary condition. The resulting yaw angle was 90°.

An influence of the vehicle-ground relative motion was observed in the mean surface pressure distribution on the vehicle bottom face. This produced only slight differences (~2.5%) in the mean side force coefficient, but resulted in a lift force coefficient approximately 11% higher when the vehicle-ground relative motion was replicated.

Cheli et al. (2011a) performed Reynolds-averaged Navier-Stokes (RANS) simulations analysing the leading car of an ETR 500 train, reproduced at 1:15 scale and subjected to a low-turbulence crosswind at 0° to 30° yaw angle. Both single track ballast and rail (STBR) and embankment scenarios were analysed. The simulation of the train movement was achieved by employing an auxiliary moving reference frame (MRF) that translated (at the train speed) with respect to the absolute reference frame (ARF) fixed to the ground.

On a STBR, the vehicle movement representation influenced the surface pressure distribution mainly on the ground leeward corner of the train nose. This produced small variations of both side force and

rolling moment coefficients (< 3%), but an increment in the lift force coefficient of ~11%. On an embankment, modifications in the surface pressure relating to a moving train became evident also on the roof and leeward side and affected a portion of the vehicle longer than the train nose. On a moving vehicle, this led to an increment of the mean lift force coefficient of ~20% and also to a growth of side force and rolling moment mean coefficients of ~10%. This suggested that wind tunnel tests might underestimate the wind-induced overturning moment coefficient relating to an embankment scenario and, in turn, determine a non-conservative assessment of the CWC.

Comparison

The two CFD investigations reported above examined different case studies and employed different computational techniques. However, it is worth noting that the results of a STBR ground simulation by Cheli et al. were in good agreement with those obtained by Hemida and Baker for the aerodynamic effects of the vehicle-ground relative movement simulation. Both analyses found a small impact of such a relative movement on side and rolling moment mean coefficients and both indicated an increment of the mean lift coefficient.

In comparison with past experimental campaigns, a certain level of agreement can be argued between the indications obtained through CFD studies and the results of Humphreys (1995). Such an agreement consists of outlining the largest impact of the vehicle movement simulation on the lift, rather than side, mean force coefficient. Furthermore, regarding the mean side force coefficient, the small variations between static and moving model tests found by CFD simulations are consistent with experimental results of Cooper (1981) and of Bocciolone et al. (2008).

3.6   Discussion and closing remarks

The examination of the three main methodologies available for investigating the aerodynamic behaviour of rail vehicles in crosswinds suggests that wind tunnel tests on static scale trains currently represent the best option. However, the analysis of this technique has shown that its inability of reproducing the vehicle movement leads to an approximation of the conditions actually experienced by a real travelling train. Hence, it can be hypothesised that a margin of error affects the non-dimensional aerodynamic coefficients measured through such static model experiments.

A number of previous studies were undertaken in order to assess the effect of simulating the vehicle movement on the aerodynamic behaviour of trains in crosswinds. However, these studies did not give a robust indication of the hypothesised effect. Considering steady aerodynamic coefficients, a small impact of the vehicle motion could be inferred on the side force, while a larger influence is suggested on the lift. Nevertheless, since different investigations did not agree, a confirmation of such indications would be required. It would also be desirable to quantify the influence of these effects on the mean rolling moment coefficient, which is more strictly related to the assessment of overturning risk. In terms of unsteady aerodynamic coefficients, the examination of the influence produced by train movement simulation is at an early stage. These parameters have been investigated only in a restricted number of cases. When analysed, then, their estimations relating to moving model tests were associated with large experimental uncertainties. These were caused either by uncontrollable wind conditions (where a natural wind simulation was employed), or by *mechanical noise* affecting the time series recorded by on-board force balances.

An evaluation of the experimental approach has highlighted the following major challenges relating to undertaking moving model tests in crosswinds:

- A significant level of *mechanical noise* was found in the time series of the forces and moments detected on a moving vehicle model. Common to all the previous campaigns, this noise tended to

have a frequency content falling within the aerodynamic range of interest, thus preventing an effective use of numerical filtering protocols. Consequently, it became a problem for the identification of the actual aerodynamic contributions from the recorded forces, particularly in relation to the analysis of unsteady effects (Humphreys, 1995; Baker and Humphreys, 1996).

The source of such a noise was identified in the vibrations induced on a running model by track (or guideway) irregularities. These vibrations were inevitably detected by on-board balances and particularly affected the vertical component of the force. To mitigate this issue, particular care was paid to maximise the track (or guideway) smoothness. Furthermore, specific test procedures and data processing methods were adopted. Combinations of *wind-on* and *wind-off* runs were carried out in some cases (Howell, 1986). Alternatively, multiple runs were performed to enable the calculation of ensemble average time histories. These measures proved beneficial in reducing the interference caused by *mechanical noise* on the estimation of the mean aerodynamic load coefficient. However, they were not equally effective when applied to the calculation of the unsteady aerodynamic coefficients.

- Where mechanical propulsion systems were employed, a certain level of flow interference was caused by the model supporting frame. This happened on the leeward side of the vehicle relating to the arrangement adopted by Howell (1986) and, more importantly, in the train underbody during experiments undertaken by Baker (1986) and Humphreys (1995). In this case, indications were found that the presence of a slot in the ground in between the rails caused unrealistic disruptions in the underbody flow. Hypothesising a relevant effect of such a flow interference principally on the lift force coefficient, some controversies emerged in the interpretation of the relative results.

- Difficulties were encountered in the analysis of moving model test data because of the short duration of the time series relating to a train travelling in actual crosswind conditions. This

duration was typically of the order of a few tenths of a second and depended on the combination of vehicle speed and track length affected by the simulated airflow.

Because of the stochastic nature of the turbulent flow developing around a train, such short time series showed a significant run-to-run variability. In this regard, to obtain accurate estimations of mean aerodynamic coefficients, the calculation of their ensemble averages based on a series of multiple runs was highly beneficial. However, the short duration of the time series also limited the frequency resolution achievable through spectral analyses and compromised the viability of conventional (Gumbel) extreme value analyses (Cook, 1985) to estimate the peak aerodynamic coefficients (Baker and Humphreys, 1996).

- The Reynolds numbers achieved in most of the previous moving model experiments were relatively low. They were determined by the low maximum vehicle speed deliverable by the propulsion system and by the use of small geometrical scales. The latter were adopted in a number of cases either to limit the vehicle length (and thus increase the duration of the time series recorded whilst the train travels across the crosswind simulation) or, in the presence of an ABL simulation, to match the turbulence length scale.

Except in the campaign of Cooper (1981), Reynolds numbers of past moving model tests were smaller than those typically reached in current low-turbulence wind tunnel tests on static trains ($\sim 1 \times 10^{6}$), and sometimes even significantly less than the nominal critical Reynolds number (2-2.5×10^{5}). In this regard, however, the discussion in section 3.4.1 suggests that the use of sharp-edged vehicle geometries, as well as that of an ABL simulation, could have helped to avoid relevant Reynolds number effects.

In view of further research, the complexity and variety of these challenges suggest that any future experimental investigation will most likely have to accept some compromises in its arrangement and, thus, the accuracy in the aerodynamic assessment of the vehicle movement simulation will be limited.

However, a margin of improvement can be identified with respect to what has been achieved so far. An on-board pressure measuring system of the type outlined in section 3.4.2.2 seems viable for a moving model train. Replacing a force balance, such a system should ensure much less sensitivity to track-induced vibrations, thus enabling a more accurate analysis of unsteady aerodynamic effects. Furthermore, providing information on the train surface pressure distribution, it would also enable a more in depth assessment of the aerodynamic impact of the vehicle movement. In addition, undertaking tests at the TRAIN rig, the particular design of the propulsion system (section 4.3.1) would minimise flow interference around the moving vehicle. Without compromising either the track quality or the vehicle speed, this would ensure a more realistic representation of the underbody flow and a better consistency in the comparison between static and moving model tests.

An evaluation of the numerical approach outlines how CFD simulations, once properly validated, could be the way forward in order to achieve an accurate representation of vehicle movement in the presence of a crosswind. Inherently free of the technical issues that affect physical tests, they offer wide flexibility in terms of vehicle and ground geometries and, to some extent, also of onset winds. Furthermore, they are likely to benefit from the development of computational technology. The main limitation to their employment, currently, is that an accurate validation has not yet been achieved. Thus, a significant value for CFD benchmarking would be the availability of experimental results comprising not only load coefficients, but also surface pressure data relating to both static and moving model tests. Hence, even considering the numerical approach, further value is added to the development of enhanced scale moving model experiments of the type described above.

Chapter 4

Experimental methodology

4.1 Introduction

Chapter 4 describes the methodology adopted in this research. Section 4.2 presents the type of experiments that have been undertaken and introduces the case study that was examined. Section 4.3 outlines the features of the TRAIN (Transient Railway Aerodynamic Investigation) rig facility, where such experiments were carried out and, in addition, in appendix A can be found a detailed description of the crosswind generator (CWG) that was developed in this facility as part of this project. The characteristics of the train scale-model are described in section 4.4, while section 4.5 reports the details of the trackside and on-board instrumentation that were employed. Finally, sections 4.6 and 4.7 illustrate the experimental setup and test procedure adopted for static and moving model tests, respectively.

4.2 TRAIN rig experimental campaign

The experimental campaign undertaken in the TRAIN rig comprised two experimental phases. In phase one, a scale-model train was tested in static conditions under the effect of a side wind. In the second phase, moving model experiments in crosswinds were undertaken. The comparison between the two datasets enabled the impact of the vehicle movement simulation on the aerodynamic behaviour of a train in a crosswind to be evaluated.

The static and moving model test sessions were designed in order to minimise any difference in the setup other than the train movement simulation. The same train scale-model, the same measuring

equipment and the same wind simulation provided by the new TRAIN rig CWG were used throughout both series of experiments.

4.2.1 Case study

The case study analysed during static and moving model tests was agreed within the AeroTRAIN consortium. As summarised in table 4.1, it consisted of a 1:25 scale Class 390 Pendolino train, on Approximate Flat Ground (AFG), subjected to a turbulent relative wind at 30° nominal yaw angle.

Train geometry	Class 390 Pendolino train (simplified)
Geometrical scale	1:25
Nominal yaw angle ( )	30°
Ground scenario	Approximate Flat Ground (AFG)
Crosswind characteristics	Incident turbulence (according to the CWG performance)

Table 4.1 Case study – details of train model used for this study

The selection of the train geometry was made by some of the AeroTRAIN partners in the light of the availability of existing data from earlier campaigns for additional comparisons (Baker, 2003; RSSB, 2009b), while the geometrical scale was the standard for TRAIN rig experiments. The nominal yaw angle of 30° was chosen to represent the '*low yaw angle range*' (described in section 2.4.1), that is between 0° and 40°-50°.   = 30° was thus well within the boundaries. Furthermore, although one nominal yaw angle may correspond to a variety of combinations between wind velocity and train speed, 30° is often considered as the top of the realistic range for high-speed trains (Cheli et al., 2011a). A ground simulation as close as possible to the conventional flat ground (FG) (CEN, 2010) was adopted in order to examine the simplest case possible. This will provide a fundamental reference for further investigations concerned with more realistic and critical scenarios, such as like ballast and rail or embankments. The simulated crosswind, finally, was characterised by an incident turbulence according to performance of the newly developed CWG (illustrated in section 4.3.2).

4.3 TRAIN rig facility

The TRAIN rig was built by British Rail Research at the end of the 1980s as a research laboratory dedicated to undertaking moving model tests on scale rail vehicles (Pope, 1991; Baker et a., 2001; Johnson and Dalley, 2002). Situated in Derby (UK), since 2009 the facility is owned and operated by the University of Birmingham (Quinn, 2009-2011).

**testing
room**

**control room
&
workshop**

Figure 4.1 TRAIN rig aerial view (Microsoft Corporation and Blom, 2009)

The rig is located in the white building portrayed in the aerial view of figure 4.1. It comprises of a control room from which the facility is operated, a workshop dedicated to the scale-model instrumentation and setup, and a long and narrow testing room. Inside the latter, three straight tracks run parallel for 150 m in length and are equipped with two mechanical propulsion systems that can catapult 1:25 scale vehicle models at speeds of up to 75 m/s (section 4.3.1). The tracks are mounted on a concrete deck and supported approximately 1.2 m above the ground, by a series of concrete piers. All the components and devices that make up the propulsion system are accommodated under the deck. The CWG, indicated in the following as 'new CWG' to distinguish it

from the previously existing system described in appendix A, spans a portion of the tracks 6.35 m long and provides a horizontal airflow perpendicular to the direction of travel (section 4.3.2). An internal view of the facility is shown in figure 4.2, while figure 4.3 provides some details concerning the dimensions of the building and the arrangement of the tracks.

Figure 4.2 TRAIN rig internal view
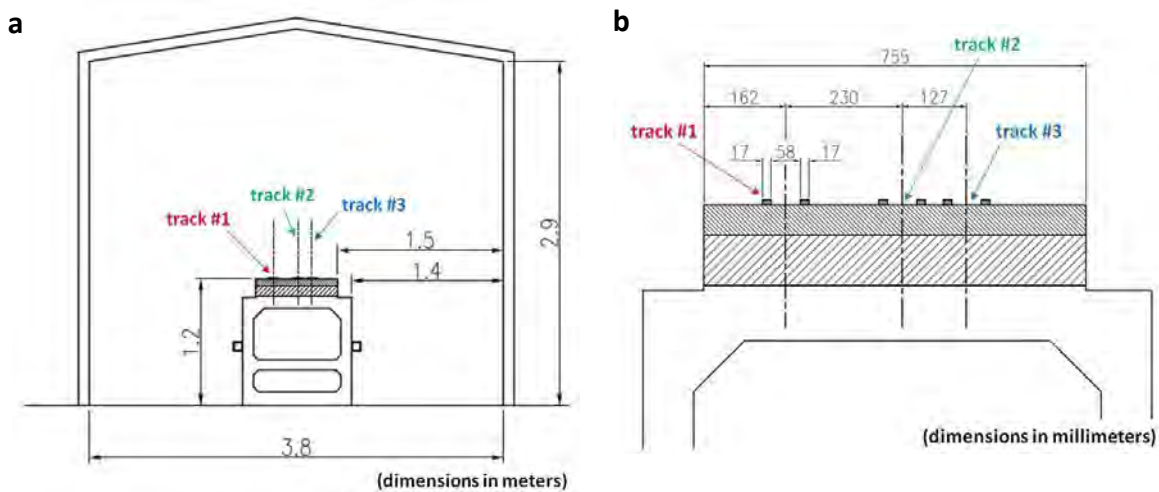
Figure 4.3 TRAIN rig testing room a) Testing room transverse section b) Testing tracks layout

Of the 150 m length of track, the two end-portions (each 50 m long) are dedicated to accelerate and brake the model while the central 50 m correspond to the actual test section over which the train travels at approximately constant speed.

In the present rig configuration (illustrated in figure 4.4), three different areas can be identified within the test section. According to the direction of travel on track 1, the first section (~12 m long)

is dedicated to investigating either train aerodynamic phenomena in open air (e.g., slipstreams and pressure pulses) or aerodynamic induced effects on trackside structures. The second section is ~23 m in length and is where measurements concerning train aerodynamics in tunnels are undertaken. Finally, the CWG is situated within the third section.
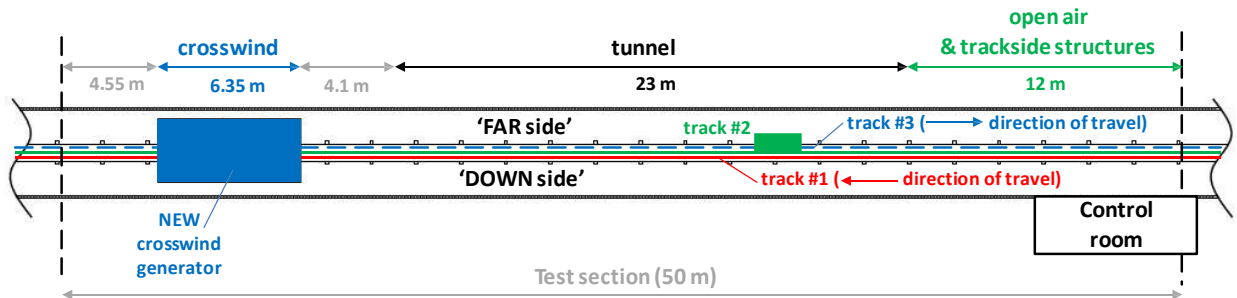
Figure 4.4 TRAIN rig testing room: test section configuration

4.3.1 Model vehicles propulsion system

Two mechanical propulsion systems are currently operational at the TRAIN rig. They are identical in design but are installed with opposing orientations in order to provide tracks 1 and 3 with opposite directions of travel (figure 4.4). Each system comprises a launching and a braking mechanism and is operated from a control panel placed in the control room, since, for safety reasons, access into the testing room is forbidden during operation. The launching mechanism is based on the use of pre-tensioned elastic bungees that, during the launch phase, are connected to the vehicle model by a 'firing-rope' guided by a pulley system. The braking mechanism employs a piston dragged through a deformable tube (made of polyurethane) by a cord that engages with the scale train at the beginning of the braking section. Such a device dissipates the energy associated with the vehicle movement and ensures a gentle deceleration that does not damage the model.

A schematic of the propulsion system is illustrated in figure 4.5, while further details are included in appendix C, where a detailed description of the firing procedure is provided. For purposes of discussion in the following, however, it is worth noting here that the launching and braking mechanisms are independent from one another and interact with the model only during the acceleration and deceleration phases, respectively. This means that whilst the train travels within the

test section, once it has been accelerated to the desired speed and before hitting the brake, it is completely unlinked to the propulsion system and runs on its own wheels guided by the rails.
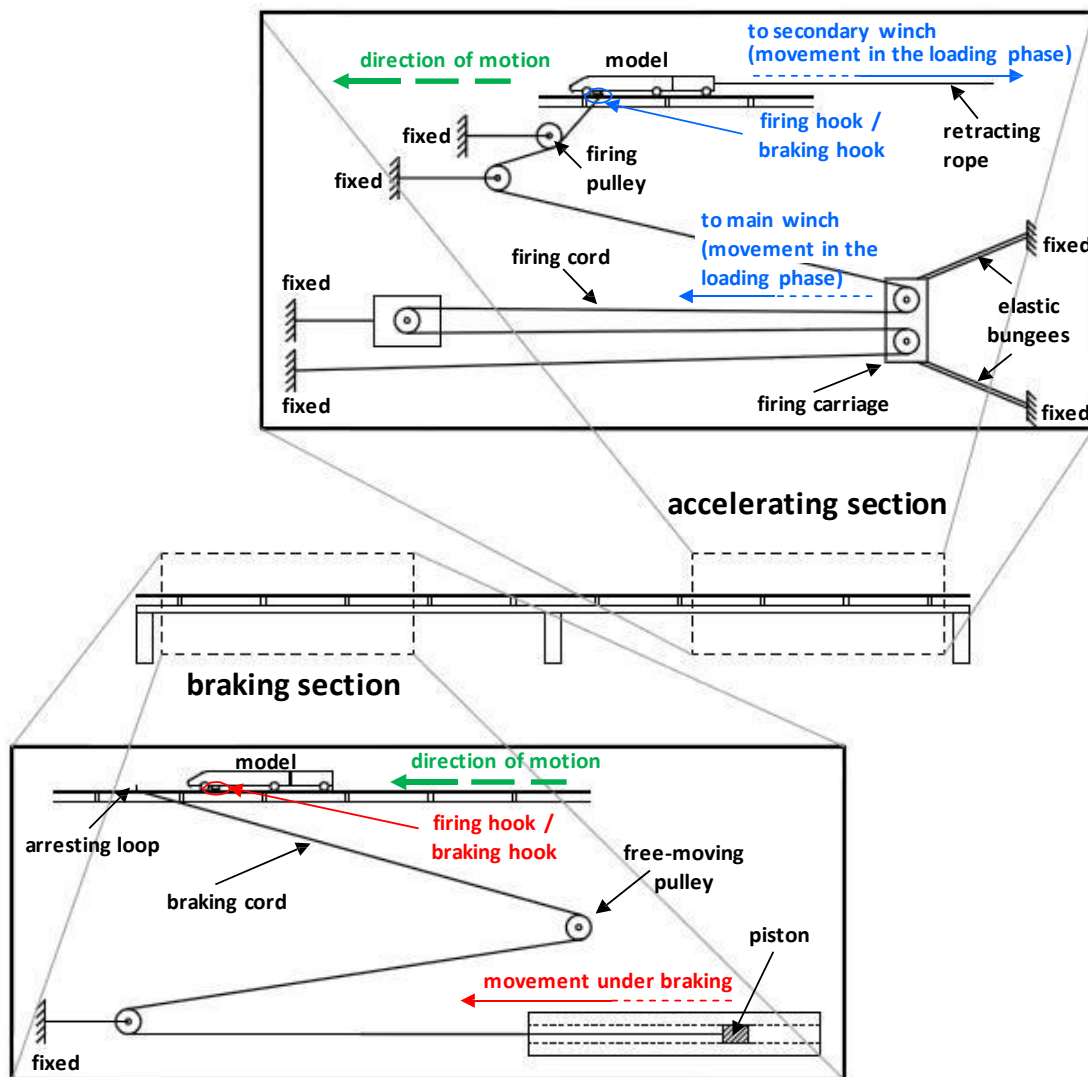
Figure 4.5 Schematic of the TRAIN rig propulsion system

One drawback of this propulsion system is that the vehicle speed decreases slightly along the test section due to friction and aerodynamic drag. An average speed decay of < 0.05 m/s per meter has been estimated for trains running in open air (at a nominal speed > 20 m/s). However, since the deceleration depends both on the characteristics of the train and on the trackside conditions, larger decays occur, for example, when the vehicles travel in tunnels or in crosswinds (section 4.7).

For tests in the presence of a crosswind simulation, the advantage of the TRAIN rig propulsion system is that it minimises the flow interferences around the vehicle. Slight distortions on the underbody

flow might occur because the wheel-sets of the scale-model do not entirely replicate the bogies of a real train. As further detailed in 4.4, a special design for the wheel-sets is required in order to withstand the high loads to which the scale-model is subjected during the launch and braking phases and to prevent derailment. However, when the model travels within the test section of the track, it is not attached to any external support, nor is there a slot in the ground between the rails. As discussed in section 3.6, the use of intrusive train supports and the presence of such a slot caused in the past unrealistic simulations of the flow around and underneath the vehicle. In this respect, therefore, the TRAIN rig enables an improvement.

4.3.2   New crosswind generator

The crosswind generator (CWG) which is currently in the TRAIN rig was designed and constructed as part of this PhD work. A previous crosswind generator (PCWG) already existed at the beginning of this project. However, past research (Baker et al., 2001) and an initial assessment showed that the crosswind simulation delivered by this device was inadequate for the present study (as detailed in appendix A). Consequently, a completely new system was developed.

The design of the new CWG was heavily constrained by the size of the building. Since no alterations were possible to the building envelope, not only had the entire apparatus to be accommodated inside it, but also the possibility of sucking and / or exhausting the air outside was precluded. To achieve the best possible flow simulation under such restrictions, a development process through prototype testing was carried out (figure 4.6). For details, please refer to appendix A.

Phases

Deliverables

- Assessment of the PCWG
- New CWG feasibility study

• Decision to develop a new CWG

Design specifications

Preliminary design

- Position within the TRAIN rig testing room
- Overall design
- Fans selection
- Fans configuration
- Air channel layout

Design optimization (through prototype tests)

- Prototype design and construction
- Optimization of the flow simulation:
  - Exact position of the fans
  - Air channel detailed design
  - Choice between blow-through and suck-through design

Final design

- Design for construction:
  - Electric circuit and control panel
  - Fans supporting frame
  - Air channel structural design
- Construction drawings

Construction and 'tuning'

- Installation
- Optimization of the final system (minor adjustments of the final design)
- Final Moving model test configuration
- Static test configuration

Flow characterization

- Flow measurements:
  - Moving model test configuration
  - Static test configuration

Figure 4.6 New CWG design process

As illustrated in figure 4.7, the new CWG is an open-circuit design in which the air is drawn through an enclosed duct positioned over the tracks and then recirculated inside the building. The air channel is horizontal and perpendicular to the tracks. The test section extends 1.685 m in the mean flow direction (transverse to the track), is 1 m high above the top of the rail (TOR) and spans a portion of track ( ) 6.35 m long. The airflow within the duct is generated by a bank of 16 axial flow fans [Ziehl-Abegg, FC071-4DF.7M.V6] (Ziehl-Abegg, 2010), that are positioned at the trackside and arranged in two rows of eight units. Schematics of the system in its '*final configuration*' are given in figure 4.8 and 4.9, while its characteristics are summarised in table 4.2. It should be noted, in figure 4.8 (detail A), the presence of a notch in the ground between the rails. This notch represents a difference between the Approximate Flat Ground (AFG) simulation adopted in these tests and the conventional FG, but was essential in order to enable the transit of the model along the track.
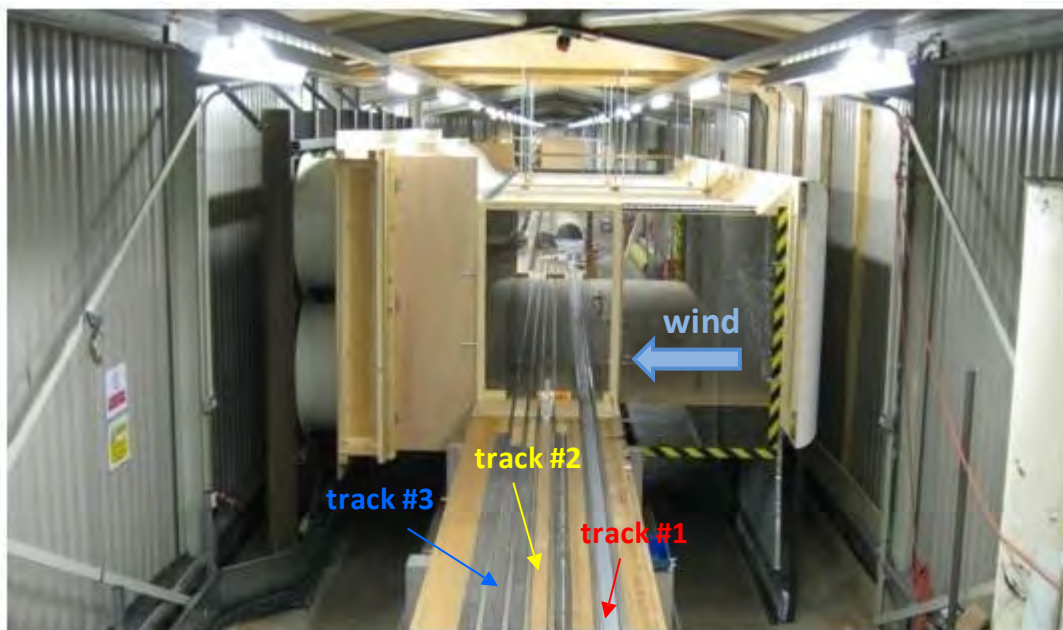
Figure 4.7 TRAIN rig internal view of the new CWG
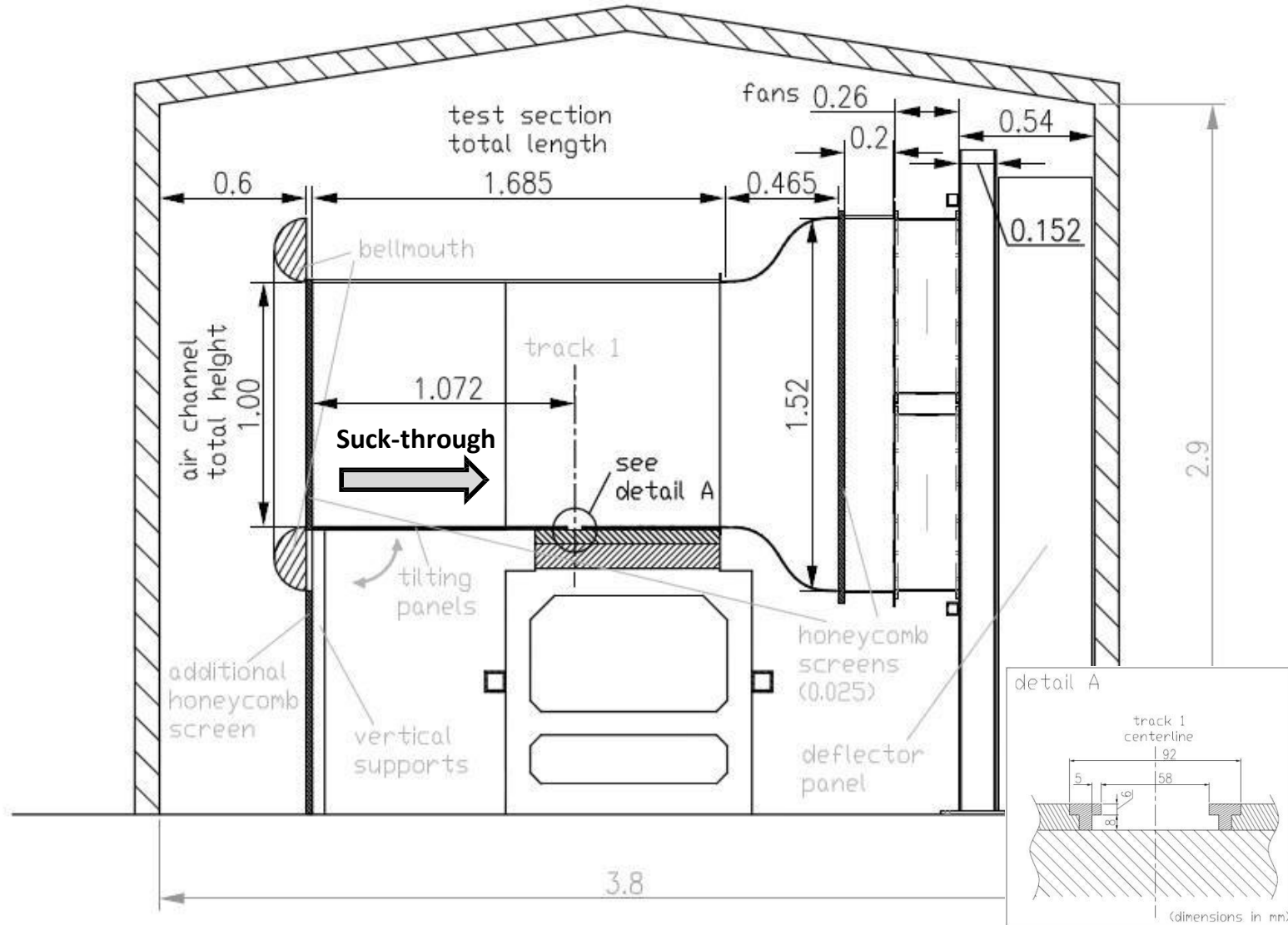
Figure 4.8 Schematic of the CWG final configuration (transverse section and ground simulation details)
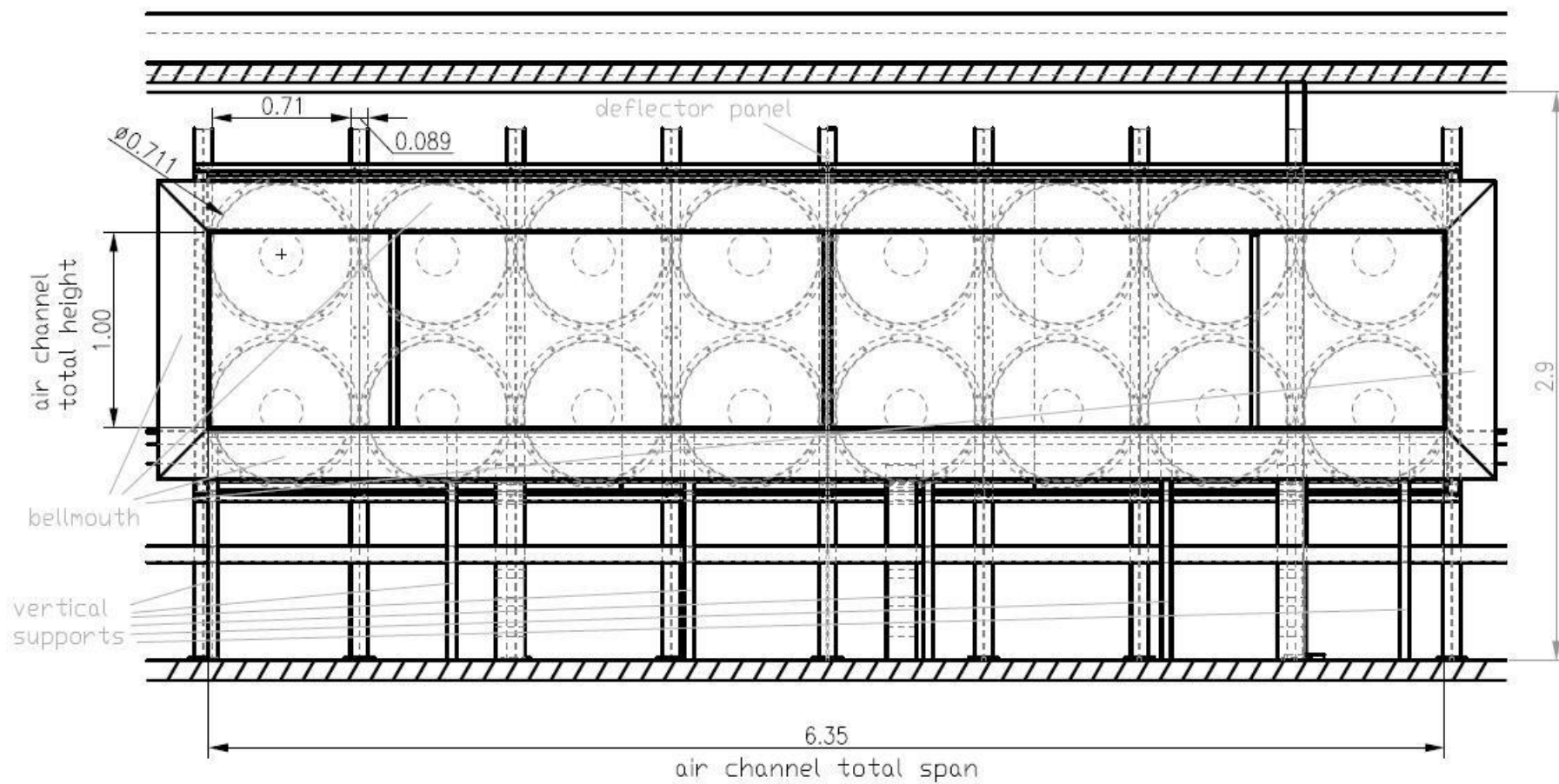
Figure 4.9 Schematic of the CWG final configuration (front view)

Position (within the TRAIN rig testing room)	• Towards the end of the test section according to track 1 travel direction (figure 4.4)
	• Flow fans on the far side of the testing room
	• Distances from the walls:
	  − Suction side: 0.6 m
	  − Discharge side: 0.54 m

Overall configuration	• Open circuit design • Suck-through design • Flow fans at the trackside moving the air horizontally and perpendicularly to the tracks • Ducted test-section (over the tracks)

Fans model	**Ziehl-Abegg FC071-4DF.7M.V6**
	• Type: AXIAL flow fans
	• Size:
	  − Nominal Diameter (ND): 0.71 m
	  − Case dimensions: 0.785 External Diameter (CD).; 0.26 m length
	• Motor:
	  − Integrated into the impeller hub
	  − 3-phases 400V ±10% (Y) 50Hz (4-poles)
	  − Nominal rotational speed: 1350 rpm
	  − Current consumption: 5.3 A (full-speed); 18 A (startup)
	• Number of blades: 6

Fans arrangement	• 16 units arranged in 2 rows of 8 units each

Air-channel layout	• Straight horizontal air channel directed perpendicularly to the tracks
	• Test-section size (Span x Height x Length): 6.35 x 1 x 1.685 m
	• Vertical expansion between the fans and test-section (expansion ratio 1.52)
	• Bellmouth and one aluminium honeycomb screen at the inlet
	• Additional aluminium honeycomb screen between the air channel and the floor, underneath the inlet section
	• Vertical deflector panel aligned to wind direction and positioned at mid-span between the fans and the wall
	• One aluminium honeycomb screen downstream of the expansion
	• Honeycomb screen specifications:
	  − Material: treated extra-hard 3003 alloy aluminium foil
	  − Size: 9 mm (cell diameter); 25.4 mm (length); 60 µm (foil thickness)
	• Portion of air channel spanning the 'down side' of the tracks to be semi-permanent (to allow access all along the testing room)

Table 4.2 CWG final specifications

In addition to the CWG *final configuration* described above, which was employed for the moving model experiments, a dedicated CWG arrangement was developed in order to undertake static tests. This consisted of a '*static track bed*' (24 mm thick) installed on the top of the actual TRAIN rig tracks that included a turntable in order to enable rotation of the train model with respect to the wind. By reproducing the same notch in the ground between the rails that characterised the ground simulation adopted for the moving model tests (outlined in figure 4.8), the use of this *static track bed* ensured consistency in such a ground simulation between static and moving tests. Furthermore, it enabled to anchor the model to the ground by clamping the wheel-sets of the train's leading car between the edges of the notch. A schematic and a photograph of the CWG configuration adopted for static tests are illustrated in figures 4.33 and 4.34, respectively, in the following section 4.6.

4.3.2.1   Crosswind simulation

Once the new CWG had been installed, flow measurements were carried out to characterise the crosswind simulation. These measurements comprised a reference horizontal wind profile (HWP) and two vertical wind profiles (VWPs). The former consisted of 64 spanwise measuring positions distributed parallel to the tracks, 0.2 m upstream of track 1, at 0.12 m height (i.e. the chosen reference height   equivalent to 3 m at full-scale). The VWPs were measured both 0.2 m upstream of track 1 and 0.15 m downstream of the air channel inlet, at spanwise positions 26 and 28. These positions were at 0.6 m and 0.4 m from the mid-span, respectively, and were chosen because (at the reference height) they were in front of the centre of the fan blades and in front of the impeller hub, respectively. Relating to the static model tests CWG configuration, additional HWPs were investigated. They were measured at   , both 0.2 m upstream of track 1 and 0.15 m downstream of the inlet, within the air channel span where the train model was positioned during the static tests (i.e. between stations 15 and 33). The measurement positions and the reference system that was adopted are illustrated in figure 4.10.
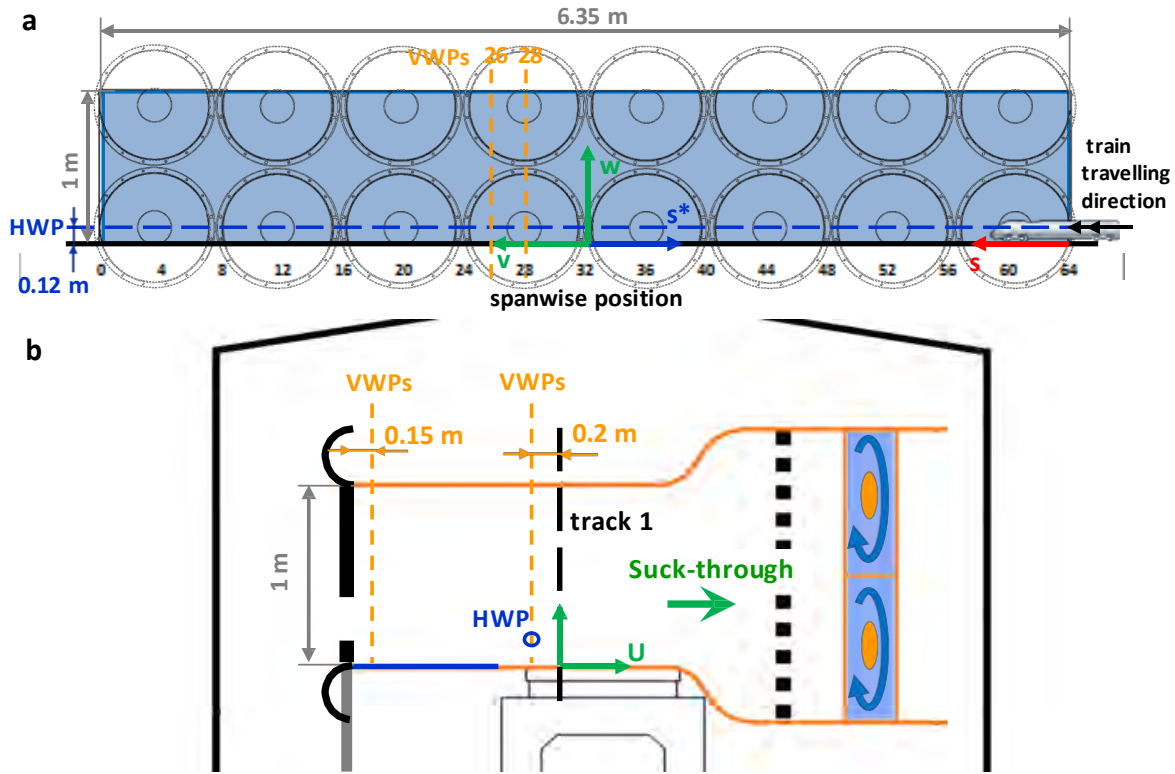
Figure 4.10 CWG flow characterisation reference system. a) Front view b) Side view

A set of Cobra probes [Turbulent Flow Ltd, series 100] (TFI, 2012) in combination with a manually operated traversing system were used to undertake the flow measurements. The specifications of the probes and data acquisition system are described in section 4.5.2, while the details of the experimental procedure are illustrated in appendix A.

According to the conventions in figure 4.10, in this thesis identifies the horizontal component perpendicular to the track and is referred as the nominal streamwise wind velocity, while and are the nominal lateral and vertical velocities, respectively. The mean (i.e., time average) value of each component is indicated with an overbar, while the relative turbulence intensities are denoted by , and (according to the conventions detailed in section 2.3).

The main characteristics of the crosswind simulation delivered by the new CWG are described in the following. The complete sets of flow measurements and a comparison with the performance of the previous crosswind generator are reported in appendix A.4.

Moving model tests configuration

Figure 4.11 illustrates the HWPs of the three mean wind velocity components (figures 4.11a and 4.11b), the mean differential static pressure (figure 4.11e), the turbulence intensities (figure 4.11c) and the integral length scales (figure 4.11d). In figure 4.11a and 4.11e, spanwise positions 16 and 35 are highlighted since where the trackside reference probes were placed during moving model tests (section 4.7). Table 4.3 reports spanwise averages associated with the HWPs presented in figure 4.11 and relative to the central part of the air channel that excludes one-half of the fan at both ends (i.e. between spanwise positions 5 and 59).
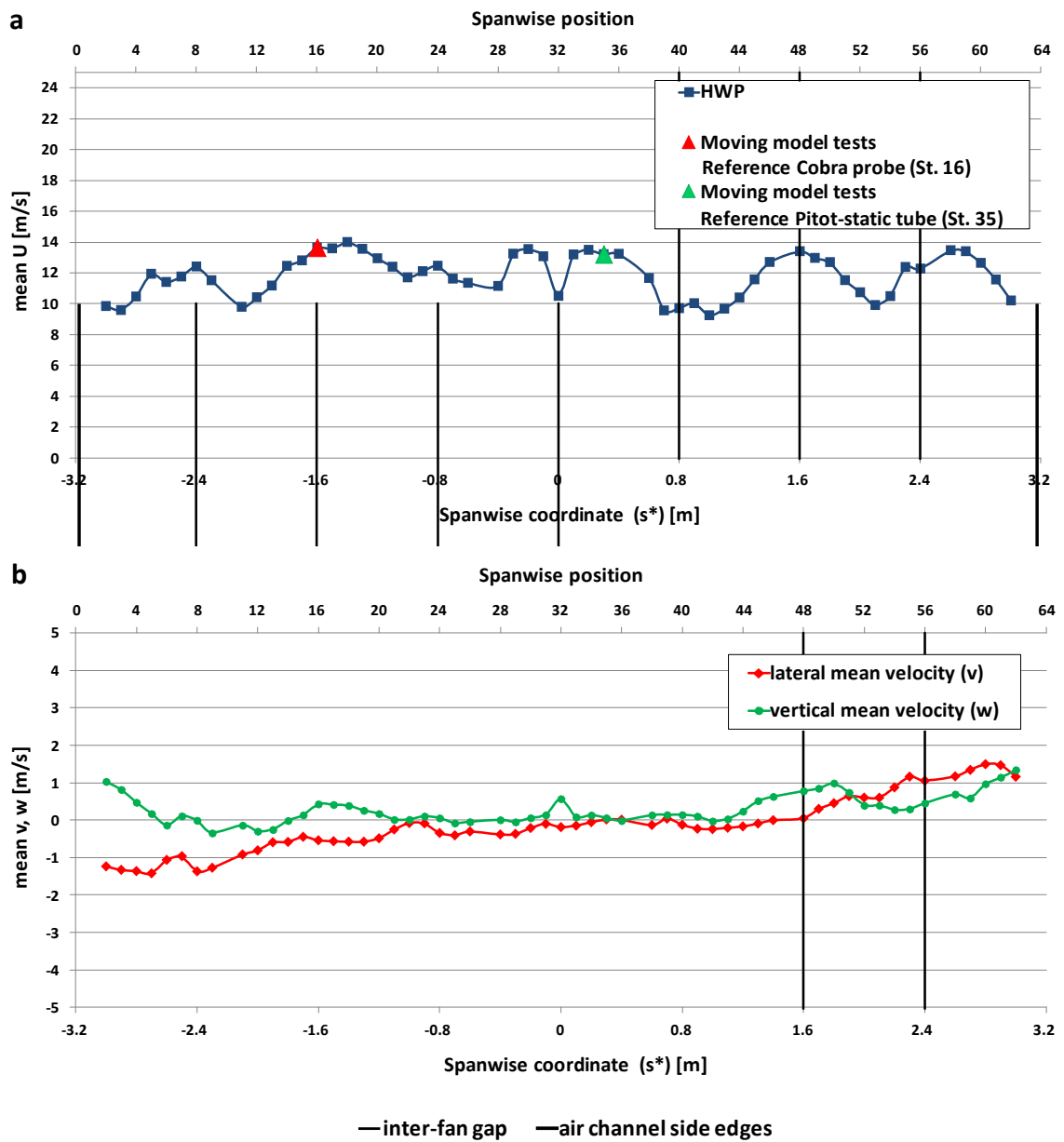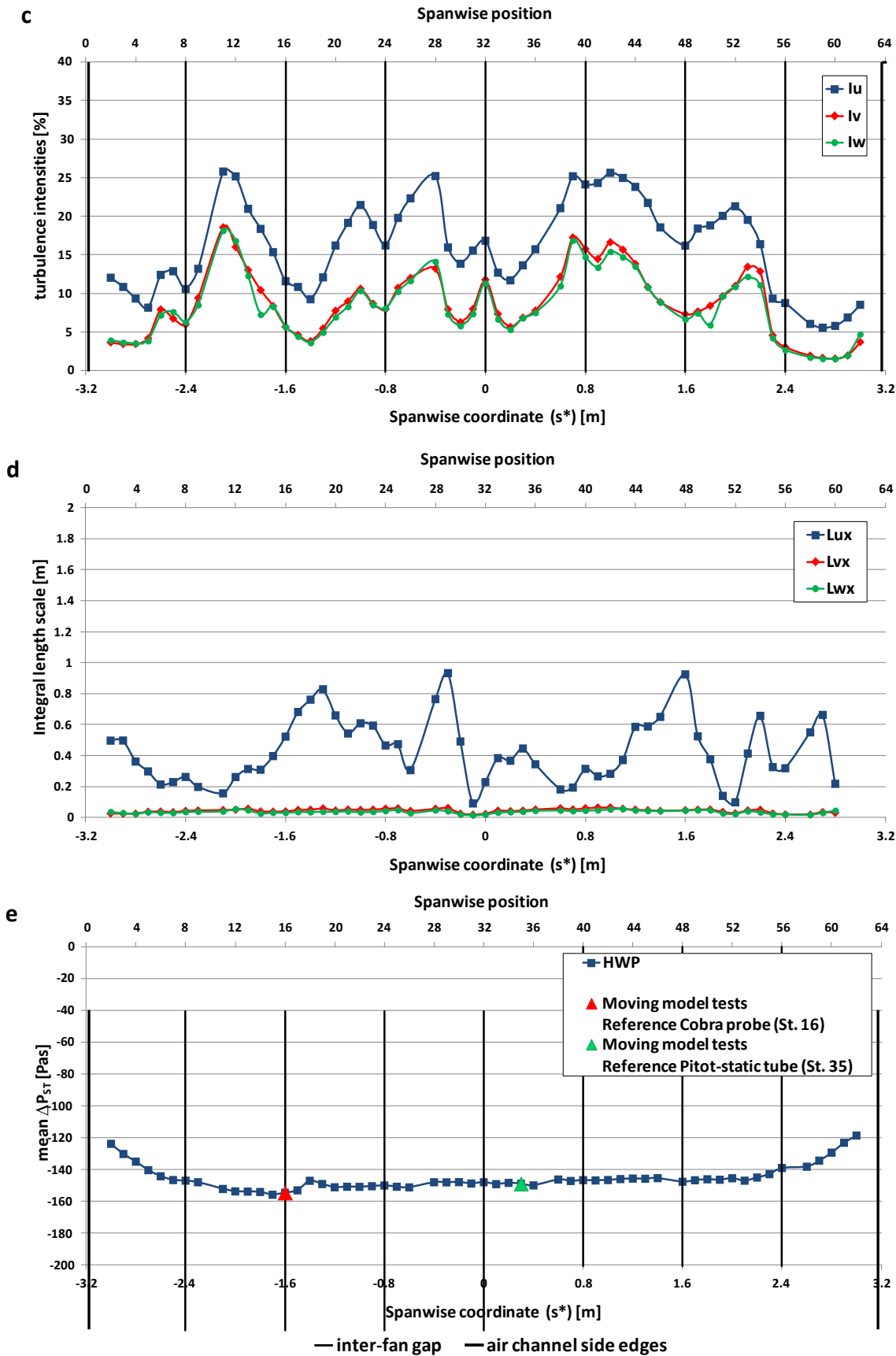
Figure 4.11 Crosswind simulation (moving model tests configuration): HWP. a) Streamwise mean velocity ( ). b) lateral and vertical mean velocities ( ). c) Turbulence intensities. d) Streamwise integral length scales. e) Mean differential static pressure ( )

SPANWISE AVERAGES	[m/s]	[m/s]	[m/s]	[%]	[%]	[%]	[m]	[m]	[m]	[Pa]
CENTRAL SPAN (pos. 5 – 59)	12	0	0.2	17	9	9	0.42	0.05	0.04	- 150

Table 4.3 Crosswind simulation (moving model tests configuration): spanwise averages at reference height

A limited spanwise uniformity can be observed in the HWPs for both the streamwise mean velocity and turbulence intensities, with a relationship emerging between the spanwise evolution of the two quantities (since the highest values of ,   and   occur in association with the wind holes). Figure 4.11b shows negative and then positive lateral mean velocities respectively on the left and right hand side of the CWG. According to the conventions in figure 4.10, this indicates a lateral velocity directed from the side edges towards the centre of the air channel and suggests that the flow is sucked in not only from the top and bottom of the inlet section, but also from either side. A certain level of spatial inhomogeneity can be noted in figure 4.11d also for the streamwise turbulence length scales   , while figure 4.11e outlines a negative and relatively homogeneous mean differential static pressure, apart from the areas at both ends of the air channel.

Figure 4.12 illustrates the VWPs of the streamwise mean wind velocity and turbulence intensity and the mean differential static pressure (measured at spanwise positions 26 and 28, both downstream of the air channel inlet and upstream of track 1).
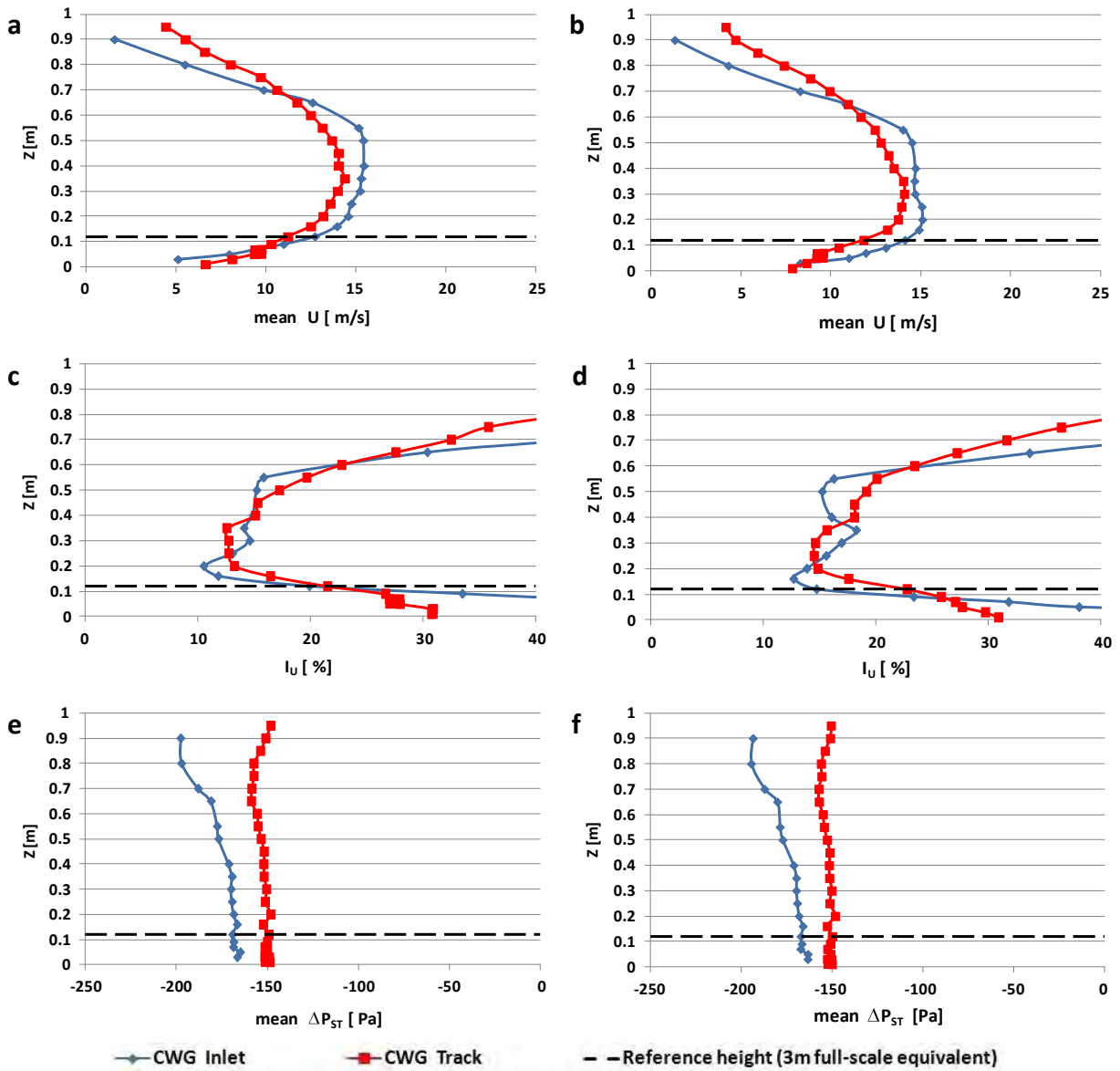
Figure 4.12 Crosswind simulation (moving model tests configuration): VWPs. a) Streamwise mean velocity ( ) at spanwise pos. 26. b) Streamwise mean velocity ( ) at spanwise pos. 28. c) Streamwise turbulence intensity ( ) at spanwise pos. 26. d) Streamwise turbulence intensity ( ) at spanwise pos. 28. e) Mean differential static pressure ( ) at spanwise pos. 26. f) Mean differential static pressure ( ) at spanwise pos. 28.

In the lower half of the air channel a decrease of streamwise mean wind velocity and an increment of mean differential static pressure can be observed moving from the inlet to track 1. Furthermore, at both positions, the streamwise mean wind velocity increases with the height. Similar to the evolution of an ABL profile, this trend represents a significant progress with respect to the PCWG performance (appendix A) and has been achieved by adopting a suck-through design. The examination of the upper half of the air channel outlines an asymmetry with respect to the air channel mid-height, with

a tendency of lower velocities and higher turbulence intensities to occur. This is consistent with larger irregularities and a higher level of turbulence in the flow recirculating in the top part of the building (rather than underneath the air channel).

A spanwise inhomogeneity of the mean wind velocity, which affects both the HWP and the VWPs, is larger than what would be desirable. Since it was caused by the space limitations imposed onto the new CWG, this spanwise inhomogeneity could not be reduced further. However, it is outlined in appendix A that the quality of the crosswind simulation provided by the new CWG led to significant improvements with respect to that delivered by the previous apparatus.

Static tests configuration

Figure 4.13 illustrates the HWPs of the three mean velocity components and mean differential static pressure that were measured in the presence of the CWG static test arrangement (additional data are included in appendix A). A comparison is presented between the HWP measured 0.15 m downstream of the inlet and 0.2 m upstream of track 1 (both at = 0.12 m) and also data relative to the moving model test CWG arrangement (from figure 4.11) are superimposed. Spanwise positions 15 and 16 are highlighted since this is where the reference trackside probes were placed during the static tests (section 4.6). The air channel span corresponding to the position of the first car and second half-car of the train model (section 4.4) are highlighted in grey.
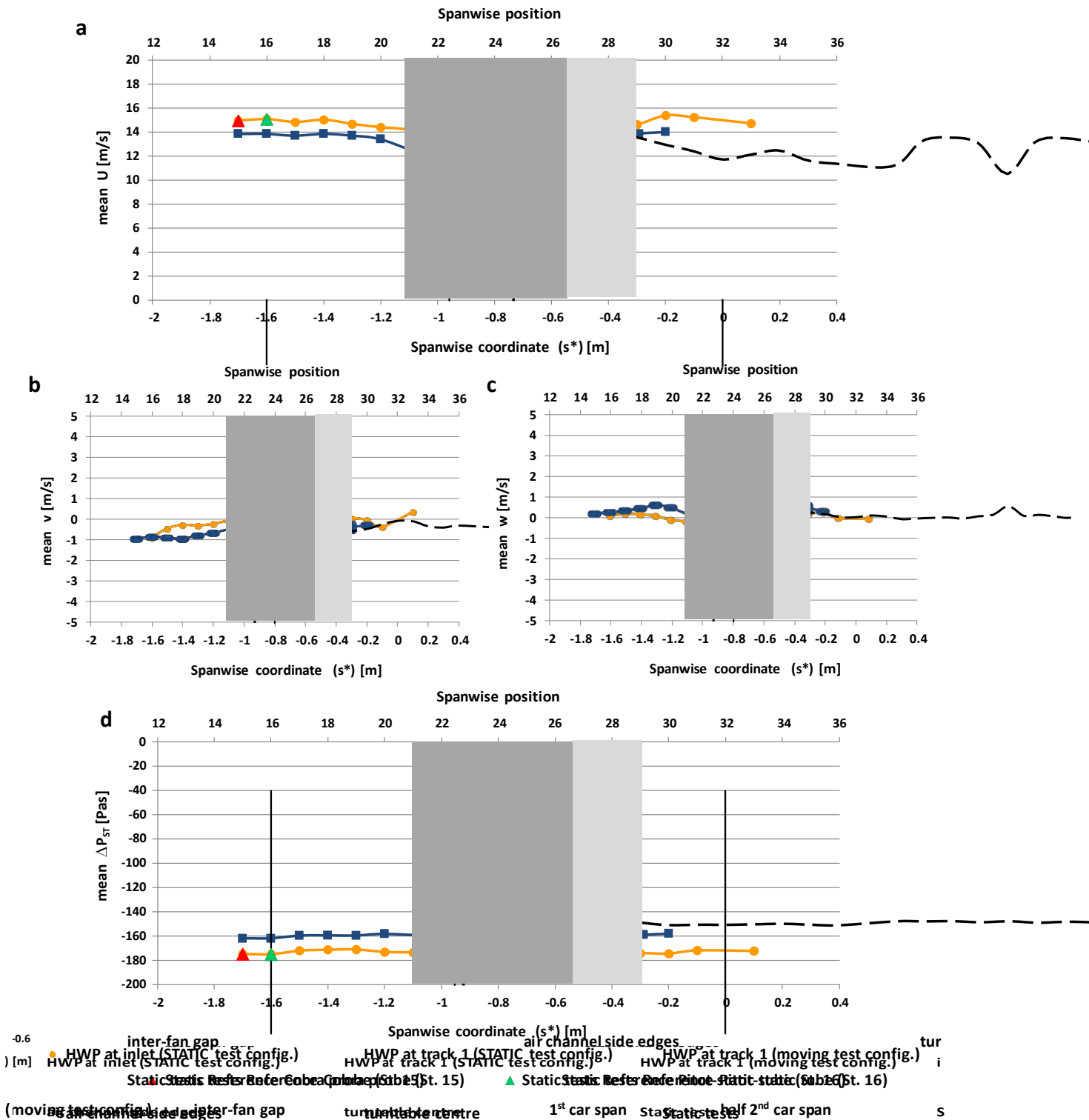
Figure 4.13 Crosswind simulation (static tests configuration): mean wind velocity HWP. a) Streamwise component ( ). b) lateral component ( ). c) vertical component ( ). d) differential static pressure ( )

The HWPs of the three mean velocity components denote a good level of spanwise uniformity within the span portion corresponding to the train position. Consistent with what is observed in figure 4.12, a reduction of the streamwise velocity and an increment of the mean static differential pressure

occur between the inlet and track 1. Upstream of track 1, an improved spanwise uniformity is reached with respect to the HWP relative to the moving model test arrangement. The spanwise averages associated with both the HWPs are reported in tables 4.4. In the view of static tests, such values were estimated considering only the span portion where the train model was placed (i.e., spanwise positions from 18 to 30).

SPANWISE AVERAGES	[m/s]	[m/s]	[m/s]	[%]	[%]	[%]	[m]	[m]	[m]	[Pa]
INLET	14.4	0	-0.1	12	3	4	1.21	0.05	0.08	- 174
TRACK 1	13.2	-0.5	0.3	12	5	5	0.94	0.07	0.05	- 159

Table 4.4 Crosswind simulation (static tests configuration): spanwise averages at reference height (span portion between positions 18 and 30)

4.4   Train scale-model

Figure 4.14 Class 390 Pendolino 1:25 scale-model on the TRAIN rig track

The 1:25 scale train used in the TRAIN rig experiments was a simplified model of a Class 390 Pendolino. The model consisted of a full reproduction of the leading car followed by a partial trailing car. For the purposes of this research only the leading car was considered, while the half-car was included to ensure a realistic flow around the length of the vehicle (according to the EN 14067-6

(CEN, 2010)). The model construction was contracted to Derwent Patterns Ltd, a Derby (UK) based model-making company familiar with the construction of such train models. A photograph of the model is shown in figure 4.14, while the overall dimensions are illustrated in figure 4.15.
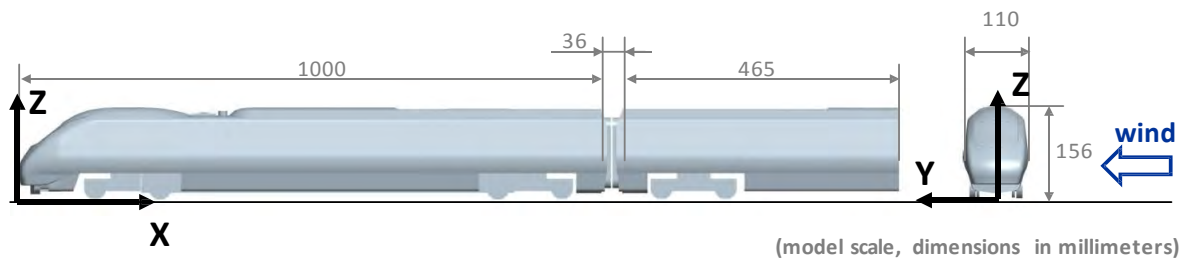
Figure 4.15 Class 390 Pendolino 1:25 scale-model (overall dimensions and reference system)

TRAIN rig models require an internal structure capable of withstanding the high loads transmitted during the launch and braking phases. Furthermore, they also have to include specifically designed wheel-sets that make them compatible with the propulsion system. Finally, excessive mass should be avoided so as not to limit the maximum achievable speed. Constructed in accordance to this design-practice, the Class 390 scale-model had an internal metal framework made up by a chassis and a spine joined together, and a shell that reproduced the external train geometry. The arrangement for the model is outlined in figure 4.16.

Figure 4.16 Class 390 Pendolino internal model structure

Model chassis

The model chassis consists of a metal bar of the type shown in figure 4.17a that carries the firing / braking hook and the two principal wheel-sets that ensure the vehicle movement. It is the element through which the loads acting on the model are transmitted into the track. Therefore, it has to ensure sufficient strength and rigidity without excessive total mass. On the Class 390 scale-model, the chassis consisted of an aluminium square hollow section with a side of 38 mm, a thickness of 3 mm and a length of 632 mm, which allowed it to have each wheel-set coincident with one of the bogies. As shown in figure 4.17b, each wheel-set comprised a pair of *'L-shaped brackets'* mounted between the wheels and the sides of the bar. These brackets were complying with the standard TRAIN rig design: specifically shaped in order to have their bottom wings fitting around the rail heads (whose '*T-shape*' is outlined in detail A of figure 4.8), they act as anti-lifting devices and prevent the model derailing but are the reason for the notch that is required in the track (figure 4.8).
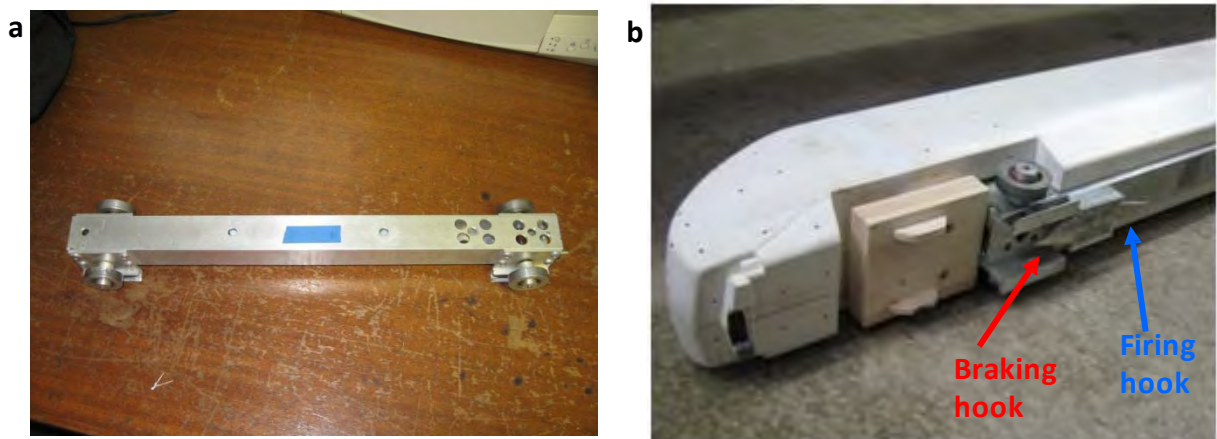
Figure 4.17 TRAIN rig scale-model chassis a) Typical chassis b) Front wheel-set and firing / braking hook on the Class 390 Pendolino model

Model spine

The spine is an aluminium rectangular hollow section (typically 30 mm x 55 mm) that runs along the length of the model. It is connected onto the top of the chassis through a set of three spacers. By design, the spine provides the link between the chassis and the external shell and, since it is not subjected to high loads, it does not require particularly high stiffness. For this reason, on the Class 390 scale-model it had a wall thickness of 1 mm and presented circular holes on both sides. This

reduced the weight and, more importantly, the holes gave good accessibility to the inside cavity, where the electric cables for the on-board instrumentation were accommodated (section 4.5.1).

Model shell

The model shell comprises two half-shells for each car. They are made of glass-fibre reinforced plastic (GRP or '*fibreglass*') and are approximately 3 mm thick. Having split the envelope of the train on a vertical plane oriented along the central-longitudinal axis, the two half-shells of the same car are symmetrical and reproduce one side of the external geometry each (with the exception of the bogies). A number of pins and transverse brackets located on their internal sides provide connection to the spine. Once assembled onto the latter, each pair of half-shells is held in position by wrapping it with tape (figure 4.14). To ease replaceability in case of damage (which is not uncommon during moving model tests), the bogies are modelled separately from the rest of the train, made of balsa-wood and then screwed onto the external shell (figure 4.17b).

An external shell split on the vertical-longitudinal plane is normally adopted for TRAIN rig scale-models because it allows quick inspection and maintenance to the internal framework. In this case, it was also indispensable to enable the installation, setting and periodic checking of the on-board instrumentation. In order to prevent unrealistic flow interferences, extra positioning pins were added to minimise any possible misalignment between the two half-shells. Furthermore, their joint all around the train perimeter was covered by tape in order to avoid any gap and further smooth any artificial irregularity (figure 4.14).

Compared to the reference geometry of a real Class 390 Pendolino train, the TRAIN rig scale-model had a number of minor alterations. Modifications for ease manufacturing were implemented by reducing the details on the train roof and by simplifying the shape of the bogies. The bogies were only partially modelled on the leading car. As highlighted in figures 4.18a and 4.18b, both the rear part of the first bogie and the front part of the second bogie were replaced by the chassis wheel-sets. Furthermore, an additional trailing wheel was accommodated at the tail of the train to prevent

excessive oscillation (figure 4.18c). Finally, on the first car, a slight modification in underbody geometry between the bogies consisted of the chassis beam protruding ~3 mm from the original profile (figure 4.17b). This had to be accepted in order to preserve a correct scaling of the distance between the train body above the ground.

Figure 4.18 Class 390 Pendolino model: details of the bogies a) First bogie on the leading car b) Second bogie on the leading car c) Bogie on the half trailing car

These geometrical alterations of the nominal train geometry should be taken into account wherever a comparison between TRAIN rig and other wind tunnel tests results is performed (appendix H). However, the use of the same scale-model enabled a comparison between static and moving model test results with no reduction in consistency.

4.5 Instrumentation

A variety of on-board and trackside measurements were collected during TRAIN rig tests. The on-board measurement system collected the surface pressures detected at a number of taps on the train and, for moving model tests, the signal from an on-board light-beam detector. The trackside measurements involved the ambient and crosswind conditions and, for moving model tests, the train speed and the signals from a pair of trackside light-beam detectors.

4.5.1 On-board pressure measuring system

An internal measuring system capable of monitoring the crosswind loads on the train is necessary for

this project that the only viable option was to use a stand-alone system, completely accommodated undertaking moving model experiments in crosswinds (section 3.4.2). Considering the characteristics

of the propulsion system and of a typical TRAIN rig scale-model, it became clear at the beginning of

excessive oscillation (figure 4.18c). Finally, on the first car, a slight modification in underbody inside the scale train and unlinked to the external background.

As discussed in chapter 3, in a wind tunnel static force measurements are normally undertaken in order to obtain the non-dimensional aerodynamic coefficients relating to rail vehicles. However, previous research has outlined significant difficulties arising from the use of force balances during moving model tests. Relying on this past experience and following an assessment study, an on-board system based on surface pressure measurements was used for the TRAIN rig campaign. Hence, direct measurements of the pressure distribution on the vehicle surface were undertaken, while the overall forces and moments were estimated by discrete integration.

The on-board pressure measuring system that was developed consisted of a battery-powered stand-alone data logger, 15 miniaturised differential pressure transducers and one light-beam detector. A set of three-core electric cables connected the sensors to the logger. A total of 165 pressure taps were installed on the scale-model leading car and connected to the transducers via silicon tubing. Finally, a second set of silicon tubing, a small sealed reservoir and a pressure manifold, all accommodated inside the scale-model, formed the reference pressure circuit. A schematic diagram of both the pressure and electronic circuits is illustrated in figure 4.19.
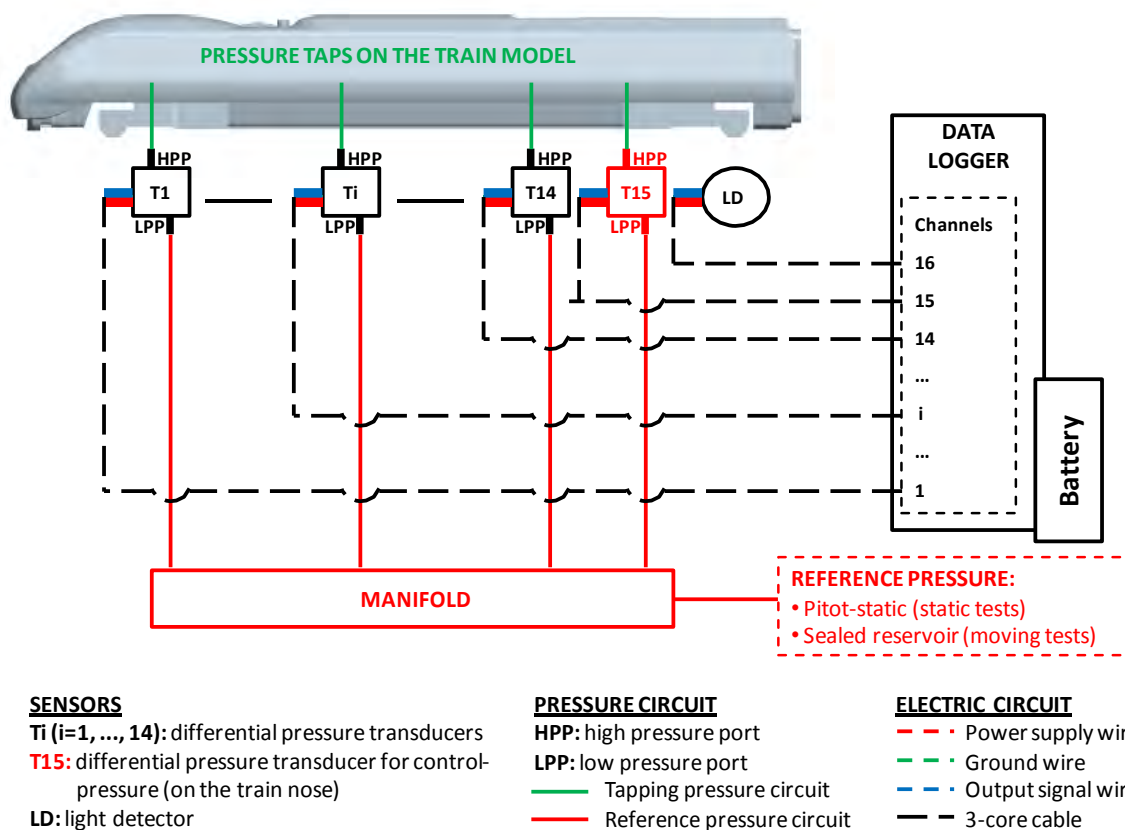
Figure 4.19 On-board pressure measuring system: schematic of the electronic and pneumatic circuits

4.5.1.1   Stand-alone data logger

The data logger employed on the scale train was custom-built for this application. This was necessary in light of the limited space available inside the model and taking into account the relatively severe accelerations (~2 to 3 g and higher) to which it was subjected during the launch and braking phases. The design and construction of the electronic system, as well as the development of its control software, were carried out by Mr. Mani Entezami of the Birmingham Centre for Railway Research and Education (BCRRE). Technology currently under development for a wide range of applications was used (Entezami et al., 2011).

The on-board data logger comprises two printed circuit boards (PCB) and one battery (figure 4.20) and presents the characteristics detailed in table 4.5. The system has a 16-bit resolution, is capable of monitoring 16 analogue channels at a maximum sampling rate of 4kHz and uses an SD memory card integrated into the mainboard for data storage. In addition, it provides a power supply (at 5 V) and

sampling to be started and stopped remotely from a computer or to be self-triggered. The self-trigger criterion can be set either as a countdown or as one of the channels' output signals exceeding a pre-determined threshold. The communication between the logger and a computer is provided by a USB cable and a dedicated software was developed (as part of the package) for controlling the device. This software enables the setting, sampling / real-time monitoring and data downloading (into a .tsv file format). A screenshot of the software main interface and an example of a data output file are shown in figure 4.21.
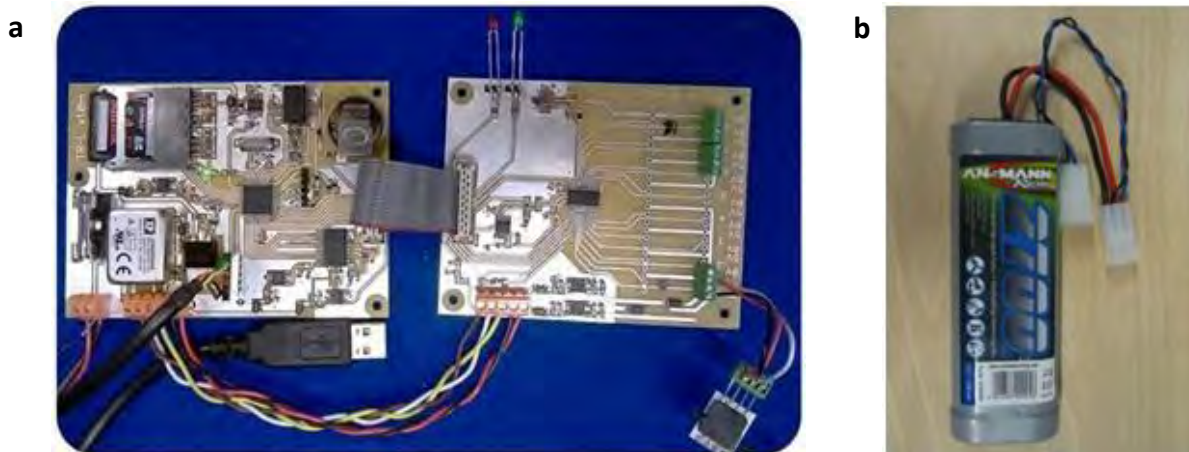
Figure 4.20 On-board stand-alone data logger a) Main boards b) Battery

Model Name	RRLog16
Resolution	16 bits
Number of channels	16
Voltage range	0 - 5 V
Sampling Rate	4 kHz (maximum)
Storage	4 GB (expandable up to 32 GB)
PC connection	USB 1.0 / 2.0
Power supply	7.2V 2700mA NiMH Battery
Dimensions	140 x 80 x 15 mm (PCB 1) 110 x 80 x 15 mm (PCB 2) 135 x 47 x 25 mm (battery)
Environmental operating conditions	0 °C to +80 °C overall.

Table 4.5 On-board data logger specifications

Figure 4.21 On-board data logger a) Control software main panel b) Data output file

As shown in figure 4.22, the entire data acquisition system (i.e., data logger PCBs and battery) was installed inside the trailing vehicle of the Class 390 Pendolino scale-model. Two LEDs were fitted into the model envelope on the windward side towards the tail of the train to enable immediate and continuous monitoring of the logger working state (figure 4.23a). In addition, on the train tail were accommodated also an activation / deactivation switch (figure 4.23b) and a multi-pin circular socket that allowed computer access and battery recharging.
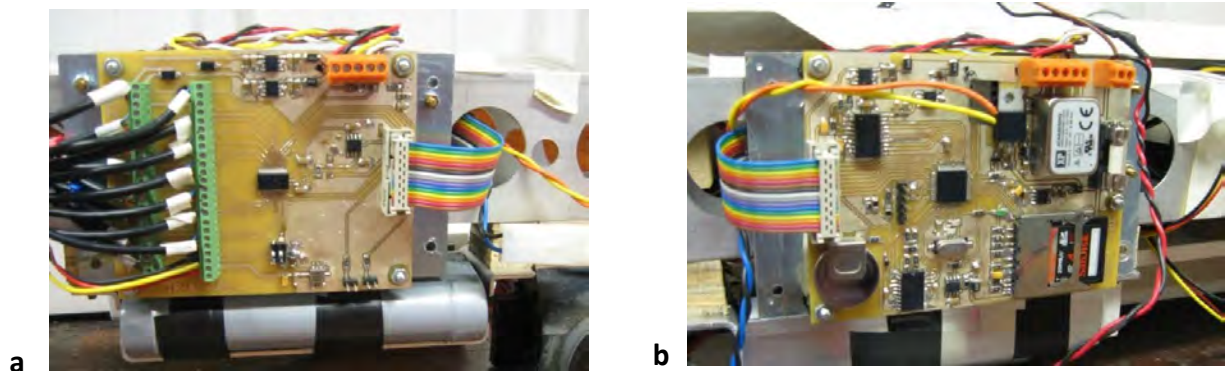
Figure 4.22 On-board data logger mounted inside the Class 390 model trailing car a) Windward side b) Leeward side
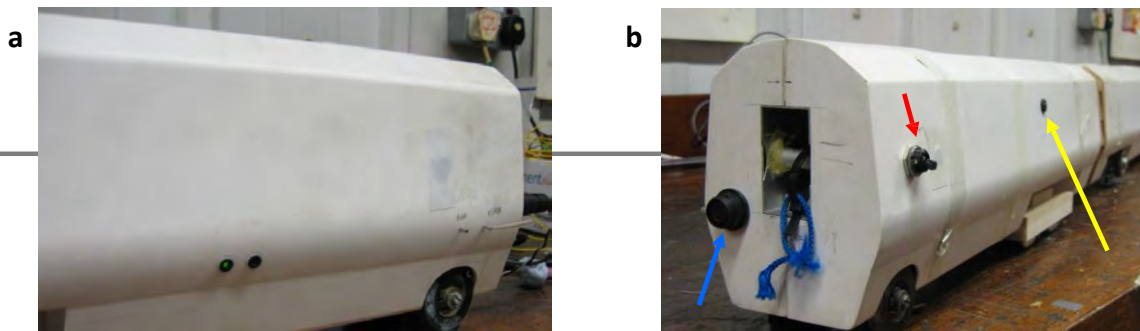
-PIN CONNECTOR

ON / OFF SWITCH

ONBOARD LIGHT DETECTOR

Figure 4.23 On-board data logger external interfaces a) LEDs on the windward side b) On-board light-beam detector, on / off switch and multi-pin connector on the leeward side and on the rear

4.5.1.2 Pressure transducers

A total of 15 pressure transducers [Sensortechnics, HCLA12X5PB] (Sensortechnics, 2012) were used in the on-board measuring system (figure 4.24). These are piezoresistive miniaturised-amplified differential low pressure sensors with a ±1250 Pa range, similar to those adopted in the past on-board measuring systems illustrated in section 3.4.2.2. Extremely compact, they are compatible with the power supply (5 V) and the analogue intput signal range (0 – 5 V) of the data logger.
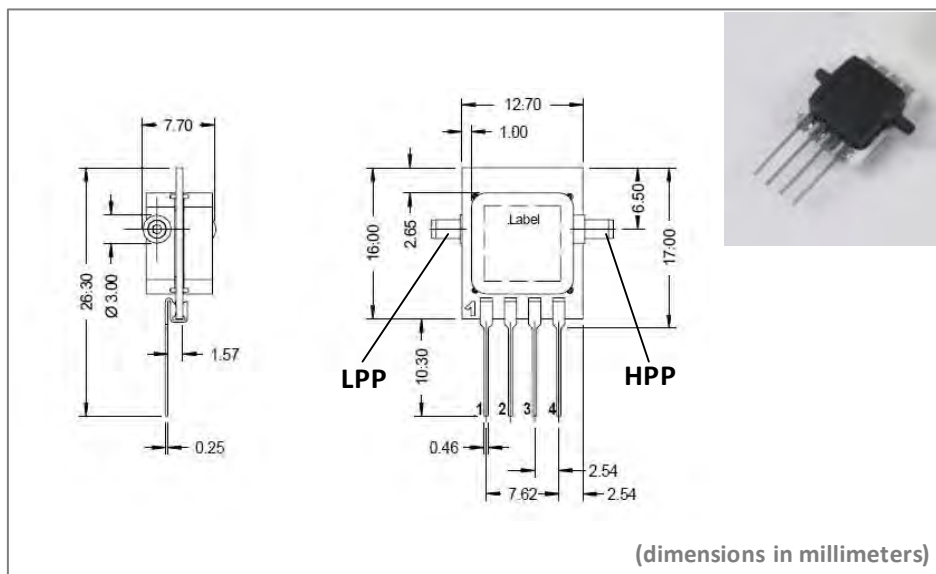
Figure 4.24 Miniaturised differential pressure transducers (Sensortechnics, 2012)

As differential sensors, these transducers have two pressure ports each, identified as high and low pressure ports and indicated as HPP and LPP, respectively. It should be noted that these designations are nominal and, as these sensors can measure both positive and negative differential pressure, the arrangement does not affect performance. In the arrangement that was adopted, the HPP monitored the pressure at the taps on the vehicle surface, while the LPP were provided with a common reference pressure (figure 4.19). According to the manufacturer's specifications (Sensortechnics, 2012), the HCLA12X5PB transducers have a typical non-linearity and hysteresis error which is 0.05% of the full scale span (FSS = 2500 Pa). To refine this estimation, and to identify individual calibration curves for each sensor, a static calibration against a Betz micro-manometer was performed (appendix B).

The transducers were mounted inside the first car of the scale train by attaching them onto the spine using a pressure sensitive adhesive (figure 4.25).
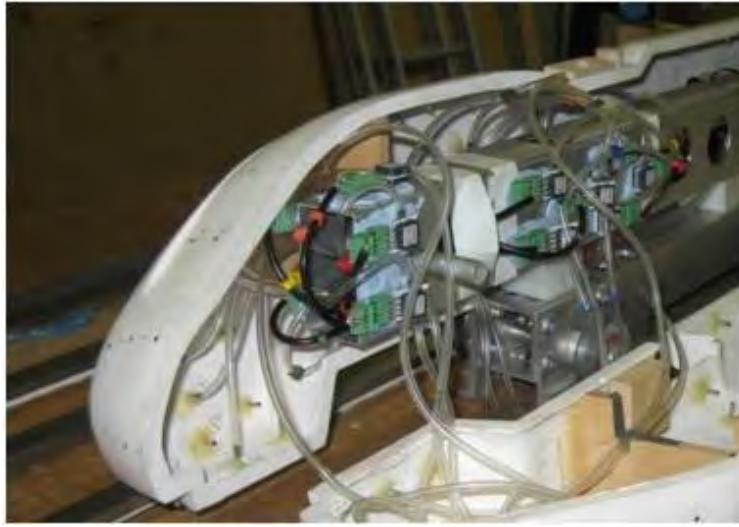
Figure 4.25 Miniaturised pressure transducer installation inside the Class 390 model

4.5.1.3 On-board light-beam detector

One light-beam detector was employed as part of the on-board measuring system. A phototransistor sensor [Vishay Intertechnology Inc., VISHAY-TEPT5600] (VISHAY, 2011) was powered and monitored (on channel 16) by the on-board data logger simultaneously to the pressure transducers (figure 4.19). Sensitivity was calibrated to deliver ~4.6 V when the sensor was exposed to normal lighting and ~0 V when it was illuminated by a strong light-beam. This on-board light-beam detector was accommodated inside the trailing vehicle and its sensor was exposed on the leeward side (figure 4.23b). Having set a series of light sources at specified locations along the track (figure 4.36), during moving model tests the signal from this sensor provided a number of 'position markers' on the time histories of the pressure transducers for alignment purposes (section 5.3).

4.5.1.4 Pressure taps

A total of 165 pressure taps were provided on the train's leading car. One reference tap was positioned on the nose of the train (figure 4.26) while the other 164 were distributed on 14 loops. Figure 4.26 shows the position of these loops along the vehicle and table 4.6 reports their distances

from the nose (normalised to the first car length $\quad$ = 1000 mm). In addition, figure 4.27 illustrates the distribution of the taps on the perimeter of each loop.

The pressure tap on the nose was constantly monitored on channel 15 of the data logger during any test that was carried out, so as to assess the consistency of the data from different runs. The pressure taps on loops 1 to 8 (110 in total, indicated in figure 4.26 with black lines) were monitored in groups of 14, through subsequent runs, during both static and moving model experiments. During static tests, pressures were measured also at all taps on loops from 9 to 14. During moving model tests, instead, extra measurements with respect to those on loops from 1 to 8 were undertaken on loops from 9 to 13, but only at taps in the train underbody. Accordingly, train sections corresponding to loops 9 to 14 are highlighted in red in figure 4.26, where dotted lines indicate rings having a reduced number of taps (i.e., 6 or 7 rather that 12 to 14).
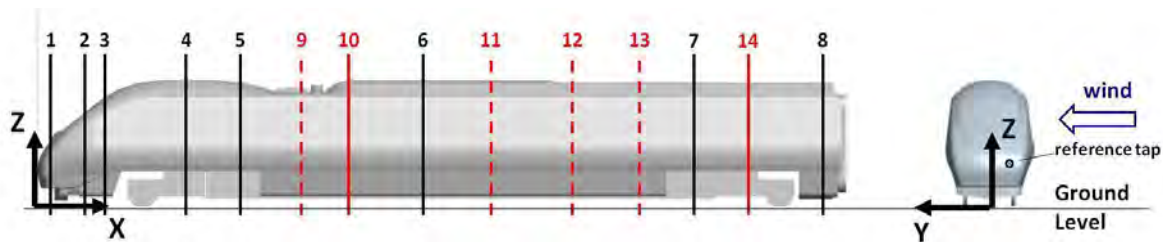
Figure 4.26 Distribution along the Class 390 leading vehicle of the loops of pressure taps (red lines indicate loops on which pressures were measured only in the train underbody during moving model tests; dotted lines indicate loops with pressure taps only on the roof and underbody)

Loop	1	2	3	4	5	6	7	8
X_j/L	0.018	0.055	0.085	0.185	0.25	0.48	0.81	0.97

Loop	9	10	11	12	13	14
X_j/L	0.325	0.39	0.56	0.665	0.75	0.89

Table 4.6 Longitudinal positions of the loops of pressure taps (in red loops on which pressures were measured only in the train underbody during moving model tests)
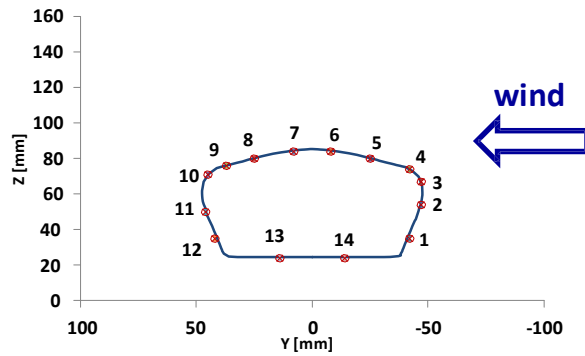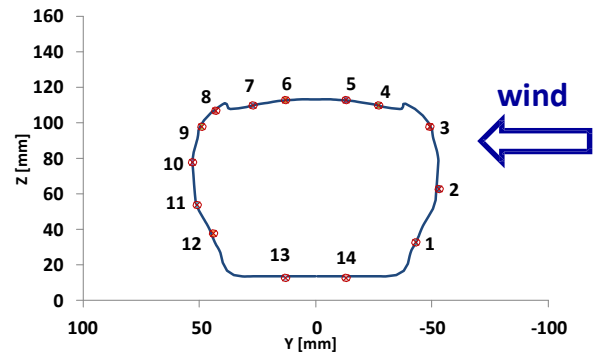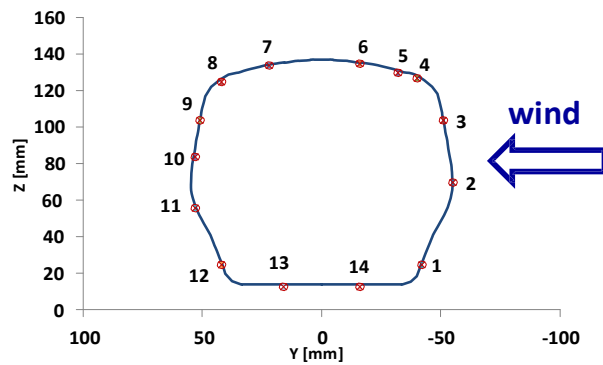
Loop 1, Loop 2, Loop 3, Loop 4, Loop 5, Loop 6, Loop 7, Loop 8
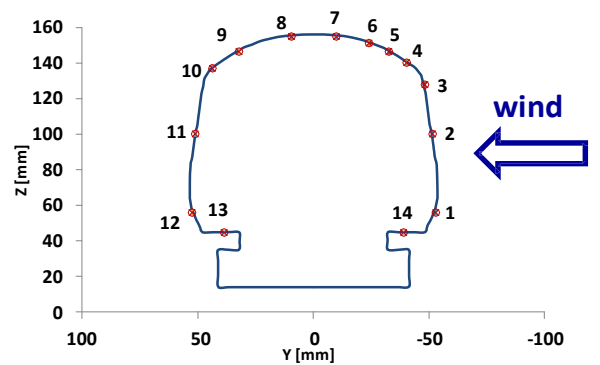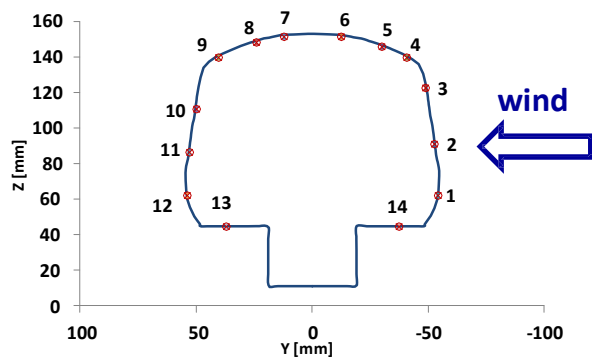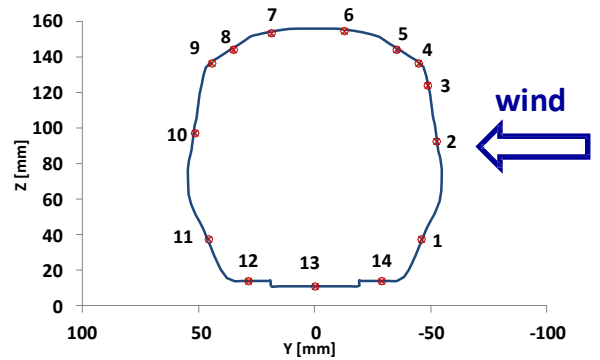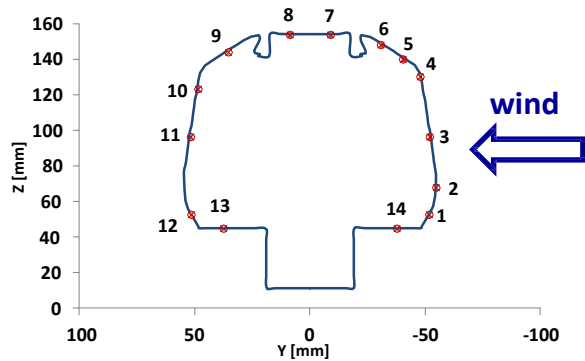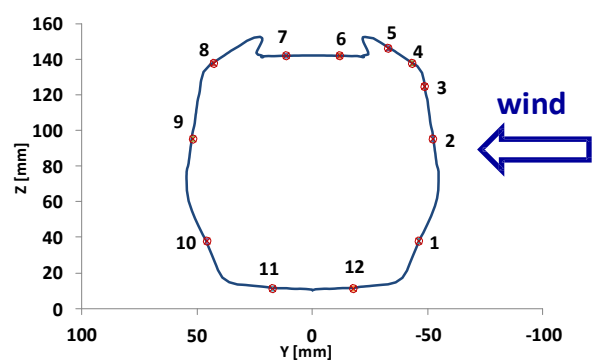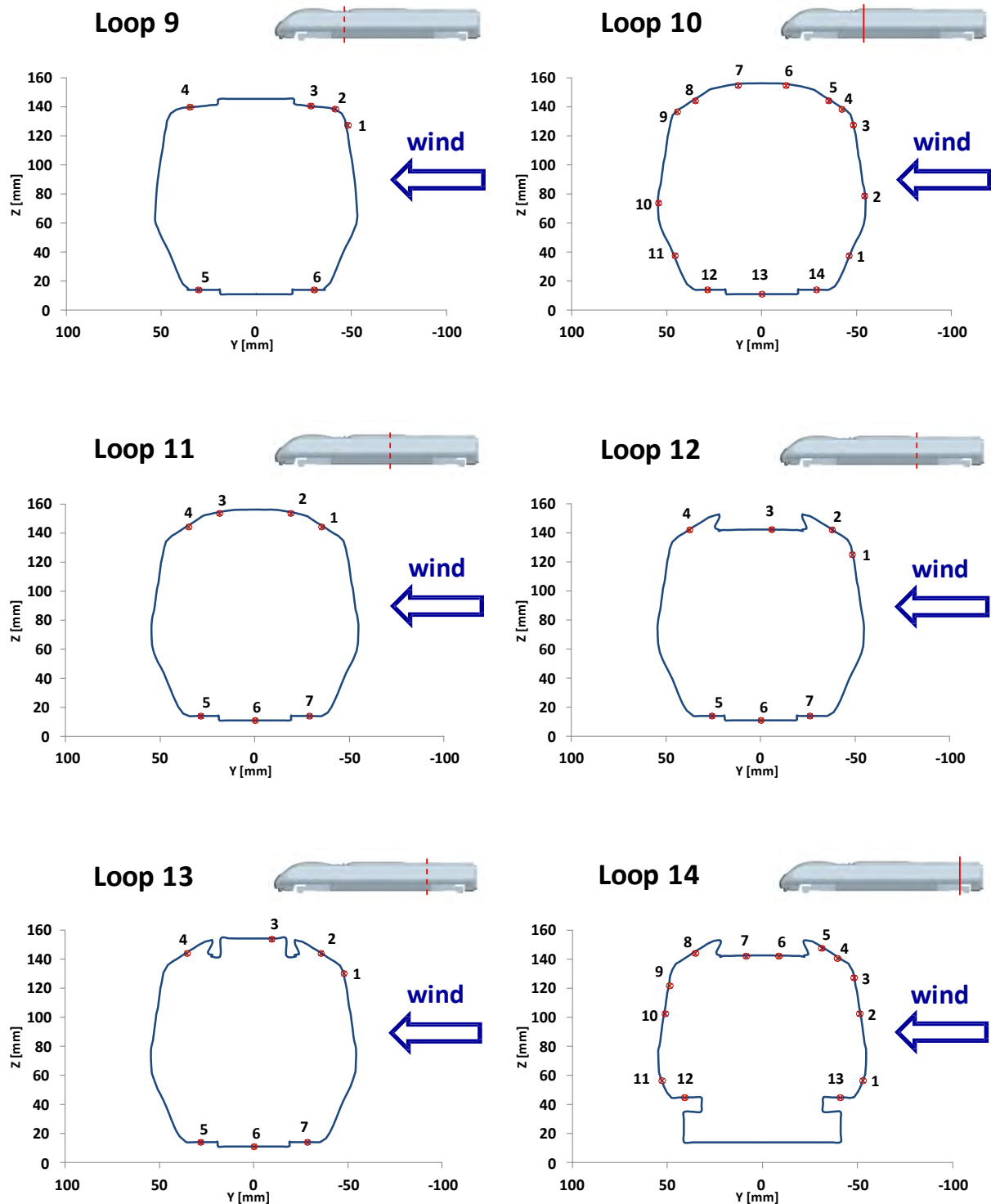
Figure 4.27 Distribution of pressure taps on each loop

The pressure taps were made of a series of stainless steel '*tube-inserts*' fitted into pre-drilled holes in the GRP model shell. These *tube-inserts* had a 1.5 mm inner diameter (ID) and a 2 mm outer diameter (OD) and were 12 mm long. Once set with no overhang on the external side, they were

glued using an epoxy structural adhesive on the interior side of the shell to provide the internal pressure ports illustrated in figure 4.28.

a

b
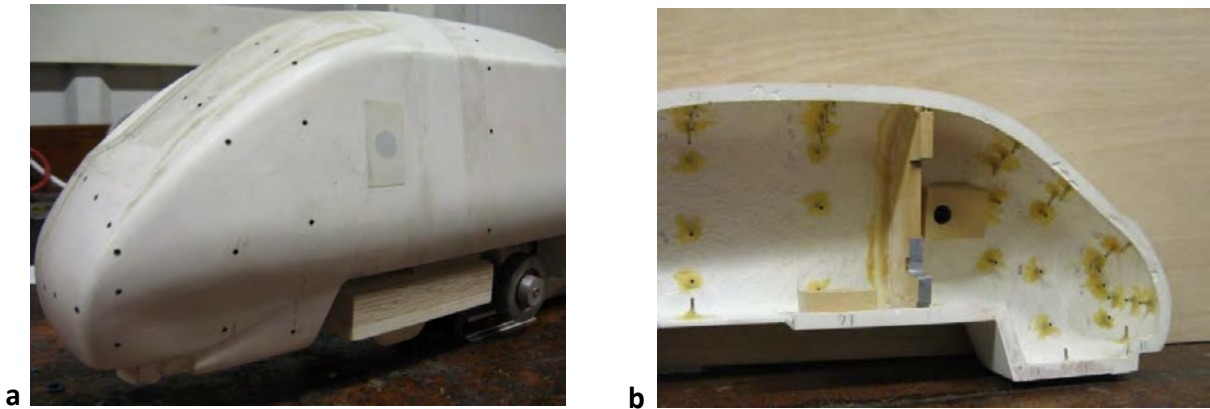
Figure 4.28 Pressure taps installation on the Class 390 model

4.5.1.5   Pneumatic circuit

Silicon tubing having 1.6 mm ID and 3.2 mm OD was used to connect the taps to the HPP of the transducers (figure 4.29a). Since channels 15 and 16 on the data logger were used for monitoring the *'reference pressure tap'* on the train nose and the light-beam detector, respectively, 14 channels remained available for simultaneous pressure measurements on the body of the first car. As further detailed in sections 4.6 and 4.7, the pressure was measured on different groups of 14-taps by opening the model and switching the tubing connection in subsequent runs (section 4.6.1 and 4.7.1; appendix C).

Tubing lengths up to 0.6 m were used for connecting the pressure taps to the transducers. Estimating the lowest resonance frequency according to Feather (1961), as $f = \frac{c}{4L}$, where c is the speed of sound conservatively taken as ~300 m/s, while and are the tubing length and inner diameter, respectively, the lengths prevented resonances at less than ~125 Hz. Considering that the raw data were low-pass filtered at 70 or 120 Hz, for static and moving model tests, respectively

(chapter 5), significant tubing resonance interference was avoided.

A second set of silicon tubing formed the reference pressure circuit that, through a manifold, provided a common reference to the LPP of all the transducers (figure 4.29b). For static tests, the

reference pressure was the wind static pressure detected by a Pitot-static tube positioned inside the CWG (section 4.5.2.2). For moving model tests, it was taken from a sealed reservoir installed inside the model trailing car. As outlined in chapter 5, a unified normalisation was introduced through proper data reduction to keep consistency between static and moving model test.
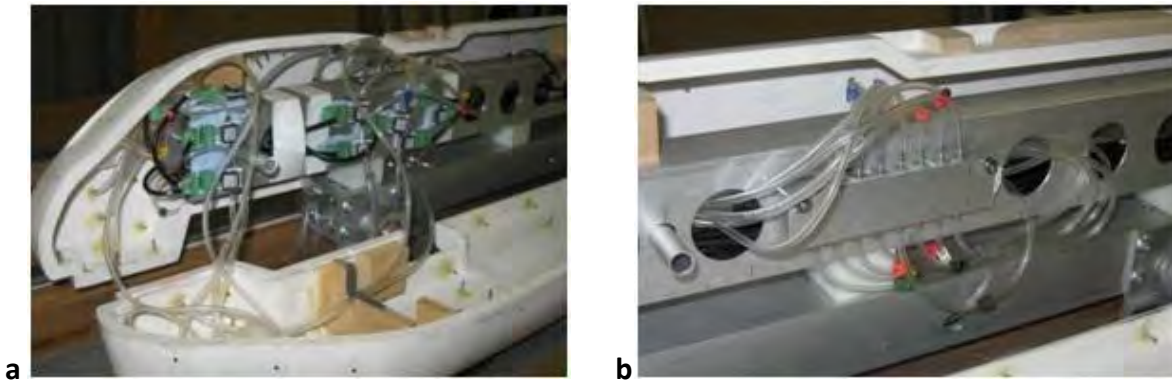
Figure 4.29 Pneumatic circuit a) Connection to the pressure taps b) Manifold in the reference pressure circuit

4.5.2 Trackside measurements

4.5.2.1 Ambient conditions

The ambient conditions of temperature, ambient pressure (i.e., barometric pressure) and relative humidity were monitored in still air during all experiments. A weather station [Oregon Scientific Inc., BAR208HGA] (Oregon Scientific, 2012) measured temperature and relative humidity, while a barometer [Greisinger Electronic GmbH, GBP3300] (GREISINGHER, 2012) measured the barometric pressure. The measuring resolutions were ±1 °C, ±1% and ±10 Pa, the accuracies ±2 °C, ±10% and ±200 Pa, respectively. All measurements were manually recorded into an Excel spreadsheet file.

4.5.2.2 Wind measurements

Measurements of crosswind velocity and static pressure were undertaken both in dedicated flow characterisation sessions and during the static and moving model experiments. In the first situation,

a set of Cobra probes was used for mapping the horizontal and vertical wind profiles delivered by the

new CWG (section 4.3.2.1). In the second situation, one Cobra probe and one Pitot-static tube were

employed for monitoring the actual wind conditions at two reference locations during each run (of

both static and moving model tests).

The characteristics and specifications of the equipment are described in the following, while the experimental setup adopted for the flow characterisation and for static and moving model tests are illustrated in appendix A and in sections 4.6 and 4.7, respectively.

Cobra probes

Cobra probes of the type illustrated in figure 4.30 [Turbulent Flow Ltd, series 100] (TFI, 2012) were used for measuring wind velocity and static pressure. These are 4-hole pressure probes capable of resolving the three components of the mean and fluctuating velocity within a 45° 3D-angle with a maximum frequency response of 2kHz. In addition, they measure the wind static differential pressure, i.e., the wind static pressure with respect to the ambient pressure in still air, to which they are vented using a silicon tubing system from the base: = . The manufacturer provides Cobra probes already calibrated and together with a '*TFI data acquisition system*' that includes also a control software package (section 4.5.2.5). The measurement accuracy (as declared by the manufacturer) is 0.3 m/s and ±1° for the velocity magnitude and direction, respectively, while it is approximately ±5 Pa for the differential static pressure. Positioning and alignment of the probes was checked at the beginning of each test session, ensuring accuracies of ±5 mm and ±2°, respectively.

a   b

Figure 4.30 Series 100 Cobra probe (TFI, 2012)

Pitot-static tube

A Pitot-static tube connected with two differential pressure transducers [Sensortechnics HCLA02X5PB] (Sensortechnics, 2012) was also employed during the static and moving model experiments. One transducer measured the wind dynamic pressure ( ) as the difference between

the total and static pressure from the Pitot-static tube. Consistent with the Cobra probes, the other transducer monitored the wind differential static pressure (   ) as the difference between the static pressure from the Pitot-static tube and the barometric pressure in still air (figure 4.31). Apart from the reduced measuring range, which in this case is ±250Pa, these transducers are of the same type as those used on board the train model (static calibration provided in appendix B). They were powered by a power supply unit [Caltek Industrial Ltd., PSD 30/3B] (BST, 2007) and monitored (as external analogue inputs) using the *TFI data acquisition system*.
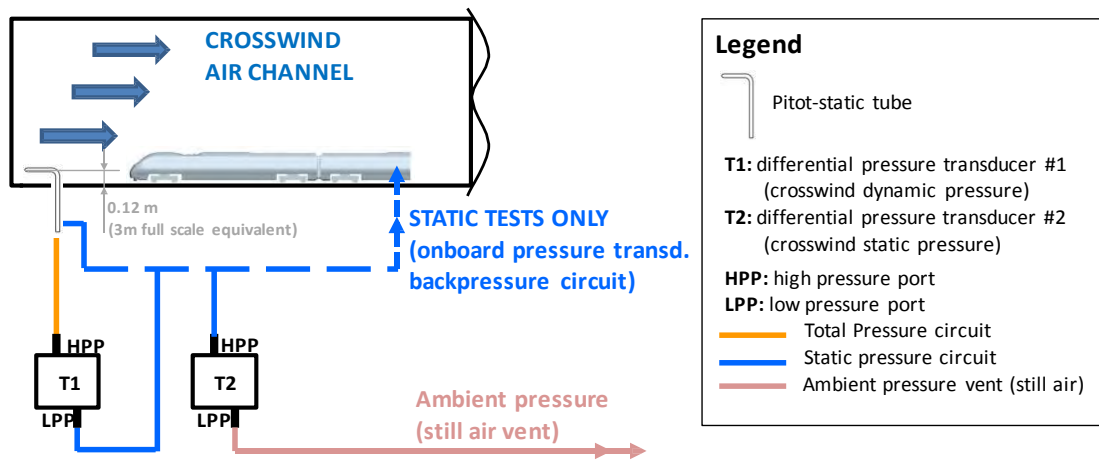
Figure 4.31 Pitot-static tube pressure circuit

4.5.2.3 Train speed

During moving model tests, the vehicle speed at the entry and exit of the crosswind section was detected by two speed detectors (with an accuracy of ±0.1 m/s). Each of these consists of two pairs of photoelectric units that, once positioned as illustrated in figure 4.32, create two light gates at a distance of 1 m along the track. The system measures the time delay between the interruption of such light-beams caused by the train passing, calculates the vehicle speed and displays it on an output screen. During the tests, the readings of the train speed measurements were entered manually into an Excel spreadsheet file after every run.

Figure 4.32 Vehicle speed measuring device and trackside light source and light-beam detector

4.5.2.4 Trackside light sources and light-beam detectors

During moving model experiments, two light sources were positioned along the track at either side of the CWG, with two light-beam detectors placed in front of them on the opposite side of the track (figure 4.32 and 4.36). These light-beam detectors were of the same type as that used on board the scale-model (section 4.5.1.3), were powered by the same unit used for supplying the Pitot-static tube pressure transducers and their signals were sampled by the *TFI data acquisition system* simultaneously to the flow measurements . Delivering a steady signal at ~0 V that peaked (at ~5 V) when the train passed in front of them (since it broke the light-beam projected from the light source), these sensors enabled the time histories of the trackside measurements to be synchronised with the train transit through the CWG (section 5.2.2.2).

4.5.2.5 Data acquisition system

All the trackside measurements were recorded using the *TFI data acquisition system* provided by the Cobra probe manufacturer (TFI, 2012). It consists of an interface-unit connected to a computer via USB cable and a software package called '*Device Control*'. The interface-unit includes an integrated analogue-to-digital (A/D) converter and enables monitoring (in parallel) of four cobra probes and 6 external analogue inputs via (BNC) coaxial connectors.

4.6   TRAIN rig static model tests

The methodology applied for TRAIN rig static tests was similar to that commonly used in conventional wind tunnel experiments on static vehicles. Accordingly, using the CWG static test *track bed* (section 4.3.2), the train model was mounted statically inside the air channel and rotated with respect to the oncoming wind in order to simulate the required 30° yaw angle (figure 4.33 and 4.34).
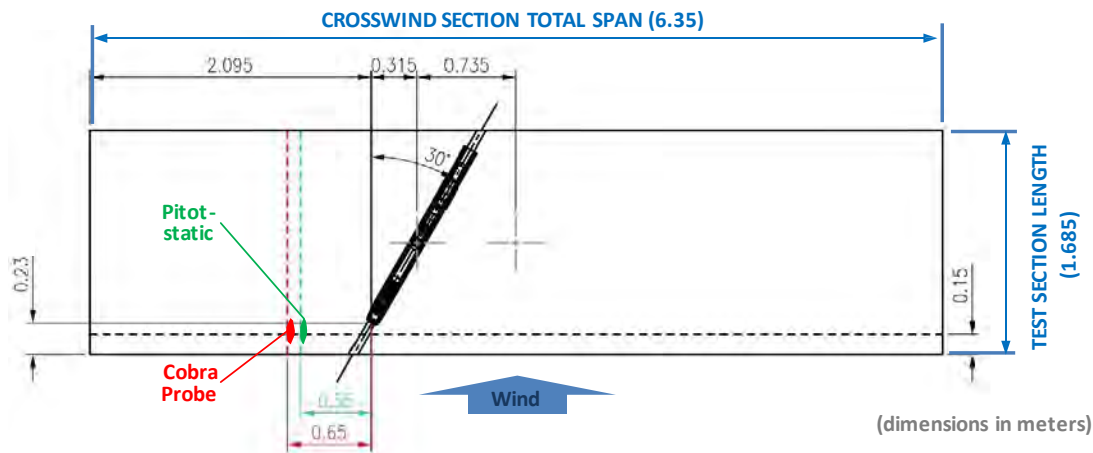
Figure 4.33 TRAIN rig static tests: train model position and trackside instrumentation setup

Figure 4.34 View of the Class 390 scale-model inside the CWG during the static tests

Figures 4.33 shows how the train model was placed slightly to the left of the CWG mid-span. In light of the flow characterisation (section 4.3.2.1), this position was chosen in order to gain a better spanwise uniformity in the onset wind. In addition, in figure 4.34, the short distance (~0.23 m) between the nose of the train and the honeycomb at the inlet of the air channel can be observed.

This arrangement was the best possible considering the dimensions of the train model and the length of the CWG in the streamwise flow direction. However, it is acknowledged that such a test configuration had some limitations. It is likely that the reduced distance between the inlet and the train nose was not sufficient to ensure an undisturbed onset wind. In addition, it prevented the residual unsteadiness and turbulence in the ingested flow (that remained once it had passed through the inlet honeycomb screen) from significantly reducing upstream of the train. This caused, in turn, a sensitivity of the surface pressure on the train to alterations in the environment external to the air channel. These alterations were difficult to keep under control and caused a run-to-run variability in the pressure measurements on the train nose that led to a relatively high experimental uncertainty (section 5.4).

As explained in section 4.5.2.2, one Cobra probe and one Pitot-static tube were employed for monitoring the reference wind conditions. In a conventional wind tunnel setup, the reference wind measurement would be taken upstream of the model, at a distance such that the wind profile can be assumed undisturbed. In the TRAIN rig arrangement this approach could not be adopted because of space limitations and, therefore, the alternative layout illustrated in figure 4.33 was adopted. The probes were positioned at a reference height above the ground of   = 0.12 m, 0.15 m downstream of the channel inlet, shifted approximately 0.55 and 0.65 m to the left (according to the wind direction) with respect to the train nose. Dedicated preliminary measurements showed that such a lateral separation prevented any mutual flow interference between the probes and the train.

Related to these static tests, the wind velocity and differential static pressure measurements for calculating the non-dimensional aerodynamic coefficients were those detected by the Pitot-static tube, while those from the Cobra probe were used as a backup. Furthermore, the Pitot-static tube provided the reference pressure to the on-board differential pressure transducers through the pneumatic circuit illustrated in figure 4.31. An assessment was carried out to verify that the pressure fluctuations transmitted through such a reference pressure circuit did not interfere with the dynamic

component of the differential pressure measured by the on-board pressure transducers and no significant interferences were found.

4.6.1 Static test procedure

Since a limited number of simultaneous channels were available on the on-board data logger, the process in figure 4.35 was iterated and multiple runs were carried out in order to monitor all the pressure taps on the train's leading car.
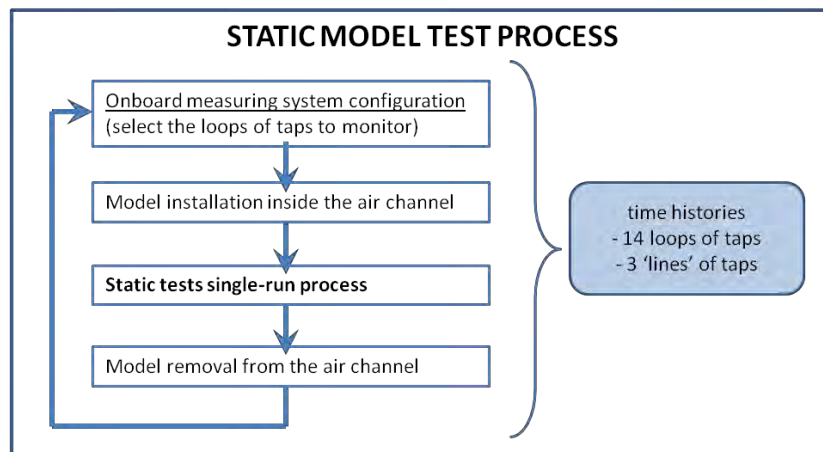
Figure 4.35 TRAIN rig static test process

Before positioning the Class 390 scale train inside the air channel, the leading car was opened to set the configuration of the on-board pressure measuring system, i.e., to connect the pressure transducers to the desired group of taps. After that, once the scale-model had been closed, it was anchored inside the CWG and then a single-run was carried out (following the procedure described in full in appendix C). During each test, time histories 30 s long were recorded in still air conditions (i.e., before switching on the CWG) in order to monitor the 'zero pressure offset' (   ) of both on-board and trackside pressure transducers. Then, in the presence of a stabilised crosswind simulation, time histories of 60 s were sampled at 4 kHz, for the on-board pressure measurements, and at 1 kHz for trackside measurements. The former sampling frequency was chosen for consistency with the moving model test, while the latter was sufficient for resolving the spectral content of the simulated wind. After completion of the run, finally, the train was removed from the CWG and the process was repeated.

As anticipated in section 4.5.1.4, during static tests surface pressures were measured at all the taps available on the Class 390 leading car. Firstly, the pressure taps on the same loop were monitored simultaneously during each run and all the loops were characterised in sequence. Then, extra runs were carried out investigating 3 'lines of taps', i.e., groups of measuring points distributed longitudinally along the vehicle (figure 7.6 in section 7.4). Typically, each measuring configurations was tested only once. However, loops 2 and 6   were monitored several times to assess the measurement repeatability (section 5.4).

4.7   TRAIN rig moving model tests

The TRAIN rig moving model experiments consisted of multiple series of runs carried out by propelling the scale train along the TRAIN rig test track 1 whilst the CWG was running in full-operational mode.

Figure 4.36 illustrates the arrangement of the trackside instrumentation described in section 4.5.2 inside and in proximity of the CWG.
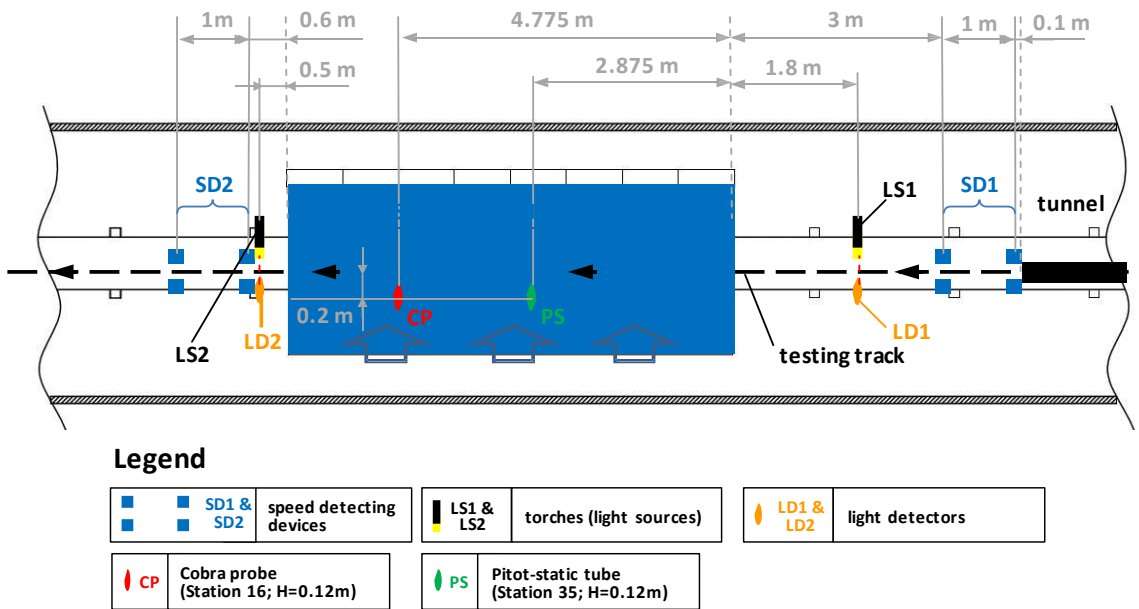
Figure 4.36 TRAIN rig moving model tests: trackside instrumentation arrangement

Before starting the moving model experiments, a number of preliminary tests were undertaken for calibration purposes: the on-board data logger was tested in operation, the vehicle speed and

launching processes were calibrated and the design adopted for the on-board reference pressure circuit was assessed.

Vehicle speed and launching process calibration

For the moving model experiments in this study, a nominal vehicle speed of 20.8 m/s was required in order to achieve a 30° nominal yaw angle of the relative crosswind. This was in light of the 12 m/s spanwise average of the streamwise mean wind velocity (   ) taken at the reference height   = 0.12 m. The speed decay experienced by the scale-model whilst travelling within the CWG was ~1.1 m/s. Caused by the combined effect of friction and aerodynamic drag, this was measured during preliminary tests and later confirmed by the statistics relative to the entire test campaign. Accordingly, assuming a linear decrement, the target speed at the entry of the CWG was set as 21.4 m/s.

To achieve this target, the nominal launching tension to be applied to the TRAIN rig elastic *launching* mechanism (section 4.3.1) was identified as 7.25 kN, with a margin of ±0.15 kN resulting from susceptibility of the propulsion system performance to ambient conditions, particularly the temperature.

A tolerance range of ±0.6 m/s with respect to the target was accepted in light of the run-to-run vehicle speed variability inherent in the characteristics of the TRAIN rig propulsion system. This ensured average yaw angles within ±1° with respect to the nominal target of 30°. The vehicle speed range provided the criterion for assessing the acceptability of each run: if the measured train speed did not fall within this range, the data relating to that specific run were discarded.

Assessment of the on-board reference pressure circuit

As explained in section 4.5.1.5, during moving model experiments the reference pressure to the on-board pressure transducers was provided by an on-board sealed reservoir. Hence, as a sealed system, the reference pressure circuit was susceptible to pressure drifts caused, for example, by

variations in the ambient temperature. However, the short duration of a moving model test run, during which the total train travelling time was ~3 s, mitigated this possible issue. The reference pressure drift measured during a typical test was less than ±2 Pa, i.e. less than the estimated instrumentation accuracy (appendix B). Furthermore, to prevent excessive drift during one entire session (which comprised multiple runs), the design of the reference pressure circuit was implemented so as to give the possibility of venting the a circuit between any two successive runs, with no need to open the train model.

4.7.1 Moving model test procedure

The moving model test process was based on two levels of iterations, as illustrated in figure 4.37. As for static tests, subsequent sessions were undertaken monitoring the surface pressure on different loops / lines of taps. In any of these sessions the configuration of the on-board measuring system was set by opening the leading car, connecting the transducers to the desired group of taps, and then reclosing the model. Due to time limitations and to the availability of the TRAIN rig, pressure measurements undertaken during moving model tests included a reduced number of the pressure taps with respect to static tests. As explained in section 4.5.1.4, the taps on each loop from 1 to 8 (figure 4.27) were monitored simultaneously. In addition, the underbody pressure taps on loops 9 to 13 and 3 'lines of taps' (the same investigated during static tests) were characterised.
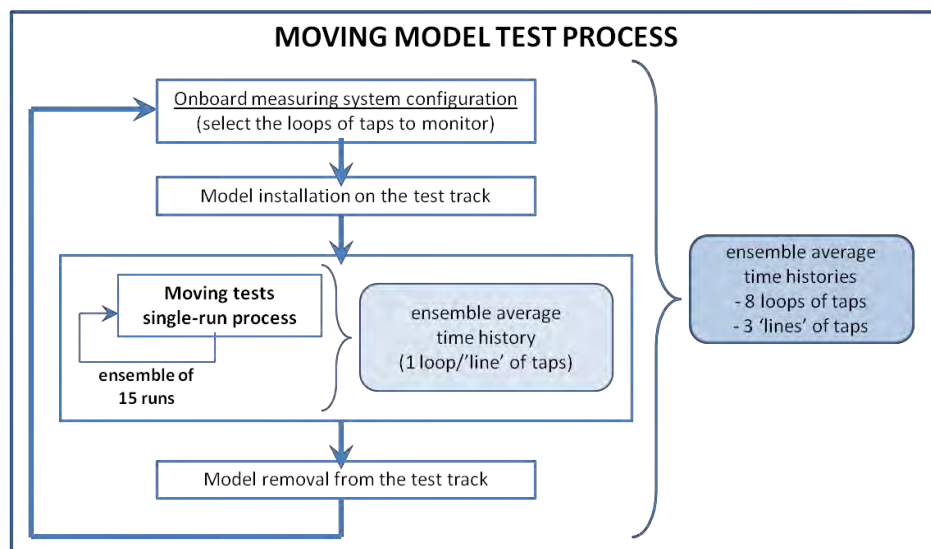
Figure 4.37 TRAIN rig moving model test process

A second level of iteration was introduced in the process by performing ensembles of runs to investigate each group of pressure taps. For each tap, this enabled an ensemble average time series to be calculated from a collection of 15 single-run time histories (section 5.2.2.3), which a sensitivity study had indicated to be sufficient for obtaining stable ensemble averages (appendix D). Consistent with the discussion in sections 3.5 and 3.6, this test procedure allowed to obtain reliable estimates for the mean non-dimensional aerodynamic coefficients despite the shortness of the time series. Furthermore, it reduces the *mechanical noise* interference in the estimation of such coefficients (appendix E). Finally, it also enabled the evaluation of non-dimensional peak aerodynamic coefficients through the analysis illustrated in section 7.2.

During each moving model test run, data were sampled continuously by the trackside instrumentation at 1 kHz over 240 s. The on-board pressure measuring system, by contrast, was triggered by the on-board data logger using an automatic countdown and data were sampled at 4 kHz for 40 s. Both on-board and trackside time histories were recorded over time windows longer than the time spent by the train transiting through the CWG. This allowed the collection of additional measurements that enabled a proper data reduction to ensure consistency with the normalisation adopted for the static tests (section 5.2). Please refer to appendix C for the full details of the single-run moving model test procedure.

Data reduction and experimental uncertainty

5.1   Introduction

Chapter 5 presents the methodologies adopted for processing the experimental data through a series of computer programs that were developed using Matlab and MS Excel. Firstly, the electronic signals were converted into measurements corresponding to physical variables. Secondly, these measurements were combined in order to express the results in a non-dimensional form, as is normal practice for scale-model tests. The calculation procedures and the conventions adopted within such processing are presented in sections 5.2 and 5.3, with consideration of the pressure and aerodynamic load coefficients, respectively. In addition, section 5.4 reports the analysis of the experimental uncertainty associated with the results presented in the following chapters 6 and 7.

5.2   Surface pressure distribution

The data concerning the pressure distribution on the train are expressed in this thesis in terms of the non-dimensional pressure coefficient. Time histories of this coefficient were obtained from the time series measured for the surface pressures using equation 5.1.

$$C_{Pij}\left(t\right) = \frac{P_{ij}\left(t\right) - \overline{P}_{ST,SW}^{*}}{\frac{1}{2}\rho\left(\overline{V}_{rel,SW}^{*}\right)^{2}}$$

(5.1)

where:

- is the time (synchronised to the on-board data acquisition system) obtained via:

$$t = t_{SAMP} = \frac{N_{SAMP} - 1}{f_{SAMP}}$$

(5.2)

where   is the ordinal number of each sample in a time series, while   is the sampling frequency adopted (i.e., 4 kHz). For ease, the subscript '$SAMP$' is omitted in equation (5.1) and in the following.

- The combined index   identifies the pressure tap, with   associated with the loop and   with the tap on such loop according to the numeration in figure 4.27.

- $P_{ij}(t)$ is the instantaneous surface pressure at the tap   , at the time   .

- ρ is air density which was calculated from the ambient temperature, barometric pressure and wind static pressure through the ideal gas law, i.e.,   = temperature, barometric pressure and J/(kg·K) (CEN, 2010).

-         is the reference pressure and consists of the '*corrected double-average wind static pressure*' defined below.

-          , is the reference wind velocity termed as the '*corrected double-average wind velocity relative to the train*' and defined in the following.

In the notations of   and   an overbar denotes a time average, the subscripts '*SW*' denote a spatial average in the track direction within the CWG (i.e., a spanwise average) and the superscript '*'' expresses a correction to the data that takes into account the streamwise gradients assessed during the CWG flow characterisation and reported in appendix A.4. To ensure consistency between static and moving model tests, the same reference pressure and reference wind velocity were used in both cases. However, due to the differences in the test arrangements and methodologies, they were obtained from the raw data through different calculations.

5.2.1   Static model tests

During the static tests the wind velocity relative to the vehicle coincided with the onset wind velocity. Hence, the reference velocity relative to the train was given by:

$$\overline{V}_{rel,SW}^{*} = \overline{U}_{SW}^{*} \tag{5.3}$$

where is the '*corrected double-average of the streamwise wind velocity*' and will be defined subsequently. Substituting equation (5.3) into equation (5.1) yields:

$$C_{Pij}(t) = \frac{P_{ij}(t) - \bar{P}^{*}_{ST\ SW}}{\frac{1}{2}\rho\left(\bar{U}^{*}_{SW}\right)^{2}} \tag{5.4}$$

5.2.1.1 On-board pressure measurements

The electronic signals recorded by the on-board data logger during each run of the static tests are indicated as , where the index identifies the pressure tap, while identifies the pressure transducer that was used for monitoring such a tap, with = 1, ..., 15. Of the 15 transducers available (i.e., T1 to T15), T1 to T14 monitored the pressure on the taps of the same loop, or line, which, as explained in section 4.6.1, changed from one run to another. In addition, the transducer T15 measured the pressure on the tap on the train nose (figure 4.26) during every run. The measurements from this transducer allowed an assessment of the run-to-run consistency of the data and, in turn, to check if any major issue had occurred during each individual run. If this was the case, the measuring system was checked, fixed and then the run was repeated. If not, the data were processed as explained below.

Low-pass data filtering

The time histories were filtered using a numerical low-pass Butterworth filter (MathWorks, 2012). This low-pass filter had a cutoff frequency of 70 Hz in order to remove the resonance peak identified in the spectrum of the electronic signal ( ) at a frequency of approximately 135 Hz (see figures 5.1a and 5.1b). Occurring approximately at the fan blade passing frequency, this peak echoed what was found in the spectrum of the wind static pressure (appendix A.4) and, as such, was interpreted as an interference in the flow caused by the fans.
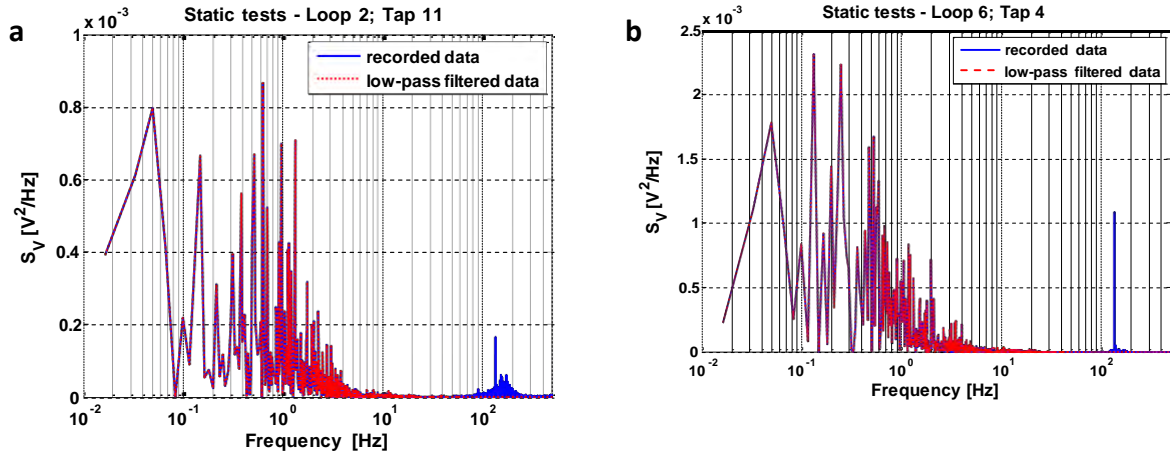
Figure 5.1 Original and low-pass filtered power spectrum of the static tests on-board data series a) Tap 11 on loop 2 b) Tap 4 on loop 6

The cutoff frequency of 70 Hz was adopted for consistency with the moving model tests data (section 5.2.2.1) in light of the different frequency scaling factor (section 7.2.1). As illustrated in figure 5.1, it ensured that the frequency content of the signal was preserved, apart from the disturbance at 135 Hz.

Data conversion

The filtered time series, (   ), were converted from electronic signals into actual differential pressure measurements   using the '*cubic calibration curves*' given by:

$$\Delta P_{ij}(t) = C_{3,k} \cdot \Delta V_{ij,k}(t)^3 + C_{2,k} \cdot \Delta V_{ij,k}(t)^2 + C_{1,k} \cdot \Delta V_{ij,k}(t) \tag{5.5}$$

the zero pressure offsets indicates the difference between the (filtered) time histories the calibration (measured in still air), while the $C_{1,k}$, $C_{2,k}$, $C_{3,k}$ are the calibration coefficients associated with each transducer   (appendix B.3).

Given the experimental arrangement adopted for the static tests (section 4.6),   can be expressed as

$$\Delta P_{ij}(t) = P_{ij}(t) - P_{ST,Loc}(t) \tag{5.6}$$

It corresponds to the difference between the pressure at the tap   on the train surface and the local wind static pressure. As a stationary time varying quantity,   is given by the sum of a time

average (i.e., mean) component   and a fluctuating component   (with zero mean). As discussed in section 4.6, a dedicated assessment proved a negligible contribution from the latter, thus leading to rewrite equation (5.6) as follows:

$$\Delta P_{ij}(t) = P_{ij}(t) - \overline{P}_{ST,Loc}$$

(5.7)

5.2.1.2 Trackside measurements
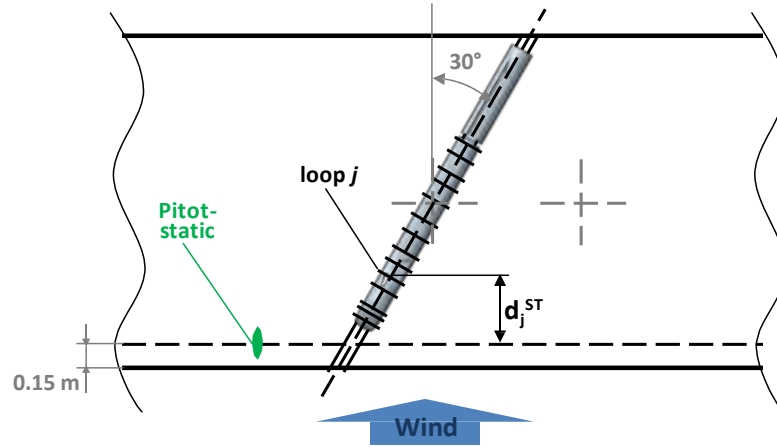
Figure 5.2 Static tests model and instrumentation setup

As explained in section 4.6, during the static tests the Pitot-static tube (indicated in figure 5.2) provided the reference pressure for the on-board pressure transducers. Furthermore, in combination with a pair of trackside differential pressure transducers, it measured the local wind dynamic pressure   and the local wind static differential pressure   , i.e., the local wind static pressure with respect to the ambient pressure in still air: =   , where τ is the time associated with the trackside data acquisition system. An '*actual linear calibration curve*' and the calibration coefficients specified in appendix B were adopted for converting the electronic signals from the trackside pressure transducers into dynamic and static pressure measurements.

Reference pressure

Relating to each static test, the mean of the local static differential pressure (=   ) was calculated by time averaging the time history   over its entire 60 s duration. Secondly, the spanwise average   was obtained from   as:

$$\overline{\Delta P}_{ST,SW} = K_{F_{ST}}^{ST} \cdot \overline{\Delta P}_{ST,Loc} \qquad (5.8)$$

where = 0.997 is the spanwise average-to-local ratio defined in appendix A.4.2. Finally, the *corrected double-average* static differential pressure (defined as) was calculated as:

$$\overline{\Delta P}_{ST,SW}^{*} = \overline{P}_{ST,SW}^{*} - P_{AMB} = \overline{\Delta P}_{ST,SW} + m_{P_{ST}}^{ST} \cdot d_{j}^{ST} \qquad (5.9)$$

where (= 20.8 Pa/m) is the streamwise mean static pressure gradient indicated in appendix A.4.2, while is the streamwise projection of the distance between the loop of taps ( ) and the position of the reference Pitot-static tube (figure 5.2). The values of corresponding to the different loops of pressure taps are specified in table 5.1.

Loop	1	2	3	4	5	6	7	8
[mm]	98	130	156	242	299	498	783	922

Loop	9	10	11	12	13	14
[mm]	363	420	567	658	732	853

Table 5.1 Static tests: streamwise projection distances for gradient corrections

Reference wind velocity

The time series of the local wind velocity was obtained from that of the dynamic pressure as:

$$U_{Loc}(\tau) = \sqrt{\frac{2q_{Loc}(\tau)}{\rho}} \qquad (5.10)$$

The local mean wind velocity was given by the time average of over its 60 s duration. Then, similar to the reference pressure, the spanwise average of the mean wind speed was estimated through the spanwise average-to-local ratio = 0.952 (appendix A.4.2) as:

$$\overline{U}_{SW} = K_{U}^{ST} \cdot \overline{U}_{Loc} \qquad (5.11)$$

Finally, the reference wind velocity indicated in equation 5.4 was calculated as:

$$\overline{U}_{SW}^{*} = \overline{U}_{SW} + m_{U}^{ST} \cdot d_{j}^{ST} \qquad (5.12)$$

where = -1.66 —— is the streamwise gradient for the streamwise mean wind speed (appendix A.4.2).

5.2.1.3 Pressure coefficient

The instantaneous values of the pressure coefficient were calculated as:

$$C_{P_{ij}}(t) = \frac{\Delta P_{ij}(t) + \overline{\Delta P}_{ST,Loc} - \overline{\Delta P}_{ST,SW}^{*}}{\frac{1}{2}\rho\left(\overline{U}_{SW}^{*}\right)^{2}}$$

(5.13)

By substituting the quantities on the right hand side with the expressions obtained above, the correspondence with the definition of given in equation (5.4) can be shown as follows:

$$C_{P_i}(t) = \frac{P_{ij}(t) - \cancel{\overline{P}}_{ST,Loc} + \cancel{\overline{P}}_{ST,Loc} - \cancel{\overline{P}}_{AMB} - \overline{P}_{ST,SW}^{*} + \cancel{\overline{P}}_{AMB}}{\frac{1}{2}\rho\left(\overline{U}_{SW}^{*}\right)^{2}} = \frac{P_{ij}(t) - \overline{P}_{ST,SW}^{*}}{\frac{1}{2}\rho\left(\overline{U}_{SW}^{*}\right)^{2}}$$

(5.14)

5.2.2 Moving model tests

In a crosswind moving model test, the wind velocity relative to the train is given by the vector sum of the onset wind velocity and the vehicle speed. As such, the following reference wind velocity was adopted:

$$\overline{V}_{rel,SW}^{*} = \sqrt{\left(\overline{U}_{SW}^{*}\right)^{2} + V_{tr,SW}^{2}}$$

(5.15)

where is the *corrected double-average* streamwise wind velocity, whose value differs from that of the static tests, and is the average train speed within the crosswind section. Calculation processes for both of these quantities are provided below.

Substituting equation (5.15) into (5.1), the pressure coefficient becomes:

$$C_{P_{ij}}(t) = \frac{P_{ij}(t) - \overline{P}_{ST,SW}^{*}}{\frac{1}{2}\rho\left(\left(\overline{U}_{SW}^{*}\right)^{2} + V_{tr,SW}^{2}\right)}$$

(5.16)

As explained in section 4.7, a series of 15 moving model test runs were carried out monitoring each pressure tap. Accordingly, ensemble average time series of the pressure coefficient defined in equation (5.16) were calculated from sets of 15 single-run time histories as explained in section 5.2.2.3.

5.2.2.1 On-board pressure measurements
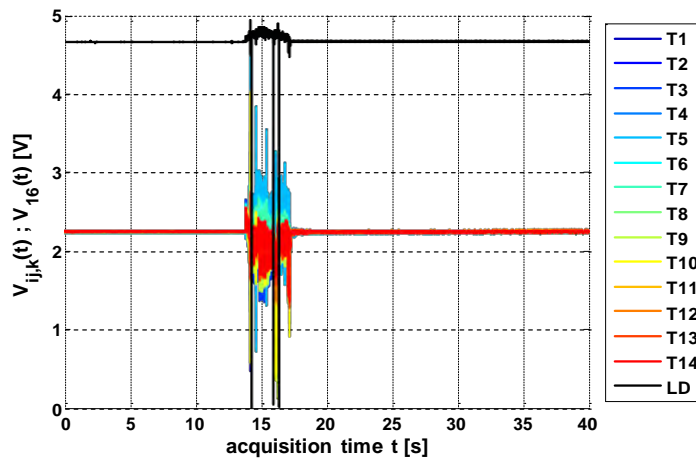
Figure 5.3 Example of moving model tests single-run on-board time series (loop 2)

As for the static tests, so during the moving model tests, the transducers from T1 to T14 monitored the pressure on each loop, or line, of taps (section 4.7.1). In addition, the transducer T15 measured the pressure on the taps on the train nose to assess the consistency from run to run and, therefore, the acceptability of the data. These signals are indicated below as   , with   = 1, ..., 15, while the   is the on-board light-beam detector that was monitored during the moving model tests. Figure 5.3 shows an example of the electronic signals recorded by the on-board data logger during a single test. The coloured lines are the time histories for the pressure transducers (i.e. T1 to T14), while the black line is the signal of the on-board light-beam detector (LD). Troughs of this signal (reaching ~0 V) indicate the instants when the light-beam detector, mounted on the scale-model trailing car, transited in front of each of the three light sources positioned at the trackside. The first of these was placed at the end of the track acceleration section, whilst the other two (i.e. LS1 and LS2) were at either end of the CWG (figure 5.6 in the following). As discussed in section 4.7.1, it can be observed in figure 5.3 that the 40 s acquisition time included not only the launch, but also two intervals during which the train was stopped on the track.

Data conversion

The electronic signals   from the 15 pressure transducers were converted into pressure measurements   using the same '*cubic calibration curves*' specified in equation (5.5).

was given by $\quad$ = $\quad$, which is the difference between the electronic signals

and the zero pressure offsets $\quad$ measured as explained in appendix C.

It was discussed in section 4.7 that the reference pressure provided by the sealed reservoir during moving model tests could be assumed to be time-invariant within the time interval of interest. Indicating this reference pressure as $\quad$, the differential pressure $\quad$ detected by the on-board pressure transducers can be expressed as:

$$\Delta P_{ij}(t) = P_{ij}(t) - P_{RES} \tag{5.17}$$

When the train was not moving on the track, but stationary in still air, the pressure detected at all taps corresponded to the atmospheric pressure ($\quad$). Denoting as $\quad$ the time averages of $\quad$ calculated over the initial 5 s of each time history (when the train was actually stationary in the acceleration section), then equation (5.17) gives:

$$\Delta P_{ij,0} = \overline{\Delta P_{ij}(t)}\Big|_{0 < t < 5} = P_{AMB} - P_{RES} \tag{5.18}$$

Time history trim

The portion of time histories associated with the train travelling within the CWG (indicated as $\quad$) were isolated from the full-length records using the signal of the on-board light-beam detector ($\quad$). The times $\quad$ and $\quad$ at which the on-board light-beam detector transited in front of the trackside light sources LS1 and LS2 (figure 5.6 in the following) were identified as those corresponding with the second and third peak of the $\quad$ signal (figure 5.3). From these times, the instants $\quad$ and $\quad$, i.e., when the loop with the monitored taps entered and exited the crosswind section, respectively, were calculated from the combination of the following known data: the distance of the light sources from the CWG entry and exit (figure 5.6); the distance between the on-board light-beam detector and loop of taps under investigation (section 4.5.1); the velocity of the vehicle measured by the trackside speed measuring devices at the entry and exit of the crosswind section. Accordingly, the trimmed time histories illustrated in figure 5.4 were obtained as:

$$\Delta P_{ij,CW}\left(t\right)=\Delta P_{ij}\left(t\right)\Big|_{t_{IN}<t<t_{EX}} \tag{5.19}$$

where   indicates the *'shifted (discrete) time'* defined as   =   and varying between 0 and

.
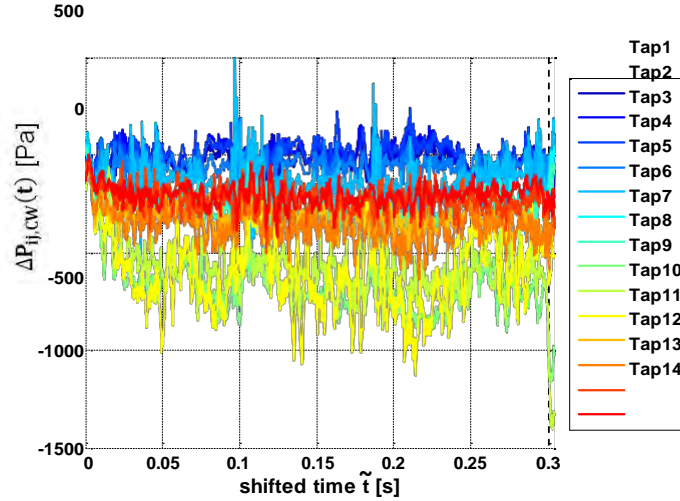
Figure 5.4 Example of moving model tests single-run trimmed on-board time series (loop 2)

Reference train speed

The average train speed within the crosswind section was calculated as:

$$V_{tr,SW}=\frac{L_{CW}}{t_{EX}-t_{IN}} \tag{5.20}$$

where   = 6.35 m is the total span of the CWG along the track (section 4.3.2).

Low-pass data filtering

Figure 5.5 shows that the moving model experiments were affected by interference on the surface pressure measurements occurring at frequencies close to the fan blade passing frequency (i.e., ~135 Hz). In light of the train movement and of the related Doppler effect (Parker, 1993), not surprisingly the resonant peak embraced a frequency range slightly wider than that observed in figure 5.1, relating to the static tests. A numerical Butterworth low-pass filter at 117 Hz was applied to remove such interference from the trimmed time histories   . The cutoff frequency was consistent with that adopted for filtering the static test data in light of the different time scaling ratios relative to the two series of tests (discussed in section 7.2).
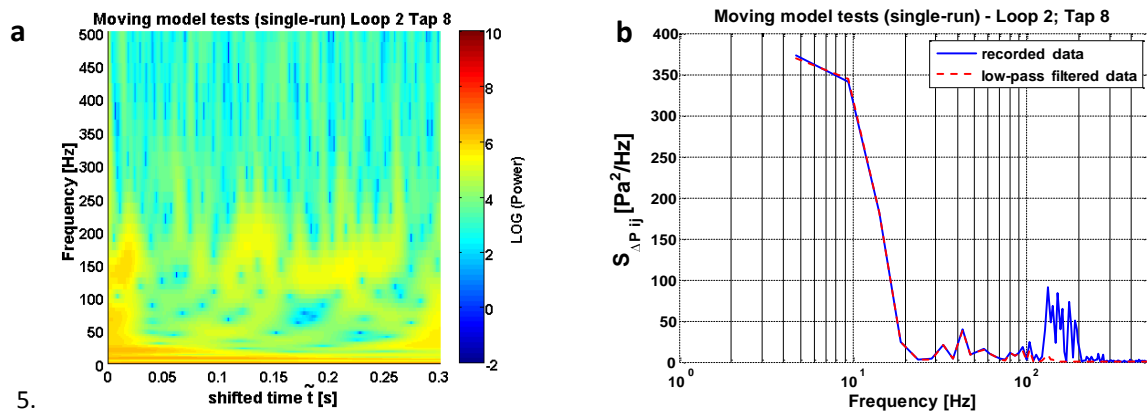
**Figure 5.5 Low-pass filtering of trimmed on-board data series from moving model tests (tap 8 on loop 2)
a) Wavelet power spectrum via continuous wavelet trasform using the Morelet wavelet, calculated using the
Matlab script from Torrence and Compo (n.d.) b) Power spectrum**

5.2.2.2   Trackside measurements
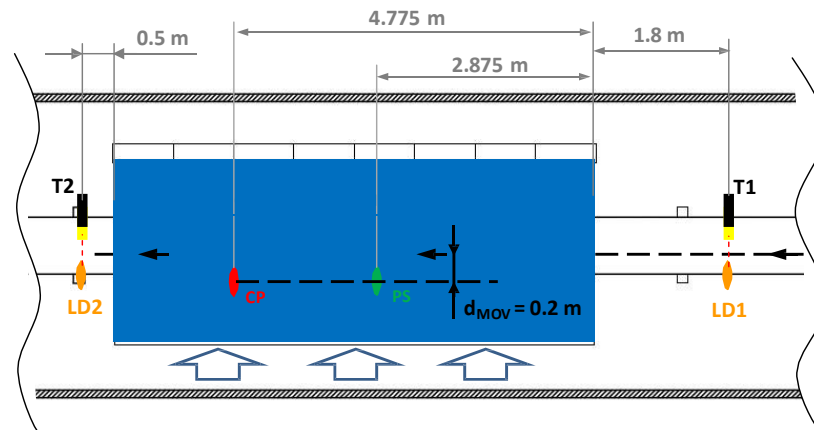
Figure 5.6 Moving model tests instrumentation setup

During moving model tests the reference wind velocity and reference pressure were measured by
the Cobra probe (CP) indicated in figure 5.6. Since the acquisition system provided by the
manufacturer was used (section 4.5.2.5), the electronic signals from the Cobra probe were
automatically converted into physical measurements comprising of the three velocity components

) and of the wind static differential pressure   .

Time history trim
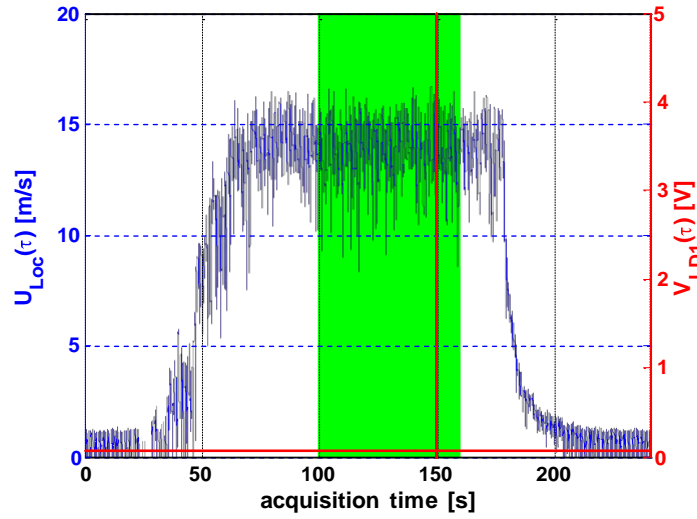
Figure 5.7 Example of trackside measurements time series from moving model tests

Figure 5.7 illustrates an example of a time series of the onset wind streamwise velocity (τ) that was continuously recorded for 240 s during a moving model test. As discussed in appendix C, it can

be noticed in this figure that such a time series included not only the time when the fans were

running at full speed, but also the start-up and stopping transitions and a still air condition occurring

both at the beginning and at the end of each run. The actual time at which the train transited across

the CWG was identified analysing the signal from the trackside light-beam detector (LD1) at the

crosswind section entry. As shown in figure 5.7, a 5 volts peak was associated with the train passing

in front of this sensor, which indicated the model running through the CWG within the next 0.5 s.

Denoting as the time instant at which the peak occurred, a time interval of 60 s (i.e. =

) was defined from 50 s before , to 10 s after it. This time interval (highlighted in

green in figure 5.7), was specifically defined in order to include a period of time during which the fans

were running at full speed. As such, it was assumed as the reference time interval for trimming the

Cobra probe time histories and to obtain:

$$U_{Loc,CW}\left(\tau\right) = U_{Loc}\left(\tau\right)\Big|_{\tau_{60,1} < \tau < \tau_{60,2}} \qquad (5.21)$$

$$\Delta P_{ST,Loc,CW}\left(\tau\right) = \Delta P_{ST,Loc}\left(\tau\right)\Big|_{\tau_{60,1} < \tau < \tau_{60,2}} \qquad (5.22)$$

for the streamwise velocity and differential static pressure, respectively. From these, then, time averages were calculated to obtain the local reference wind velocity and local reference wind static differential pressure (i.e.   and   , respectively).

It is acknowledged that a 60 s time interval was significantly longer than the actual time spent by the train travelling within the crosswind section (i.e., ~0.3 s). Nevertheless, the approach undertaken enabled reliable estimations of the spanwise averages of both wind velocity and static pressure from one local measurement. Due to the lack of spatial correlation found for any of these quantities at spanwise distances larger than ~0.2 m (appendix A.4.1), no such extrapolation could have been done unless long-term (stabilised) time averages had been considered.

Reference pressure

The *double-average* static differential pressure   and its *corrected* value   were obtained from the local mean value   through calculations analogous to those carried out for the static test data and given by:

$$\overline{\Delta P}_{ST,SW} = K_{F_{ST}}^{MOV} \cdot \overline{\Delta P}_{ST,Loc} \tag{5.23}$$

$$\overline{\Delta P}_{ST,SW}^{*} = \overline{P}_{ST,SW}^{*} - P_{AMB} = \overline{\Delta P}_{ST,SW} + m_{P_{ST}}^{MOV} \cdot d_{MOV} \tag{5.24}$$

where   = 0.2 m is the distance between the measuring position and the track centreline illustrated in figure 5.6, while   = 0.963 and   = 27.5 Pa/m are the spanwise average-to-local ratio and streamwise mean static pressure gradient, respectively (appendix A.4.1).

Reference onset wind velocity

The *corrected double-average* streamwise wind velocity   was calculated through the spanwise average-to-local ratio   = 0.876 and the gradient   = -2.63 —— (appendix A.4.1) as:

$$\overline{U}_{SW} = K_{U}^{MOV} \cdot \overline{U}_{Loc} \tag{5.25}$$

$$\overline{U}_{SW}^{*} = \overline{U}_{SW} + m_{U}^{MOV} \cdot d_{MOV} \tag{5.26}$$

5.2.2.3 Pressure coefficient

Single-run actual time histories

Having processed the raw data as explained above, the time histories for the pressure coefficient (relating to any tap   ) were calculated as:

$$C_{Pij}(t_r)\big|_r = \frac{\Delta P_{ij,CW}(t_r)\big|_r - \Delta P_{ij,0}\big|_r - \overline{\Delta P}^*_{ST,SW}\big|_r}{\frac{1}{2}\rho_r\left(\left(\overline{U}^*_{SW}\big|_r\right)^2 + \left(V_{tr,AVG}\big|_r\right)^2\right)}$$

(5.27)

where the subscript   is added to the notation to distinguish each individual run from the others. Developing the terms in equation (5.27) in light of the relations illustrated above, the equivalence with the definition given in equation 5.16 is shown as follows:

$$C_{Pij}(t_r)\big|_r = \frac{P_{ij,CW}(t_r)\big|_r - \cancel{P_{RES}\big|_r} - \left(\cancel{P_{AMB}\big|_r} - \cancel{P_{RES}\big|_r}\right) - \left(\overline{P}^*_{ST,SW}\big|_r - \cancel{P_{AMB}\big|_r}\right)}{\frac{1}{2}\rho_r\left(\overline{V}^*_{rel,SW}\big|_r\right)^2} = \frac{P_{ij,CW}(t_r)\big|_r - \overline{P}^*_{ST,SW}\big|_r}{\frac{1}{2}\rho_r\left(\overline{V}^*_{rel,SW}\big|_r\right)^2}$$

(5.28)

Normalised non-dimensional time

Because of the tolerance of ± 0.6 m/s accepted for the train speed (section 4.7), the duration of the single-run trimmed time history varied from run to run. For normalisation purposes, the following *normalised (discrete) time* was defined:

$$t^*_r = \frac{t_r \cdot V_{tr,SW}\big|_r}{L_{CW}}$$

(5.29)

It was based on the *shifted (discrete) time* that has been introduced in section 5.2.2.1, on the total span of the crosswind section   and on the train reference speed   , calculated according to equation (5.20). For any run, this quantity varied from 0 to 1 and the corresponding 'time vector' was given by:

$$t^*_r = \left\{0, \Delta t^*_r, 2 \cdot \Delta t^*_N, \ldots, 1\right\} \qquad \text{with } \Delta t^*_r = \frac{V_{tr,SW}\big|_r}{f_{SAMP} \cdot L_{CW}}$$

(5.30)

Furthermore, it can be observed that such a normalised time was equivalent to the normalised spanwise position within the air channel:

$$t_r^* = \frac{t_r \cdot V_{tr,SW}\big|_r}{L_{CW}} = \frac{s}{L_{CW}} \tag{5.31}$$

where   is the distance along the track between loop   on the train and the entry of the CWG.

Since   (in equation 5.32) depended on   , the train speed run-to-run variability generated a mismatch in the discretisation of this variable when associated with different runs. Therefore, a *nominal normalised (discrete) time* was introduced. Indicated as   , it had a fixed (non-dimensional) time step   shorter than   (for any   ) and was given by:

$$t_N^* = \left\{0, \Delta t_N^*, 2 \cdot \Delta t_N^*, ..., 1\right\} \qquad \text{with } \Delta t_N^* = 0.0001 \tag{5.32}$$

Extending the correspondence highlighted in equation (5.31),   can also be interpreted as a *nominal spanwise normalised position* (   ) within the crosswind section.

Single-run interpolated time histories

In order to calculate properly an ensemble average time series, a set of synchronised single-run time histories was required. Noting the above, however, this was not necessarily guaranteed by the   time histories defined in equation (5.27). To overcome this issue, an *interpolated* time series (   ) was calculated from each of the   by performing a piecewise linear interpolation with respect to the nominal normalised time   (figure 5.8).
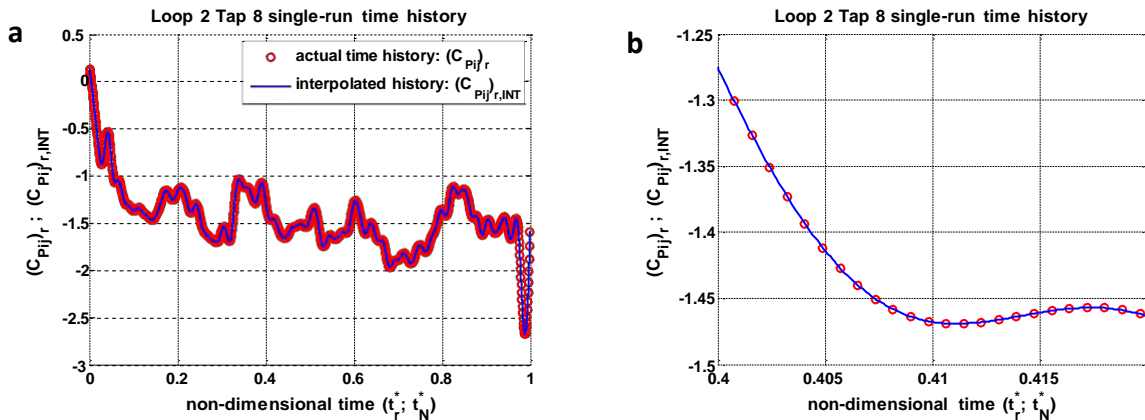
Figure 5.8 Example of interpolated time series for the on-board pressure measurements of the moving model tests (tap 8 on loop 2) a) Complete trimmed time series b) Detail from figure 5.8a

Ensemble average time history

The ensemble average time histories for the pressure coefficient, indicated by   and
illustrated by a black line in figure 5.9 below, were calculated from sets of R = 15 single-run
interpolated time histories as:

$$C_{Pij}(t_N^*)\Big|_{ENS} = \frac{\sum_{r=1}^{R} C_{Pij}(t_N^*)\Big|_{r,INT}}{R} \quad \forall t_N^* \in [0,1] \tag{5.33}$$
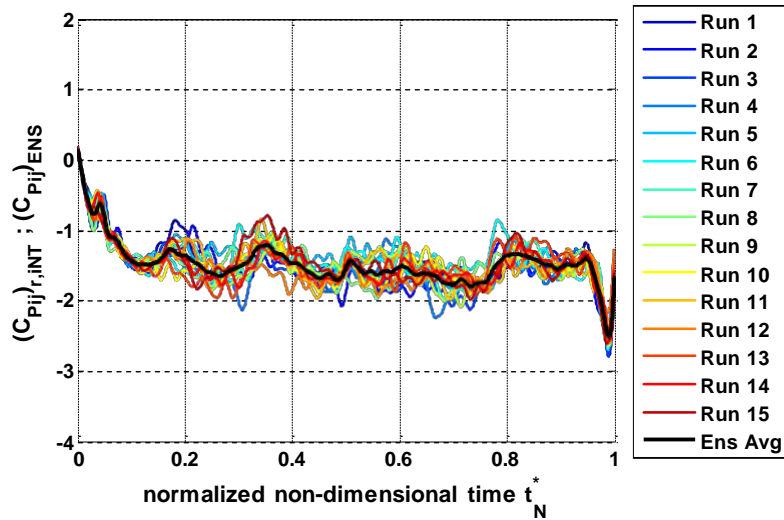
Figure 5.9 Example of single-run and ensemble average time series for the moving model tests surface pressure coefficient (tap 8 on loop 2)

5.3   Aerodynamic forces and moments

Consistent with the approach discussed in section 2.4.2, non-dimensional aerodynamic coefficients
for the side and lift forces and for the rolling moment, referred both to a central longitudinal   -axis
and to the leeward rail, were examined in this research. According to the reference system that was
adopted (illustrated in figure 5.10), the definitions of these non-dimensional coefficients are given in
equations (5.34).
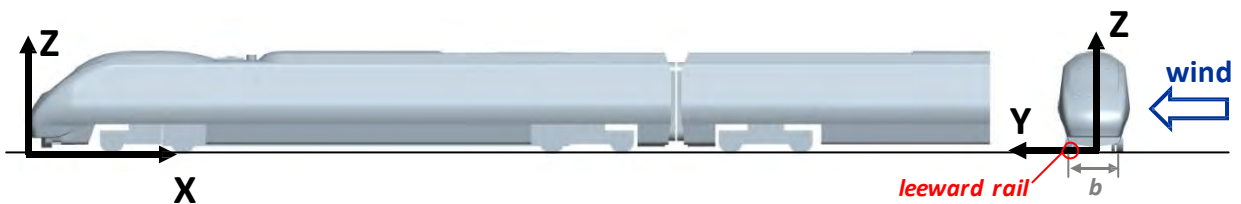
Figure 5.10 Train model reference system

$$C_Y = \frac{F_Y}{\frac{1}{2}\rho V_{ref}^2 A_{ref}}$$ (5.34a)

$$C_Z = \frac{F_Z(\theta)}{\frac{1}{2}\rho V_{ref}^2 A_{ref}}$$ (5.34b)

$$C_{M_X} = \frac{M_X}{\frac{1}{2}\rho V_{ref}^2 A_{ref} H_{ref}}$$ (5.34c)

$$C_{M_{X,lee}} = \frac{M_{X,lee}}{\frac{1}{2}\rho V_{ref}^2 A_{ref} H_{ref}}$$ (5.34d)

In equations (5.34)   and   are the coefficients relative to side and lift forces (i.e.,   and   ), respectively, while   and   are the rolling moment coefficients referred to the   -axis and to the leeward rail, respectively. In addition,   indicates the air density and   ,   and   identify the reference values for wind velocity and for the area and height of the vehicle, respectively, shown in table 5.2.

	Static tests	Moving model tests
ρ	Calculated from the average temperature and pressure using the ideal gas law	
V_{ref}	$\overline{U}_{SW}^*$	$\sqrt{\left(\overline{}_{SW}\right)^2 + V_{tr,SW}^2}$
A_{ref}	Nominal side area of the Class 390 leading car (77m² full-scale equivalent)	
H_{ref}	Nominal height of the Class 390 leading car (3.1m full-scale equivalent)	

Table 5.2 Reference quantities for non-dimensional load coefficients normalisation

It is worth noting that both the rolling moments (and their corresponding coefficients) were defined as positive along the respective axes following the 'right-hand screw' rule. Therefore, they became negative when tending to overturn the vehicle. Furthermore, the following relationship can be specified between   and   :

$$C_{M_{X,lee}} = C_{M_X} - C_Z \frac{b/2}{H_{ref}}$$ (5.35)

where   is track gauge, which corresponds to the standard value of 1.435 m at full-scale.

Since only surface pressure measurements were carried out in the TRAIN rig tests, in this thesis the aerodynamic loads and the relative non-dimensional coefficients were estimated by integrating the

surface pressure field on the train's discretised geometry, which is specified in figures 5.11 and 5.12.

As detailed in the following sections, the integration was performed in two steps: first, '*load coefficients per unit length*' were calculated integrating the pressure on each loop; secondly, by discrete integration along the vehicle of these coefficients per unit length (relating to stripes of varying length), the '*overall load coefficients*' were obtained.

Figure 5.11 and table 5.3 below detail the longitudinal division of the Class 390 leading vehicle into eight stripes, including one loop of taps each. Figure 5.11 illustrates the polygons used for approximating the original profiles of the train cross-sections where the loops of pressure taps (from loop 1 to loop 8) were positioned. According to this discretisation, each facet of the discretised train surface is identified in the following by the combined index ' ', where stands for the loop (or stripe), while ' ' relates to the position of the facet on each stripe (following the counterclockwise numeration in figure 5.12).
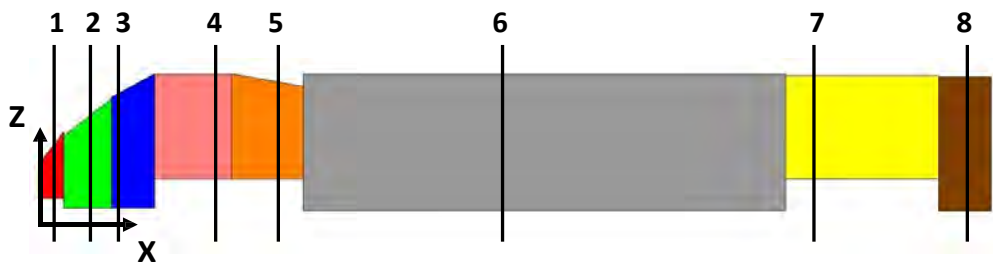
Figure 5.11 Class 390 model longitudinal discretisation (8 stripes)

Stripe	1	2	3	4	5	6	7	8
X_{in} [mm]	0	25	75	120	200	275	780	940
X_{fin} [mm]	25	75	120	200	275	780	940	1000
length L_j [mm]	25	50	45	80	75	505	160	55

Table 5.3 Class 390 discretised model: longitudinal stripes extension (8 stripes)
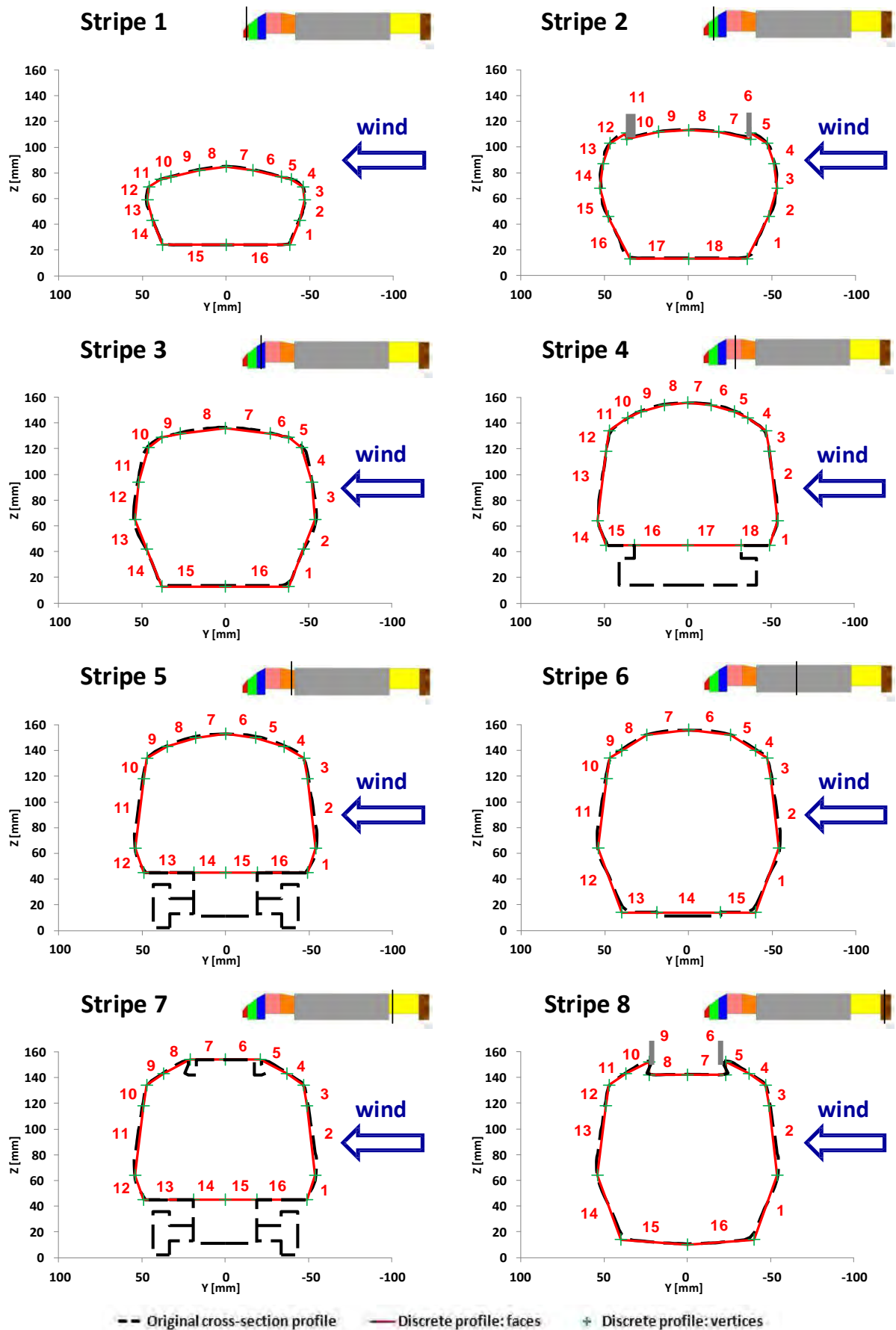
Figure 5.12 Class 390 model discretised cross-sections (loops 1 to 8)

The reason why this reference discretisation presented eight longitudinal stripes is that, during moving model tests, the pressure taps on the same loop were monitored simultaneously only on loops from 1 to 8 (section 4.7). The use of the same model discretisation for extrapolating the load coefficients from pressure measurements collected during static and moving model tests ensured consistency in the comparison between the two set of results. However, since the pressure distribution was monitored also on loops from 9 to 14, during static tests, and at extra taps in the underbody of loops from 9 to 13, during moving model tests, alternative discretisations based on a larger number of stripes were considered to enable sensitivity analyses (appendix F).

Since no pressure measurements were collected on the bogies, these were excluded from the discrete train geometry. Apart from this, figures 5.11 outlines that a generally good approximation of the original geometry was provided by the use of polygonal loop profiles. Ideally, every facet of the (symmetrical) discretised model should have contained one single tap. In practice, since a non-symmetrical distribution for the taps was chosen to increase measurements in the regions where high pressure gradients were expected, no perfect matching could be achieved. Therefore, where one facet ( ) did not include any pressure tap (, for computational purposes its pressure was taken equal to that measured at one of the taps on the adjacent facets according to table 5.4.

Loop (j)	1	2	3	4	5	6	7	8
Facet (I)	Pressure tap (i)							
1	1	1	1	1	1	1	1	1
2	2	2	2	2	2	2	3	2
3	3	2	2	3	3	3	4	3
4	4	3	3	4	4	4	5	4
5	5	3	4	5	5	5	6	5
6	5	4	5	6	6	6	7	6
7	6	4	6	7	7	7	8	6
8	7	5	7	8	8	8	9	7
9	8	6	7	9	9	9	9	7
10	9	7	8	9	10	10	10	8
11	10	7	9	10	11	10	11	8
12	10	8	10	11	12	11	12	9
13	11	9	11	11	13	12	13	9
14	12	10	12	12	13	13	13	10
15	13	11	13	13	14	14	14	11
16	14	12	14	13	14		14	12
17		13		14				
18		14		14				

Table 5.4 Class 390 discretised model: facets-pressure taps correspondence (loops 1 to 8)

5.3.1 Load coefficients per unit length

The '*load coefficient per unit length*' are indicated in the following by   ,   and   and refer to the side and lift forces and to the rolling moment about the   -axis and about the leeward rail, respectively. Calculated for each stripe ( ) and expressed in m⁻¹, they were defined as (Sanquer et al., 2004):

$$C_{Y_j}^* = \sum_I \frac{C_{P_{I,j}} A_{I,j} \left(\mathbf{n}_{I,j} \bullet \mathbf{y} \right)}{A_{ref} L_j} \tag{5.36a}$$

$$C_{Z_j}^* = \sum_I \frac{C_{P_{I,j}} A_{I,j} \left(\mathbf{n}_{I,j} \bullet \mathbf{z} \right)}{A_{ref} L_j} \tag{5.36b}$$

$$C_{Mx_j}^* = \sum_I \frac{C_{P_{I,j}} A_{I,j} \, \left\| \mathbf{d}_{I,j} \times \mathbf{n}_{I,j} \right\|}{A_{ref} H_{ref} L_j} \quad \mathbf{x} \tag{5.36c}$$

$$C_{Mx,lee_j}^* = \sum_I \frac{C_{P_{I,j}} A_{I,j} \, \left\| \mathbf{d}_{I,j} \times \mathbf{n}_{I,j} \right\|}{A_{ref} H_{ref} L_j} \quad \mathbf{x} \tag{5.36d}$$

where: is the value of the pressure coefficient associated with each facet , obtained from (associated with each tap) through table 5.4 and assumed to be uniform within the extension of each facet; represents the stripe's length specified in table 5.3. Furthermore, as illustrated in figure 5.13 considering a 2D simplification, is the normal unit vector associated with each flat surface (directed towards the inside of the body); **x**, **y** and **z** are the unit vectors associated with the , and axes, respectively; is vector perpendicular to the longitudinal axis ( ) and directed from this to the mid point of the each facet ; , finally, is the corresponding of but originating from the leeward rail.
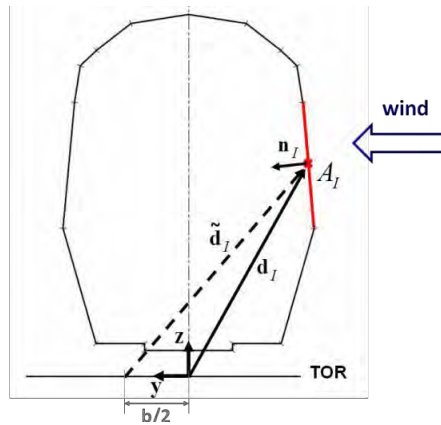
Figure 5.13 Reference quantities for the calculation of the load coefficients per unit length

5.3.2 Overall load coefficients

Assuming the load coefficients per unit length to be constant within each stripe, the corresponding parameters referred to the entire vehicle were calculated as follows:

$$C_Y = \sum_j \left[\sum_I \frac{C_{P_{I,j}} A_{I,j} \left(\mathbf{n}_{I,j} \bullet \mathbf{y} \right)}{A_{ref} L_j} \right] L_j = \sum_j C_{Y_j}^* L_j \tag{5.37a}$$

$$C_Z = \sum_j \left[\sum_I \frac{C_{P_{I,j}} A_{I,j} \left(\mathbf{n}_{I,j} \bullet \mathbf{z} \right)}{A_{ref} L_j} \right] L_j = \sum_j C_{Z_j}^* L_j \tag{5.37b}$$

$$C_{M_X} = \sum_j \left[\sum_I \frac{C_{F_{I,j}} A_{I,j} \left\| \mathbf{d}_{I,j} \times \mathbf{n}_{I,j} \right\|}{A_{ref} H_{ref} L_j} \mathbf{x} \right] L_j = \sum_j C_{Mx_j}^* L_j \tag{5.37c}$$

$$C_{M_X,lee} = \sum_j \left[\sum_I \frac{C_{F_{I,j}} A_{I,j} \left\| \mathbf{d}_{I,j} \times \mathbf{n}_{I,j} \right\|}{A_{ref} H_{ref} L_j} \mathbf{x} \right] L_j = \sum_j C_{Mx,lee_j}^* L_j \tag{5.37d}$$

5.4   Analysis of experimental uncertainty

A measurement error corresponds to the difference between the measured and the true (unknown) value of either a physical quantity or a derived property (Taylor, 1996; Tavoularis, 2005). The measurement uncertainty represents the quantification of such a difference. To assess the experimental uncertainty associated with the results obtained through the TRAIN rig experiments, the following analysis was undertaken.

5.4.1   Mean aerodynamic coefficients

The results relating to the train steady aerodynamics are presented in chapter 6 of this thesis in terms of mean pressure coefficients and mean load aerodynamic coefficients. A primary analysis was carried out for assessing the level of uncertainty associated with the former and, from this, the margin of error associated with the load coefficients was estimated through the propagation theory (Taylor, 1996).

With consideration of the experimental techniques and data reduction methods that were adopted, two main sources of experimental uncertainty were identified:

- bias limit (E_{BIAS})

- random uncertainty (E_{RND})

The bias limit is the uncertainty determined by the characteristics and performances of the employed instrumentation. For example, the bias limit relative to the mean pressure coefficient depended on the individual accuracies of each instrument according to the 'propagation of error' (Taylor, 1996):

$$E_{BIAS} = \sqrt{\sum_k \left(\frac{\partial \overline{C}_P}{\partial b_k} \delta b_k \right)^2} \tag{5.38}$$

where   indicates any generic individual quantity that was directly measured (and from which   was calculated) and   is the respective bias limit. The single contributions were added in quadrature considering them independent and not correlated.

In principle, the bias of one instrument can be determined by a number of causes, like hysteresis and non-linearity. As such, the bias affecting the measurements obtained using that instrument is not necessarily constant but may vary, for example, within the measuring range. For the differential pressure transducers employed in this work the bias was assessed through a static calibration that was performed (appendix B). For the rest of the instrumentation, it was taken from the manufacturers' specifications. Since no information was available on the statistical distribution of the bias, the conservative assumption of a uniform distribution was made and a bias *limit* (which is considered in this analysis) was defined as the largest possible bias associated with any of the employed instruments.

The random uncertainty accounts for the variability intrinsic in the testing process and relating to the unsteadiness and stochastic nature of the physical phenomenon under investigation. In this analysis, the margin of random uncertainty was defined through a statistical analysis of the data, assuming a normal distribution and considering a confidence level of 95%.

The total uncertainty was given by the sum of the bias limit and the random uncertainty:

$$E_{TOT} = E_{BIAS} + E_{RND} \tag{5.39}$$

Since the two contributions consider different aspects, there was no evidence of any correlation. Hence, the algebraic sum (rather than the sum in quadrature) was considered in order to adopt a conservative approach (Taylor, 1996).

5.4.1.1 Mean pressure coefficients

Bias limit

Static model tests

Table 5.5 specifies the individual contributions considered for estimating the bias limit relative to the static tests through the propagation of error.

	Quoted accuracy	Instrument	Source of information
	±5 Pa	On-board pressure transducers	
	±4 Pa	Pitot-static & trackside pressure transducer	Static calibration (appendix B)
	0.3 m/s	Pitot-static & trackside pressure transducer	
	0.005 kg/m^3	Derived from: ambient temperature, ambient pressure, wind static pressure	Instrument manufacturer's specifications

Table 5.5 Quoted accuracies of the static tests instrumentation

The bias limit for the air density was calculated through the propagation of error in relation to the ideal gas law. The individual accuracies accounted for the ambient temperature and barometric pressure were ±2 °C and ±200 Pa, respectively (as specified in section 4.5.2.1). It was also assessed that the approximation (inherent in the ideal gas law) associated with neglecting the air humidity falls within the estimated uncertainty of 0.005 kg/m^3.

The bias limit estimated for the pressure coefficients for each pressure tap are summarised in figure 5.14a, below.

Moving model tests

The individual contributions evaluated for estimating the bias limit associated with moving model tests are indicated in table 5.6.

	Quoted accuracy	Instrument	Source of information
	±5 Pa	On-board pressure transducers	Static calibration (appendix B)
	±3 Pa	On-board pressure transducers	
	±5 Pa	Cobra probe	Instruments' specifications
	0.3 m/s	Cobra probe	Instruments' specifications
	0.1 m/s	On-board light-beam detector & trackside speed measuring devices	Instruments' specifications
	0.005 kg/m^3	Derived from: ambient temperature, ambient pressure, wind static pressure	Instrument manufacturer's specifications

Table 5.6 Quoted accuracies of the moving model tests instrumentation

It can be observed that the accuracy of the on-board pressure measurements is counted twice, relatively to both ⬚ and ⬚, as indicated in equation (5.27). Although measured by the same instrument, such quantities were obtained processing different portions of the same time history and, therefore, they represent independent measurements. The individual accuracies for the wind velocity and static pressure measurements correspond to the Cobra probe's specification. The bias limit of the train speed is determined by the performance of both the trackside speed detecting devices and the on-board data acquisition system. The air density, finally, was treated as for the static tests.

Figure 5.14d below illustrates the bias limits associated with the mean pressure coefficients at the different taps.

Random uncertainty

Static model tests

During the static tests, single experiments were carried out on different days monitoring the loops of taps 2 and 6 (respectively on the nose and in the centre of the first car). The availability of a series of seven records for each of those loops enabled a statistical analysis to estimate the random uncertainty. The mean pressure coefficients ⬚, associated with each pressure tap ⬚ on loop ⬚ (with ⬚ = 2 or 6) and obtained by averaging the time series from different runs (*r*) as explained in section 6.2, were considered. Since seven runs represented a restricted statistical population in the view of performing a standard statistical analysis, a bootstrap method was applied (Zoubir and Boashash, 1998). Using the Matlab bootstrap toolbox available from Zoubir and Iskander (n.d.), a bootstrap population of ⬚ = 1000 samples (each indicated as ⬚) was extracted (drawing with replacement) from the original ⬚ values. Based on the '*bootstrap principle*', the estimation for the random uncertainty of the original data with a 95% confidence limit was obtained from the standard deviation calculated over the bootstrap population (⬚) as:

$$E_{RND,i} \cong \pm 2\sigma \frac{BS}{C_{Pi}} = \pm 2 \sqrt{\frac{\sum_{b=1}^{B}\left(\bar{C}_{Pi}\big|_b - \frac{1}{B}\sum_{b=1}^{B}\bar{C}_{Pi}\big|_b\right)^2}{B-1}} \tag{5.40}$$

Since single-run repetitions were available only for loops 2 and 6, the random uncertainty on the other loops was extrapolated from the estimations obtained for these. The different 'flow regions' specified in table 5.7 were defined on loops 2 and 6. Any region included adjacent pressure taps presenting similar values of both mean pressure coefficient and random uncertainty, assuming that taps of the same group were characterised by similar flow conditions. A nominal random uncertainty was calculated for each region by averaging the individual $E_{RND,i}$. Since loops 1 and 3, both on the train nose, were included in the same flow region relating to loop 2, their random uncertainties were assumed to be the same as those estimated for this loop. Analogous extrapolation, then, was undertaken by extending the estimations obtained for loop 6 to loops 4, 5, 7 and 8.

Loop 2 - nose				Loop 6 – car centre			
Tap #	$E_{RND,i}$	Flow Region		Tap #	$E_{RND,i}$	Flow Region	
1	0.034			1	0.009		
2	0.050	Windward	0.039	2	0.007	Windward	0.009
3	0.033			3	0.012		
4	0.009			4	0.031	Roof Windward	0.023
5	0.020	Roof	0.023	5	0.018		
6	0.032			6	0.019		
7	0.030			7	0.013		
8	0.095			8	0.017	Roof	0.015
9	0.070			9	0.016		
10	0.098	Leeward	0.076	10	0.013	Leeward	0.010
11	0.044			11	0.006		
12	0.071			12	0.014		
13	0.007	Underbody	0.011	13	0.005	Underbody	0.008
14	0.016			14	0.005		

Table 5.7 Random uncertainties on the static tests mean pressure coefficients

A summary of the random uncertainties for all pressure taps is illustrated in the figure 5.14b below.

Moving model tests

The random uncertainty for the moving model tests was quantified in relation to the run-to-run variability of the mean pressure coefficient. For this purpose, the mean pressure coefficients

relative to any tap   were calculated by time averaging the steady portion of the single-run time series obtained from each single-run (*r*). The standard deviation   was calculated over the population of 15 values (one per run) obtained for each pressure tap. Finally, the random uncertainty (with a 95% confidence limit) associated with the mean pressure coefficient   was estimated as:

$$E_{RND,i} = \pm 2 \frac{\sigma_{\bar{C}_{Pi}}}{\sqrt{R}}$$

(5.41)

and is shown in figure 5.14e.

Overall uncertainty
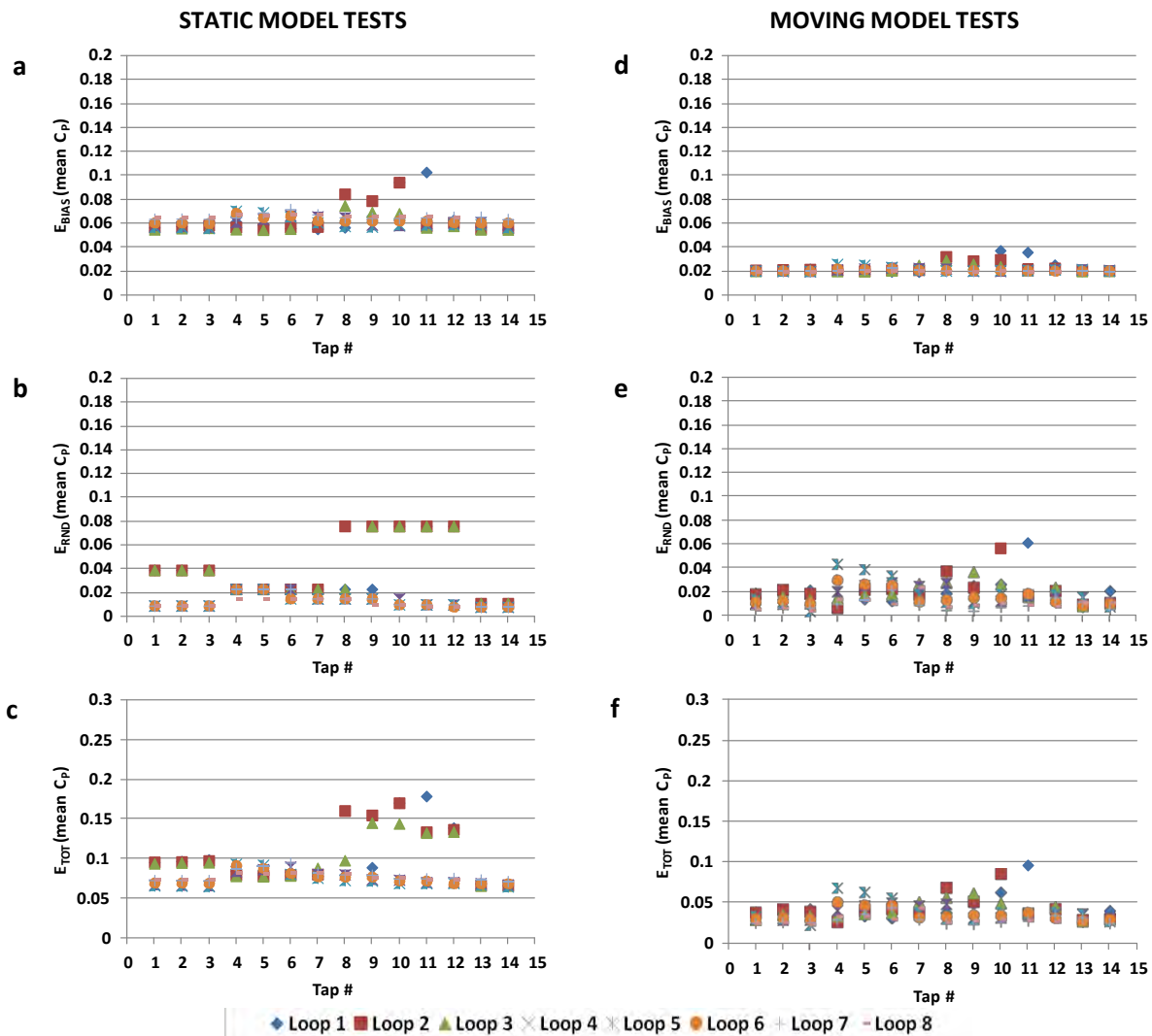
Figure 5.14 Uncertainties on the mean pressure coefficients a) Static tests bias limit b) Static tests random uncertainty c) Static tests overall uncertainty d) Moving model tests bias limit e) Moving model tests random uncertainty f) Moving model tests overall uncertainty

Figure 5.14 summarises the various uncertainties estimated for each pressure tap. The bias limit, random and overall uncertainties are illustrated for static and moving model experiments. In addition, table 5.8 indicates the average and maximum values relating to each contribution and to the total uncertainty. The averages were calculated from the individual uncertainties associated with all the pressure taps, while the maxima were given by the largest.

	Bias limit		Random uncertainty		Overall uncertainty	
	Average	Maximum	Average	Maximum	Average	Maximum
STATIC	0.063	0.103	0.023	0.076	0.086	0.179
MOVING	0.022	0.037	0.017	0.061	0.039	0.098

Table 5.8 Average and maxima uncertainties on the mean pressure coefficients

It can be observed that the estimated overall uncertainty is larger for static than for moving model tests. Since the random uncertainty is similar in both cases, such a difference is largely due to a discrepancy in the bias limit. A larger bias limit for static tests was essentially determined by the lower reference wind speed during these experiments. According to the propagation of error expressed in equation (5.38), all the contributions   associated with the individual instruments are weighted on the derivative of   with respect to any of them. Following from equation (5.1), the bigger the reference wind velocity, the lower the derivative of   with respect to any   . Therefore, a higher reference wind speed associated with moving model tests led to a reduced impact on   associated with any individual contribution specified in table 5.6.

5.4.1.2   Mean load coefficients

The experimental uncertainties related to the mean load aerodynamic coefficients were estimated from those relative to the mean pressure coefficients. The propagation of error was calculated through the equations in section 5.3 assuming the contribution from each facet of the discrete geometry as independent and random (and thus accounting for cancellations by summing them in quadrature). Considering a generic load coefficient   (with   = ,   ,   ,   ), the experimental uncertainty of the corresponding coefficients per unit length (   ) was given by:

$$E^*_{n,j} = \sqrt{\sum_I \left(\frac{\partial C^*_{I,j}}{\partial C_{P_{I,j}}^{n,j}} E^{TOT} \right)^2}$$

(5.42)

where indicate the stripe and is the total uncertainty relating to associated with each facet on the loop . Estimations obtained for static and moving model experiments are illustrated in figure 5.15 and detailed in table 5.9.
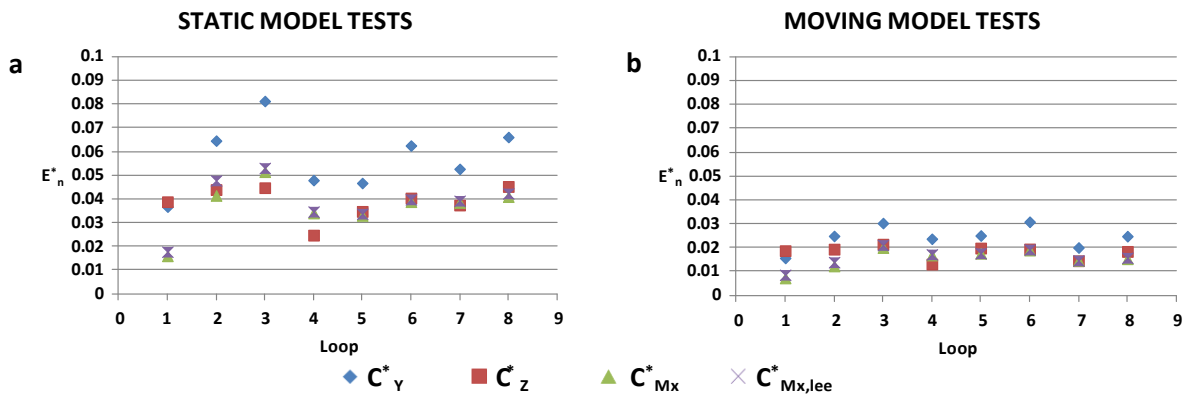
Figure 5.15 Overall uncertainties on the mean load coefficients per unit length a) Static tests b) Moving model tests

	Average Uncertainty			
	(mean)	(mean)	(mean)	(mean)
STATIC	0.057	0.039	0.037	0.039
MOVING	0.024	0.018	0.015	0.016

Table 5.9 Average total uncertainties on the mean load coefficients per unit length

Uncertainties relating to the overall load coefficients were obtained as:

$$E_n = \sqrt{\sum_I \left(\frac{\partial C_n}{\partial C^*_{n,j}} E^*_{n,j} \right)^2}$$

(5.43)

leading to the values in table 5.10.

	STATIC MODEL TESTS	MOVING MODEL TESTS
(mean)	0.034	0.016
(mean)	0.022	0.01
(mean)	0.021	0.01
(mean)	0.022	0.01

Table 5.10 Total experimental uncertainties on the overall mean load coefficients

It is acknowledged that the estimation provided here does not account for any uncertainty introduced by the discrete train geometry or by the assumptions made during the pressure integration process, for example, the assumption of pressure uniformity on each facet. This contribution is difficult to quantify without comparing these results with those obtained through forces and moments measurements. These considerations are taken into account where the TRAIN rig results are compared to those from the wind tunnel tests (appendix H). However, since the same discrete geometry and the same assumptions were adopted for both static and moving model tests, the effect of the model discretisation is assumed to be approximately the same on both sets of results and, as such, not of primary relevance for the assessment of the vehicle movement simulation. A sensitivity analysis to support this assumption is included in appendix F, where a second train geometry discretisation is evaluated in combination with the static tests results.

5.4.2   Peak aerodynamic coefficients

Peak aerodynamic coefficients are analysed in chapter 7 in order to investigate the unsteady aerodynamic loads on the train. Two series of coefficients are defined (section 7.2), i.e., the peak-over-mean (*PoM*) and peak-over-peak (*PoP*), and then presented in a '*normalised form',* having been divided by the mean coefficients (calculated in chapter 6).

In light of such a normalisation, the random uncertainty was considered the only significant contribution to the uncertainty of the peak normalised coefficients. It was estimated through statistical analyses of the processed data with consideration of the error propagation theory and, consistent with the approach undertaken above, it was based on the assumption of a normal distribution and considered a confidence level of 95%.

5.4.2.1 Peak normalised coefficients per unit length

Peak-over-mean (PoM) normalised coefficients

Static model tests

The uncertainty of the PoM coefficients for the static tests was assessed based on the extra measurements carried out on the loops of taps 2 and 6, respectively on the nose and in the centre of the train's leading car. From any of the seven records available for each of these loops, the PoM coefficients were obtained as detailed in section 7.2.2. Once the standard deviation of the values ( ) had been calculated, their uncertainty was estimated as . Combining these uncertainties with those found for the mean coefficients (according to the propagation of error), the uncertainty relative to the PoM normalised coefficients was found. Similar to what was done for the mean coefficients, finally, the estimation concerning loop 2 was extended to the other loops on the train nose (i.e., loops 1 and 3), while the estimation relating to loop 6 was applied to the loops from 4 to 8 (figure 5.16a).

Moving model tests

For the moving model tests, the uncertainty of the PoM normalised coefficients associated with one loop was estimated by computing such parameters from the data collected during each individual run, and then obtaining the standard deviation ( ) over a population of 15 values, corresponding to the total number of runs carried out for each loop. Consistent with the static tests, the range of variation was taken as . The uncertainty relative to the PoM normalised coefficients (figure 5.16b), then, was determined by combination (according to the propagation of error) of the uncertainties relating to the PoM coefficients with those estimated for mean coefficients.
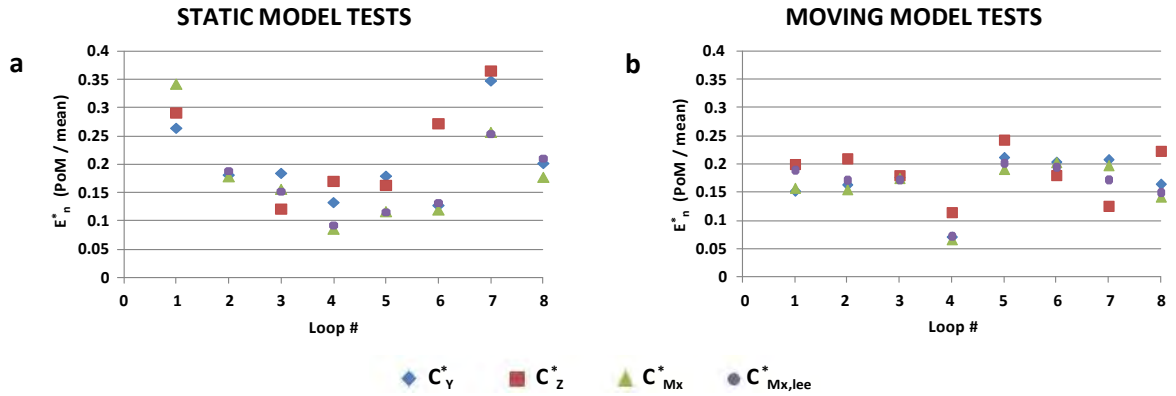
Figure 5.16 Uncertainties on the PoM normalised load coefficients per unit length a) Static tests b) Moving model tests

It can be observed in figure 5.16 that the uncertainty estimated for the PoM normalised coefficients relating to moving model experiments is of the same order as that concerning static tests. This is remarkable if it is taken into consideration that, for the moving model tests, such an uncertainty includes the extra contribution of *mechanical noise* caused by track-induced vibrations. A dedicated analysis (appendix E) outlined how vibrations propagating through the train model frame affected the on-board measuring system employed in this study. However, what is observed in figure 5.16 suggests that the use of pressure transducers (rather than of a force balance) significantly mitigates the impact of *mechanical noise* in the frequency range of aerodynamic interest.

Peak-over-peak normalised (PoP) coefficients

As detailed in section 7.2.1, PoP coefficients were obtained dividing PoM coefficients by the gust factor squared. PoP normalised coefficients, then, were given by the ratio between PoP and corresponding mean coefficients. Accordingly, the uncertainty of the PoP normalised coefficients was evaluated through the propagation theory based on the uncertainty reported above for both PoM and mean coefficients, as well as on the uncertainty of the gust factor . The random uncertainty associated with this parameter was mainly related to the fluctuations of the actual wind conditions taking place when the peak aerodynamic loads were measured. These included the variability of the peak and mean wind velocities actually occurring during any individual run (i.e., the run-to-run variability) and the spanwise variations of the wind velocity within the CWG. The run-to-run

variability was estimated examining the time histories recorded by a reference probe that was kept in a fixed position during the entire flow characterisation. The spatial inhomogeneity of the simulated wind was assessed by evaluating the spanwise variations of (outlined in figure 7.2) with respect to the spanwise average . The estimated ranges of variation are specified in table 5.11 for both static and moving model tests. Considering the two sources of uncertainty as independent, their contributions were summed in quadrature to determine the overall uncertainty affecting .

	STATIC MODEL TESTS	MOVING MODEL TESTS
Spanwise variation	0.06	0.05
Run-to-run variation	0.016	0.016

Table 5.11 Uncertainties on the gust factor

The estimates obtained for the overall uncertainty of the PoP normalised coefficients are illustrated in figure 5.17 for both static and moving model experiments.
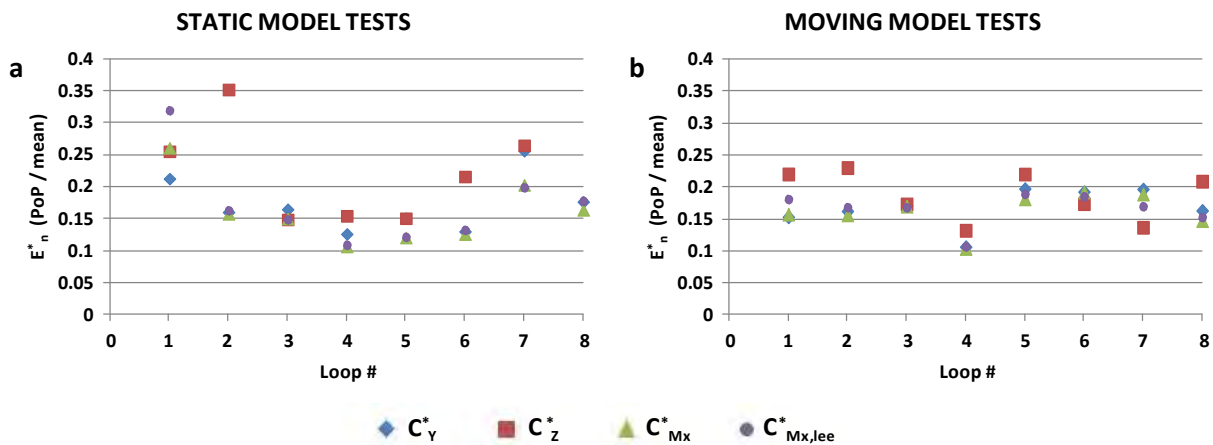
Figure 5.17 Uncertainties on the PoP normalised load coefficients per unit length a) Static tests b) Moving model tests

5.4.2.2 Overall peak normalised coefficients

As detailed later in section 7.3, the PoP coefficients relative to the overall aerodynamic loads were obtained by integration of the PoP coefficient per unit length along the train leading vehicle, and then computing the ratio with respect to the corresponding overall mean load coefficients. The margins of uncertainty for the PoP overall normalised coefficients were calculated through the propagation theory and are specified in table 5.12.

	STATIC MODEL TESTS	MOVING MODEL TESTS
(PoP/mean)	0.074	0.094
(PoP/mean)	0.123	0.102
(PoP/mean)	0.068	0.088
(PoP/mean)	0.072	0.089

Table 5.12 Uncertainties on the overall loads PoP normalised load coefficients

Chapter 6

Steady aerodynamics: results and discussion

6.1 Introduction

Chapter 6 analyses the experimental data relative to the train aerodynamics under the action of a stationary relative wind. These data are expressed through a number of non-dimensional mean coefficients that were given by time averages of the corresponding time series obtained through the data reduction process described in chapter 5. Static and moving model test results are illustrated in section 6.2 and 6.3, respectively. Furthermore, section 6.4 presents a comparison between these and discusses the effects of the vehicle movement simulation.

6.2 Static model tests

6.2.1 Surface pressure distribution

For static tests, the mean values of the pressure coefficient (,) were calculated by averaging the time histories defined in equation (5.4) over their entire duration:

$$\overline{C}_{Pij} = \overline{C_{Pij}(t)} = \frac{\overline{P_{ij}(t)} - \overline{P}^*_{ST,SW}}{\frac{1}{2}\rho\left(\overline{U}^*_{SW}\right)^2} \tag{6.1}$$

All the quantities in equation (6.1) correspond to those introduced in chapter 5 and the normalisation criteria are those defined in section 5.2.1. Accordingly, the results presented below are referred to the *double-average* of the streamwise velocity and wind static pressure (and respectively), both corrected in order to take into account the respective streamwise gradients. (For a sensitivity analysis relating to the use of such a normalisation the reader is referred to appendix F).

As explained in section 4.6, during the static tests all the 164 pressure taps available on the leading car of the Class 390 scale-model were monitored. The values obtained for the mean pressure coefficient are indicated in table 6.1. Figure 6.1 illustrates the pressure distribution relating to each of the 14 cross-sections equipped with rings of taps. In addition, the variation of the pressure distribution along the vehicle is outlined by the contour plots in figure 6.2. Please note that the experimental uncertainties relating to the mean coefficients presented in this section 6.2 and in section 6.3, which has been estimated in section 5.4.1, will be evaluated and discussed in the final section 6.4, covering the comparison between static and moving model tests.

Tap	Loop													
	1	2	3	4	5	9	10	6	11	12	13	7	14	8
1	0.277	0.277	0.137	0.294	0.231	-0.104	0.172	0.173	-0.555	-0.017	-0.156	0.104	0.093	0.066
2	0.387	0.325	0.278	0.206	0.195	-0.867	0.197	0.172	-0.650	-0.448	-0.471	0.127	0.084	0.095
3	0.526	0.428	0.311	-0.081	-0.044	-0.612	-0.214	-0.063	-0.309	-0.665	-0.457	0.101	-0.086	-0.023
4	0.620	0.285	0.159	-0.506	-0.977	-0.357	-0.599	-0.714	-0.282	-0.216	-0.248	-0.252	-0.385	-0.363
5	0.461	0.051	0.029	-0.644	-0.925	-0.288	-0.585	-0.533	-0.221	-0.185	-0.145	-0.545	-0.424	-0.263
6	0.208	-0.288	-0.236	-0.794	-0.776	-0.190	-0.715	-0.615	-0.147	-0.091	-0.026	-0.676	-0.854	-0.384
7	-0.022	-0.338	-0.833	-0.746	-0.533		-0.547	-0.364	-0.131	-0.043	-0.006	-0.453	0.027	-0.335
8	-0.285	-1.474	-1.202	-0.715	-0.309		-0.424	-0.334				-0.278	-0.172	-0.184
9	-0.838	-1.298	-1.001	-0.354	-0.246		-0.375	-0.344				-0.218	-0.183	-0.230
10	-1.779	-1.763	-0.961	-0.289	-0.418		-0.345	-0.347				-0.222	-0.228	-0.217
11	-2.011	-0.373	-0.348	-0.449	-0.410		-0.341	-0.338				-0.268	-0.247	-0.235
12	-0.698	-0.580	-0.451	-0.465	-0.426		-0.285	-0.206				-0.309	-0.267	-0.146
13	-0.390	-0.038	-0.130	-0.504	-0.426		-0.200	-0.167				-0.317	-0.090	
14	0.024	-0.157	-0.119	0.354	0.199		-0.249	-0.176				-0.007		

Table 6.1 Static tests: mean pressure coefficients on the loops of taps 1 to 14 (in red loops on which pressures were measured only in the train underbody during moving model tests; experimental uncertainties specified in figure 5.14 in section 5.4.1.1).
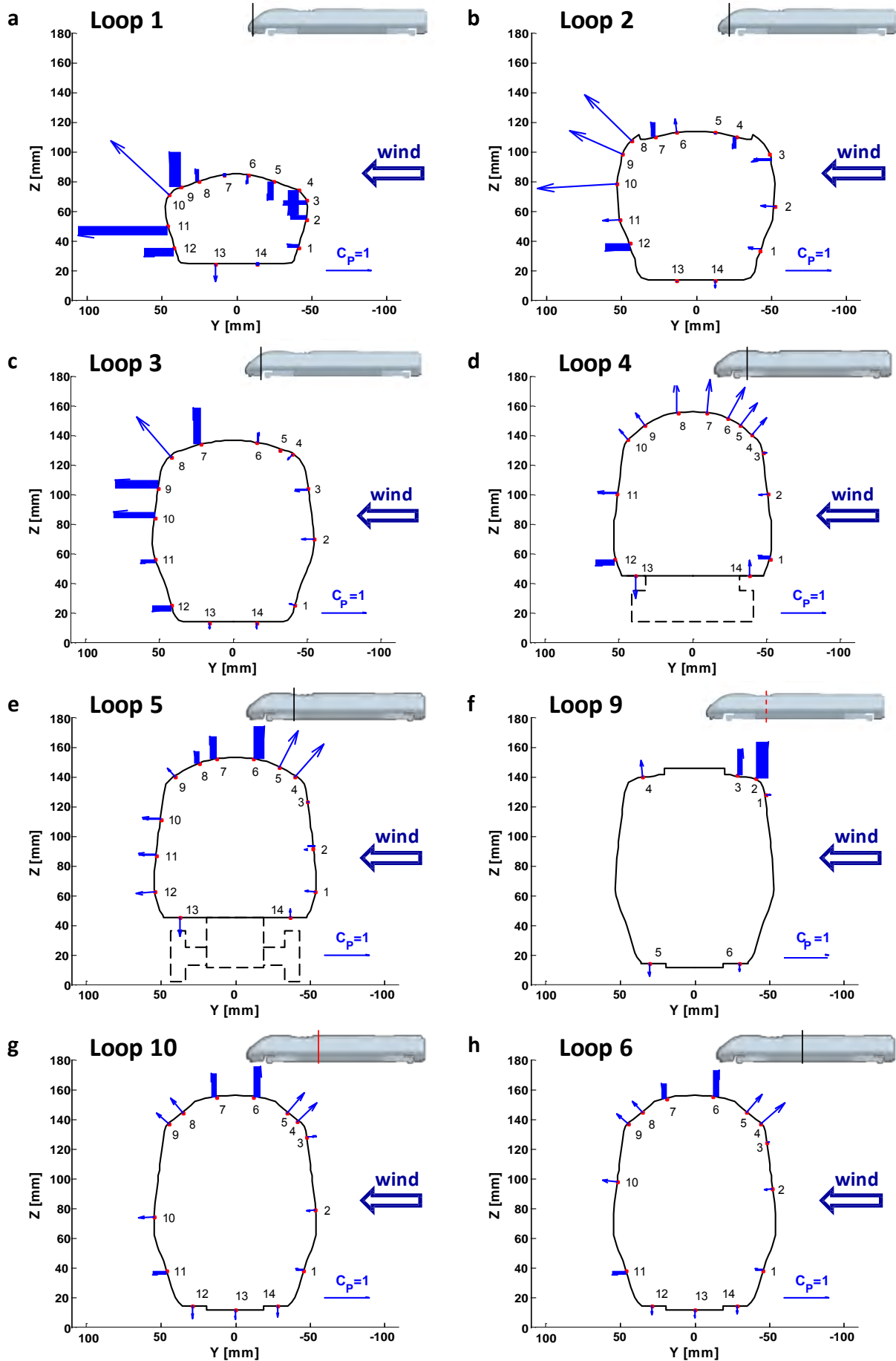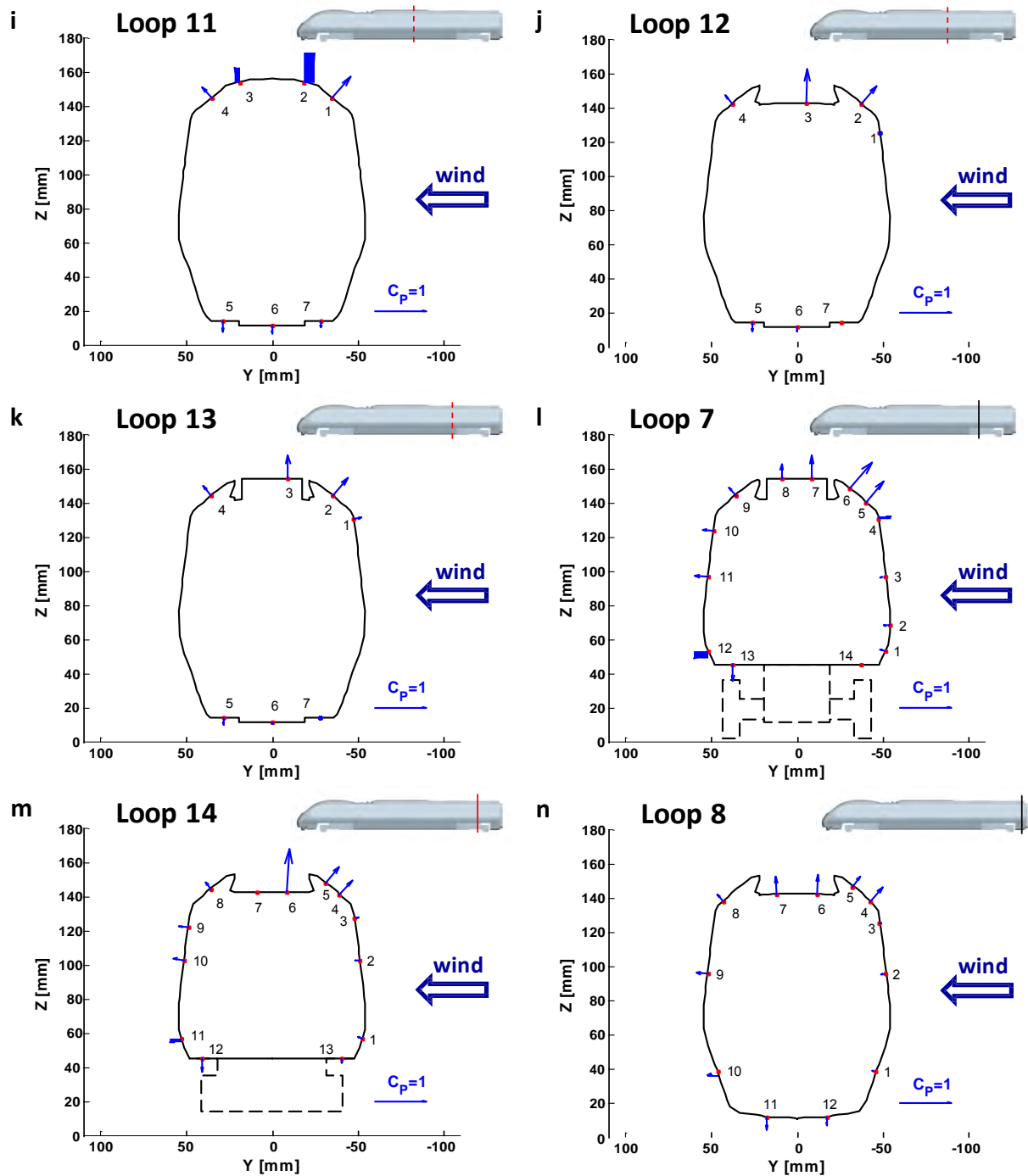
Figure 6.1 Static tests: mean pressure coefficient distribution on each loop of taps (loops 1 to 14)
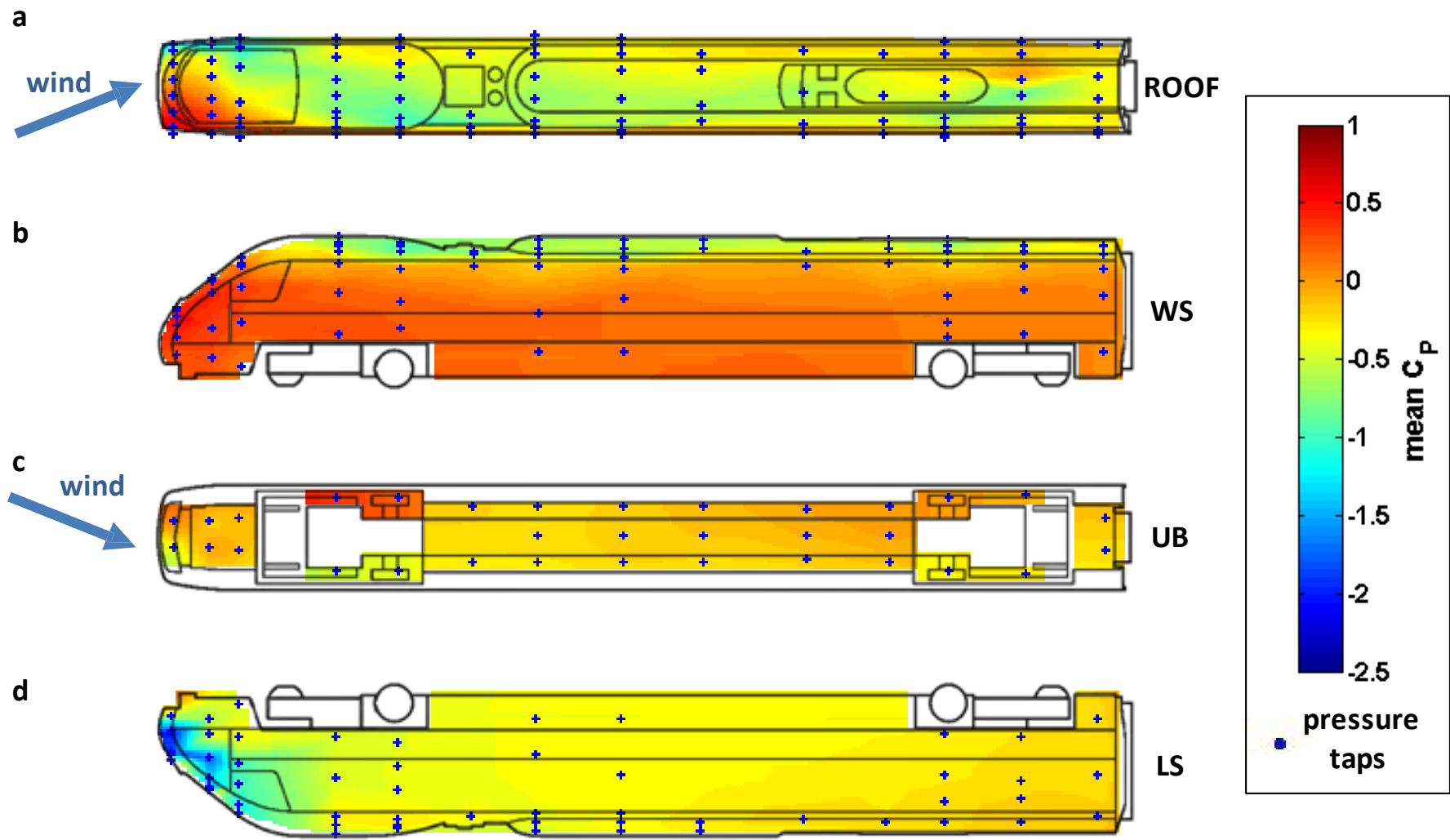
Figure 6.2 Static tests: contour plots of the mean pressure coefficient

In table 6.1 and in figure 6.1 the loops of pressure taps are ordered moving from the nose to the tail of the train. The number of each loop, as well as the number of the pressure taps, are those introduced in figures 4.26 and 4.27 (section 4.5.1.4).

In figure 6.1, the reference system is the same as in chapter 4. Accordingly, the various loops of taps are displayed as seen by an observer looking at the train from the front and the wind is blowing from the right. The pressure taps are identified by red dots on the perimeter of each section while a vector directed normally to the vehicle surface represents the mean pressure coefficient. The length of the vector is proportional to the magnitude of   according to the scale specified on the bottom right corner of each graph. The same scale is used for all loops to ease comparisons. Vectors directed towards the internal of the cross-section are associated with a positive   (i.e., indicating stagnation), while those directed away from the bodies indicate negative pressures.

The contour plots in figure 6.2 were obtained by interpolating the experimental data measured at the pressure taps. They present the roof, windward side (WS), underbody region (UB) and leeward side (LS) of the Class 390 leading car maintaining the same colour scale to ease comparison between different faces of the vehicle.

Different patterns of pressure distribution can be identified along the train. Since the Class 390 leading car has a streamlined design, the cross-sections on the front of the train present a significant and progressive increase in their height and cross-sectional area. This part, i.e. the train 'nose', extends up to the front bogie embracing loops 1, 2 and 3 and is characterised by positive values of on the windward side and on the windward portion of the roof. This indicates a stagnation region determined by the relative wind directly impinging on the train surface. On the windward face the magnitude of   appears uniform on each single loop (considering, for example, taps 1 and 2), with a positive peak occurring at the roof windward corner on loop 1 and 2. A slight decrease of   is observed moving from loop 1 towards loop 3. On the roof, the mean pressure coefficient presents a

negative gradient moving from the windward to the leeward side. As highlighted in figure 6.2a, the transition from stagnation to suction tends to shift progressively upwind.

The region of suction that characterises the leeward side of the roof includes also the entire leeward face of the train nose, with a suction peak arising along the roof leeward corner. The highest magnitude of such a peak occurs on loop 1 and reaches values of   of the order of -2. Moving from loop 1 to loop 3, although the intensity of the suction progressively reduces, the peak remains evident and tends to move upward, following the edge of the roof leeward corner. This echoes previous results obtained for rail vehicles of similar shapes subjected to a crosswind at 30° yaw angle (e.g. Copley, 1987; Hemida and Karjnovic, 2009a) and suggests the presence, on the leeward face of the nose, of one or more vortices attached to the train surface. The attenuation of the low pressure peak observed from loop 1 to 2 and 3 supports the hypothesis of such vortices progressively rolling up and moving away from the train.

One aspect to consider while looking at the pressure distribution in the nose underbody region is that there is a physical downward step between loop 1 and loop2. As highlighted in the side views in figure 6.2, this determines the underbody on loop 1 being at a larger distance from the ground with respect to loops 2 and 3. The mean pressure coefficient is slightly negative in the entire area except at the windward tap on loop 1, where a small positive value is probably induced by a stagnation area occurring upstream of the aforementioned physical downward step. The suction peak appearing on the lee tap on loop 1 might be associated with the initial development of a lee-side vortex along the low edge of the train. The low pressure region in the underbody on loops 2 and 3 is compatible with the development of a (relatively weak) recirculation developing downstream of the physical downward step.

The nose of the vehicle ends by the front bogie, with the maximum height of the cross-section reached on loop 4. From this section to the end of the first car, both the windward and leeward faces are characterised by relatively uniform pressure distributions. A stagnation region embraces the

windward side, showing   values sensibly lower than those on the train nose and a slight negative

gradient moving towards the train tail. The area of suction that occurs on the leeward face presents

magnitudes of   significantly lower than those found on the nose. There is no suction peak arising

on any of the loops from 4 to 8, and a slight attenuation in the intensity of the suction is found

towards the rear. The fact that a smooth pressure distribution on the leeward face is reached already

on loop 4 suggests that a complete detachment of the leeward vortices that form on the train nose

has occurred by that stage.

The geometry of the roof induces an evolution of the pressure distribution along the top face of the

vehicle that is less regular than that observed on the windward and leeward sides. The loops from 4

to 8 see the roof entirely embraced by an area of low pressure that includes a suction peak. Although

such a peak tends to occur on the windward corner, its exact position and intensity vary along the

vehicle. It can be observed in figures 6.1 and 6.2 that for all the loops on the train body (i.e.,

excluding the nose) the suction peak on the roof represents the lowest   of the entire section.

However, it can also be observed that the magnitude of this peak is less than that of the peak on the

leeward side of the train nose. On the first bogie, where the roof presents a large radius and 'well

rounded' profile, the suction peak occurs approximately on the centreline of loop 4, and then drifts

towards the windward corner on loop 5 (figure 6.1d and 6.1e). Presenting a significant variation in its

profile, the roof on loop 9 shows a suction peak on the windward corner (figure 6.1f). In the central

portion of the vehicle, which includes loops 10, 6 and 11, the roof maintains a constant (smooth-

edged) profile. As shown in figures 6.1g to 6.1i, the pressure distribution is characterised by a less

intense trough of   spread on the windward portion of the roof. In the rear part of the first car,

finally, there is a further significant modification in the shape of the roof, which takes the sharp

edged profile of loop 12 highlighted in figures 6.1j-n. Where the roof central notch is empty, as

happens on loops 12, 14 and 8, the edge on the upper windward corner induces flow separation. This

determines the onset of flow recirculation within the notch and thus an intense low pressure peak

arises. On loops 13 and 7, instead, since the space within the notch is occupied, no recirculation occurs. The pressure distribution, hence, is similar to that observed in the centre of the vehicle and the low pressure reached at the roof windward corner represents the trough.

The train underbody is characterised by significant variations in the flow field along the vehicle. This is mainly caused by 'interference' generated by the mock bogies and by the wheel-sets (see section 4.4) on the flow developing in the gap between the train and the ground. On loops 4 and 5 at the front bogie, figures 6.1d and 6.1e show positive   values on the bottom face positioned over the windward wheel and mock bogie. This suggests that the flow directly impinging on the wheel-set is stagnating in the cavity delimited by the train body, the wheel-set assembly and the half-bogie that was modelled. Conversely, in the symmetric cavity on the opposite side of the train the mean pressure coefficient becomes negative. As discussed in section 4.4, the geometry of the half-bogies and of the wheel-sets of the TRAIN rig scale-model was different from that of the bogies on a real Class 390 Pendolino train. Therefore, it is acknowledged that the observations concerning the pressure distribution in proximity of the scale-model bogies might offer an approximate representation only of what happens on a real train.

Along the portion of train body between the two bogies the geometry of the train bottom face remains uniform. This induces a pressure distribution presenting negative values of   and no sudden variations. A tendency to have the highest (relative) suction on the leeward side of the underbody region is shared by all the loops. Furthermore, a slight increment of the mean pressure coefficient is found moving from the front towards the rear. The combination of these two effects determines a positive gradient in the underbody surface pressure directed from the leeward side of the front bogie towards the windward side of the rear bogie (figure 6.2c). Such a trend appears to be determined by the underbody blockage associated with the presence of the rear bogie (Copley, 1987), which induces 'relative stagnation' in the area upstream of the wheel-set. Similar to what is observed at the front, on the rear wheel-set the underbody pressure is significantly lower on the

cavity on the leeward side than on the windward side. However, since the magnitudes of on loops 7 and 14 are generally reduced with respect of those on loops 4 and 5, the mean pressure coefficient on the windward cavity does not reach positive values. On loop 8, positioned at the tail of the leading car, after the rear bogie, decreases to values similar to those on loop 9 downstream of the front bogie.

6.2.2 Aerodynamic load coefficients per unit length

The mean load coefficients per unit length were obtained from the mean pressure coefficients through equations (5.36) in section 5.3.1. They were calculated for cross-sections 1 to 8 and for sections 10 and 14. The other loops were not considered because they were equipped with only a partial distribution of pressure taps. Figure 6.3 illustrates the evolution of and , side and lift force coefficients per unit length, respectively, with respect to the longitudinal position of each loop normalised on the vehicle length (i.e.). In figure 6.4a and 6.4b, the rolling moment coefficients per unit length and are shown. They refer to the -axis (corresponding to the vehicle centreline and positioned at the top of the rail (TOR)) and to the leeward rail, respectively, and see their overall values illustrated together with the individual contributions from the side and lift forces. According to the reference system adopted, negative values of both and correspond to moments that tend to overturn the vehicle. Therefore, an inverted vertical axis is adopted in the figures for ease of interpretation. Figure 6.5, finally, outlines the lateral and vertical coordinate of the centre of pressure on each section. These were calculated by dividing the individual contributions to the rolling moment from side and lift forces by the corresponding force coefficient (and multiplying the result by).
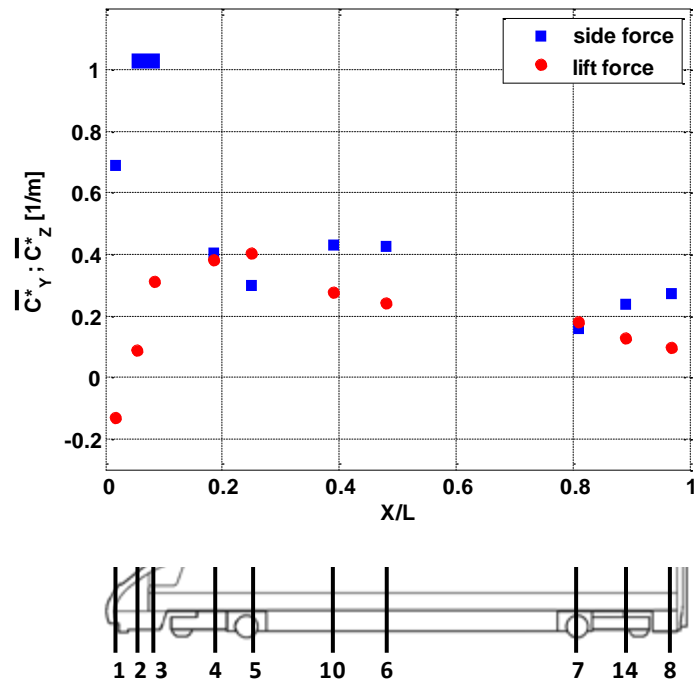
Figure 6.3 Static tests: mean load coefficients per unit length of the side and lift forces (experimental uncertainties specified in figure 5.15 in section 5.4.1.2)
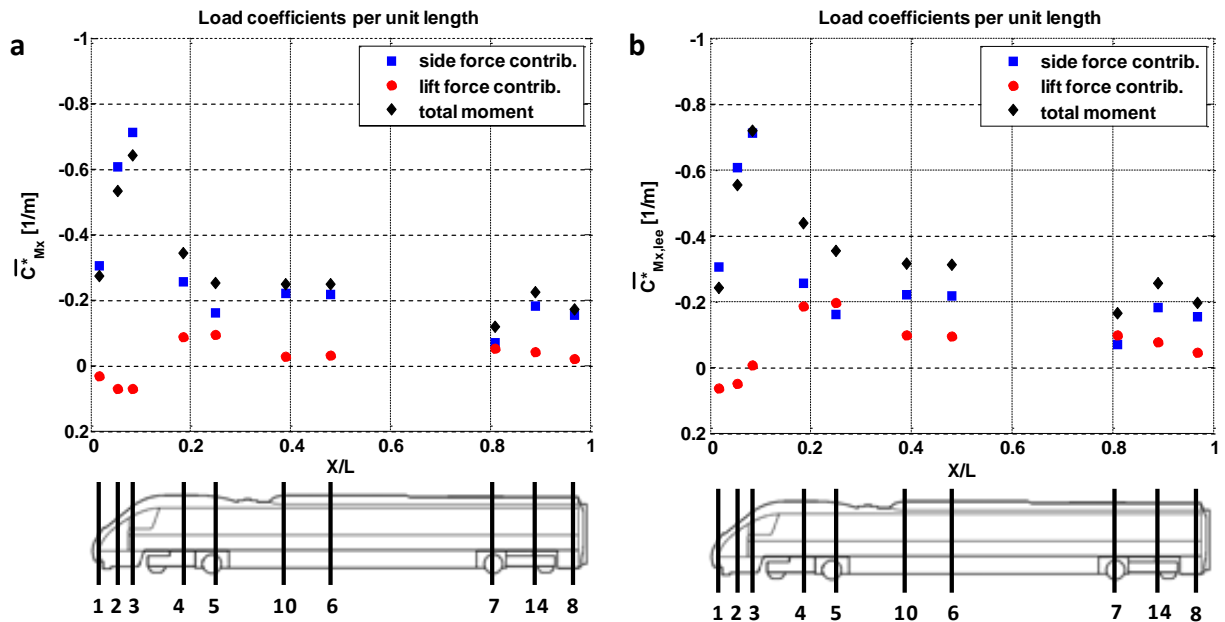
Figure 6.4 Static tests: mean load coefficients per unit length (inverted vertical axis; experimental uncertainties specified in figure 5.15 in section 5.4.1.2). a) *X*-axis rolling moment **b)** Leeward rail rolling moment
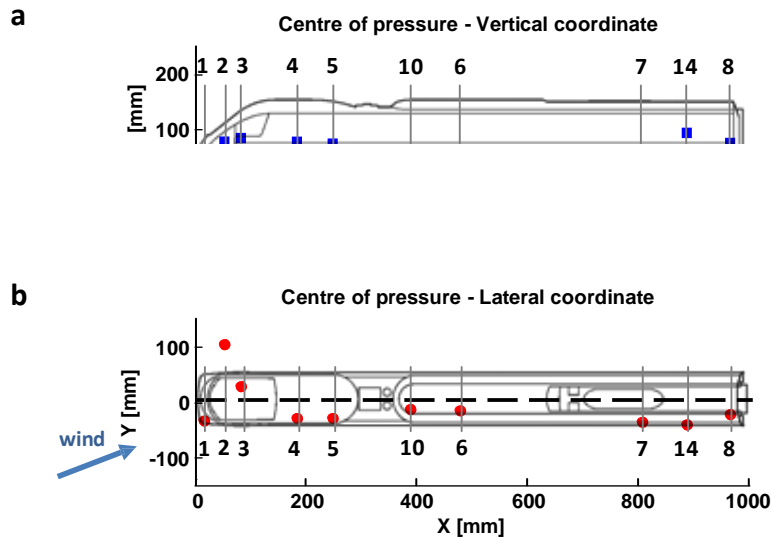
Figure 6.5 Static tests: position of the centre of pressure on each loop a) Vertical coordinate b) Lateral coordinate

The blue square markers in figure 6.3 show that the entire vehicle is characterised by positive values of side force coefficients (per unit length). This indicates a lateral net force directed in the wind direction and reflects the stagnation and suction pressure regions identified respectively on the windward and leeward side of the train. The maximum values of side force coefficients, slightly larger than 1, are reached on loops 2 and 3 on the nose of the train. This is not surprising in light of the intense low pressure peak previously observed on the leeward side of the sections. Although the most intense suction on the lee face occurs at of loop 1, the corresponding   remains slightly lower because of the limited height of the cross-section.

In the central part of the vehicle, the side force coefficients on loops 10 and 6 are significantly lower than these on the nose. This is due to the absence, in this part of the vehicle, of any low pressure peak on the leeward face and also to a negative contribution associated with the suction region on the roof windward corner. Even if no data were available between loop 6 and 7, since the geometry of the vehicle between these two loops is consistent with that of loop 6, it may be inferred that similar values of   could occur for 0.3   0.75. Slight variations could perhaps be expected

just at the upper end of this range (i.e. 0.65 ÷ 0.75) because of the variation in the roof profile.

On the loops relating to both wheel-sets figure 6.3 indicates that low side force coefficients occur. Since the bogies were not included in the vehicle discrete geometry (section 5.3), this could be caused by the reduced height of the integration surface. Finally, on the tail of the car, the low outlined in figure 6.3 appears consistent with the reduced intensities of the pressure field found on the windward and leeward faces of loop 8.

The lift force coefficient per unit length is essentially determined by the balance between the pressure on the roof and in the underbody region of each loop. Positive values of this parameter (indicating a force directed upwards) are found for all sections except on loop 1 on the train nose. On loop 1, a negative contribution is determined both by the intense stagnation that extends over large parts of the roof and by the low pressure in the underbody region. Furthermore, since the leeward suction peak embraces only a small part of the roof, its positive contribution to the overall value of is limited. Although a similar condition affects loop 2, the reduced magnitude and extensions of the stagnation region on the roof lead to a positive   On all other sections, a positive lift force coefficient is determined by the fact that the suction on the upper face of the train is more intense than that in the underbody region, with a significant contribution given by the low pressure peak developing on the roof. Accordingly, the largest   .are reached on loops 4 and 5, where such a suction peak is particularly intense. Moving from there to the rear of the train, then, the lift force coefficient tends to decrease, which is consistent with the observed slight attenuation of the low pressure peak on the roof.

The examination of figure 6.4 outlines that the side force generates an overturning moment (i.e. negative   ) on all the examined loops of pressure taps. The corresponding vertical coordinate of the centre of pressure is illustrated in figure 6.5a. The intensity of the rolling moment varies along

the vehicle following the trend observed for the side force coefficient. A different tendency can be observed by looking at the contribution to the rolling moment given by the lift force. On the nose of the train such a contribution is opposite to that of the side force and thus assumes positive values. Associated with a lift force directed downward, on loop 1 this determines a centre of pressure positioned on the windward side of the car (figure 6.5b). On loop 2 and 3, instead, where the vertical component of the aerodynamic load points upward, this implies a shift of the line of action of the vertical force to the leeward side. Such a behaviour is mainly caused by the strong suction peak on the leeward side of the vehicle nose. Along the remaining length of the vehicle the lift force produces negative , thus contributing to increase the magnitude of the total rolling moment coefficient. The intensity of such contribution reflects the evolution of the lift force coefficient and reaches its maximum for loops 4 and 5. As illustrated in figure 6.5b, in the presence of positive values, from loop 4 to the end of the car, the centre of pressure for the vertical force remains on the windward side of the train.

It is worth noting that on loop 2 the centre of pressure is indicated in a 'theoretical position' external to the vehicle. According to the calculation method adopted, this results from the windward and leeward portions of the section generating vertical forces directed respectively downward and upward, which produce a relatively high rolling moment associated with a small lift force.

On the entire leading car, the side force has the dominant impact on the overturning moment coefficient (with the only exception being around the rear bogie). Comparing figure 6.4a and 6.4b, it can be noticed that the side force contribution to and is the same. According to equation (5.35) in section 5.3, this is consistent with the -axis being at the same height as the leeward rail. Furthermore, the contribution of the side force is dominant with respect to that given by the lift force on any loop. However, the markers associated with the lift force contribution denote a different behaviour depending on the loop. On loop 1 and 2, as to so to the lift force gives a stabilising contribution and, in turn, leads these coefficients to be slightly smaller than for the

situation with only the side force. However, while on loop 1 such a lift force contribution to   is larger than to   , on loop 2 it is the opposite. This depends on the position of the centre of pressure. On loop 3, the positive (i.e., stabilising) contribution given by the lift force to   becomes negative to   . Finally, on any loop of pressure taps from the front bogie to the tail of the leading car, the lift force increases the negative magnitudes of   as well as it does for   , thus enhancing the rolling moment that tends to overturn the train.

6.2.3 Overall aerodynamic load coefficients

The overall mean load coefficients were calculated from the corresponding mean coefficients per unit length through equations (5.37) in section 5.3.2. To ensure consistency with the moving model experiments, a discrete integration along the train was performed based on a vehicle discretisation comprising eight longitudinal stripes, which corresponded to the loops from 1 to 8. (A second estimation based on a longitudinal discretisation comprising of 14 stripes is presented in appendix F).

The values estimated for the aerodynamic load coefficients of the entire vehicle are illustrated in figure 6.6a and detailed in table 6.2, while figure 6.6b shows the position of the centre of pressure on the   -   vertical plane.
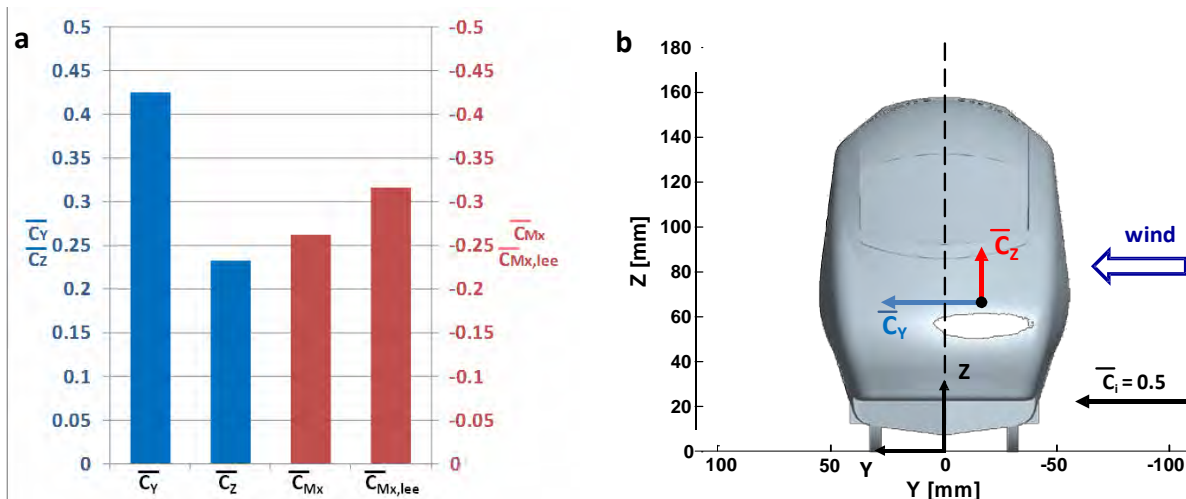
Figure 6.6 Static tests: train overall aerodynamics (experimental uncertainties specified in table 5.10 in section 5.4.1.2). a) Mean overall aerodynamic coefficients b) Position of the overall centre of pressure

	0.425
	0.233
	-0.262
	-0.316

Table 6.2 Static tests: mean overall aerodynamic load coefficients (experimental uncertainties specified in table 5.10 in section 5.4.1.2)

These results reflect the behaviour of the load coefficients per unit length. Positive values of   and   indicate overall lateral and vertical forces directed according to wind and pointing upward, respectively. Negative values for   and   , where the negative scale is specified in figure 6.6a on the inverted vertical axis on the right, denote overall moments that tend to overturn the train. Accordingly, the centre of pressure is positioned at ~1.7 m above the ground and shifted on the windward side of the centreline by ~0.4 m (using full-scale dimensions). These trends are consistent with what is typically observed on leading cars of high speed trains at 30° yaw angle (Sanquer et al., 2004; Bocciolone et al., 2008; Baker, 2011). Furthermore, an encouraging level of agreement can be found with standard wind tunnel static tests performed as part of the AeroTRAIN project (appendix H) as well as with previous data relative to the same nominal train geometry (Baker, 2003).

6.3   Moving model tests

6.3.1   Surface pressure distribution

For moving model experiments the mean pressure coefficients   were given by:

$$\overline{C}_{Pij} = \overline{C_{Pij}\left(t_N^*\right)\Big|_{ENS}}\,\Bigg|_{0.2<t_N^*<0.9} \tag{6.2}$$

where   is the normalised time,   are the ensemble average time series defined in equation (5.33) in section 5.2.2.3 and an overbar indicates a time average. Furthermore, it is worth noting the equivalence between   and   , i.e., the spanwise coordinate normalised on the crosswind section span:

$$t_N^* = \frac{t \cdot V_{tr,CW}}{L_{CW}} = \frac{s}{L_{CW}} = s_N \tag{6.3}$$

Equation (6.2) indicates that the averaging time does not correspond to the entire duration of the moving model ensemble average time series. Rather, it includes only the interval of between 0.2 and 0.9, where the time series denote a relatively stable behaviour.

Figure 6.7 shows an example of the typical evolution of the pressure coefficient while the model train travels within the crosswind section. 15 single-run time histories are illustrated together with the corresponding ensemble average time series and the averaging time interval is highlighted in green. The variations of that characterise both ends of the time histories explain why such portions of data were not included in the time averaging process. They reflect the transitions in the train surface pressure occurring when the vehicle has just entered the crosswind section and when it approaches the exit. Although they were not examined as part of this research, it is worth noting that, in a future development, the data relating to such transitions offer the possibility to investigate transient aerodynamic phenomena (section 8.2).
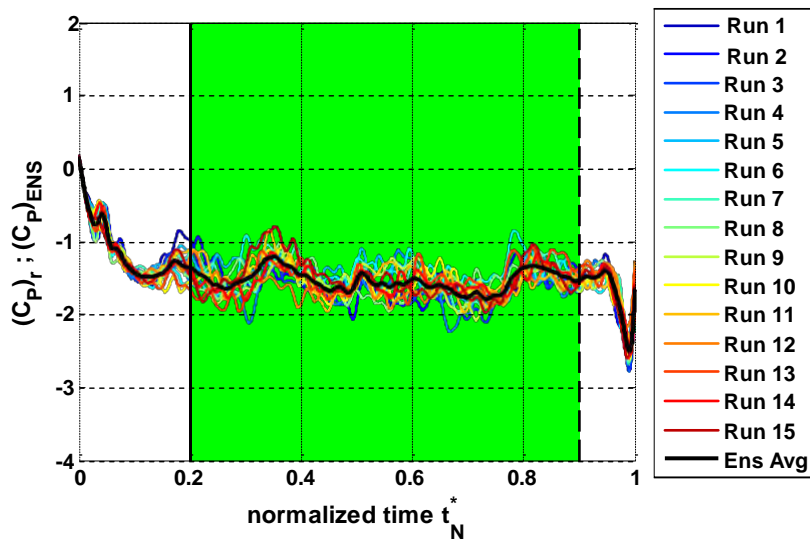
Figure 6.7 Moving model tests: example of averaging time interval for the mean pressure coefficients calculation (tap 8 on loop 2)

As explained in section 4.7, during moving model experiments all the pressure taps on loops from 1 to 8, plus the underbody taps on loops from 9 to 13, were monitored (124 pressure taps in total). For the purposes of discussion, the pressure coefficient time histories relating to the taps on loops 2 on the nose and loop 6 in the centre of leading car are illustrated in figures 6.8 and 6.9, respectively.

a Loop 2

b Loop 2 Tap 1

c Loop 2 Tap 2

d Loop 2 Tap 3

e Loop 2 Tap 4

f Loop 2 Tap 5

g Loop 2 Tap 6

h Loop 2 Tap 7
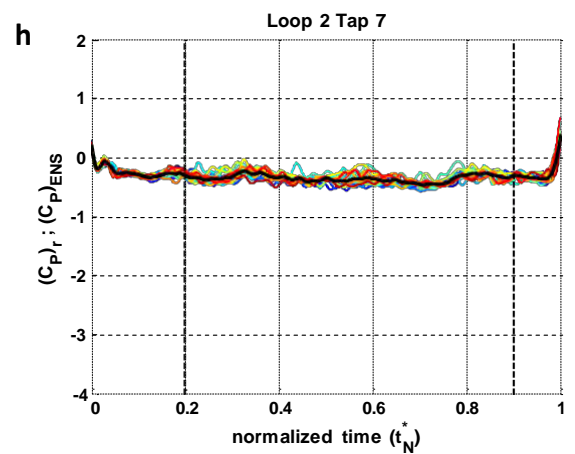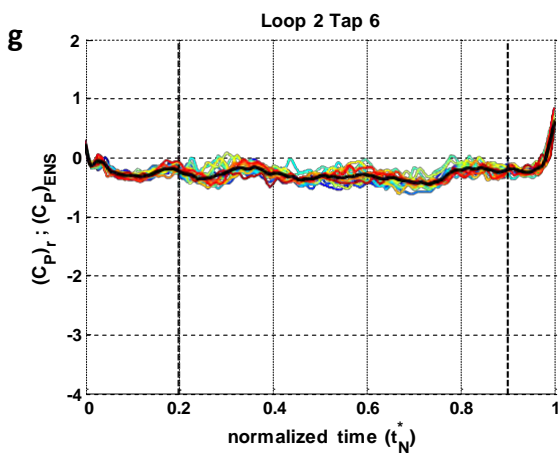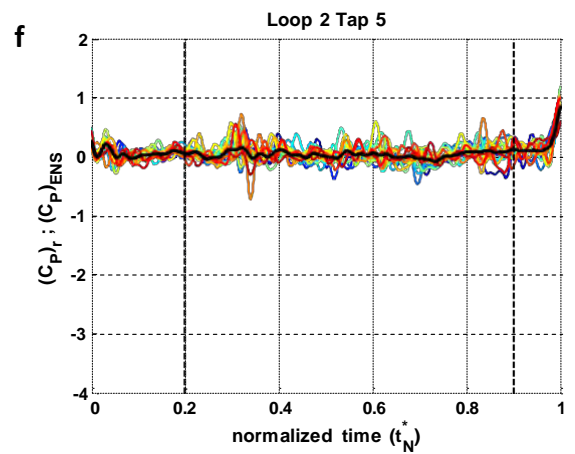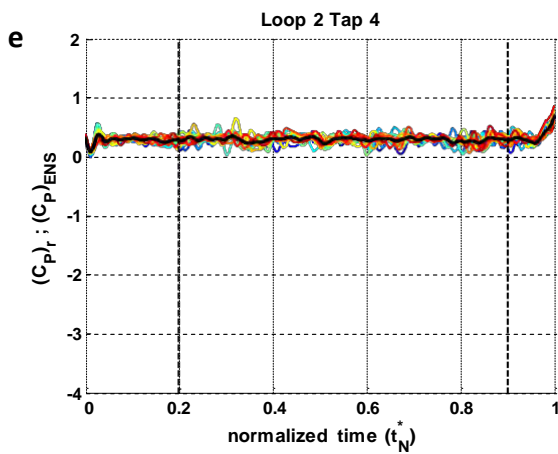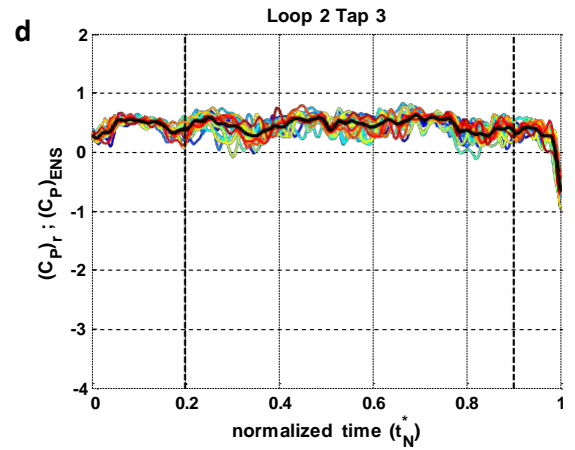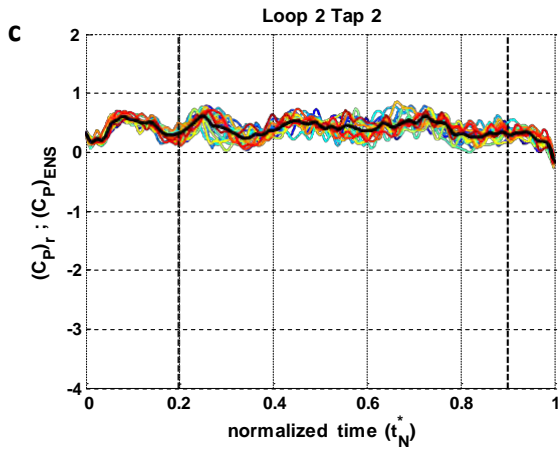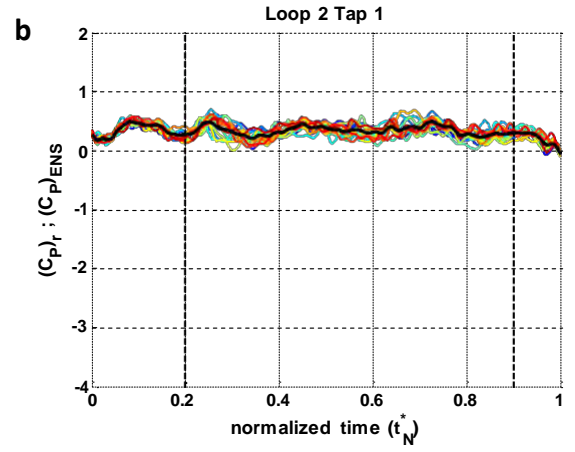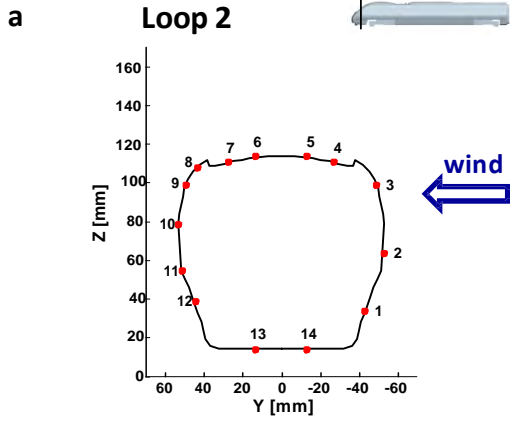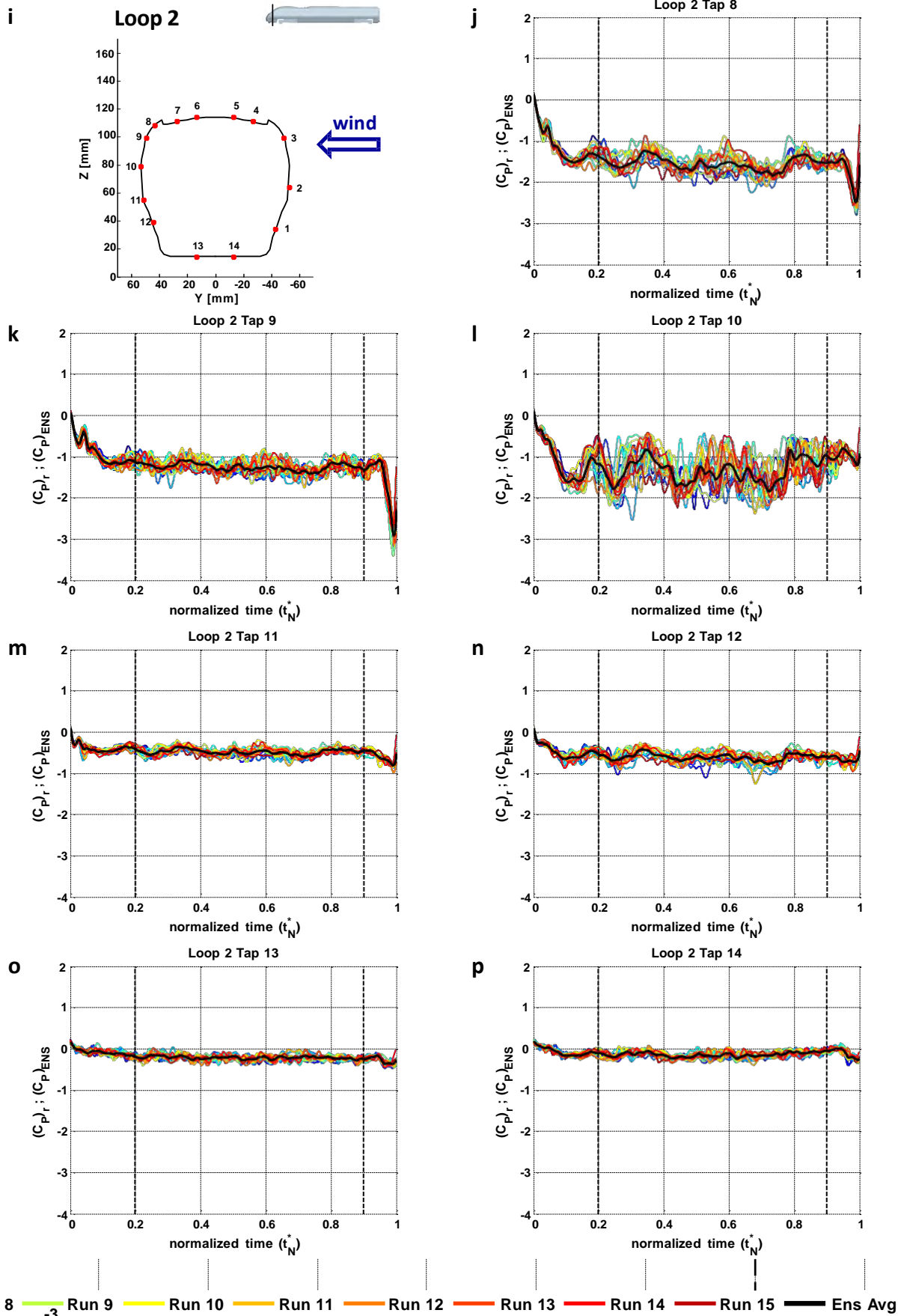
Figure 6.8 Moving model tests: single-run and ensemble average time series of the pressure coefficient on loop 2 on the train nose

a Loop 6

b Loop 6 Tap 1

c Loop 6 Tap 2

d Loop 6 Tap 3

e Loop 6 Tap 4

f Loop 6 Tap 5

g Loop 6 Tap 6

h Loop 6 Tap 7
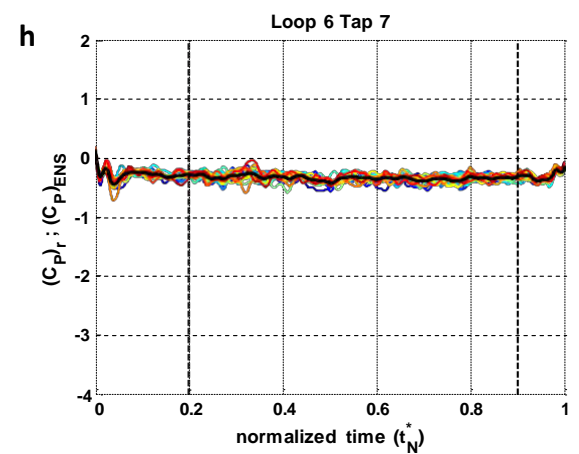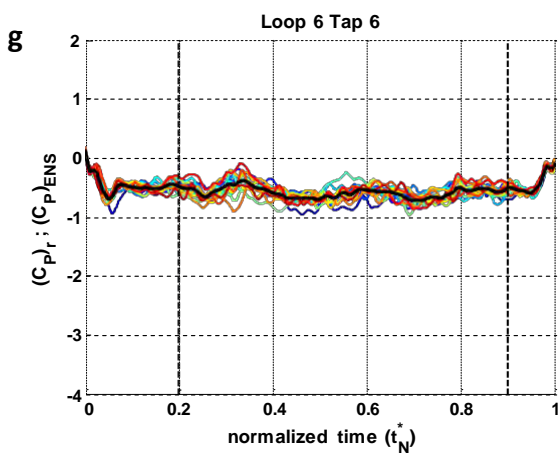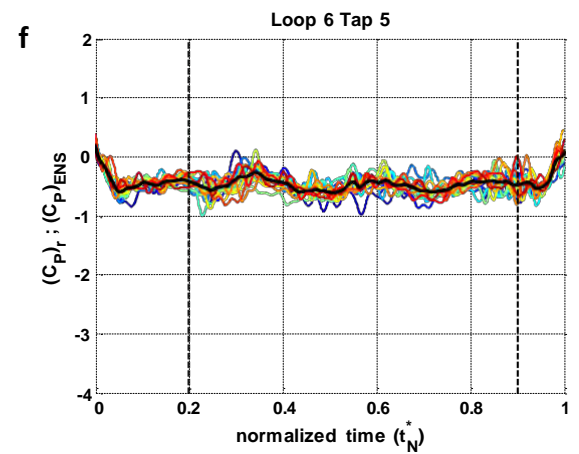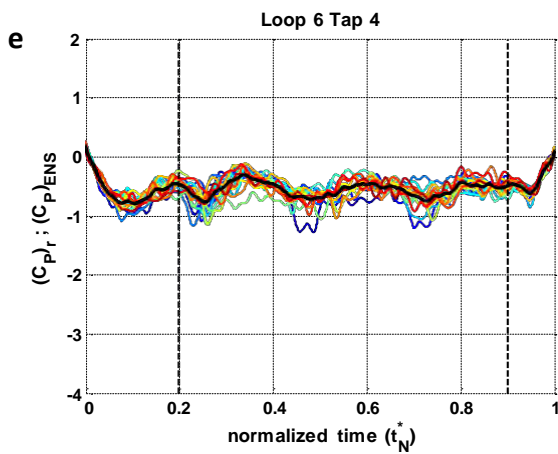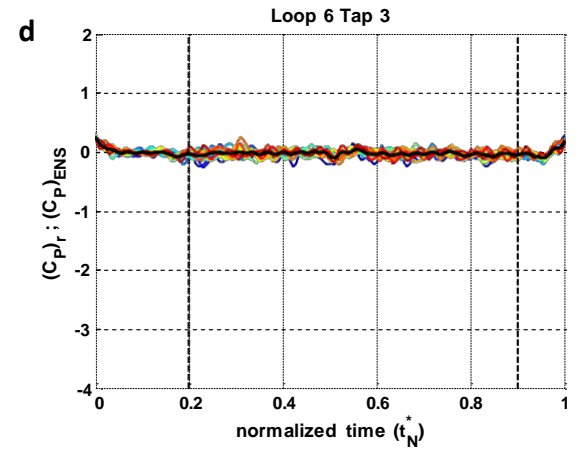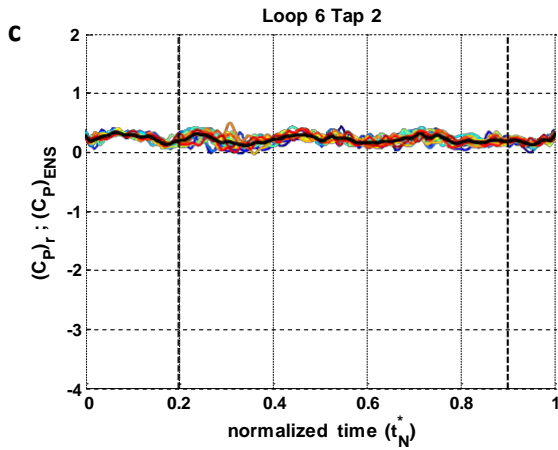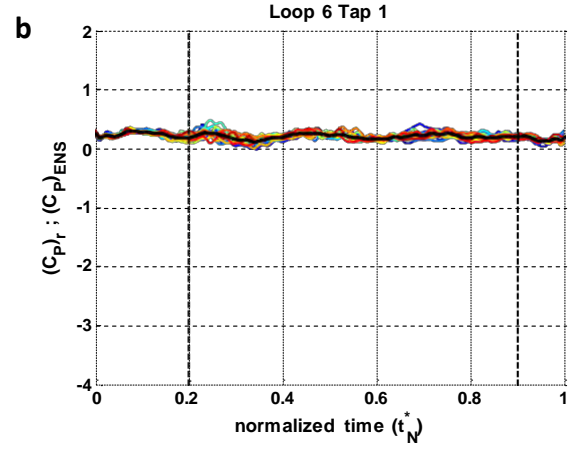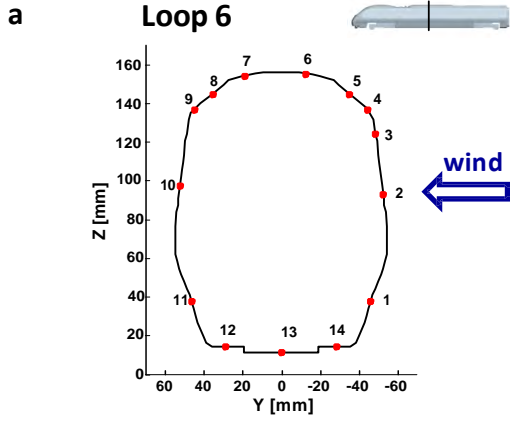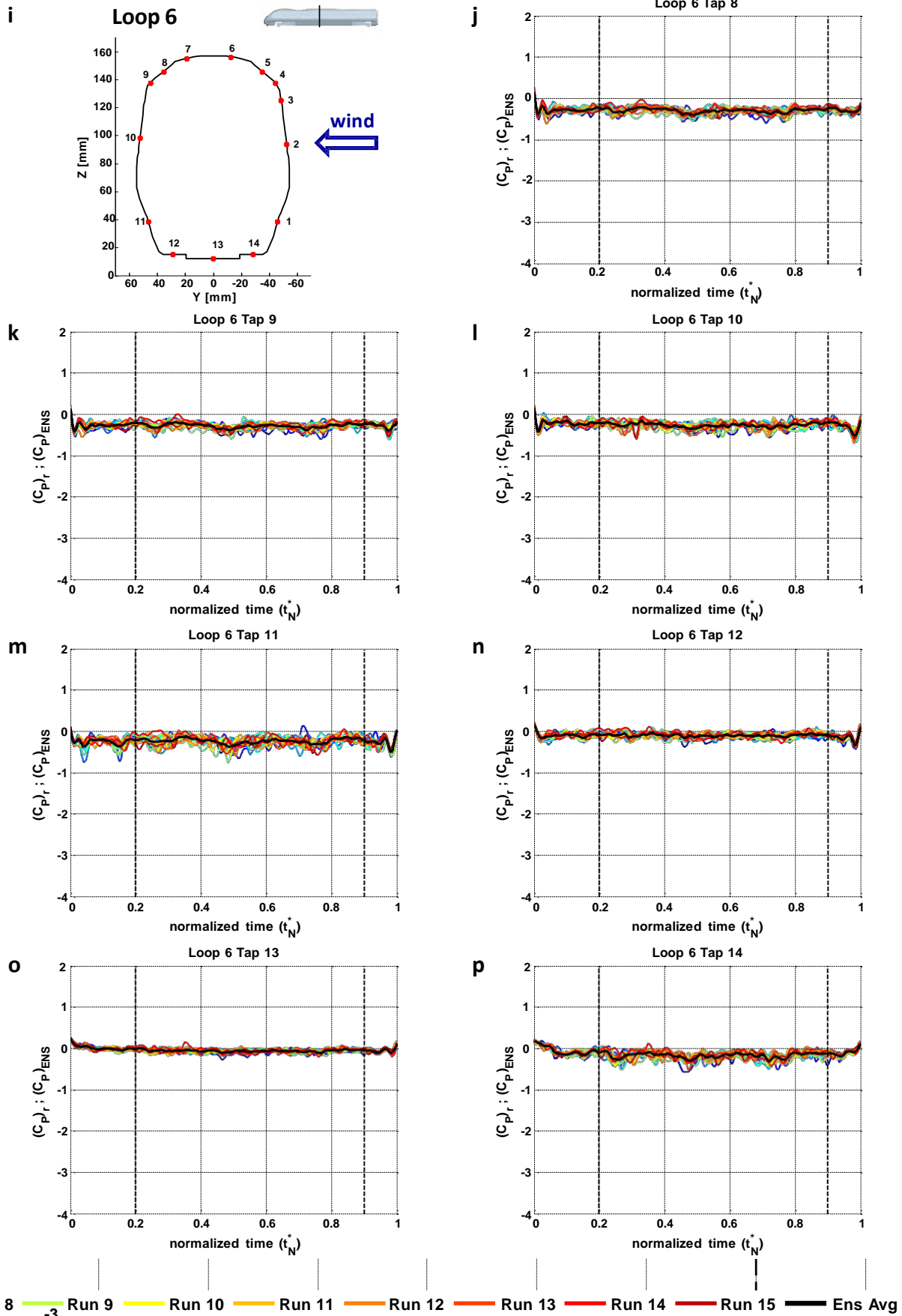
Figure 6.9 Moving model tests: single-run and ensemble average time series of the pressure coefficient on loop 6 in the centre of the leading car

In figures 6.8 and 6.9, a good consistency can be observed in the evolution with respect to the non-dimensional time of different single-run time series relating to the same pressure tap. There is agreement both in the average values of   reached in the central (steady) portion of the time window and in the shape and intensity of the transient oscillations outlined at both ends.

Any time history associated with one individual run is characterised by a series of relatively short time-scale (i.e., high frequency) fluctuations. Comparing different runs relative to the same pressure tap, these fluctuations have similar amplitude. However, a degree of scatter in the instantaneous values of   corresponding to the same non-dimensional time   denotes a lack of synchronisation between oscillations occurring during different runs. Therefore, since these are not synchronous, the fluctuations 'cancel out' within the ensemble averaging process and, therefore, do not appear in the ensemble average time series.

These oscillations are compatible with surface pressure variations induced by the turbulent flow developing around the train once subjected to the crosswind. In addition, since we are dealing with a moving vehicle, a *mechanical noise* interference' caused by vibrations induced by the track irregularities and sensed by the on-board measuring system, cannot be excluded (appendix E). A comparison between different pressure taps reveals a variation in the amplitudes of these short time-scale fluctuations. Larger amplitudes tend to occur in combination with the lowest values of   , for example, on taps 8 to 10 on loop 2 and on tap 4 on loop 6. This is consistent with the presence of areas of suction associated with vortices attached to the train surface, or of regions of recirculation characterised by an increased level of turbulence.

Specific observations need to be made regarding tap 5. Large fluctuations, in comparison with the adjacent taps 4 and 6, are shown by the single-run time series relating to this tap both on loop 2 and 6 (and also on the other loops, not shown here). This was assessed to be caused by a technical problem with the measurement chain associated with one particular channel on the data logger (i.e., channel 5). The increased amplitude in the short time-scale oscillations, therefore, was not a

symptom of actual variations in the surface pressure, but rather was determined by electronic noise. The numerical low-pass filter applied to the raw data (section 5.2.2.1) was beneficial in mitigating this interference. However, since the noise also had low frequency components, a residual effect remained on the filtered time series. With respect to the steady aerodynamic analysis, this issue did not compromise the reliability of the measurements. Having monitored one pressure tap originally associated with channel 5 using a different channel, good agreement was found in the two series of mean coefficients that were obtained. With respect to the analysis of the peak aerodynamic coefficients, this interference was further mitigated by the moving average filter that was applied in the time domain (section 7.2). Any remaining effect still affecting the data, then, was accounted for in the uncertainty analysis (section 5.4.2).

The examination of figures 6.8 and 6.9 reveals also a second type of oscillations. These can be identified both on the single-run and ensemble average time histories and their amplitudes vary significantly from one tap to another, with the largest occurring on at tap 10 on loop 2, where the suction peak occurs. They persist for the entire duration of the time series and have a relatively long time-scale, of the order of approximately 0.2 times the total length of the time window.

Rather than being caused by the turbulent nature of the flow surrounding the train, or by mechanical or aerodynamic induced noise, it is inferred that these long time-scale fluctuations are related to the spanwise inhomogeneity in the mean wind relative to train (appendix A). To support this interpretation, appendix G outlines how such an inhomogeneity causes variations both in the magnitude and in the yaw angle of the relative wind velocity seen by a train whilst travelling through the CWG. Furthermore, consistent with the dependence of the pressure coefficient on both these quantities (section 2.4.2), it highlights the correspondence of the long time-scale oscillations in the time series with the spanwise evolution of the magnitude and yaw angle of the relative wind.

The data reduction method applied here assumes that the mean pressure coefficient depends only on the mean values of both the reference wind velocity and yaw angle. Accordingly, the variability of

the mean relative wind is taken into account by considering its effect on the spanwise averages of the relative velocity and of the yaw angle (which, most importantly, was 30° as in the static tests). The assumption made, which is not uncommon in wind engineering (Richards et al., 1995), is in accordance with the *Quasi-Steady* theory discussed in section 2.4.2.2 (Cook, 1985; Baker, 1991b). In addition, a discussion on its application in this particular context is included in appendix G, where an alternative data reduction method is also evaluated.

The mean pressure coefficients on loops 1 to 8, obtained according to the assumptions specified above, are presented in table 6.3. The results relative to the additional taps in the underbody region are in table 6.4. Figure 6.10 illustrates the mean pressure distribution on the examined cross-sections using the same conventions adopted in figure 6.1 (for static tests). Finally, figure 6.11 shows a set of contour plots obtained by interpolating the values of   relating to the pressure taps on the four faces of the train's leading car.

The analysis of the mean pressure coefficients from the moving model tests indicates that the pressure distribution over the vehicle is similar to that obtained in the static tests. Even if some differences appear on a number of pressure taps, in general   has the same order of magnitude described in section 6.1.1. Similarities can be observed on each loop in the trend of the variation of   around the vehicle, as well as in its evolution from the nose to the tail of the train. For, an in depth comparison with static experiments, the reader is referred to section 6.4.

Tap	Loop							
	1	2	3	4	5	6	7	8
1	0.450	0.328	0.170	0.385	0.252	0.191	0.190	0.177
2	0.570	0.407	0.377	0.242	0.223	0.200	0.223	0.201
3	0.653	0.457	0.376	-0.084	-0.024	-0.041	0.193	0.046
4	0.684	0.291	0.107	-0.512	-1.077	-0.567	-0.198	-0.373
5	0.469	0.032	-0.025	-0.636	-0.996	-0.497	-0.433	-0.258
6	0.159	-0.307	-0.335	-0.775	-0.795	-0.611	-0.690	-0.370
7	-0.086	-0.366	-0.979	-0.708	-0.430	-0.358	-0.440	-0.338
8	-0.374	-1.586	-1.374	-0.657	-0.289	-0.307	-0.259	-0.157
9	-0.987	-1.280	-1.077	-0.291	-0.241	-0.291	-0.202	-0.178
10	-2.108	-1.374	-0.853	-0.234	-0.403	-0.273	-0.174	-0.217
11	-1.995	-0.494	-0.371	-0.397	-0.411	-0.242	-0.191	-0.203
12	-1.064	-0.622	-0.614	-0.556	-0.474	-0.105	-0.318	-0.088
13	-0.365	-0.232	-0.127	-0.585	-0.489	-0.078	-0.342	
14	0.399	-0.162	-0.233	0.448	0.263	-0.192	0.089	

Table 6.3 Moving model tests: mean pressure coefficients on the loops of taps 1 to 8 (experimental uncertainties specified in figure 5.14 in section 5.4.1.1).

Loop 9		Loop 10		Loop 11		Loop 12		Loop 13	
Tap		Tap		Tap		Tap		Tap	
5	-0.368	12	-0.276	5	-0.174	5	-0.212	5	-0.105
6	-0.217	13	-0.139	6	-0.113	6	-0.074	6	0.094
		14	-0.259	7	-0.122	7	-0.062	7	0.107

Table 6.4 Moving model tests: mean pressure coefficients at the underbody pressure taps on loops 9 to 13.
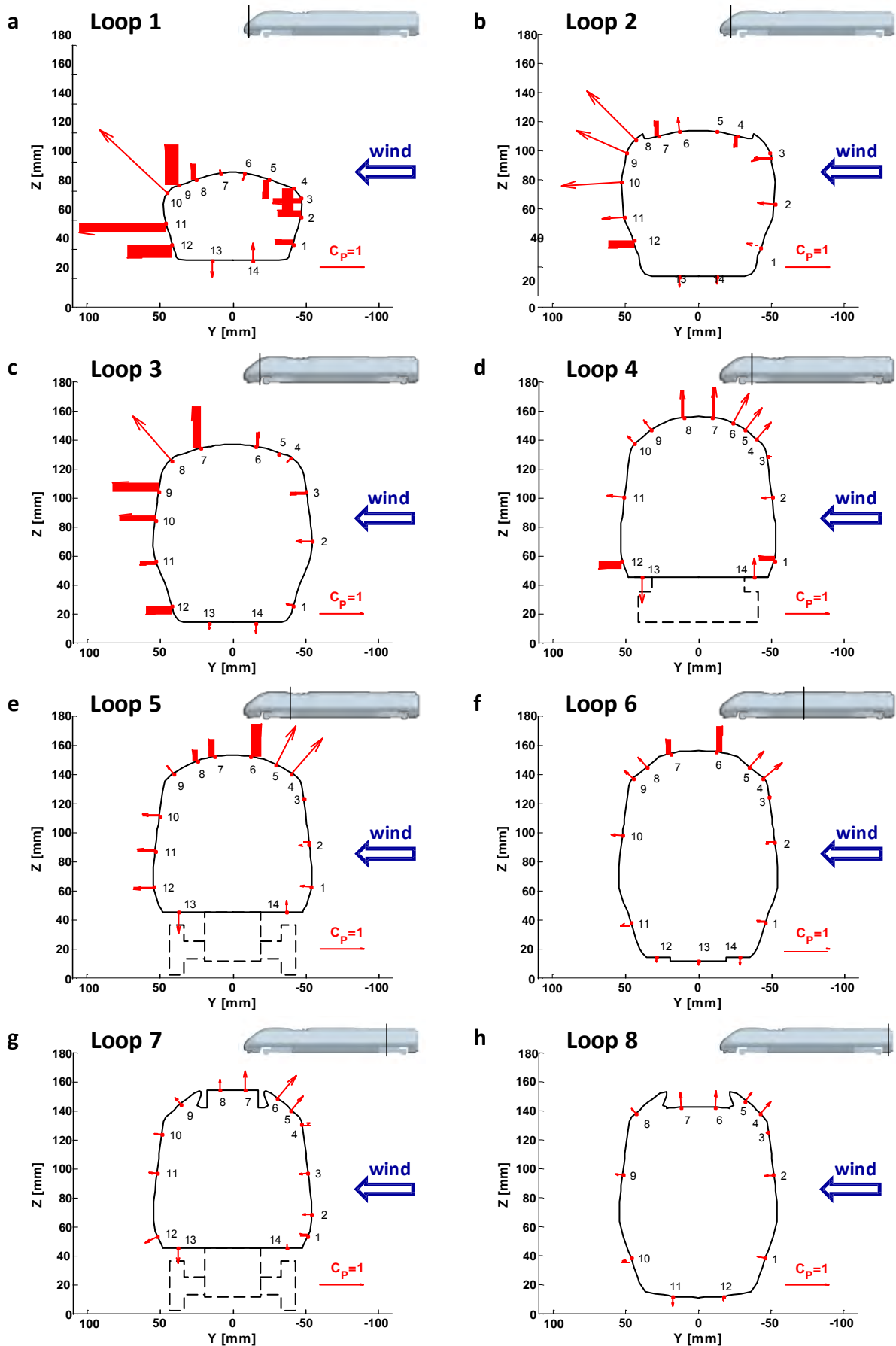
Figure 6.10 Moving model tests: mean pressure coefficient distribution on each loop of taps (loops 1 to 8)
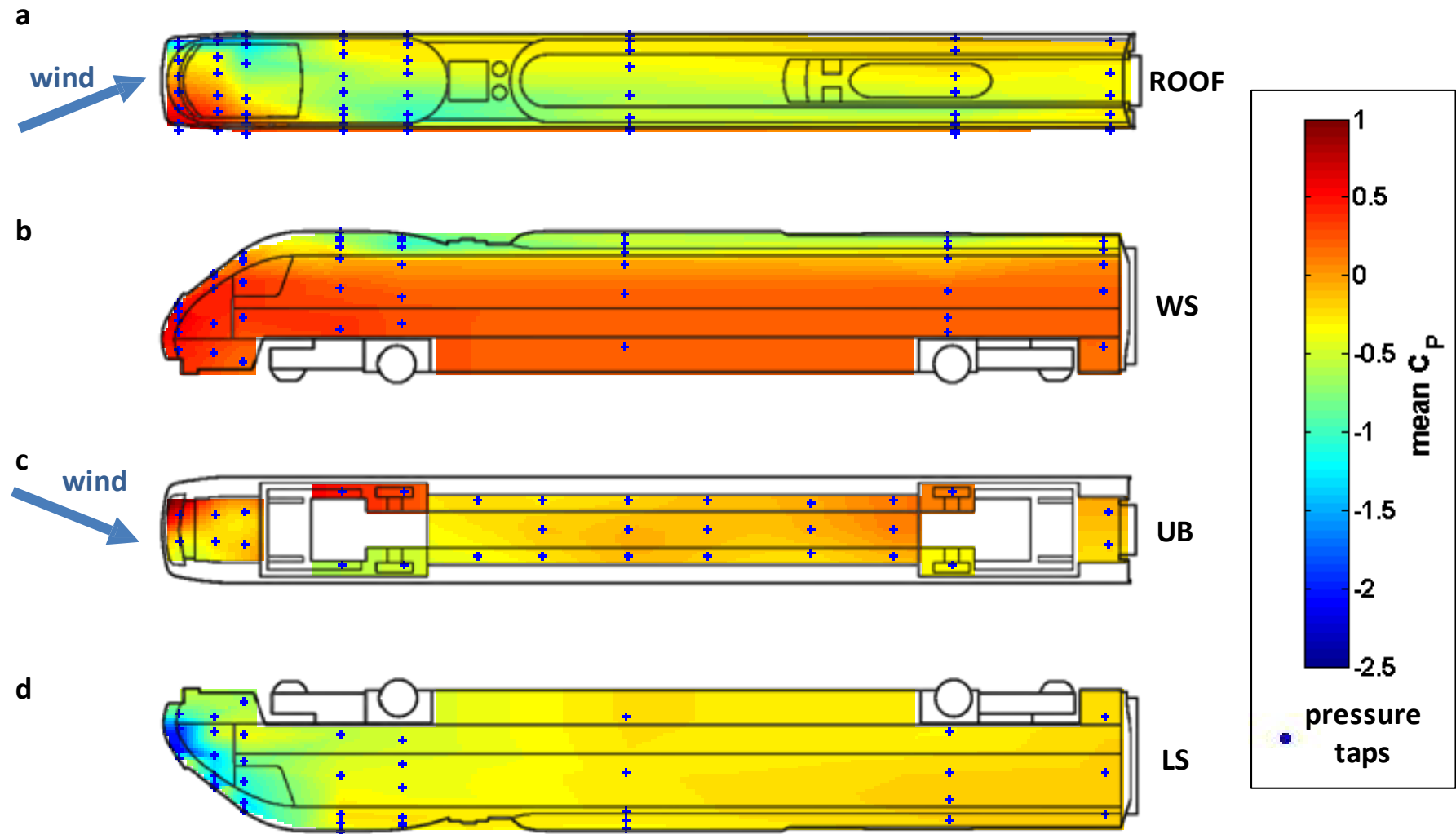
Figure 6.11 Moving model tests: contour plots of the mean pressure coefficient

6.3.2 Aerodynamic load coefficients per unit length

Since pressure taps on the same loop were monitored simultaneously during the same run, time series for the load coefficients per unit length could be obtained from those of the pressure coefficients. The instantaneous values   ,   ,   and   were calculated for each loop (from 1 to 8) through equations (5.36) in section 5.3.1 and, as for   , examples of the evolution of such coefficients are shown relating to loops 2 and 6 (in figures 6.12 and 6.13, respectively).

Figure 6.12 Moving model tests single-run and ensemble average time series of the load coefficients per unit length on loop 2 on the train nose a) Side force b) Lift force c) *X*-axis rolling moment d) Leeward rail rolling moment

Figure 6.13 Moving model tests: single-run and ensemble average time series of the load coefficients per unit length on loop 6 in the centre of the leading car a) Side force b) Lift force c) *X*-axis rolling moment d) Leeward rail rolling moment

The single-run time series denote similar characteristics to those illustrated for   . Short time-scale fluctuations (whose amplitude is larger for   ) occur for the entire duration of these time series and are not synchronous between different runs. As such, at a certain time instant, either a peak or a trough can occur, depending on which time history is taken into account. By contrast, there is a good correspondence between individual runs in the transient at the beginning of the time series and in the long time-scale fluctuations, which are both clearly visible in the ensemble average time series also. The long time-scale fluctuations are evident in the side force and, although slightly attenuated, in the rolling moment coefficients. They show higher amplitudes on loop 2 on the nose rather than on loop 6 in the centre of the vehicle and, as discussed relating to the pressure coefficient (and in appendix G), appear related to the spatial non-uniformity of the relative wind.

The mean load coefficients per unit length (identified by an overbar) were obtained from the instantaneous values according to the same procedure applied for the pressure coefficients. They were the time averages of the ensemble average time histories restricted to   between 0.2 and 0.9. Alternatively, the same results could be obtained substituting the mean pressure coefficients in equations (5.36) in section 5.3.1.

and   are illustrated in figure 6.14, while figure 6.15 shows   and   . Additionally, the vertical and lateral coordinates of the centre of pressure on each loop of taps are displayed in figure 6.16. As specified in the diagram included in each figure, all the results were obtained for the loops from 1 to 8.

In agreement with what was observed for the mean pressure coefficients, the data presented here denote only minor discrepancies from those obtained with the static tests. There is a good correspondence between the static and moving results in the magnitude of the coefficients and also in their trend along the vehicle. As for   , so in this case, a detailed comparison between the two sets of experimental data is included in section 6.4.
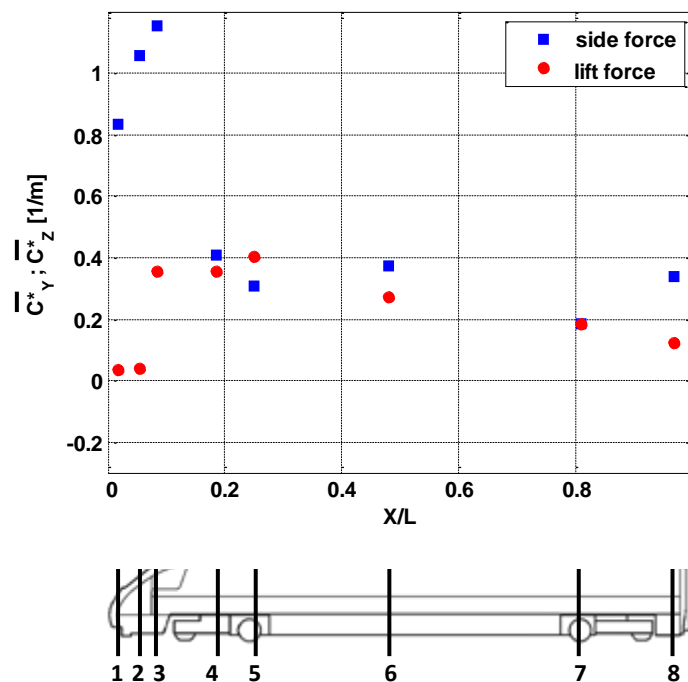
Figure 6.14 Moving model tests: mean load coefficients per unit length of the side and lift forces (experimental uncertainties specified in figure 5.15 in section 5.4.1.2)
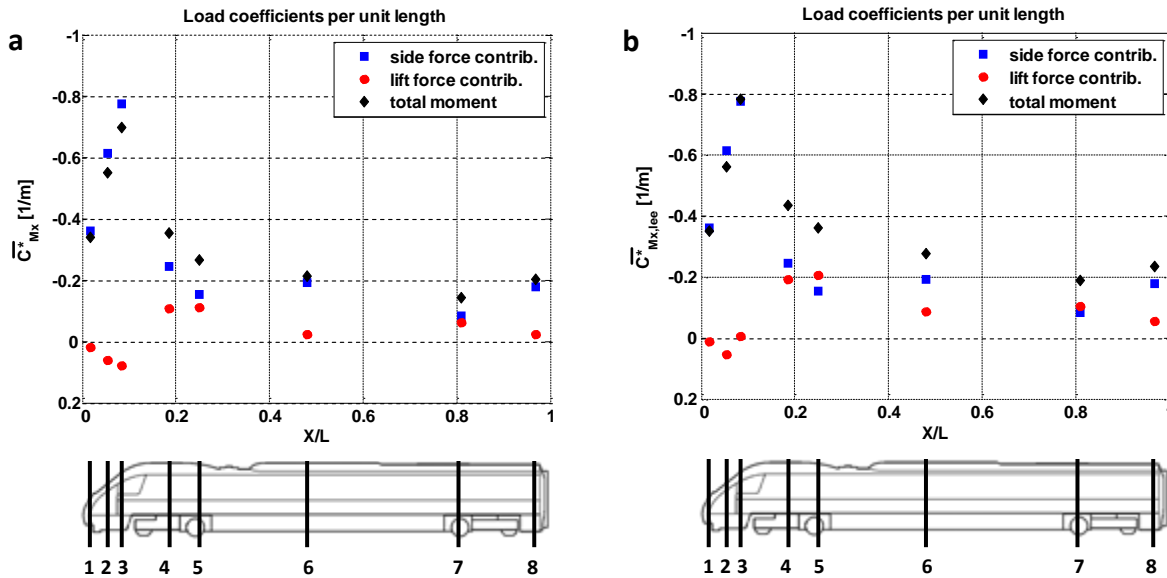
Figure 6.15 Moving model tests: mean load coefficients per unit length (inverted vertical axis; experimental uncertainties specified in figure 5.15 in section 5.4.1.2). a) *X*-axis rolling moment **b)** Leeward rail rolling moment
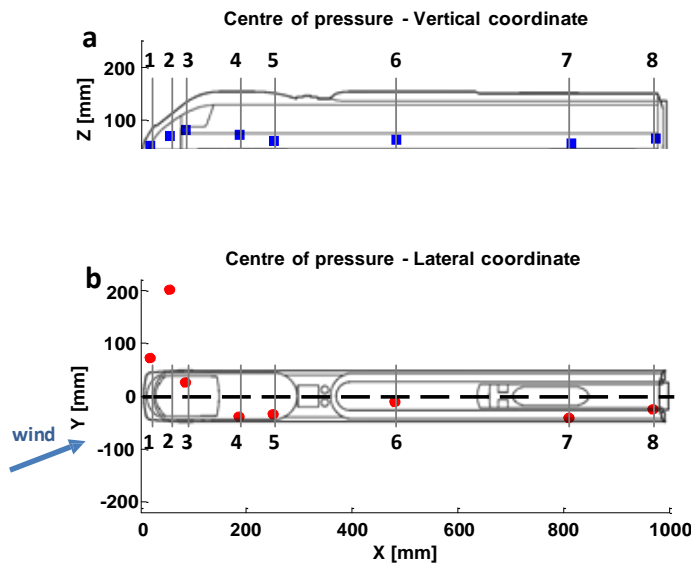
Figure 6.16 Moving model tests: position of the centre of pressure on each loop a) Vertical coordinate b) Lateral coordinate

6.3.3 Overall aerodynamic load coefficients

The numerical values obtained for , ,   and   are illustrated in figure 6.17a and specified in table 6.5. The estimated lateral and vertical coordinates of the centre of pressure are indicated in figure 6.17b. Once again, although no major differences appear with respect to the static tests results, the reader is referred to section 6.4 for an in depth discussion.
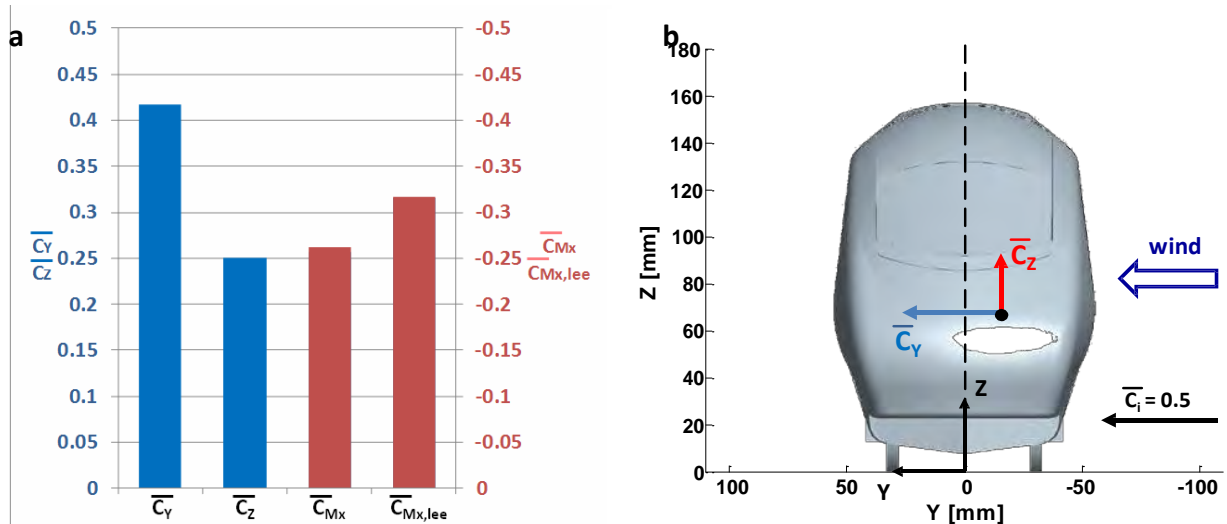
Figure 6.17 Moving model tests: train overall aerodynamics (experimental uncertainties specified in table 5.10 in section 5.4.1.2). a) Mean overall aerodynamic coefficients b) Position of the overall centre of pressure

	0.417
	0.251
	-0.257
	-0.316

Table 6.5 Moving model tests: mean overall aerodynamic load coefficients (experimental uncertainties specified in table 5.10 in section 5.4.1.2).

6.4 Comparison between static and moving model tests

6.4.1 Surface pressure distribution

Figure 6.18 presents the comparison between static and moving model tests results (indicated in blue and red, respectively) for the mean pressure coefficients relating to pressure taps on loops from 1 to 8. In each figure the cross-section of the loop under investigation is shown in combination with the values to ease identification of the tap positions. Furthermore, error bars are included to denote the *overall* experimental uncertainties estimated in section 5.4.1, assuming normally distributed data and considering a 95% confidence level.
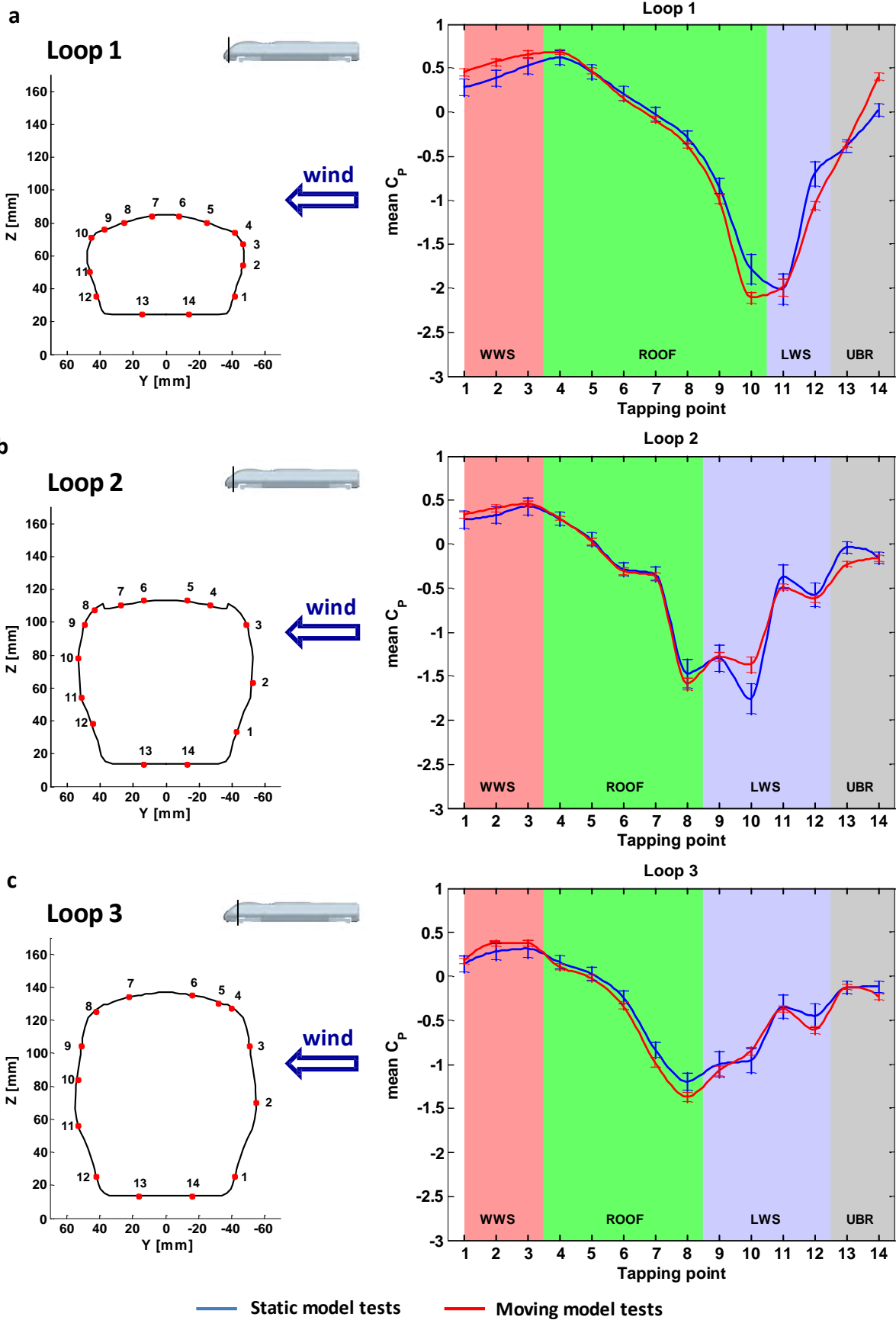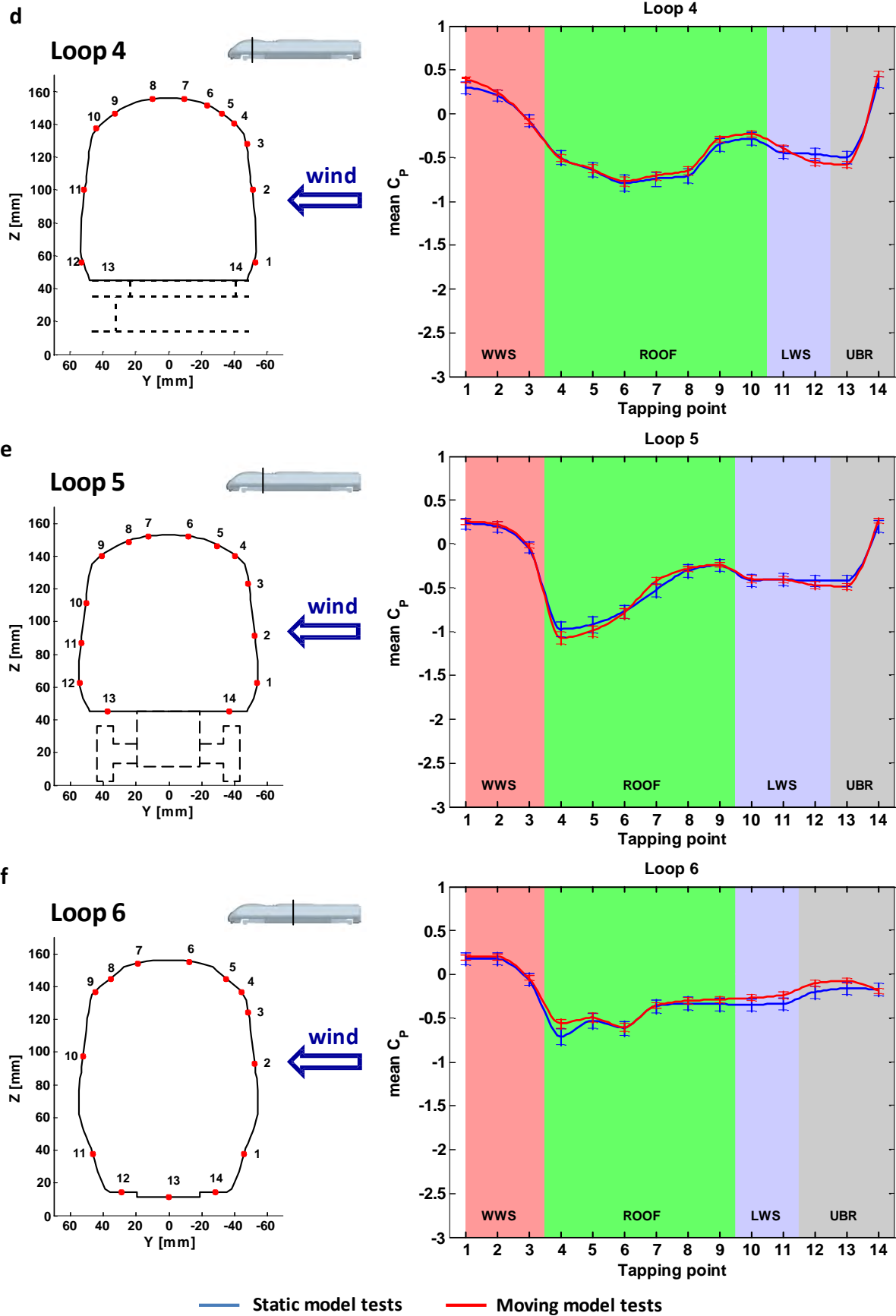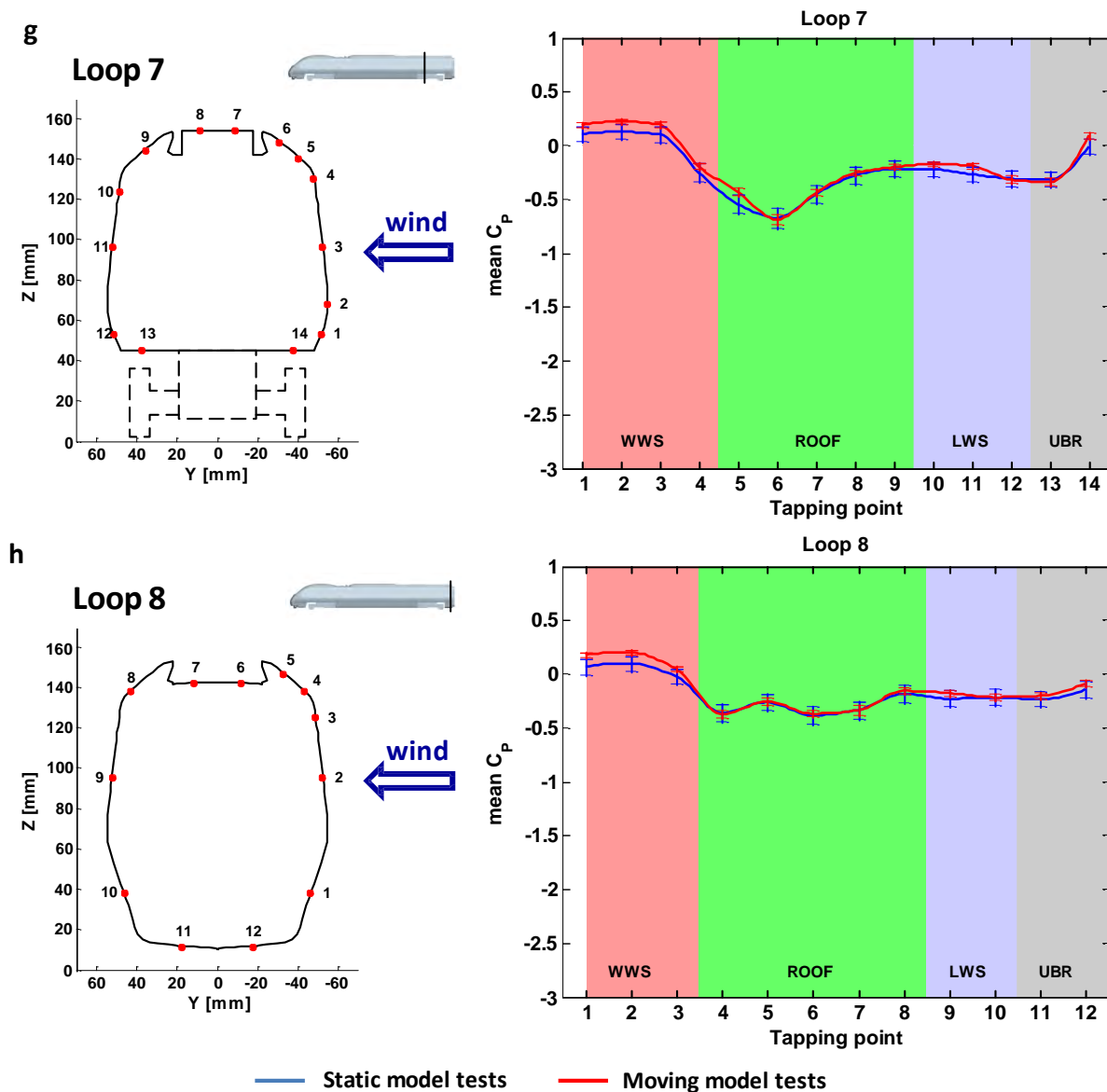
Figure 6.18 Static vs moving model tests comparison: mean pressure coefficient distribution on the loops of taps 1 to 8

Figure 6.18 highlights a general agreement between static and moving model tests. For the vast majority of the examined pressure taps, the mean pressure coefficient has the same order of magnitude and shows the same trend in both cases. Similarities can be observed in how it varies on each loop and in its evolution from the nose to the tail of the train. Differences in   that slightly exceed the estimated uncertainty appear only on the nose of the train.

On the train nose the results from moving model tests tend to show increased magnitudes of   , both positive and negative. The only exception occurs at tap 10 on the leeward side of loop 2, where

a stronger suction peak was found from static (rather than moving) tests. On loop 1, on a moving train an enhanced stagnation arises both on the windward face (tap 1, 2 and 3) and on tap 14 on the windward side of the underbody region. In addition, lower (negative)   can be observed at the bottom of the leeward face (tap 12) and also on the suction peak positioned on the roof leeward corner (tap 10). The same variation with respect to the static tests can be observed also at tap 8 on loop 3. It suggests that on a moving train a slight increase in the strength of the vortices developing on leeward side of the vehicle occurs. In the underbody region, the vehicle movement causes an enhanced stagnation at the windward tap on loop 1 and stronger suctions both at tap 13 on loop 2 and at tap 14 on loop 3. This is consistent, on a moving train, with a change in the pattern and intensity of the recirculation that was inferred based on the static test results.

The higher magnitudes of   observed on a moving train appear to be an actual effect of the vehicle-ground relative movement simulation. It has been discussed in section 3.3.3 that the relative wind seen by a moving vehicle has a skewed vertical profile, which differs in magnitude and orientation of the mean velocity from that of the onset wind impinging on a static train. Accordingly, at heights lower than Z (i.e., for most of its height) a moving train experiences increased relative wind velocities and reduced yaw angles. As suggested by Cheli et al. (2011a), in principle both these aspects might contribute to determine the variation between static and moving model results. In particular, since only the reference wind speed is used for calculating   , the increased local-to-reference velocity ratio characterising the moving tests can explain the enhanced magnitudes of their coefficients. Within this view, the results of tap 10 on loop 2 (where a reduced intensity of the suction peak was found on a moving vehicle) represent an anomaly, the cause of which is hypothesised to be a slight shift in the position of the top leeward vortex.

Considering the loops from 4 to 8, the agreement found between static and moving model tests is generally good and, to some extent, remarkable. Where present, any variations are smaller than the estimated margin of uncertainty. Within such a margin, the most evident differences appear on the

suction peak on the roof leeward corner of loops 5 and 6, and on the windward face on loops 7 and 8. In addition, some discrepancies can be observed on loop 6, both on the leeward face and leeward side of the underbody region. Apart for loop 6, these slight variations follow the main trend described on the nose of the train (i.e., increased magnitudes of   are associated with moving model test data). Since it appears an isolated tendency, what is observed on loop 6 could be interpreted as the effect of an experimental error. It is acknowledged, however, that since all these differences fall within the margin of uncertainty, it can only be hypothesised that they reflect actual pressure differences between moving and static tests rather than being entirely caused by experimental errors (section 6.4.4).

The following figure 6.19 illustrates a specific comparison between static and moving model test results with consideration of the pressure distribution in the underbody region. Being the closest to the ground, this area was expected the most sensitive to the effects of the vehicle movement simulations. For this reason, extra pressure taps (in addition to those on loop 1 to 8) were monitored during moving model experiments. Figure 6.19c presents a comparison at each pressure tap: it distinguishes increments from reductions and specifies whether the variation is larger or smaller than the estimated overall experimental uncertainty (   ). Figure 6.19d highlights the areas of the underbody region where the differences in the mean pressure coefficient exceed the margin of uncertainty.
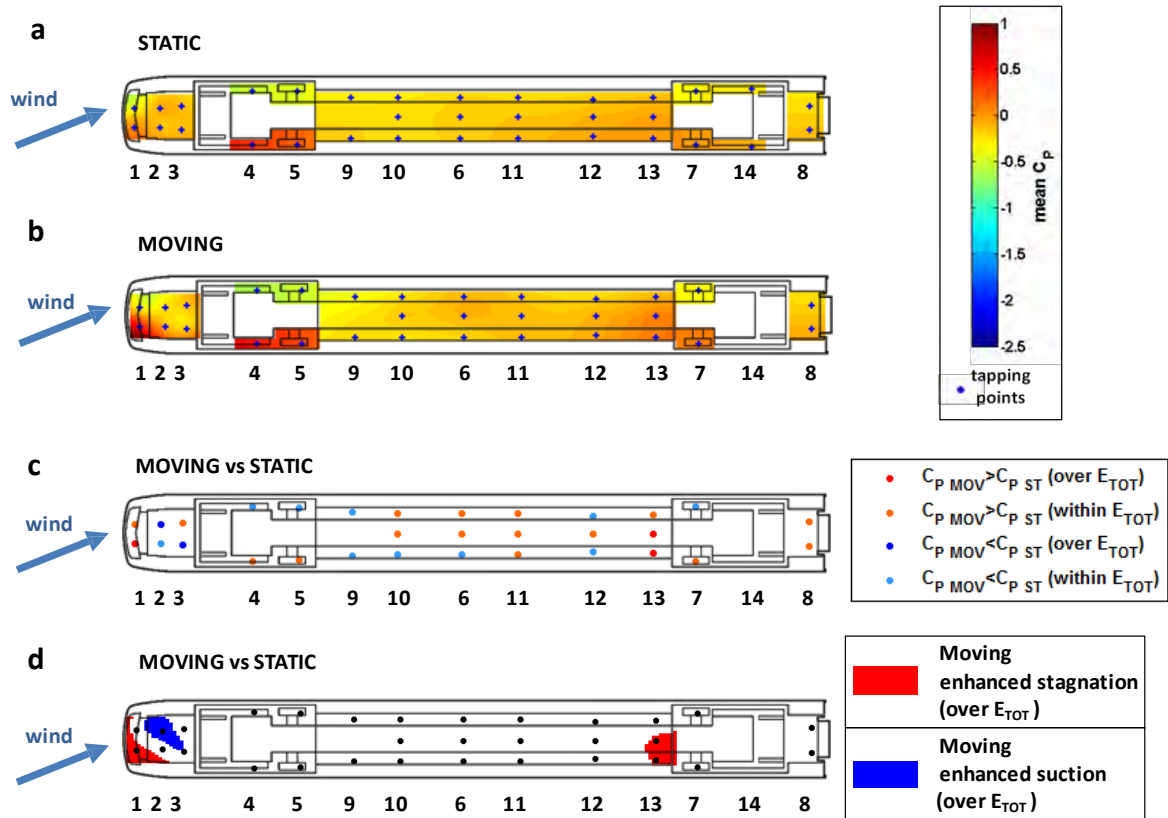
Figure 6.19 Static vs moving model tests comparison: mean pressure coefficient in the underbody region a) Static tests contour plot b) Moving model tests contour plot c) Mean pressure coefficient variation at the pressure taps d) Mean pressure coefficient variation exceeding the experimental uncertainty extrapolated from the contour plots

Consistent with what was discussed relating to figure 6.18, most of the variations between static and moving model experiments exceeding the margin of uncertainty are found in the underbody of the train nose. Furthermore, both in the centre and in the rear of the vehicle the data relating to the extra pressure taps in the underbody confirm the good agreement between static and moving model tests.

In the area between the wheel-sets the positive pressure gradient found in static conditions, and directed from the leeward side of the front bogie towards the windward side of the rear bogie, is confirmed also by moving model test results. An increment of   exceeding the margin of uncertainty is found on a moving vehicle on loop 13, immediately upstream of the rear bogie, where the vehicle movement simulation causes an enhancement of '*relative stagnation*'. As for the intensified high pressure region on the windward face of the nose, this effect appears compatible

with the differences in the wind profile perceived by a moving train (i.e. a higher local relative wind velocity in proximity to the ground).

Apart from loop 13, any other underbody pressure tap between the bogies shows differences between the static and moving test results that are smaller than the margin of experimental error. Examining the trend within such a margin, on the majority of the taps it occurs $\quad >\quad$. Since most of $\quad$ are negative, this indicates a reduced suction, and thus an opposite behaviour with respect to the increased magnitude observed above. Since, as mentioned, these discrepancies are lower than $\quad$, it cannot be excluded that they are (entirely) due to measurement errors. One alternative interpretation, however, might be that what observed on a moving vehicle is determined by the reduced yaw angle that is perceived in the presence of a skewed relative wind profile.

6.4.2 Aerodynamic load coefficients per unit length

The comparison between static and moving model tests in terms of mean load coefficients per unit length is illustrated in figures 6.20 to 6.23. $\quad$, $\quad$, $\quad$ and $\quad$ are shown, respectively, with consideration of the eight stripes that characterise the vehicle discretised geometry (section 5.3) and error bars are included to show the margin of uncertainty estimated in section 5.4.1. In addition, Figure 6.24 presents the vertical and lateral coordinates of the centre of pressure.
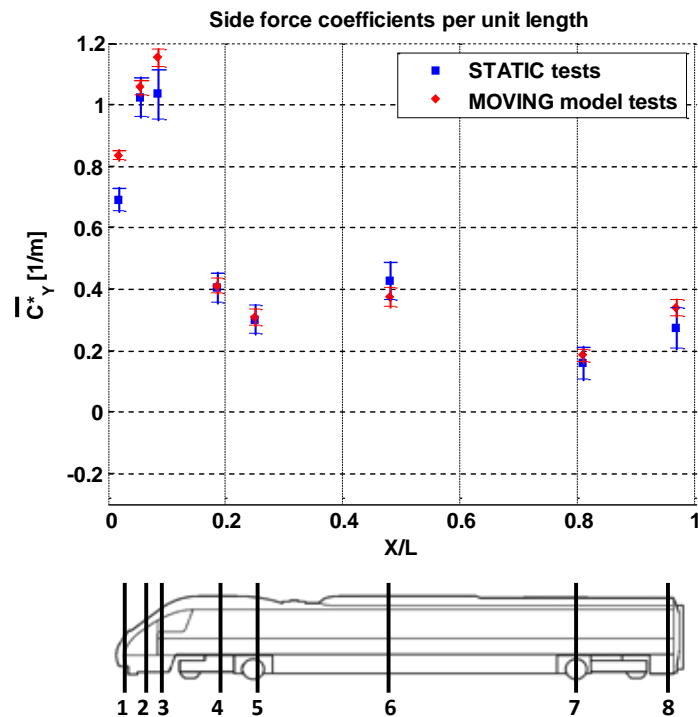
Figure 6.20 Static vs moving model tests comparison: mean side force coefficient per unit length
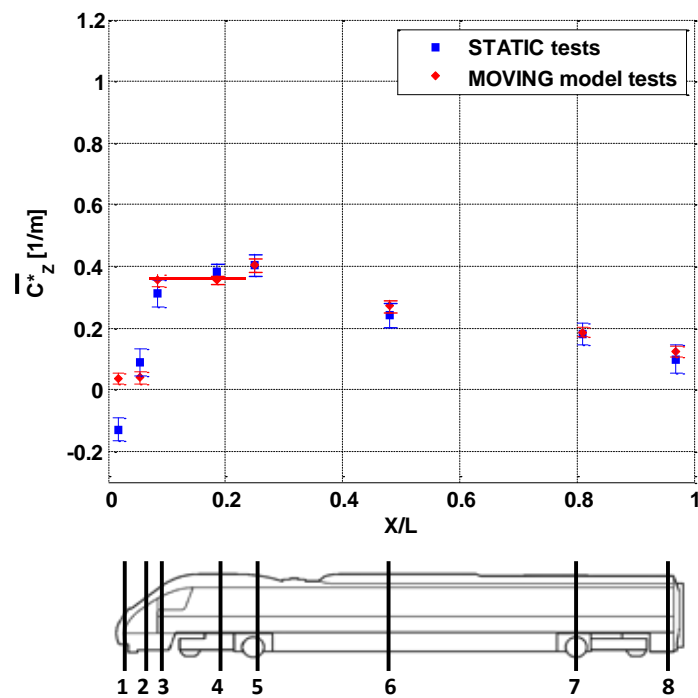
Figure 6.21 Static vs moving model tests comparison: mean lift force coefficient per unit length
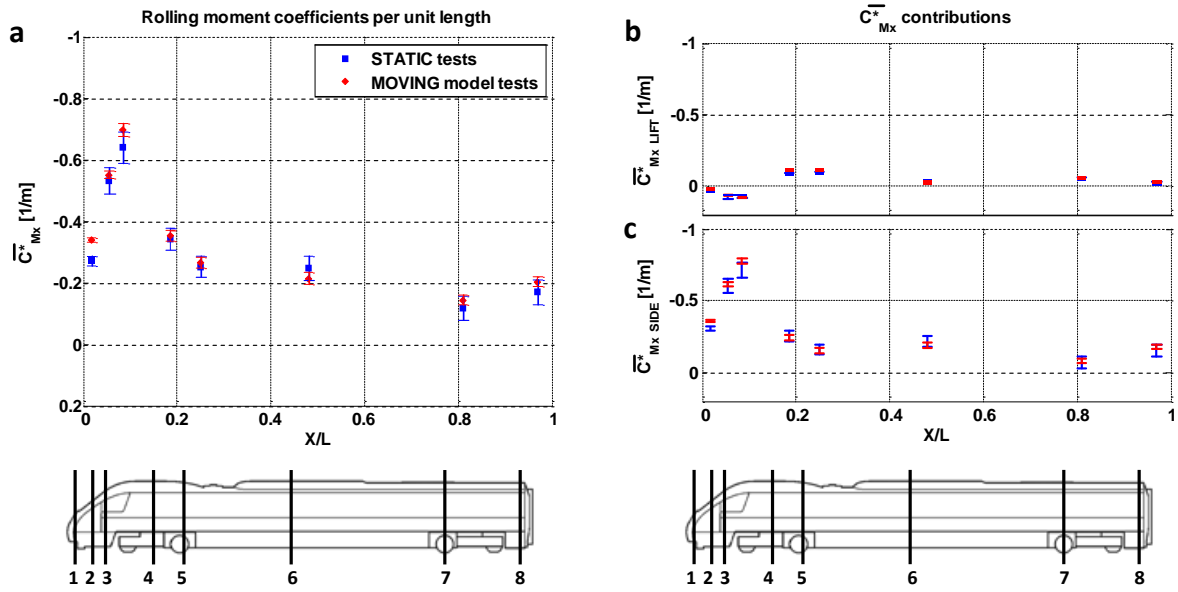
Figure 6.22 Static vs moving model tests comparison: *X*-axis mean rolling moment coefficient per unit length (inverted vertical axis) a) overall rolling moment (per unit length) b) lift force contribution c) side force contribution
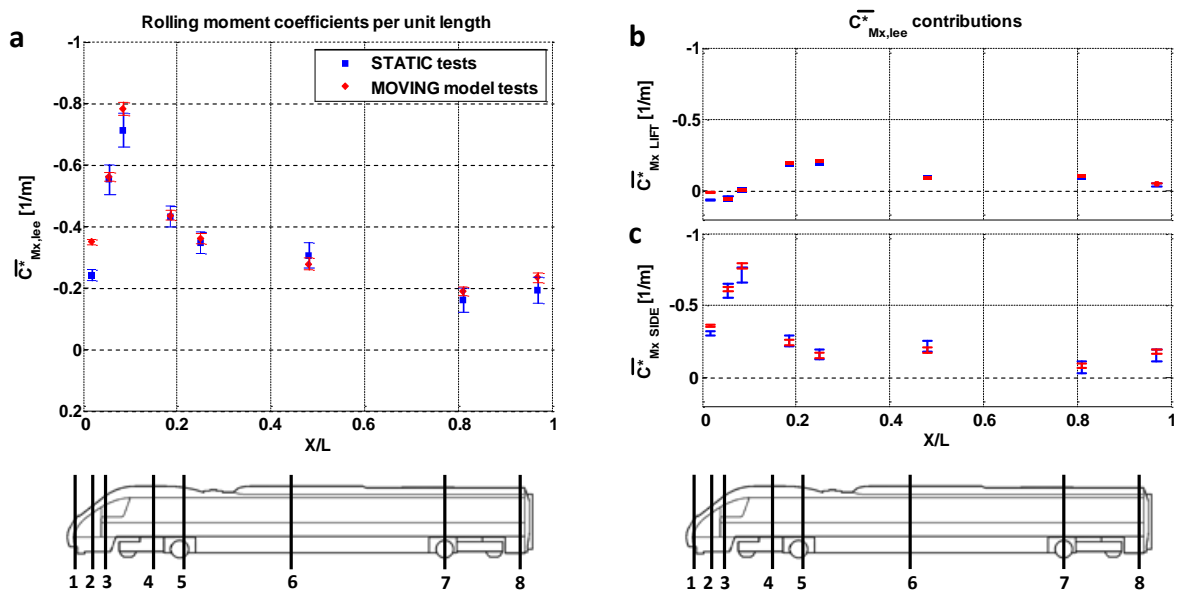
Figure 6.23 Static vs moving model tests comparison: Leeward rail mean rolling moment coefficient per unit length (inverted vertical axis) a) overall rolling moment (per unit length) b) lift force contribution c) side force contribution
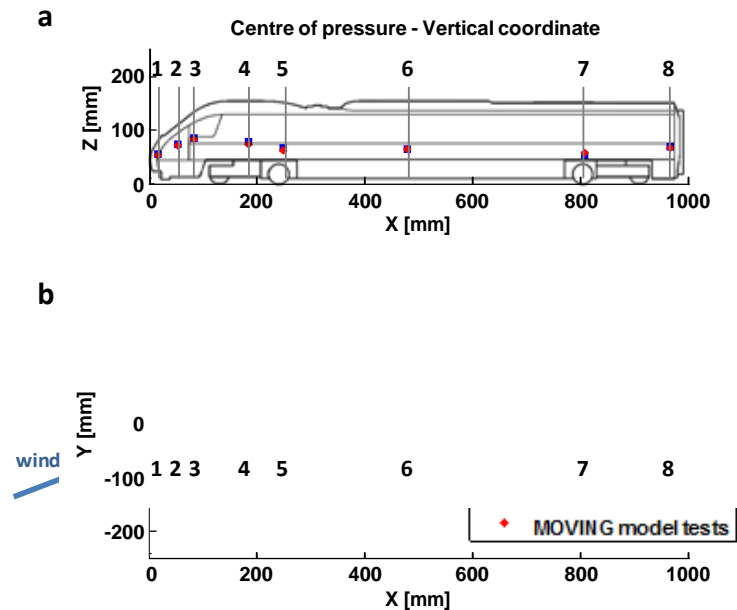
Figure 6.24 Static vs moving model tests comparison: Position of the centre of pressure on each loop a) Vertical coordinate b) Lateral coordinate

Consistent with what was observed for the surface pressure distribution, the mean load coefficients per unit length show general agreement between static and moving model tests. The best correspondence appears in the central and rear part of the train, where no differences exceed the uncertainty margin. Only on the nose, some discrepancies larger than such a margin of uncertainty arise.

On loop 1, the moving model test results show an increased magnitude of the mean side force coefficient. In addition,   shifts from negative (as obtained from static experiments) to slightly positive. This means that the lift force direction switches from downward to upward. Such a variation is determined by the higher pressure found (on a moving train) on the windward side of the underbody region and also by the enhanced suction on the roof leeward corner (figure 6.18a). Figure 6.24 highlights that, because of the modified pressure distribution, the line of action of the lift force moves from the windward to the leeward side of the vehicle. The combination of these two changes determines, on a moving vehicle, that the lift force contribution to the rolling moment remains stabilising (i.e. positive) as it is on a statically tested train (figures 6.22c and 6.23c). In terms of overall values of   and   , the effect of the side force is dominant in both static and moving model

tests. Accordingly, what was observed above leads to slightly larger overturning moments (i.e., larger negative magnitudes) in moving model conditions.

On loop 3, a significant variation between the two set of results can be observed only for   . This parameter is higher in moving model tests, although the increment is not as large as on loop 1. Neither of the other coefficients shows any discrepancy exceeding the margin of uncertainty.

On loops 4 to 8 all the differences between static and moving test results are less than the estimated experimental uncertainty. For all the coefficients there is a remarkable agreement on loops 4 and 5; while a tendency of having slightly larger magnitudes on a moving train (attenuated on the lift force parameter) can be observed on loops 7 and 8 at the rear of the train. On loop 6 in the centre of the vehicle, instead, appears a different trend: while   is slightly higher, in moving model conditions (and consequently the rolling moment coefficients) slightly drops compared to the static tests. Not surprisingly, this variation in the behaviour along the vehicle echoes what is observed in figure 6.18f for pressure distribution. The lower side force coefficient per unit length reflects the attenuated suction found on the leeward face. Still a reduced suction, but this time on the pressure taps 13 and 14 in the underbody region, determines the increment in   . In this respect, a counter effect is due to the attenuation of low pressure regions at both the roof corners. The impact of such variations in terms of   , however, is limited since they involve two small portions of the train's upper surface. Furthermore, occurring at the two corners, where the roof has an inclination, only part of the related aerodynamic forces is projected in the vertical direction. Once integrated according to equations (5.36), the dominant pressure variations are those under the train.

Figure 6.24 shows a good agreement between static and moving model tests concerning the position of the centre of pressure. The only two differences are in the lateral coordinate on loop 1 and 2. The former has been explained above relating to the trend of   , while the latter is not surprising in light of what discussed in section 6.1.1 regarding the characteristics of the pressure distribution on loop 2.

6.4.3 Overall aerodynamic load coefficients
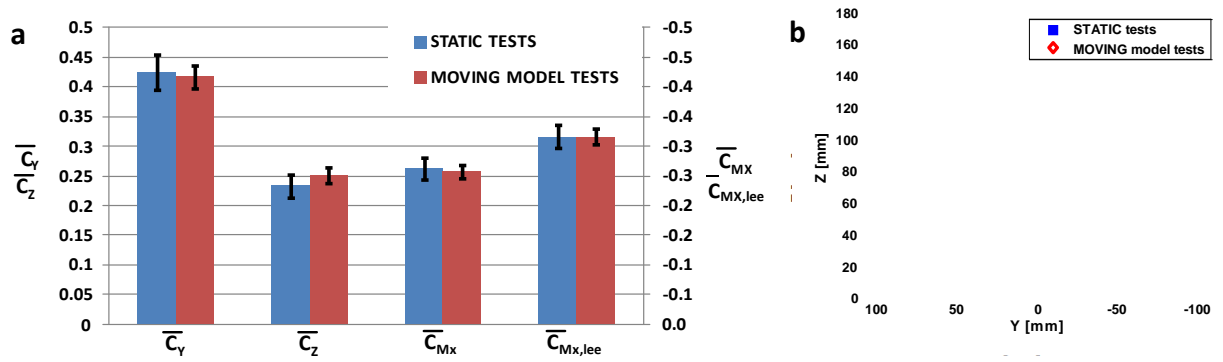
Figure 6.25 Static vs moving model tests comparison: mean overall aerodynamics a) Mean overall load coefficients b) Position of the overall centre of pressure

Figure 6.25 and table 6.6 illustrate a comparison between static and moving model experiments taking into account the mean overall aerodynamic coefficients and the position of the centre of pressure. Error bars (as well as percentage values in table 6.7) indicate the margins of uncertainty estimated in section 5.4.1. It is worth remarking here that, since the same train model discretisation was used, and the same assumptions were made in the pressure integrations process for both static and moving model tests, these aspects are not evaluated within the estimated error margins.

	STATIC TESTS	MOVING TESTS	Magnitude VARIATION |MOV. – ST.|
	0.425	0.417	-2%
	0.233	0.251	+8%
	-0.262	-0.257	-2%
	-0.316	-0.316	0%

Table 6.6 Static vs moving model tests comparison: mean overall aerodynamic load coefficients

	E_{TOT}		E_{TOT} %		
	STATIC	MOVING	STATIC	MOVING	ST. + MOV.
	0.034	0.016	8%	4%	12%
	0.022	0.01	9%	4%	13%
	0.021	0.01	8%	4%	12%
	0.022	0.01	7%	3%	10%

Table 6.7 Static vs moving model tests comparison: total experimental uncertainties for the overall load coefficients

Reflecting what was discussed for the pressure distribution and the load coefficients per unit length, the overall static and moving model test results are in good agreement. In terms of the side force and rolling moment overall coefficients the differences are smaller than 2% and, as such, the agreement looks remarkable. With consideration of the lift force, a slightly larger variation (with the moving test results being ~8% larger) can be observed. For all the coefficients, however, the discrepancies between the two set of results fall within the margin of uncertainty.

6.4.4 Discussion

Reynolds number effect

As discussed in chapters 4 and 5, the experimental setup, test methodology and data reduction methods employed for this research were developed in order to ensure the best consistency possible between static and moving model tests. The objective was to minimise any difference other than vehicle movement simulation. However, since the CWG does not allow the fans' rotational speed to vary, there was a difference in the reference mean wind velocity (relative to the train) and, in turn, in the Reynolds number. During static tests, the reference wind velocity coincided with the onset wind speed at the reference height, while during moving model experiments it was given by the vector sum of the latter with the train speed. Consequently, the Reynolds number achieved in static and moving model test conditions (based on a nominal vehicle height of 3.1 m at full-scale) were approximately $= 1.2 \times 10^5$ and $= 2 \times 10^5$, respectively.

If a critical Reynolds number of $2\text{-}2.5 \times 10^5$ was taken as a reference, the Reynolds numbers achieved in the TRAIN rig tests could suggest that a Reynolds number effect might have occurred between static and moving model tests. However, as discussed in section 3.4.1, such a critical Reynolds number refers to scale-model vehicles tested at 90° yaw angle and subjected to a low-turbulence flow and, as such, represents a conservative threshold. Hence, since the tests of the present research investigated a 30° yaw angle and were characterised by an onset wind with a relatively high level of

turbulence, it is assumed that no significant Reynolds number effect has arisen between the static and moving model experiments.

Unfortunately, not having the chance of varying the fans' rotational speed prevented a Reynolds number check. However, the assumption is consistent with the findings from a number of previous studies on smooth-edged trains (section 3.4.1). For example, the Reynolds number check performed by Baker (1986) in the presence of a turbulent onset wind (with ~10% turbulence intensity) indicated no significant Reynolds number effects for Re > 0.6×10^5 (which is less than both values achieved in the TRAIN rig tests). Furthermore, the results of Cheli et al. (2011b) showed that at 30° yaw angle the Reynolds number effect between $= 1.3 \times 10^5$ and $= 2 \times 10^5$ is very limited. In addition, the hypothesis that no significant Reynolds number effects occur between the static and moving model tests is supported also by the very good agreement that the TRAIN rig results show in the pressure distributions over the roof and leeward side of the train (figure 6.18), which suggests a good consistency in the position of the boundary layer separation point.

Interpretation of the experimental uncertainty

The experimental uncertainties reported by the error bars in the figures of this section 6.4, and specified in table 6.7, are the total uncertainties defined in section 5.4.1 and, as such, are given by the sum of two contributions: random uncertainty and bias limit. The former was estimated on a statistical basis assuming normally distributed data and considering a 95% confidence level. The bias limit, instead, was calculated through the propagation of error based on the quoted accuracy of the measurement instruments and, since a uniform distribution was assumed, it represents the range where the actual bias affecting any of the results is expected to lie. Hence, it is worth noting that a total uncertainty does not necessarily indicate the actual errors associated with any of the reported results. Rather, it is the limit within which such an actual error is thought to lie with a very high probability.

In this view, if the variations between static and moving model test results exceed the margin of uncertainty then, since it is very unlikely that an experimental error larger than such a margin might have occurred, the variations are interpreted as symptoms of actual physical differences. If the variations fall within the margin of uncertainty, instead, there is a higher probability that an experimental error equal (or larger) to them might have occurred, thus determining them entirely. However, notwithstanding such a higher probability, this is not certain. Therefore, the possibility cannot be excluded that the actual error affecting the measurements was smaller than the observed variations. Accordingly, in a conservative approach, no physical differences between static and moving model tests are associated to variations of the results smaller than the total uncertainty. However, in a less conservative view, physical interpretations can be given also to such variations.

Effect of the vehicle movement simulation

The simulation of the vehicle movement determines perceptible variations of the mean surface pressure on the train only in limited areas of the vehicle. The largest of these variations occur at pressure taps around the train nose, where they are generally larger than the margin of experimental uncertainty. On the rest of the leading car these differences become smaller and exceed the experimental uncertainty only on a restricted number of underbody pressure taps.

On a train subjected to a crosswind at yaw angle around 30°, the front part of the vehicle is naturally the most exposed to the action of the relative wind. In the centre and in the rear, a stronger interaction develops between this relative wind and the slipstream moving along the train. Therefore, the characteristics of the freestream relative wind are likely to have a strong influence on the surface pressure distribution on the train nose, while a dominant effect of the vehicle-induced turbulence is expected on the train body.

In this view, as a difference in the mean relative wind, the skewed wind profile perceived by a moving train (but not by a static train) can explain the larger variations in the mean surface pressure field found on the train nose (section 6.4.1). The discrepancies observed in the mean underbody

pressure in proximity of both bogies, instead, are consistent with a high sensitivity to the relative wind characteristics (and, in turn, to the simulation of the vehicle movement) caused by the underbody blockage associated with the presence of the wheel-sets.

The behaviour of the aerodynamic load coefficients per unit length echoes what has been observed for the pressure coefficient. They show differences between static and moving model tests that exceed the margin of uncertainty only on the train nose, in particular on loop 1, where higher magnitudes occur on a moving vehicle.

The examination of the overall mean load coefficients shows that all the variations found between the static and moving model tests fall within the margin of experimental uncertainty. This is consistent with the behaviour of the load coefficients per unit length in light of the integration process discussed in section 5.3. The overall load coefficients are given by the averages of the corresponding coefficients per unit length weighted with the length of the longitudinal stripes (which the discretised vehicle was divided into). Accordingly, despite relatively large differences between static and moving tests were found for the coefficients per unit length relating to the train nose, the short length of the stripes in this part of the vehicle led to a small impact of these differences on the overall load coefficients.

If the variations of the overall mean load coefficients within the margin of uncertainty are taken into consideration, moving model tests lead to a reduction of ~2% of the side force and rolling moment coefficient   and to differences smaller than 1% for   . On the lift force coefficient, instead, the vehicle movement simulation produces an increment of ~8%.

Considering the overall mean lift force coefficient, it has been assessed that the largest portion of its increment (i.e., about 6% of the total 8%) is determined by the growth of the mean lift force coefficient per unit length (   ) associated with loop 6. As discussed in section 6.4.1, this is caused by the attenuation of the suction in the underbody of such a loop. Since the stripe associated with loop

6 embraces approximately half of the vehicle length, the question arises whether the variation of

is caused by the large weighting associated with loop 6 within the integration process or by the

actual pressure differences occurring in the whole underbody between the two bogies. To address

this doubt, the sensitivity analysis presented in appendix E.4 was carried out by considering an

alternative model discretisation, which included the additional underbody pressure data measured

on loops 9 to 13 during both static and moving model tests. This analysis confirms the increment of

the lift force coefficients from static to moving model tests. Such an increment, however, is smaller

than what was originally estimated (i.e., 3% instead of 8%). Consequently, it warns that the use of a

relatively coarse model discretisation in the central part of the leading car might lead to a slight

overestimation of the aerodynamic effect of the vehicle movement on the mean overall lift force

coefficient.

Comparison with previous studies

As discussed in section 3.6, there is a lack of agreement between the outcomes of previous studies

concerned with assessing the aerodynamic effect of the train movement simulation in the presence

of crosswinds. Not surprisingly, therefore, the results of this research are consistent with some of the

previous works, whilst differing from others.

A first comparison has been made with past moving model experiments. With regard to the mean

side force coefficient, the static and moving model tests provided by the present research are in

agreement with the results of Cooper (1981), Humphreys (1995) and Bocciolone et al. (2008). A

discrepancy, instead, arises with respect to the significant decrement in   found in moving model

tests by Baker (1986) and Howell (1986).

Considering the lift force coefficient, the agreement found here between static and moving model

tests, whose variation is smaller than the experimental uncertainty, echoes the indications of Cooper

(1981), Humphreys (1995) and Bocciolone et al. (2008). However, if the behaviour of   is evaluated

within the margin of uncertainty, the tendency is to increase when the vehicle movement is simulated confirms the findings of Humphreys (1995). It differs from the higher lift force coefficients that Howell (1986) obtained from static tests.

A second comparison can be made with respect to the CFD simulations developed by Hemida and Baker (2010) and by Cheli et al. (2011a). In this regard, the variations of overall mean load coefficients found are in agreement with the trends found in both these studies (which are, in turn, consistent with each other) for any of the examined coefficients, with a consistency in the order of ±3%.

Finally, a third comparison can be made between the level of accuracy achieved in the present investigation (table 6.7) and that of previous test campaigns. On the one hand, the uncertainties relating to the TRAIN rig static tests are sensibly larger than those typically achieved in a wind tunnel static test. This was determined by the limitations in the experimental setup that were caused, in turn, by the constraints posed for the CWG design. On the other hand, the uncertainties estimated for the moving model tests denote significant progress with respect to the past. The total uncertainty estimated at ~4% is significantly lower than the ~15% reported by Cooper (1981). Furthermore, it is of the same order of the '*measurement repeatability*' of ~3% estimated by Baker and Humphreys (1996), with respect to which it represents a considerable improvement because it includes the bias and, as discussed in appendix D, has been achieved through a significantly lower number of runs (i.e. 15 vs. 50).

Chapter 7

Unsteady aerodynamics - results and discussion

7.1   Introduction

Chapter 7 presents the analysis of the fluctuating aerodynamic loads acting on a train under the effect of a stationary relative crosswind and illustrates a comparison between static and moving model experiments. The study of the peak aerodynamic load coefficients per unit length is reported in section 7.2, while section 7.3 presents the estimation of the peak coefficients relative to the overall crosswind forces and moments. In addition, section 7.4 analyses the correlation between the time-varying wind-induced surface pressure fluctuations occurring along the train.

7.2   Peak load coefficients per unit length

As illustrated in section 2.4.2.2, the analysis of the peak load coefficients enable the evaluation of the unsteady aerodynamic behaviour of a train in crosswinds within the *amplitude domain*, which is mainly concerned with the vehicle overturning (Baker 1991c; Baker et al., 2004; Sanquer et al., 2004; Baker, 2010a; RSSB, 2001).

Based on the data collected during the TRAIN rig static and moving model experiments, the peak coefficients relating to the aerodynamic loads per unit length were estimated according to the procedures described in the next sections 7.2.1 and 7.2.2. In addition, an uncertainty analysis was developed in order to assess the accuracy of these estimations (section 5.4.2).

7.2.1 Definitions and scaling factors

Two series of peak coefficients were calculated: the peak-over-mean (PoM) and the peak-over-peak (PoP) coefficients. They are defined, respectively, as

$$C_n^* = \frac{\hat{l}_n^*}{\frac{1}{2}\rho A_{ref} V_{ref}^2} \quad \text{(PoM)} \tag{7.1}$$

$$\hat{C}_n^* = \frac{\hat{l}_n^*}{\frac{1}{2}\rho A_{ref} \hat{V}_{ref}^2} \quad \text{(PoP)} \tag{7.2}$$

where indicates the peak value of the generic aerodynamic load per unit length (with = , ,

,), while and are the mean and peak values of the reference (wind) velocity, respectively. Defining a gust factor as:

$$G = \frac{\hat{V}_{ref}}{\overline{V}_{ref}} \tag{7.3}$$

it follows that the PoM and PoP coefficients are related by the following relation:

$$\hat{C}_n^* = \frac{C_n^*}{G^2} \tag{7.4}$$

According to the approach suggested by Baker (1991c) and discussed in section 2.4.2.2, the peak aerodynamic load coefficients (PoM and PoP) are normalised with respect to the mean load coefficients:

$$\frac{C_n^*}{\overline{C}_n^*} = \frac{\hat{F}_n^*}{\overline{F}_n^*} \quad \text{(PoM normalised)} \tag{7.5}$$

$$\frac{\hat{C}_n^*}{\overline{C}_n^*} = \frac{\hat{l}_n^*/\overline{F}_n^*}{\hat{V}_{ref}^2/\overline{V}_{ref}^2} \quad \text{(PoP normalised)} \tag{7.6}$$

As for steady aerodynamics, the peak coefficients taken into consideration in this study were relative to: side and lift forces, rolling moment referred to the -axis and rolling moment about the leeward

rail. The reference velocity indicated in equations (7.1-7.6) is the relative wind velocity and the mean and peak values that were adopted are detailed in section 7.2.2. The averaging time considered for calculating the peak values (of both loads and velocity) was equivalent to 3 seconds at full-scale (FS). This is consistent with the critical wind gust duration of 1 to 3 s discussed in section 2.4.2.2 and indicated by Baker (1991c).

Dealing with scale-model experiments, the actual averaging time considered for processing the data was determined according to the time scaling factor ( ). Following the similitude theory (Barlow et al., 1999), this factor was determined by the combination of the length ( ) and velocity ( ) scaling ratios as:

$$\lambda_T = \frac{\lambda_L}{\lambda_V} \qquad\qquad (7.7)$$

Table 7.1 specifies the scaling ratios adopted in this study for static and moving model tests. The length scaling factor was the same in both cases and equalled the geometrical scale of the train model, i.e. 1:25. The difference in the relative mean wind velocities (determined by the use of the same onset wind simulation for both static and moving model tests) led to a variation in the scaling ratio for the velocity, and in turn of the time, between the two cases. The ratio between moving and static tests reference velocities ( ) was defined based on the data from the flow characterisation (section 4.3.2.1) and estimated as 1.67. The scaling velocity ratio was selected for convenience to be unitary for the static tests, thus determining in the moving model case   =   = 1.67:1. Accordingly, static and moving model experiments were characterised by respective time scaling factors of 1:25 and (1:25)/(1.67:1), which led to 3 s FS equivalent averaging times equalling 0.12 s and 0.072 s, respectively.

	STATIC MODEL TESTS	MOVING MODEL TESTS
λ_L	1:25	1:25
	14.4 m/s	24 m/s
$\gamma_V = \dfrac{V_{ref}^{MOV}}{V_{ref}^{ST}}\left(= \dfrac{\lambda_V^{MOV}}{\lambda_V^{ST}} = \dfrac{\lambda_T^{ST}}{\lambda_T^{MOV}}\right)$	—— =	
λ_V	1:1	1.67:1
$\lambda_T = \dfrac{\lambda_L}{\lambda_V}$	1:25	——
3s (FS equivalent)	0.12 s	0.072 s

Table 7.1 Scaling factors, reference velocity, peak coefficients averaging time intervals

7.2.2 Estimation process

During the majority of the TRAIN rig experiments the pressure taps on the same loop were monitored simultaneously during the same run. Thus, it was possible to obtain the time series for the load coefficients per unit length from those of the local pressure (according to equations (5.36) in section 5.3.1). From these, PoM coefficients defined in equation (7.1) were calculated as explained in the following.

For static tests, each 60 s long time history recorded for each loop of taps was split into three records of 20 s (which is the shortest time ensuring statistically stable records). A 3 s (full-scale equivalent) moving average filter was applied and the maximum value of the averaged time series was obtained. The PoM coefficient was given by the average of the three maxima.

For moving model tests, the moving average process was applied to each of the single-run time histories relating to each loop. For consistency with static tests, the transitions experienced by the moving train at the entry and exit of the crosswind section were not included within the time averaging interval. Once a series of 15 maxima (one for each run) had been found, their average gave the PoM coefficient relative to each individual loop.

The PoP coefficients were obtained by dividing the PoM coefficients by the gust factor squared (equation (7.4)). Such a gust factor was estimated from the wind data collected during the flow characterisation (section 4.3.2.1), as explained below. PoM and PoP *normalised* coefficients were obtained by dividing the PoM and PoP coefficients by the mean coefficients presented in chapter 6. As such, the mean values used for normalisation were slightly different between static and moving model tests.

As specified in table 7.2, the adopted reference mean velocities were those defined in equations (5.3) and (5.15) in sections 5.2.1 and 5.2.2, relating to static and moving model tests, respectively. The reference peak velocities, instead, were taken as the spanwise averages of the local peak velocities (calculated at each spanwise position (figures 7.1 and 7.2). The portion of the CWG span taken into account for computing the spanwise averages was the same considered in sections 4.3.2.1 for the spanwise averages mean velocities (i.e. the spanwise positions 5 to 59 for moving model experiments, and the positions 18 to 30 for static tests).

The local peak wind velocities were given by the maxima of the 3 s (FS equivalent) averaged time series obtained from the 60 s long flow characterisation velocity time histories. Their definition, however, changed from static to moving model tests. For the static tests, the moving average filter was applied over the time histories of the streamwise wind speed . For the moving model tests it was applied on the time histories of the local relative wind velocity, which was given by the vector combination of the streamwise and lateral components of the wind velocity with the train speed (according to equation (A.2) in appendix A). For moving model tests, it is acknowledged that the characteristics of the actual relative wind seen by the travelling train are determined by the combination of the temporal and spatial variations of the simulated (turbulent) flow along the track, with the latter depending on the lateral correlation of the simulated turbulent structures. In principle, therefore, the calculation of an actual reference peak velocity would require the characteristics of such a relative wind to be determined. Nevertheless, its extrapolation is not

straightforward because of the spanwise variability of the simulated crosswind. Although representing an approximate estimation of the actual relative peak velocity, the reference value adopted here is similar to that employed by Humphreys (1995) for investigating peak aerodynamic load coefficients through moving model experiments. Furthermore, it is also consistent with the method adopted in the UK standard (RSSB, 2001).

The gust factor   , was obtained as the ratio between the spanwise average of the peak and mean reference wind velocities defined above.

	STATIC MODEL TESTS	MOVING MODEL TESTS
$\overline{V}_{ref}$	$\overline{U}_{SW}^{*}$	$\overline{V}_{rel,SW}^{*} = \sqrt{\left(\overline{U}_{SW}^{*}\right)^2 + V_{tr,SW}^2}$
$\hat{V}_{ref}$	$\hat{U}_{SW}^{*}$	$\hat{V}_{rel,SW}^{*}$ where, from eq. (A.2), $V_{rel}^{*} = \sqrt{\left(U^{*}\right)^2 + \left(V_{tr} - v\right)^2}$
G_{SW}	$\dfrac{\hat{U}_{SW}^{*}}{\overline{U}_{SW}^{*}} = \dfrac{\hat{U}_{SW}}{U_{SW}} = 1.22$	$\dfrac{\hat{V}_{rel,SW}^{*}}{\overline{V}_{rel,SW}^{*}} = \dfrac{\hat{V}_{rel,SW}}{V_{rel,SW}} = 1.10$

Table 7.2 Reference wind velocities (mean and peak) and gust factors
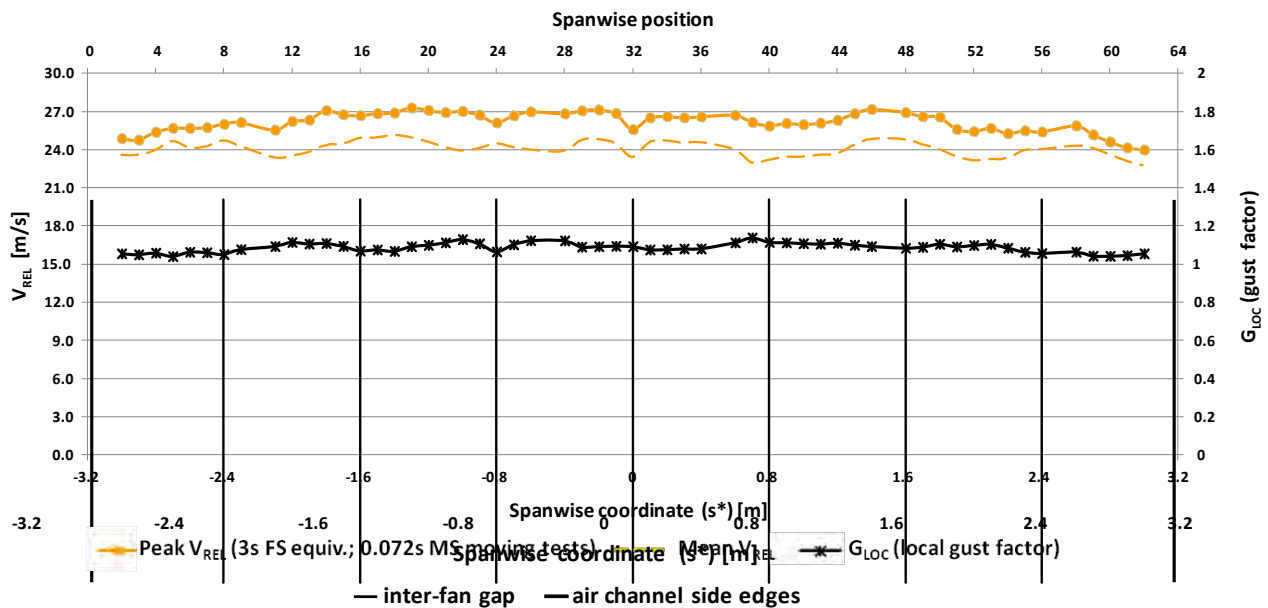
Figure 7.1 Peak reference wind velocity and gust factor for the moving model tests
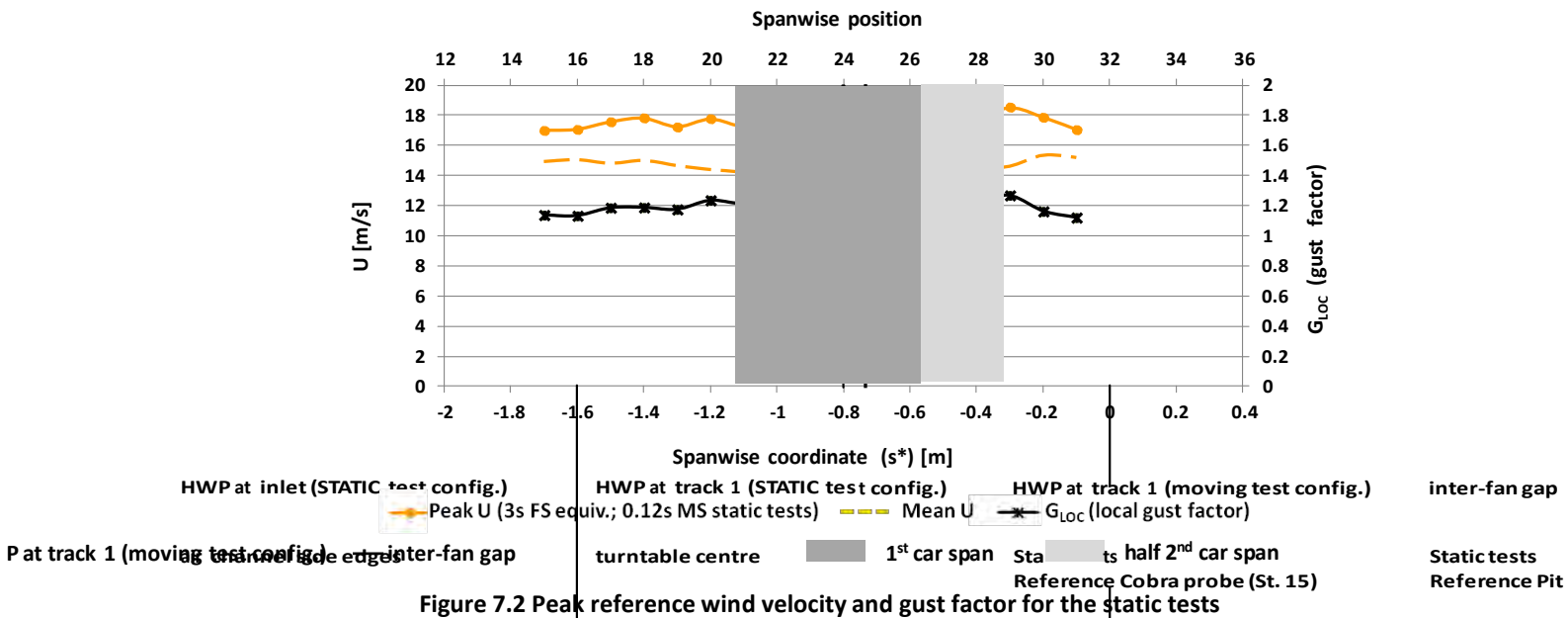
Figure 7.2 Peak reference wind velocity and gust factor for the static tests

7.2.3 Comparison between static and moving model tests and discussion

7.2.3.1 *Peak-over-mean normalised coefficients*

The PoM normalised (i.e. PoM / mean) coefficients relating to the aerodynamic load per unit length are illustrated in figure 7.3. This figure examines the side and lift forces and the rolling moment coefficients for both the static and moving model tests. The error bars relative to each set of data represent the margin of experimental error estimated through the analysis reported in section 5.4.2.1 (assuming a normal data distribution and considering a 95% confidence level).
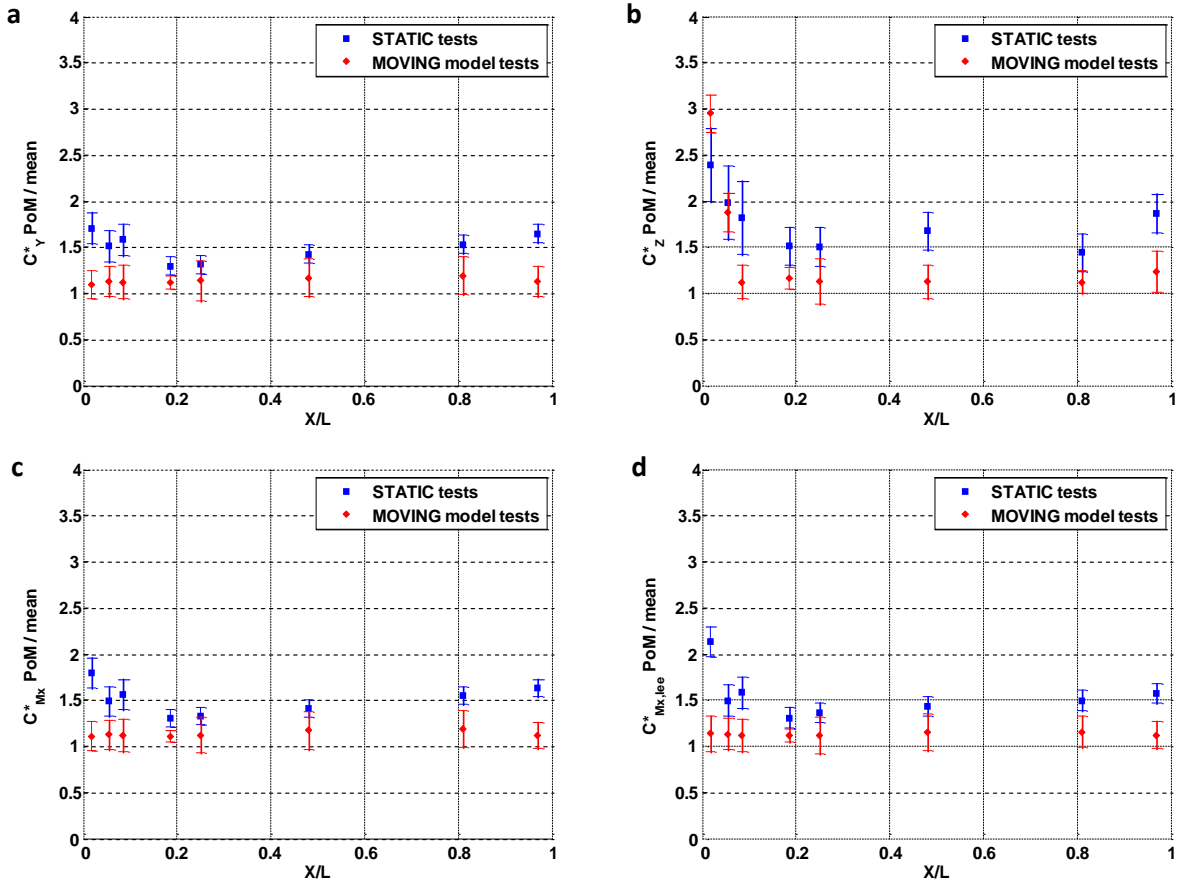
Figure 7.3 Peak-over-mean normalised coefficients of the aerodynamic loads per unit length. Static vs moving model tests comparison

Substituting into equation (7.5) the expressions of the aerodynamic loads given either by the *Quasi-Steady* or by the *Quasi-Steady corrected* formulation (section 2.4.2.2), it can be seen that the PoM normalised coefficients are proportional to the ratio between the peak and mean relative wind velocity squared. In this view, it is not surprising that, in figure 7.3, all the PoM normalised coefficients are larger than 1.

Comparing static and moving model tests, a significant variation between the two sets of results can be observed. With the exception of the lift force on loop 1, all the PoM normalised coefficients obtained through static tests are larger than those from moving model experiments and their variations exceed the estimated uncertainty in the majority of the cases. As such, these results suggest an actual (physical) difference between the peak aerodynamic loads experienced by the train in the two test conditions.

As discussed in section 7.2.1, the use of the same onset wind simulation for both static and moving model tests led to a greater mean relative wind velocity for the latter. Accordingly, if the turbulence intensity perceived by a moving train is approximated by the turbulence level of the onset wind divided by such a mean relative velocity (Baker, 2010b), then it becomes lower than that perceived by a train tested statically. Since the reference peak wind velocity reflects the turbulence intensity in the relative wind, not only the vehicle movement, but also the higher ratio between peak and mean wind velocity perceived by a static train could explain the larger PoM normalised coefficients observed in the static test results. The anomalous trend concerning the lift force on loop 1, instead, is consistent with the very small value of the mean load coefficient associated with the moving model case.

In light of these considerations, the examination of the PoM normalised coefficients is not conclusive for assessing the impact of the vehicle movement, specifically. By contrast the analysis of the PoP normalised coefficients is promising for this purpose. As highlighted in equation (7.6), these parameters express the ratio between the peak and mean loads with respect to the ratio between the peak and mean reference velocities. As such, since they take into account the different turbulence intensity perceived by a static rather than moving train, it can be assumed that their variations from one to the other test condition (if any) are mainly caused by the vehicle movement simulation.

7.2.3.2 *Peak-over-peak normalised coefficients*

Figure 7.4 presents the comparison between static and moving model test results in terms of the PoP normalised coefficients. Consistent with the previous section, error bars represent the uncertainty estimated in section 5.4.2.1 and the same four aerodynamic loads per unit length are examined.
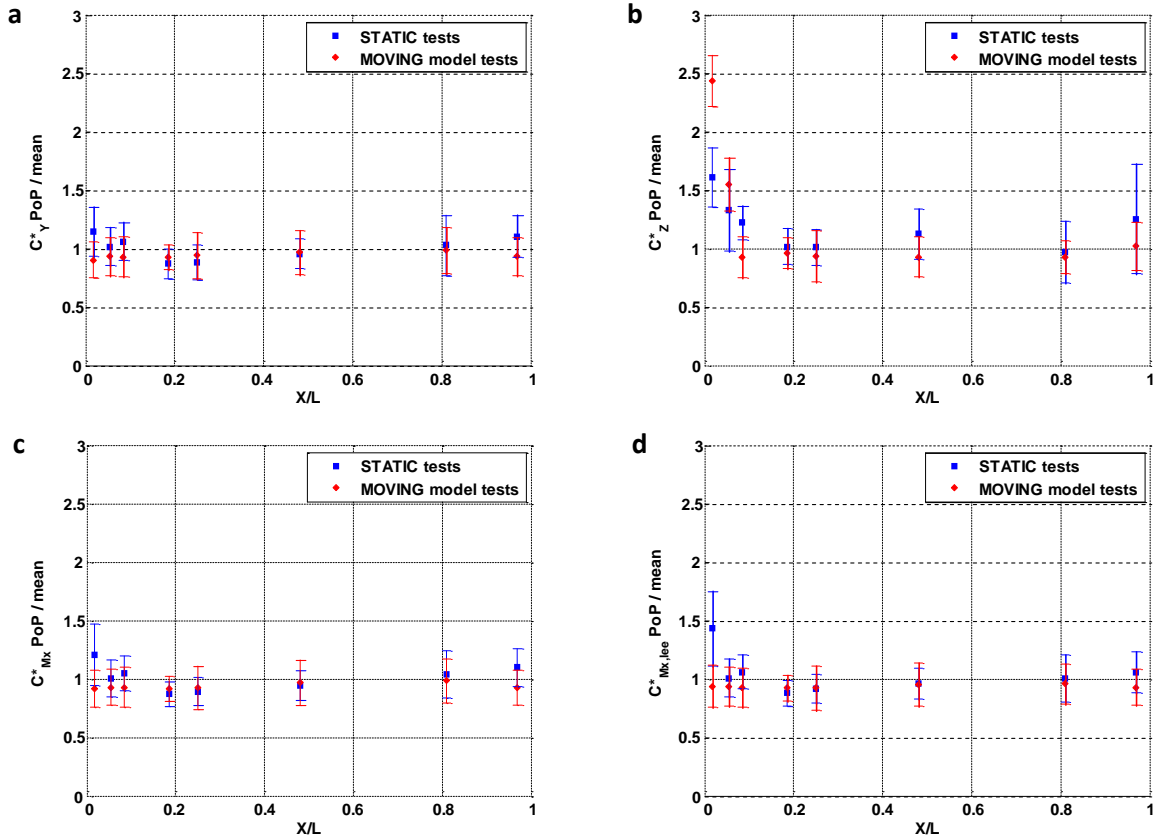
Figure 7.4 Peak-over-peak normalised coefficients of the aerodynamic loads per unit length. Static vs moving model tests comparison

It can be noticed in figure 7.4 that the PoP normalised coefficients are generally lower that the corresponding PoM normalised coefficients. This is not surprising in light of equation (7.4) and of the values of the gust factor (> 1) employed in the calculations (table 7.2). Most of the PoP normalised coefficients have values close to 1 and, if the uncertainty margin is taken into consideration, only a small number of results are greater than 1. These are the lift coefficients on loops 1 and 2 in both the static and moving model tests and, for static tests only, the lift coefficient on loop 3 and the rolling moment coefficient referred to the leeward rail on loop 1.

A good agreement can be noticed between static and moving model test results. Only the lift coefficients on loop 1 denote a difference that exceeds the estimated uncertainty, with the moving model test results being the largest. If the variations between the two sets of data are examined within the uncertainty margin, the agreement between the best estimates is remarkable for the coefficients relating to the side force and both the rolling moments on loops from 4 to 7. On the

loops on the nose and on the tail of the leading car, instead, larger values were obtained from static tests. Larger coefficients associated with static tests are also observed for the lift force, with the exception of loop 1 and 2 on the train nose. In these sections the opposite trend is apparent.

According to the interpretation of the PoP normalised coefficients suggested by Baker (1991b), the values very close to 1 illustrated in most of the cases by figure 7.4 suggest a *Quasi-Steady* behaviour (section 2.4.2.2). In this view, it is not surprising that none of the PoP normalised coefficients is less than 1 beyond the margin of uncertainty. Dealing with loads per unit length, this indicates a better correlation with respect to what is normally found for the overall aerodynamic forces and moments (Baker et al., 2004). The fact that most of the results larger than 1 are relative to the lift force is compatible with the presence of lift force fluctuations caused by the development of turbulence as an effect of the wind-vehicle interaction. With regard to the large lift force PoP normalised coefficients occurring on loops 1 and 2, a contribution to enhancing the force fluctuations can be inferred from the rolling vortices on the leeward face and on the roof leeward corner of the train (as hypothesised in chapter 6). At the same time, however, it is worth mentioning that an alternative explanation could be given based on the very small values of the corresponding mean coefficients (Baker and Humphreys, 1996).

In terms of the comparison between static and moving model test results, the general agreement indicated by the PoP normalised coefficients per unit length suggests a limited impact of the vehicle movement. This is similar to what was observed regarding the mean aerodynamic coefficients per unit length. In light of this, the differences outlined in section 7.2.3.1 appear to support the idea, with regard to the PoM coefficients, that the use of the mean reference wind velocity in the normalisation leads to insufficient consideration of the variation (between static and moving model tests) of the turbulence level in the relative wind. Therefore, the normalised PoP, rather than PoM coefficients appear to be the most appropriate parameters to investigate the influence of the vehicle movement on the train unsteady aerodynamics.

7.3 Overall peak load normalised coefficients

The analysis of the overall peak aerodynamic loads is presented here with consideration of the PoP normalised coefficients. These were obtained as the ratios between the PoP and the corresponding mean coefficients, both referred to the overall aerodynamic loads. The latter had been calculated within the analysis of the steady aerodynamic loads (section 6.4.3). The overall PoP coefficients, by contrast, were computed as explained below.

In light of the methodology adopted for most of the tests in this research (chapter 4), the pressure taps on each loop were monitored during different runs. This means that there was no synchronisation between the surface pressure fluctuations measured on different loops. Therefore, there was no possibility of obtaining time histories of the overall aerodynamic loads from the surface pressure measurements collected during different runs. The PoP coefficients for the overall aerodynamic loads, hence, were calculated by integrating along the train the PoP coefficients relative to each individual loop. Although this method is the same used for computing the overall mean load coefficients, its application relating to peak aerodynamic loads implies the assumption of perfectly correlated surface pressure fluctuations along the entire vehicle. Based on previous experimental results (Baker, 1991b, Baker 2010a), it is acknowledged that this is likely to be a conservative assumption. Therefore, a discussion on such conservativeness is included in the following section 7.4.2 based on the analysis of the correlation of the pressure fluctuations along the train.

Figure 7.5 illustrates the PoP normalised coefficients of the overall aerodynamic loads for both the static and moving model tests. In addition, the corresponding numerical values are specified in table 7.3. The side and lift forces are presented together with the rolling moments referred to   -axis and to leeward rail. The error bars indicate the margin of uncertainty estimated in section 5.4.2.2.
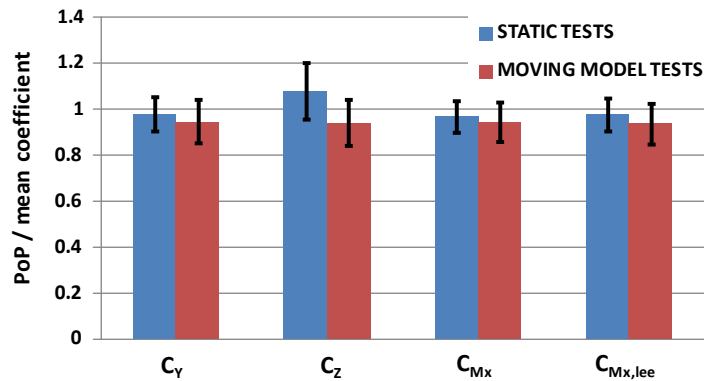
Figure 7.5 Peak-over-peak normalised coefficients of the overall aerodynamic loads. Static vs moving model tests comparison

		STATIC TESTS	MOVING TESTS	Magnitude VARIATION |MOV. – ST.|
$\hat{C}_Y$	C_Y	0.98	0.95	-3%
$\hat{C}_Z$	C_Z	1.08	0.94	-13%
$\hat{C}_{Mx}$	C_{Mx}	0.97	0.95	-2%
$\hat{C}_{Mx,lee}$	$C_{Mx,lee}$	0.98	0.94	-4%

Table 7.3 Peak-over-peak normalised coefficients of the overall aerodynamic loads. Static vs moving model tests comparison

		E_{TOT} STATIC	E_{TOT} MOVING	E_{TOT} % STATIC	E_{TOT} % MOVING	E_{TOT} % ST. + MOV.
$\hat{C}_Y$	C_Y	0.074	0.094	8%	10%	17%
$\hat{C}_Z$	C_Z	0.123	0.102	11%	11%	22%
$\hat{C}_{Mx}$	C_{Mx}	0.068	0.088	7%	9%	16%
$\hat{C}_{Mx,lee}$	$\overline{C}_{Mx,lee}$	0.072	0.089	7%	9%	17%

Table 7.4 Peak-over-peak normalised coefficients of the overall aerodynamic loads: experimental uncertainties.

With consideration of any of the four aerodynamic loads, for both static and moving model tests, the PoP normalised coefficients have values close to 1. As long as the uncertainty margin is taken into consideration, it can be observed that PoP normalised coefficients correspond to 1 in all cases. Nevertheless, if the best estimates are evaluated, it can be noted that all the coefficients, with the exception the lift force relating to the static tests, tend to be slightly less than 1. All these aspects, as well as their interpretation, are consistent with what observed with regard to the PoP normalised coefficients relating to aerodynamic loads per unit length.

The comparison between static and moving model results outlines a general agreement. Not only do the differences between the corresponding PoP normalised coefficients fall within the estimated uncertainty for the four examined loads, but also the uniformity is remarkable in three of the four cases (with variations < 4%). Only the lift force shows a tendency of the static test coefficients to be higher with respect to those obtained from the moving model experiments. This behaviour reflects the trend observed above with consideration of the peak coefficients relating to the aerodynamic loads per unit length. Furthermore, noting that the PoP coefficients reported here have been normalised on the corresponding mean coefficients, the tendency noted for the lift force is consistent with the higher overall mean lift force coefficients found for the moving model tests (figure 6.25 in section 6.4.3).

Noting the (conservative) assumption of peak pressure correlation made in the calculation process, the present sets of overall PoP normalised coefficients can be evaluated with respect to those obtained from previous investigations specifically concerned with rail vehicles. For example, a series of static tests were carried out by Baker (2003), both at full-scale and on a scale-model in a conventional wind tunnel. Interestingly, a Class 390 Pendolino train geometry (very similar to that adopted in this research) was investigated. The agreement of those with the present results appears encouraging in the sense that the PoP normalised coefficients for both the side force and the rolling moment (relating to 30° yaw angle) are very close to 1 in both studies.

Regarding the assessment of the aerodynamic effect associated with the moving vehicle simulation, previous experiments on a railway container (Humphreys, 1995; Baker and Humphreys, 1996) can be used for comparison. A good agreement can be found between the results presented here and those from static tests undertaken in this previous study, for which the PoP normalised coefficients were close to 1. However, there is a significant difference in the PoP normalised coefficients relating to moving model tests. While for the present tests they are still approximately unitary, the values found by Baker and Humphreys are of the order of 2, for both side and lift forces. The main reason for this

discrepancy is hypothesised in the *mechanical noise* interference that, during moving model tests, is most likely to have affected the performance of the force balance employed by Baker and Humphreys. This interference, rather than an actual difference with respect to static tests, might have caused the increment found in the past moving model PoP normalised coefficients (section 3.5.1). Furthermore, since its effect on the measurements undertaken in this campaign has been significantly mitigated thanks to the use of a pressure measuring system (appendix E), it could also explain the differences between the present and past moving model tests results.

7.4 Correlation of aerodynamic pressure fluctuations along the vehicle

7.4.1 Static and moving model test results

To assess the correlation of the unsteady pressure fluctuations along the train, dedicated series of tests were carried out monitoring simultaneously groups of pressure taps belonging to different loops. This is similar to the approach undertaken by Coleman (1990) in a wind tunnel study on a scale lorry.
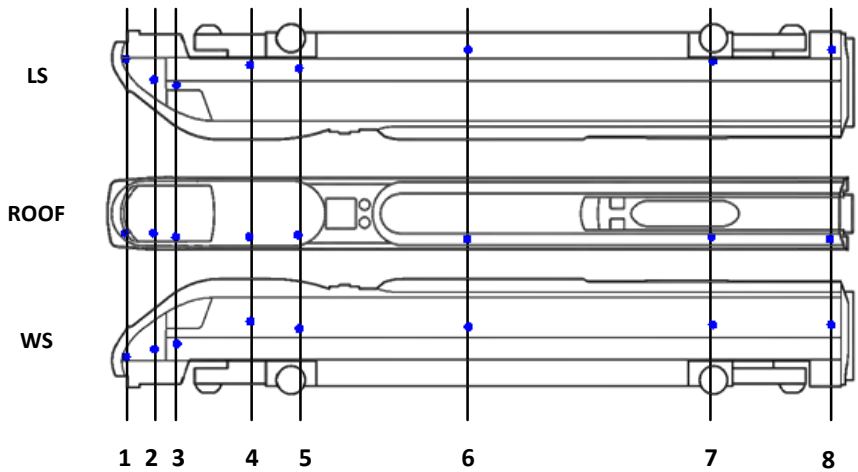
Figure 7.6 '*Lines of pressure taps*': pressure tap distribution along the vehicle

The three different '*lines of pressure taps*' illustrated in figure 7.6 were investigated. For each of these, positioned on the windward side (WS), on the roof and on the leeward side (LS) of the vehicle, respectively, table 7.4 specifies the pressure taps taken into consideration on each loop with respect to the numbering system in figure 4.27.

Loop #	Tap #		
	WS	Roof	LS
1	2	5	11
2	2	4	10
3	2	5	10
4	2	5	12
5	2	5	12
6	2	5	11
7	3	6	12
8	2	5	10

Table 7.5 *'Lines of pressure taps'*: pressure taps on each loop (numbering system defined in section 4.5.1.4)

The correlation between the pressure loads on different loops was analysed through the calculation of the time delayed cross-correlation coefficient, defined as:

$$\rho_{x,y}(\tau) = \frac{\overline{x'(t) \cdot y'(t+\tau)}}{\sigma_x \cdot \sigma_y}$$

(7.8)

where   and   are the fluctuating component of the two (stationary) signals (and   ) taken into consideration,   and   are the respective standard deviations,   is the time and   is the time delay (i.e., the lag) and the overbar indicates indicate a time average. In this case,   and   represent the time series of the pressure coefficient relating to two different taps of the same line. Each time series was calculated from the pressure measurements according to the data reduction method explained in chapter 5. Therefore, the corresponding time delayed correlation coefficient, indicated in the following as   , was computed for any pair of pressure taps (and   ) belonging to the same line.

For static tests, the entire 60 s long time histories obtained (from the raw data) for   at each pressure taps were taken into account for calculating   . For moving model tests, instead, the stationary portion of any individual single-run time history (i.e., 0.2   0.9) was considered (section 6.3.1). This produced a total of fifteen   time series associated with each pair of pressure taps (one per each run). From these, the final values of the time delayed cross-correlation coefficients were obtained through an ensemble averaging process. An example of this computation

is illustrated in figure 7.7 with consideration of two pairs of measuring points on the windward face

of the vehicle. Here, as well as in the following figures 7.8, 7.9 and 7.10, is presented with respect to a normalised lag = (where is the reference mean wind velocity and is

length of the train's leading car). Since changes from static to moving model tests, the use of

eases comparison between the two sets of results.
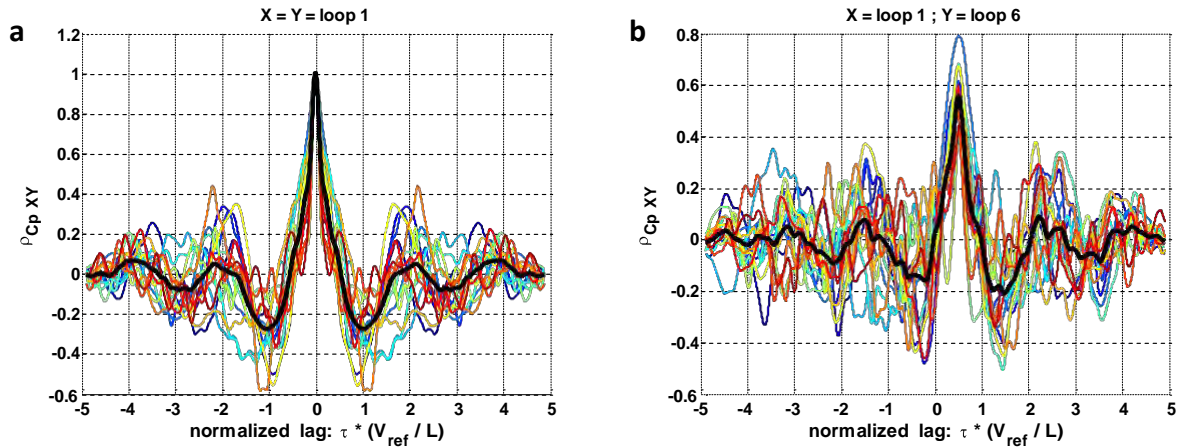
Figure 7.7 Time delayed cross-correlation coefficient, line of pressure taps on the windward side. Moving model tests, ensemble averaging process (the coloured lines represents the single-run data series; the black line is the ensemble average).

Figures 7.8, 7.9 and 7.10 report the time delayed cross-correlation coefficients relating to the lines of

pressure taps on the WS, on the roof, and on the LS, respectively. For each line, a reference pressure

tap on four different loops is considered: loop 1 on the nose, loop 4 on the front bogie, loop 6 in

the centre and loop 8 on the tail of the leading car (figure 7.6). For any of these cases, each figure

illustrates with respect to a pressure tap on any loop varying from 1 to 8, both at positive

and negative non-dimensional lags. Accordingly, in light of equation (7.8), when = , then

coincides with the autocorrelation coefficient, which has a unitary maximum at = 0 and varies

symmetrically between positive and negative lags.

STATIC TESTS
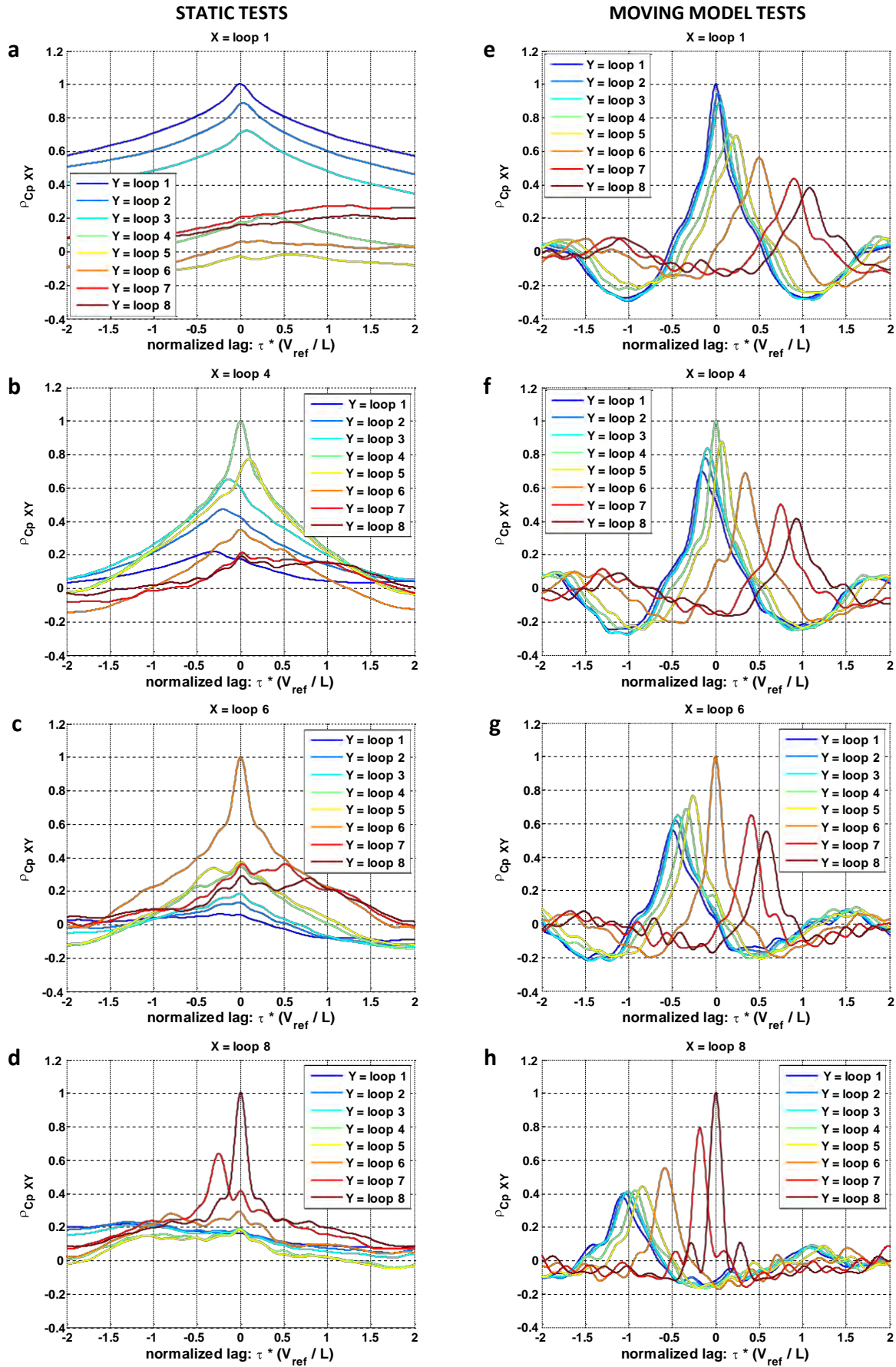
MOVING MODEL TESTS

Figure 7.8 Time delayed cross-correlation coefficient, line of pressure taps on the windward side. Static vs moving model tests

STATIC TESTS
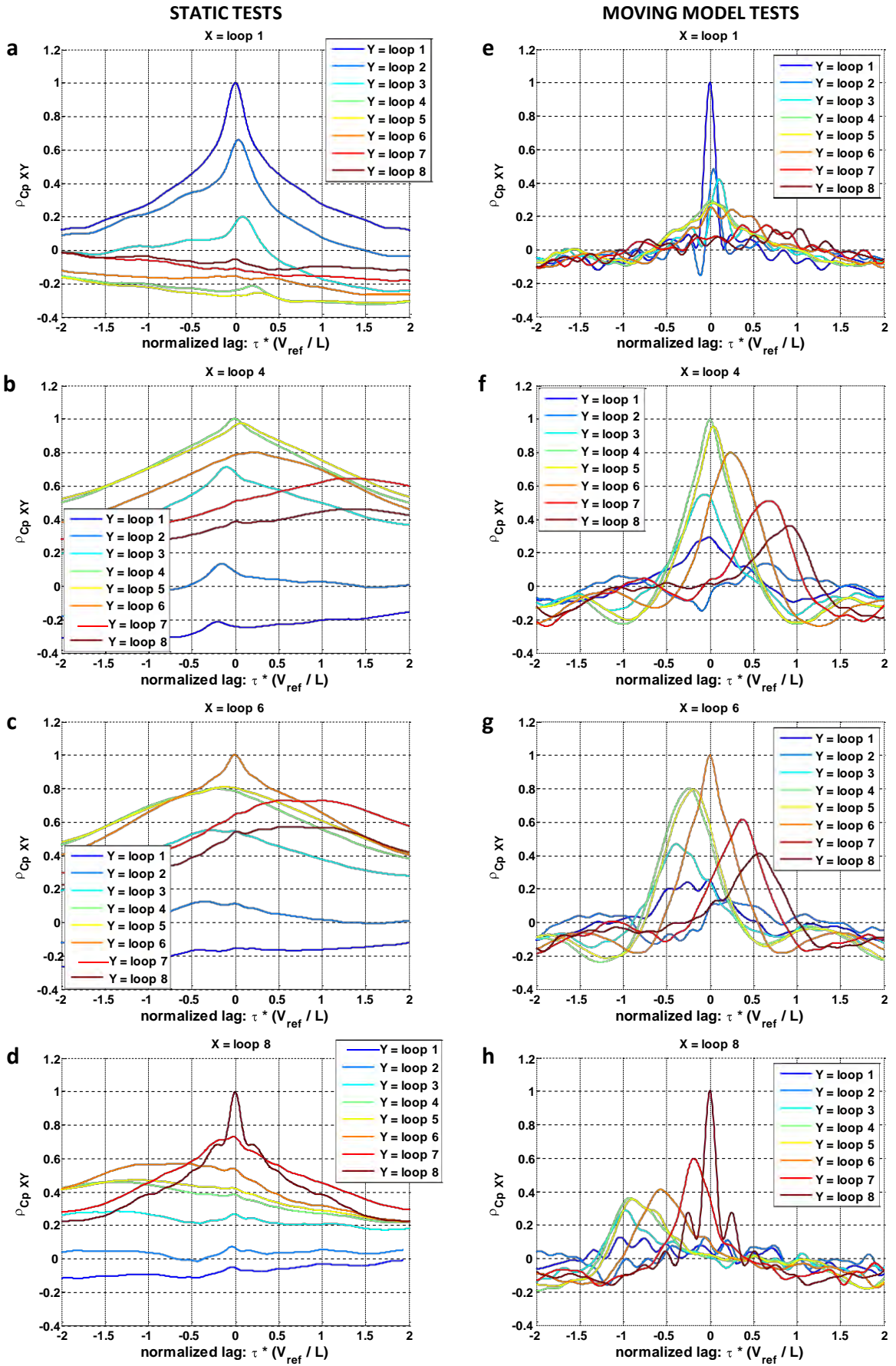
MOVING MODEL TESTS

Figure 7.9 Time delayed cross-correlation coefficient, line of pressure taps on the roof. Static vs moving model tests

STATIC TESTS
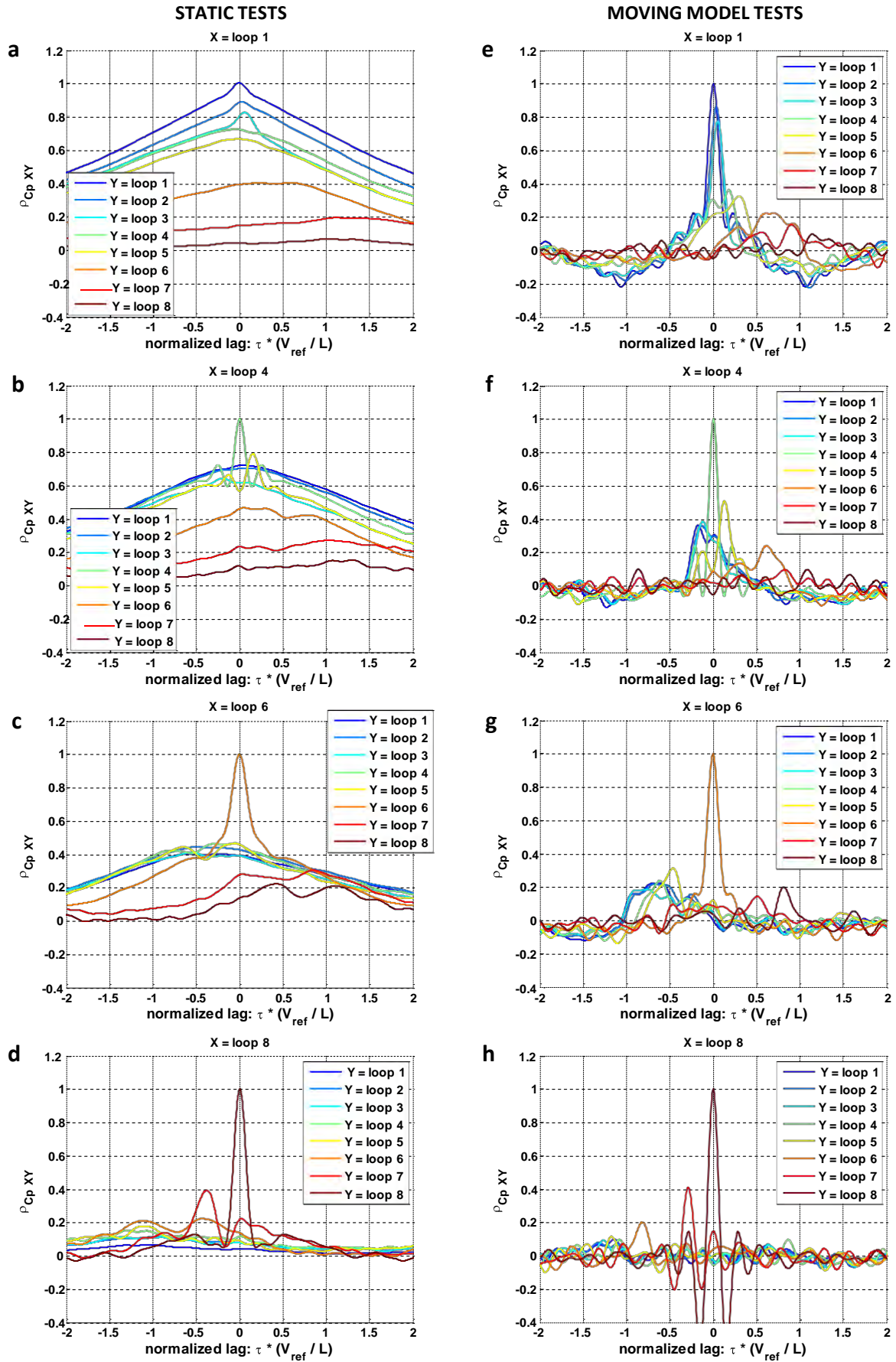
MOVING MODEL TESTS

Figure 7.10 Time delayed cross-correlation coefficient, line of pressure taps on the leeward side. Static vs moving model tests

Static model test results

Relating to the line of pressure tap on the WS, Figure 7.8 a-d shows a correlation between the fluctuations extending to limited portions of the vehicle, but not to its entire length. On loop 1, maximum values of   greater than 0.7 indicate a good correlation with the three loops on nose (figure 7.8a). Examining loop 4, although with lower maxima, a series of peaks can still be identified in the cross-correlation coefficients associated with loops 2, 3 and 5. Loop 6 appears weakly correlated even with the adjacent loops 4 and 5, as well as with loops 7 and 8: this is not surprising in light of the relatively large distance that separates such loops from any of the others. Loop 8, finally, denotes a peak in   only with respect to the adjacent loop 7. In terms of their evolution with respect to   , the aforementioned correlation peaks are significantly wide relating to loop 1 on the nose of the train, while tend to progressively sharpen moving towards the rear.

Figure 7.9 a-d illustrates a partially different behaviour relating to the line of pressure taps on the roof. On loop 1, although still present the indication of a correlation extending up to loop 3, has lower maxima than on the WS and the peaks are sharper. Conversely, stronger correlations than those occurring on the WS appear on loops 4, 6 and 8. Loop 4 is correlated with loop 5 (maximum   > 0.9) as well as with any other loop other than 1 and 2 (maxima   > 0.4). The latter condition is also observed for loop 6 and loop 8 with respect to all loops except, respectively, loops 1 and 2 and loops 1, 2 and 3. Excluding loop 1, furthermore, comparing the same loops, the correlation peaks on the roof are wider than those on the WS.

The tendency of the cross-correlation coefficients on the LS line of pressure taps, presented in figure 7.10 a-d, is similar to that observed on the WS. The correlation does not extend all along the vehicle length, but is strong between the loops on the front. Both on loops 1 and 4, it is slightly stronger than on the WS. Higher maxima of   are reached on loop 1, considering the correlation with loop 4 and 5, and on loop 4 considering the correlation with loop 1 and 2. Furthermore, while on loop 1 the correlation peaks are approximately as wide as on the WS, on loop 4 they appear to be wider. In

addition, the autocorrelation coefficient on loop 4 shows a secondary peak (symmetrical with respect

on $\;$ = 0) which reaches approximately $\;$ = 0.7. The behaviour of $\;$ on loops 6 and 8 is in

agreement with what found on the WS. In both cases, the autocorrelation peak is sharp. On loop 6, it

occurs in combination of weak cross-correlations with respect to any other loops, with a slight

increment (from the WS results) in the $\;$ referred to loops 1 to 5 on the train front. On loop 8,

instead, the only relevant cross-correlation peak is associated with the adjacent loop 7.

Moving model test results

In figures 7.8 e-h, the moving model test results show well defined $\;$ peaks relating to any pair of

loops that were examined. This denotes a good correlation extended to the entire length of the

vehicle. Maxima higher than 0.8 are reached between adjacent loops (like between loop 1 and loops

2 and 3, or between loop 4 and 5). Moreover, cross-correlation coefficients higher than 0.4 are kept

even between loop 1 and loop 8, respectively on the nose and on the tail of the vehicle. Although not

as wide as for the static tests, the shape of these peaks remains consistent considering different

distances between loop $\;$ and loop $\;$ (i.e. within each figure from 7.8e to 7.8g) and also considering

a different reference loop $\;$ (i.e. comparing two of these figures). The exceptions, where sharper

peaks occur, are represented by the autocorrelation peaks on loop 6 and 8 and, on loop 8, also by

the cross-correlation with respect to loops 6 and 7. On loop 8, finally, a pair of positive secondary

peaks (approximately symmetrical with respect to primary peak) arises both on the autocorrelation

and on the cross-correlation correlation with respect to loop 7.

As for static, so for moving model tests, figures 7.9 e-g relating to the line of pressure taps on the

roof outline a different behaviour between loop 1 and the others. Furthermore, some differences can

be noticed with respect to $\;$ relating to the line of pressure taps on the WS. On loop 1, apart

from a sharp autocorrelation peak, weak cross-correlations are found with respect to any other loop.

On loops 4 and 6, $\;$ behaves consistent to what it does on the WS: a series of correlation peaks

associated with the loops from 3 to 8 reach maxima of   approximately equal or larger of 0.4.

Similar, but associated with slightly lower maxima, is the trend on loop 8. On loops 4 and 6 the shape of the correlation peaks is alike to that observed in the vast majority of the results associated the WS line of pressure taps. On loop 8 the peaks are slightly sharper and, as on the WS, the autocorrelation coefficient shows a pair of symmetrical positive secondary peaks.

A significant change, with respect to any of the other two lines of pressure taps, is outlined by the cross-correlation coefficients on the LS of the vehicle.   maxima greater than 0.4 are reached only by the autocorrelation or by the cross-correlation that relates pairs of adjacent loops (i.e. any couple of loops between 1 to 3, loops 4 and 5 and loops 7 and 8), for which the peaks are sharper than any of those found on the roof or on the WS. Apart from that, a weak correlation with never exceeding 0.2 characterises all other cases. On loop 4, two secondary peaks with a magnitude of the order of 0.2 and symmetrical with respect to the primary peak arise on the autocorrelation. On loop 8 both the autocorrelation and cross-correlation coefficients with respect to loop 7 show a series of oscillations that lead to the arising of a series of negative and positive secondary peaks. These peaks occur for both positive and negative   , are approximately symmetrical on the primary peak, and their magnitude progressively reduces when the non-dimensional lag increases.

7.4.2 Discussion

A peak in the cross-correlation coefficient, i.e. when   ≠   and therefore the pressure taps on different loops are evaluated, can be observed in a number of cases. If present, such a peak arises at   and has its maximum lower than 1. Maximum values of   occur at positive lags when loop   is downstream (i.e. towards the rear of the train) of loop   and at negative lags when loop   is upstream of loop   . This indicates that the   fluctuations occur subsequently (in time) on the loop downstream with respect to that upstream. An example of this behaviour is given by the moving model results reported in figure 7.8 e-h and 7.9 f-h (for the line of pressure taps on the WS and on

the roof, respectively). In figure 7.8e the cross-correlation is calculated between a pressure tap on the train nose (= loop 1) and a measuring point progressively moved towards the rear (= loop 1 to 8). It can be noticed here that, when the distance between the two loops becomes larger, not only does the lag at which the maximum occurs increase, but also the magnitude of the maximum decreases, which denotes that the correlation progressively deteriorates when the spatial separation increases.

Whether = or ≠ , not only the lag and magnitude of the maximum, but also the evolution of with respect to the (non-dimensional) lag provides useful information. The width of the peak indicates the duration (in time) of the correlation: the broader the peak, the longer the time during which the correlation lasts. Considering the relation between the surface pressure fluctuations and the characteristics of the turbulent flow field developing around the train, the analysis of this aspect gives an indication on the time (and length) scales of turbulence: the wider the peak, the longer the time (and the larger the length) of such scales. Therefore, the larger become the dimensions of the vortices and turbulence structures.

The presence of a pair of symmetrical secondary peaks has been observed in the autocorrelation coefficients relating to loop 4 and loop 8. On loop 4, these secondary peaks characterise both static and moving tests results of the LW line of pressure taps. On loop 8, they are evident on the moving model test data on any side of the train, while barely visible on the static test results. It is hypothesised that such secondary peaks indicate the presence, near the pressure taps under investigation, of a separation point from which a series of wake vortices originates. In this view the secondary peaks are associated with periodic fluctuations in the local surface pressure that, in turn, are compatible with the cyclic formation and detachment of vortical structures from the vehicle surface. This interpretation is consistent with the particular positions along the train where the secondary peaks are found. On loop 8, the formation and detachment of wake vortices is more likely to be induced by the geometrical discontinuity represented by the inter-car gap between the first

and second vehicle. Between loop 3 and loop 4, instead, detachment of the leeward rolling vortices forming on the nose of the train is consistent with what was previously hypothesised in light of the mean pressure coefficient distribution (sections 6.2.1 and 6.3.1).

Comparison between static and moving model tests

The results in figures 7.8, 7.9 and 7.10 denote that a correlation exists between the pressure fluctuations occurring at different longitudinal positions along the train, both on a static and on a moving model. The characteristics of such correlations, however, are not the same in the two cases and the following main differences can be observed:

- On any side of the train, wider correlation peaks characterise the train model tested statically. According to the interpretation given to the peak width, this suggests that the time and length scales of turbulence surrounding the scale-model train are smaller when it is tested in moving model conditions.

- On the WS, for the moving model tests, correlation peaks arise between any pair of loops, even if positioned at the opposite ends of the leading car. This indicates a correlation between the pressure fluctuations all along the windward face of the vehicle. In static test conditions, instead, such fluctuations are correlated only within limited portions of the train length.

- When the train is moving, on loop 8 a series of well-defined secondary peaks arise in the autocorrelation. On a statically tested model, instead, such peaks are extremely smooth. This suggests a difference in the mechanism of formation and detachment of the wake vortices from the tail of the leading car.

One interpretation for these differences can be given in relation to the characteristics of the relative wind turbulence perceived by the train in the two test conditions. During static tests, the integral turbulence scales relative to the train correspond to those of the onset wind. In such a condition, the longitudinal turbulence scales   appears to determine the width of the cross-correlation peaks and

thus the duration (in time) of a series of pressure fluctuations occurring at one pressure tap and caused by the same vortex. The portion of the vehicle actually subjected to one typical onset wind turbulent structure, instead, and thus the occurrence of correlation peaks between different loops, is more likely to be related to the lateral integral scales (   ). This situation changes with consideration of a moving train, which travels across the onset wind turbulence structures whilst these moves perpendicularly to the track (along the streamwise mean wind direction). According to the theory of Cooper (1984) (section 2.3.1), in this condition the turbulence scales seen by the vehicle depend on both the longitudinal and lateral scales of the onset wind (and   , respectively), on the mean wind velocity ( ) and on train speed   . In this case, hence, it is the combination of all these factors that determines both the width of the   peak and the correlation of the pressure fluctuations along the vehicle (i.e., the occurrence of cross-correlation peaks between different loops).

The decrease observed in the width of the correlation peaks is consistent with the reduction of the turbulence length scales seen by a moving train with respect to those perceived by a static train (which, based on the flow characterisation data reported in full in appendix A, are approximately 0.3 m and 1 m, respectively). Analysing the correlation along the vehicle, the persistence of cross-correlation peaks between loop 1 and loop 8 on a moving train suggests that it travels quickly enough to run through the crosswind turbulent structures (for the entire length of the first car) before these have entirely moved downstream of the track. When it is statically tested, instead, the lateral length scales do not appear to be sufficiently large to embrace the entire leading car.

An alternative explanation for the variations between static and moving model experiments takes into account the characteristics of turbulence generated by the flow-vehicle interaction. According to this second approach, the modifications in the peak width could be ascribed to different length (and time) scale of the vortices forming on the train surface, with larger turbulent structures corresponding to wider peaks. The correlation of the pressure fluctuations along the train is instead

related to the way these vortices develop and progressively detach from the surface of the vehicle. The shorter the portion of train within which such a correlation can be observed, the shorter the distance along which the vehicle-induced turbulent structures remains attached to the train.

There is no general indication as to whether one or another of the two aspects mentioned above is prevailing in determining the differences found between static and moving model test results. Neither any specific observation can be made for excluding a combination of both. Nonetheless, in light of the characteristics identified on the mean surface pressure distribution (sections 6.2.1 and 6.3.1), the dominance of one rather than the other can be inferred relating to different areas of the train.

On the windward face, the rather uniform stagnation region observed in the analysis mean pressure distribution has been ascribed to the onset wind directly impinging on the vehicle. Suggesting a limited impact of the vehicle-induced turbulence, this supports the hypothesis that on the windward face the effect of differently perceived onset wind turbulence could be dominant for explaining the differences found (in figure 7.8) between static and moving model tests. Conversely, on the leeward face in the front portion of the train and in part of the roof the mean pressure distribution indicates a significant contribution to the   fluctuations from the vortices developing on the train surface. Accordingly, it is more likely that a modification in the characteristics of the vehicle-induced turbulence has a major role in determining the variations observed in figures 7.9 and 7.10 around the roof and the leeward face. In light of the interpretation given above to the secondary autocorrelation peaks, finally, the latter consideration can be extended also to the interpretation of the different behaviour observed in the correlation coefficients relating to loop 8.

Assessment of the overall peak coefficients estimation

The analysis of the time delayed cross-correlation reported above outlines that there is a correlation between the pressure fluctuations occurring on different loops along the train. The characteristics of this correlation depend both on the portion and on the side of the vehicle taken into consideration and changes between static and moving model tests.

Based on this, a correlation is likely to exist between the aerodynamic loads per unit length arising on different loops. Where two loops are correlated, this means that there is a *'specific dependence'* between the instantaneous aerodynamic loads per unit length arising on each of them. Since such a *specific dependence* does not necessarily imply a perfect correlation, the conservativeness of the assumption made in section 7.3 for calculating the peak coefficients for the overall aerodynamic loads is confirmed.

To calculate the overall peak coefficients two subsequent integrations are performed. The first integration is in the *time domain* and consists of a moving average run over the recorded time series for finding the peak coefficients per unit length. The second integration is performed in space, along the train, and leads from the coefficient per unit length to those associated with the entire vehicle. As such, the overall peak coefficients are related both to the width and to the persistence along the vehicle of the correlation peaks observed in figures 7.8 to 7.10.

The comparison between the cross-correlations relative to static and moving model tests has outlined a number of differences concerning both of these aspects. Indicating that the vehicle movement has an effect on the correlation of the surface pressure fluctuations, this suggests that such an effect could influence also the magnitude of the overall peak coefficients. It cannot be excluded, therefore, that the same assumption made in both cases within the overall peak coefficients calculation might have introduced different approximations depending whether the train is tested statically or in moving conditions. Nevertheless, because of the differences in the results concerning the three lines of pressure taps that were examined, no rigorous extrapolation leading

from the correlation of the local pressures to the correlation of the loads per unit length can be made.

Within this research, hence, it is acknowledged that the data collected do not enable the implementation of a more accurate calculation for the overall peak coefficients. However, it is worth noting that the experimental method developed in the present work is viable to pursue further this investigation. Using the TRAIN rig facility and employing an on-board pressure measuring system, the method reduces the interference produced by the mechanical vibrations on the on-board measurements collected during moving model tests, thus addressing one of the major challenges outlined by the past experiments. As such, if an increased number of channels were available in the on-board data logger, it could be employed in order to overcome the limit reached in this research (as recommended in section 8.2).

Chapter 8

Conclusions and recommendations for further work

8.1   Conclusions

The main aim of the present research was to assess the influence of the modelling of the vehicle movement on the aerodynamic behaviour of a rail vehicle in the presence of crosswinds. To this end, and to accomplish the objectives stated in section 1.3, the following tasks were completed:

- A new crosswind generator was designed and installed in the TRAIN rig facility (reported in chapter 4 and appendix A).

- An on-board pressure measuring system was developed and integrated inside a scale-model train suitable for TRAIN rig moving model tests (chapter 4).

- An experimental methodology for undertaking moving model experiments in the presence of a crosswind simulation at the TRAIN rig was developed (chapters 4 and 5; appendices C, D and E).

- The surface pressure distribution on a scale-model train subjected to a crosswind was measured: two series of experiments were undertaken in the TRAIN rig, testing the same scale-model in static and moving model conditions (chapters 6 and 7; appendix F).

- A comparison between the results obtained from these experiments was carried out and the effects of the modelling of the vehicle movement on the train steady and unsteady aerodynamic coefficients were assessed (chapters 6 and 7; appendices F and G).

- A set of experimental data viable for CFD benchmarking was produced. These data include both the pressure distribution on the train and the information regarding the characteristics of the onset wind simulation adopted during the tests.

With regard to the upgrade of the test facility, as well as to the development of the measuring system and of the test methodology adopted in this research, the conclusions below can be drawn from the work presented in chapters 4 and 5:

1. After the development and installation of the new CWG, the TRAIN rig has been demonstrated to be a viable facility to undertake moving model experiments on rail vehicles in crosswinds.

2. The characteristics of the TRAIN rig mechanical propulsion system ensure the following main advantages relating to moving model tests in crosswinds:

    - Good run-to-run vehicle speed repeatability;

    - Minimum flow interference around the vehicle and, particularly, in the underbody region;

    - Simulation of a variety of yaw angles by varying the vehicle speed (in the range between 0 and 75 m/s) at Reynolds numbers equal to or larger than 1.2×10^5.

3. The new CWG represents a significant improvement on the existing apparatus. The constraint imposed to its dimensions by the narrow space available inside the existing building means that the new system delivers a relatively crude simulation of a natural wind. Notwithstanding such a limitation, it has been shown that the quality of the crosswind simulation is sufficient to undertake valuable investigations. Furthermore, the current CWG configuration also enables static model experiments in crosswinds.

4. An on-board pressure measuring system suitable for installation in TRAIN rig scale-models has been successfully developed. With respect to using a force balance, the employment of such a system for moving model tests gives the following benefits:

    - Ensures a reduced sensitivity of the collected data to *mechanical noise* caused by the vibrations of the vehicle model induced by track irregularities;

    - Enables a detailed comparison between static and moving tests, not only in terms of overall aerodynamic load coefficients, but also of local pressure distribution;

    - Delivers experimental data that allow for accurate CFD validation (Sterling et al., 2010).

5. The newly developed TRAIN rig firing procedure that includes the operation of the new CWG and of the on-board measuring system allows it to perform up to 15 runs per day with an estimated data acceptance rate greater than 85 % (on average). This is similar to the performance associated with TRAIN rig tests in the absence of any crosswind simulation (i.e. up to 20 runs per day with an acceptance rate of at least 90% (Gilbert, n.d.)) and such values appear satisfactory in light of the increased complexity of crosswind experiments.

6. The experimental methodology suggested by Baker (1986) and Humphreys (1995), based on ensembles of runs, has been demonstrated to be adequate for TRAIN rig moving model tests in crosswinds. Series of 15 runs have been found sufficient for obtaining statistically stable ensemble averages.

7. With regard to the steady aerodynamic investigation, such a moving model test methodology has led to estimations of the overall aerodynamic mean load coefficients with a random uncertainty of the order of 2% and a total uncertainty (including the bias) of approximately 4%. Such an accuracy level is comparable with that obtained in the past campaign of Humphreys (1995). However, having been reached through a significantly lower number of runs (i.e., 15 vs. 50), it testifies the advantages inherent in the use of the TRAIN rig facility and of an on-board pressure measuring system.

8. The analysis of the unsteady aerodynamics from moving model tests has been eased by the reduction of *mechanical noise* obtained through the employment of an on-board pressure measuring system rather than an on-board force balance. However, the short duration of the time series recorded during a single, moving model test run, prevents the peak aerodynamic coefficients being obtained through a conventional extreme value analysis, according to the methods of Gumbel or Lieblein. Furthermore, a challenge has been identified in the definition of a representative reference wind velocity to be used in the computation of such parameters.

9. An estimation method has been developed for obtaining the peak-over-peak normalised load coefficients from the data collected through series of 15 TRAIN rig moving model test runs. Such coefficients were referred to a 3 s full-scale equivalent gust-time, based on a peak reference wind velocity and normalised with respect to the corresponding mean load coefficients. The accuracy of these estimations is in the order of 10%.

The results presented in chapters 6 and 7 led to the following conclusions regarding the aerodynamic behaviour of a Class 390 Pendolino leading car, subjected to a 30° yaw angle crosswind on a flat ground:

1. The mean surface pressure distributions and the mean load coefficients measured during the TRAIN rig tests (both on a static and on a moving model) are in qualitative agreement with those found in previous studies relating to streamlined rail vehicles investigated on similar ground scenarios and exposed to low yaw angle side winds (Baker, 1991a; Hemida and Krajnovic, 2009a; Cheli et al., 2011a).

2. The characteristics of the surface pressure distribution suggest a similarity with what was observed in previous research also concerning the flow field surrounding the train (Copley, 1987; Baker, 1991a; Baker, 2010b). The main features of such a flow field are a series of intense vortices on the leeward side of the vehicle that develop on the nose and then, moving towards the tail, progressively distance and finally detach from the train to form the wake.

3. The quantitative comparison between the mean aerodynamic coefficients obtained from the TRAIN rig static and moving model tests reveals the following:

   - The time averaged pressure distributions relating to the two test conditions are in good agreement around the entire vehicle. The vast majority of the observed differences fall within the estimated margin of uncertainty. An exception to this occurs on the first loop of pressure taps on the train nose, where moving model tests show larger magnitudes of the non-dimensional pressure coefficient. Such differences are consistent with the skewed wind

profile, and particularly with the higher local relative wind velocity, perceived by a moving rather than by a static train (between the ground and the reference height).

- The mean pressure field on the underbody of a moving train shows a suction that is slightly less intense than that that found on a static train. Since these measured variations are smaller than the uncertainty margin, however, their rigorous interpretation in physical terms is not possible.

- The time average properties of the flow developing in proximity to the train, which were inferred based on the mean surface pressure distributions, suggests a good consistency between the static and moving model tests.

- The two series of mean load coefficients per unit length are in remarkable agreement along the entire vehicle. Consistent with what happens for the surface pressure, an exception occurs at the train nose. Here, the results from the static tests are lower than those from the moving tests for both the side force and rolling moment coefficients while, in terms of lift force, the direction of such a force switches in direction from upward (on a moving train) to downward. These differences exceed the uncertainty margin.

- The overall mean aerodynamic coefficients show an agreement between static and moving model tests to the level of accuracy of the present comparison. Any discrepancies between the corresponding parameters associated with the two different test conditions are all smaller than the estimated experimental uncertainty (which is approximately 10 to 13%). Slight decrements in the order of 2 to 5% characterise the moving model tests side force and rolling moment coefficients, while the lift force coefficient shows an increment estimated between 3 and 8%.

4. The comparison of the TRAIN rig overall mean load coefficients, calculated by discrete integration of the surface pressure distribution, with those obtained through standard wind tunnel static tests on the same (nominal) train geometry shows an encouraging level of

agreement. This supports the reliability of the results as well as of the experimental setup and the test methodology that have been developed in the TRAIN rig.

5. The 3 s (full-scale equivalent) peak-over-peak normalised coefficients of the loads per unit length are equal to 1 (to the estimated uncertainty) in the vast majority of the cases examined, for both static and moving model tests. This indicates a *Quasi-Steady* behaviour of the peak loads arising on the individual cross-section of the vehicle. Exceptions occur only on the train nose, where normalised lift force peak coefficients larger than 1 occur, which are likely to be related to the (hypothesised) formation of a series of intense vortices on the roof leeward corner of the vehicle.

6. The peak-over-peak normalised coefficients of the overall aerodynamic loads have been estimated by integrating along the vehicle the normalised peak-over-peak load coefficients per unit length associated with each loop of pressure taps. Postulating a complete correlation of the aerodynamic load fluctuations along the train, this approach leads to values equal to 1 (to the estimated level of accuracy). Although implying a *Quasi-Steady* behaviour on the overall aerodynamic loads fluctuations, these results should be interpreted with care in the light of the limitations inherent in the initial assumption (discussed at the following point 10).

7. Comparing the peak-over-peak normalised coefficients from static and moving model tests, the following indications are obtained:

   • The aerodynamic load coefficients per unit length in the two test conditions are in general agreement. The only discrepancy larger than the estimated uncertainty arises on the train nose. Here, the higher peak normalised coefficient of the lift force on a moving train is more likely to be determined by the lower mean force coefficients used within the normalisation.

   • The coefficients relating to the overall aerodynamic loads are also in general agreement. However, as with the interpretation of such parameters discussed at point 6 above, so the analysis of their variations depends on the implications of the initial assumption on the

correlation between the peak loads per unit length, which was made in the computation and is addressed at point 10.

8. The analysis of the time-delayed cross-correlation coefficient between the pressure fluctuations occurring along the train suggests the following differences between static and moving model tests:

    - On any side of the vehicle, the time and length scales of turbulence experienced by the train reduces when it moves;

    - On the windward side of the train, the pressure fluctuations on a scale-model moving train are correlated along the entire leading car. Conversely, in static test conditions such fluctuations are correlated only within limited portions of the vehicle length;

    - When the train motion is replicated, there is a variation in the mechanism that leads to the formation and detachment of the wake vortices at the rear of the leading vehicle.

9. These results indicate that there is an effect of the vehicle movement on the pressure fluctuations occurring on the train. One cause of this effect can be hypothesised as the different onset wind turbulence perceived by the train when tested in static rather than moving conditions, i.e., the different size of the turbulent length scales in the freestream relative wind. In addition, it can also be considered that the simulation of the vehicle movement might alter the characteristics of the turbulent structures generated by the train-wind interaction.

10. The differences found in the correlation of the pressure fluctuations along the vehicle relating to static or moving model tests suggest that the vehicle movement might also influence the correlation of the aerodynamic loads per unit length and, in turn, the magnitude of the overall peak load coefficients. In light of the limited correlation observed for the surface pressure, the assumption of a perfect correlation along the vehicle made in the computation of the overall peak coefficients looks conservative for both a static and a moving train. Furthermore, in light of the differences outlined between static and moving model test results, it appears that the weight

of such an assumption could be different in the two cases. Nevertheless, no quantification of such a difference is enabled by the data collected in this research, due to the limited number of simultaneous channels available in the on-board measuring system.

According to the above, the effect of the modelling of the vehicle movement on the aerodynamic behaviour of the train can be assessed as follows to the level of accuracy reached in the present comparison:

1. There are only minor and localised variations in the mean pressure distributions on the train whether tested in static or moving conditions. This suggests an overall similarity in the characteristics of the time averaged flow field surrounding the vehicle in the two cases and leads to the conclusion that there is no significant impact of the vehicle movement simulation on the overall mean aerodynamic load coefficients. Accordingly, the results of this research disprove the hypothesis (made in section 1.2) of the vehicle movement simulation having an effect on the train steady aerodynamic behaviour in crosswinds. Hence, they support the adequacy of wind tunnel static tests for investigating the train overall mean aerodynamic load coefficients.

2. There is agreement in the magnitude of normalised peak-over-peak aerodynamic load coefficients per unit length obtained through static and moving model tests. Nevertheless, differences found in the correlation of the pressure fluctuations along the vehicle suggest an impact of the train movement on the overall peak-over-peak aerodynamic load coefficients. This confirms the initial hypothesis concerning the train unsteady aerodynamic behaviour and places a doubt on the capability of static tests to provide an accurate estimation of the peak coefficients of the overall aerodynamic loads.

8.2   Recommendations for further work

1. The experimental data collected in this research should be used for CFD benchmarking. This would enable an accurate validation of the numerical simulations, thus overcoming the previous limitations caused by a lack of experimental surface pressure measurements taken on moving trains in crosswinds.

2. The results of the present work suggest that the vehicle movement simulation might have an effect on the correlation of the aerodynamic load fluctuations arising along the vehicle and, in turn, on the magnitude of the overall peak load coefficients. The use of the pressure measuring system that was developed in this research appears extremely promising to assess this indication. To such end, however, an upgrade of the on-board data logger would be required to increase the number of channels and, in turn, to enable a larger number of pressure taps to be monitored simultaneously.

3. Previous experimental studies have suggested that, when a train subjected to a crosswind is investigated on an embankment, the presence of this infrastructure scenario might enhance the impact of the vehicle movement simulation with respect to what occurs on a flat ground (section 3.3.3). Furthermore, CFD simulations (Cheli et al., 2011a) have warned that, in such a case, wind tunnel tests on static vehicles could lead to a relatively large underestimation of the overall mean aerodynamic load coefficients. To assess this indication at an experimental level, and to validate the CFD results, a further series of crosswind moving model tests could be undertaken in the TRAIN rig. In this view, with only minor adjustments, the windward side of an embankment (i.e. an escarpment) could be implemented within the current CWG. Then, static and moving model tests could be undertaken using the instrumentation and methodology developed in this research.

4. It has been observed in section 6.3.1 that an analysis of transient aerodynamic loads could be undertaken examining the initial and final portions of the time series recorded whilst the scale-

model train travels within the CWG. This analysis would enable the assessment of the methods currently in use to predict such loads, which typically rely on a *Quasi-Steady* (or *Quasi-Steady corrected*) formulation and employ aerodynamic loads coefficients obtained through wind tunnel static tests (EC, 2008, CEN, 2010).

References

ACIN, 2012. Betz micromanometer - Factory Standard for pressure calibration. Available at http://www.acin.nl. Last accessed on 07/12/2012.

ATSB, 2008. Derailment of train 3DA2K near Tarcoola, South Australia, 1 November 2006. Transport Safety Report. Rail Occurrence Investigation No. 2006/012. Final. Australian Transport Safety Bureau.

ATSB, 2010. Derailment of train 2PM6 near Loongana, Western Australia, 11 November 2008. Transport Safety Report. Rail Occurrence Investigation RO-2008-013. Final. Australian Transport Safety Bureau.

Baker, C.J., 1985. The determination of topographical exposure factors for railway embankments. Journal of Wind Engineering and Industrial Aerodynamics 21, 89-99.

Baker, C.J., 1986. Train aerodynamic forces and moments from moving model experiments. Journal of Wind Engineering and Industrial Aerodynamics 24, 227-251.

Baker, C.J., 1991a. Ground vehicles in high cross winds part I: Steady aerodynamic forces. Journal of Fluids and Structures 5, 69-90.

Baker, C.J., 1991b. Ground vehicles in high cross winds part II: Unsteady aerodynamic forces. Journal of Fluids and Structures 5, 91-111.

Baker, C.J., 1991c. Ground vehicles in high cross winds part III: The interaction of aerodynamic forces and the vehicle system. Journal of Fluids and Structures 5, 221-241.

Baker, C.J., 2002. The Wind Tunnel Determination of Crosswind Forces and Moments on a High Speed Train, in: SchulteWerning, B., Gregoire, R., Malfatti, A., Matschke, G. (Eds.), TRANSAERO - A European Initiative on Transient Aerodynamics for Railway System Optimization. Springer, Berlin, pp. 46-60.

Baker, C.J., 2003. Wind overturning study: Full scale and wind tunnel measurements to determine the aerodynamic force and moment parameters of Mark 3 and Class 390 vehicles - Overview Report. University of Birmingham.

Baker, C.J., 2010a. The simulation of unsteady aerodynamic cross wind forces on trains. Journal of Wind Engineering and Industrial Aerodynamics 98, 88-99.

Baker, C.J., 2010b. The flow around high speed trains. Journal of Wind Engineering and Industrial Aerodynamics 98, 277-298.

Baker, C.J., 2011. A meta-analysis of train crosswind aerodynamic force coefficient data, in: Proceedings of the ICWE-13th International Conference on wind Engineering, Amsterdam, The Netherlands.

Baker, C.J., Bouferrouk, A., Perez, J., D., I.S., 2008. The integration of cross wind forces into train dynamic calculations, in: World Congress on Rail Research. Seoul, South Korea.

Baker, C.J., Cheli, F., Orellano, A., Paradot, N., Proppe, C., Rocchi, D., 2009. Cross-wind effects on road and rail vehicles. Vehicle System Dynamics: International Journal of Vehicle Mechanics and Mobility 47, 983 - 1022.

Baker, C.J., Dalley, S.J., Johnson, T., Quinn, A., Wright, N.G., 2001. The slipstream and wake of a high-speed train. Proceedings of the Institution of Mechanical Engineers, Part F: Journal of Rail and Rapid Transit 215, 83-99.

Baker, C.J., Humphreys, N.D., 1996. Assessment of the adequacy of various wind tunnel techniques to obtain aerodynamic data for ground vehicles in cross winds. Journal of Wind Engineering and Industrial Aerodynamics 60, 49-68.

Baker, C.J., Jones, J., Lopez-Calleja, F., Munday, J., 2004. Measurements of the cross wind forces on trains. Journal of Wind Engineering and Industrial Aerodynamics 92, 547-563.

Baker, C.J., Sterling, M., 2009. Aerodynamic Forces on Multiple Unit Trains in Cross Winds. Journal of Fluids Engineering-Transactions of the Asme 131.

Barlow, J.B., Rae, W.H., Pope, A., 1999. Low-Speed Wind Tunnel Testing, 3rd ed. ed. John Wiley & Sons, New York.

Baron, A., 2001. Alcune note sul corso di Fluidodinamica (in Italian). Department of Aerospace Engineering, Politecnico di Milano, Milano.

BBC, 2007. BBC News: Strong wind topples Chinese train. Available at http://news.bbc.co.uk/1/hi/world/asia-pacific/6403959.stm. Last accessed on 8/11/2012.

Bocciolone, M., Cheli, F., Corradi, R., Muggiasca, S., Tomasini, G., 2008. Crosswind action on rail vehicles: Wind tunnel experimental analyses. Journal of Wind Engineering and Industrial Aerodynamics 96, 584-610.

Bradshaw, P., Pankhurst, R.C., 1964. The design of low-speed wind tunnels. Progress in Aerospace Sciences 5, 1-69.

BST, 2007. PSD Series - High Performance Regulated DC Power Supply (Digital Display). Available at http://www.bstcaltek.com. Last accessed on 07/12/2012.

Cairns, R.S., 1994. Lateral Aerodynamic Characteristics of Motor Vehicles in Transient Crosswinds. PhD Thesis. College of Aeronautics Department of Aerospace Science, Cranfield University.

CEN, 2005. Eurocode 1: Actions on structures - Part 1-4: General actions - Wind actions, EN 1991-1-4: 2005. European Commitee for Standardization, Brussels.

CEN, 2010. Railway Applications - Aerodynamics - Part 6: Requirements and test procedure for cross wind assessment, EN 14067-6. Brussels.

Chadwick, A., Garry, K.P., Howell, J.P., 2000. Transient Aerodynamic Characteristics of Simple Vehicle Shapes by the Measurements of Surface Pressures. SAE Technical Paper 2000-01-0876.

Cheli, F., Corradi, R., Diana, G., Ripamonti, F., Rocchi, D., Tomasini, G., 2007. Methodologies for assessing trains CWC through time-domain multibody simulations, in: 12th International Conference on Wind Engineering. Cairns, Australia.

Cheli, F., Corradi, R., Rocchi, D., Tomasini, G., Maestrini, E., 2008. Wind Tunnel Tests on Train scaled Models to Investigate the Effect of Infrastructure Scenario, in: BBAA VI International Colloquium on Bluff Bodies Aerodynamics & Applications. Milano, Italy, July 20-24.

Cheli, F., Rocchi, D., Schito, P., Tomasini, G., 2011a. Steady and moving high-speed train crosswind simulations. Comparison with wind-tunnel tests, in: Proceedings of the 9th World Congress on Railway Research, WCRR 2011, Lille, France.

Cheli, F., Rocchi, D., Tomasini, G., 2011b. Study of the Reynolds effects on aerodynamic coefficients of a railway vehicle through wind tunnel tests, in: Proceedings of the ICWE-13th International Conference on wind Engineering, Amsterdam, The Netherlands.

Chiu, T.W., 1991. A two-dimensional second-order vortex panel method for the flow in a cross-wind over a train and other two-dimensional bluff bodies. Journal of Wind Engineering and Industrial Aerodynamics 37, 43-64.

Chiu, T.W., Squire, L.C., 1992. An experimental study of the flow over a train in a crosswind at large yaw angles up to 90°. Journal of Wind Engineering and Industrial Aerodynamics 45, 47-74.

Cogotti, A., 2008. Evolution of performance of an automotive wind tunnel. Journal of Wind Engineering and Industrial Aerodynamics 96, 667-700.

Coleman, S.A., 1990. The aerodynamics of ground vehicles in cross winds PhD Thesis. University of Nottingham.

Cook, N.J., 1985. The designer's guide to wind loading of building structures. Part1: Background, damage, wind data and structural classification. Building Research Establishment, Butterworths, London.

Cooper, K.R., 1991. The wind tunnel simulation of wind turbulence for surface vehicle testing. Journal of Wind Engineering and Industrial Aerodynamics 38, 71-81.

Cooper, R.K., 1979. The probability of trains overturning in high winds, in: Proceedings of the 5th International Conference on Wind Engineering, Fort Collins, USA.

Cooper, R.K., 1981. The Effect of Cross-Winds on Trains. Journal of Fluids Engineering 103, 170-178.

Cooper, R.K., 1984. Atmospheric turbulence with respect to moving ground vehicles. Journal of Wind Engineering and Industrial Aerodynamics 17, 215-238.

Copley, J.M., 1987. The three-dimensional flow around railway trains. Journal of Wind Engineering and Industrial Aerodynamics 26, 21-52.

Diedrichs, B., 2003. On computational fluid dynamics modelling of crosswind effects for high-speed rolling stock. Proceedings of the Institution of Mechanical Engineers Part F-Journal of Rail and Rapid Transit 217, 203-226.

Diedrichs, B., 2005. Computational Methods for Crosswind Stability of Railway Trains. A literature survey. Thesis. Aeronautical and Vehicle Engineering, KTH Engineering Sciences.

Diedrichs, B., 2010. Aerodynamic crosswind stability of a regional train model. Proceedings of the Institution of Mechanical Engineers Part F-Journal of Rail and Rapid Transit 224, 580-591.

Ding, Y., Sterling, M., Baker, C.I., 2008. An alternative approach to modelling train stability in high cross winds. Proceedings of the Institution of Mechanical Engineers Part F-Journal of Rail and Rapid Transit 222, 85-97.

Dorigatti, F., Sterling, M., Rocchi, D., Belloli, M., Quinn, A.D., Baker, C.J., Ozkan, E., 2012. Wind tunnel measurements of crosswind loads on high sided vehicles over long span bridges. Journal of Wind Engineering and Industrial Aerodynamics 107, 214-224.

Dyrbye, C., Hansen, S.O., 1999. Wind Loads on Structures. John Wiley & Sons Ltd.

EC, 2008. TSI - Technical Specification for Interaoperability of the trans-European high-speed rail system, 'Rolling stock' Sub-System, TSI-HS 2008/232/EC. Official Journal of the European Union.

Entezami, M., Hillmansen, S., Weston, P., Papaelias, M., 2011. Fault detection and diagnosis within a wind turbine mechanical braking system, in: The Eighth International Conference on Condition Monitoring and Machinery Failure Prevention Technologies. Cardiff.

ERA, 2009. AeroTRAIN (Aerodynamics: Total Regulatory Acceptance for the Interoperable Network). Seventh Framework Programme., Annex I - "Description of Work".

ESDU, 1974. Characteristics of atmospheric turbulence near the ground. Part 1: definitions and general informations, Data item 74030. Engineering Sciences Data Unit International plc, London.

ESDU, 2001. Characteristics of atmospheric turbulence near the ground. Part 2: single point data for strong winds (neutral atmosphere), Data item 85020. Engineering Sciences Data Unit International plc, London.

ESDU, 2002. Strong winds in the atmospheric boundary layer Part 1: hourly-mean wind speeds, Data item 82026. Engineering Sciences Data Unit International plc, London.

Feather, N., 1961. An Introduction to the physics of Vibrations and Waves. Edinburgh University Press, Edinburgh.

Gawthorpe, R.G., 1994. Wind effects on ground transportation. Journal of Wind Engineering and Industrial Aerodynamics 52, 73-92.

Gilbert, T., n. d. Aerodynamic effects of high speed trains in confined spaces. PhD Thesis. in progress, University of Birmingham.

Greisinger, 2012. GPB 3300 Precision Barometer - Operating Manual. Available at http://www.greisinger.de. Last accessed on 07/12/2012.

Hemida, H., Baker, C., 2010. Large-eddy simulation of the flow around a freight wagon subjected to a crosswind. Computers & Fluids 39, 1944-1956.

Hemida, H., Krajnovic, S., 2009a. Exploring flow structure around a simplified ICE2 train subjected to a 30 degrees side wind using LES. Engineering Applications of Computational Fluid Mechanics 3, 28-41.

Hemida, H., Krajnovic, S., 2009b. Transient Simulation of the Aerodynamic Response of a Double-Deck Bus in Gusty Winds. Journal of Fluids Engineering-Transactions of the Asme 131.

Holmes, J.D., 2007. Wind Loading on Structures, 2nd ed. Taylor & Francis, London.

Howell, J.P., 1986. Aerodynamic response of maglev train models to a crosswind gust. Journal of Wind Engineering and Industrial Aerodynamics 22, 205-213.

Hudson, 2009. The Basics of Axial Flow Fans. Available at http://www.hudsonproducts.com. Last accessed on 26/10/2010.

Humphreys, N.D., 1995. High Cross Wind Gust Loads on Ground Vehicles from Moving Model Experiments. PhD Thesis. University of Nottingham.

Johnson, T., 1996. Strong; wind effects on railway operations — 16th October 1987. Journal of Wind Engineering and Industrial Aerodynamics 60, 251-266.

Johnson, T., Dalley, S., 2002. 1/25 scale moving model tests for the TRANSAERO project, in: SchulteWerning, B., Gregoire, R., Malfatti, A., Matschke, G. (Eds.), Transaero-European Initiative on Transient Aerodnamics for Railway System Optimisation, pp. 123-135.

Jonsson M., Kowalski t., Loose S., Richard H., 2012. Measurements of aerodynamic coefficients of the Class390 on a 6 m high embankment configuration in the Cryogenic Wind Tunnel Cologne. DLR, Cologne, Germany.

Li, Y., Hu, P., Xu, Y., Zhang, M., Liao, H., 2011. Aerodynamic characteristics of vehicle-bridge system under cross wind by wind tunnel tests with moving vehicle model, in: Proceedings of the ICWE-13th International Conference on wind Engineering, Amsterdam, The Netherlands.

Macklin, A.R., Garry, K.P., Howell, J.P., 1996. Comparing Static and Dynamic Testing Techniques for the Crosswind Sensitivity of Road Vehicles. SAE Technical Paper 960674.

Mair, W.A., Stewart, A.J., 1985. The flow past yawed slender bodies, with and without ground effects. Journal of Wind Engineering and Industrial Aerodynamics 18, 301-328.

Martinez-Vazquez, P., Baker, C.J., Sterling, M., Quinn, A., Richards, P.J., 2009. The Flight of Wind Borne Debris: An Experimental, Analytical, and Numerical Investigation. Part II (Experimental Work), in: The Seventh Asia-Pacific Conference on Wind-Engineering. Taipei, Taiwan, November, 8-12, 2009.

MathWorks, 2012. Butterworth filter (Signal Processing Toolbox). Available at http://www.mathworks.co.uk/help/signal/ref/butter.html. Last accessed on 10/12/2012.

Matschke, G., Heine, C., 2002. Full scale tests on side wind effects on trains. Evaluation of aerodynamic coefficients and efficiency of wind breaking devices, in: SchulteWerning, B., Gregoire, R., Malfatti, A., Matschke, G. (Eds.), Transaero-European Initiative on Transient Aerodnamics for Railway System Optimisation, pp. 27-38.

Matschke, G., Tielkes, T., Deeg, P., B., S.-W., 2000. Effects of Strong Cross Winds on High-Speed Trains – a Risk Assessment Approach, in: PSAM 5 International Conference on Probabilistic Safety Assessment and Management. Osaka, 27th of Novemeber - 1st of December.

Mehta, R.D., Bradshaw, P., 1979. Design rules for small low-speed wind tunnels. Aeronautical Journal 83, 443-449.

Microsoft_Corporation, Blom, 2009. TRAIN rig aerial view. Available at www.bing.com/maps/. Last accessed on 3/02/2010.

Muggiasca, S., 2002. Caratterizzazione dei carichi aerodinamici associate al vento trasversale su convogli ferroviari tramite misure in galleria del vento (in Italian). M.Sc. Thesis. Dipartimento di Meccanica, Politecnico di Milano.

Oregon_Scientific, 2012. Oregon Scientific Advanced Weather Station - User Manual. Available at http://uk.oregonscientific.com. Last accessed on 07/12/2012.

Parker, S.P., 1993. Doppler Effect, McGraw-Hill Encyclopedia of physics, 2nd ed. McGraw-Hill, New York, London, pp. 305-307.

Pope, C.W., 1991. The simulation of flows in railway tunnels using a 1/25th scale moving model facility, in: Proceedings of the Aerodynamics and Ventilation of Vehicle Tunnels, 709-737. Elsevier.

Quinn, A.D., 2009-2011. The TRAIN (Transient Railway Aerodynamics INvestigation) Rig. Available at http://www.windresearch.org/mmr.html. Last accessed on 24/01/2012.

Quinn, A.D., Sterling, M., Robertson, A.P., Baker, C.I., 2007. An investigation of the wind-induced rolling moment on a commercial vehicle in the atmospheric boundary layer. Proceedings of the Institution of Mechanical Engineers Part D-Journal of Automobile Engineering 221, 1367-1379.

Richards, P.J., Hoxey, R.P., Wanigaratne, B.S., 1995. The effect of directional variations on the observed mean and rms pressure coefficients. Journal of Wind Engineering and Industrial Aerodynamics 54–55, 359-367.

Rocchi, D., Schober, M., Cheli, F., Orellano, A., Tomasini, G., 2009. Comparison of wind tunnel test results on the ATM train. EUROMECH COLLOQUIUM 509; Vehicle Aerodynamics; External Aerodynamics of Railway Vehicles, Trucks, Buses and Cars.

RSSB, 2001. Calculation of Enhanced Permissible Speeds for Tilting Trains, Railway Safety approved Code of Practice GC/RC 5521. Rail Safety and Standards Board Limited, London.

RSSB, 2009a. Resistance of Railway Vehicles to Roll-Over in Gales, Railway Group Standard GM/RT 2142. Rail Safety and Standards Board Limited, London.

RSSB, 2009b. Recommendations for Determination of Aerodynamic Rolling Moment Coefficient, GM/RC 2542 (Railway Group Recommendations for GM/RT 2142). Rail Safety and Standards Board Limited, London.

Sanquer, S., Barre, C., de Virel, M.D., Cleon, L.M., 2004. Effect of cross winds on high-speed trains: development of a new experimental methodology. Journal of Wind Engineering and Industrial Aerodynamics 92, 535-545.

SCART, 2012. Simulation Centre of Aerodynamic Research in Transportation - Tunnel Simulation Facility. Available at http://scart.dlr.de/site/test-facilities/tsg/index.htm#c73. Last accessed on 30/11/2012.

Schetz, J.A., 2001. Aerodynamics of high-speed trains. Annual Review of Fluid Mechanics 33, 371-414.

Schober, M., Weise, M., Orellano, A., Deeg, P., Wetzel, W., 2010. Wind tunnel investigation of an ICE 3 endcar on three standard ground scenarios. Journal of Wind Engineering and Industrial Aerodynamics 98, 345-352.

Sensortechnics, 2012. HCLA Series miniature amplified low pressure sensors - Data Sheet. Available at www.sensortechnics.com. Last accessed on 06/12/2012.

Simiu, E., Scanlan, R.H., 1996. Wind Effects on Structures, 3rd ed. John Wiley & Sons, Inc., New York.

Sterling, M., Baker, C., Bouferrouk, A., Oneil, H., Wood, S., Crosbie, E., 2009. An investigation of the aerodynamic admittances and aerodynamic weighting functions of trains. Journal of Wind Engineering and Industrial Aerodynamics 97, 512-522.

Sterling, M., Baker, C.J., Quinn, A.D., Hoxey, R.P., 2005. Pressure and velocity fluctuations in the atmospheric boundary layer. Wind and Structures 8, 13-34.

Sterling, M., Quinn, A.D., Hargreaves, D.M., Cheli, F., Sabbioni, E., Tomasini, G., Delaunay, D., Baker, C.J., Morvan, H., 2010. A comparison of different methods to evaluate the wind induced forces on a high sided lorry. Journal of Wind Engineering and Industrial Aerodynamics 98, 10-20.

Surrey, D., Cooper, R.K., Davenport, A., 1988. Aerodynamics of urban transit vehicles. Canadian Journal of Civil Engineering 15, 37-48.

Suzuki, M., Tanemoto, K., Maeda, T., 2003. Aerodynamic characteristics of train/vehicles under cross winds. Journal of Wind Engineering and Industrial Aerodynamics 91, 209-218.

Tavoularis, S., 2005. Measurement in fluid mechanics. Cambridge University Press, Cambridge.

Taylor, J.R., 1996. An introduction to error analysis : the study of uncertainties in physical measurements, 2nd ed. University Science Books, Sausalito, Calif.

TFI, 2012. Catalogue Pages. Available at http://www.turbulentflow.com.au/Downloads/Downloads.html. Last accessed on 07/12/2012

TheJapanTimesonline, 2008. News: Wind blamed for fatal 2005 JR East accident. Available at http://www.japantimes.co.jp/text/nn20080403a4.html. Last accessed on 8/11/2012.

Torrence, C., Compo, G.P., n. d. A Practical Guide to Wavelet Analysis. Available at http://paos.colorado.edu/research/wavelets/. Last accessed on 10/12/2012

UNIFE, 2009-10. TrioTRAIN (Total Regulatory Acceptance for the Interoperable Network). Available at www.triotrain.eu. Last accessed on 14/01/2013.

Ushijima, M., 2006. Strong wind measures of East Japan Railway Company, in: IRSC International Rail Safety Conference. Dublin.

Vishay, 2011. Ambient Light Sensor - TEPT5600. Available at http://www.vishay.com/. Last accessed on 07/12/2012.

Yoshida, Y., Muto, S., Imaizumi, T., 1977. Transient Aerodynamic Forces and Moments on Models of Vehicles Passing Through Cross-Wind. SAE Technical Paper 770391.

Ziehl-Abegg, 2010. Technical Data - Axial Fans Series FC. Available at http://www.ziehl-abegg.com. Last accessed on 3/02/2010.

Zoubir, A.M., Boashash, B., 1998. The bootstrap and its application in signal processing. IEEE Signal Processing Magazine 15, 56-76.

Zoubir, A.M., Iskander, R.D., n. d. Bootstrap Matlab toolbox. Available at http://www.csp.curtin.edu.au/downloads/bootstrap_toolbox.html. Last accessed on 08/03/2012.

Appendix A

TRAIN rig crosswind generator

A.1   Introduction

This appendix describes the development of a new crosswind generator (CWG) for the TRAIN rig that was undertaken in the course of this research. Section A.2 illustrates the previously existing crosswind generator (PCWG) and examines its main features and limitations. Sections A.3 and A.4 details the development process that led to the new system and the characteristics of the crosswind simulation that it delivers, respectively. Finally, an assessment of the new CWG is presented in section A.5.

A.2   Previously existing crosswind generator

A.2.1   Configuration

When the TRAIN rig was acquired by the University of Birmingham, the facility was equipped with a previously existing crosswind generator (PCWG). Such a PCWG was accommodated inside the testing room, positioned towards the end of the test section (according to the direction of travel on track 1) in an area partially overlapping the location of new system (figure A.1).
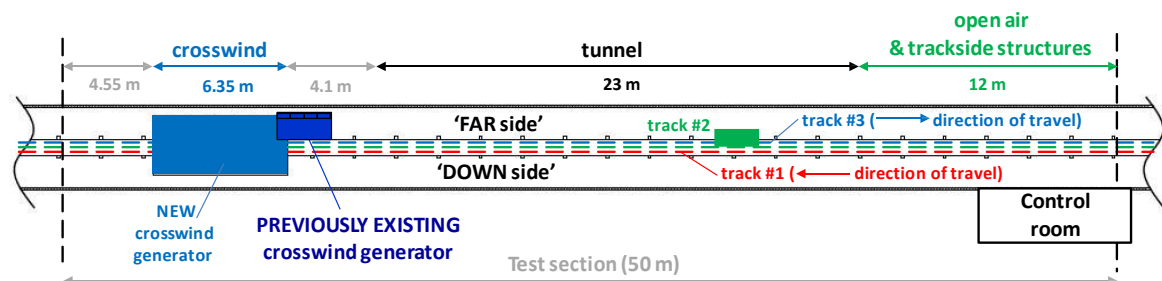
Figure A. 1 Location of the PCWG within the TRAIN rig testing room.

The PCWG consisted of a bank of four axial flow fans that were placed between the tracks and the side wall of the building, on the *far side* of the testing room (figure A.1). The jet of air that was generated was directed perpendicularly to the tracks by the nozzle illustrated in figure A.2.
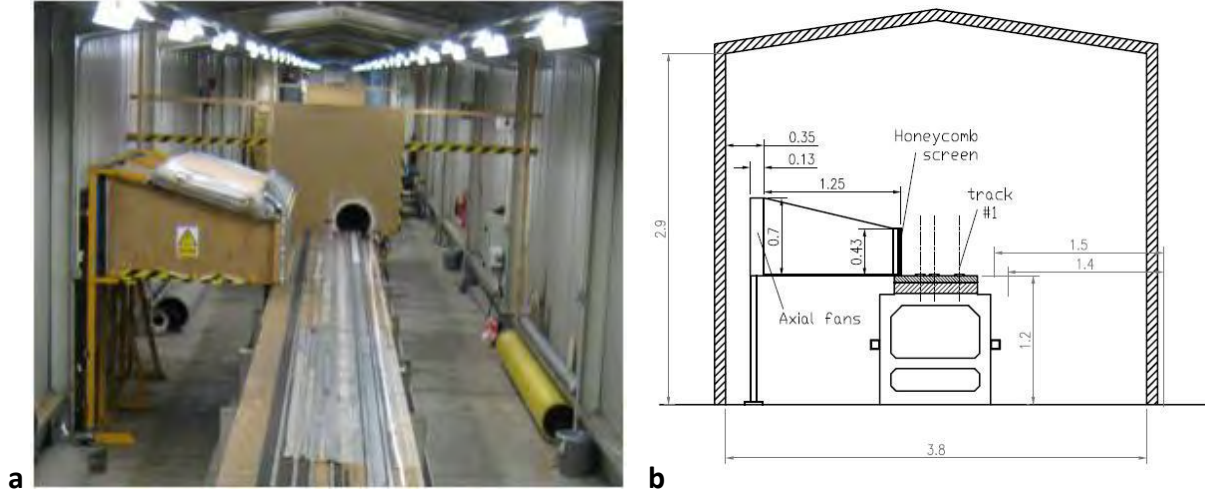
Figure A.2 PCWG overall configuration. a) TRAIN rig photograph. b) TRAIN rig transverse section scheme

The axial fans [Clarke Air Movers] were electrical-powered single-phase units operating at 900 rpm. Nominal diameter and flow rate were 0.6 m and ~2.8 m^3/s, respectively. The nozzle had a total length (transverse to the track) of 1.25 m and a contraction ratio of 1.65. Its cross-section at the exit was 2.85 m long (along the track) and 0.43 m high. Inside this nozzle, a set of four vertical deflectors had been adopted in order to reduce the swirl in the airflow delivered by each fan (figure A.3b). In addition, to further smooth the lateral and vertical velocity components in the airflow before it reached the tracks, the aluminium honeycomb screen in figure A.3a (with hexagonal cells of 3/8 inches equivalent diameter and 1 inch in length) was positioned at the nozzle exit.
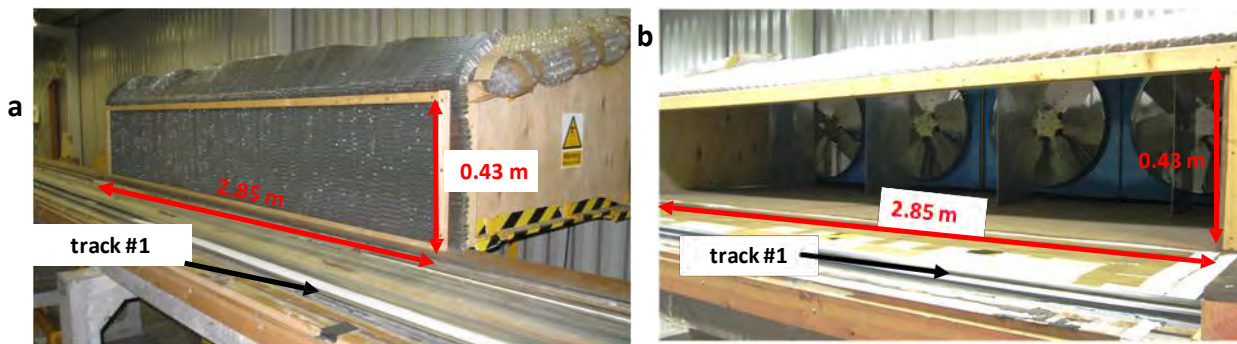
Figure A.3: PCWG detailed view. a) Base configuration. b) Air channel internal details

A.2.2 Performance (flow simulation)

Experimental flow characterisation

In the early stages of this project, a dedicated measurement session was undertaken for characterising the flow delivered by the PCWG. The horizontal wind profile (HWP) on the centreline of track 1 was investigated within the 2.85 m full span of the air-jet, at the reference height   = 0.12 m (figures A.4). In addition, vertical wind profiles (VWPs) were measured relating to four spanwise positions (i.e., positions 3, 15, 20 and 29 specified in figure A.4a).
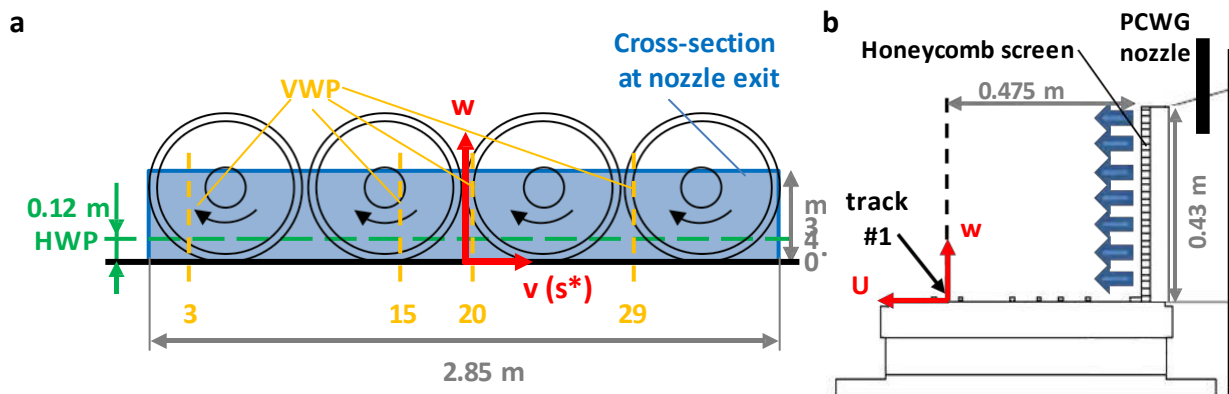
Figure A.4 PCWG: flow characterisation reference system. a) Front view b) Side view

Flow measurements were carried out using a set of four Cobra probes [Turbulent Flow Ltd, series 100] (TFI, 2012) in combination with their bespoke data acquisition system (whose specifications are described in section 4.5.2.5). Three of the four probes were installed on a manually operated traversing system and moved during a number of subsequent runs in order to measure the flow at different positions along the HWP and VWPs specified above. The fourth probe was kept in a fixed location in order to provide an insight into the run-to-run variability. Time histories of 60 s were recorded at a sampling frequency of 500 Hz during each run. The raw data were then processed using Matlab and MS Excel in order to obtain the time averages of the three velocity components over the entire length of the time histories and the relative turbulence intensities. According to the conventions in figure A.4, and consistent with those adopted in chapter 4, in the following   is the '*nominal streamwise velocity*' and identifies the component in the direction of the nominal main

wind (i.e., horizontal and perpendicular to the tracks), while   and   are the lateral and vertical velocities, respectively. Their mean values are indicated with an overbar, while the relative turbulence intensities are denoted by   ,   and   .

Crosswind simulation with honeycomb screen

Figure A.5 illustrates the HWPs of the mean wind velocities and turbulence intensities and, in figure A.5a, compares the streamwise velocity data to those measured by Baker et al. (2001) during a previous research project. In addition, the spanwise averages of both velocity magnitudes and turbulence intensities are specified in table A.1.

Figure A.5 PCWG: HWP on track 1 at reference height. a) Mean velocity components b) Turbulence intensities
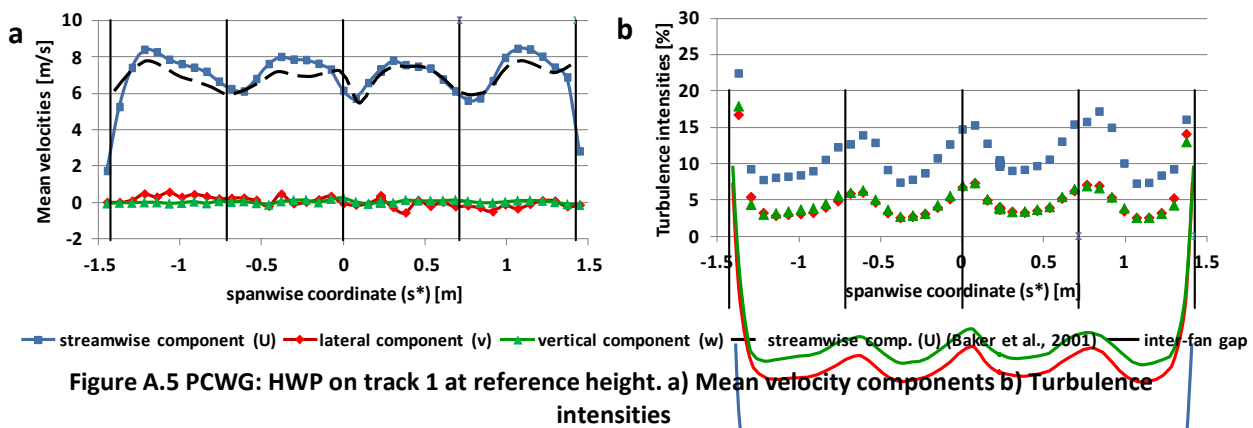
	Spanwise averages	
Velocity component	**Mean velocity**	**Turbulence intensity**
Streamwise (U)	7.2 m/s	11%
Lateral (v)	0.1 m/s	4%
Vertical (w)	0 m/s	4%

Table A.1 PCWG: HWP spanwise average characteristics

The data of the mean streamwise velocity confirmed the spanwise irregularities previously reported by Baker et al. (2001). Peak values of the order of 8 m/s were found at the fans centrelines in combination with relatively low turbulence intensities (below 10%), while 'wind holes' with minimum velocities of approximately 6 m/s (and turbulence levels in the order of 15%) occurred in the areas between two adjacent fans. The spanwise averages of the streamwise mean wind speed and of the streamwise turbulence intensity were approximately 7.2 m/s and 11%, respectively.

Lateral and vertical mean wind velocities were both close to zero across the entire span. Different from the streamwise velocity, they did not show any major spanwise fluctuation. Such fluctuations, however, were found on the turbulence intensities   and   (figure A.5b), which followed a similar trend to that of   . Their magnitudes fluctuated between 2.5% and 7%, while their spanwise averages were ~4%.

The consistency between the spanwise variations in the simulated wind and the position of the fans suggested that the spatial inhomogeneity in the HWP could have been caused by the interaction between the individual air jets delivered by the fans. The irregularities in the flow could not be entirely smoothed before the wind reached the track because of the short distance available.

VWPs of the streamwise mean velocity turbulence intensity are illustrated in figures A.6a and A.6b, respectively. The differences between data relating to the fan centrelines (3 and 15) and to the '*inter-fan gaps*' (20 and 29) were in agreement with the spanwise variations observed in the HWP. Furthermore, it can be observed in figure A.6a that each VWP tended to have a velocity peak at heights of ~0.05 m and 'wind hole' at between 0.15 and 0.2 m above the ground (i.e. at mid-height of the air jet).
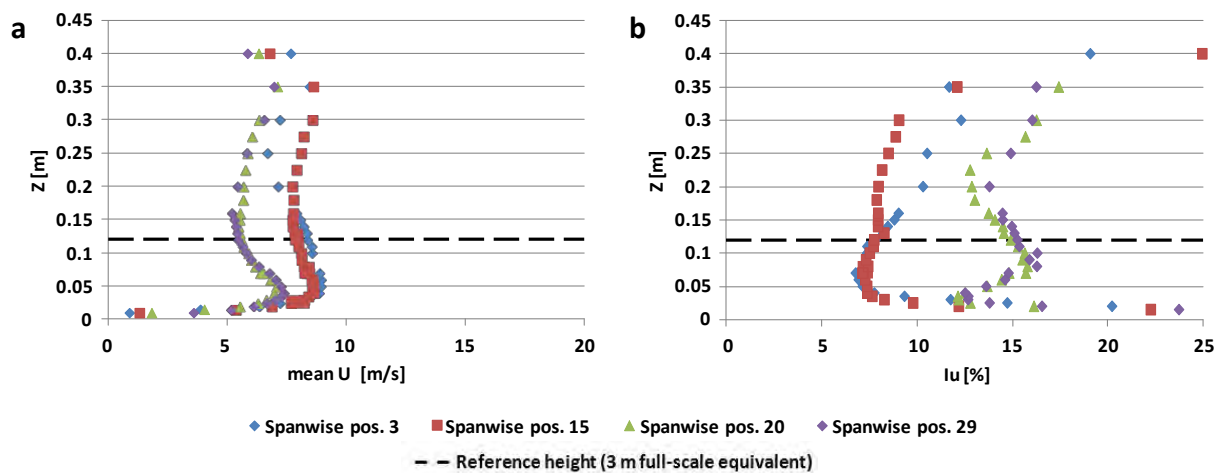
Figure A.6 PCWG: VWP on track 1 a) Streamwise mean velocity b) Streamwise turbulence intensities

The VWPS in figure A.6 were quite different from an atmospheric boundary layer (ABL) wind profile (described in section 2.3). Their behaviour was compatible with the characteristics of the flow delivered by axial fans, for which the streamwise velocities reach their maxima at the tip of the impeller's blades (therefore at the top and bottom of the air jet cross-section) while have their minima in front of the impeller hub (i.e., at mid-height) (Hudson, 2009). Furthermore, because it prevented the diffusion of the air jet downwards, it was inferred that board supporting the tracks caused the peak streamwise velocity observed in the lower part of the VWPs.

A.2.3 Limitations

The PCWG had been originally built in order to investigate crosswind effects on train slipstreams (Baker et al., 2001). The flow characterisation reported above outlined that the crosswind simulation provided by such a system was not optimal, and to some extent not adequate, in order to investigate crosswind aerodynamic loads on rail vehicles. Table A.2 reports the main limitations of the PCWG in relation to their level of criticality, which were identified not only in relation to the case study of this research (section 4.2.1), but also to possible future developments (section 8.2).

Limitations	Level of criticality
Low crosswind mean velocity	Not Satisfactory
Spatial characteristics of the crosswind profile: **- HWP (spanwise inhomogeneity)** **- VWP (vertical evolution)**	Not Satisfactory Not Satisfactory
Extension of the air jet cross-section	Not Satisfactory
Flexibility to alternative ground simulation	Not Adequate

Table A.2 Limitations of the PCWG

Low crosswind mean velocity

In light of the spanwise average of the streamwise mean wind velocity, the train speed required in order to simulate a 30° yaw angle would have been ~12.5 m/s. Although reachable using the TRAIN rig propulsion system (section 4.3.1), this value lies at the very bottom of the vehicle speed range. The use of the PCWG, hence, would have led to non-optimal exploitation of the test facility. The

maxima Reynolds numbers to be achieved, for example, would have been approximately 1.2×10^5 for moving model tests, and 6×10^4 during static model experiments. Although of the same order of those obtained during previous moving model test campaigns (section 3.5), such values would have been approximately half of those actually obtained using the new CWG (section 6.4.4). Furthermore, for such a low vehicle speed, previous experience with the TRAIN rig propulsion system indicated that inconsistencies in train speed tended to arise. Potentially leading to a lower run acceptance rate for moving model tests, this posed a warning relating to an increment of the total number of runs required and, consequently, to a longer duration of the campaign.

Spatial characteristics of the crosswind profile

A good crosswind simulation should present a spanwise uniformity and a VWP possibly resembling an ABL (or at least presenting a positive gradient upwards). In this regard, however, a major constraint was posed by the narrow space available inside the TRAIN rig.

Extension of the air jet

The air jet delivered by the PCWG embraced a track portion 2.85 m long and a height of approximately 0.43 m (figure A.4). Compared to the size of the scale-model train's leading car, such an area did not seem satisfactory in any of its dimensions.

The extension of the air jet along the track (which was less than three times the length of train's leading car) represented a limitation relatively to the length of the time histories that would have been recorded during moving model experiments. Previous researches on moving models found that a train entering a sudden cross wind gust covers a distance corresponding to 1.5 times the length of the leading car before experiencing stable aerodynamic loads (Baker, 1986). Accordingly, for the current case study, it was estimated that the use of the PCWG would have led to time series (associated with the train subjected to stabilised crosswind loads) shorter than 0.1 s. However, from a measurement and analysis perspective, the longer the train spent in the cross wind the better. Too short of a time could have either required an excessive total number of runs to be carried out for

obtaining stable ensemble averages (section 4.7), or led to a large random uncertainty associated with the results (section 5.4).

The vertical extension of the air jet appeared excessively low in comparison to the maximum height of the train model (since it was only two times larger). The model blockage ratios calculated for the moving and static model tests were in the order of 15% and 8%, respectively. Both, hence, would have required to use blockage corrections (CEN, 2010), with a margin of uncertainty associated with employing a conventional correction method for moving model tests. Further concern, then, rose with consideration of the wake blockage. The total height of the simulated crosswind jet did not seem sufficient in order to allow a proper development of the vortices and turbulent structures forming around and downstream of the train.

Flexibility to alternative ground simulations

The PCWG did not offer any flexibility in terms of ground configuration, thus preventing any infrastructure scenario other than a FG to be simulated. In this regard, the considerations in section 3.3.3 have highlighted that an embankment potentially represents a criticality relating to the effect of the vehicle movement simulation on the crosswind aerodynamic loads. Although it was not an actual constraint for the present research, hence, this further limitation represented a significant restriction on one of the major future developments (section 8.2).

A.3 Development of the new CWG

In parallel to the analysis of the PCWG, a feasibility study was undertaken on the development of a new system. This study involved a detailed examination of the space into which such a new system could have been incorporated and consisted also of a research relating to the air flow fan technology available. The former task clarified the potential constraints affecting a new design; the latter provided useful indication on the actual margin of improvement achievable with respect to the PCWG.

Noting the above analysis of the PCWG and the indication from the feasibility study, a decision was made to construct a new CWG. Consequently, the development process illustrated in figure A.7 was undertaken as detailed in the following.

Phases

- Assessment of the PCWG
- New CWG feasibility study

Design specifications

Preliminary design

Design optimization
(through prototype tests)

Final design

Construction and 'tuning'

Flow characterization

Deliverables

- Decision to develop a new CWG

- Position within the TRAIN rig testing room
- Overall design
- Fans selection
- Fans configuration
- Air channel layout

- Prototype design and construction
- Optimization of the flow simulation:
  - Exact position of the fans
  - Air channel detailed design
  - Choice between blow-through and suck-through design

- Design for construction:
  - Electric circuit and control panel
  - Fans supporting frame
  - Air channel structural design
- Construction drawings

- Installation
- Optimization of the final system (minor adjustments of the final design)
- Final Moving model test configuration
- Static test configuration

- Flow measurements:
  - Moving model test configuration
  - Static test configuration

Figure A.7 New CWG design process

A.3.1 Design specifications and challenges

The design specifications for the new CWG were a compromise between the requirements and the constraints related to such a system. The design requirements, presented in table A.3, represented the best possible characteristics that the new system should have had in relation to its application. The design constraints were the restrictions imposed by the necessity of integrating the new CWG

into an already existing facility. Table A.4 indicates each of these constraints in combination of its main implications on the design (in terms of overall configuration and relating to the requirements defined in table A.3).

Design requirements (ideal)		Improvements with respect to the PCWG
Spanwise mean wind speed (at $\quad$ = 0.12 m)	$\square$ 11.5 m/s	Ease run-to-run vehicle speed consistency (V_{tr} $\square$20 m/s) Increased Reynolds number ($\square$ 2x10^5 c.a. for moving tests)
Quality of the flow simulation	• Spanwise uniformity • Low turbulence level	Ease stationary aerodynamic investigation and static *vs.* moving model test comparison Test flexibility (chance of obtaining an ABL simulation using passive turbulence generators)
System configuration	Ducted test section (over the tracks)	Better suitability to static tests Well-defined blockage corrections (if needed)
Air channel cross-section	Span $\square$ 4m Height $\square$ 1m	Longer time series from moving tests Low blockage ratios (<5%)
Wind direction	perpendicular to the track	-
Viability to static tests		-
Ground simulation flexibility		Capability of testing alternative infrastructure scenarios (e.g. ballast and rail, escarpment)

Table A.3 New CWG design requirements

Design constraints	Main implications on the design	Impacts on design requirements
Unavailability of any area outside the TRAIN rig building	New system to be accommodated inside the building in the trackside area (fans at less than 2 m from the tracks)	• reduced flow spatial uniformity • low turbulence simulation not achievable
No modifications to the existing building envelope	• No chance of sucking and/or exhausting the air outside • No chance of lifting the roof for accommodating a return channel	• reduced flow spatial uniformity • ABL flow simulation not achievable • limited maximum wind velocity • open-return air channel
Max power available: 100 A	Limitation on the fans' power demand (and therefore on maximum flow rate).	• limited maximum wind velocity • limited CWG extension
Interdiction from permanently occupying the entire area on the *down-side* of the tracks (figure A.1)	The fans had to be installed on the far-side of the testing room. Semi-permanent design for the air channel structure on the down-side	• increased design complexity

Table A.4 New CWG design constraints

The design specifications were defined relative to any design requirement and, in light of the constraints, a different '*level of challenge*' was associated with each goal. As outlined in table A.5,

none of the initial objectives was discarded and the aim for the new system was set to be a significant improvement with respect to the previously existing apparatus. Nevertheless, a relaxation of the initial requirements had to be accepted regarding the quality of the crosswind simulation.

Design Specifications			
	Initial (ideal) requirements	**Level of challenge**	**Relaxed requirements**
Spanwise mean wind speed	11.5m/s (V_{tr}≈20m/s at 30°yaw)	Moderate	
Quality of the flow simulation	~~————~~	High	
	~~Spanwise uniformity~~	High	Best spanwise uniformity possible
	~~Low turbulence level~~	High	Lowest turbulence possible
System configuration	Ducted channel (over the tracks)	Moderate	
Air channel cross-section	Span □ 4m	Moderate	
	Height □ 1m	Moderate	
Mean wind direction	Perpendicular to the tracks	Low	
Suitability to static tests		Moderate	
Ground simulation flexibility		Moderate	

Table A.5 New CWG design specifications

The main design challenge involved in the new CWG design consisted in keeping the entire system as compact as possible for accommodating it inside the TRAIN rig testing room. As shown in the transverse section in figure A.2b, the internal width of the building is only 3.8 m, with less than 1.5 m (where the fans had necessarily to be accommodated) available between the track board and the wall, on either side. In light of experience gained from the PCWG, this made a smooth (i.e., low turbulence) and spatially uniform wind simulation extremely difficult to achieve.

The impossibility of modifying the building envelope enhanced the level of the challenge. It forced the choice of an open-channel design (since the roof was not sufficiently high for accommodating a return channel). Furthermore, preventing the air from being sucked or exhausted outside, it necessarily led to recirculating the flow inside the building. This was expected to further increase the challenge of obtaining a low turbulence and uniform flow simulation. In addition, in order to avoid any risk concerning the structural integrity of the building, it also advised to aim for the minimum

requirement in terms of mean wind velocity (i.e., $\square$ 11.5 m/s according to the requisite in table A.3). As discussed in the following, then, a further and more stringent limitation in such sense came from the maximum available power supply.

A.3.2 Preliminary Design

Consistent with the design specifications, the new CWG aimed to combine an extreme compactness in the along-wind direction with a large lateral extension. As such, this system aimed to be very different with respect to a conventional wind tunnel. At a preliminary stage, however, the low-speed wind tunnel design-practice (Barlow et al., 1999, Bradshaw and Pankhurst, 1964, Metha and Bradshaw 1979) provided useful guidelines for developing and assessing a number of options concerning the overall configuration of the new CWG. In addition, still in the preliminary design phase, the research on the flow fans technology available on marked (initiated as part of the feasibility study) was continued and a number of suppliers were contacted in view of a final selection. The details of the preliminary design that was developed are specified in table A.6, while the system layout is illustrated in figure A.8.

Position (within the TRAIN rig testing room)	• Towards the end of the test section (track 1 travel direction) • (partially overlapping the area occupied by the PCWG) • Flow fans on the *far side* of the testing room
Overall configuration	• Open circuit design • Blow-through / suck-through design (**to be defined: TBD**) • Flow fans at the trackside moving the air horizontally and perpendicularly to the tracks • Ducted test-section (over the tracks) • Spanwise mean wind velocity: 11.5 m/s

Fans' model	• Ziehl-Abegg FC071-4DF.7M.V6
	• Type: AXIAL flow fans
	• Size:
	  − Nominal Diameter (ND): 0.71 m
	  − Case dimensions: 0.785 External Diameter (CD).; 0.26 m length
	• Motor:
	  − Integrated into the impeller hub
	  − 3-phases 400V ±10% (Y) 50Hz (4-poles)
	  − Nominal rotational speed: 1350 rpm
	  − Current consumption: 5.3 A (full-speed); 18 A (startup)
	• Number of blades: 6

Fans' arrangement	• 16 units arranged in 2 rows of 8 units each • distance from the wall: **TBD**
Air-channel layout	• Straight horizontal air channel directed perpendicularly to the tracks • Test-section size (Span x Height x Length): 6.4 x 1 x 1.5 m c.a. • Vertical contraction between the fans and test-section • (contraction ratio 1.5) • Aluminium honeycomb screen and variable porosity grids (specifications **TBD**) • Portion of air channel spanning the *down side* of the tracks to be semi-permanent (to allow access all along the testing room)

Table A.6 New CWG preliminary design

Figure A.8 New CWG preliminary design scheme and overall dimensions

The new CWG configuration consisted of a horizontal air channel perpendicular to the tracks. This was found the most effective solution since it could satisfy the design specifications with a relatively simple design, which avoided excessive complexities either structural or aerodynamic.

As illustrated in figure A.8, the air channel presented a vertical contraction (with a ratio of 1.5) between the fans and the test-section. The test section (i.e., the channel portion over the tracks where a constant cross-section was maintained) had a total length of ~1.55 m in the along-wind direction. This was sufficient to enable static tests with the train model being yawed with respect to crosswind. In order to not permanently occupy the *down side* of the testing room (as prescribed in table A.4) the fans were placed on the opposite side (i.e., the *far side*). For the same reason the bottom part of the air channel extending through the *down side* was designed to be semi-permanent.

The extension required for the cross-section of such an air channel necessarily implied the employment of a series of fans. In this respect, axial fans became the preferred choice (with respect, for example, to centrifugal blowers) because of their viability to be arranged in arrays. The limitation in the electric power supply available to the new CWG precluded the employment of high-speed

units (driven by 3-phases 2-poles motors and normally intended for industrial applications). Nonetheless, a preliminary estimation indicated that the specified minimum mean wind speed (of 11.5 m/s) was more likely to be achieved using axial fans equipped with 3-phases 4-poles motors. The selected fans are illustrated in figure A.9: they were [Ziehl-Abegg, FC071-4DF.7M.V6] (Ziehl-Abegg, 2010). Having the motor integrated into the impeller hub, these fans have an extremely compact design that made them suitable to this application. In total, the new CWG employs a series of 16 of these units, arranged at the trackside in two rows of eight fans each for a corresponding total span of the air channel of ~6.4 m.

D2 = 0.71 m   D1 = 0.785 m   B = 0.26 m
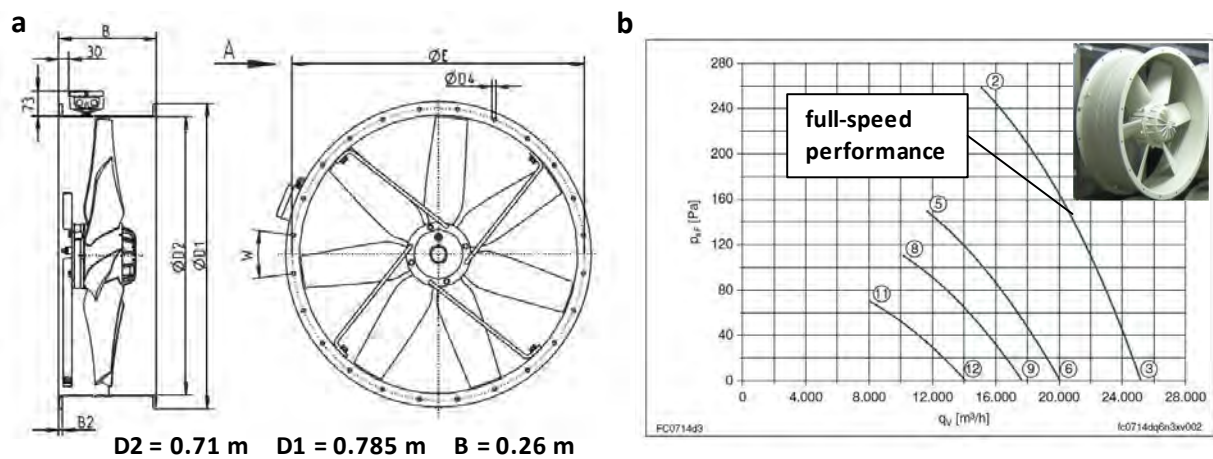
Figure A.9 New CWG axial flow fans [Ziehl-Abegg, FC071-4DF.7M.V6] (Ziehl-Abegg, 2010)
a) Dimensions b) Performance

A.3.3   Design through prototype testing

A.3.3.1   *Unresolved issues in the preliminary design*

Although numerous details of the design had been addressed within the preliminary design phase, as highlighted in the previous table A.6 there were three major aspects still to be defined (TBD):

- the choice between blow-through and suck-through configuration;

- the exact position of the fan array at the trackside (i.e., their distance from the wall of the building);

- the characteristics and arrangement of the aluminium honeycomb screens and grids (if any) to be used for reducing the turbulence level and smoothing the flow irregularities;

According to the preliminary design, both a blow-through and a suck-through configuartions were compatible with the overall layout chosen for the new CWG. Using the same fans, depending on their orientation, they could have been operated either in blowing or in sucking mode. In principle, a suck-through design would have favoured a better flow uniformity with respect to a blow-through configuration. Having the test section upstream (rather than downstream) of the fans was expected to reduce the swirl in the velocity field as well as the spatial inhomogeneity and the turbulence level. Nevertheless, such an option might have been not suitable to ground simulations different from the flat ground (FG), and particularly to an escarpment. There was the concern that sucking the flow from the top of the escarpment a region of recirculation could have developed upstream the escarpment. If such a region had been much larger than that normally occurring at full-scale, it would have led to an unrealistic representation of the wind conditions typically occurring in reality. For this reason, a blow-through design was taken into account as the base option, while a suck-through design required a specific investigation to prove its viability.

Regardless the choice between blow-through and suck-through configuration, because of the narrow gap available at the trackside, the fans had necessarily to be placed at a short distance from the tracks so as from the wall of the building. In order improve the flow quality and not to deteriorate the fans performance, in an ideal situation both distances should have been maximised. However, since it was not possible in this case, additional indications were needed in order to find the best compromise possible.

At a preliminary design stage, the use of a set of variable-porosity grids and aluminium honeycomb screens was planned in order to reduce the turbulence level and to improve the spatial homogeneity of the flow. These devices would have been selected and positioned depending on which design configuration (between blow-through and suck-through) had been chosen. However, considering the peculiarity of the new CWG, their design and selection could not entirely rely on the guidelines relative to conventional wind tunnels and, therefore, required specific investigations.

In order to address the three issues mentioned above, and to validate the assumptions made within the preliminary design, a prototype of the new CWG was built. Using this prototype a dedicated experimental campaign was undertaken for exploring the sensitivity of the wind simulation to a series of design options.

A.3.3.2   *Prototype design and construction*

In order to investigate multiple design configurations, a major requirement for the CWG prototype was to enable the air channel layout to be rapidly modified. In this view, it was accepted to reproduce only a portion (approximately 2.3 m long) of the entire 6.4 m span planned for the final CWG installation. It was acknowledged that a prototype of this size might not have properly simulated the flow recirculation inside the building as it would have been induced by the 16 fans of the new CWG running all together. However, a larger size of prototype would have dramatically increased both the complexity of its realisation and the time required for carrying out a comprehensive design optimisation.

As illustrated in figure A.10a, the prototype comprised of 6 fans (arranged in pairs on two rows) supported by a steel frame that was mounted on wheels (figure A.10b). This particular feature was crucial for providing the prototype with the required flexibility: it enabled different distances between the fans and the wall to be investigated and also eased accessibility to the air channel from the fan side. The air channel was constructed according to the layout defined in the preliminary design (figure A.8). As shown in figure A.11, it presented a modular design and, as such, consisted of four adjacent sections properly aligned one to the other. Each of these sections was independently supported and, therefore, suitable to be individually removed and modified. This solution ensured good accessibility to any portion of the air channel, enabled the implementation of multiple layouts and minimised the setup time required for switching from one configuration to another.
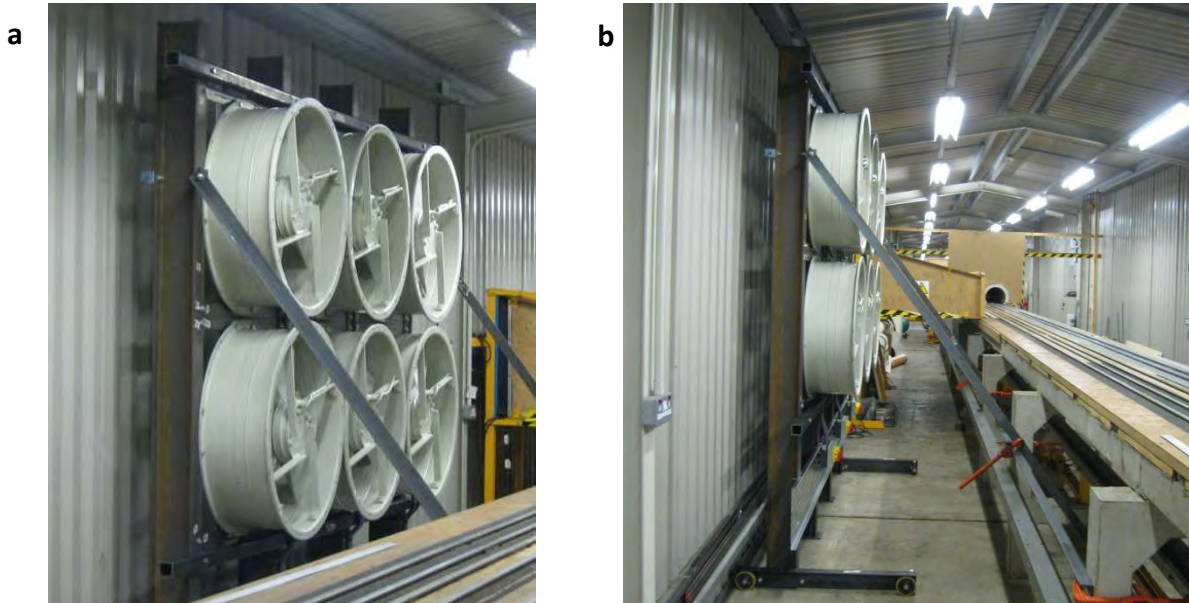
Figure A.10 CWG prototype a) Axial fans b) Fans' movable supporting frame
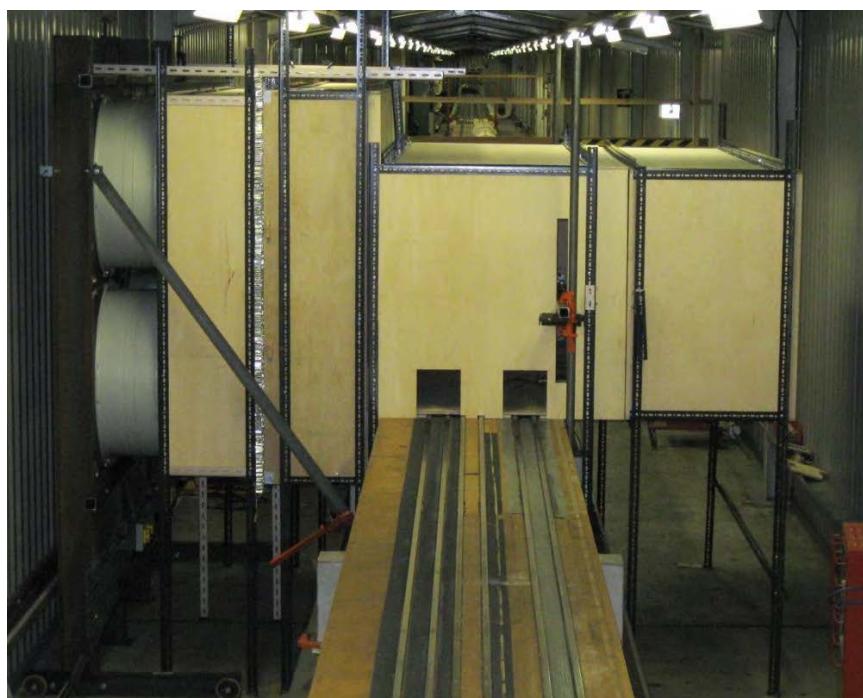
Figure A.11 CWG prototype general view

A.3.3.3 Prototype test campaign

In the first phase of the prototype test campaign, the blow-through design was investigated in combination with a number of air channel configurations, all relating to a FG simulation. The analysed options included:

- two distances of the fans from the wall of the building;

- two different lengths (25mm and 50mm respectively) of an aluminium honeycomb screen having a cell equivalent diameter of 9 mm;

- multiple layouts presenting a non-uniform porosity of the honeycomb screen;

- various arrangements presenting an array of spires (of different sizes) positioned upstream the track (either at the inlet of the test section or immediately downstream of the fans and upstream of the contraction).

During the second phase, the fans were reverted in order to implement a suck-through design. Two different configurations were tested with consideration of a FG scenario, depending on whether the air channel inlet was '*free*' or equipped with a honeycomb screen and a bellmouth profile (on the bottom edge). Furthermore, an additional test was carried out in the presence of an escarpment ground simulation. Apart from the ballast on the top, which was not be reproduced, the escarpment geometry corresponded to the 1:25 scale windward side of a '*6 m standard railway embankment*' (EC, 2008), the slope of which is 3:2 (expressed by the length-to-depth ratio).

The configurations relative to a FG scenario were tested in order to assess the quality of the flow simulation. The escarpment was investigated to address the aforementioned concern on the suitability of the suck-through design to such a ground simulation. For purposes of discussion concerning the definition of the final CWG design, the data relative to 6 of the (totally 23) investigated configurations are presented in the following. They include four different options for the blow-through design, and two arrangements relating to the suck-through design. Such configurations, which are identified with letters from '*A*' to '*F*', have their details reported in table A.7 and are illustrated in figures A.12 and A.13.

Configuration	Ground simulation		Air channel layout
A (figure A.12a)	FG	Blow-through	• fans-wall distance: 0.4 m (small) • honeycomb screen: 9 mm (cell equiv. diameter); 25 mm length
B (figure A.12b)			• fans-wall distance: 0.4 m (small) • honeycomb screen: 9 mm x 50 mm
C (figure A.12b)			• fans-wall distance: 0.53 m (large) • honeycomb cell: 9 mm x 25 mm
D (figure A.12c)			• fans-wall distance: 0.53 m (large) • honeycomb screen: 9 mm x 25 mm • spires at the test-section inlet
E (figure A.13a,b)	FG	Suck-through	• fans-wall distance: 0.53 m (large) • honeycomb screen downstream of test-section (cell: 9 mm x 25mm)
F (figure A.13c,d)	Escarpment		• honeycomb screen at the air channel inlet (cell: 9 mm x 25 mm) • bellmouth (at the inlet bottom edge)

Table A.7 CWG prototype: selection of tested configurations
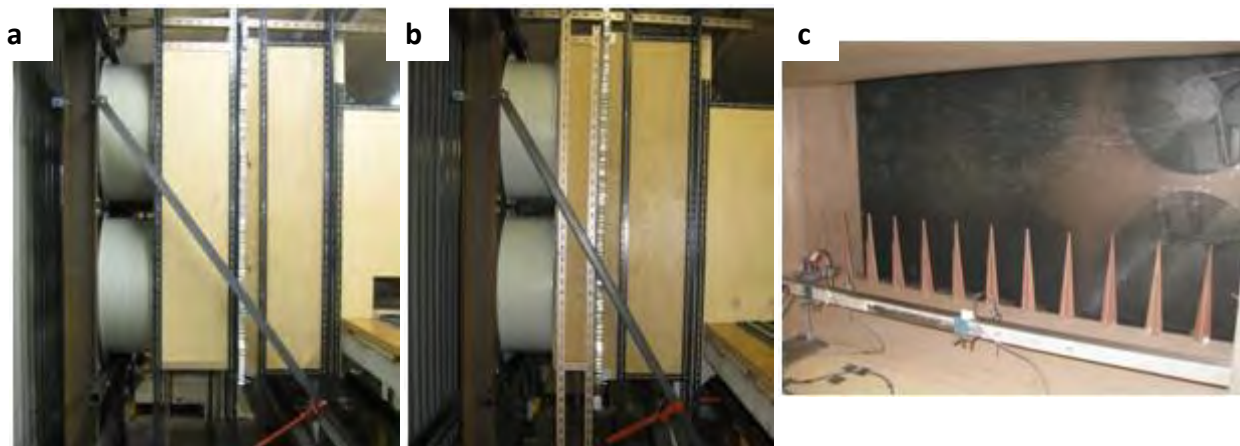
Figure A.12 CWG prototype blow-through design a) Configuration A b) Configuration B and C c) Configuration D
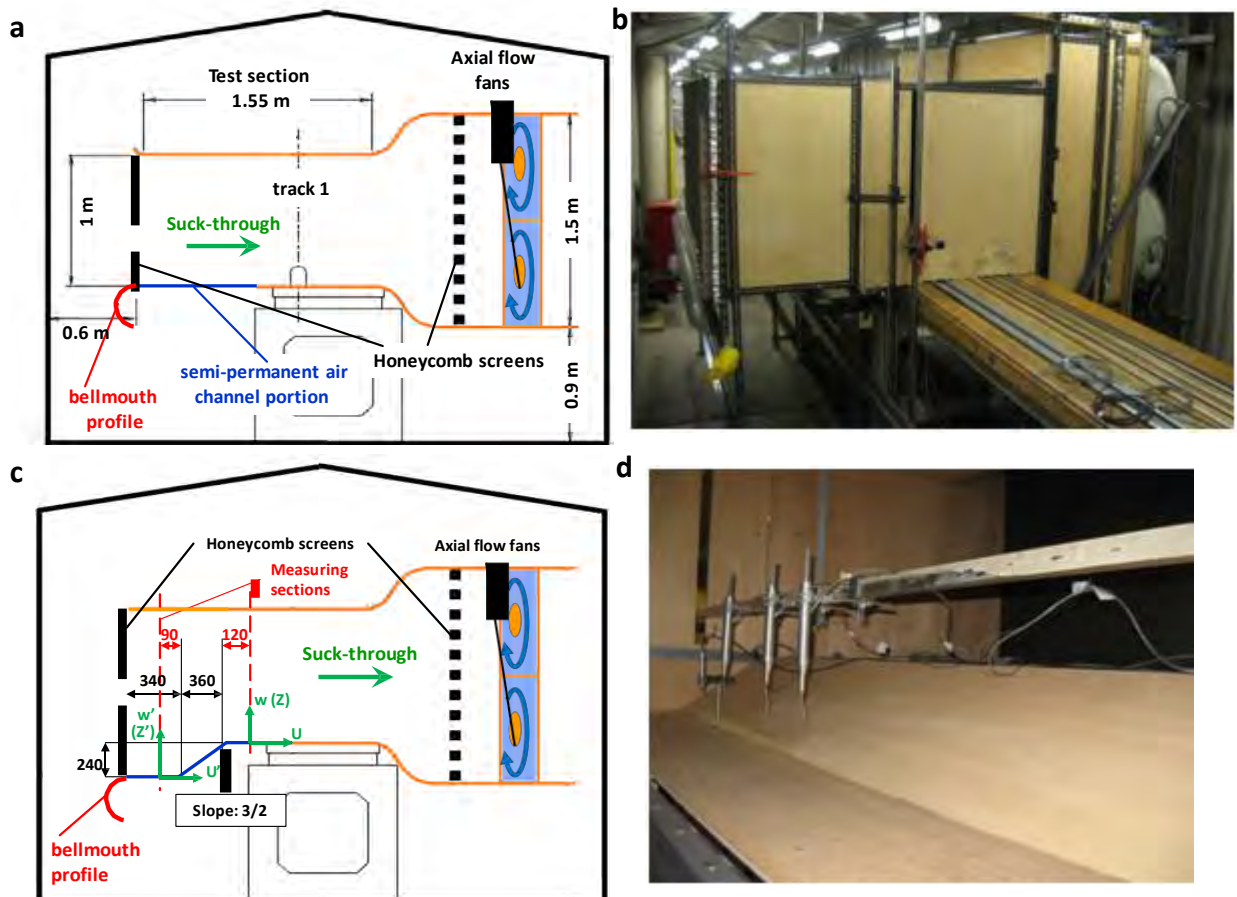
Figure A.13 CWG prototype suck-through design a) Configuration E (FG) b) Configuration F (Escarpment)

Experimental arrangement

The flow measurements iterated during the prototype test campaign were carried out using the same instrumentations and same methodology adopted for characterising the PCWG (specifications of which are reported in section 4.5.2.2). The arrangement used is shown in figure A.15. As illustrated in figure A.14, relating to a FG simulation both the HWP and VWPs were measured at the centreline of track 1. The HWP comprised a total of 23 spanwise measurement positions, all at   = 0.12 m above the ground. The VWPs were investigated on 6 of these positions within 0.01 and 0.7 m above ground. The spanwise coordinate and the conventions for the positive directions of the velocity components are specified in figure A.14. In addition, the investigation carried out on configuration F comprised flow measurements both upstream and on the top of the escarpment. As outlined in figure A.13c, in this case the VWPs were characterised at spanwise positions 9, 12 and 14.
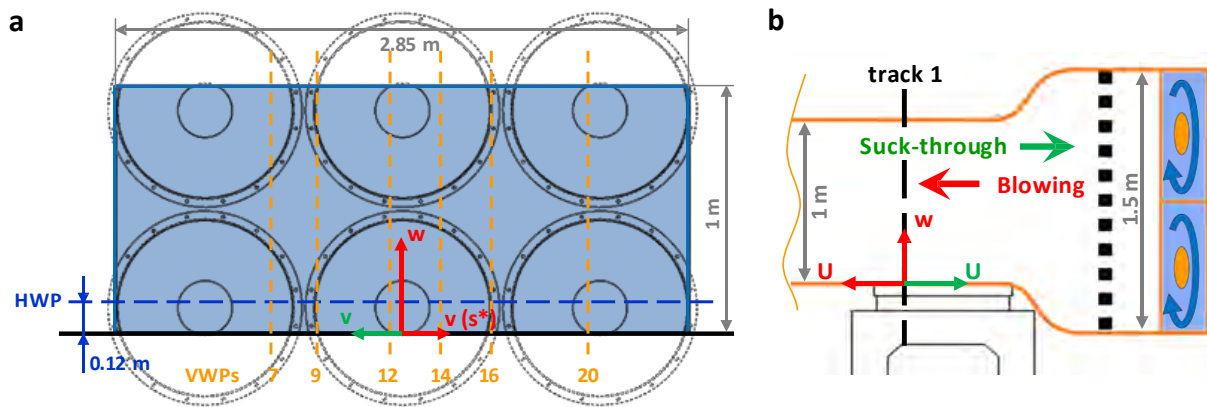
Figure A.14 CWG prototype: FG simulation flow characterisation reference system. a) Front view b) Side view

Figure A.15 CWG prototype: flow measurements instrumentation setup

FG simulation results and discussion

For configurations A to E in table A.7, the mean wind velocity and turbulence intensity are examined in the following. With consideration of the HWP, the streamwise ( ), lateral ( ) and vertical ( ) mean components are illustrated in comparison with those measured for the PCWG (figures A.16 and A.19). For the VWPs the streamwise mean velocity and turbulence intensity are reported relating to two spanwise positions: one in between two adjacent pairs of fans (station 9 in figures A.17 and A.20), the other in front of the central pair of units, in proximity of the middle of the air channel (station 14 in figures A.18 and A.21). Figures A.16 to A.18 illustrate a comparison between the four blow-through configurations (A to D). Figures A.19 to A.21, present one of such configurations (i.e., D) in contrast to configuration E relating to the suck-through arrangement.

To ease interpretation of the results, a series of contour plots relative to the vertical air channel cross-section on track 1 were produced by interpolation of the measured data. Figure A.22 illustrates

the flow field associated with the streamwise mean velocity   relating to the prototype

configurations C, D and E, while figure A.23 illustrates the mean wind velocity relative to a moving

train   . Such a quantity was given by the vector sum of the horizontal components of the onset

wind velocity and the nominal train speed (which was properly assumed in order to achieve a 30°

yaw angle, and thus depended on the spanwise average of   obtained for each configuration).

Furthermore, in figure A.23 a comparison is arranged between the PCWG and the prototype

configurations D and E.
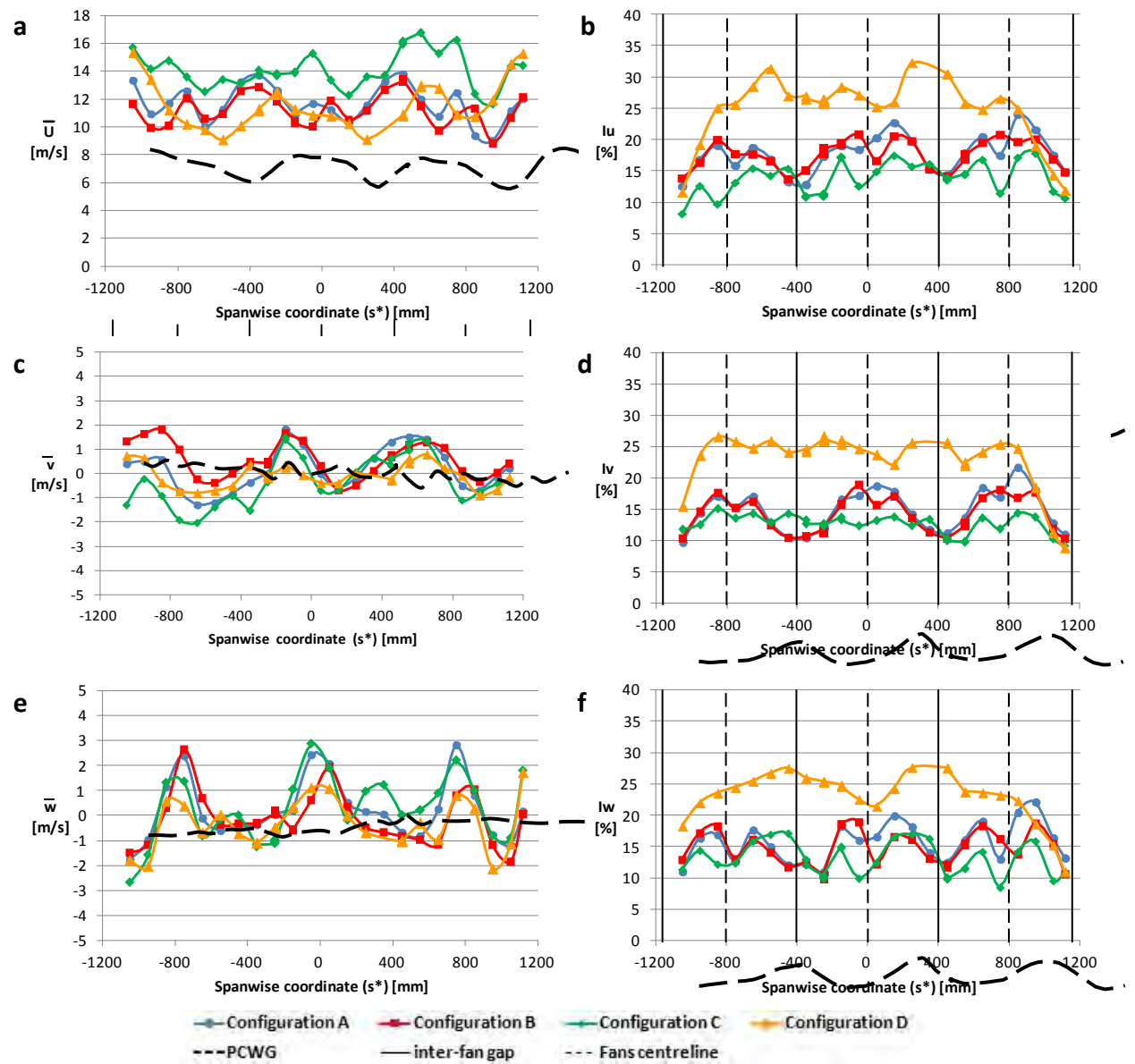
Figure A.16 CWG prototype blow-through design options: HWP on track 1 at reference height.
a) Streamwise mean velocity b) Streamwise turbulence intensity c) Lateral mean velocity
d) Lateral turbulent intensity e) Vertical mean velocity f) Vertical turbulence intensity
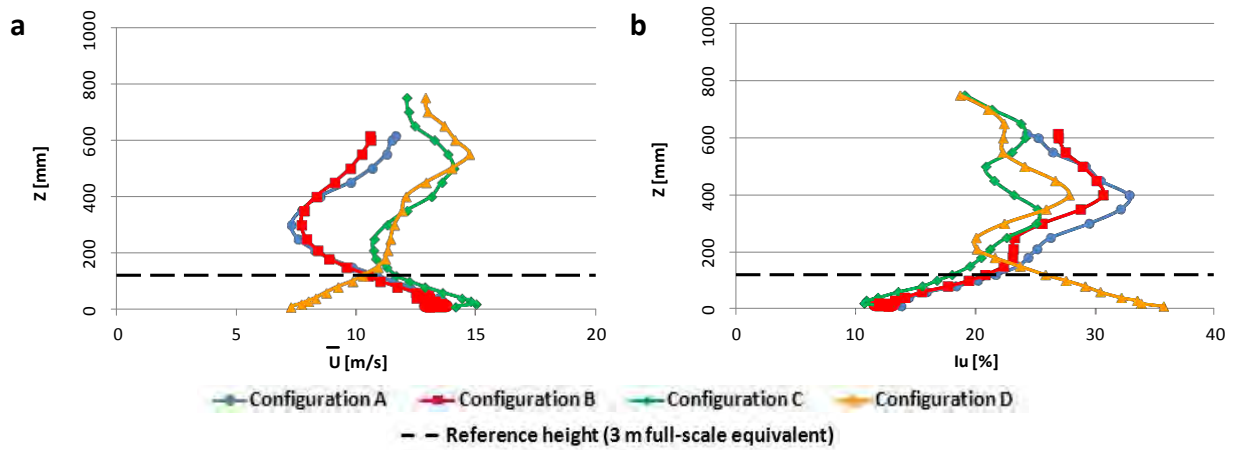
Figure A.17 CWG prototype blow-through design options: VWP on track 1 at spanwise position 9 a) Streamwise mean velocity b) Streamwise turbulence intensity
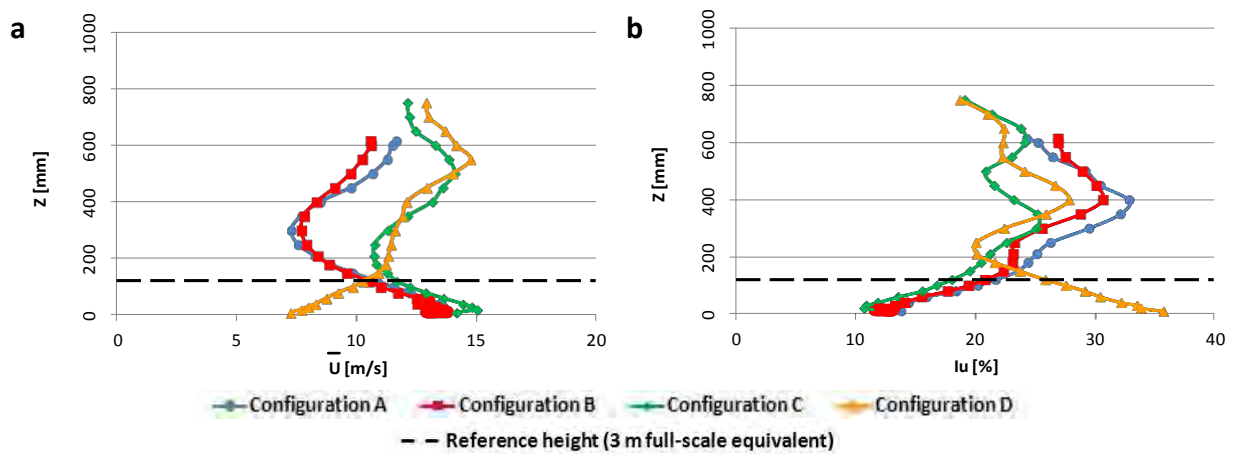
Figure A.18 CWG prototype blow-through design options: VWP on track 1 at spanwise position 14 a) Streamwise mean velocity b) Streamwise turbulence intensity
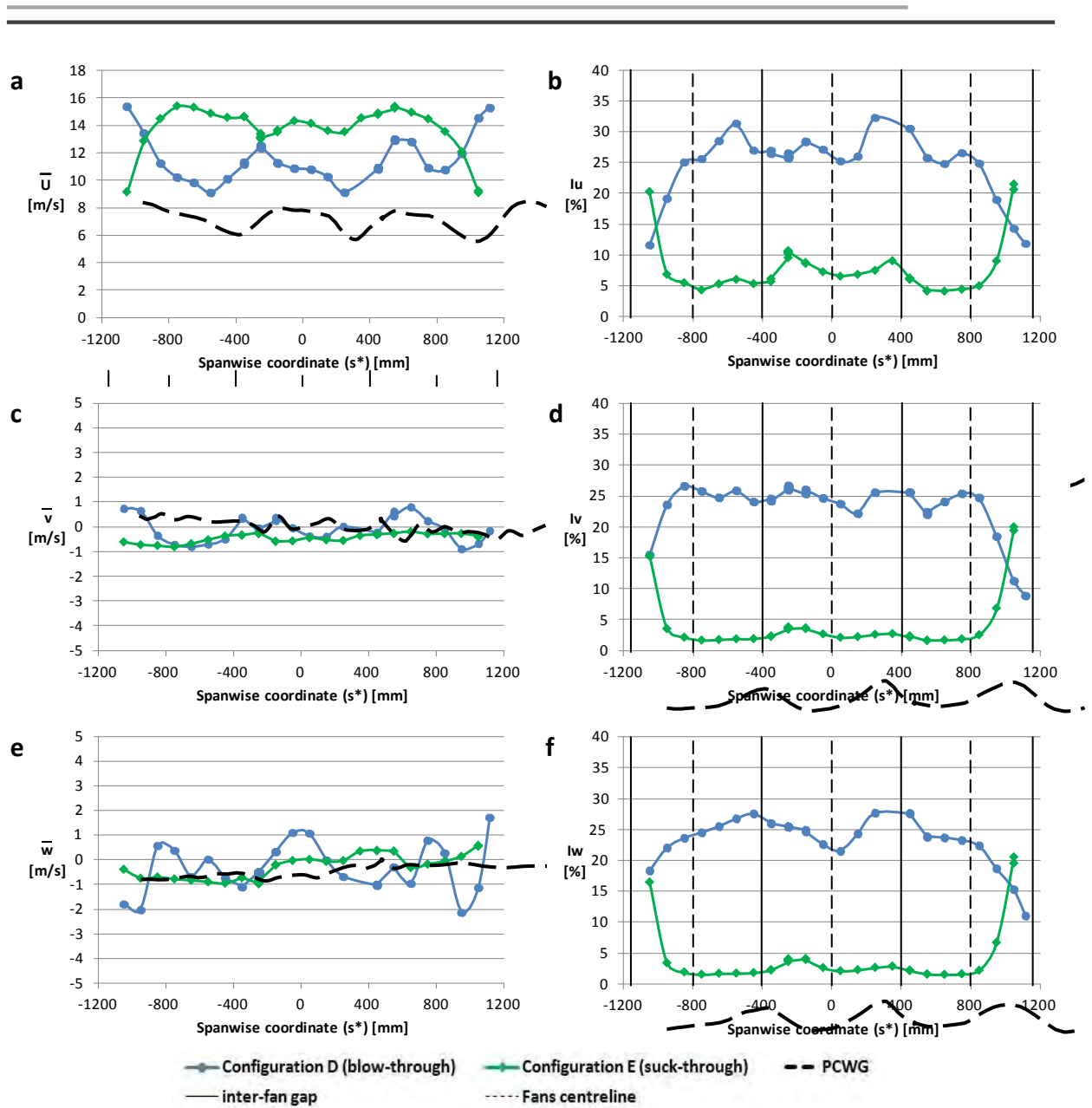
Figure A.19 CWG prototype such-through vs blow-through design: HWP on track 1 at reference height.
a) Streamwise mean velocity b) Streamwise turbulence intensity c) Lateral mean velocity
d) Lateral turbulent intensity e) Vertical mean velocity f) Vertical turbulence intensity

a

b

Configuration D (blow-through)   Configuration E (suck-through)

— — Reference height (3 m full-scale equivalent)
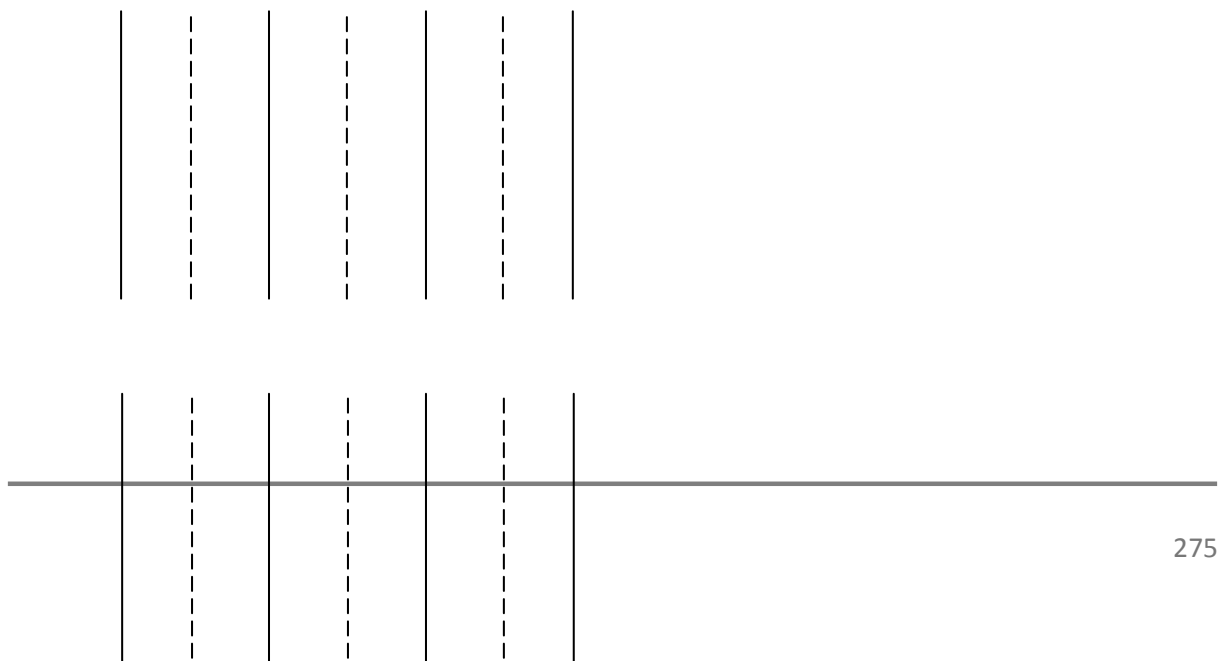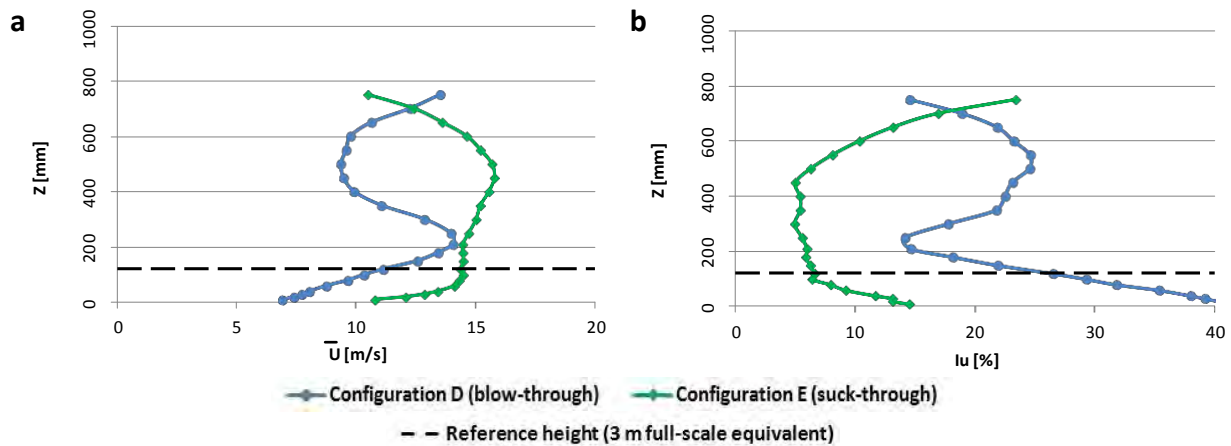
**Figure A.20 CWG prototype such-through vs. blow-through design: VWP on track 1 at spanwise position 9
a) Streamwise mean velocity b) Streamwise turbulence intensity**

a

b

Configuration D (blow-through)   Configuration E (suck-through)

— — Reference height (3 m full-scale equivalent)
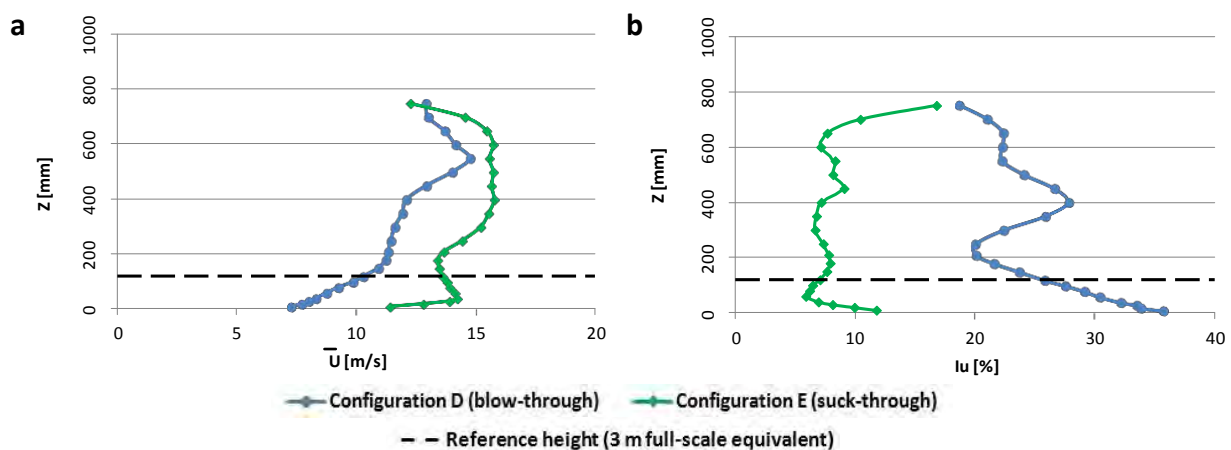
**Figure A.21 CWG prototype such-through vs. blow-through design: VWP on track 1 at spanwise position 14
a) Streamwise mean velocity b) Streamwise turbulence intensity**
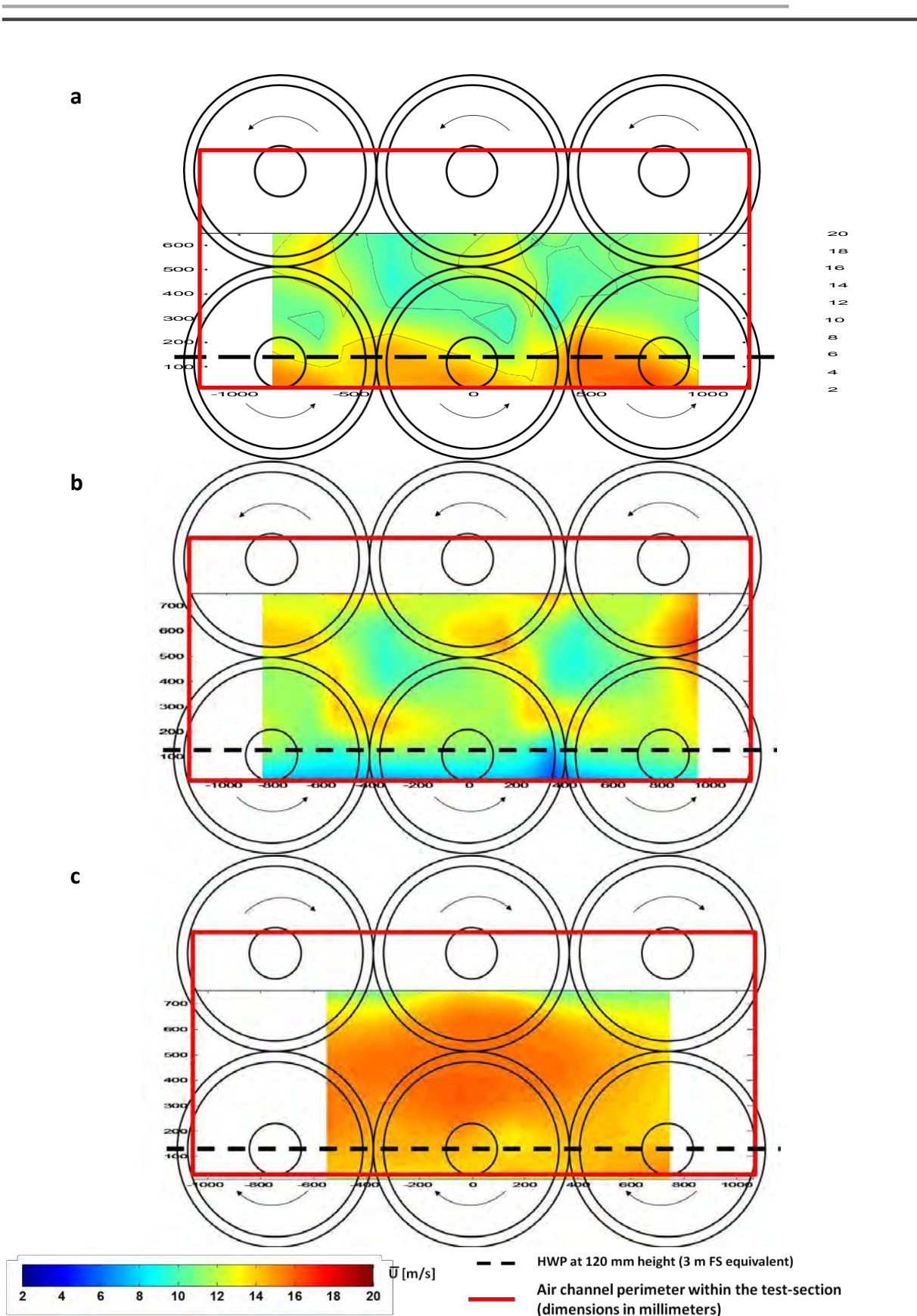
Figure A.22 CWG prototype: contour plots of the onset streamwise mean velocity.
a) Configuration C (blow-through) b) Configuration D (blow-through) c) Configuration E (suck-through)
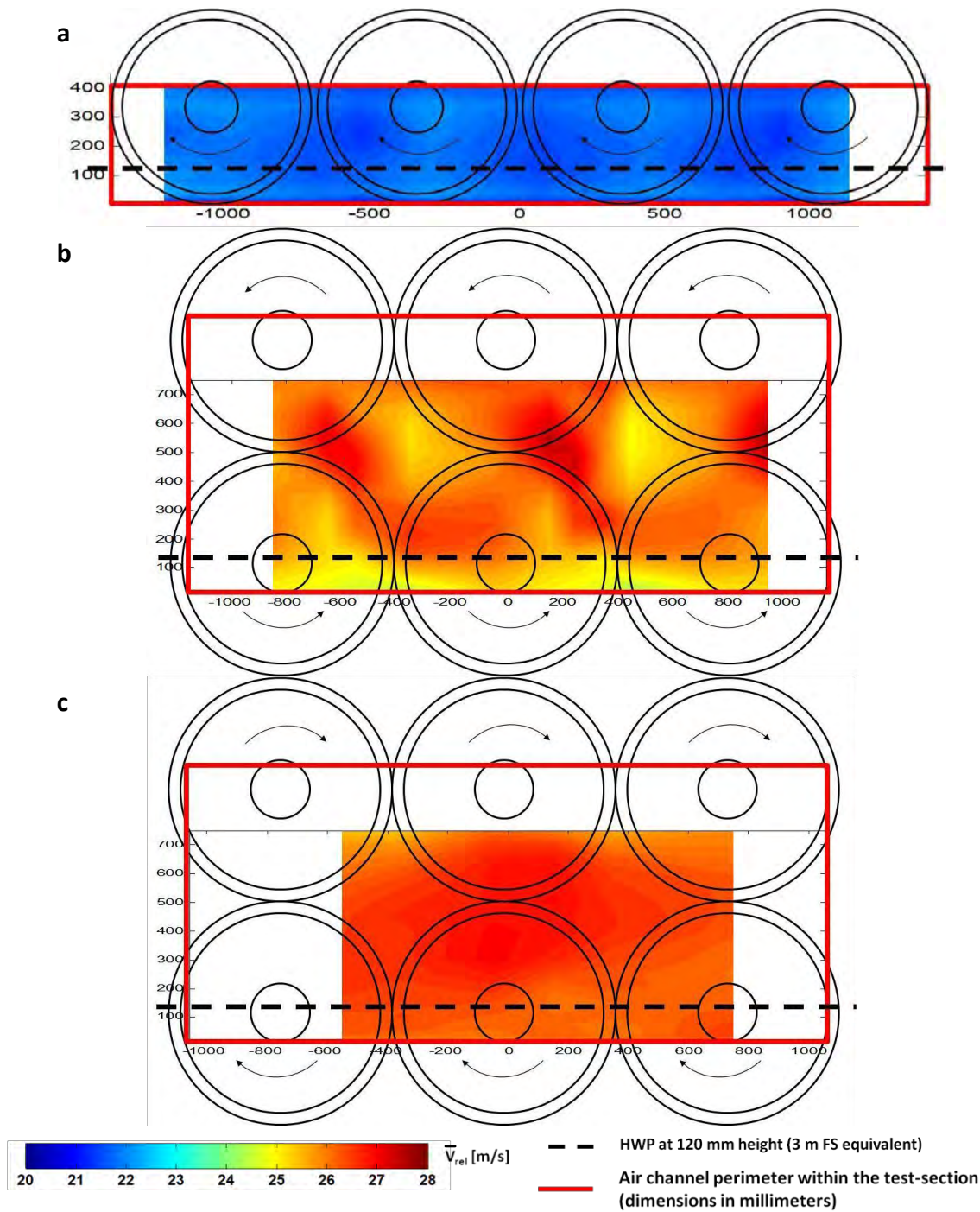
Figure A.23 CWG prototype: contour plots of the mean velocity reltive to a running train at 30° yaw angle ( ).
a) PCWG b) Configuration D (blow-through) c) Configuration E (suck-through)

The spanwise averages relative to the HWPs displaced in the figures above are reported in table A.8 (for the streamwise mean wind velocity and the three turbulence intensities). In addition, table A.9 reports the peak-to-peak spanwise variations and the run-to-run variations of the streamwise mean velocity. In both tables, a comparison is presented involving the air channel prototype configurations from A to E and the PCWG.

Spanwise averages (at)	PCWG	CWG Prototype configuration				
		A	B	C	D	E
[m/s]	7.2	12.03	11.72	14.25	11.25	14.11
I_U [%]	10.5	17.72	17.54	13.43	27.59	7.46
I_V [%]	4.2	14.01	12.99	12.41	25.43	2.63
I_W [%]	4.3	14.23	13.31	12.25	23.73	2.69

Table A.8 CWG prototype: HWP spanwise average streamwise mean wind velocity and turbulence intensities (Configurations A, B, C, D, E)

Streamwise mean velocity ( ) at [m/s]	PCWG	CWG Prototype configuration				
		A	B	C	D	E
peak-to-peak spanwise variation	2.85	3.76	3.66	4.50	5.86	2.40
run-to-run (2σ) spanwise variation	0.13	0.28	0.34	0.14	0.21	0.52

Table A.9 CWG prototype: HWP spanwise peak-to-peak variation of the streamwise mean wind velocity (Configurations A, B, C, D, E)

The flow characterisation data outline that any of the five prototype configurations taken into account here produced a sensible increment in the streamwise mean wind velocity with respect to that delivered by the PCWG. The spanwise averages in table A.8, relative to the selected reference height (i.e.,   = 0.12 m), indicate that four configurations (A, B, C and E) met or exceeded the 11.5 m/s mean wind velocity specification and that configuration D was also close to meeting such a target. In terms of average mean wind velocity, hence, the prototype confirmed the performance estimation made during the preliminary design and denoted an improvement with respect to the PCWG represented by the higher onset wind speed that was achieved. Furthermore, figure A.23

confirms such an improvement also regarding the mean wind speed relative to a travelling in view of the higher velocity that was achieved.

Unfortunately, the blow-through design led to a 'non-optimal quality' of the flow regardless of the specific air channel configuration. The HWPs in figure A.16 show a rather large peak-to-peak spanwise variability not only in the streamwise mean velocity (quantified in table A.9), but also in the lateral and vertical components. This suggested the presence of a significant swirl in the flow despite the use of a honeycomb screen, which was reflected also by values of lateral and vertical turbulence intensities of the same order of   . A further spatial inhomogeneity in the flow obtained through a blow-through design was outlined by the VWPs. On the spanwise position 9, between adjacent fans, the streamwise mean velocities in figure A.17 shows a wind hole at mid-height of the air channel. At station 14 (figure A.18), a low velocity peak tends to occur at approximately 300 mm above the ground level. These two regions of low wind speed seemed to be induced by a reduced (local) flow rate in the areas in front either of the space in between four adjacent fans or of the hubs of the fans' impellers, respectively. As illustrated in figure A.22a, it was observed as the wind holes were slightly shifted upwards and on the right hand side with respects to such areas. This was compatible with a drift of the flow generated by the CCW fans' rotation and by the air channel contraction.

The agreement between the data relative to configuration A and B indicated that doubling the length of honeycomb did not significantly reduced the swirl in the flow. A comparison between configurations A and C (both based on a blow-through design) revealed that an increased distance between the fans and the wall led to an increment of the streamwise mean wind speed. Neither of the variable porosity grids configurations that were tested (not shown here) proved to be effective in smoothing the spatial irregularities in the streamwise velocity field. To this end, the only modification to the air channel layout capable of generating a sensible improvement was the implementation of an array of spires at the inlet of the test section (configuration D in figure A.12c). The use of these

devices determined a reduction in the mean streamwise velocity near the ground, thus leading to a positive gradient upwards for heights < 0.2 m (figures A.17a and A.18a).

A significant improvement in the quality of the flow field was achieved in combination with a suck-through design. In the presence of configuration E, the HWP was characterised by a significantly improved spatial uniformity (figure A.19, A.22 and A.23). The streamwise mean wind speed presented higher values across the entire span and was associated with a reduced variability and with lower turbulence intensities. In addition, the lateral and vertical mean velocity components showed low peak-to-peak fluctuations in combination of low turbulence intensities. This suggested a reduction of the flow swirl induced by impellers' rotation with respect to any of the blow-through configurations. Furthermore, Figures A.20 and A.21 illustrate that the VWPs had a more regular evolution compared to that ensured by the best option associated with a blow-through design (i.e., configuration D).

Escarpment ground simulation results and discussion

The streamwise mean wind velocity field on the top and upstream of the escarpment is illustrated in figure A.24a and A.24b, respectively. The low velocities measured upstream of the escarpment suggested that a flow separation might have occurred in that area. Nevertheless, this did not necessarily indicate an unrealistic simulation of the flow conditions since, in light of the escarpment slope (i.e., approximately 34°), a region of recirculation is expected in that area even in the presence of a natural atmospheric wind at full-scale. In order to assess the accuracy of the crosswind simulation, a comparison was arranged between the flow field measured during the prototype tests and the reference mean wind profile over an escarpment indicated in the ESDU 82026 (2002).

Figure A.24 CWG prototype suck-through design escarpment ground simulation: streamwise mean wind velocity a) top of the escarpment b) upstream the escarpment

The comparison was carried out considering the ratio between the streamwise mean wind speed on the top and upstream the escarpment (and   , respectively) defined as:
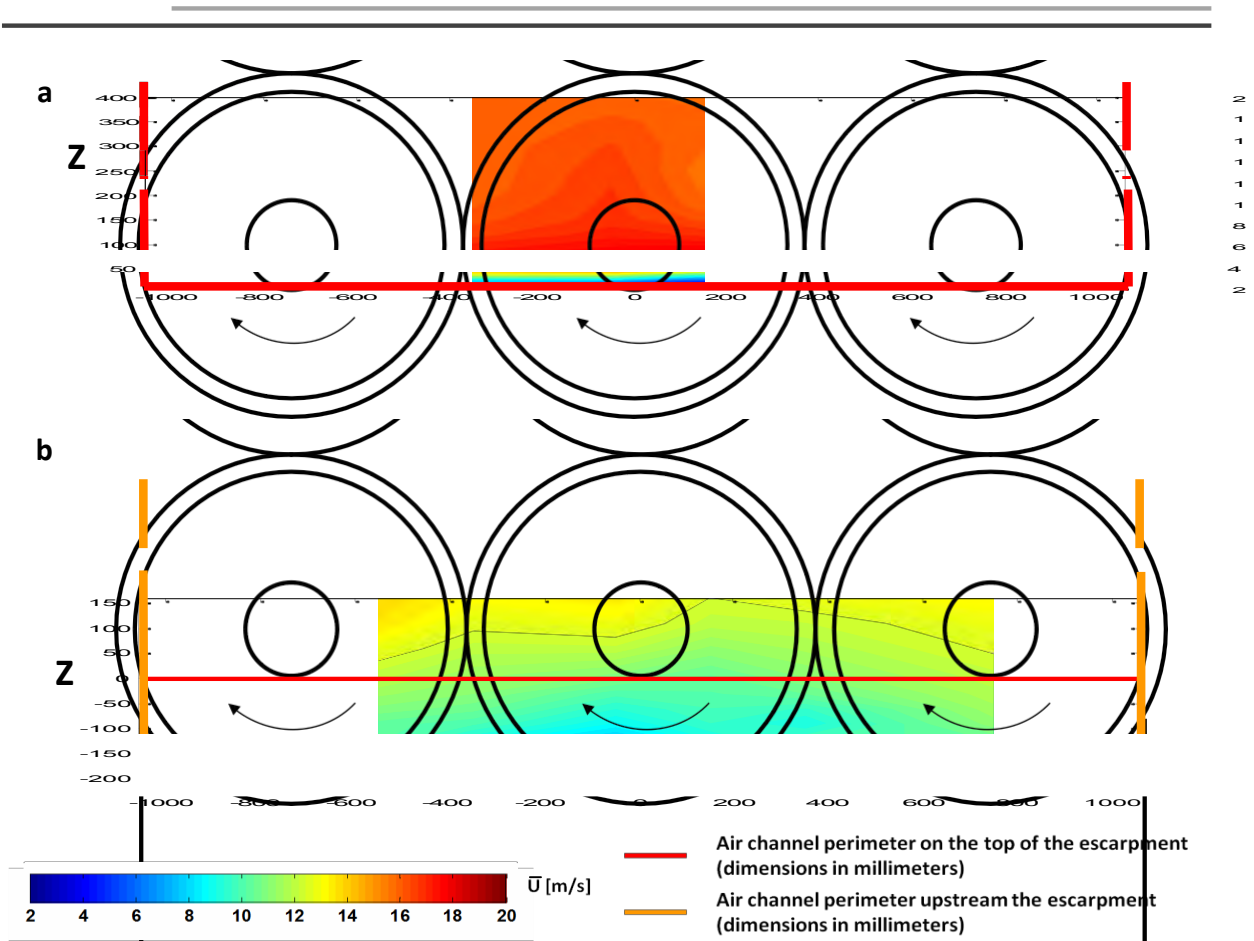
$$K_L = \frac{U_{top}\left(z/H_{esc}\right)\big|_{z=z}}{U_{us}\left(z'/H_{esc}\right)\big|_{z=z}}$$

(A.1)

where the vertical coordinate is normalised with respect to the escarpment depth   and, as indicated, the two wind velocities are associated with the same height above the ground (i.e., according to the conventions in figure A.13c).
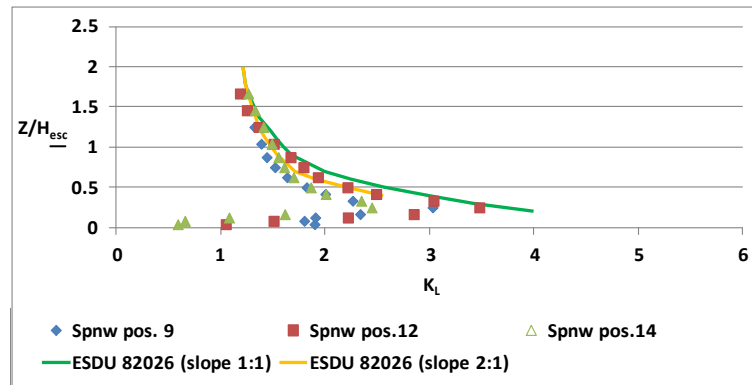
Figure A. 25 Streamwise velocity ratio over an escarpment (CWG prototype vs ESDU 82026 (2002))

The comparison is illustrated in figure A.25, where both series of data from the ESDU 82026 (relative to 1:1 and 2:1 slope escarpments, respectively) and the three VWPs measured on the CWG prototype are considered. As outlined, a good agreement was found between the measured and reference data with respect to most of the heights within the escarpment depth (i.e.,   ). Therefore, the viability of a suck-through design to an escarpment ground simulation was supported.

A.3.3.4   Selection of the final design configuration

The CWG prototype tests showed that, in combination of a blow-through design, the extremely short distance between the axial fans and the testing track did not allow the swirl and spatial irregularities in the flow to be appropriately smoothed. Configuration D (which employed an array of spires) was the best of the blow-through configurations tested. Although it presented a streamwise mean wind speed slightly lower than the target value, as well as a relatively high spanwise variability in HWP, it ensured allowed to achieve VWPs with a positive gradient upward (at least for < 0.25 m).

With respect to the blow-through design options, the suck-through design led to the following improvements:

- better spatial homogeneity and higher magnitudes of the mean streamwise velocity in both HWP and VWPs;

- reduced magnitudes and spanwise variations of both the lateral and vertical velocities;

- lower turbulence levels.

In addition, the prototype tests on configuration F confirmed the suitability of a suck-through design to an escarpment ground simulation.

In light of these considerations based on the prototype tests, the decision was made to construct the new CWG based on a suck-through design corresponding to the prototype configuration E.

A.3.4 Final design, construction and 'tuning'

The details of the final CWG design are specified in table A.10, where the progresses and variations with respect to the preliminary design (presented in table A.6) are highlighted in bold.

Position (within the TRAIN rig testing room)	• Towards the end of the test section (track 1 travel direction) • (partially overlapping the area occupied by the PCWG) • Flow fans on the *far side* of the testing room • **distance between the fans and the wall: 0.54 m**
Overall configuration	• Open circuit design • ~~Blow-through /~~ **suck-through** design • Flow fans at the trackside moving the air horizontally and perpendicularly to the tracks • Ducted test-section (over the tracks) • Spanwise mean wind velocity (at) : 11.5 m/s

Fans' model	• Ziehl-Abegg FC071-4DF.7M.V6
	• Type: AXIAL flow fans
	• Size:
	  – Nominal Diameter (ND): 0.71 m
	  – Case dimensions: 0.785 External Diameter (CD).; 0.26 m length
	• Motor:
	  – Integrated into the impeller hub
	  – 3-phases 400V ±10% (Y) 50Hz (4-poles)
	  – Nominal rotational speed: 1350 rpm
	  – Current consumption: 5.3 A (full-speed); 18 A (startup)
	• Number of blades: 6

Fans' arrangement	• 16 units arranged in 2 rows of 8 units each

Air-channel layout	• Straight horizontal air channel directed perpendicularly to the tracks
	• Test-section size (Span x Height x Length): 6.35 x 1 x **1.685 m**
	• Vertical ~~contraction~~ **expansion** between the fans and test-section (contraction ratio 1.52)
	• **Bellmouth and one honeycomb screen at the inlet**
	• **One honeycomb screen ~~and variable porosity grids~~ downstream the expansion**
	• **Honeycomb screen specifications:**
	  – **Material: treated extra-hard 3003 alloy aluminium foil**
	  – **Size: 9 mm (cell diameter); 25.4 mm (length); 60 μm (foil thickness)**
	• Portion of air channel spanning the *down side* of the tracks to be semi-permanent (to allow access all along the testing room)

Table A.10 New CWG final design

Once the final CWG design had been completed, the following details concerning the construction of the new system were defined to enable the installation.

- A steel frame for supporting the fans was designed. It comprised of a set of steel columns and angle beams bolted together and anchored to the floor (figure A.26a).

- Concerning the air channel, load was transferred directly onto the concrete structure which supported the tracks and onto the steel frame which supported the fans. In addition, a series of additional steel columns (anchored to the floor) were installed on the *down side* of track (please refer to figures 4.8 and 4.9 in section 4.3.2) to provide additional support. Finally, to suspend the roof of the air channel, the aerial support system illustrated in figure A.26b was developed.
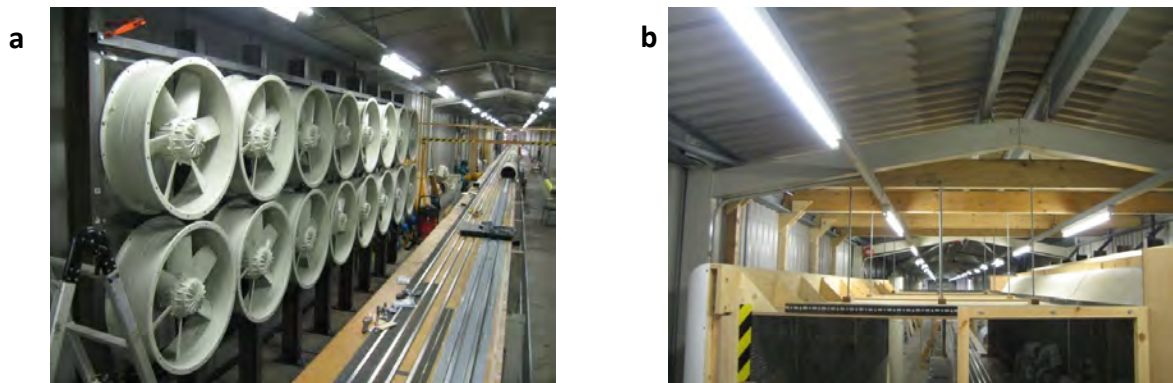
Figure A.26 CWG construction details. a) Fans' supporting frame b) Air channel aerial supports

- To operate the 16 fan units an electronic circuit was designed and integrated into one single control panel. This panel was placed in proximity of the CWG, on the *far side* of the testing room. In addition, to ease the CWG operation during moving model tests (and to enable emergency stop), remote start / stop switches were installed on the *down side* of the testing room (on both sides of the CWG), as well as in the control room. The current configuration of the control circuit enables the fans to be operated only at full speed. In order to limit the power demand at the start-up, an automatic system ensures that the fans switch on two by two, one pair every approximately 5 s (leading to a total start-up time of approximately 50 s).

The manufacturing and installation of the steel frame supporting the fans was completed by the technical staff of the Civil Engineering Laboratories of the University of Birmingham with the support of a local contractor (Rampart Carriage & Wagon Services Ltd). The construction of the air channel was contracted to Derwent Pattern Ltd. The design and installation of the electronic control circuit was carried out by R.D. Jukes & Co. Ltd.

For an illustration of the new CWG, please refer to figures 4.7 to 4.9 in section 4.3.2.

After the new CWG had been constructed, flow measurements were undertaken for characterising the crosswind simulation. In first instance, the reference HWP at = 0.12 m above the ground (i.e., 3 m full-scale equivalent height) was measured 0.2 m upstream of the centreline of track 1 (figure A.27). Instrumentation and measurement technique were the same adopted during the flow characterisations relating to the PCWG and to the CWG prototype.

Figure A.27 CWG flow characterisation reference system. a) Front view b) Side view

The results of these initial measurements, which are illustrated in figure A.28 below, showed a slight deterioration of the CWG performance in its '*base configuration*' with respect to what predicted by

prototype tests. The spanwise averages of the streamwise mean wind velocity and turbulence intensity, which were approximately 10.5 m/s and 20%, were respectively lower and higher than expected. Furthermore, the spanwise irregularity in the HWP was relatively large, with two wind holes (where   dropped to a minimum of ~6 m/s) occurring at both sides of the air channel, in between 0.8 and 1.6 m from the mid-span.
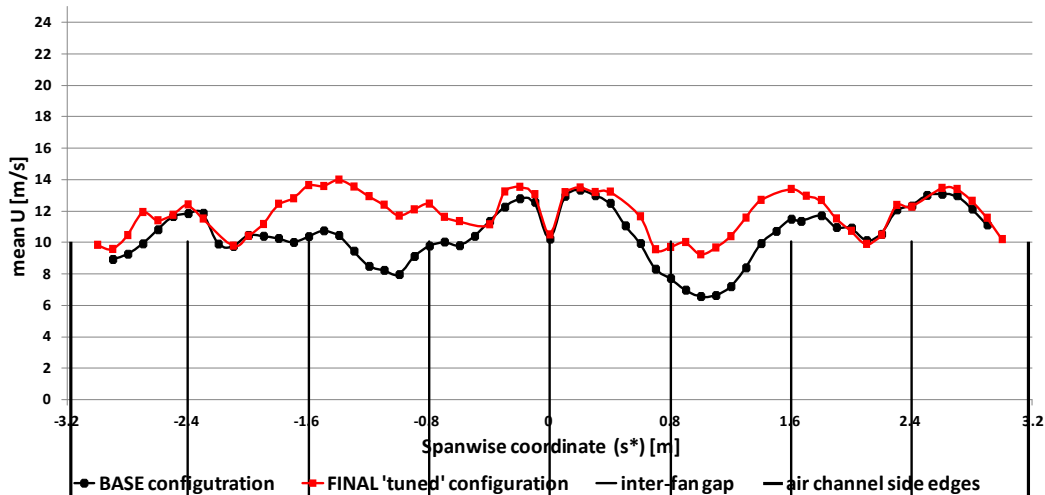
Figure A.28 CWG tuning phase: reference HWP of the streamwise mean velocity

To explain what happened, although the CWG presented an open circuit configuration, it was analysed as a closed system in light of the extremely narrow space available between the air channel and the building envelope (as outlined in figures 4.8 and 4.9 in section 4.3.2). In this view, part of the high turbulence and spatial non-uniformities affecting the flow within the test section were assumed to originate because the air stream was recirculating outside the air channel. This was consistent with flow disruptions possibly caused by structures such as the concrete piers sustaining the tracks and the air channel aerial support. Furthermore, a backpressure arising at the fans' discharge was inferred to propagate upstream and to reach the test-section, thus determining a reduction of the wind velocity measured on track 1 with respect to what predicted by prototype tests. Induced by the sudden diversion undertaken by the flow exhausted by the fans when it impinges the wall of the building, this backpressure was likely to have affected also the performance of the prototype. However, an enhancement of its effect was inferred for the CWG final installation. Since the number

of fans was higher in this case (i.e., 16 instead of 6), this enhancement appeared consistent with a stronger interaction occurring between the flow exhausted by adjacent units.

Following these considerations, a 'tuning process' was undertaken in order to improve the quality of the crosswind simulation. During this process a series of minor adjustments were implemented and their effects were investigated by repeating the flow characterisation. At the end, two of these adjustments were permanently adopted as part of the '*CWG final (tuned) configuration*'. A vertical deflector panel, oriented in the streamwise direction and spanning almost the entire height of the building, was positioned in the gap between the fans and the wall (on the *far side* of the testing room). This limited the interaction between the air streams discharged by the fans and favoured the flow recirculation. Furthermore, in order to smooth irregularities in the airflow before it was intaken into the air channel, an additional aluminium honeycomb screen was mounted between the air channel and the floor, under the inlet (please refer to figures 4.8 and 4.9 in section 4.3.2).

In terms of HWP, the benefit obtained with respect to the initial performance is outlined in figure A.28. As minor adjustments, these alterations could not entirely remove the spanwise irregularities in the flow. Nevertheless, they led to a better uniformity by reducing the peak-to-peak spanwise mean velocity variation and also by determining a reduction in the turbulence intensity (whose spanwise average decreased from ~20% to ~17%). In addition, they produced an increment in the spanwise average mean wind velocity to reach ~12 m/s.

The CWG *final configuration*, which was used for the tests of this research and is currently in place in the TRAIN rig, consists of the *final design* specified in table A.10 and enhanced according to the two adjustments discussed above. In addition, the dedicated arrangement described in section 4.3.2 and illustrated in figures 4.33 and 4.34 in section 4.6 was developed to enable static model tests to be undertaken.

A.4   New CWG performance

Including the extract already presented in 4.3.2.1, this section illustrates the characteristics of the flow simulation delivered by the new CWG and, as such, employed for the experiments of this research. Flow measurements were undertaken using the instrumentation and methodology adopted for any of the flow characterisations carried out during the new CWG development. Accordingly, the experimental uncertainty associated with the results presented below is determined by the combination of the following factors:

- The bias limit of the instrumentation, specified in section 4.5.2.2.

- The random uncertainty associated with the stochastic nature of the turbulent wind simulation. This was estimated by assessing the run-to-run variation of measurements recorded by one reference probe kept in a fixed position during different runs. Inferring a normal distribution of the data and considering a 95% confidence level, this contribution was quantified in approximately ± 0.3 m/s for   , ± 0.1 m/s for both   and   and ±2 Pa for the mean differential static pressure (   ).

- The accuracy in positioning and aligning the probes. Since Cobra probes were aligned by eye and the traversing system was manually operated, such accuracies were estimated in ±5 mm and ± 2°, respectively.

A.4.1   Moving model tests configuration

A.4.1.1   Crosswind simulation

As illustrated in figure A.27 (in the previous section A.3.4), the reference HWP consisting of 64 spanwise positions was measured at   = 0.12 m above the ground (i.e., 3 m full-scale equivalent height), 0.2 m upstream of the centreline of track 1. In addition, two VWPs were characterised at spanwise positions 26 and 28, positioned both 0.2 m upstream of the centre of track 1 and 0.15 m downstream the air channel inlet. HWPs and VWPs are illustrated in figures A.29 and A.30, respectively.

a

Spanwise position

b

Spanwise position

c

Spanwise position

— inter-fan gap   — air channel side edges

d

Spanwise position

e

Spanwise position
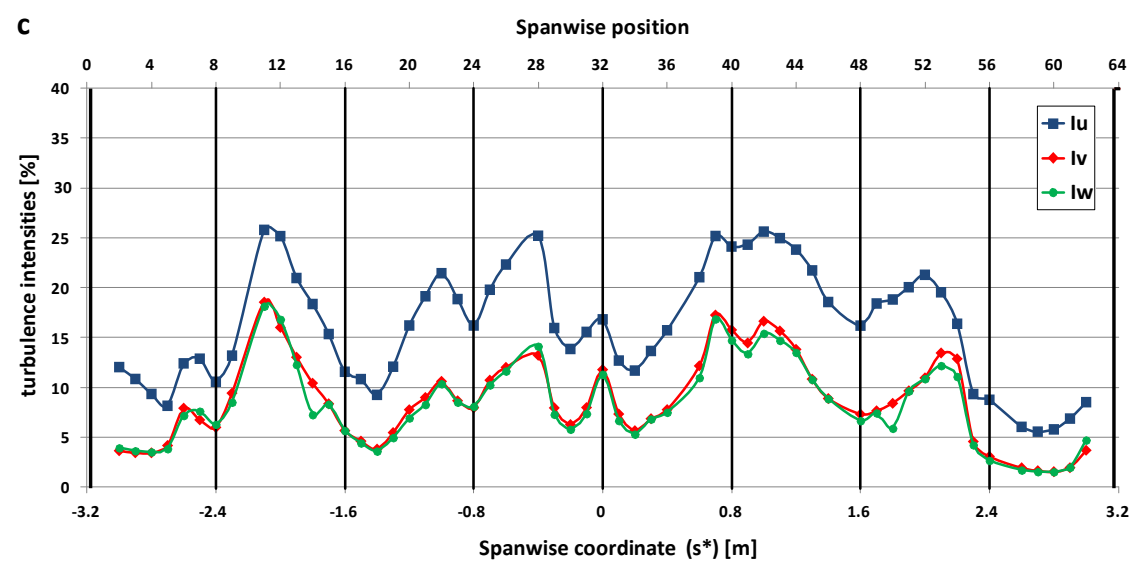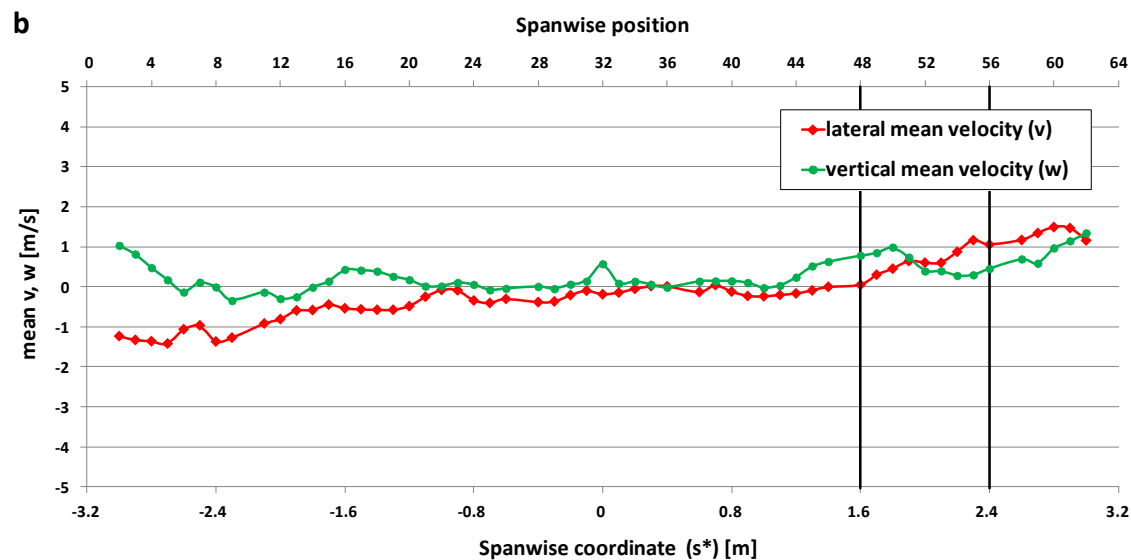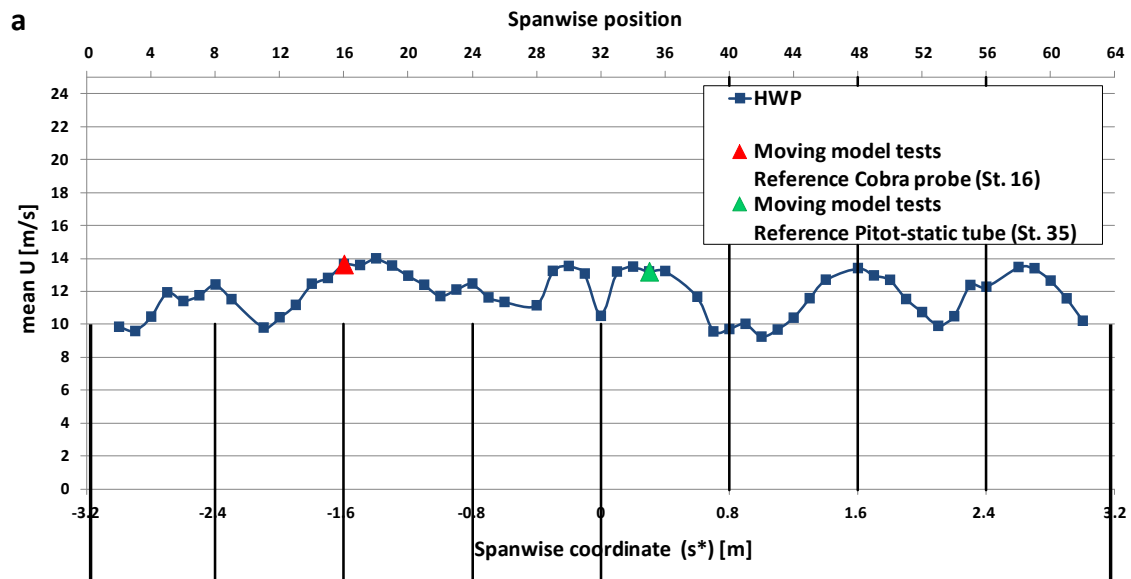
—inter-fan gap   —air channel side edges
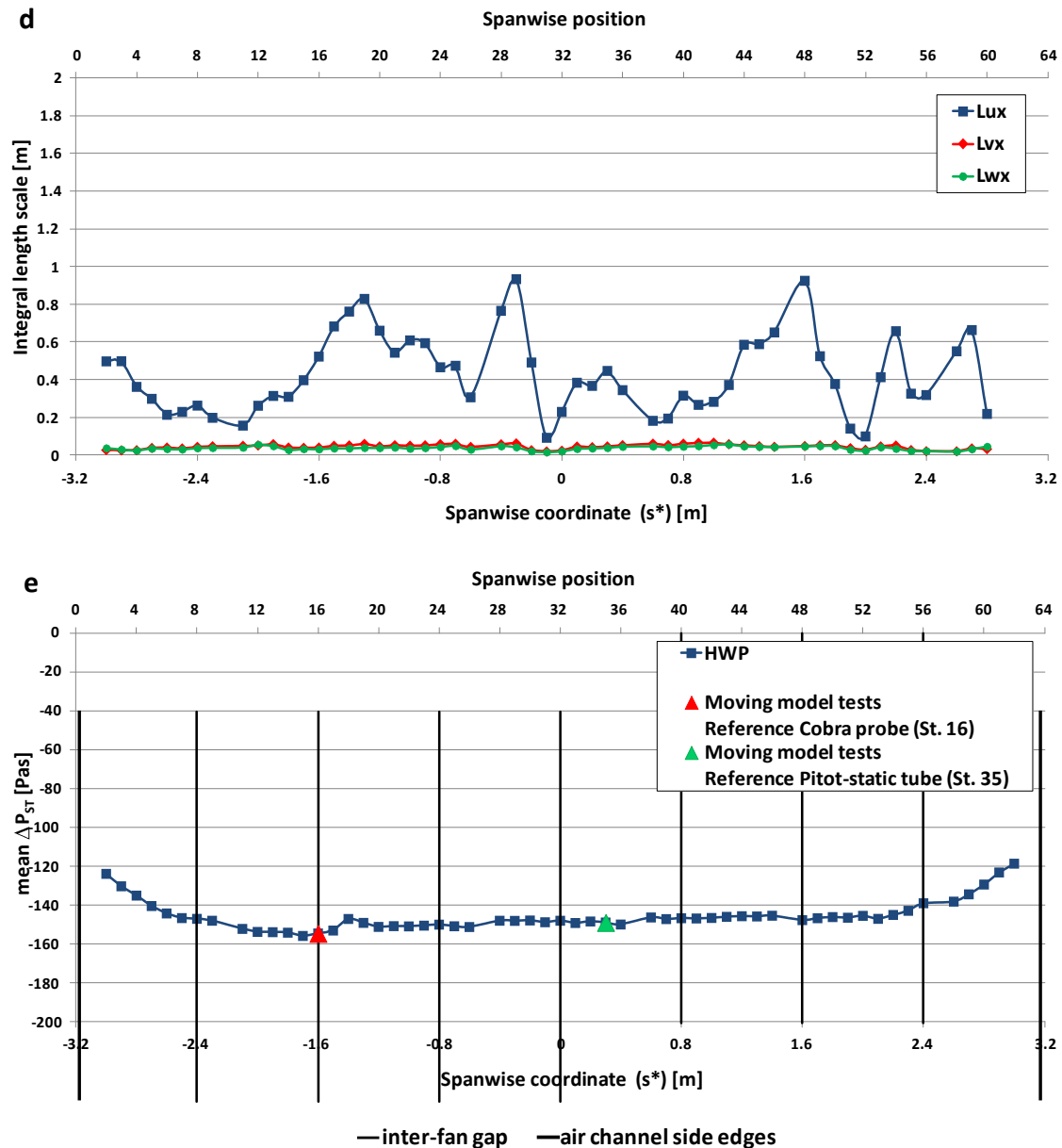
Figure A.29 Crosswind simulation (moving model tests configuration): HWP. a) Streamwise mean velocity ( ). b) lateral and vertical mean velocities ( ). c) Turbulence intensities. d) Along-wind integral length scales. e) Mean differential static pressure ( )

The streamwise velocity HWP in figure A.29a corresponds to that obtained at the end of the '*tuning process*' and previously shown in figure A.28 above. In figure A.29a, as in figure A.29e, the spanwise positions 16 and 35 are highlighted since those where the trackside reference probes were placed during the moving model tests (section 4.7). Figure A.29b shows negative and then positive lateral mean velocities respectively on the left and right hand side of the CWG. As discussed in section 4.3.2.1, in light of the conventions specified in figure A.27, this indicates a lateral velocity directed

from the side edges towards the centre of the air channel and suggests the flow being sucked in not only from the top and bottom of the inlet section, but also from either side.

The spanwise evolution of the streamwise turbulence intensity appears to be related to that of the mean velocity, with high values of the latter associated with reduced   and, vice-versa, the highest turbulence intensities relating to the wind holes. Reduced in magnitude,   and   follow a similar trend as   .

The turbulence integral length scales in figure A.29d were calculated from a single-point measurement fitting the Von Karman spectrum (ESDU, 2001) into the normalised spectra obtained from the experimental data (figure A.32). While a certain spanwise uniformity was found for   and   , it can be observed that larger   tend to occur in the areas characterised by higher wind velocities. That being said, it is acknowledged that previous studies have indicated a degree of scatter of approximately one order of magnitude associated with the estimations of such quantities (Sterling et. al., 2005).

Figure A.29e outlines that a negative and homogeneous (apart in the side areas) mean differential static pressure is produced inside the air channel by the fans operating in sucking-mode.
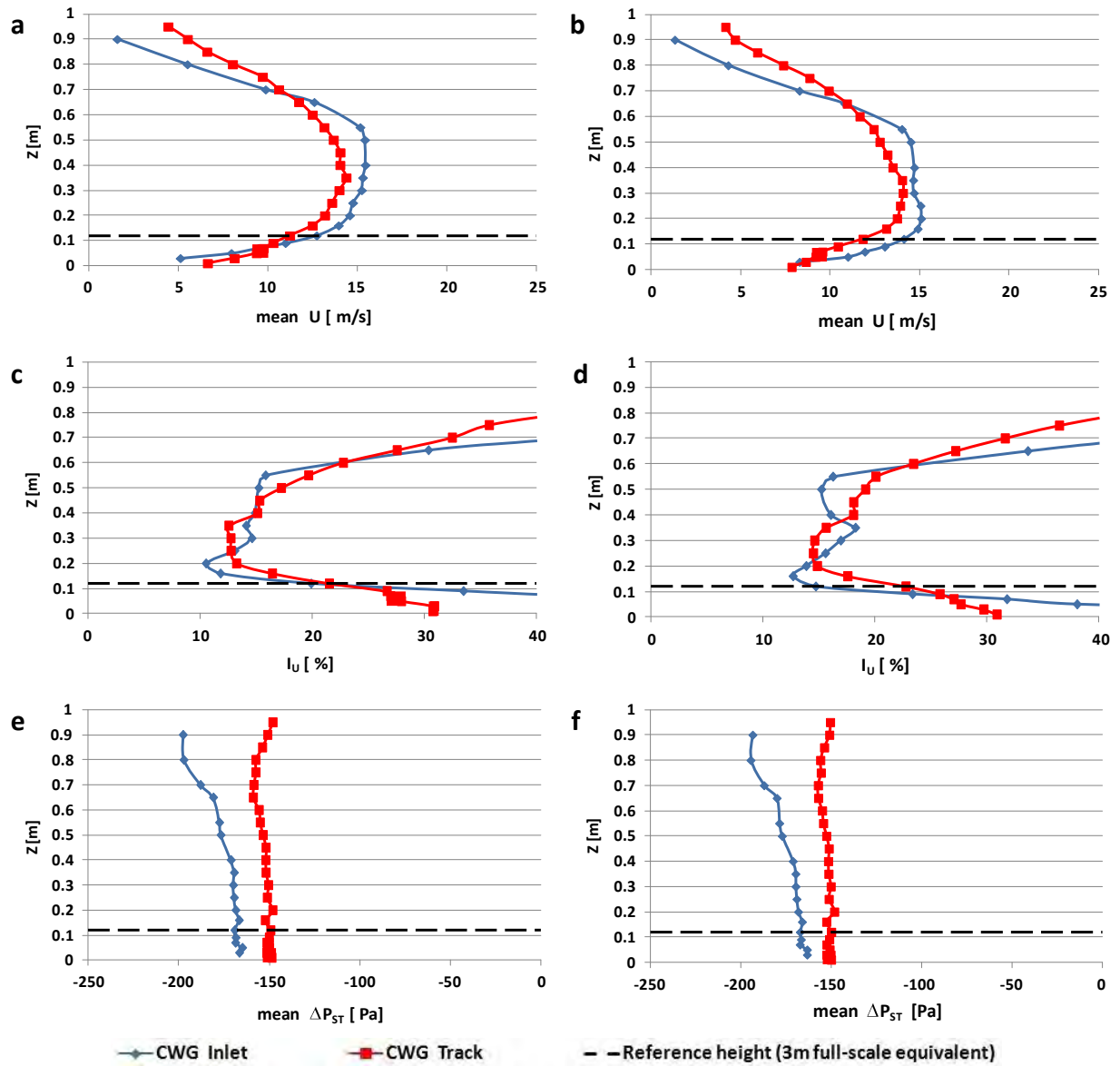
Figure A.30 Crosswind simulation (moving model tests configuration): VWPs. a) Streamwise mean velocity ( ) at spanwise pos. 26. b) Streamwise mean velocity ( ) at spanwise pos. 28. c) Streamwise turbulence intensity ( ) at spanwise pos. 26. d) Streamwise turbulence intensity ( ) at spanwise pos. 28. e) Mean differential static pressure ( ) at spanwise pos. 26. f) Mean differential static pressure ( ) at spanwise pos. 28.

Figure A.30 illustrates the VWPs of the mean streamwise velocity, of the turbulence intensity and of the mean differential static pressure. For each of these quantities, examined at the spanwise positions 26 and 28 specified in figure A.27a, a comparison is arranged between the VWPs measured 0.15 m downstream of the inlet and 0.2 m upstream of track 1. The increment of the mean streamwise velocity with respect to the height in the lower half of the air channel is encouraging and confirms the indication of the prototype tests regarding the effectiveness of a suck-through design.

However, an asymmetry can be observed about the air channel mid-height, with a tendency of lower velocities and higher turbulence intensities occurring in the upper portion. Consistent with section A.3.4, it is inferred that this might be caused by disruptions in the flow forming whilst it is recirculated inside the building. Accordingly, the different characteristics of the inlet flow on the top and the bottom half of the air channel might depend on whether it is ingested after recirculating above or below the air channel. In this view, the results in figure A.30 suggest a higher level of non-uniformity and of turbulence associated with the flow recirculating in the top part of building.

Considering the lower portion of the cross-section (i.e., < 0.7 m), the comparison between VWPs measured 0.15 m downstream of the inlet and 0.2 m upstream of track 1 shows a tendency of the streamwise wind velocity to decrease in the along-wind direction, while an increment can be observed regarding to the mean differential static pressure. Along with observations made in section A.3.4, it is hypothesised that these trends are caused by the propagation throughout the air channel of the backpressure generated by the flow discharged from the fans impinging on the wall of the building.

Spectral analyses performed on the flow characterisation data are reported in figures A.31 and A.32. Four spanwise positions are examined: the two positions where the reference trackside probes were placed during the moving model tests (i.e., 16 and 35), and the other two where the VWPs were measured.
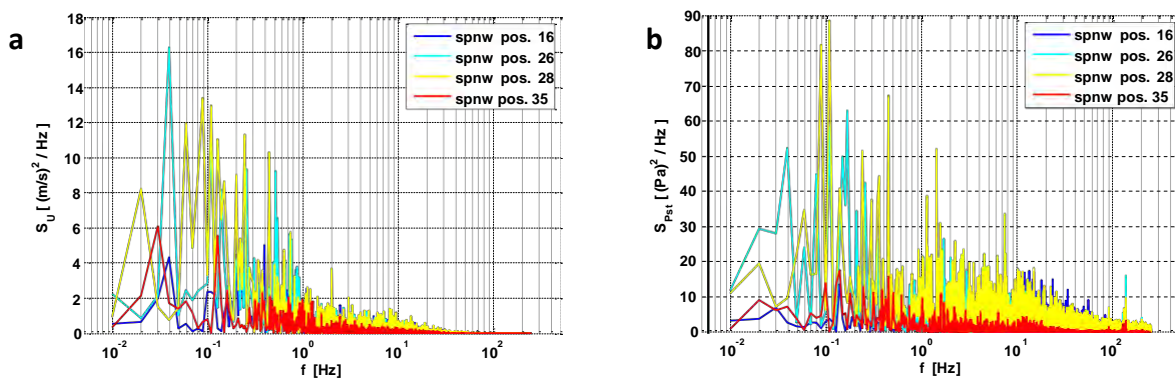
Figure A.31 Crosswind simulation (moving model tests configuration): wind spectra. a) Streamwise velocity b) Differential static pressure

Not surprisingly, figure A.31 reveals that the limited spanwise homogeneity observed in the HWP is echoed by variations shown by the spectra of both the streamwise velocity (a) and the differential static pressure (b). In figure A.31b, it is worth drawing attention on a resonant peak that arises at frequencies in between 130 and 140 Hz. Visible in the spectra of the differential static pressure, this peak does not appear in those of the streamwise velocity. In light of a fans' (nominal) blade passing frequency of 135 Hz (given by 6 blades rotating at 1350 rpm), such resonance is interpreted as a fan-induced interference.

The same data illustrated in figure A.31a for the streamwise velocity are presented in a normalised form in figure A.32, with the standard wind engineering normalisations (Dyrbye and Hansen, 1999) adopted for both spectra and frequency, and in combination with the Von Karman spectrum associated with the integral length scales indicated in figure A.29d.
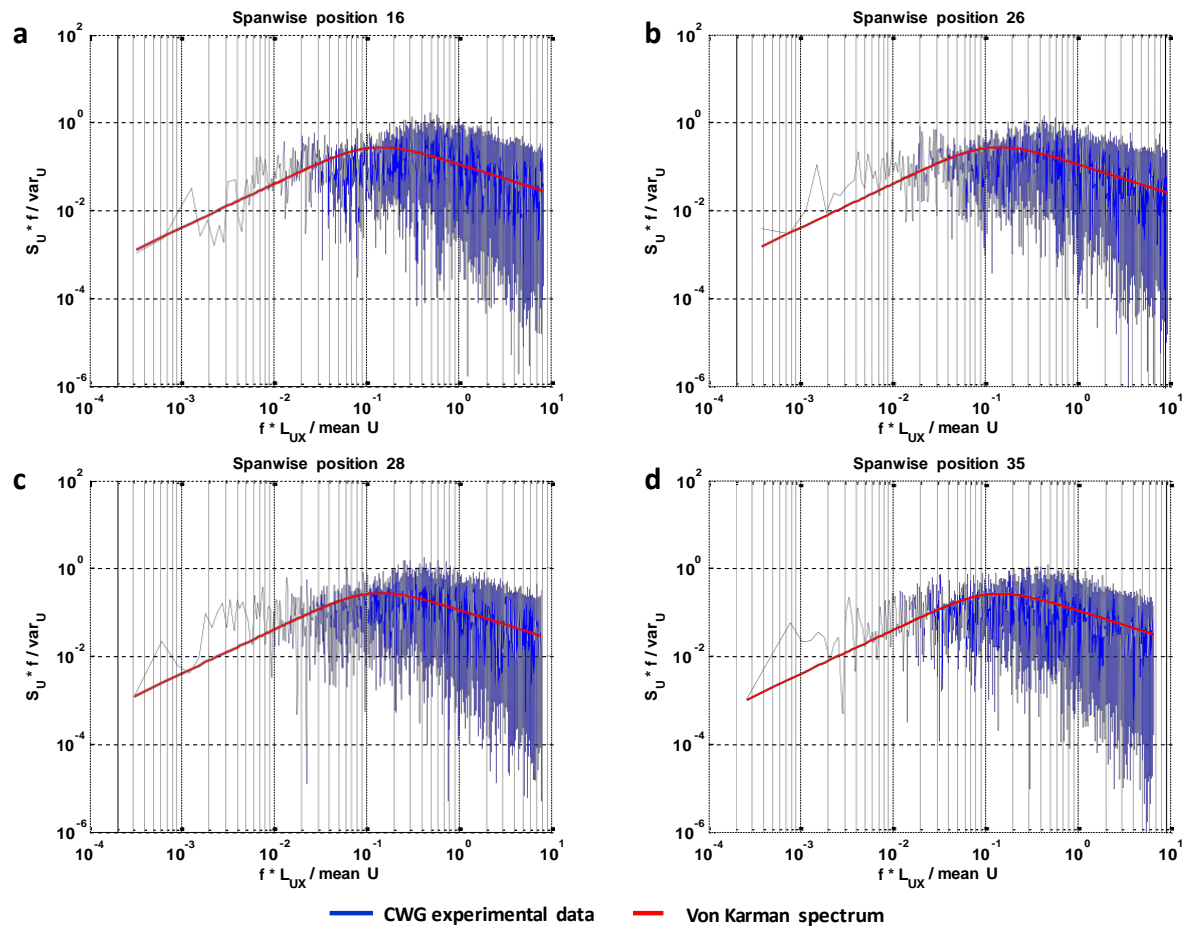
Figure A.32 Crosswind simulation (moving model tests configuration): normalised wind spectra for the streamwise velocity. a) Spanwise position 16. b) Spanwise position 26. c) Spanwise position 28. d) Spanwise position 35.

Duplicating table 4.3 (in section 4.3.2.1), table A.11 below reports the spanwise averages relative to the HWP presented in figure A.29 and calculated considering the central part of the air channel (between spanwise positions 5 and 59).

SPANWISE AVERAGES	[m/s]	[m/s]	[m/s]	[%]	[%]	[%]	[m]	[m]	[m]	[Pa]
CENTRAL SPAN (pos. 5 – 59)	12	0	0.2	17	9	9	0.42	0.05	0.04	- 150

Table A.11 Crosswind simulation (moving model tests configuration): spanwise averages at reference height

Table A.12 reports an additional estimation performed for the lateral turbulence integral scales at the spanwise position 24. According to the definitions of these parameters (ESDU, 1974), this estimation was based on a series of dedicated two-points simultaneous measurements carried out to enable calculation of the cross-correlation coefficient variation with respect to the spanwise distance from station 24.

	[m]	[m]	[m]
Spanwise position 24 (s* = - 0.8 m)	0.14	0.06	0.04

Table A.12 Crosswind simulation (moving model tests configuration): estimated lateral turbulence length scales

To enable processing of the moving model experiments raw data (section 5.2.2), the spanwise average-to-local ratios   and   , relating to the mean streamwise velocity and mean differential static pressure, respectively, were calculated from the flow characterisation data. They are reported in table A.13 relating to spanwise positions 16 and 35, where the trackside reference measuring probes were positioned. As highlighted in table A.13, the reference trackside sensor used for moving model tests was a Cobra probe placed at station 16.

Flow measurements were carried out 0.15 m downstream of the inlet and 0.2 m upstream of track 1 only for the VWPs at spanwise positions 26 and 28. Accordingly, the along-wind gradients (and   ) were estimated from such data. Taking into account measurements relating to the reference

height (i.e., = 0.12 m), the values indicated in table A.13 are the averages between the streamwise gradients obtained at each position.

spanwise average to local ratios	**spanwise position 16** (moving model test reference Cobra probe)		
	spanwise position 35 (moving model test reference Pitot-static tube)	0.905	0.999
Along-wind gradient			

Table A.13 Crosswind simulation (moving model tests configuration): spanwise average-to-local ratios and along-wind gradients for streamwise mean velocity and mean differential static pressure

A.4.1.2   Mean crosswind relative to a moving train at 30° yaw angle

As discussed in section 2.3.1, the relative wind seen by a moving train is given by the vector combination of the onset wind (in a fixed reference system) and of the vehicle speed. Accordingly, the mean wind experienced by a scale-model train during moving model experiments was calculated based on the onset wind data detailed in the previous section. Furthermore, a nominal train speed ( ) was considered that had a 20.8 m/s spanwise average (which ensured a nominal yaw angle) and a linear decrement within the crosswind section that led to a total speed decay of 1.1 m/s. Figure A.33 illustrates the '*velocity triangle*' defined consistent with the conventions adopted in this thesis.
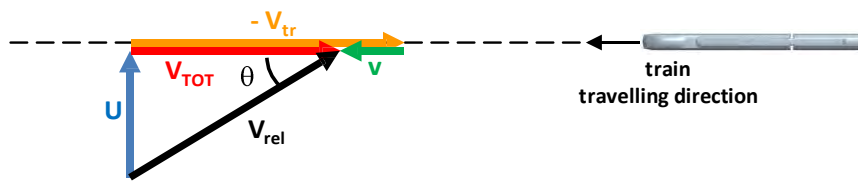
Figure A.33 Relative wind simulation (moving model tests): velocity triangle

Time histories of the relative wind velocity ( ) were calculated from the time series of the onset wind (recorded during the flow characterisation) associated with any spanwise position (*s**) as:

$$V_{rel}\left(t,s^{*}\right)=\sqrt{\left[U\left(t,s^{*}\right)\right]^{2}+\left[V_{TOT}\left(t,s^{*}\right)\right]^{2}}$$

(A.2a)

$$V_{TOT}\left(t,s^*\right)=V_{tr}\left(s^*\right)-v\left(t,s^*\right) \qquad \text{(A.2b)}$$

where t indicates the time and the different velocity components follow the conventions reported in figure A.27. The relative mean velocity   was given by the time average of each time history over its entire duration.

The HWP of the relative mean wind velocity is illustrated in figure A.34, where the individual contributions from which   has been determined are also specified. The corresponding spanwise average values are reported in table A.14.
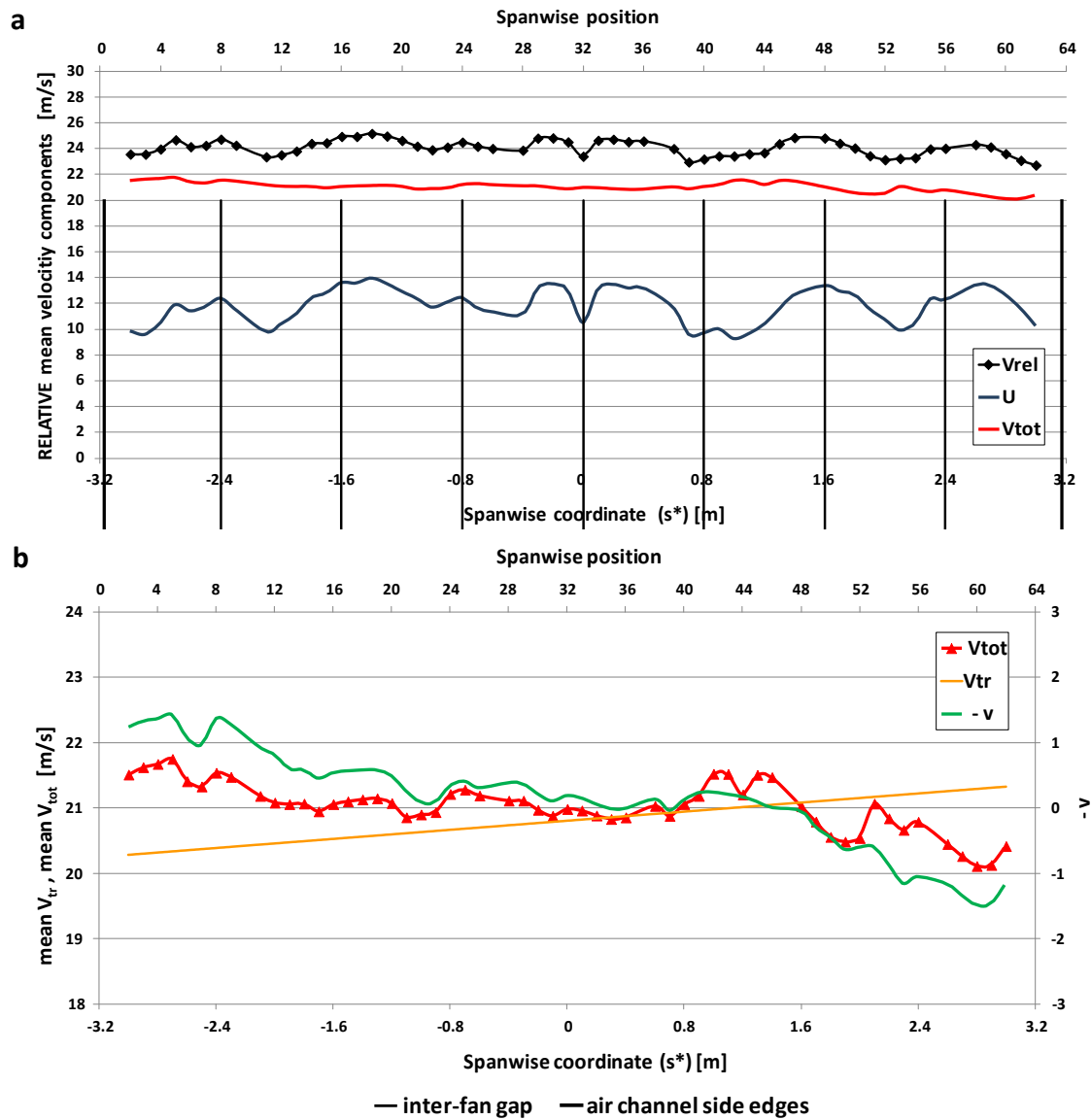
Figure A.34 Relative wind simulation (moving model tests): HWP. a) Relative mean wind velocity (and individual components). b) Lateral mean velocity components

SPANWISE AVERAGES	[m/s]	[m/s]	[m/s]	[m/s]	[m/s]
CENTRAL SPAN (pos. 5 – 59)	24	12	20.8	20.8	0

Table A.14 Relative wind simulation (moving model tests): spanwise averages at reference height

Figure A.34a outlines that the spanwise inhomogeneity of both streamwise and lateral velocity components is reflected in the behaviour of the relative mean wind velocity. Although the largest contribution to this irregularity is related to spanwise fluctuations of   , the largest peak-to-peak variation occurring on the HWP of   is significantly reduced in comparison with that characterising the HWP of   . Figure A.34b highlights that spanwise fluctuations occur also on the lateral mean wind velocity. However, it is interesting to observe that the lateral wind velocity, which increases in the direction of travel (i.e., from the right to the left hand side of figure A.34), has a trend that is opposite to the decrease of the train speed associated to the vehicle deceleration. As such, it is shown in figure A.34 that there is a 'compensation' between these two effects, which leads to a resultant lateral mean wind velocity relative to the train (   ) presenting an increased spanwise homogeneity.

A.4.2 Static tests

Dedicated flow measurements were carried out to characterise the crosswind simulation obtained in the presence of the CWG static test arrangement in a free channel (i.e., with no train model in place). HWPs were investigated both at inlet and in proximity of track 1 (as indicated in figure A.27b) at the reference height   = 0.12 m and spanning the portion of air channel width between the spanwise positions 15 and 33. This portion of span included the area where the scale-model train was positioned during static tests, which is highlighted in grey in the figures below.

Figure A.35 illustrates the HWPs of the three mean velocity components, while the turbulence intensity and integral length scale relating to the streamwise velocity are presented in figure A.36. The mean differential static pressure, then, is reported in figure A.37. In each figure, a comparison is made between HWPs measured 0.15 m downstream of the inlet and 0.2 m upstream of track 1. In

addition, the data obtained through the flow characterisation of the moving model test arrangement are superimposed.
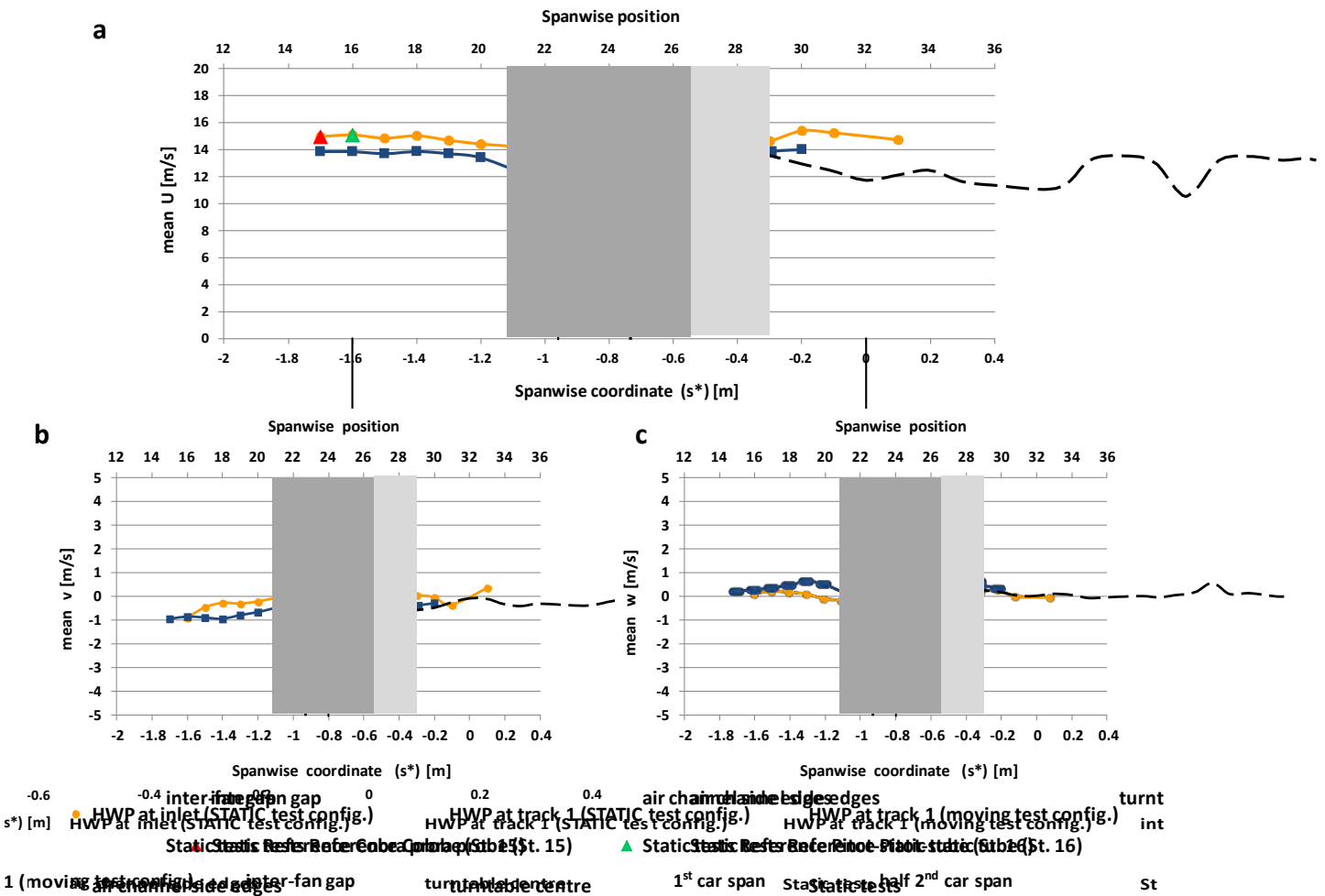
Figure A.35 Crosswind simulation (static tests configuration): mean wind velocity HWP. a) Streamwise component ( ). b) lateral component ( ). c) vertical component ( ).
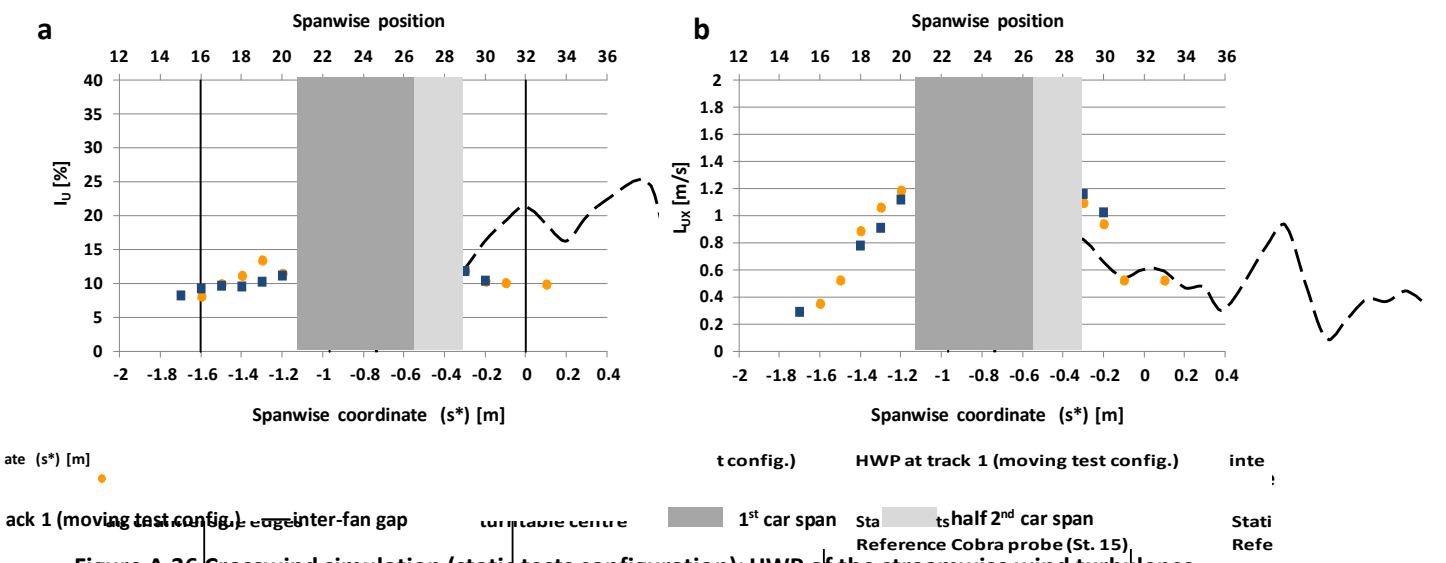
Figure A.36 Crosswind simulation (static tests configuration): HWP of the streamwise wind turbulence. a) Turbulence intensity ( ). b) Integral length scale ( ).
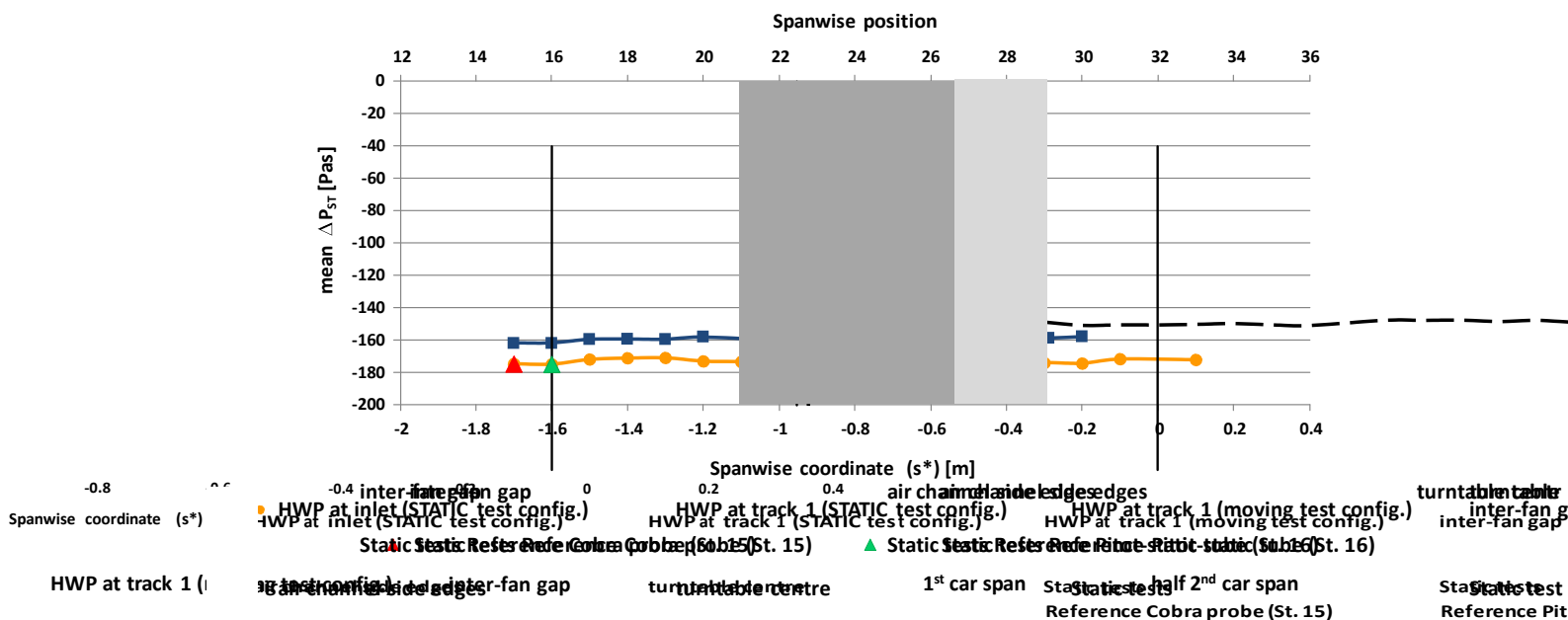
Figure A.37 Crosswind simulation (static tests configuration): mean differential static pressure (   ) HWP

The HWPs of the three mean velocity components (illustrated in figure A.35) denote a good level of spanwise uniformity within the span portion corresponding to where the train was positioned. A decrement in the streamwise velocity, which is quantified in table A.17 below, can be noticed between the inlet and track 1. At track 1, furthermore, a limited agreement can be observed with respect to the HWP relative to the CWG arrangement for moving model tests. The largest variations, however, which occur between the spanwise positions 24 and 29, work in favour of a better uniformity achieved in the presence the CWG arrangement for the static tests.

The turbulence intensity and integral length scales of the streamwise velocity are presented in figure A.36. A comparison between HWPs relating to the inlet and to track 1 indicates that, where changes occur,   tends to increase while   tends to reduce moving along-wind.

During the flow characterisation performed in the presence of the CWG static test configuration, a high sensitivity of the wind simulation was observed with respect to the presence (and position) of the additional vertical supports required underneath the air channel to sustain the tilting panels. This detail, as the presence of the notch in the ground oriented with a 30° angle with respect to the

streamwise direction, are hypothesised to have caused the aforementioned variations with respect to the HWP relating to the moving model test wind simulation.

The HWPs for the mean differential static pressure illustrated in figure A.37 confirm the positive gradient estimated in section A.4.1.1 (table A.17). Measurements referred to track 1 outline a difference with respect to the moving model test HWP, which remains quite consistent spanwise. This suggests that it might have been due to a different cause from that discussed regarding the variations of   and   . For example, it might have been caused by the slight offset of the ground level (and by the consequent slight reduction of the total channel height) determined by the addition of the static track bed which was part of the static test arrangement (section 4.3.2).

Tables A.15 and A.16 report the spanwise averages of the HWPs illustrated above (relating to both positions, 0.15 m downstream of the inlet and 0.2 m upstream of track 1). In the view of processing the data from static model tests, these values were estimated considering the spanwise positions from 18 to 30, which included the portion of span where the train model was placed. Furthermore, table A.17 reports the spanwise average-to-local ratios (and   ) and the along-wind gradients (and   ) for the mean streamwise velocity and mean differential static pressure, respectively.

	[m/s]	[m/s]	[m/s]	[%]	[%]	[%]	[m]	[m]	[m]	[Pa]
Spanwise average	14.4	0	-0.1	12	3	4	1.21	0.05	0.08	- 174

Table A.15 Crosswind simulation (static tests configuration): inlet spanwise averages at reference height (span portion between positions 18 and 30)

	[m/s]	[m/s]	[m/s]	[%]	[%]	[%]	[m]	[m]	[m]	[Pa]
Spanwise average	13.2	-0.5	0.3	12	5	5	0.94	0.07	0.05	- 159

Table A.16 Crosswind simulation (static tests configuration): track 1 spanwise averages at reference height (span portion between positions 18 and 30)

spanwise average to local ratios	**spanwise position 15** (static test reference Cobra probe)	0.952	0.981
	spanwise position 16 (static test reference Pitot-static tube)		
Along-wind gradient			

Table A.17 Crosswind simulation (static tests configuration): spanwise average-to-local ratios and along-wind gradients for streamwise mean velocity and mean differential static pressure

As for the moving model test configuration, so for the static test arrangement these coefficients were estimated based on the flow characterisation data. For the spanwise average-to-local ratios both spanwise positions where the trackside probes were located during the static tests were taken into considerations (with the Pitot-static tube at station 16 having been used as reference). The along-wind gradients were estimated from the spanwise averages indicated in tables A.15 and A.16.

Figure A.38 illustrates the spectra of the streamwise velocity and mean differential static pressure at three different spanwise positions (i.e., 22, 24 and 26) that were all within the portion of span where the scale-model leading car was positioned. As observed in figure A.31b above, so in figure A.38b a resonant peak arises at approximately 135 Hz (i.e., the blade passing frequency) only in the spectra of the differential static pressure.
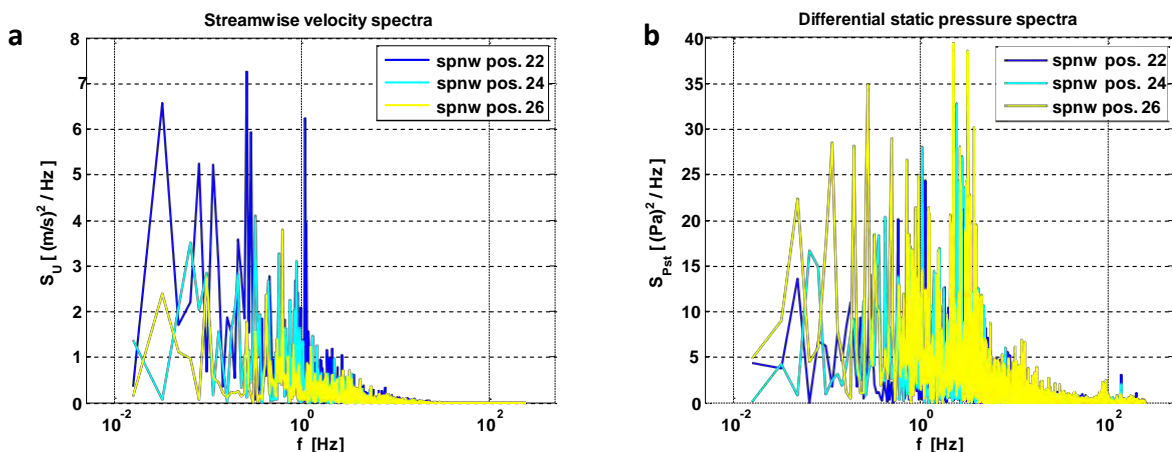
Figure A.38 Crosswind simulation (static tests configuration): wind spectra at the air channel inlet. a) Streamwise velocity b) Differential static pressure

A.5   New CWG assessment

One criterion to assess the new CWG relies on the examination of the characteristics and performance of such a system with respect to the design specifications (table A.5). In this view, as outlined in table A.18, the new CWG has been successful in meeting the design objectives set at the beginning of the development process. The spanwise mean wind velocity, the configuration of the system and the dimensions of the test section have met the respective targets. In addition, the new CWG is suitable to both moving and static tests and enables ground simulations different from a FG scenario in both cases. Not surprisingly, the characteristics of the crosswind simulation confirm the challenge posed by the extremely narrow space available inside the TRAIN rig building, where the apparatus had to be accommodated. Even in this regard, however, the performance of the newly constructed system is satisfactory because it meets the relaxed specifications that had been set following the initial feasibility study (section A.3.1).

	Design specification	Level of challenge	Final installation	Accomplished
Spanwise mean wind speed (at)	(at 30° yaw)	M (=) H (>)		✔
Quality of the flow simulation	Best spanwise uniformity possible	Relaxed spec.	(see figure A.40)	✔
	Lowest turbulence possible	Relaxed spec.		✔
System configuration	Ducted channel (over the tracks)	M	Closed test-section	✔
Air channel cross-section	Span $\square$ 4m Height $\square$ 1m	M	Span = 6.35 m Height = 1 m	✔
Mean wind direction	Perpendicular to the tracks	L	Perpendicular to the tracks	✔
Suitability to static tests		M	suitable	✔
Ground simulation flexibility		M	(Approximate) flat ground Escarpment	✔

Table A.18 New CWG assessment with respect to the design specification

A second assessment criterion for the new CWG relies on a comparison with the PCWG. As discussed in section A.2.3, the decision to construct a new CWG was made in order to overcome the limitations

of such a previously existing system (table A.2) and thus to improve the TRAIN rig crosswind test capability. In the following, figure A.39 illustrates the features of previous and new CWG and table A.19 presents a comparison of their performance. The spanwise average properties of the simulated mean wind (i.e., streamwise velocity and turbulence intensity), as well as the characteristics of the static and moving model experiments enabled by each system are examined. In addition, a further comparison in terms of crosswind simulation is illustrated in figures A.40 and A.41. The former examines the HWPs and one VWPs of the onset wind streamwise mean velocity (   ), the latter evaluates the HPWs of the relative mean wind velocity (   ) experienced by a moving train subjected to 30° yaw angle.

	PCWG	New CWG
Overall configuration	• blow-through design • open jet over the tracks	• such-through design • open circuit with ducted test-section
Fans	• axial flow fans • single-phase low speed (930 rpm) • 6 units	• axial flow fans • 3-phases 4 poles motor (1350 rpm) • 16 units
Air jet / test-section extension	• Span: 2.85 m • Height: 0.43 m • Length: 0.75 m (track board width)	• Span: 6.35 m • Height: 1 m • Length: 1.685 m
Ground simulations	• (Approximate) Flat Ground only •	• (Approximate) Flat ground • Escarpment
Spanwise mean wind (at)	• •	• •
Moving tests performance (C390 Pendolino model, 1:25 scale, 30° yaw angle)	• Maximum blockage ratio: 15% • Train speed: ~12.5 m/s • Re: ~1.2×10^5	• Maximum blockage ratio: 3% • Train speed: ~20.8 m/s • Re: ~2×10^5
Static tests performance (C390 Pendolino model, 1:25 scale, 30° yaw angle)	• Blockage ratio: 8% • Re: ~6×10^4	• Blockage ratio: 1% • Re: ~1.2×10^5

Table A.19 Comparison between new CWG and PCWG: characteristics and performance

Figure A.39 New CWG assessment: TRAIN rig internal view a) PCWG b) New CWG
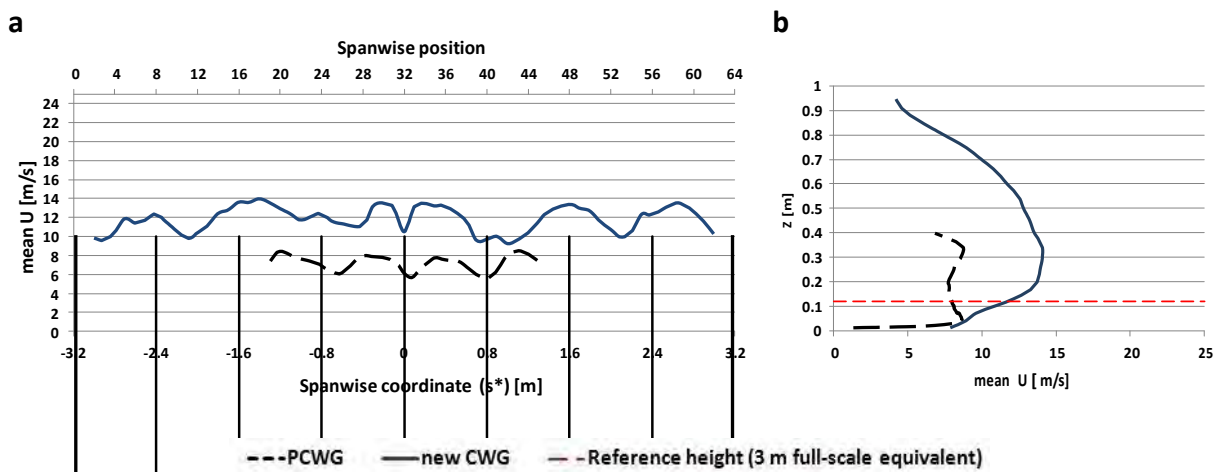
Figure A.40 Comparison between new CWG and PCWG: streamwise mean wind velocity ( )
a) HWP b) VWP (PCWG spanwise position 15; new CWG spanwise position 28)
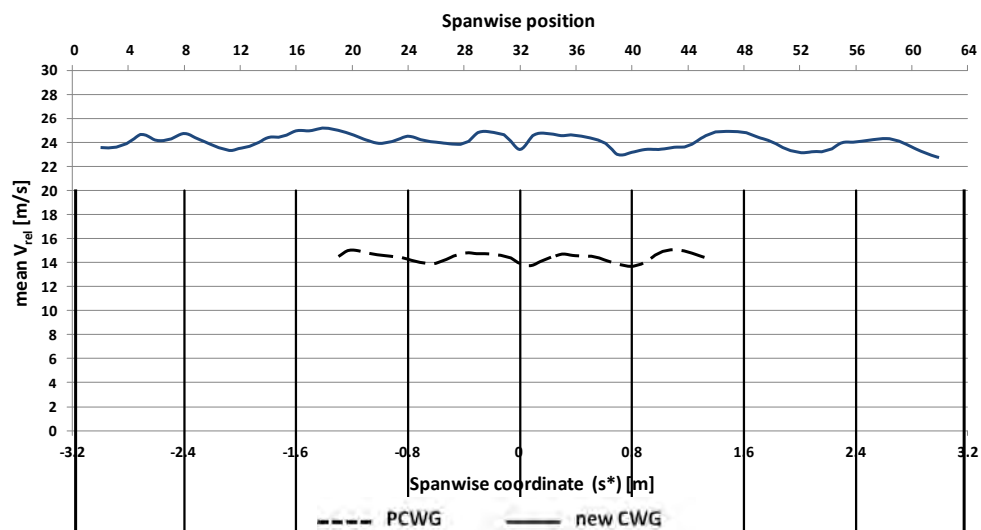
Figure A.41 Comparison between new CWG and PCWG: relative mean wind velocity ( ) at 30° yaw angle
(PCWG   = 12.5 m/s; new CWG   = 20.8 m/s)

Examining the overall layout and dimensions of the previous and of the current system, the significant change represented by the new CWG can be appreciated in figure A.39. The open-jet blow-through design of the PCWG has been replaced by a ducted test section associated with a suck-through design. Furthermore, a bank of 4 low-speed fans has been substituted by an array of 16 units running at higher speed. Finally, both the length along the track and the height of the crosswind section have been more than doubled. This ensures a significant reduction of the blockage ratios (which during the tests of this research did not exceed 3%) and eases the analysis of moving model tests data (section 5.2.2).

It is demonstrated in table A.19 and in figures A.40 and A.41 that the new CWG ensures an increment of spanwise mean wind velocity (at the   = 0.12 m) from ~7.2 to ~12 m/s. This enabled the moving model tests of this research (that aimed for 30° yaw angle) to be carried out at a higher vehicle speed (nominally, 20.8 m/s rather than 12.5 m/s) and, in turn, led to a higher relative mean wind velocity. In addition, it allowed to keep a good run-to-run consistency in the train speed and, therefore, contributed to reach a relatively high run acceptance rate (i.e., ~85%) during the moving model tests.

A degree of spanwise irregularity affects the HWP relating to the new CWG. However, in light of the constraints imposed to the design, this was not a critical improvement to be aimed for. Furthermore, a good progress in the quality of the wind simulation is represented by the VWPs (of the streamwise mean velocity) delivered by the new CWG, which are characterised by a positive gradient upwards. As indicated by the results of prototype tests, this achievement is mainly related to the adoption of a suck-through design.

Appendix B

Pressure transducers calibration

B.1 Introduction

This appendix illustrates the static calibration performed for the differential pressure transducers employed in this research. The HCLA12X5PB and HCLA02X5PB differential pressure transducers used for on-board and trackside measurements, respectively, were calibrated in comparison to a Betz micro-manometer [Acin Instrumenten bv], which consists of a liquid U-manometer and has an accuracy of 1 Pa and a resolution of ±0.5 Pa (ACIN, 2012).

B.2 Calibration process

The transducers of the same type were calibrated in parallel by connecting them to the Betz using a close pneumatic circuit. Such a circuit comprised of two separate arms. One connected the HPP of the transducers to the high pressure port of the Betz unit and, in parallel, to a manual pump. The other connected the LPP of the transducers to the low pressure port of the Betz unit. Using the manual pump, a nominal differential pressure (   ) was applied to the system and then increased step by step, in order to cover the entire nominal measuring range of the transducers (i.e., ±1250 Pa and ±250 Pa for the on-board and trackside transducers, respectively). At each step of this process, the nominal differential pressure was set according to the reading provided (in Pascal) on the scale of the Betz unit. Once the system had stabilised, time histories of the electronic signals delivered by every transducer (indicated in this appendix by *t*) were recorded for 10 s and averaged over their entire duration to obtain the corresponding 'time averaged actual voltage readings'   .

Data recorded for a differential pressure of zero Pascal (i.e.,   ) provided 'zero pressure offset'

voltages, i.e., the output voltages (one for each transducer) associated with no pressure difference.

Indicated as   , they were the reference values with respect to which each output voltage variations

    (corresponding to a nominal differential pressure   ) was calculated:

$$\Delta V_t \left(\Delta P_N \right) = V_{Rt} \left(\Delta P_N \right) - V_{0t} \tag{B.1}$$

It was noticed that   showed a quite high sensitivity to the input voltage provided by the power

supply unit and, as such, presented a slight difference from the nominal voltage of 2.25 V declared by

the manufacturer. Furthermore, it was found that   varied from one transducer to another, even in

the presence of the same input voltage (supplied in parallel by the same power supply unit).

Consequently, as explained in chapter 4 and 5 (and further detailed in the following appendix C)

dedicated data acquisitions were carried out during the static and moving model tests of this

research in order to monitor and take into account any drift of the 'zero pressure offset' associated

with each individual transducer.

The data collected during the calibration process are illustrated in figure B.1a and B.1b relating to the

on-board and trackside transducers, respectively, with the output voltage variations indicated on the

horizontal axis and the corresponding nominal differential pressures specified on the vertical axis. As

expected according to the manufacturer specifications a linear trend can be observed for both series

of transducers.
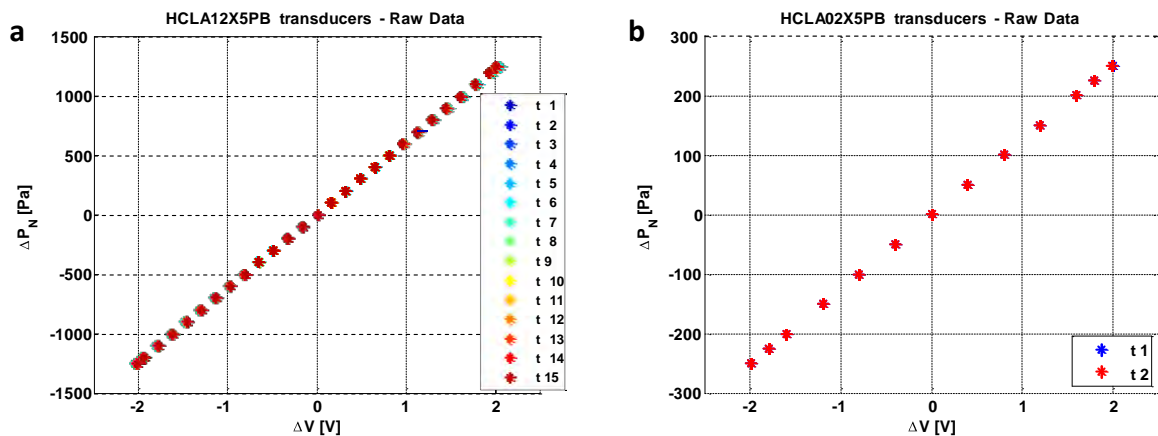
Figure B.1 Pressure calibration raw data a) On-board transducers b) Trackside transducers

B.3   On-board pressure transducers (HCLA12X5PB)

B.3.1   Nominal Linear Calibration (NLC)

A '*Nominal Linear Calibration*' (NLC) curve was defined as:

$$\Delta P_{NLC,t} = \Delta V_t \cdot K_{NLC}$$
(B.2)

where   is the nominal linear calibration factor, while   is the measurement of differential

pressure (expressed in Pascal) obtained using this particular calibration.   is the same for all the

(HCLA12X5PB) transducers that have the same range and corresponds to   .

To assess the accuracy of the NLC, a 'nominal linear calibration error' (   ) was defined as

$$E_{NLC,t}\left(\Delta P_N\right) = \Delta P_{NLC,t} - \Delta P_N$$
(B.3)

It is the difference, in terms of differential pressure, between the value calculated in accordance to

the NLC and the nominal value measured by the Betz manometer. The variation of this error within

the measuring range was calculated for each transducer and is illustrated in figure B.2.
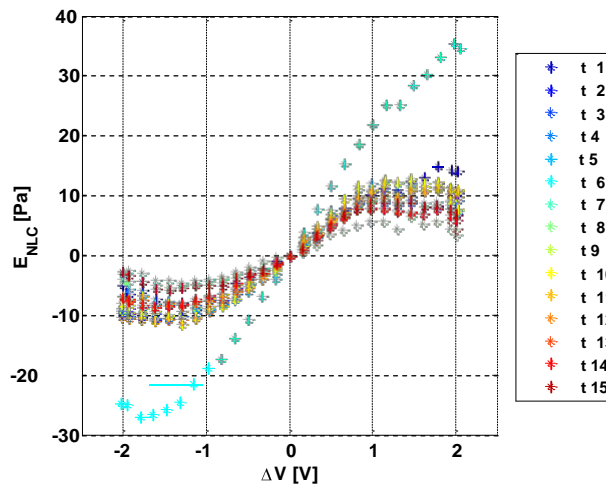
Figure B.2 Nominal linear calibration error (on-board transducers)

The data indicate that the calibration error tends to reach the maximum in between   V and

          , both in the positive and negative range. For 14 over the totally 15 transducers that were

used, such a maximum is of the order of ±12 Pa. Only transducer 6 shows a maximum error of

approximately ±30Pa.

B.3.2 Actual Linear Calibration (ALC)

A linear regression analysis was performed in order to reduce the calibration error associated with the NLC. Considering each transducer individually, the line of best fit through the data reported in figure B.1 was calculated imposing the passage through the origin. This led to obtain the '*actual linear calibration factors*' (one for each transducer) specified in table B.1.

Transducer (t)	1	2	3	4	5	6	7	8
[Pa/V]	619.4	619.1	620.3	619.4	620.5	609.2	621.8	622.5

Transducer (t)	9	10	11	12	13	14	15
[Pa/V]	619.3	619.3	619.8	619.1	621.2	620.9	621.7

Table B.1 Actual linear calibration factors (on-board transducers)

Using these calibration factors, the corresponding ALC curves were given by:

$$\Delta P_{ALC,t} = \Delta V_t \cdot K_{ALC,t}$$
(B.4)

and the associated calibration errors were calculated as:

$$E_{ALC,t}\left(\Delta P_N\right) = \Delta P_{ALC,t} - \Delta P_N$$
(B.5)

Figure B.3 shows the evolution of over the measuring range. The largest magnitudes of such an error occur at about V and, since less than ±8Pa, they are smaller with respect to what observed for the NLC. Furthermore, since a dedicated calibration factor was defined for each transducer, the discrepancy previously observed in the behaviour of transducer 6, in this case has been properly taken into account and, therefore, it no longer determines a large calibration error.
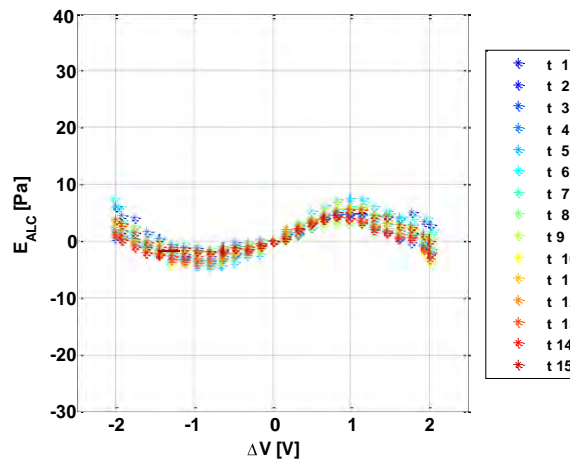
Figure B.3 Actual linear calibration error (on-board transducers)

B.3.3 Actual Cubic Calibration (ACC)

A variety of calibration curves were examined in order to interpolate the static calibration data reducing the calibration error. Such a process led to identify a set of '*Actual Cubic Calibration*' (ACC) curves (one for each transducer) having the following form:

$$\Delta P_{ACC,t} = C_{3,t} \cdot \Delta V_t^3 + C_{2,t} \cdot \Delta V_t^2 + C_{1,t} \cdot \Delta V \qquad \text{(B.6)}$$

where $C_{1,t}$, $C_{2,t}$ and $C_{3,t}$ indicate the differential pressure measurement coefficients obtained by employing static calibration data through a regression analysis. The values of these coefficients relating to each transducer are reported in table B.2.

	C_3	C_2	C_1
	[Pa/V^3]	[Pa/V^2]	[Pa/V]
t 1	1.353	-1.051	615.0
t 2	1.413	-0.139	614.4
t 3	1.489	0.217	615.4
t 4	1.534	0.077	614.3
t 5	2.507	-0.533	612.3
t 6	2.121	-1.159	602.0
t 7	1.440	-0.701	617.1
t 8	1.087	0.003	619.0
t 9	1.328	-0.209	614.9
t 10	2.159	-0.081	612.2
t 11	1.499	-0.468	614.8
t 12	1.558	0.088	613.9
t 13	1.653	0.238	615.8
t 14	1.380	0.206	616.4
t 15	1.567	-0.507	616.6

Table B.2 Actual cubic calibration factors (on-board transducers)

Consistent with the above, the corresponding calibration error was given by:

$$E_{ACC,t}\left(\Delta P_N\right) = \Delta P_{ACC,t} - \Delta P_N \qquad \text{(B.7)}$$

and its distribution over the measuring range is illustrated in figure B.4. It can be observed that a significant reduction in this error has been achieved using the ACC rather than either the NLC or the ALC: the errors of all the transducers are similar and have magnitudes of the order of ±4 Pa.
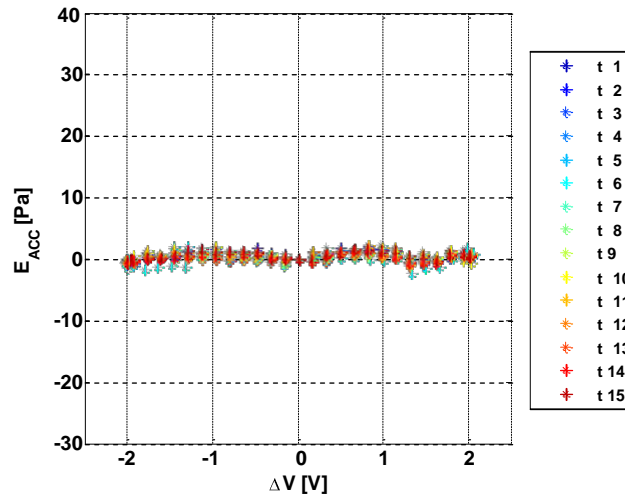
Figure B.4 Actual cubic calibration error (on-board transducers)

B.4 Trackside pressure transducers (HCLA02X5PB)

An analysis corresponding to that described in section B.3 was carried out also for the two trackside pressure transducers that were employed in combination of the Pitot-static tube. The static calibration data being shown in figure B.1b, the procedure described in the previous section was applied to obtain the different calibrations curves and the relative calibration errors illustrated in the following. It is worth noting that in this case a ALC was adopted because an ACC would have produced no benefit in comparison with it.

B.4.1 Nominal Linear Calibration (NLC)
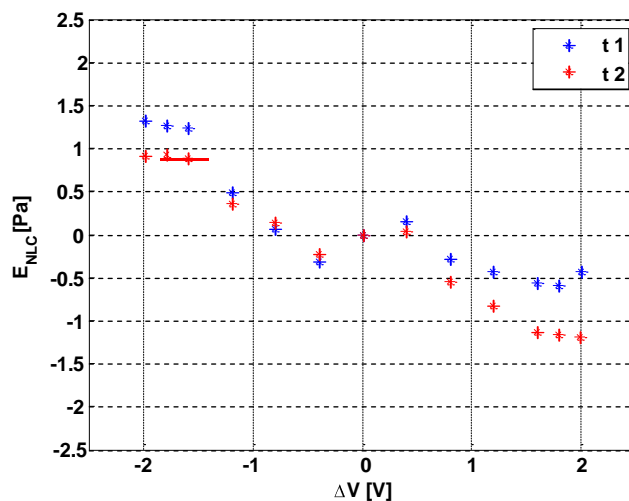
Figure B.5 Nominal linear calibration error (trackside transducers)

[Pa/V]	125
Max [Pa]	±1.5

Table B.3 Nominal linear calibration factors (trackside transducers)

B.4.2 Actual Linear Calibration (ALC)
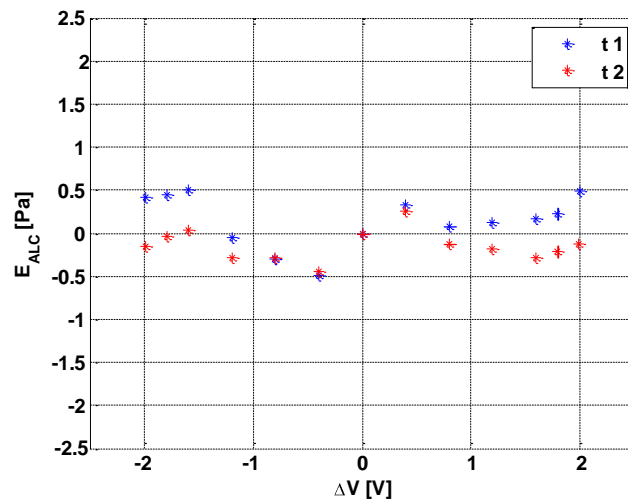
Figure B.6 Actual linear calibration error (trackside transducers)

	t 1	t 2
[Pa/V]	125.46	125.53
Max [Pa]	±1	±1

Table B.4 Actual linear calibration factors (trackside transducers)

Appendix C

TRAIN rig test procedures

C.1   Introduction

This appendix includes a description of the test procedures that were applied for the TRAIN rig experiments undertaken in this research. Section C.2 presents the procedure for the static tests. Section C.3 illustrates the standard operation of the TRAIN rig propulsion system and, in addition, the test procedure that was developed to enable moving model experiments in the presence of a crosswind simulation.

C.2   Crosswind static tests

Table C.1 illustrates the sequence of tasks that were carried out during any run of the static tests and, at each step, it specifies the status of both the CWG and the instrumentation.

The sequence starts with the scale-model train already positioned inside the air channel. First, the reference pressure circuit was set by connecting it to the static pressure signal from the Pitot-static tube. After that, the on-board data logger was connected to a laptop positioned outside the CWG (using a 10 m long communication cable) in order to control the on-board measuring system in real time and launch the data acquisition manually (i.e., without using self-triggering). Before the fans were activated, the Cobra probe was zeroed (using the specific function enabled in the *Device Control* software) to remove any 'zero velocity offset'. Furthermore, time histories of 30 s were sampled in still air conditions recording the 'zero pressure offset' ( ) associated with each of the on-board and trackside pressure transducers (these data were used in the data reduction illustrated in section 5.2.1).

	Task	CWG status	Trackside instr. status	On-board instr. status
1	Setting of reference pressure circuit of the on-board pressure transducers	off	stand by	stand by
2	Plug in of the logger-laptop communication cable into the model	off	stand by	stand by
3	**Still air data acquisition** (zero pressure offset record) - trackside instruments - on-board measuring system	off	data sampling: T_{SAMP} = 30 s F_{SAMP} = 1 kHz	data sampling: T_{SAMP} = 30 s F_{SAMP} = 4 kHz
4	Cobra probe zeroing	off	stand by	stand by
5	**CWG switch on**	start up (50 s)	stand by	stand by
6	**Crosswind data acquisition** - trackside instruments - on-board measuring system **Manual data recording:** - ambient conditions	full operation running	data sampling: T_{SAMP} = 60 s F_{SAMP} = 1 kHz	data sampling: T_{SAMP} = 30 s F_{SAMP} = 4 kHz
7	**CWG stop**	stopping	stand by	stand by
8	**Data download**	stopping	stand by	stand by
9	Unplug of the logger-laptop communication cable from the model	stopping	stand by	stand by
10	Removal of the reference pressure line connection.	stopping	stand by	stand by

Table C.1 Sequence of tasks for a static test single-run

Once the CWG had been switched on, a start up time of approximately 50 s was required to reach the full-operational mode. After that, in a settled crosswind, time histories of 60 s were recorded for both the on-board and trackside measurements, while the readings concerning the ambient conditions were manually recorded. The acquisition time was consistent with what is typically adopted for similar wind tunnel experiments (Sanquer et al., 2004) and was found sufficient for obtaining statistically stable conditions in these particular tests. Since the two data acquisition systems (i.e., on-board and trackside) were independent, they were not perfectly synchronised (which was not specifically required for the purposes of these experiments) and different sampling frequencies were used. Trackside measurements were sampled at 1 kHz, which largely covered the spectral content of the simulated wind (appendix A). The surface pressure distribution on the train, instead, was sampled at 4 kHz for consistency with the moving model tests.

After completion of the data acquisition, the data collected by the on-board system (and automatically stored in the internal memory card) were downloaded into the computer. Finally, to prepare the model for removal from the CWG, the connection between the logger and the laptop was removed, as well as the link between the Pitot-static tube and the on-board reference pressure circuit.

C.3 Moving model tests

The standard TRAIN rig operation for moving model tests requires to execute two types of activities. A first group of tasks comprise of the activation and deactivation of the propulsion system and need to be completed once per day, at the beginning and at the end of the session. A second series of activities form the '*firing process*' and, as such, have to be repeated for each run. For standard TRAIN rig tests (which do not involve a crosswind simulation) these activities consist of setting up the launching and braking mechanisms, operating the trackside instrumentation and executing the firing (through the *firing procedure* described below). For experiments carried out in the presence of a crosswind simulation, they include also the operation of the CWG, of the on-board pressure measuring system and of trackside flow measuring instrumentation.

C.3.1 Model vehicles propulsion system and *firing procedure*

Firing mechanism

The firing mechanism is based on the use of pre-tensioned elastic bungees in combination with a rope and pulley system set according to the scheme shown in figure C.1. The *firing procedure* consists of two phases: '*loading'* and '*launch*'. During the *loading* the bungees are put under tight using a main winch to pull the firing carriage in the direction indicated in figure C.1. To keep the firing rope constantly tensioned, a secondary winch progressively retracts the train model on the track within the acceleration section. Both winches are driven by electric motors. The tension applied into the system is measured by a load-cell mounted on the firing carriage and its value is monitored in

real time and shown by a digital display on the control panel. This tension determines the vehicle speed and its target value is set based on a calibration curve that depends on the mass of the model.
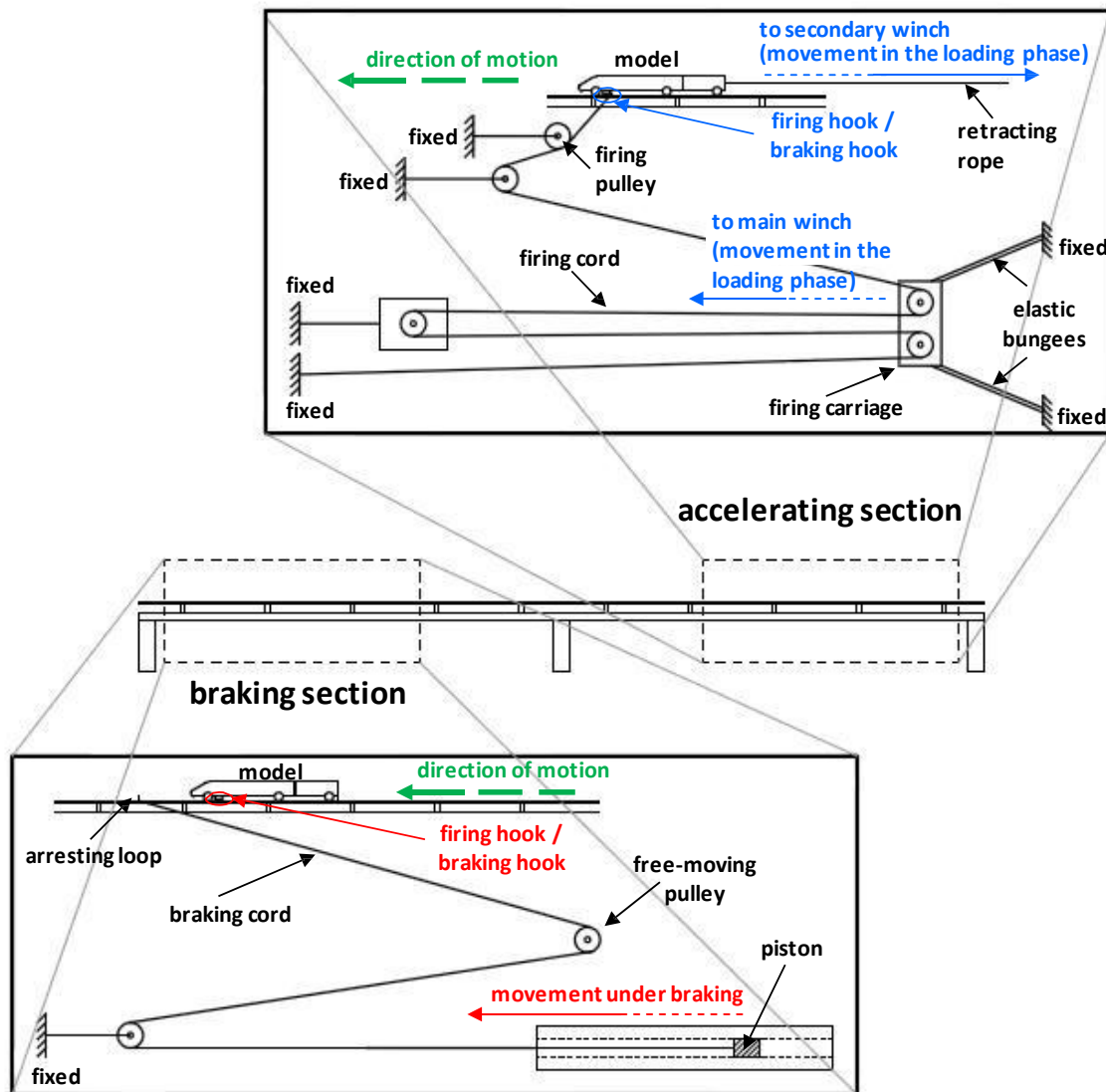
Figure C.1 TRAIN rig propulsion system scheme

Once the desired level of tension is reached, the *launch* starts by releasing the connection between the main winch and the firing carriage (pressing the '*firing button*' on the control panel). As soon as this happens the bungees retract, so dragging the firing carriage back into its original position. Since the firing rope runs through two pulleys positioned on that carriage, a force is transmitted through the rope and reaches the vehicle model. The initial impulse is sufficient for braking the elastic bound that links the vehicle to the retracting rope. Once free to move forward, the model is pulled by the firing rope and accelerates until it runs over the firing pulley at the end of the launch section. At this

point the firing rope automatically detaches from the firing hook underneath the train chassis (figure 4.17b in section 4.4) and projects the model into the test section at the desired speed.

Braking mechanism

The braking mechanism comprises one primary and two auxiliary systems. The primary brake is based on a piston dragged through a deformable tube (made of polyurethane) by a Kevlar rope that catches the vehicle model at the entry of the braking section. By dissipating the energy associated with the vehicle movement, this system ensures a gentle deceleration in order not to damage the model. The secondary brake employs an elastic cord anchored into a fixed point and terminating with a loop that is set on the track for catching the model approximately in the middle of the decelerating section. The tertiary brake consists of a '*buffer stop*' made of impact absorbing foam positioned at the end of the track. These auxiliary systems come into operation only if the primary brake fails.

C.3.2 Crosswind moving model tests

Table C.2 below illustrates the moving model test procedure developed as part of this research and adopted for undertaking moving model tests in the presence of a crosswind simulation. The sequence of tasks assumes that the train scale-model has been already positioned on the track and that the configuration of the pressure measuring system has been already set. In table C.2, tasks related to standard TRAIN rig operation are written in grey, while in black are those concerning the CWG and the instrumentation. Individual activities are listed in the chronological order of execution and a nominal timescale referred to the acquisition time interval of the trackside instrumentation is included in the first column (with a run-to-run variability range of ±10 s to be assumed). In addition, the status of the train model, of the CWG and of the additional instrumentation employed for crosswind tests is specified relating to every activity.

	MOVING MODEL TESTS SINGLE-RUN PROCESS				
Time [s]	**Task**	**Train model status**	**CWG status**	**Trackside instr. status**	**On-board instr. status**
-	**Braking mechanism preparation**	standing still (braking area)	Off	stand by	stand by
-	**Launching mechanism preparation**	standing still (accel. area)			stand by (battery charging)
0	**Trackside instrumentation setting** - light sourcees switch on - Cobra probe zeroing - trackside data acquisition launch	standing still (at the edge between test and accel. section)		data sampling T_{SAMP} = 240 s F_{SAMP}= 1 kHz	
10	Operator walking from the CWG to the acceleration section				
20					
30	**CWG switch on**		**Start up (50 s)**		
40	**On-board instrumentation setting** - reference pressure circuit venting - reference pressure circuit sealing - on-board data acquisition launch - removal of the logger-laptop communication cable				
50					
60					**trigger countdown (90 s)**
70	Testing room clearing				
80	**Loading & Launch process**		**full operation (110 s)**		
90	• control panel activation • speed detectors activation				
100	• loading phase	**moving backwards (within the accel. section)**			
110					
120					
130					
140	• wait	**standing still (within the accel. section)**			**data sampling** T_{SAMP} = 40 s F_{SAMP} = 4 kHz
150					
160					
170	• **MODEL LAUNCH (c.a. 3 s)**	**RUNNING**			
180	• control panel deactivation	standing still (braking area)			
190	**CWG stop**		stopping inertial slow down		stand by
200	**Manual data recording**				
210	- ambient conditions				
220	- train speed measurements				
230	Operator walking from the control room to the braking section				
240					
-	Light sourcees switch off				
-	**On-board data download**		off	stand by	**data downloading**

Table C.2 Sequence of tasks for a moving model test single-run

Most of the tasks relating to the operation of the CWG and of the instrumentation specifically required for crosswind tests were executed after the propulsion system had been set up and before the model was fired. Therefore, the *loading and launching process* described above was not modified, but it was just timed in order to make sure that the launch was performed whilst the on-board measuring system was sampling.

The flow measuring instrumentation at the trackside was manually operated and data were sampled at 1 kHz (as in the static tests) and recorded continuously for 240 s. Of these, the ~110 s recorded whilst the CWG was in full operation provided information on the crosswind conditions. In addition, the initial 20 s relating to a still air condition provided the 'zero pressure offset' (   ) for the trackside pressure transducers that was used for data reduction (section 5.2.2.2).

Different from the trackside measurements, the data acquisition of the on-board pressure measuring system was started by using an automatic trigger based on a 90 s countdown. The countdown was calibrated to ensure sufficient time for the operator to leave the testing room and the *loading* phase of the firing procedure to be completed (with a margin of 10-20 s in case of minor issues or delays). A countdown timer integrated in the data logger control software enabled the proper timing of the *launch*. Once triggered, the on-board data logger sampled data at 4 kHz for 40 s. The highest sampling frequency available was used in order to reduce any aliasing-related issue and to maximise the number of samples collected when the train was travelling within the CWG. Considering the combination of the nominal vehicle speed and the CWG total span (i.e., 20.8 m/s and 6.35 m, respectively), ~1220 samples were recorded in ~0.3 seconds.

Since the launch was normally executed 10 to 20 s after the on-board data logger had started sampling, both ends of the time histories were recorded whilst the train was standing still on the track, either before or after the launch. Considering that at those stages the on-board reference pressure circuit was sealed, the offset between the ambient pressure and the reference pressure was measured. This information was used for assessing the reference pressure drift as discussed in

section 4.7. Furthermore, through proper the data reduction (section 5.2.2), it enabled the moving model surface pressure measurements to be normalised with respect to the crosswind static pressure, thus keeping consistency with the convention adopted for static tests.

In addition to the activities specified in table C.2, during any moving model test session, time histories of 30 s were recorded three times a day (approximately every four hours) whilst the scale-train was standing on the track in still air, with the reference pressure circuit vented. These records provided measurements for the 'zero pressure offset' of the on-board pressure transducers (whose stability during a four-hour session was measured in the order of ±1 Pa).

Appendix D

Moving model tests - Sensitivity to the number of runs

D.1 Introduction

This appendix presents a sensitivity study performed in order to determine the number of moving model test runs required to obtain stable ensemble averages. This study was undertaken using the data collected during the early stages of the measurement campaign, when sets of 20 runs were carried out monitoring the pressure taps on loop 2 and loop 6, and comprises two different analyses. Presented in sections D.2 and D.3, respectively, these analyses provided consistent indications and led to use series of 15 runs in order to calculate the ensemble averages time series of the present research.

D.2 Correlation coefficient analysis

The first sensitivity analysis relied on the calculation of a correlation coefficient between ensemble average time histories based on a different number of runs. First, ensemble average time histories were computed based on single-run time series (relating to each pressure tap i) for a total number of runs ( ) increasing from 2 to 20. Secondly, the correlation coefficient was calculated between each pair of these ensemble average time histories and , associated with n-1 and n number of runs (with 3 $\leq$ $\leq$ 20), respectively. Finally, the increment of such a correlation coefficient with respect to the total number of runs (n) was determined as:

$$\Delta\left(\rho_i\right)_n = \left(\rho_i\right)_{n-1,n} - \left(\rho_i\right)_{n-2,n-1} \quad (\text{with } 4 \leq n \leq 20) \tag{D.1}$$

Low values of $\quad$ indicate that the increment in the number of runs from $\quad$ -1 to $\quad$ leads to small modifications in the ensemble average time histories. Therefore, the closer the values of $\quad$ are to zero, the higher is the stability of the ensemble averages.

Figure D.1 Moving model tests total number of runs: correlation analysis
a) loop 2   b) loop 2   c) loop 6   d) loop 6
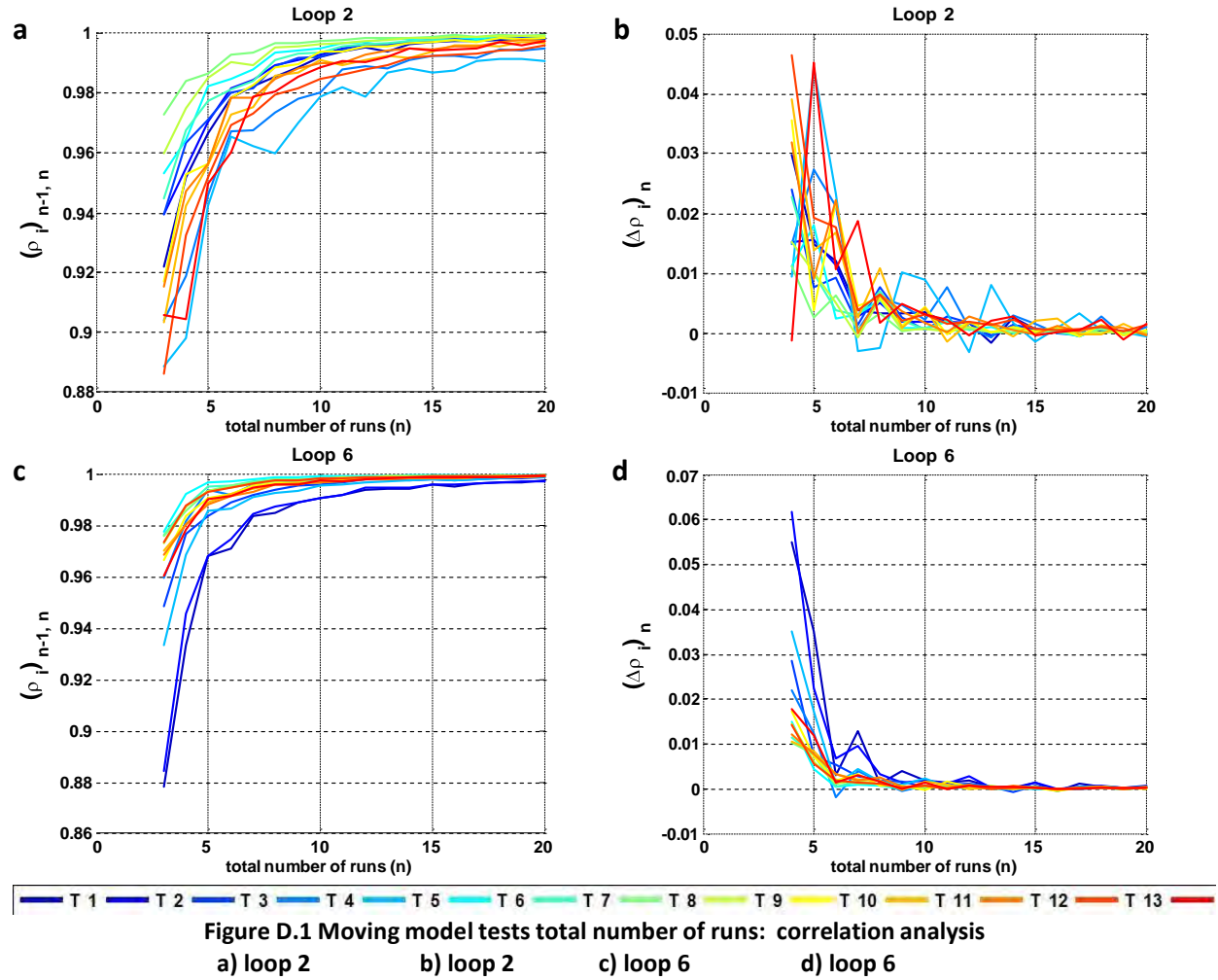
As illustrated in figures D.1a and D.1c, the correlation coefficients $\quad$ tend to progressively increase with respect to the number of runs both on loop 2 and on loop 6, positioned respectively on the nose and in the centre of the train. Furthermore, since the gradient becomes progressively smaller, figure D.1b and D.1c show that $\quad$ decreases with the total number of runs and reaches values very close to zero for $n = 10$ on loop 6 and $n = 15$ on loop 2.

D.3   Standard deviation analysis (Bootstrap method)

The second sensitivity analysis examined the evolution of the standard deviation of the ensemble average time histories with respect to an increasing total number of runs ( ).

Considering each pressure tap   (on loops 2 and 6), the 20 (in total) single-run time histories formed a normally distributed population indicated as   , where   identifies a generic single-run. The equivalent of the mean and standard deviation relating to this population, defined with respect to the total number of runs ( ), were two time histories indicated as   and

and are referred to in the following as '*ensemble average*' and '*ensemble standard deviation*', respectively. In addition, a '*standard deviation of the ensemble average time history*' was defined as follows:

$$\sigma_{\left(C_{Pi,ENS}\right)_n}(t) = \frac{\left(C_{Pi,STD}(t)\right)_n}{\sqrt{n}} = \frac{\sqrt{\frac{1}{n-1}\sum_{r=1}^{n}\left(C_{Pi,r}(t) - \left(C_{Pi,ENS}(t)\right)_n\right)^2}}{\sqrt{n}} \tag{D.2}$$

This parameter indicates (at any instant in time   ) the semi-amplitude of the 68% confidence interval associated with   and, as such, it provides an indication on the uncertainty relating to the best estimate provided by such an ensemble average time history (Taylor, 1996). Therefore, the smaller   , the more accurate the estimation provided by   .

In order to monitor the variation of such an uncertainty with respect to the total number of runs ( ),   was computed for   raising from 2 to 20. In addition, its time-average   (over the entire time window associated with the train travelling within the crosswind section) was also calculated.

Since the total number of single-run time histories was rather small (i.e., 20), there was a doubt that the outcome of such a conventional statistical analysis might have been not particularly robust. Therefore, also a bootstrap method (Zoubir and Boashash, 1998) was applied and an additional analysis was performed using the Matlab bootstrap toolbox from Zoubir and Iskander (n.d.). For each pressure tap , a series of = 500 bootstrap realisations having 20 single-run time histories each, were extracted drawing with replacement from the original population . These bootstrap realisations are indicated in the following as , with an *apex* added in the notation to distinguish them from the original population, and a subscript (varying from 1 to = 500) indicating their ordinal number. According to the bootstrap principle, the *standard deviation of the ensemble average time history* (defined in equation (D.1)) was estimated as follows:

$$\sigma_{\left(C_{Pi,ENS}\right)_n}(t) \cong \sigma^{BS}_{\left(C_{Pi,ENS}\right)_n}(t) = \sqrt{\frac{\sum_{b=1}^{B}\left(\left(C_{Pi,ENS}(t)\right)'_{b,n} - \frac{1}{B}\sum_{b=1}^{B}\left(C_{Pi,ENS}(t)\right)'_{b,n}\right)^2}{B-1}} \tag{D.2}$$

In equation (D.2), indicates an ensemble average time history calculated from the first single-run time histories that formed the bootstrap realisation and the superscript ' ' is included in the notation of in order to distinguish the parameter estimated through the bootstrap method from the one defined in equation (D.1). As in the above, in order to monitor the evolution with respect to the total number of runs, and the corresponding time-average were calculated for varying from 2 to 20.

The evolution of and of with respect to the number of runs is illustrated in figures D.2a and D.2b for the pressure taps on loop 2, and in figures D.2c and D.2d for those on loop 6. In all figures the error bars indicate the standard deviation of (or) calculated over their time duration.

Figure D.2 Moving model tests total number of runs: standard deviation analysis
a) loop 2   b) loop 2   c) loop 6   d) loop 6
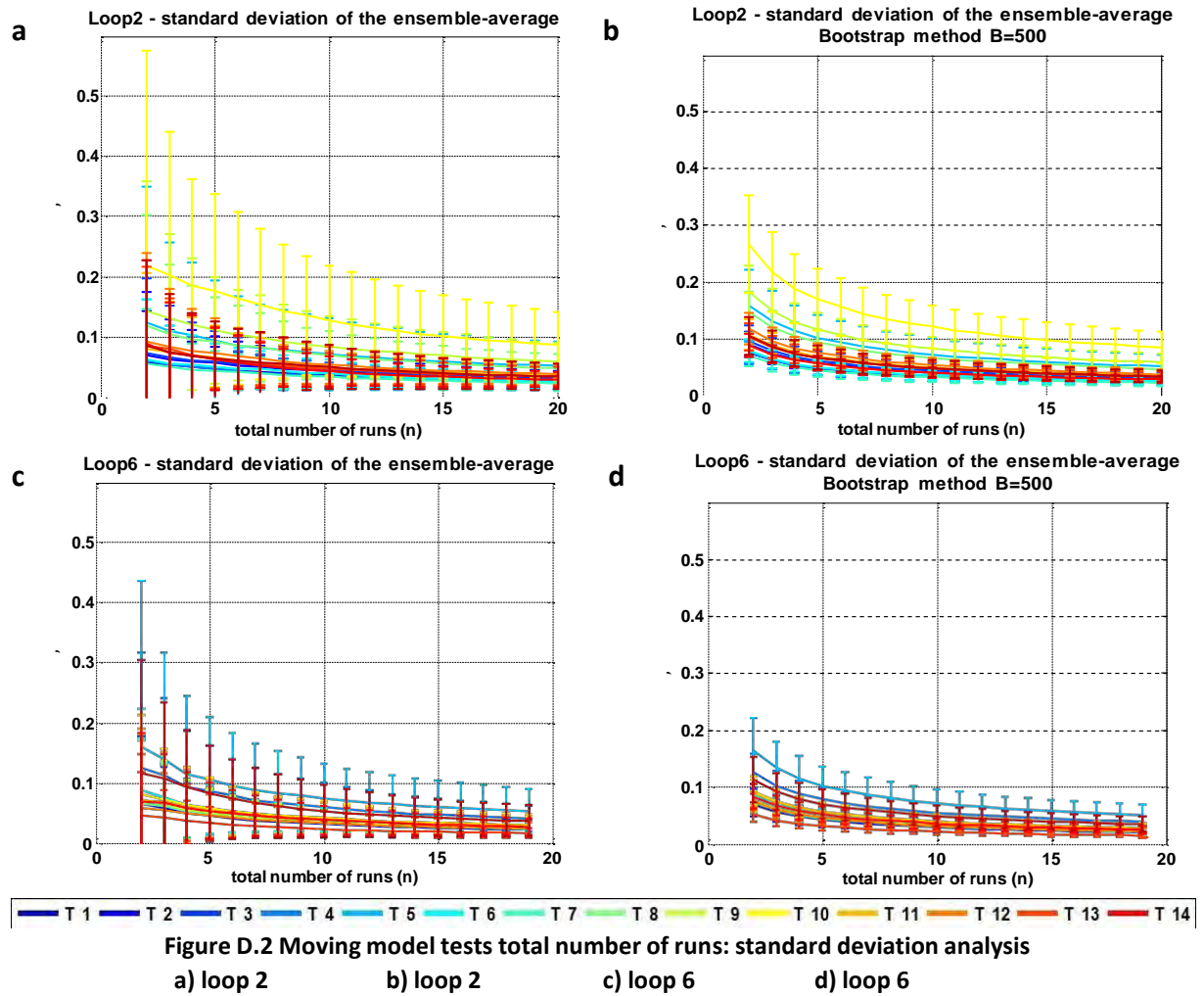
Figure D.2 outlines a good agreement between the estimations based on the two approaches expressed by equations (D.1) and (D.2). Considering loop2, figures D.2a and D.2b show that both of

and   depend on the pressure tap, with their highest magnitudes associated with

tap 10 (on the leeward side of the train). For any pressure tap both parameters progressively

decrease with respect to the total number of runs and become stable for   > 15, thus suggesting that

not dramatic improvement in the stability of the ensemble averages can be achieved with additional

runs. On figures D.2c and D.2d (relating to loop 6) the trend of   and   is similar to

what observed for loop 2. In this case, however, the magnitudes of both the parameters are slightly

lower and reach a good stability with only 10 runs.

Appendix E

'*Mechanical noise*' interference on moving model on-board pressure measurements

E.1 Introduction

This appendix presents the analysis carried out in order to quantify the effect of the so-called '*mechanical noise'* on the accuracy of the moving model test results. As discussed in chapter 3, when a scale-model train travels along a track, it typically experiences a series of vibrations caused by the track irregularities. If an on-board force balance is employed, to some extent these vibrations are detected by such a measuring system and lead to a series of spurious fluctuations in the recorded time series. Commonly referred as *mechanical noise*, in the past such fluctuations have led to a relatively large margin of uncertainty associated with experimental results obtained through tests on moving model vehicles, particularly relating to the estimations of unsteady aerodynamic coefficients (Baker and Humphreys, 1996). Hence, one of the objectives of the present research was the mitigation of the interference induced by *mechanical noise* through the development and use of a novel on-board measuring system.

The novelty related to such an on-board measuring system consists of the fact that it monitors the pressure on the train surface rather than the overall aerodynamic loads acting on the vehicle. In order to assess the advantages related to this design, this appendix assesses which portion of the overall experimental uncertainty (estimated in section 5.4) is associated with *mechanical noise*. Section E.2 describes a dedicated moving model test and the following data reduction that were carried out in order to isolate the interference caused by the model mechanical vibrations. Based on

this analysis, then, the uncertainties produced by *mechanical noise* on mean and peak normalised

aerodynamic coefficients are estimated in sections E.3 and E.4, respectively.

E.2 Analysis of the moving model tests time series

As illustrated in figure E.1, during a moving model test the surface pressure detected by the on-board

differential transducers is characterised by a significant level of fluctuations.
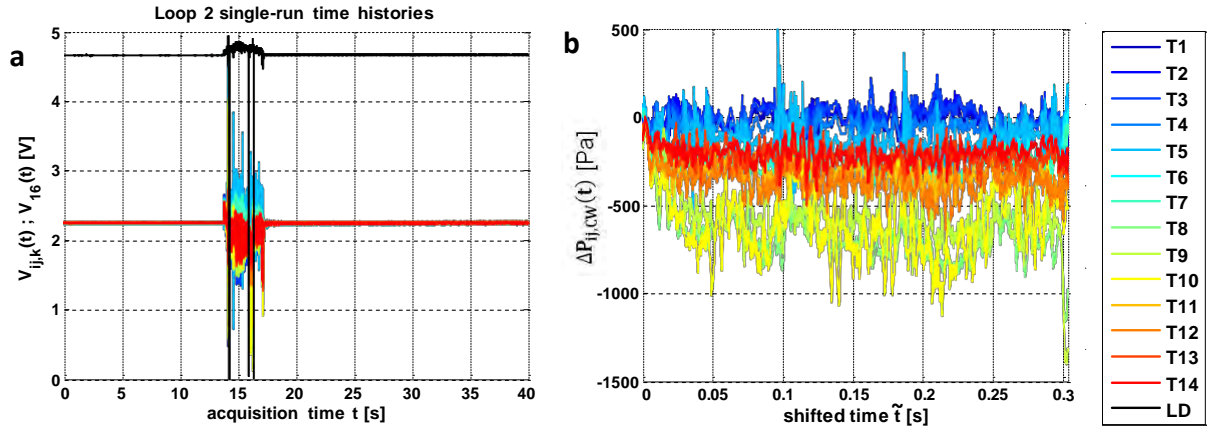
Figure E.1 Example of moving model test on-board time series (loop 2)
a) Complete run time series b) Crosswind section trimmed time series

These fluctuations reflect the surface pressure variations induced by the turbulent flow field

surrounding the train. In principle, however, contributions to these fluctuations might be given also

by a variety of 'external interferences', such as electrical disturbances, tubing resonances and the

aforementioned *mechanical noise*.

From the analysis of the time series illustrated in figure E.1 it is not straightforward to distinguish the

contributions generated by each of these sources. Hence, a 'non-conventional moving model test'

was undertaken. By occluding one of the pressure taps on the train surface, the actual surface

pressure variations were prevented from being detected. This arrangements enables the assumption

that all the fluctuations of the recorded signal were caused by electrical disturbances and *mechanical*

noise. Furthermore, if a much smaller contribution is inferred from the former, the recorded

fluctuations can be treated as entirely due to the latter.

Figure E.2 illustrates both the time history and the spectrum of the fluctuating component of the pressure signal recorded during the moving model test described above. Expressed in terms of differential pressure measurements (in Pascal), the time history includes the time interval during which the train travelled along the track at approximately constant speed. It is presented in its original form (i.e., as sampled at 4 KHz), as well as after low-pass filters have been applied at cutoff frequencies of 117 Hz and of 14 Hz, respectively. The former of these filters is the same used for data reduction (section 5.2.2.1), while the latter is equivalent to the moving average filter applied in the time domain (using an averaging time of 0.072 s) for calculating the peak coefficients (section 7.2). Table E.1 reports the standard deviations calculated for each of the three time series.
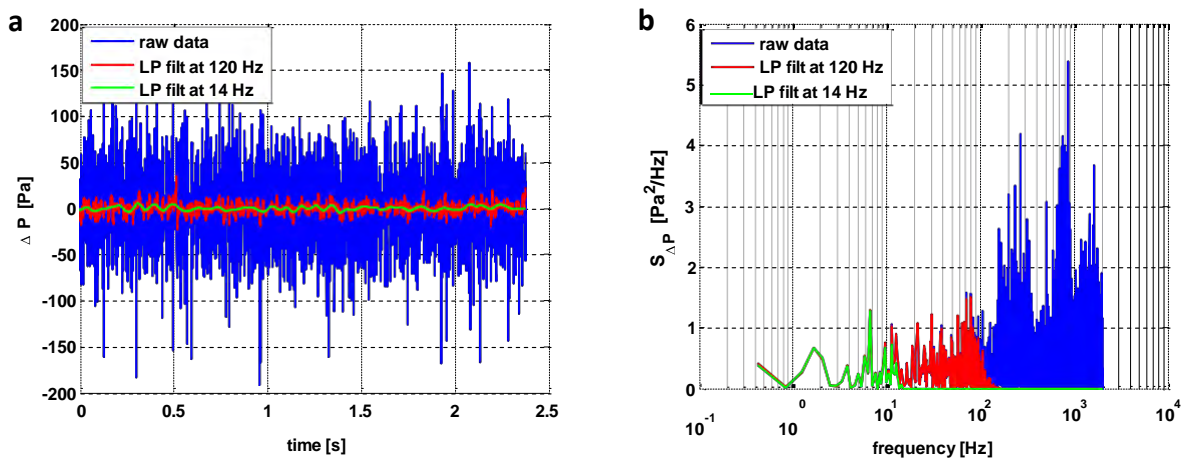
Figure E.2 Differential pressure fluctuations induced by the model vibrations during a moving model test a) Time series relative to the train travelling within the TRAIN rig test section b) Power spectra of the differential pressure time series

	Original raw data	Low-pass filtered at 117 Hz	Low-pass filtered at 14 Hz
Standard deviation ( ) [Pa]	30.2	6.2	2

Table E.1 Standard deviations of the time series illustrated in figure E.2

Evaluating the original recorded signal, the pressure fluctuations illustrated in figure E.2a lead to a relatively large standard deviation of ~30.2 Pa. However, since the spectrum in figure E.2b indicates that these fluctuations tend to occur at frequencies larger than 100-150 Hz, the majority of them are filtered out by the low-pass filter at 117 Hz used for data reduction (section 5.3.1). Accordingly, once such a filter has been applied, the pressure oscillations present significantly smaller amplitudes and

their standard deviation decreases from ~30 Pa to ~6.2 Pa (and then to ~2 Pa when the moving average time series required for calculating the peak coefficients are considered).

E.3   Mean aerodynamic coefficients

The contribution of *mechanical noise* to the experimental uncertainty was estimated through the propagation of error. Since all the raw data collected during moving model tests were filtered at 117 Hz, a standard deviation of ~6.2 Pa relative to the single-run differential pressure measurements was taken into account. Accordingly, considering a normal distribution and a 95% confidence level, the uncertainty on the differential pressure measurements is given by   Pa. In turn, the average uncertainty relating to the single-run mean pressure coefficient is   and, from this, the uncertainties specified in table E.2 have been obtained concerning the single-run overall aerodynamic load coefficients.

	Non-dim. coefficients overall aerodynamic loads
(mean)	0.016
(mean)	0.010
(mean)	0.010
(mean)	0.011

Table E.2 Uncertainties associated with the *mechanical noise* relative to the single-run overall mean load coefficients

It is important to note that the values in table E.2 are relative to the single-run mean pressure coefficients. As such, in light of the ensemble averaging process undertaken for treating the moving model test data, they provide a conservative estimation of the actual uncertainties relating to the mean pressure coefficients reported in chapter 6.

Assuming a random nature of the *mechanical noise* affecting the on-board pressure measurements, it follows that the fluctuations that such a noise induces at one particular time instant on different time series (recorded during different runs) are not always the same. Consequently, such fluctuations tend to progressively 'cancel out' within the ensemble averaging process. Hence, if a normal

distribution is hypothesised, the uncertainty that they determined on the   (calculated from an

ensemble average time history based on 15 occurrences) can be estimated as

⎯⎯   and, in turn, the uncertainties in table E.3 can be obtained through the

propagation of error.

	Non-dim. coefficients overall aerodynamic loads
(mean)	0.005
(mean)	0.003
(mean)	0.003
(mean)	0.003

Table E.3 Uncertainties associated with the *mechanical noise* relative to the 15-runs ensembles overall mean load coefficients

With consideration of the non-dimensional coefficients for the overall aerodynamic loads relating to

moving model tests, the values in table E.3 correspond to uncertainties of ~2% associated with

mechanical noise. By comparing them with the overall experimental uncertainties estimated in

section 5.4.1 for the moving model tests (and reported in table E.4 below), it can be observed that

the *mechanical noise* determined the largest amount of the random uncertainty.

Although what outlined is consistent with the findings of the past campaigns, the present analysis

testifies the effectiveness of using an on-board pressuring system (instead of a force balance) in

order to reduce the *mechanical noise* interference on the estimated overall mean load coefficients.

The random uncertainties of ~2% (or lower) estimated for the present moving model experiments

are slightly lower of the 3% previously reported, for example, by Baker and Humphreys (1996). More

importantly, here such smaller uncertainties are based on ensemble averages calculated from 15

runs (only), rather than from series of 50 runs (Humphreys, 1995). This indicates that the use of a

pressure measuring system for moving model tests leads not only to a slight improvement in the

experimental accuracy, but also to a significant reduction in the required number of runs.

	E_{BIAS}	E_{RND}	E_{TOT}	E_{BIAS} %	E_{RND} %	E_{TOT} %
	0.01	0.006	0.016	2%	2%	4%
	0.006	0.004	0.01	2%	2%	4%
	0.006	0.004	0.01	2%	2%	4%
	0.006	0.004	0.01	2%	1%	3%

Table E.4 Moving model tests experimental uncertainties for the overall mean load coefficients

E.4   Peak aerodynamic coefficients

Consistent with the approach described above, a normal distribution and a 95% confidence level were considered also in order to estimate the contribution of *mechanical noise* to the experimental uncertainties affecting the peak coefficients. It is explained in section 7.2.2 that, for moving model tests, the peak-over-mean (PoM) and the peak-over-peak (PoP) coefficients were calculated from single-run time series once a moving average filter (equivalent to 14 Hz low-pass filter) had been applied in the time domain. Consequently, considering a standard deviation of 2 Pa for the *mechanical noise* (table E.1), the propagation of error led to estimate the uncertainty on the peak differential pressure as   Pa and, in turn, to an uncertainty on the peak pressure coefficient

.

The effect of such uncertainties on the PoP normalised coefficients (i.e., the PoP divided by the mean coefficients) was computed through the propagation of error consistent with the calculation process reported in section 5.4.2 and produced the estimations specified in table E.5.

	Overall aerodynamic loads
(PoP/mean)	0.018
(PoP/mean)	0.019
(PoP/mean)	0.018
(PoP/mean)	0.015

Table E.5 Uncertainties associated with the *mechanical noise* relative to the single-run PoP normalised coefficients

It can be observed that the values in table E.5 are approximately one order of magnitude smaller than the total uncertainties estimated in section 5.4.2 (and reported in table E.6 below) and, with

respect to the PoP normalised coefficients obtained from moving model tests (sections 7.2.3 and 7.3), they correspond to uncertainties of ~2%. As such, they are significantly lower than the experimental error of approximately 13% found by Baker and Humphreys (1996) relating to moving model experiments based on the use of an on-board force balance.

		$E_{TOT} = E_{RND}$	$E_{TOT} \% = E_{RND} \%$
$\hat{C}_Y$	$\overline{C}_Y$	0.094	10%
$\hat{C}_Z$	$\overline{C}_Z$	0.102	11%
$\hat{C}_{Mx}$	$\overline{C}_{Mx}$	0.088	9%
$\hat{C}_{Mx,lee}$	$\overline{C}_{Mx,lee}$	0.089	9%

Table E.6 Moving model tests experimental uncertainties for the PoP normalised coefficients of the overall aerodynamic loads

The considerations above suggest that in the moving model experiments of this research the *mechanical noise* had a limited effect on the accuracy of the estimations obtained for the peak normalised coefficients. This supports the use of a pressure measuring system in order to improve the accuracy the peak coefficient estimation achievable through moving model experiments. Furthermore, in light of the significant difference between the *mechanical noise* contribution and the total uncertainty, it suggests that one (or more) alternative source might play a major role in determining the latter. Consistent with the analysis developed in section 5.4.2, one of these sources could be identified in the limited spanwise uniformity of the crosswind simulation. More importantly, most of the estimated margin of uncertainty appears to be associated with run-to-run variability observed in the PoM (and consequently PoP) coefficients. In this view, the observed uncertainty is not necessarily a symptom of an actual measurement error. Rather than that, it could be inherent in the stochastic nature of the physical phenomenon under investigation.

Appendix F

Mean aerodynamic coefficients sensitivity analyses

F.1   Introduction

This appendix reports a number of sensitivity analyses relating to the steady aerodynamic coefficients presented in chapter 6. Such analyses were part of the development of the instrumentation arrangements, test procedures and data reduction methods described in chapters 4 and 5. Section F.2 considers the static test results and analyses their sensitivity with respect to the pressure coefficient normalisation, to the position of the probe employed for monitoring the crosswind conditions and to the train model discretisation adopted for the pressure integration. Section F.3 examines the effect of the trackside reference probe position on the moving model test results. Finally, Section F.4 illustrates the sensitivity of the overall load coefficients, and particularly of their variation between static and moving model tests, with respect to the train model discretisation adopted for the pressure integration.

F.2   TRAIN rig static model tests

F.2.1   Pressure coefficients normalisation criteria

As explained in section 5.2, the static tests results for the pressure coefficient were normalised using a reference pressure and reference wind velocity given respectively by:

- the *corrected double-average* (i.e., the spanwise average of the time average) wind static pressure (   );

- the *corrected double-average* of the wind velocity relative to train, which coincides with the streamwise velocity   measured at 3 m FS equivalent above the ground ().

These quantities were calculated from local measurements provided by a Pitot-static tube (chapter 4) and allowed to properly take into consideration the characteristics of the flow simulation within the CWG.

The sensitivity analysis presented here highlights the effects, on the non-dimensional aerodynamic coefficients, associated with the individual '*corrections*' that were applied to the local measurements of both velocity and pressure to obtain the aforementioned reference values specified above. Accordingly a set of four normalisations are evaluated in the following. Indicated as N1, N2, N3 and N4 (where the latter corresponds to the option that was actually adopted for data reduction) these normalisations are defined in table F.1. The mean pressure coefficient and the load coefficients per unit length that they produce on the loops of taps from 1 to 8 are examined in figure F.1 and F.2, while the overall load coefficients are illustrated in figure F.3.

Normalisation	Reference pressure (wind mean static pressure)	Reference wind velocity (wind mean streamwise velocity)
N1	local measurement	local measurement
N2	spanwise average	spanwise average
N3	spanwise average	spanwise average + along wind gradient
N4 (final selection)	spanwise average + along wind gradient	spanwise average + along wind gradient

Table F.1 Static tests pressure coefficients normalisation criteria

a

Loop 1

Loop 8

b

Loop 2

Loop 8

c

Loop 3

Loop 8

d

Loop 4

Loop 8

e

Loop 5

Loop 8

f

Loop 6

Loop 8

Figure F.1 Effects of the normalisation criteria on the static tests mean pressure coefficients
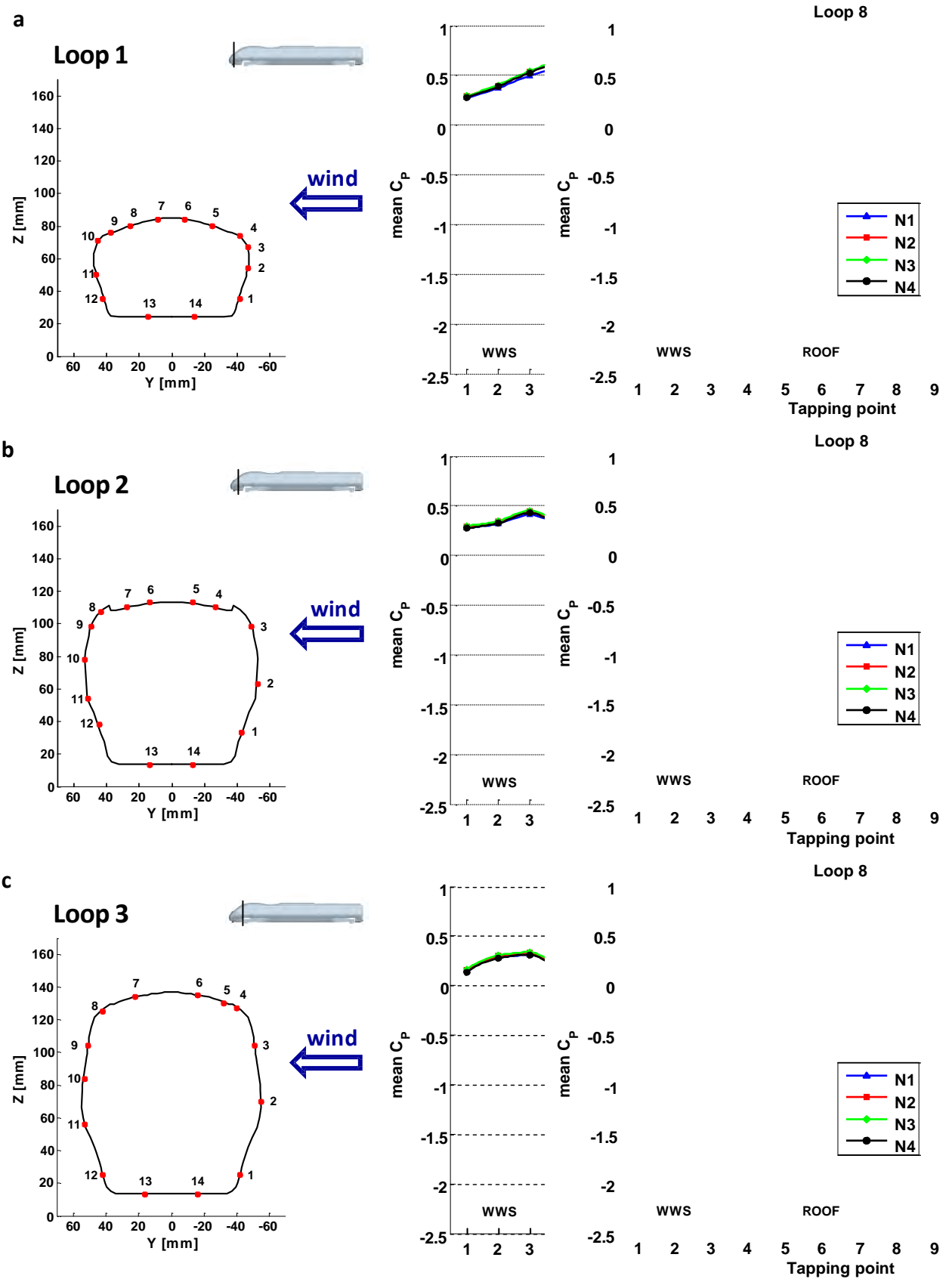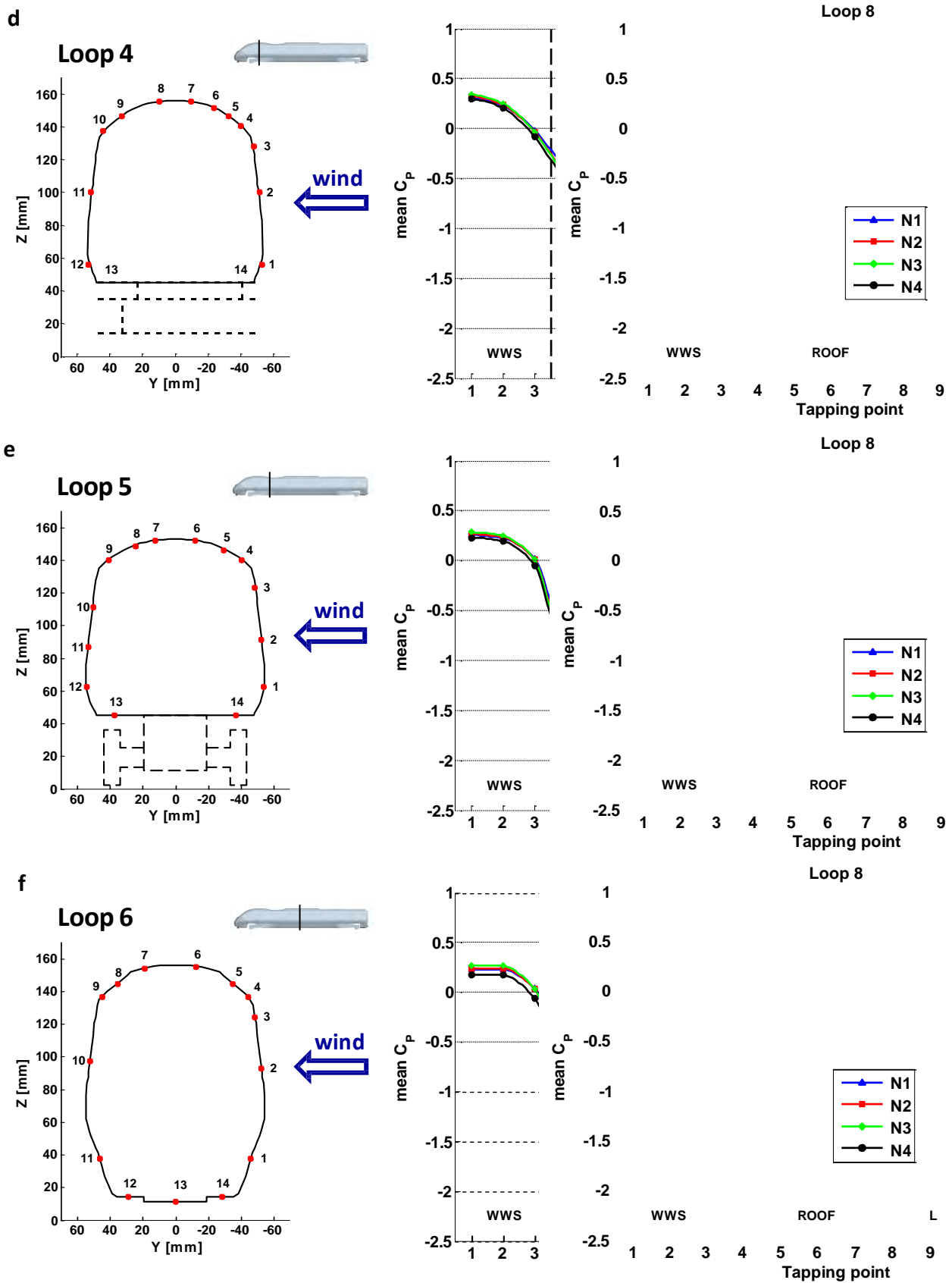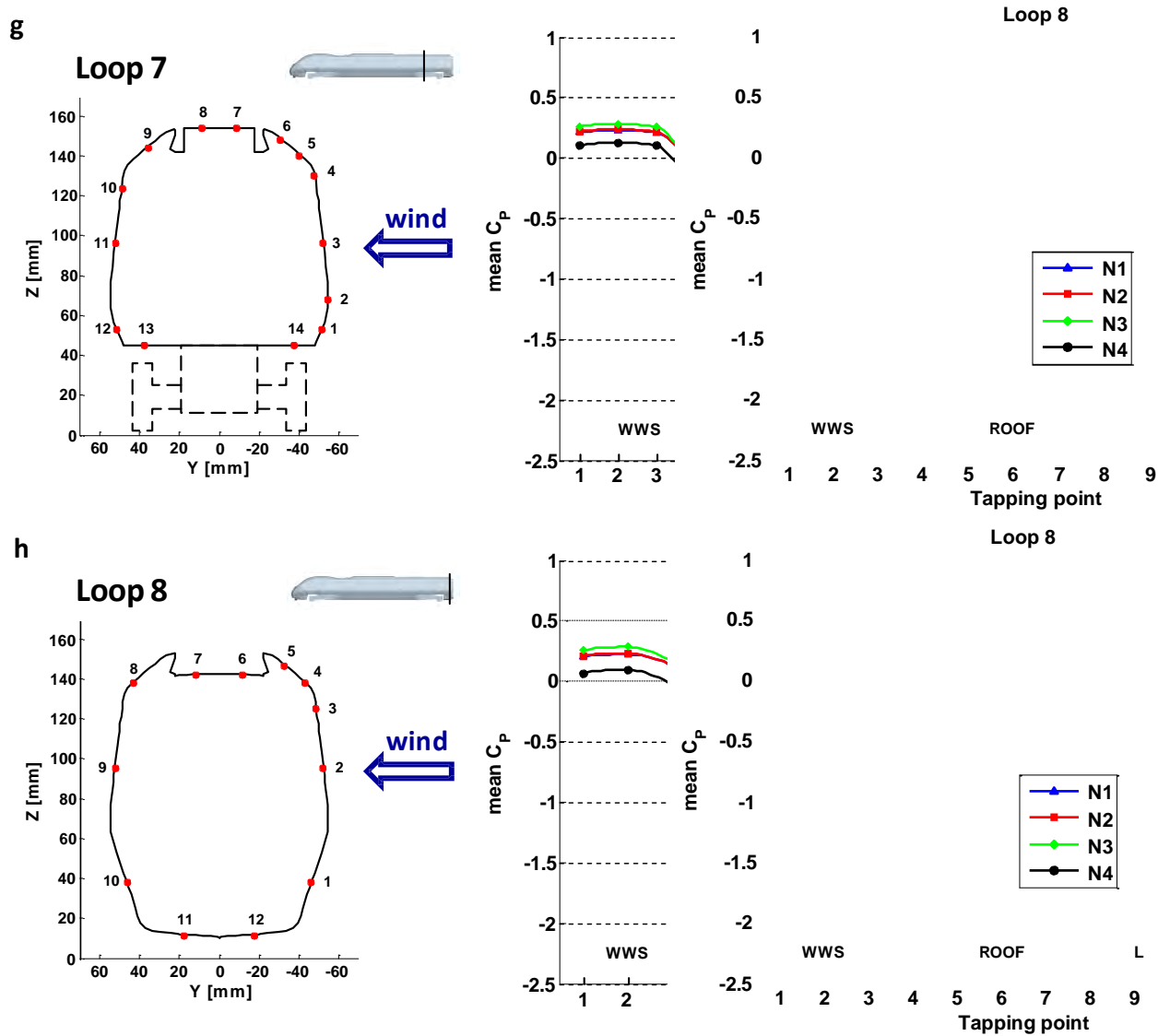
The comparison between N1 and N2 outlines the effect of correcting the local measurements by taking into consideration their spanwise averages (and   , for the differential static pressure and wind velocity mean values, respectively), which are obtained from equations (5.8) and (5.11) in section 5.2.1.2. Since the spanwise average-to-local ratios have been defined with respect to the wind profile at the inlet of the air channel, the influence of this correction remains the same on the various loops of pressure taps along the train. Furthermore, since both such ratios are less than 1, the spanwise averages are lower in magnitude than the local values, thus determining a lower wind velocity (since velocity is positive) and a higher differential static pressure (because it is negative).

A reduced reference wind velocity leads to a lower dynamic pressure and thus produces a variation of the mean pressure coefficient that depends on the magnitude of   itself. This is reflected in a stretch of the curves in figure F.1 in the vertical direction, with   that increases where it is positive, while decreases where it is negative. Accordingly, the aerodynamic load coefficients per unit length become larger in magnitude on any of the examined cross-sections (figure F.2) and lead to an increment of the corresponding parameters referred to the entire vehicle (figure F.3).

The impact of an increased reference pressure does not depend on the magnitude of the mean pressure coefficient and determines a uniform decrement of   . This is reflected in a vertical shift of the curves in figure F.1 towards lower values. Despite the impact on the pressure coefficients, any correction relating to the reference pressure does not affect the load coefficients. Accordingly, in figure F.1, the variations of   between N1 and N2 are determined by the combined effect of both the static pressure and wind velocity correction, while the differences outlined in figures F.2 and F.3 are entirely due to the wind velocity correction.

Corrections that account for the along-wind gradients of wind velocity and static pressure are applied in succession in normalisation N3 and N4, respectively. This gives the opportunity to quantify the effect of each correction. N3 is obtained from N2 by evaluating the gradient of the streamwise velocity, i.e., using a reference value given by   and calculated through equation (5.12) in section 5.2.1.2. N4, which corresponds to the final normalisation adopted in this thesis, considers also the gradient correction for the static pressure. Hence, the reference value of the mean differential static pressure is taken as   and is given by equation (5.9) in section 5.2.1.2. A negative gradient causes a reduction of velocity in the streamwise wind direction, while a positive gradient determines an increment of mean static differential pressure. According to equations (5.9) and (5.12), both gradient corrections lead to variations of the reference values (with rerspect to those used in normalisation N2) that become larger moving from the nose to rear of the train.

FigureF.1 illustrates how, on loops 1 to 3 on the nose of the train, the spanwise corrections have a larger influence than the gradient corrections on the mean pressure coefficient. Moving towards the rear, the two effects become of the same order on loops 4 and 5 and then, on loops 7 to 10, it can be seen that the evaluation of the gradients becomes prevailing. Comparing the influence, on the mean pressure coefficient, of gradient corrections for the velocity and the static pressure, they are of the same order on the front part of train (up to loop 6), while the latter becomes dominant on the rear of the vehicle.
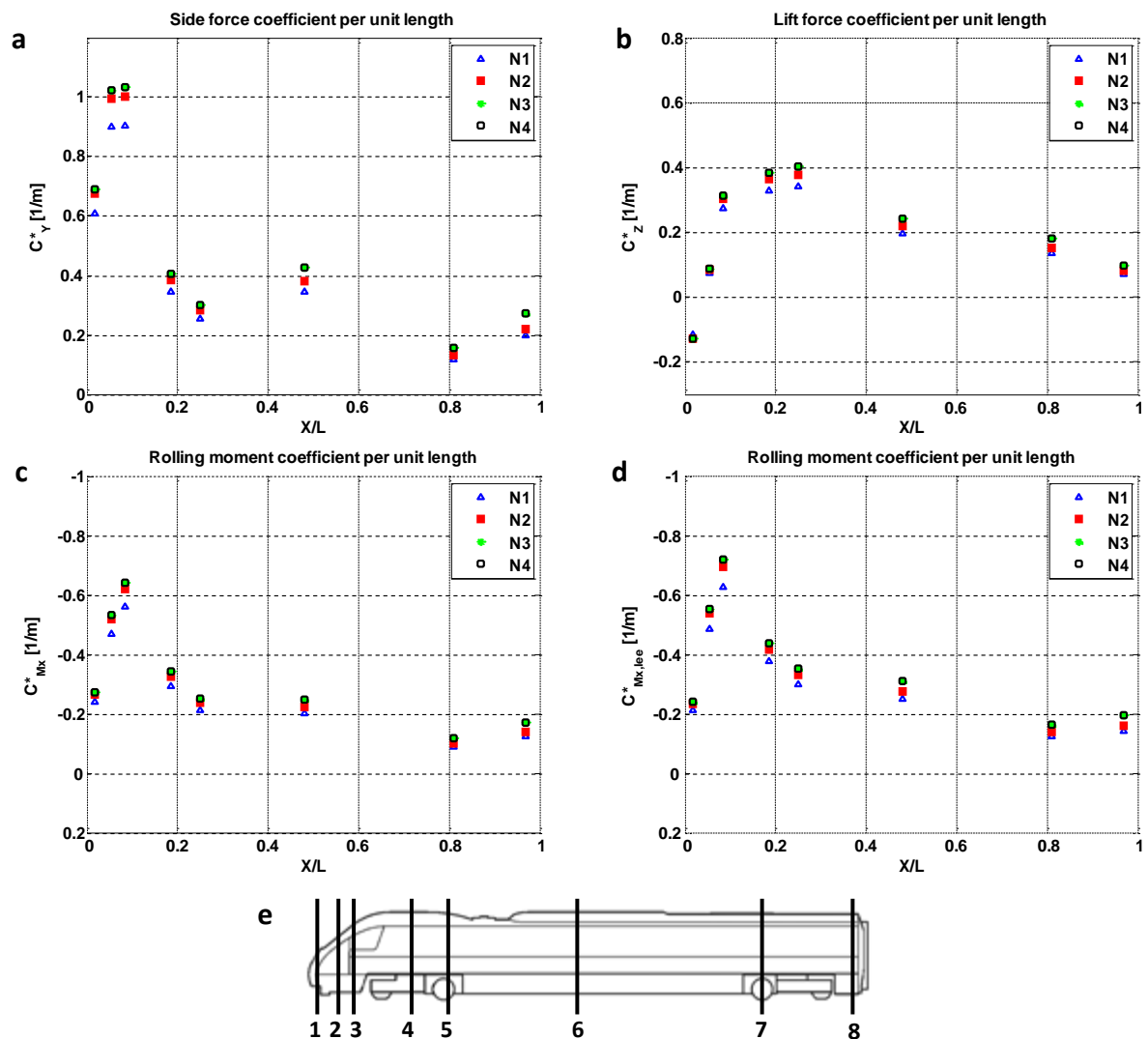
Figure F.2 Effects of the normalisation criteria on the static tests mean load coefficients per unit length

The sensitivity observed on   is reflected by the behaviour of the load coefficients per unit length illustrated in figure F.2. As discussed above, these parameters are sensitive only to corrections of

reference wind velocity, which induce larger variations when the magnitudes of the coefficients are larger. Accordingly, the most significant increments in the load coefficients per unit length are those on the nose of train, where the largest (negative) magnitudes of   occur. In this area, in light of the short along-wind distance from the position of the measuring probe (in equation (5.12)), the gradient correction produces a small variation in the reference wind velocity, and consequently also in the load coefficients per unit length. As such, the observed sensitivity is mainly related to the spanwise correction.
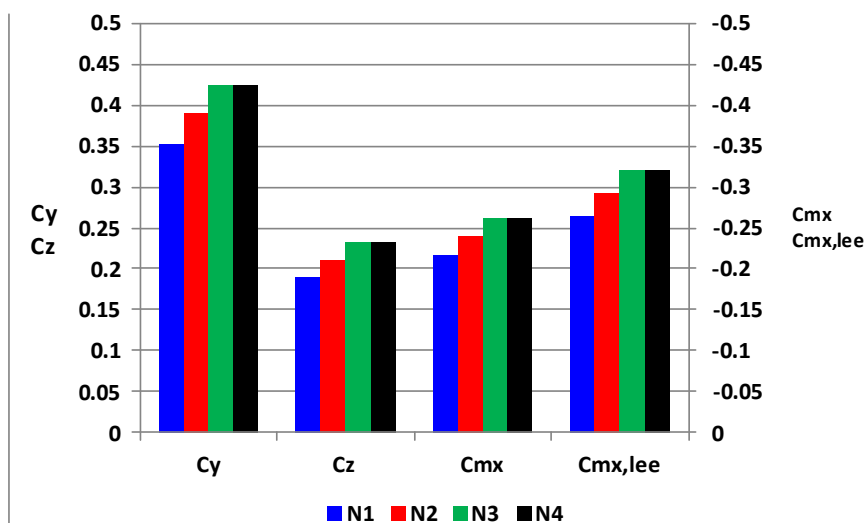
Figure F.3 Effects of the normalisation criteria on the static tests overall mean load coefficients

Figure F.3 shows that load coefficients variations induced by spanwise and gradient corrections are approximately of the same order. On the one side, the former cause larger increments in the coefficients per unit length, but only on a relatively short portion of the train (i.e., on the nose). On the other side, the smaller increments produced by the latter become significant since they affect almost two thirds of the vehicle length.

F.2.2   Position of the wind reference measurements

As detailed in chapter 4, the selection of an appropriate location for positioning the trackside reference probe (employed for measuring the wind conditions) during static tests was not straightforward. Since the limited space available within the CWG prevented the guidelines provided by the standards (CEN, 2010; RSSB, 2009b) to be followed, a preliminary series of tests were undertaken in order to address the decision. Finally, the Pitot-static tube and Cobra probe that were employed were positioned at the inlet of the air channel, at   = 0.12 m (i.e., 3 m full-scale equivalent height) shifted on the side with respect to train as illustrated in figure 4.33 in section 4.6. The Pitot-static tube, which provided also the reference pressure to the on-board pressure transducers, was the reference probe.

The analysis reported in this section was carried out in order to assess the variability of the static tests results associated with the position (and type) of the trackside reference probe. The data relative to the loop of pressure taps number 2 and 6, respectively on the nose and at the centre of the first car, are illustrated. The reference static pressure and reference wind velocity defined in section 5.2.1.2 were calculated based on the raw data collected by each of the two trackside probes during the same static test single-run (employing dedicated spanwise average-to-local ratios depending on the probe). Relating to each set of reference values, then, the mean pressure coefficients were computed. They are illustrated in figure F.4, where error bars indicate the uncertainty of   related to the bias limit associated with static pressure and wind velocity measurements.

It can be observed that the differences between the two series of results are extremely limited and falls within the estimated experimental uncertainty associated with instrumentation performance. This indicates that the sensitivity of the results to the position of the trackside reference probe can be neglected in comparison to the margin of error associated with the accuracy of the instrumentation employed. Therefore, it supports the reliability of the experimental setup that was

adopted and suggests a good accuracy of the methodology applied for extrapolating the reference values of static pressure and wind velocity from the local trackside measurements (section 5.2.1.2).
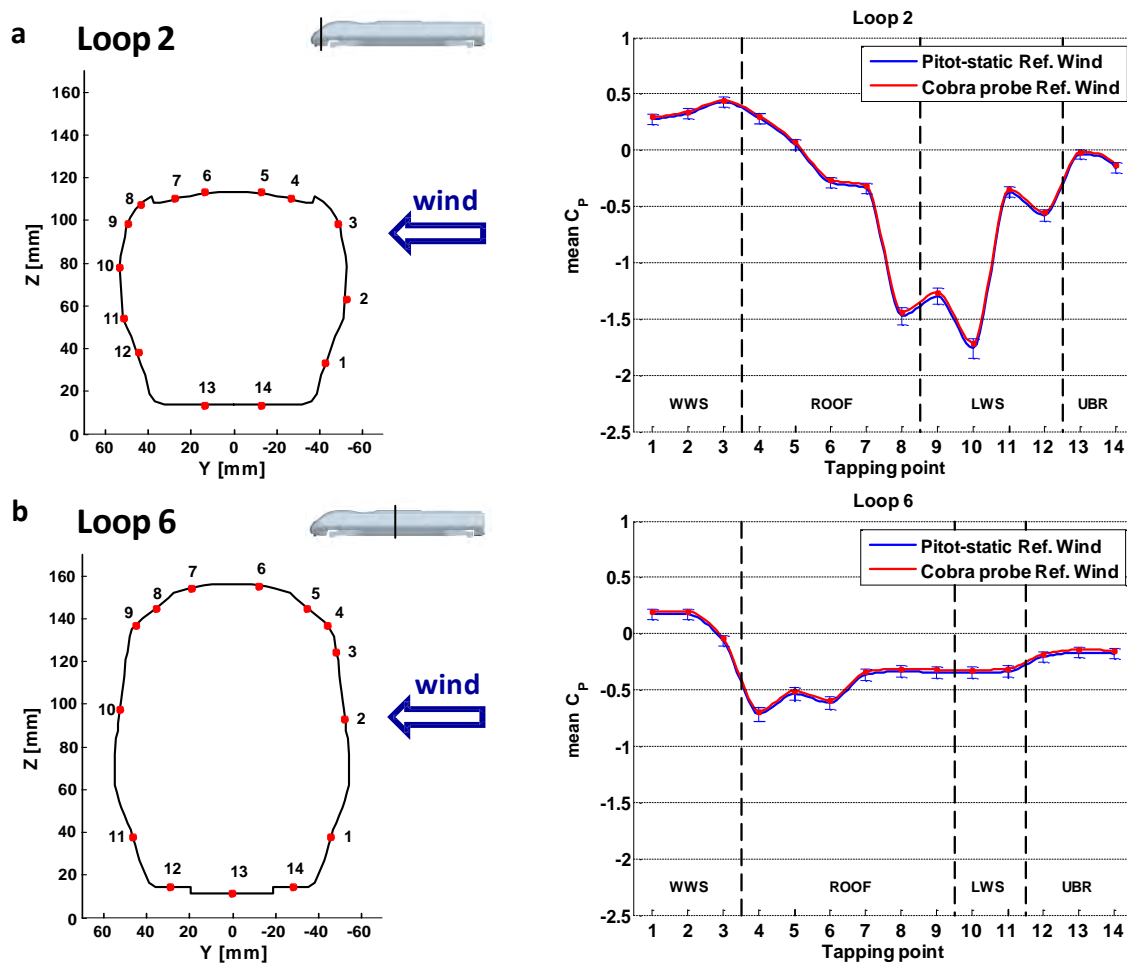
Figure F.4 Effects of the trackside wind measurements position on the static tests mean pressure coefficients

F.2.3 Total number of pressure taps and train model discretisation

The availability of supplementary pressure measurements from the static tests enabled a second estimation of mean overall load coefficients to be obtained, in addition to that reported in section 6.2.3. This was based on a train longitudinal discretisation presenting 14 stripes (rather than 8), details of which are reported in table F.2 and illustrated in figures F.5 and F.6. Furthermore, for loops from 9 to 14, table F.3 specifies the correspondence between the individual facets of each discretised geometry and the pressure taps.

Stripe	1	2	3	4	5	6	7	8	9	10	11	12	13	14
length L_j [mm]	25	50	45	80	75	85	70	55	85	75	120	75	65	90

Table F.2 Class 390 discretised model: alternative longitudinal stripes extension (14 stripes)

Figure F.5 Class 390 model alternative longitudinal discretisation (14 stripes)

Figure F.6 Class 390 model discretised cross-sections (loops 9 to 14)

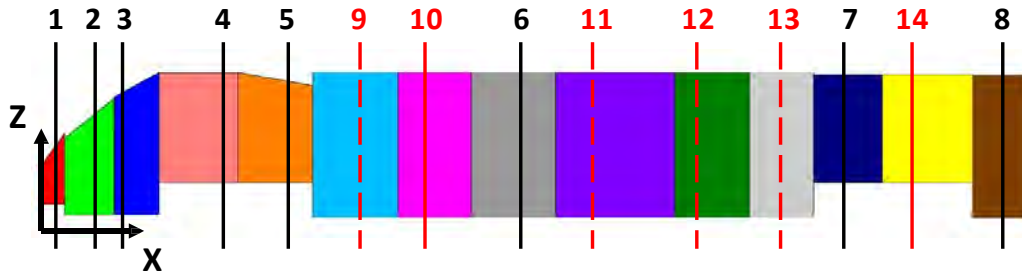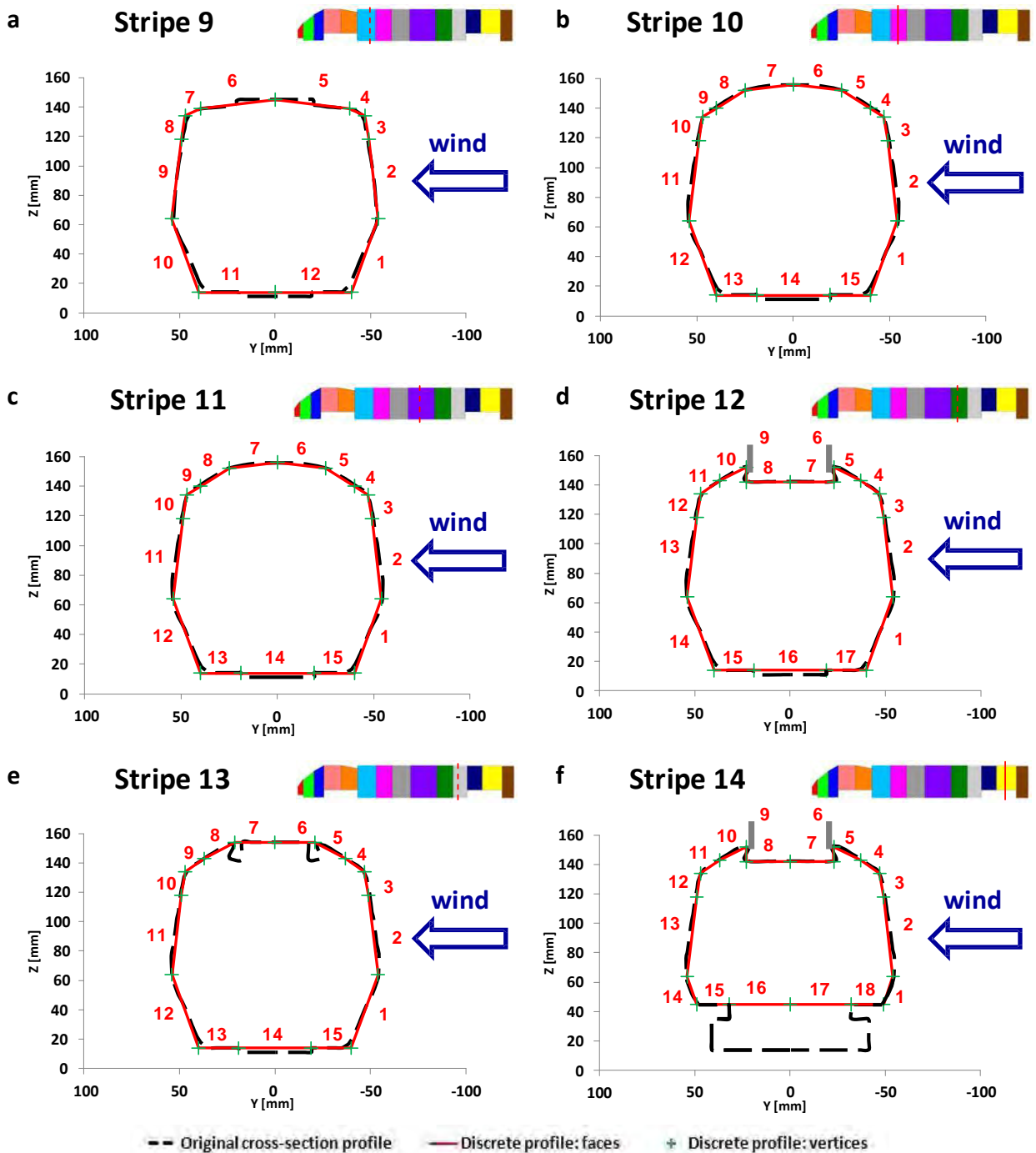| Loop	9	10	11	12	13	14
Face (I)			Pressure tap (i)			
1	1-L10	1	1-L7	1-L7	1-L7	1
2	2-L10	2	2-L7	2-L7	2-L7	2
3	1	3	3-L7	1	1	3
4	2	4	4-L7	2	2	4
5	3	5	1	2	2	5
6	4	6	2	3	3	6
7	4	7	3	3	3	6
8	10-L10	8	4	3	4	7
9	10-L10	9	4	3	4	7
10	11-L10	10	10-L7	4	10-L7	8
11	5	10	10-L7	4	10-L7	8
12	6	11	11-L7	10-L7	11-L7	9
13		12	5	10-L7	5	10
14		13	6	11-L7	6	11
15		14	7	5	7	12
16				6		12
17				7		13
18						13

Table F.3 Class 390 discretised model: facets-pressure taps correspondence (loops 9 to 14)

The overall load coefficients calculated in relation to this 14-stripes discretisation are specified in table F.4 and shown in figure F.7, where a comparison is outlined with respect to those obtained through the original 8-stripes discretisation. The two estimations are based on mean pressure coefficients computed through the same data reduction method and share their values relating to the loops of taps from 1 to 8. Accordingly, it can be assumed that the discrepancies found are entirely associated with differences in the discretisation adopted rather than to other experimental errors.

	8 Stripes	14 Stripes	Magnitude variation |14S – 8S|
	0.425	0.434	+2%
	0.233	0.239	+3%
	-0.262	-0.275	+5%
	-0.316	-0.330	+4%

Table F.4 Effects of the train discretisation on the static tests overall mean load coefficient (8 vs. 14 stripes)
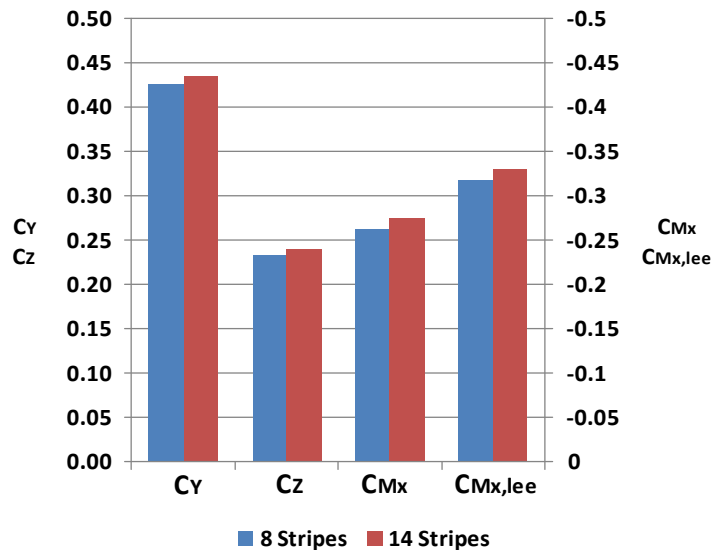
Figure F.7 Effects of the train discretisation on the static tests overall mean load coefficient (8 vs. 14 stripes)

The results denote that the 14-stripes discretisation leads to slightly larger magnitudes of all the examined load coefficients. Therefore, a tendency to slightly underestimate such coefficients can be inferred with regard to the relatively coarse 8-stripes discretisation that has been originally employed in this thesis.

F.3   TRAIN rig moving model tests

F.3.1   Position of the wind reference measurements

As explained in chapter 4, as for static so for moving model experiments a Pitot-static tube and a Cobra probe were employed at the trackside for monitoring the crosswind conditions. Both positioned at a reference height   = 0.12 m (i.e., 3 m full-scale equivalent), these sensors were placed 0.2 m upstream of the track centreline at the two spanwise locations indicated in figure 4.36 in section 4.7. In this case, the Cobra probe provided the reference measurements.

Figure F.8 illustrates the mean pressure coefficients obtained on loop 2 and loop 6 comparing the results normalised using wind speed and wind static pressure measurements from either the Cobra probe or the Pitot-static tube. Each pair of datasets relative to the same loop are based on the raw

data obtained through the same series of 15 moving model test runs (that enabled calculation of an ensemble average time history). Error bars represent the uncertainty associated with the bias limits.

Consistent to what observed for static tests, figure F.8 indicates a remarkable agreement between the two set of results, with any difference falling within the margin of error associated with the instrumentation accuracies. Hence, also with regard to moving model experiments, this sensitivity analysis supports the reliability of the test setup and data reduction method that were adopted.
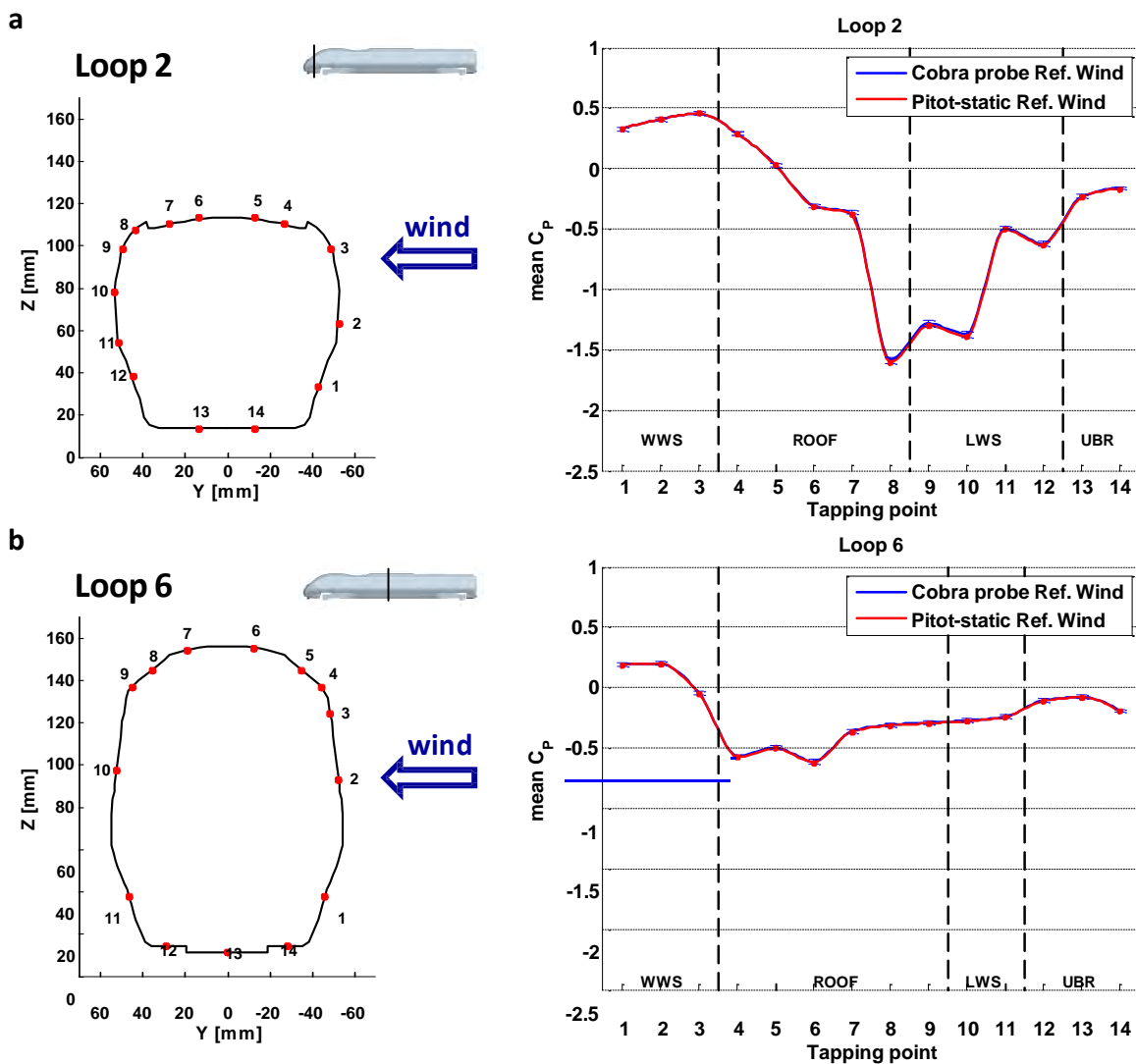
Figure F.8 Effects of the trackside wind measurements position on the moving model tests mean pressure coefficients

F.4 Comparison between static and moving model experiments

The comparison between the overall load aerodynamic coefficients associated with static and moving model tests presented in chapter 6 is based on an 8-stripes train model discretisation (figure 5.11 in section 5.3). Of these stripes, stripe 6 relating to the central part of the vehicle extends for approximately half of the length of the leading car, where the geometry of the cross-section presents a good consistency. The use of such a long stripe was dictated by the need of reducing the total number of pressure taps to monitor (particularly during moving model tests). As discussed in section 6.4.4, it led the surface pressure measured on loop 6 to have a very large weight within the integration process and, in turn, to play a key role in determining the variations between the mean overall aerodynamic coefficients associated with static and moving model tests.

The study presented here explores the sensitivity of such variations between static and moving model tests to the characteristics of the model discretisation. Unfortunately, since not all the 164 pressure taps available onto the train scale-model were investigated during moving model tests, the alternative model discretisation previously proposed in section F.2.3 was not viable for a sensitivity study involving the moving model test data. Nevertheless, additional measurements with respect to those relating to the loops of taps from 1 to 8 were undertaken during moving model tests on the underbody pressure taps on loops 9 to 13. Taking advantage from these additional measurements, the '*hybrid*' train discretisation illustrated in figure F.9 and table F.5 was employed in order to undertake a sensitivity analysis.

Such a *hybrid* discretisation comprised of a train model divided into 13 stripes. However, since only underbody pressure measurements were undertaken on loops 9 to 13, the discretised cross-sections of these loops were assumed identical to that of loop 6 (with the exception of the underbody of loop 9) and their windward, leeward and roof pressures were taken to be the same as on loop 6, according to the correspondences specified in table F.6.
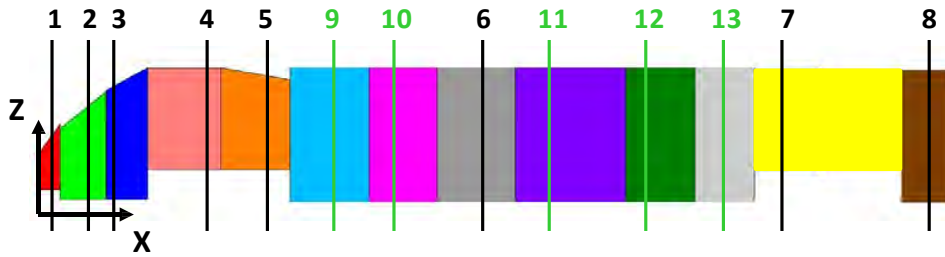
Figure F.9 Class 390 model *hybrid* longitudinal discretisation (13 stripes)

Stripe	1	2	3	4	5	6	7	8	9	10	11	12	13
length L_j [mm]	25	50	45	80	75	85	160	55	85	75	120	75	65

Table F.5 Class 390 *hybrid* discretised model: longitudinal stripes extension (13 stripes)
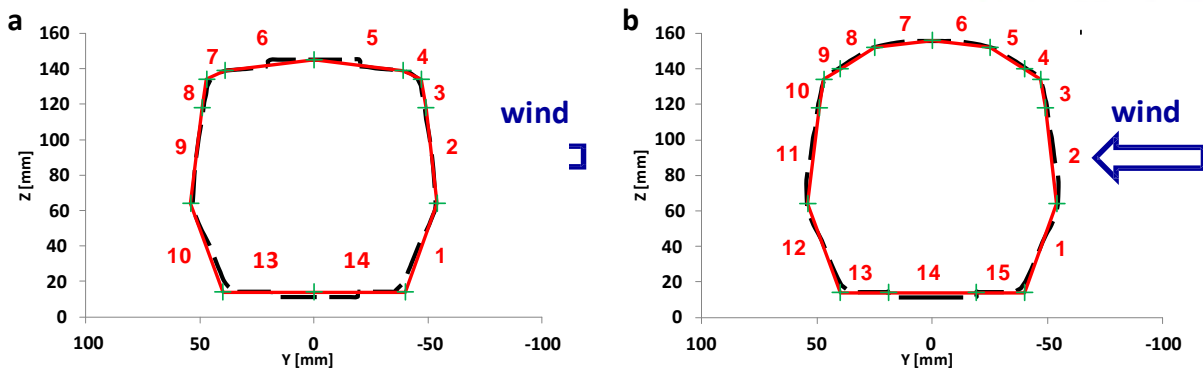
Figure F.10 Class 390 *hybrid* discretisation cross-sections. a) Loop 9 b) loops 10 to 13

Loop	9	10	11	12	13
Face (I)	Pressure tap (*i*)				
1	1-L6	1-L6	1-L6	1-L6	1-L6
2	2-L6	2-L6	2-L6	2-L6	2-L6
3	3-L6	3-L6	3-L6	3-L6	3-L6
4	4-L6	4-L6	4-L6	4-L6	4-L6
5	5-L6	5-L6	5-L6	5-L6	5-L6
6	6-L6	6-L6	6-L6	6-L6	6-L6
7	7-L6	7-L6	7-L6	7-L6	7-L6
8	8-L6	8-L6	8-L6	8-L6	8-L6
9	9-L6	9-L6	9-L6	9-L6	9-L6
10	10-L6	10-L6	10-L6	10-L6	10-L6
11	10-L6	10-L6	10-L6	10-L6	10-L6
12	11-L6	11-L6	11-L6	11-L6	11-L6
13	5	12	5	5	5
14	6	13	6	6	6
15		14	7	7	7

Table F.6 Class 390 discretised model: facets-pressure taps correspondence (loops 9 to 14)

	8-loops original model discretisation			13-loops *hybrid* model discretisation		
	STATIC TESTS	MOVING TESTS	VARIATION |MOV. – ST.|	STATIC TESTS	MOVING TESTS	VARIATION |MOV. – ST.|
	0.425	0.417	-2%	0.425	0.417	-2%
	0.233	0.251	+8%	0.237	0.243	+3%
	-0.262	-0.257	-2%	0.263	0.261	-1%
	-0.316	-0.316	0%	0.319	0.317	-1%

Table F.7 8-loops vs. 13-loops *hybrid* model discretisation: mean overall aerodynamic load coefficients, static vs. moving model tests comparison:

Table F.7 reports the mean overall aerodynamic load coefficients obtained by integrating the pressure data using this *hybrid* discretisation and compares them with those originally estimated in chapter 6 (based on a 8-stripes discretisation). While the train discretisation does not produce a relevant effect on the overall mean coefficient for the side force, it has an impact on such a parameter associated with both the rolling moments and the lift force. A *hybrid* discretisation causes lift force coefficient to increase when obtained through static tests (which is consistent with what observed for the 14-stripes discretisation examined in section F.2.3) and to decrease when measured through moving model tests. Hence, it leads to a reduction from 8 to 3% of the increment of such a coefficient originally ascribed to the simulation of the vehicle movement (section 6.4.3).

As discussed above, it is acknowledged that the use of the *hybrid* discretisation proposed here does not include any detailed information regarding the impact of the movement simulation on the pressure field on the windward, top and leeward sides of the train portion in between the bogies. However, such a discretisation does include additional information concerning the train underbody pressure. Hence, assuming that the variations on the overall lift coefficients are mainly determined by changes in the underbody pressure, the results in table F.7 suggest that what reported in section 6.4.4 might represent a slight overestimation of the aerodynamic effect of the vehicle movement simulation. However, it is worth noting that since in both cases the variations of   are well within the estimated experimental uncertainty (i.e., 13%), the findings of this sensitivity study do not affect the main conclusions drawn in chapter 6.

Appendix G

Effect of mean relative wind variations

on the moving model steady aerodynamic coefficients

G.1   Introduction

This appendix illustrates an additional analysis of the moving model test data carried out in order to investigate the sensitivity of the results presented in section 6.3 to the long time-scale fluctuations found in the time histories of non-dimensional aerodynamic coefficient. Section G.2 discusses the correspondences and, in turn, the relationship between such fluctuations and the spanwise inhomogeneity of the relative wind experienced by the scale-model train during the TRAIN rig moving model experiments. Section G.3 describes a '*modified*' data reduction method developed to obtain an alternative estimation of the mean aerodynamic coefficients. Section G.4 illustrates the results produced by the use of such a method and compares them to those originally reported in chapter 6. Finally, section G.5 discusses the sensitivity of the moving model mean aerodynamic coefficients to the use of one or the other data reduction method.

G.2   Effects of the spanwise inhomogeneity in the mean relative wind

G.2.1   Mean relative wind horizontal profile

During moving model experiments, spanwise variations in the mean wind relative to a travelling train were caused by two effects: the decrease of the vehicle speed across the crosswind section (   ) and the spanwise fluctuations of the horizontal velocity components of the mean (i.e., time average) onset crosswind (and   ). As illustrated in figure G.1, these two effects determined modifications not only in the magnitude of the relative mean wind velocity, but also in the mean yaw angle.

Indicated as , this is the angle between the mean relative wind and the direction of travel and is given by:

$$\bar{\theta} = \arctan\left(\frac{\bar{U}}{V_{tr} - \bar{v}}\right) \tag{G.1}$$

where, consistent with the notation and reference system defined in chapter 4,   and   are the nominal streamwise and lateral component of the mean wind, while   is the train speed.
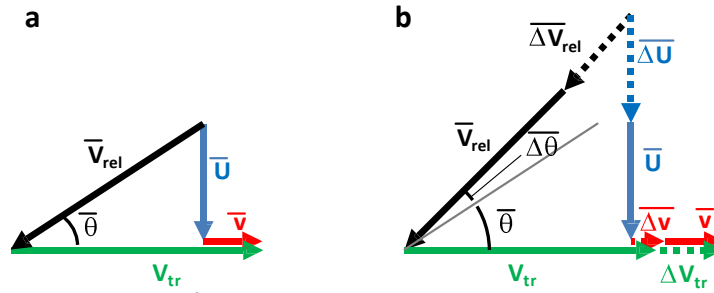

Figure G.1 Vector diagram of the mean wind velocity relative to a TRAIN moving vehicle.
a) Nominal relative mean wind b) Relative mean wind fluctuations

Figure G.2 illustrates the *nominal* horizontal profile of the mean relative wind experienced by the scale-model train travelling within the CWG. Such a *nominal* mean relative wind is based on the flow characterisation data for the onset wind horizontal profile measured at the reference height   = 0.12m (section 4.3.2.1). Furthermore, it assumes a linear decay for the train speed within the crosswind section, with an average of 20.8 m/s and a total decrement of 1.1 m/s (section 4.7).

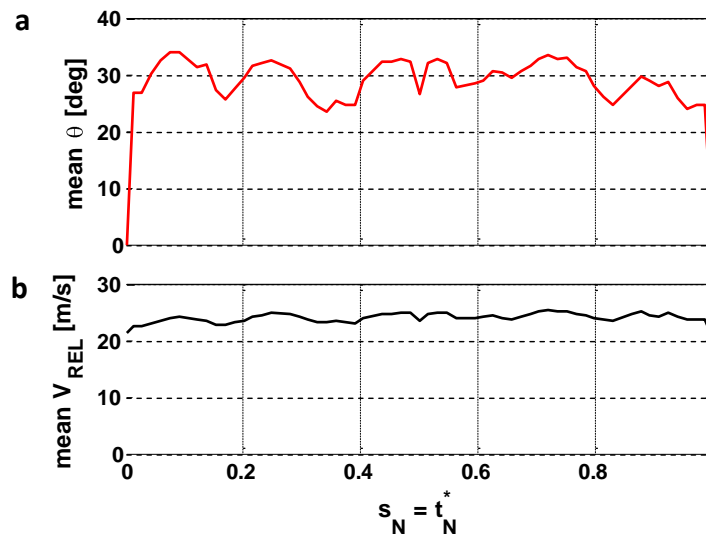**Figure G.2 Horizontal profile of the nominal mean relative wind (= 20.8 m/s,   = 0.12 m).**
**a) Yaw angle b) velocity magnitude**

Spatial variation of both velocity magnitude and yaw angle are displayed with respect to the *nominal spanwise normalised position* defined in section 5.2.2.3. To ease interpretation of the following, it is worth recalling the correspondence between and the *nominal normalised time* given by:

$$t_N^* = \frac{t \cdot V_{tr,CW}}{L_{CW}} = \frac{s}{L_{CW}} = s_N \tag{G.2}$$

G.2.2 Analysis of the non-dimensional coefficients time series

It has been observed in section 6.3.1 that some of the time histories for the non-dimensional aerodynamic coefficients obtained through moving model tests are characterised by long time-scale fluctuations. Furthermore, the hypothesis has been made that such long time-scale fluctuations could be caused by the spanwise irregularities characterising the onset mean wind simulated by the CWG.

Such a hypothesis is supported by the analysis presented in the following figures G.3 and G.4, where a correspondence is outlined between the non-dimensional aerodynamic coefficients fluctuations and the spanwise variations of the velocity magnitude and yaw angle of the *nominal* mean relative wind.
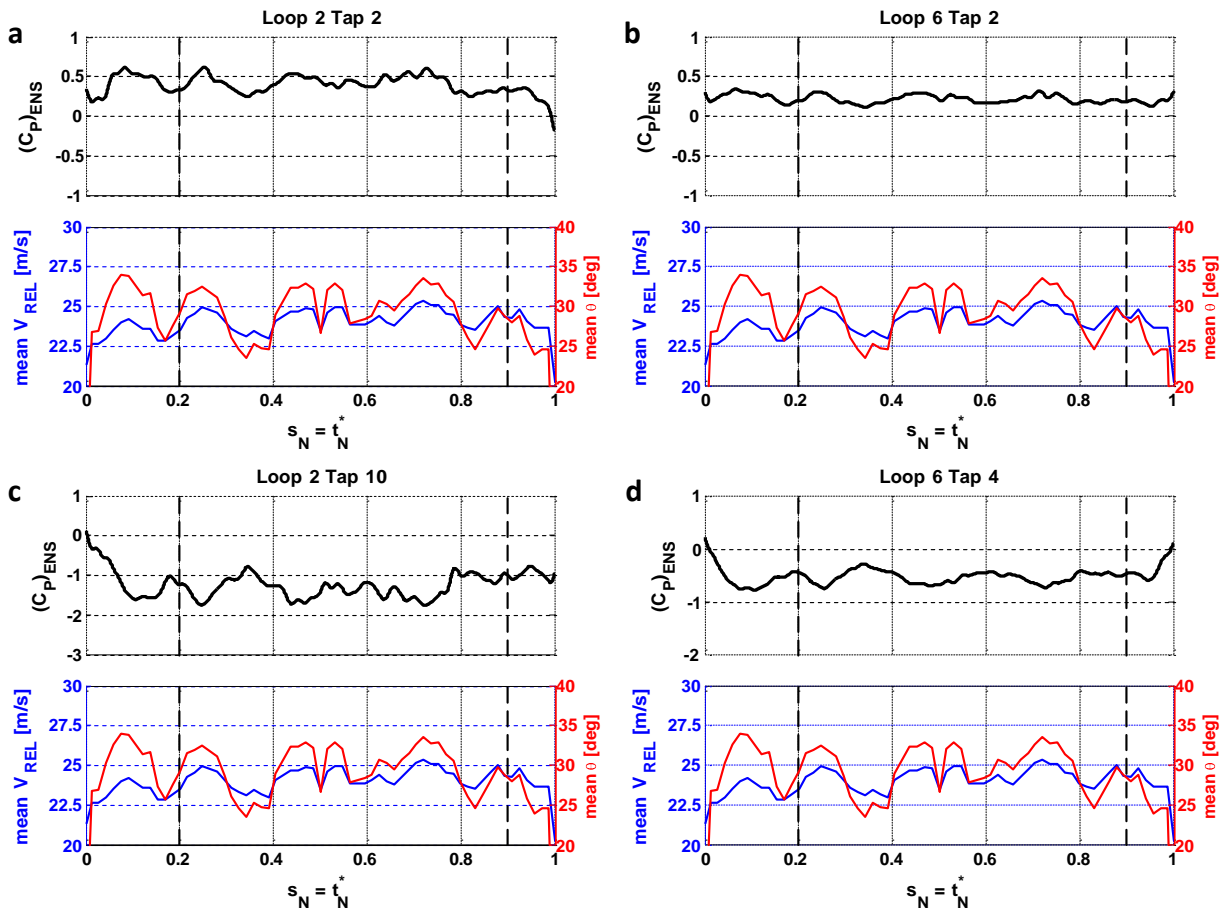
Figure G.3 Moving model tests pressure coefficient: ensemble averages time series in combination with the nominal mean relative wind (loop 2 on the train nose, loop 6 in the centre of the leading car)

Figure G.3a and G.3b outline how, in the presence of stagnation (on the windward side of the train) positive peak values of   occur in combination with mean yaw angle larger than 30° and with positive peaks of the relative wind velocity. Conversely, the opposite behaviour is highlighted in figures G.3c and G.3d relating to pressure taps positioned within areas of suction (i.e., on the leeward side on loop 2 and on the windward roof corner of loop 6, respectively). In these cases, positive peaks in the mean yaw angle and mean relative velocity correspond to troughs in the pressure coefficient.
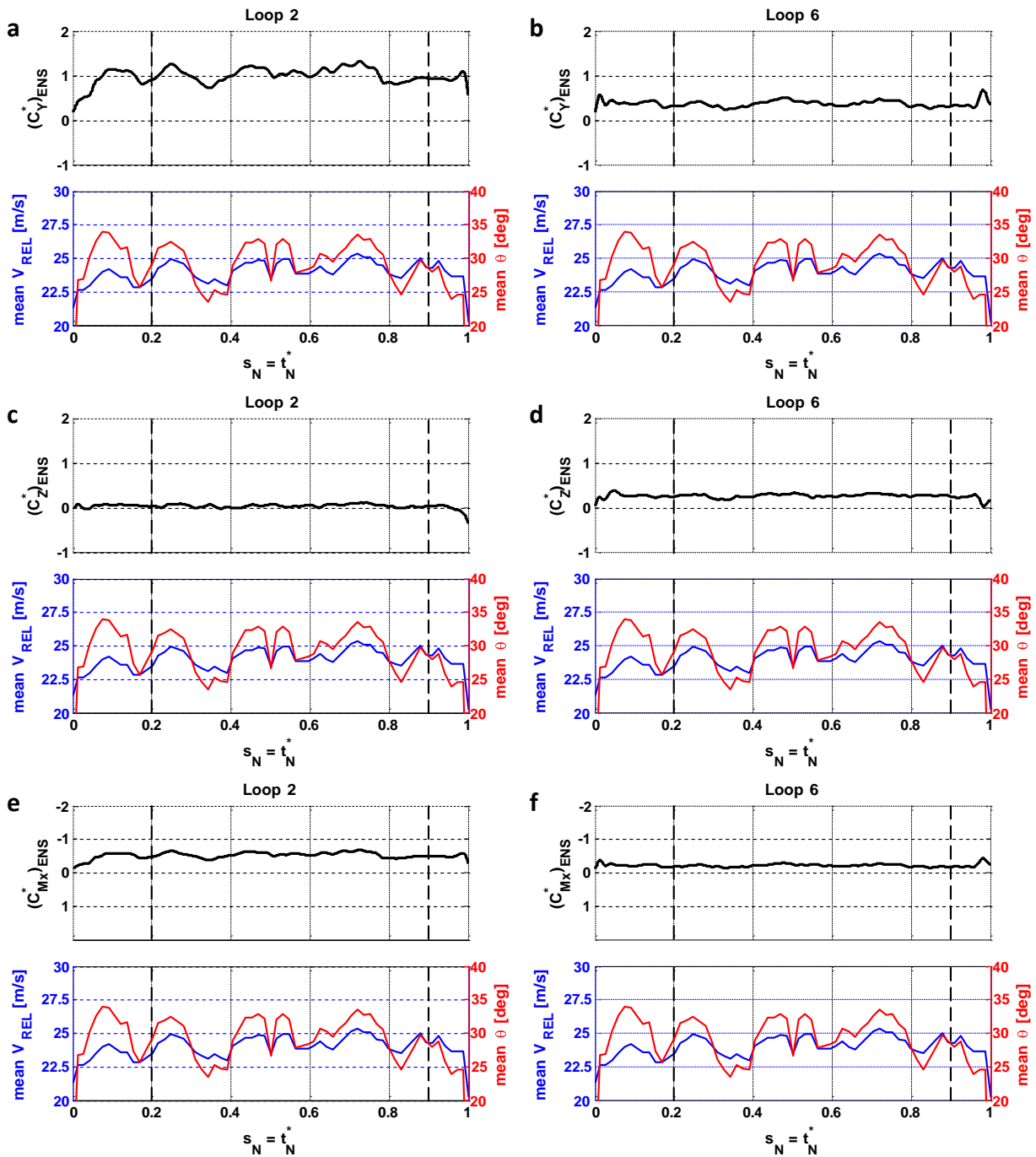
Figure G.4 Moving model tests load coefficients per unit length: ensemble averages time series in combination with the nominal mean relative wind (loop 2 on the train nose, loop 6 in the centre of the leading car)

Figure G.4 confirms the correspondence observed for the pressure coefficient also with consideration of the load coefficients per unit length: positive peaks of the side force and rolling moment coefficients occur in combination of positive peaks of both the mean relative wind velocity and the mean yaw angle.

G.3 *Modified* data reduction method

It has been illustrated in section 6.2 that a reference velocity based on spanwise averages of the mean relative wind properties is employed by the data redution method originally applied (in chapters 5 and 6) to obtain the mean aerodynamic coefficients. Such a method relies on the *Quasi-Steady* assumption and is commonly adopted in relation to experimental pressure measurements undertaken in variable wind conditions.

The '*modified*' method presented in the following proposes a development of the *original* approach. On the one side, in light of the short time-scale wind fluctuations induced by turbulence, the *modified* method cannot entirely prescind from the *Quasi-Steady* assumption. On the other side, it relaxes such an assumption by taking into account the characteristics of the mean relative wind fluctuations occurring during the moving model experiments. Accordingly, it presents a series of modifications with respect to the *original* data reduction process (in section 5.2).

For purposes of discussion, this *modified* data reduction method is described in this appendix with regard to the pressure coefficients. However, any consideration and procedure can be extended to treat also the load coefficients per unit length.

G.3.1 Mean fluctuations in the relative wind

Relative wind velocity

According to figure G.1 and considering the specific conditions experienced by a travelling train during each TRAIN rig test-run (identified by   ), the instantaneous values of the nominal streamwise and lateral components of the wind velocity (and   , respectively), as well as of the train speed are given by

$$U\left(r,s_N\right) = \bar{U}_{SW}\left(r\right) + \overline{\Delta U}\left(s_N\right) + u'\left(r,s_N\right) \qquad \text{(G.3a)}$$

$$v\left(r,s_N\right) = \bar{v}_{SW}\left(r\right) + \overline{\Delta v}\left(s_N\right) + v'\left(r,s_N\right) \qquad \text{(G.3b)}$$

$$V_{tr}\left(r,s_N\right) = V_{tr,SW}\left(r\right) + V_{tr,GRAD}\left(r\right)\cdot\left(s_N - 0.5\right) \qquad \text{(G.3c)}$$

Equation (G.3a) expresses the instantaneous nominal streamwise wind velocity as the sum of three contributions.   is the double-average (i.e., the average both in time and space, in the spanwise direction) defined in section 5.2.2. It varies (slightly) from run to run due to the intrinsic stochastic nature of the wind simulation but can be extrapolated from the wind measurements undertaken during each run.   represents the mean wind variation (with respect to   ). It depends on the spanwise position but, since it does not consider any turbulence contribution, it is assumed not to vary from run to run.   expresses the turbulence-induced fluctuations and, as such, it depends not only on the spanwise position but also changes from one run to another. In equation (G.3b), the lateral wind velocity is given by the sum of three components analogous to those described for   Finally, in equation (G.3c), the train speed is defined assuming a linear decay within the crosswind section. It is calculated as the sum of the spanwise average   (obtained through equation (5.20) in section 5.2.2.1) and the (negative) gradient   contribution (estimated as explained in the following section).

Yaw angle fluctuations

It has been discussed in section G.2.1 that variations in yaw angle ( ) are determined by modifications of the train speed as well as by fluctuations in the horizontal components of the wind velocity. Hence, for moving model tests, the instantaneous yaw angle can be written as:

$$\theta\left(r,s_{N}\right)=\overline{\theta}_{SW}\left(r\right)+\overline{\Delta\theta}\left(r,s_{N}\right)+\theta{'}\left(r,s_{N}\right) \tag{G.4}$$

where   is the average of the mean yaw angles calculated over the entire span of the crosswind section (and corresponding to 30°),   is the variation (with respect to   ) determined by the irregularity in the mean wind and by the train speed decay and, finally,   expresses the turbulence-induced fluctuations. Each of these terms can be obtained applying equation (G.1) to the train speed and wind velocities given in equations (G.3).

Considerations

The formulation reported above highlights three types of contributions to the instantaneous values of velocity magnitude and of yaw angle:

- , and , as well as the resultant , are invariant with respect to the spanwise position ( ) and vary (slightly) from run to run. Their values associated with each run can be calculated from the trackside measurements as detailed in section 5.2.

- , and are the fluctuations induced by wind turbulence. In light of the stochastic nature of such turbulence, their actual instantaneous values cannot be controlled or predicted. Neither, for practical reasons, these quantities can be measured during each run at every spanwise position. Therefore, turbulence-induced fluctuations can be treated only statistically (and are assumed to be normally distributed about their average values).

- , , and, therefore, are mean variations with respect to the spanwise averages. These quantities are functions of the spanwise coordinate (but, different from turbulence-induced fluctuations, their dependence on can be known in deterministic terms. and can be found from the flow characterisation (since, by definition, they do not vary from run to run), can be calculated for any individual run from the trackside speed measurements and, then, can be obtained from the previous quantities.

As mentioned above, the *original* method considers reference values of relative wind velocity and yaw angle based on the corresponding spanwise averages. The *modified* data reduction method presented in this appendix differs from such an *original* methods because it incorporates also the information regarding the (deterministic) spanwise variations of the mean relative wind. Accordingly, the time series are calculated using a spanwise-varying, rather than spanwise average, reference velocity. Furthermore, knowledge of the spanwise variation of (as an ensemble) is exploited to refine the estimation of the mean pressure coefficient by discarding the instantaneous values of associated with yaw angles excessively different from 30°.

G.3.2 Non-dimensional coefficients time series

The definition of   given in equation (5.16) in section 5.2.2 can be rewritten as follow in order to highlight the dependences on the normalised time   (i.e., the spanwise coordinate   ) and on the yaw angle:

$$C_{Pij2}\left(t_N^*,\theta\right) = \frac{P_{ij}\left(t_N^*,\theta\right) - \overline{P}_{ST,SW}^*}{\frac{1}{2}\rho\left[\overline{V}_{rel2}^*\left(t_N^*\right)\right]^2}$$ (G.5)

where the suffix '2' (added within the subscript indices) highlights those quantities that in this approach are calculated in a different way with respect to what done in section 5.2.2. Consistent with the previous section, then, the relative wind velocity is given by:

$$\overline{V}_{rel2}\left(t_N^*\right) = \sqrt{\left[\overline{U}_{SW2}^*\left(t_N^*\right)\right]^2 + \left[V_{tr,SW2}\left(t_N^*\right) - \overline{v}_{SW2}\left(t_N^*\right)\right]^2}$$ (G.6)

where   and   represent the streamwise and lateral component of the (onset) mean wind velocity, while   indicates the train speed. The calculation processes for each of these quantities are detailed in the following. As in the *original* method, even in this approach no spanwise dependence is taken into account for the static pressure. Its reference value in equation (G.5), hence, is the same as calculated in section 5.2.2.2.

The correspondence between *nominal spanwise normalised position*   and *nominal normalised (discrete) time*   having been recalled in section G.2.1, the notation here and in the following adopts   for consistency with section 5.2.2.

Reference onset streamwise wind velocity

The calculation of the reference onset streamwise mean wind velocity is carried out through a process similar to that described in section 5.2.2.2. In this case, however, a function of the spanwise position (rather than a spanwise average value) is extrapolated from the local measurement of wind

speed collected during each run. Based on the flow characterisation (FC) data, a velocity ratio indicated as was defined as:

$$K2_U^{MOV}\left(t_N^*\right) = \frac{\bar{U}_{C_F}\left(t_N^*\right)}{\bar{U}_{Loc,FC}}$$

(G.7)

where indicates the streamwise mean wind velocities measured at different spanwise positions (=), while represents the particular value associated with the one position where the reference probe was placed during the moving model tests.

Using such a velocity ratio, the spanwise mean velocity , and its corrected value (which took into consideration the along-wind gradient), both functions of the spanwise coordinate, are obtained respectively as

$$\bar{U}_{SW2}\left(t_N^*\right) = K2_U^{MOV}\left(t_N^*\right)\cdot\bar{U}_{Loc}$$

(G.8)

$$\bar{U}_{SW2}^*\left(t_N^*\right) = \bar{U}_{SW2}\left(t_N^*\right) + m_U^{MOV}\cdot d_{MOV}$$

(G.9)

It is worth noting that the same gradient as in section 5.2.2.2 is adopted. The data from the flow characterisation do not enable an estimation of such a quantity for each different spanwise position. However, seen the short distance , the related level of approximation on the final estimation does not appear significant.

Reference onset lateral wind velocity

The reference (onset) lateral mean wind velocity is obtained in a similar way to that illustrated for the streamwise component. The dedicated velocity ratio found from the flow characterisation data is:

$$K2_v^{MOV}\left(t_N^*\right) = \frac{\bar{v}_{FC}\left(t_N^*\right)}{\bar{v}_{Loc,FC}}$$

(G.10)

where are the mean lateral velocities across the CWG width and is the mean value at the spanwise position where the reference probe was placed during the moving model tests. From such ratio, the spanwise mean velocity is obtained as:

$$\overline{v}_{SW2}\left(s_N\right) = K2_v^{MOV}\left(s_N\right)\cdot\overline{v}_{Loc} \tag{G.11}$$

In this case, no correction is applied in terms of along-wind gradient.

Reference train speed

The train speed variation within the crosswind section is calculated on the assumption of linear decay and expressed as

$$V_{tr,SW2}\left(s_N\right) = V_{tr,SW} + V_{tr,GRAD}\cdot\left(s_N - 0.5\right) \tag{G.12}$$

where is the spanwise average of the train speed (defined and calculated as in section 5.2.2.1) while is the (negative) gradient obtained as:

$$V_{tr,GRAD} = \frac{V_{tr,EX} - V_{tr,IN}}{L_{CW}} \tag{G.13}$$

In equation (G.13), and indicate the train speed at the entry and exit of the crosswind section, which were measured during each run by the trackside speed measuring systems (section 4.5.2.3).

Pressure coefficient time histories

According to the definitions given above, the spanwise-varying reference wind speed, i.e., , can be calculated for each run. According to equation (G.5), then, in the *modified* data reduction method such a quantity is used for calculating any individual time series as described in section 5.2.2.3. First, *modified* single-run actual time histories ( ) are computed. Secondly, these are interpolated with respect to the non-dimensional normalised time . Finally, *modified* ensemble average time series are obtained through equation (5.33).

G.3.3 Mean coefficients

Mean yaw angle and *Quasi-Steady* assumption

Single-run time series for the mean yaw angle   can be calculated from those of the train speed and mean wind velocity components. From them, an ensemble average time history   can be extrapolated based on series of 15 runs. Therefore, at any instant of (non-dimensional) time   , an association can be made between ensemble average values of the pressure coefficient and ensemble average values of the yaw angle. In light of this, and invoking the *Quasi-Steady* theory, it is assumed that   , as an ensemble, depends steadily on the ensemble mean yaw angle at any normalised time instant   :

$$C_{Pij,2}\left(\theta\right)\Big|_{ENS\,2} = C_{Pij,2}\left(\overline{\theta}_{ENS}\right)\Big|_{ENS\,2} \tag{G.14}$$

Mean coefficients calculation

In the *original* method (equation (6.2) in section 6.3.1) the time averaged pressure coefficient is obtained by averaging any of the corresponding ensemble average time series over their the entire steady portion (i.e., for   ). To take into account the spanwise fluctuations of the mean yaw angle, the same approach undertaken in a number of past tests involving (uncontrollable) natural wind excitations (Cooper, 1981; Quinn, 2007) is applied in this *modified* method.

For purposes of discussion, the time series referred to the pressure tap 8 on loop 2 is taken into consideration in figure G.5. As illustrated by the horizontal blue band in this figure, a range of 30° ± 2° is defined for the yaw angle fluctuations and then the subintervals where   falls within such a range are identified within the steady portion of the time series (i.e.,   ). Highlighted by the green vertical bands in figures G.5a and G.5b, the collection of these subintervals is indicated in the following as   . The mean pressure coefficient (associated with a nominal yaw angle of 30°) is calculated as:

$$\overline{C}_{Pij\,,2} = \overline{C_{Pij}\left(t_N^*,\overline{\theta}_{ENS}\right)\Big|_{ENS\,2}}\Bigg|_{\theta_{ENS}\,\in[30°\pm2°]} = \overline{C_{Pij}\left(t_N^*\right)\Big|_{ENS\,2}}\Bigg|_{t_N^*\in T_{30}} \tag{G.15}$$

where an overbar denotes the average with respect to the normalised time which, as specified in the subscript, is computed here only over the   associated with 28° <   < 32° (i.e., for   included in the subintervals identified above and highlighted in green in figure C.5).
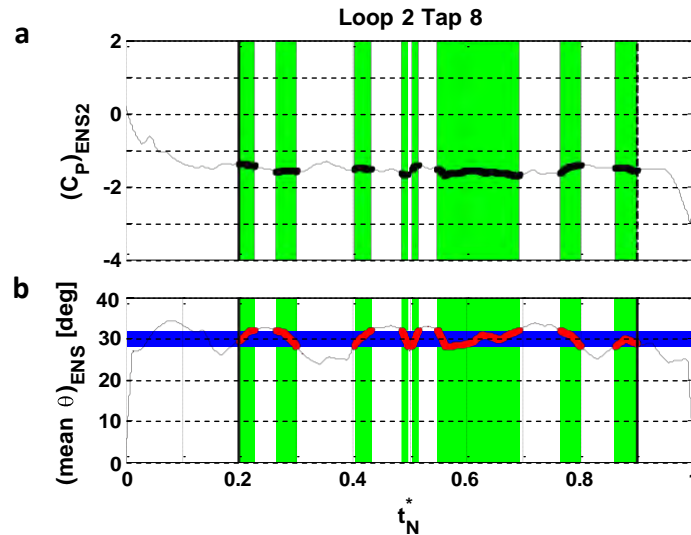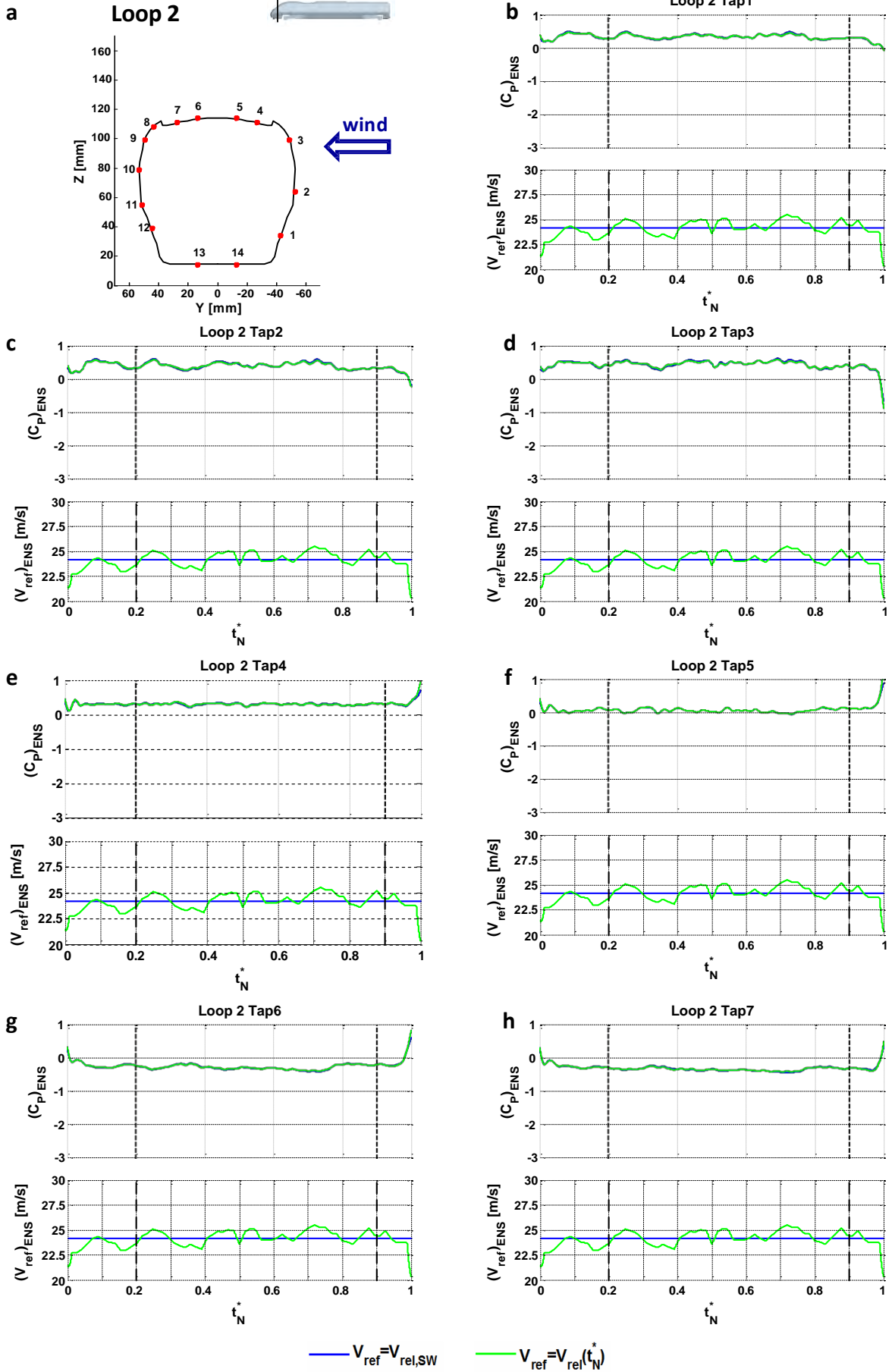

Figure G.5 Moving model tests modified data reduction method: mean pressure coefficients calculation

G.4   Second set of moving model test results

Raw data from moving model experiments were re-processed applying the *modified* data reduction method described above. This led to new ensemble averages time histories relating to both surface pressure coefficients and aerodynamic loads coefficients per unit length and, in turn, to a second series of mean coefficients for surface pressure, aerodynamic loads per unit length and overall aerodynamic loads. This second set of results is presented in the following in comparison to those reported in section 6.3.

G.4.1   Surface pressure distribution

Figures G.6 and G.7 show the ensemble average time histories of the pressure coefficients on loops 2 and 6, respectively. A comparison is arranged between   calculated according to *modified* method described above and the results obtained through the *original* method. The evolution of   with respect to the normalised non-dimensional time   is displaced in combination with spanwise variation of the *nominal* reference wind velocity used in the calculation.

a Loop 2

b Loop 2 Tap1

c Loop 2 Tap2

d Loop 2 Tap3

e Loop 2 Tap4

f Loop 2 Tap5

g Loop 2 Tap6

h Loop 2 Tap7

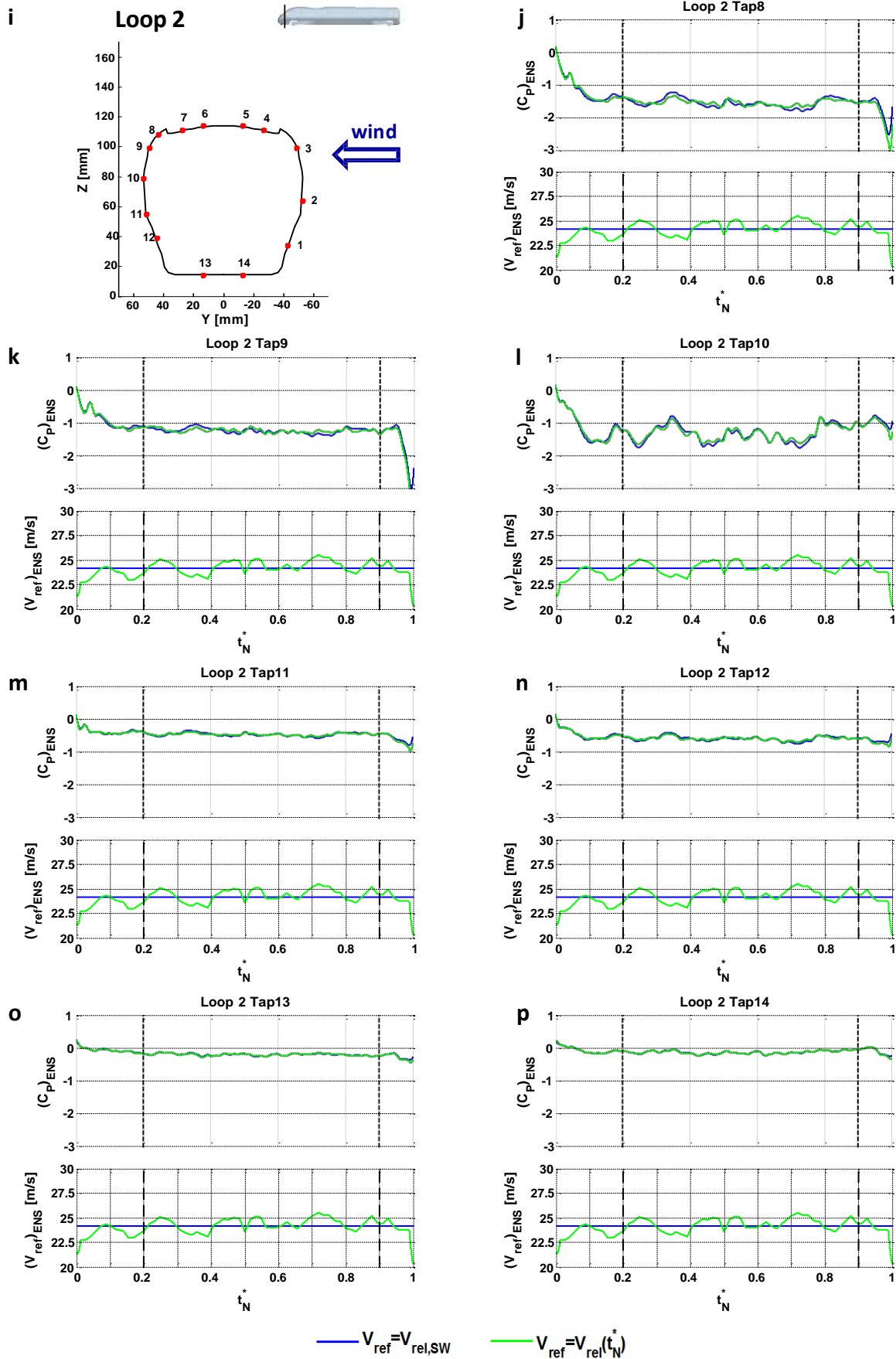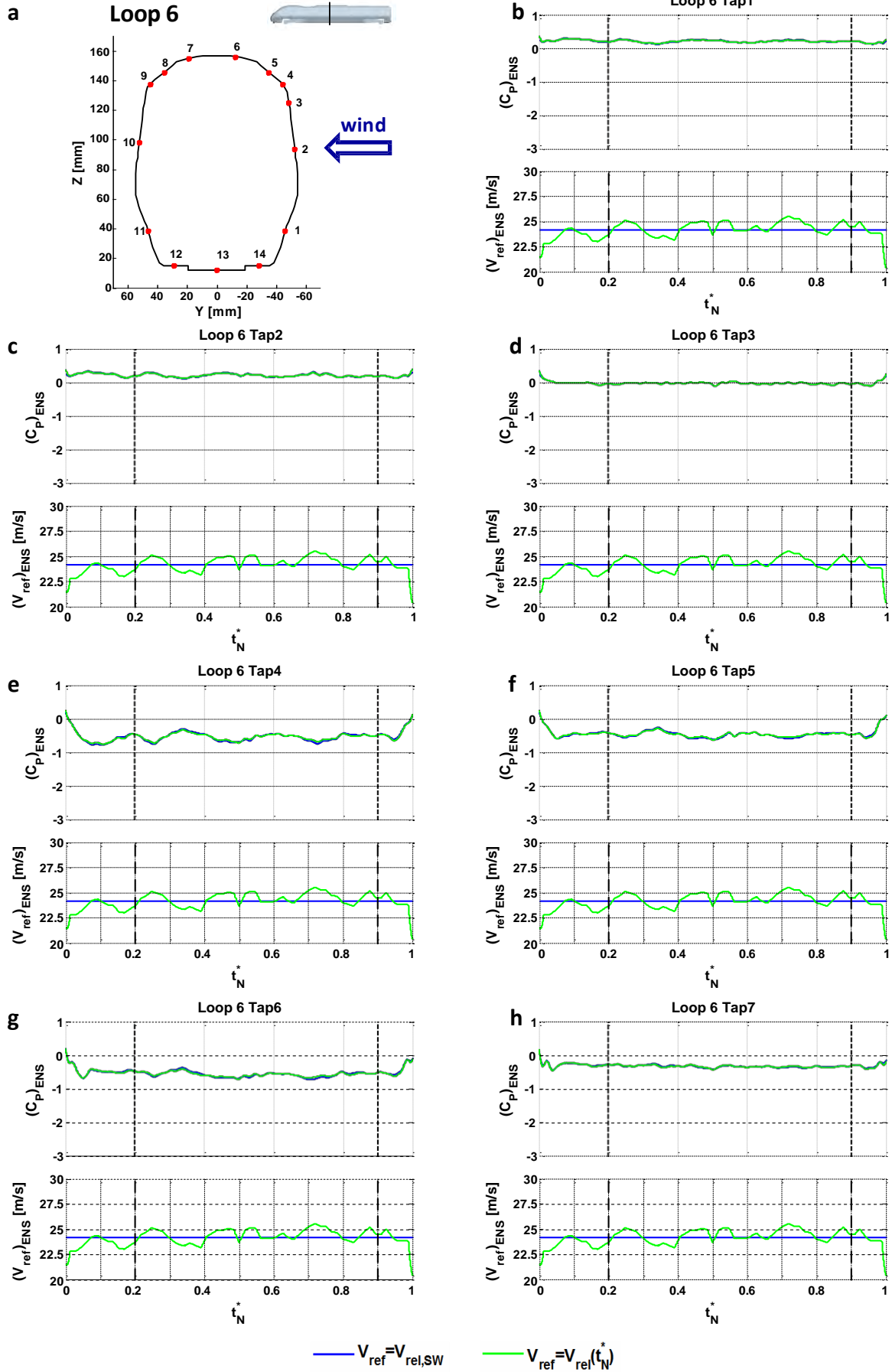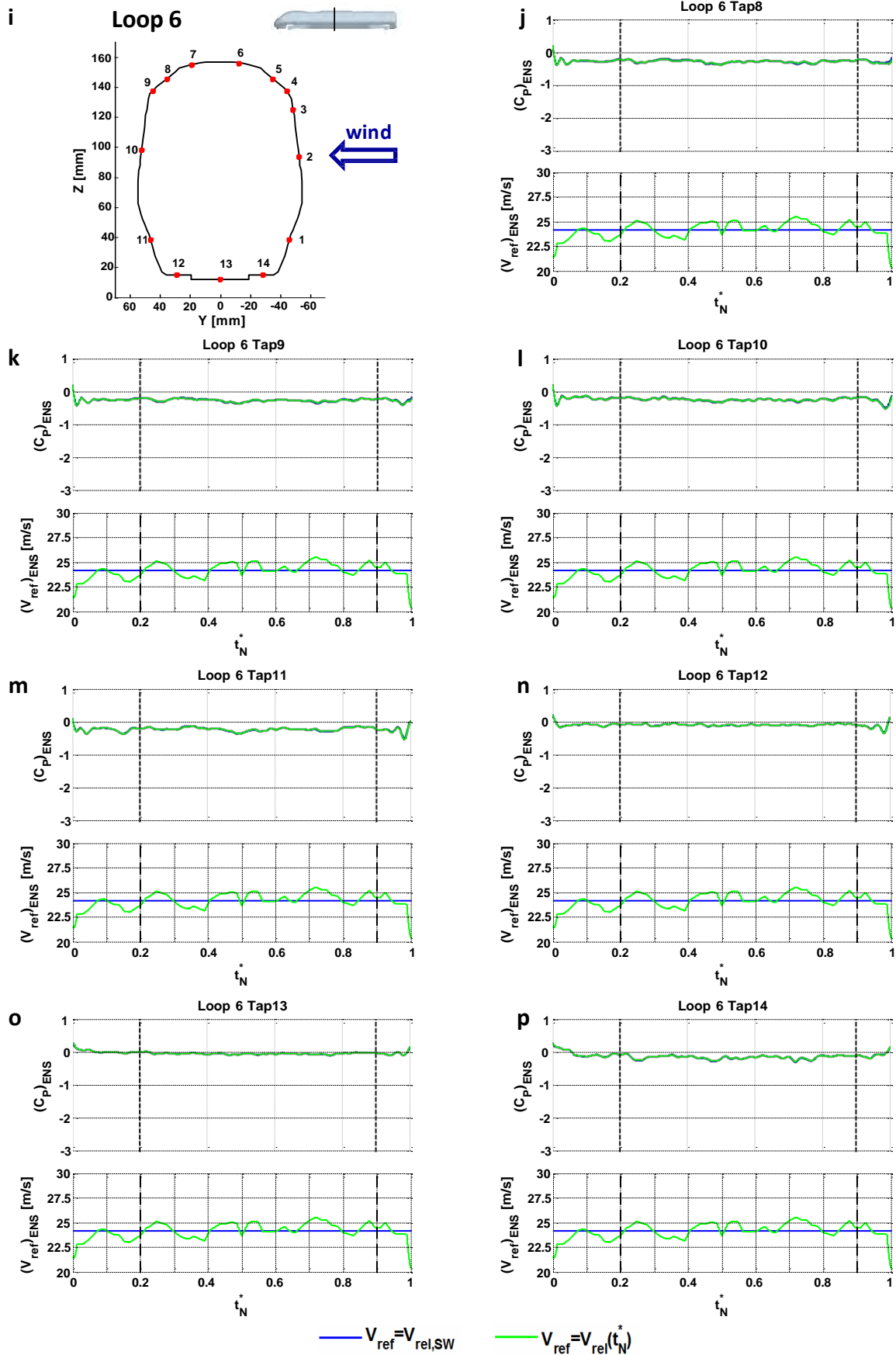$V_{ref} = V_{rel,SW}$ $V_{ref} = V_{rel}(t_N^*)$

Figure G.6 Moving model tests, original vs. modified data reduction method: pressure coefficient ensemble averages time series on loop 2 (on the train nose) in combination with the nominal mean relative wind

a Loop 6

b Loop 6 Tap1

c Loop 6 Tap2

d Loop 6 Tap3

e Loop 6 Tap4

f Loop 6 Tap5

g Loop 6 Tap6

h Loop 6 Tap7

$V_{ref} = V_{rel,SW}$ $V_{ref} = V_{rel}(t_N^*)$

Figure G.7 Moving model tests, original vs. modified data reduction method: pressure coefficient ensemble averages time series on loop 6 (centre of the leading car) in combination with the nominal mean relative wind

Figures G.6 and G.7 indicate that the *modified* method produces limited variations in the time histories of   . On the majority of the pressure taps there are no significant changes with respect to the previous set of results and, where present, these changes are quite small. The most evident modifications can be found on taps 8 to 10 on loop 2 and on taps 4 to 6 on loop 6, where suction peaks arise and, therefore, the largest amplitudes in the long time-scale fluctuations are reached. As expected, in these cases the use of a spanwise variable reference wind velocity in the *modified* method leads to a slight attenuation of such fluctuations.

Figure G.8 illustrates the mean pressure coefficients obtained through the *modified* method and presents a comparison with the *original* moving model tests results (figure 6.10 in section 6.3.1). In addition, the static test results are included. It is worth noting that no margin of experimental uncertainty is taken into consideration in this comparison because both sets of moving model test results are obtained from the same raw data. Consequently, any difference between green and blue markers in figure G.8 can be interpreted as related only to the use of a different data reduction method.

d Loop 4

e Loop 5

f Loop 6
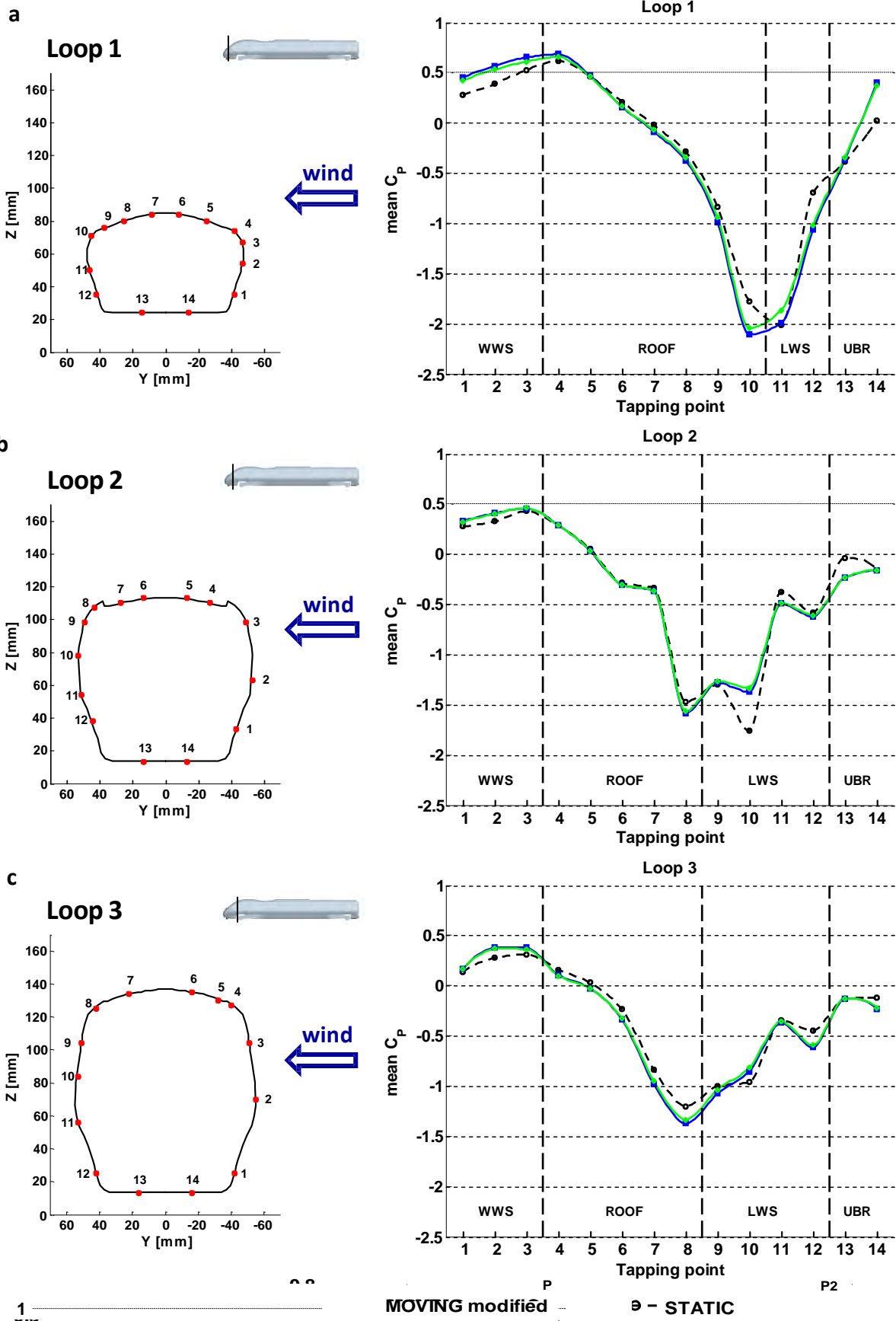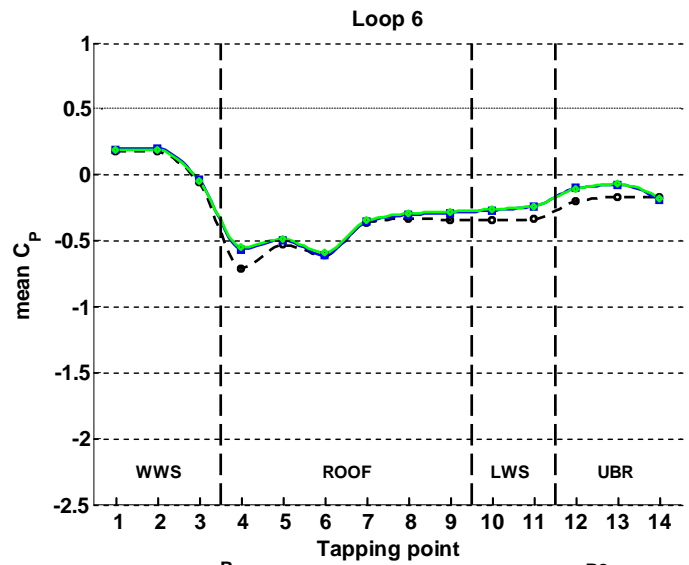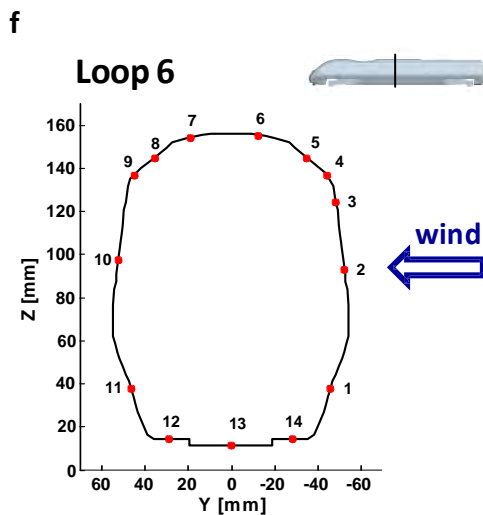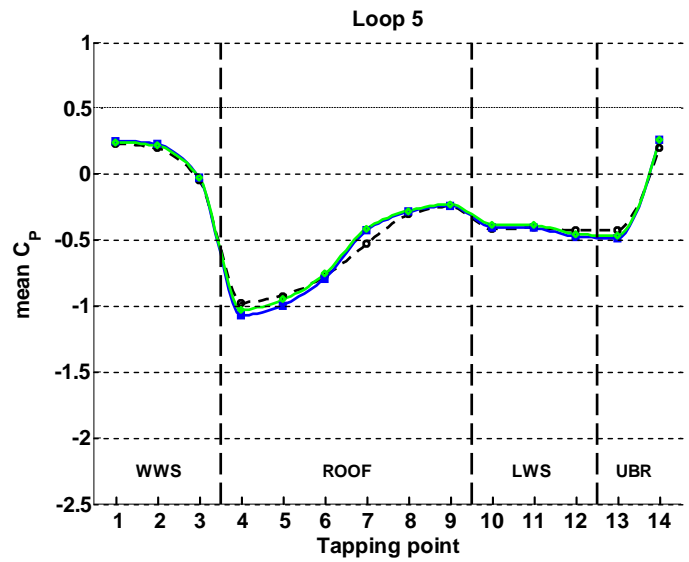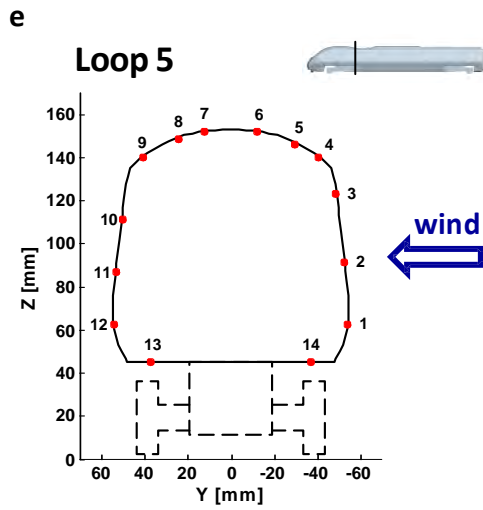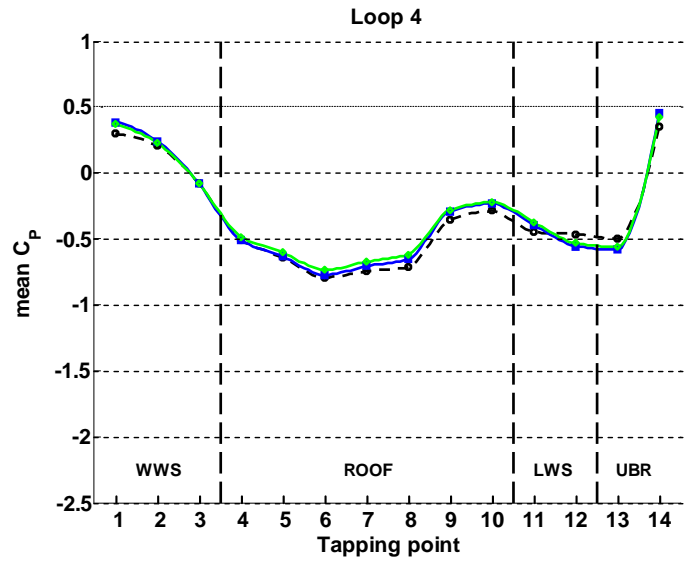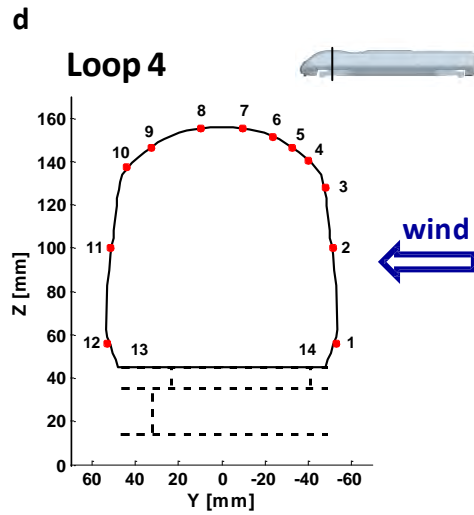
MOVING modified — STATIC
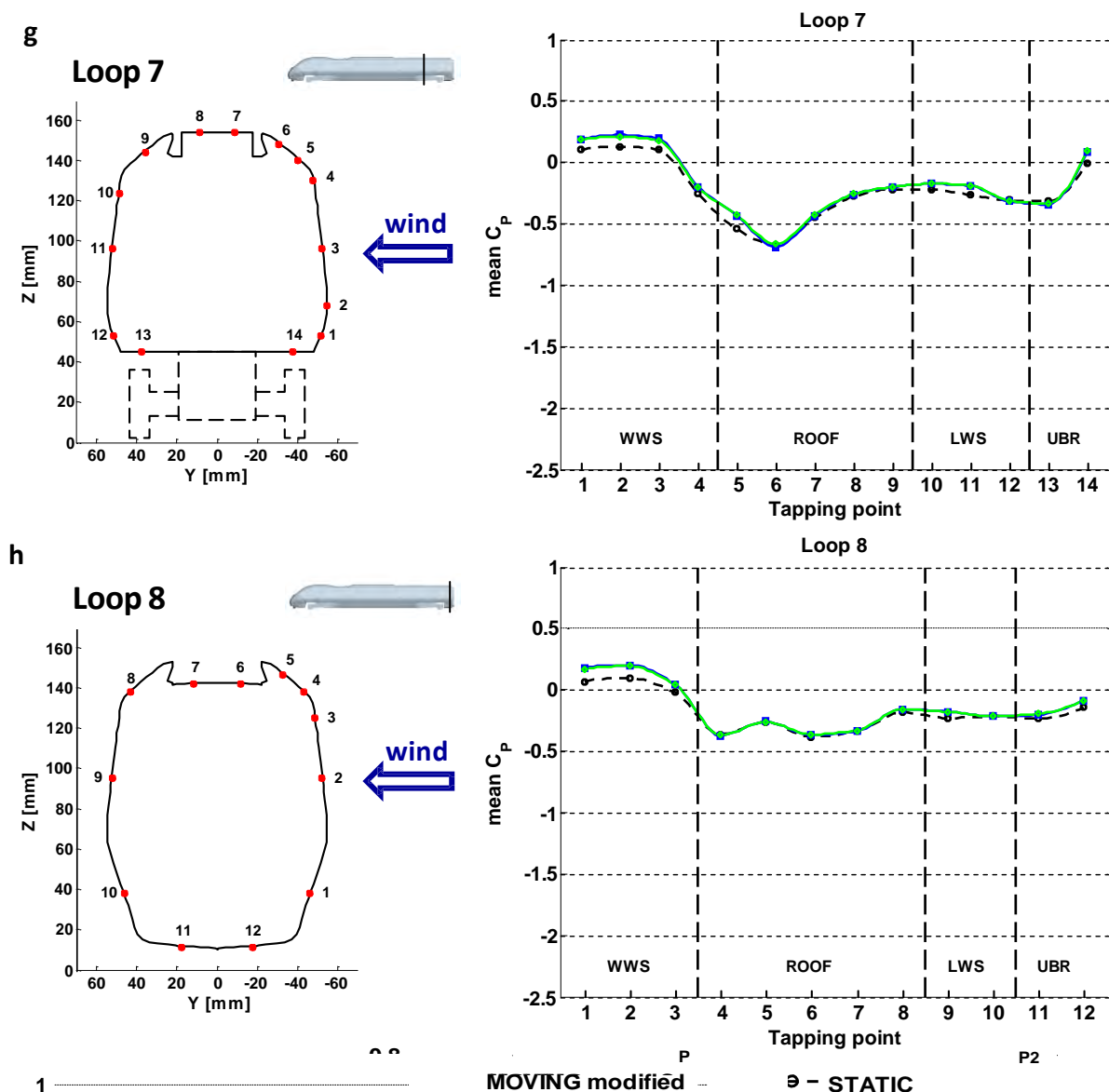
Figure G.8 Moving model tests, original vs. modified data reduction method (vs. static tests): mean pressure coefficient distribution on the loops of pressure taps 1 to 8

It appears from figure G.8 that using the *modified* data reduction method has a limited impact on the mean pressure coefficients of moving model tests. Some minor differences with respect to the *original* results can be observed in the front part of the train, from the nose to the front bogie (i.e., on loops 1 to 5). Here, the *modified* results show slightly reduced magnitudes and thus indicate slight attenuation in the intensity of both stagnation and suction areas. In the centre and rear of the train (i.e., on loop 6, 7 and 8) the agreement between the two series of moving model test results is such that no difference is perceptible. Accordingly, figure G.8 outlines that using the *modified* data

reduction method (for the moving model test data) produces negligible variations in the differences between static and moving model test results in comparison with those found in chapter 6.

G.4.2 Aerodynamic load coefficients per unit length

The ensemble averages time series of the load coefficients per unit length are illustrated in figures G.9 and G.10, relating to loops 2 and 6, respectively. Similar to the approach undertaken above for the pressure coefficient,   ,   ,   and   on each section are presented in combination with the ensemble average time history of the *nominal* reference wind velocity used in the calculations (which is the same as in figures G.6 and G.7).

Consistent to what observed for   , the *modified* data reduction method leads to reduced amplitudes of the long time-scale fluctuations in the time histories of the load coefficients per unit length. Such a modification can be observed in the side force coefficients on loops 2 and 6 and also in the rolling moment coefficients on loop 2, while considerably reduced variations characterise   and   on loop 6. With regard to   , small differences between the two set of results are visible on loop 6, but not on loop 2. This is not surprising since the long time-scale oscillations characterising the time histories of the lift force coefficient have considerably smaller amplitude than those relating to the other parameters.

Figure G.9 Moving model tests, original vs. modified data reduction method: load coefficient per unit length ensemble averages time series on loop 2 (on the train nose) in combination with the nominal mean relative wind
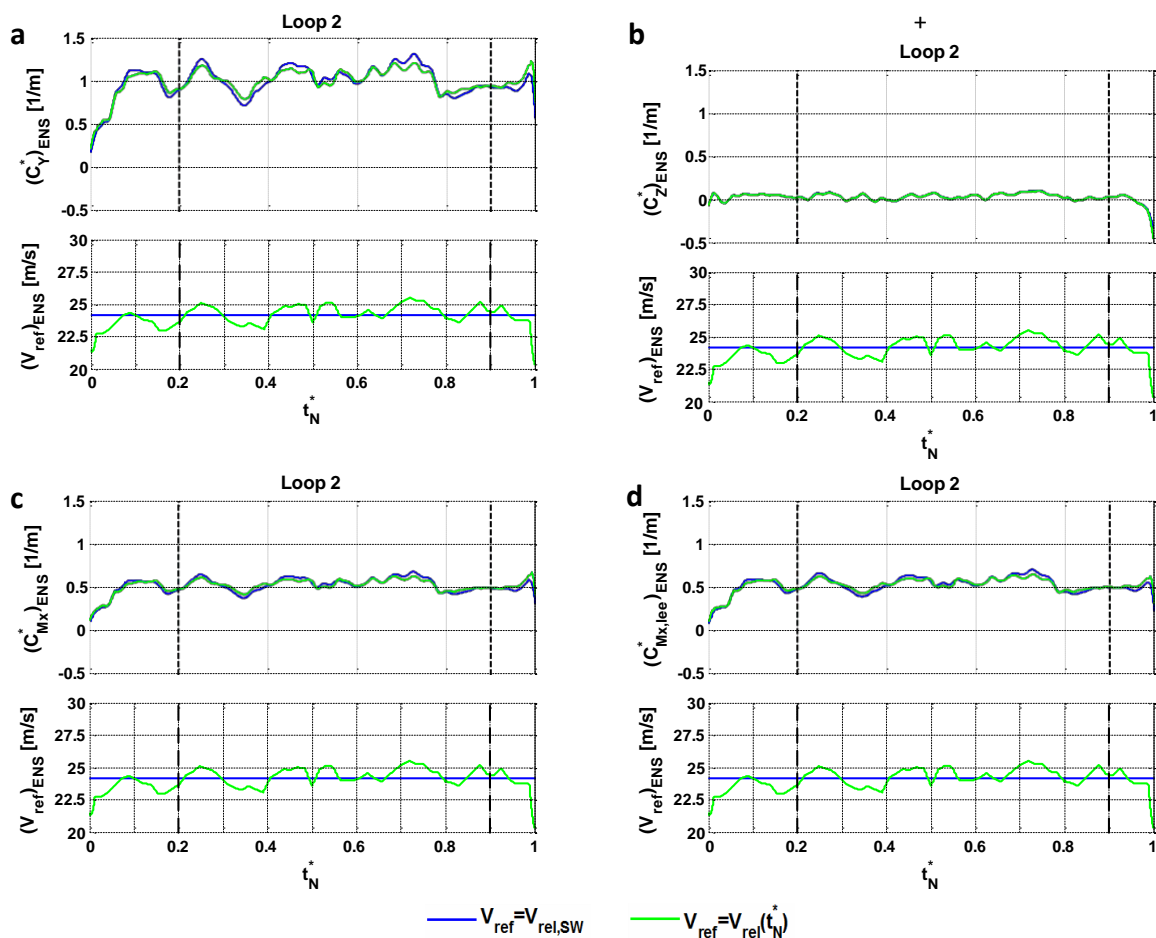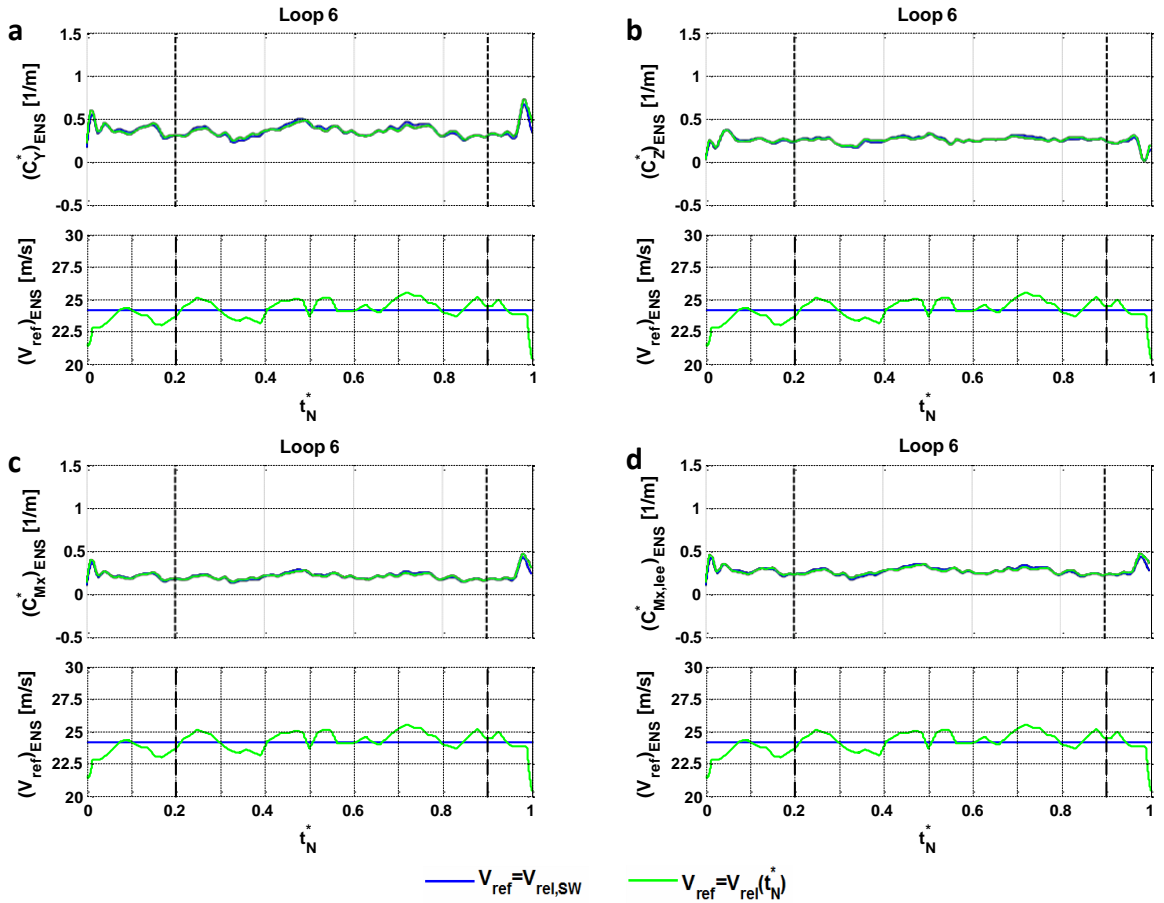
Figure G.10 Moving model tests, original vs. modified data reduction method: load coefficient per unit length ensemble averages time series on loop 6 (in the centre of the leading car) in combination with the nominal mean relative wind
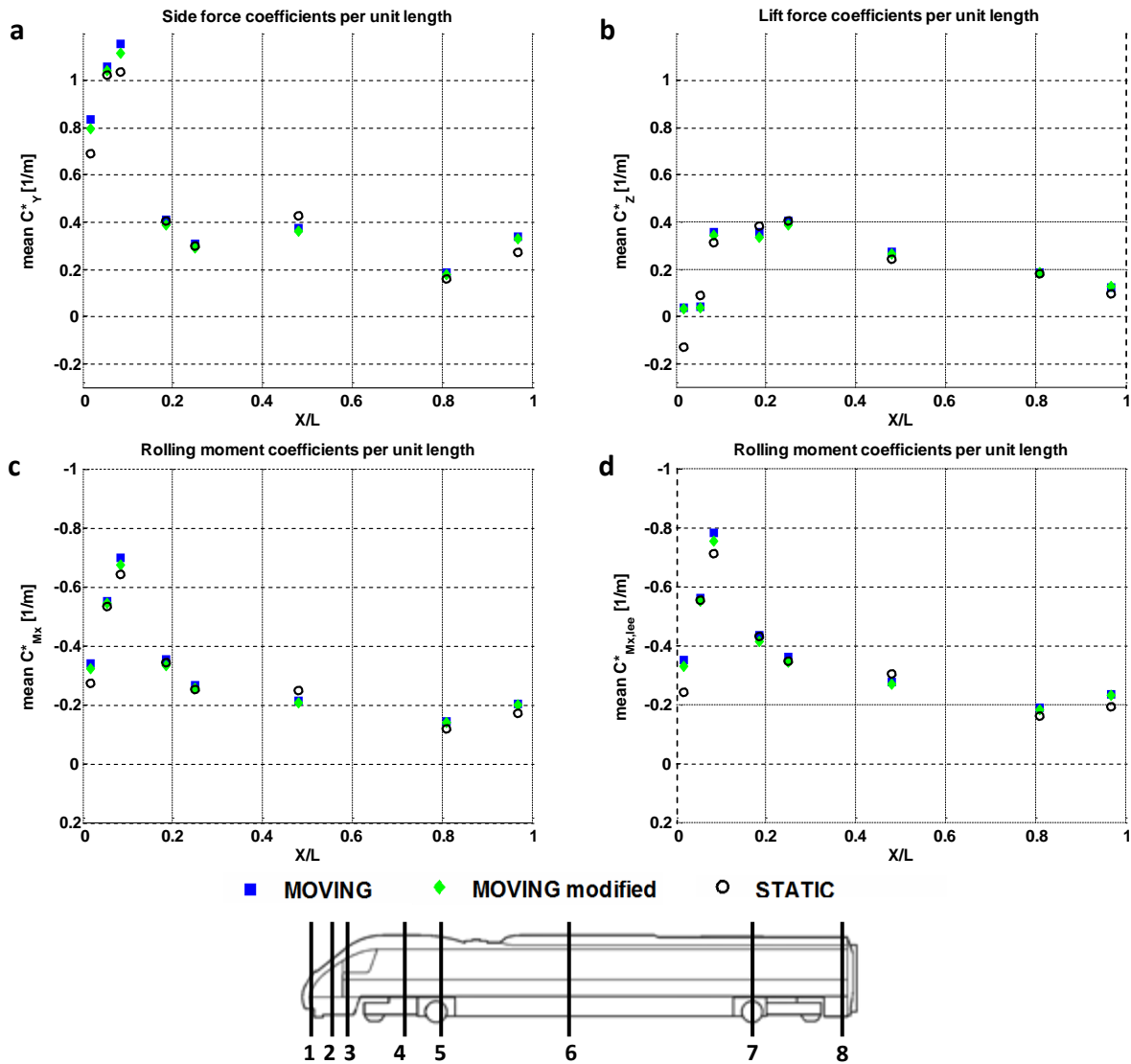
Figure G.11 Moving model tests, original vs. modified data reduction method (vs. static tests): mean load coefficients per unit length

Figure G.11 reports the mean load coefficients per unit length relative to the two series of results obtained for the moving model experiments and to the static test data. The moving model data obtained through the *modified* method denote relevant modifications with respect to those presented in section 6.3.2 only in the front part of the train. The reduced intensity observed for   is echoed here by a decrement in magnitude of the load coefficients per unit length, which is evident particularly on side force and rolling moment coefficients. As observed for the pressure distribution, however, any difference between the two series of moving model test results is smaller than the discrepancy with respect to the static tests values.

G.4.3 Overall aerodynamic load coefficients

Table G.1 and figure G.12 below illustrates the overall aerodynamic load coefficients obtained through the *modified* method. A comparison with respect to the *original* set of moving model test results is presented and, in addition, the static test values are reported. In figure G.12 the experimental uncertainty (estimated in section 5.4.1.2 assuming a normal distribution and considering a 95% confidence level) is indicated by the error bars. According to what discussed above, this uncertainty has no specific use regarding the comparison between moving model test results obtained through different data reduction methods. Nevertheless, it is included at this stage in order to ease the interpretation of the sensitivity that the static vs. moving model test comparison has with respect to the method of analysis used for processing the moving model test data.

	Moving tests ORIGINAL process	Moving tests MODIFIED process	Magnitude VARIATION |MOD. – ORIG.|	STATIC TESTS
	0.417	0.403	-3%	0.425
	0.251	0.245	-2%	0.233
	-0.257	0.248	-4%	-0.262
	-0.316	0.305	-3%	-0.316

Table G.1 Moving model tests, original vs. modified data reduction method (vs. static tests): mean overall aerodynamic load coefficients
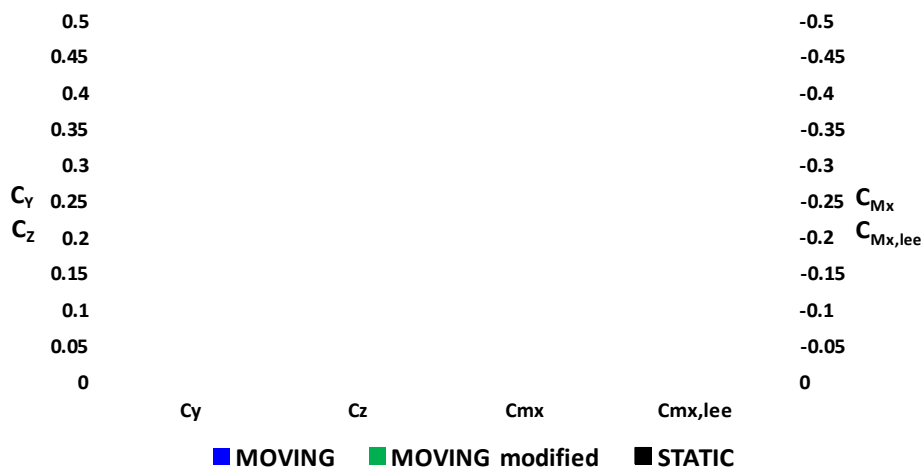

Figure G.12 Moving model tests, original vs. modified data reduction method (vs. static tests): mean overall aerodynamic load coefficients

The trend highlighted by the overall load coefficients reflects the results presented in the previous sections G.4.1 and G.4.2. The *modified* data reduction method leads to a reduction in magnitude of

the overall mean load aerodynamic coefficients. This reduction is quantified between 2% and 4%, with the largest variations occurring on the parameters relating to side force and rolling moments.

With respect to static test results, such a trend contributes to slightly increase the discrepancies originally observed in section 6.4.3 relating to   ,   and   (for which moving model tests produce lower coefficient than static tests). With regard to the lift force coefficient, which instead is larger when obtained through moving model experiments, the use of the *modified* method leads to a reduction of the difference with respect to the static test results. It is worth noting, however, that even if the *modified* method is used for computing the moving model test results, any difference with respect to the static tests data remain within the margin of experimental uncertainty.

G.5   Discussion

The examination of the ensemble average time histories obtained through the *modified* method (both for   and for the load coefficients per unit length) has shown that long time-scale fluctuations are still present, although slightly attenuated in magnitude. Within the *modified* method a spanwise varying (rather than spanwise average) reference wind velocity is used for data reduction. However, at such a stage where the ensemble average time series are computed, no modifications with respect to the *original* method are implemented to evaluate the spanwise variability of the mean yaw angle. Accordingly, the persistence of the long time-scale fluctuations suggests a strong dependence on the spanwise variation of the mean yaw angle (rather than of the relative wind velocity magnitude).

In terms of mean pressure coefficients, as well as of mean aerodynamic load coefficient per unit length, the *modified* data reduction method leads to results very similar to those presented in chapter 6. Any discrepancies with respect to the *original* results are significantly smaller than the differences with respect to the static test results. With regard to overall mean load coefficients, instead, the *modified* data reduction method produces variations in moving model test results of the same order of the differences found with respect to the static test coefficients. However, if the

margin of experimental uncertainty is taken into account, it can be observed that this is significantly larger than any variation in the results related to using one or another moving model tests data redution method. This suggests that any margin of approximation introduced by the assumptions made while processing the moving model test data is smaller than the uncertainty caused by experimental errors. Consequently, for the purposes of the present research, what outlined in this appendix supports the viability of the moving model test *original* data reduction method.

Appendix H

Wind Tunnel Static Tests

H.1   Introduction

This appendix describes the measurements undertaken in the Cryogenic wind tunnel (KKK) of DLR – DNW, in Cologne (Germany). These tests were carried out as part of the AeroTRAIN project (ERA, 2009) and investigated the same nominal train geometry (i.e., a Class 390 Pendolino) that was used in the TRAIN rig experiments. It should be noted that the wind tunnel campaign was supervised by SNCF and Alstom (two of the AeroTRAIN project partners) and the University of Birmingham had accessibility to the data as a member of the AeroTRAIN consortium. The following section H.2 reports a comparison between the overall mean load aerodynamic coefficients estimated through wind tunnel tests and those from the TRAIN rig experiments (carried out by the author of this thesis).

H.2   Comparison between wind tunnel and TRAIN rig tests

The wind tunnel tests were undertaken in accordance to the experimental procedure specified in the European standard EN14067-6 (CEN, 2010). They investigated a 1:30 scale-model train statically mounted on a flat ground scenario and subjected to a low-turbulence wind simulation. The Reynolds number was ~3×10^5. A force balance was employed for measuring the aerodynamic forces and moments and then the non-dimensional load coefficients were obtained. The full details of the experimental campaign are included in the internal test report (Jonsson et al., 2012).

Figure H.1 outlines the comparison between the results from Wind Tunnel (WT) static tests and from TRAIN rig static and moving model tests. It considers the overall mean aerodynamic coefficients relative to side and lift forces, and to the rolling moment referred to the central longitudinal   -axis

(placed at the same level as the top of the rail (TOR)) and to the leeward rail. The reference system is the same specified in figure 4.14 in section 4.4. The WT data are illustrated in the 0 to 90° yaw angle range, while those from TRAIN rig experiments are relative to a 30° yaw angle. Error bars indicate the experimental uncertainty associated with any of the datasets (the TRAIN rig experimental errors have been estimated in section 5.4.1.2, while the WT errors have been provided in the test report (Jonsson et al., 2012)).
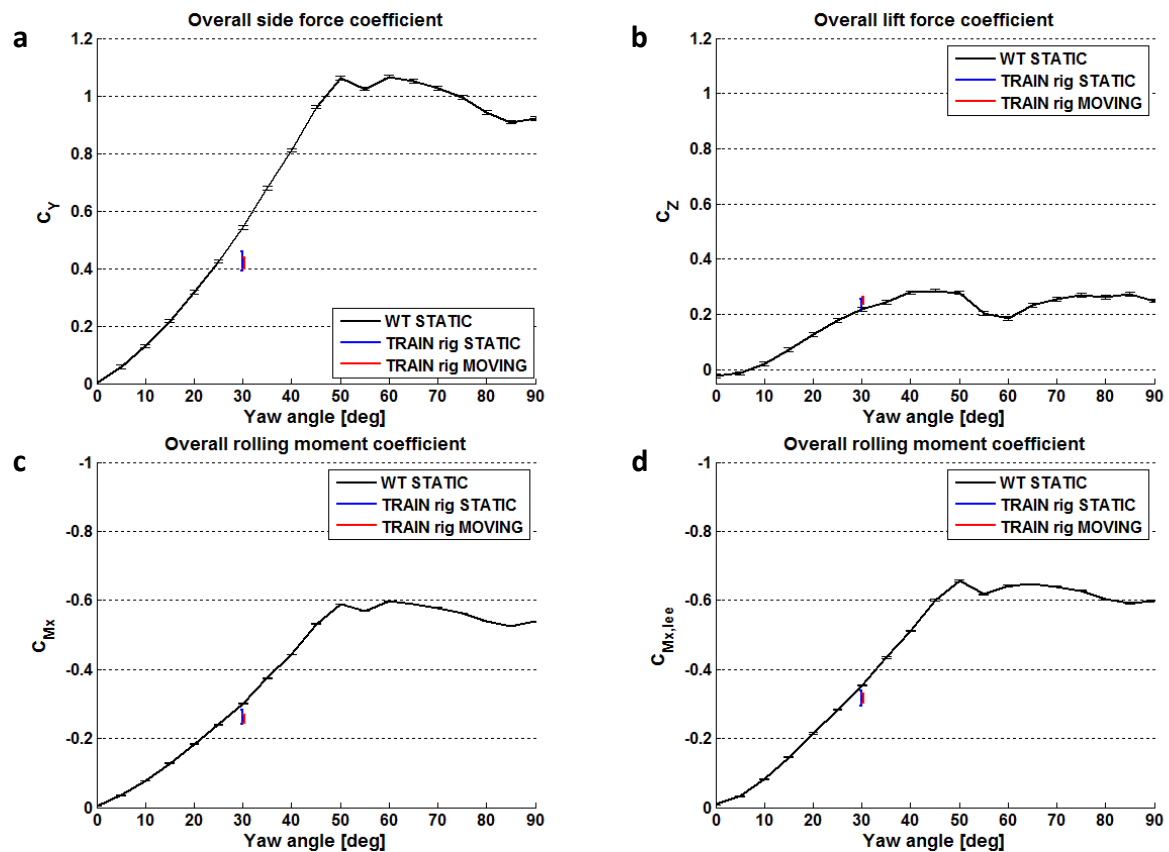
Figure H.1 Comparison between wind tunnel and TRAIN rig tests: mean overall aerodynamic coefficients

WT load coefficients show progressively increasing values between yaw angles of 0° and 50°-60°. The side force coefficient ( ) and reach peaks of approximately 1.06 and -0.6, respectively, both in the 50°-60° yaw angle range. The lift force coefficient tends to peak at slightly lower yaw angles, i.e., between 40° and 50° and its largest magnitude is ~0.28. , which is given by the combination of and , has its maximum of ~0.66 in proximity of 50° yaw angle. At yaw angles larger than 50°-60° the side force and both rolling moment coefficients tend to decrease slightly, with a deeper reduction occurring on and . The lift coefficient drops (of approximately one-third) if the yaw

angle increases over 50°, with a relative minimum at 60°. After that, it grows again to reach values of the same order of its maximum between 75° and 85° and then slightly decreases at 90°.

This trend of the overall mean load coefficients is consistent with what expected for a train's leading car presenting a streamlined design (Baker, 2011), such as the Class 390 Pendolino train. It reflects the characteristics of the flow around a high speed train as examined in section 2.4.1. Furthermore, a correspondence can be observed with respect to the results obtained for the same nominal train geometry (i.e., Class 390 Pendolino) through previous experimental campaigns (Baker, 2003).

The comparison between WT and TRAIN rig (static and moving model) test results outlines a good consistency, although a number of differences exceed the margin of experimental uncertainty. With regard to the side force and rolling moment coefficients the TRAIN rig test data underestimate the WT prediction of approximately 20% and 10-13%, respectively. The TRAIN rig results concerning the lift force coefficient, instead, are slightly higher than those obtained in the WT. If the TRAIN rig static test data are considered, however, the variation of lift force coefficient with respect to the WT results is smaller than the estimated uncertainty. These discrepancies between WT and TRAIN rig results are not surprising in light of the differences between the two experimental setups, which are specified in table H.1.

	TRAIN rig	Wind Tunnel
vehicle geometry	Simplified Class 390 Pendolino 1st car + half second coach Simplified bogies	Simplified Class 390 Pendolino 1st car + half second coach Simplified half bogies + wheel-sets Slight modification in the underbody profile
Geometrical scale	1:30	1:25
Infrastructure scenario	Conventional Flat Ground (FG)	Approximated Flat Ground (AFG)
Wind simulation	Low turbulence ($I_U \square 0.4\%$)	Turbulent ($I_U \approx 16\%$)
Reynolds number	$Re \square 3x10^5$	$Re \approx 1.2x10^5$ (Static tests) $Re \approx 2x10^5$ (Moving tests)
Type of measurements	Force measurements	Surface pressure measurements

Table H.1 Wind tunnel vs. TRAIN rig test setup

Although the same nominal train geometry was used, not only there was a small mismatch in the geometrical scale, but also the two scale-models were different in a series of other details. The TRAIN rig model presented partially different bogies and a slight modification in the underbody profile (section 4.4) with respect to the WT vehicle geometry. Furthermore, there were differences between the WT flat ground simulation and the approximate flat ground simulation adopted in the TRAIN rig (section 4.3) and also in the characteristics of the onset wind simulated in each case. While the flow simulation delivered by the CWG in the TRAIN rig presented a turbulence level of ~17%, the WT tests were carried out in low-turbulence flow conditions. In addition, the Reynolds number of ~$3x10^5$ relating to WT tests was slightly higher than those achieved in the TRAIN rig (i.e., $1.2 \ x10^5$ to $2x10^5$). Finally, while direct force measurements were undertaken in the WT, surface pressures were monitored in the TRAIN rig. In the latter case, hence, an additional margin of approximation with respect to the indicated experimental uncertainty is likely to affect the estimations of the overall mean load coefficients.

This additional margin of approximation is related to the model discretisation and to the assumptions made within the integration process (section 5.4.1.2). Despite its quantification is not straightforward, a qualitative indication is provided by the sensitivity study reported in appendix F, where the magnitudes of the mean load coefficients (obtained from TRAIN rig static tests) increases of 2 to 5% when a finer train discretisation is adopted. Therefore, it can be hypothesised that part of the discrepancies outlined in figure H.1 are caused by the use of a relatively coarse train discretised geometry. In addition, a further reason to explain the TRAIN rig underestimation of the side and rolling moment coefficients might be related to the fact that discretised geometry of the train did not include the train bogies, thus sensibly reducing the total lateral surface of the vehicle over which the pressure distribution was integrated.

Appendix I

Author's publications

I.1   Introduction

This appendix contains the following two papers written by the author as part of the PhD studies:

Dorigatti, F., Quinn, A.D., Sterling, M., Baker, C.J., 2012. Evaluation of crosswind effects on rail vehicles through moving model experiments, in: BBAA7 The Seventh International Colloquium on Bluff Body Aerodynamics and Applications Shanghai, China, 2nd-6th September.

Dorigatti, F., Sterling, M., Rocchi, D., Belloli, M., Quinn, A.D., Baker, C.J., Ozkan, E., 2012. Wind tunnel measurements of crosswind loads on high sided vehicles over long span bridges. Journal of Wind Engineering and Industrial Aerodynamics 107, 214-224.

The first paper contains a preliminary version of the results presented in chapter 6 of this thesis.

The second paper illustrates an investigation on the crosswind stability of high-sided road vehicles over long span bridges undertaken through wind tunnel tests. These tests were commissioned by ARUP and Transport Scotland and were carried out by Politecnico di Milano, while the University of Birmingham was involved in the analysis of the experimental results. Accordingly, the role of the author of this thesis has been to analyse the data and then to write the aforementioned paper.

Evaluation of crosswind effects on rail vehicles through moving model experiments

F. Dorigatti [a], A.D. Quinn [a], M. Sterling [a], C.J. Baker [a]

[a] School of Civil Engineering, University of Birmingham, Birmingham, UK

ABSTRACT: This paper presents the results obtained from two series of tests on scale-model rail vehicles, one in static and the other in moving model conditions. The experiments were carried out at the TRAIN (TRansient Aerodynamic INvestigation) rig using the recently developed crosswind generator. A 1:25 scale model of a Class 390 Pendolino train was tested on a flat ground scenario in correspondence of a 30° yaw angle. The Reynolds number was of the order of 2×10^5. The surface pressure on the train leading car was monitored in correspondence of 110 tapping points using a novel onboard stand-alone measuring system. An evaluation of the mean values for the local pressure coefficient shows limited differences between static and moving model tests only in correspondence of a restricted number of tapping points. A comparison in terms of overall mean aerodynamic coefficients indicates a good agreement between the two sets of results.

KEYWORDS: Crosswind, rail vehicles, moving model tests, static tests, mean pressure coefficient, mean aerodynamic load coefficients

1 INTRODUCTION

A train travelling through a natural turbulent crosswind is surrounded by a complex flow field which leads to a series of steady and unsteady aerodynamic forces and moments. These aerodynamic loads may induce significant changes in the vehicle dynamic behaviour in comparison to a no-crosswind condition and, in the presence of strong winds, serious accidents may happen because the train stability has been compromised [1]. To prevent the occurrence of such events, in the last two decades a series of specific methodologies have been developed for assessing the stability of trains in crosswinds [2, 3]. These methodologies are currently applied within the rolling stock certification process [4, 5] and rely on a numerical-experimental approach. While the vehicle dynamics and the characteristics of the natural wind are simulated numerically, the information regarding the wind-vehicle interaction is provided as an external input to the model in form of dimensionless aerodynamic coefficients. Such parameters depend on the train geometry and are typically obtained through wind tunnel experiments on static scale models, which represent the standard technique of investigation [4, 5]. These type of experiments have the significant advantage that they can be treated as conventional wind tunnel tests and, as such, can be carried out in traditional environmental wind tunnel facilities. However, by their very nature they do not simulate the movement of the train relative to the ground; the importance of this on the overall forces/moments acting on the train still remains largely unresolved [6].

Different studies have been undertaken in the past for evaluating the impact that the vehicle movement simulation has on the crosswind loads on trains. Since the mid 1980's the problem was approached from an experimental perspective and a number of moving model test campaigns were carried out [7, 8, 9, 10]. Despite the differences in these experiments, three common elements can be identified. Firstly, a test methodology based on carrying out series of multiple

runs was adopted. This was essential in order to collect a proper amount of data for enabling stable ensemble averages of the time histories to be calculated. Secondly, in the vast majority of the cases, the tests took place in existing wind tunnel facilities, where specifically designed propulsion systems (either mechanical [7, 8, 10] or gravity based [9]) had been integrated for providing the vehicle movement. Finally, the measuring systems employed during the tests all measured the overall forces and moments acting on the moving vehicle through the use of internal strain gauge balances. The outcomes from these previous moving model test campaigns do not appear to be entirely consistent. Bocciolone et al. [9] found no relevant discrepancies between aerodynamic loads on a train measured in stationary and moving model conditions, whereas Baker [7] and Humphreys [8] found the opposite. However, a close examination of data which did show an effect of the vehicle movement simulation yielded no definitive trends. Such inhomogeneity suggests a limited level of reliability associated with the results and was one of the motivations for the current work.

Considering the numerous issues associated with a moving model test campaign, recently, an alternative approach based on CFD analyses has been used [11]. However, before quantitative conclusions can be drawn based on numerical results, it is essential to assess the level of accuracy of CFD when applied to moving vehicles. Such a comparison requires detailed and reliable experiment data, some of which will be outlined below.

This paper presents the results obtained from a measurement campaign on scale-model rail vehicles in crosswinds, which was undertaken as part of the EU-funded AeroTRAIN project. Two series of experiments were carried out, one under static conditions and the other in moving model conditions. Contrary to previous moving model campaigns, the measuring system used for these tests monitored the local pressure distribution on the train surface rather than the overall aerodynamic loads on the vehicle. This approach enables a first comparison between static and moving tests results to be made with consideration to local values of the mean pressure in different areas of the train. By integrating the pressure distribution, a further comparison can be arranged in terms of steady overall aerodynamic loads. In what follows, the details of the examined test case, together with the characteristics of the facility, as well as of the measuring system and of the methodology, are described in section 2. Section 3 illustrates the results in terms of local values of the mean pressure coefficient and also of overall steady aerodynamic loads. Side force, lift force and rolling moment coefficients are considered and a comparison between static and moving tests is discussed. Finally, some concluding remarks are drawn in section 4.

2 EXPERIMENTAL CAMPAIGN

All of the experiments outlined below were carried out at the University of Birmingham's TRAIN (TRansient Aerodynamic INvestigation) rig (the distinctive features of which are outlined in section 2.1). A 1:25 scale model of a Class 390 Pendolino train was used for the tests. It comprised a full reproduction of the leading car followed by a dummy half trailing car: the leading vehicle was the object of investigation, while the partial second coach was provided to ensure realistic flow around the length of the train (Fig. 1a). For the purpose of the present work a Flat Ground (FG) scenario (i.e. no representation of the ballast was included) and a yaw angle (i.e. the angle between the direction of travel and the relative impacting wind) of 30° were examined. An onset turbulent crosswind characterized both series of tests, static and moving. Such flow simulation was provided by a crosswind generator that has been developed as part of this project. A more in depth description of this apparatus, as well as of the flow characteristics, is reported in what follows. The Reynolds number, based on the train height and the wind speed relative to the vehicle, was of the order of 2×10^{5}.
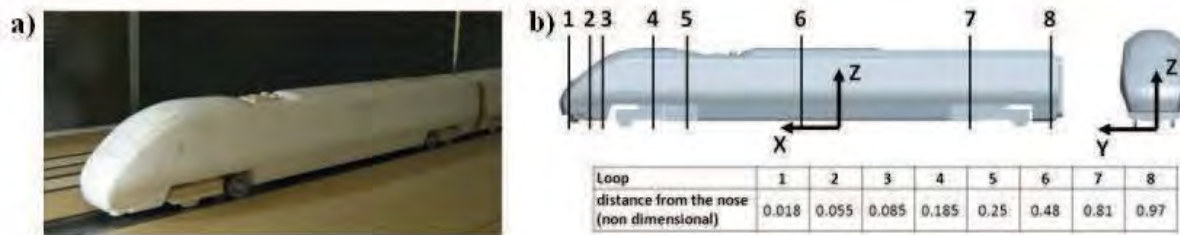
Figure 1. a) Photograph of the Class 390 Pendolino model (1:25 scale). b) Reference system and position of the loops of pressure taps on the leading car.

2.1 The TRAIN rig

The TRAIN rig is a research facility specifically dedicated to undertaking moving model tests on scale model vehicles in open-air, crosswinds and tunnels [12]. It is situated in Derby (UK) and was designed and built by British Rail Research at the end of 1980's [13]. The rig consists of a series of three straight parallel tracks, 150 meters long, equipped with a mechanical propulsion system that can catapult a 1/25 scale model up to 75 m/s. The acceleration mechanism employs a series of pre-tensioned elastic ropes driven by pulleys, while the brake is based on the use of a piston deformable tube. The facility was acquired by the University of Birmingham Centre for Railway Research and Education (BCRRE) in 2009. Since then, the capability of performing moving model experiments in crosswinds has been improved through the design and installation of a new crosswind generator.
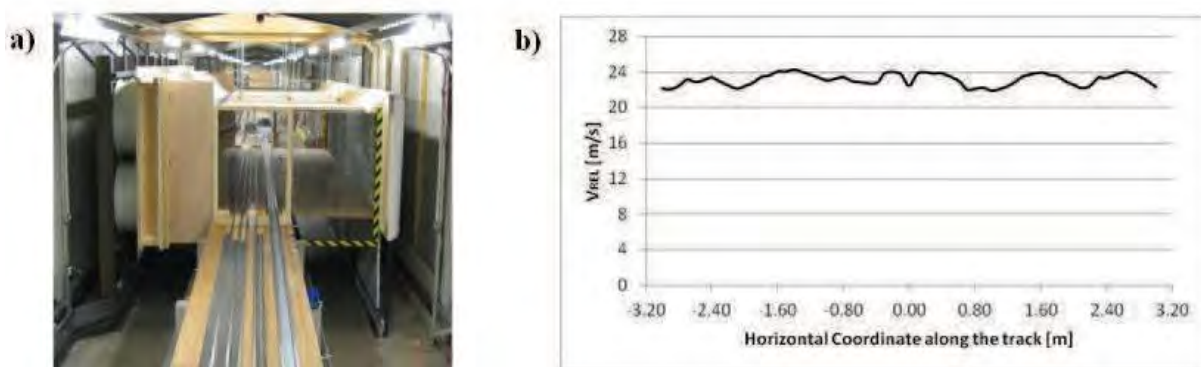

Figure 2. a) TRAIN rig internal view: new crosswind generator. b) Mean wind velocity relative to a train travelling at 20m/s c.a. and experiencing a 30° yaw angle: horizontal profile at 3m full scale equivalent height.

The new system, consists of a series of 16 axial flow fans positioned at the trackside and arranged in two rows of eight units each. The fans operate in sucking-mode and generate an airflow directed perpendicularly to the direction of travel. Such flow is enclosed in a tests section spanning a portion of the tracks 6.4m long (indicated in what follows as L_{CW}). A photograph of the new crosswind generator is shown in Figure 2a. Before the static and moving model test campaigns started, a dedicated session was carried out in order characterize the properties of the simulated crosswind in terms of mean speed, turbulence intensity and static pressure. The spanwise average of the mean wind speed (U) and turbulence intensity (I_U), measured at 3m full

scale equivalent height, are approximately 12m/s and 16%, respectively. The mean velocity profile of the relative wind, as seen by a train travelling through the crosswind section at approximately 21 m/s (thus in correspondence to a 30° yaw angle) is illustrated in Figure 2b.

2.2 Measuring Instrumentation

The experimental data collected during the tests comprised of both trackside and onboard measurements. The trackside measurements included the data regarding the ambient conditions (temperature, barometric pressure and relative humidity), the crosswind properties (velocity and static pressure within the air-channel) and the train speed (for moving model tests only). The ambient conditions were monitored using an Oregon Scientific BAR208HGA weather station and a GBP3300 digital barometer. Localized measurements of the flow speed and static pressure within the crosswind section were recorded using a set of Series 100 cobra probes (by Turbulent Flow Instrumentation Ltd) and a Pitot-static tube in combination with differential pressure transducers HCLA02X5PB (by Sensortechnics GmbH). An acquisition system run by a laptop computer was employed and data were sampled at 1KHz over a time interval of 60s. During moving model tests, the vehicle speed at the entry and exit of the crosswind generator was measured by two sets of photoelectric position finders and reflectors.

   The onboard measurements consisted mainly of the surface pressures detected on the train model. For moving model tests, they included also the output signal from a light detector. The employment of an onboard stand-alone measuring system is essential in order to enable moving model experiments. Unlike what had been done in the past, the system used for these tests monitored the local pressure distribution on the train surface rather than the overall aerodynamic loads on the vehicle. It is a purpose-built measuring system, which employs a series of miniaturized ultra-low differential pressure transducers HCLA12X5PB (by Sensortechnics GmbH) in combination with a stand-alone data logger. The data logger has a 16-bit resolution, is capable of monitoring 16 channels at a maximum sampling rate of 4KHz and presents an extremely compact design that makes it suitable to be accommodated inside the scale train model. The surface pressure was measured only on the first vehicle, which was equipped with eight loops of pressure taps distributed along its length for a total of 110 measuring positions (Fig. 1b). A series of silicon tubing connected the tapping points to the pressure ports of the transducers. Having 15 channels of the data logger available to pressure measurements, the same number of transducers was used. This enabled the pressure taps of each single loop to be monitored simultaneously. A light detector was connected to the sixteenth channel of the data logger. Having set a series of light sources at specified locations along the track, during the moving model tests the signal from such sensor provided a number of µSRVLWLRQ PDUNHUs¶. They were used while post-processing the data for trimming the records from the raw data and thus isolate the portion of time histories associated to the train travelling within the crosswind section.

2.3 Experimental setup and test methodology

The test procedure for static tests was similar to the standard methodology commonly adopted for wind tunnel experiments. The train model was mounted statically inside the air-channel and rotated with respect to the oncoming wind in order to simulate the required yaw angle (30°). Time histories of the surface pressure on the train were recorded during a time window of 60s at a sampling rate of 4KHz. It is worth noting that, having the design of the crosswind generator optimized for moving model tests, a number of restrictions were imposed on the static tests. The dimensions of the model coupled with the limited extension of the air-channel in the along-wind direction (i.e. transversally to the track) meant that the nose of train was positioned close to the

channel inlet (i.e. at a distance of approximately 0.2m). This positioning compromised the possibility of a freestream flow upstream the model and determined a high sensitivity of the pressure field on the nose of the train to minor alterations in the environment external to the air-channel. In addition, a gradient in the along-wind direction was identified by the experimental data collected during the flow characterization, either for the streamwise mean wind velocity (negative gradient) or for the static pressure (positive gradient). All these aspects were taken into account during the data processing and also within the uncertainty analysis. They led to an estimate of the experimental error for the static tests slightly larger than in moving model conditions (Fig. 6).

During the moving model experiments the train was run through the crosswind section at approximately 20.8m/s (±0.6m/s). For analysis purposes the wind velocity was doubled averaged, i.e., both in time (averaged over the measurement time) and spatially (spanwise) along the measurement domain, yielding a value of 12m/s. Hence, the required yaw angle was 30° ±1°. Considering a total span of the air-channel (L_{CW}) of 6.4m, a train travelling at the specified speed spent approximately 0.3s within the crosswind section. With an acquisition data rate of 4 KHz, this corresponded to approximately 1200 samples. A high variability was observed in the time histories of the surface pressure associated to different runs (Fig. 3b). This suggesting that no reliable indication could be obtained from the analysis of individual runs, a data analysis method based on ensembles of runs was adopted for the moving model tests [14]. For the experiments reported in this paper, a sensitivity study indicated that 15 runs were required for obtaining stable ensemble averages. Figure 3 presents an example of the results obtained by applying this moving model test procedure, with consideration of one single pressure tap on loop 2 (on the nose of the train according to Figure 1b).
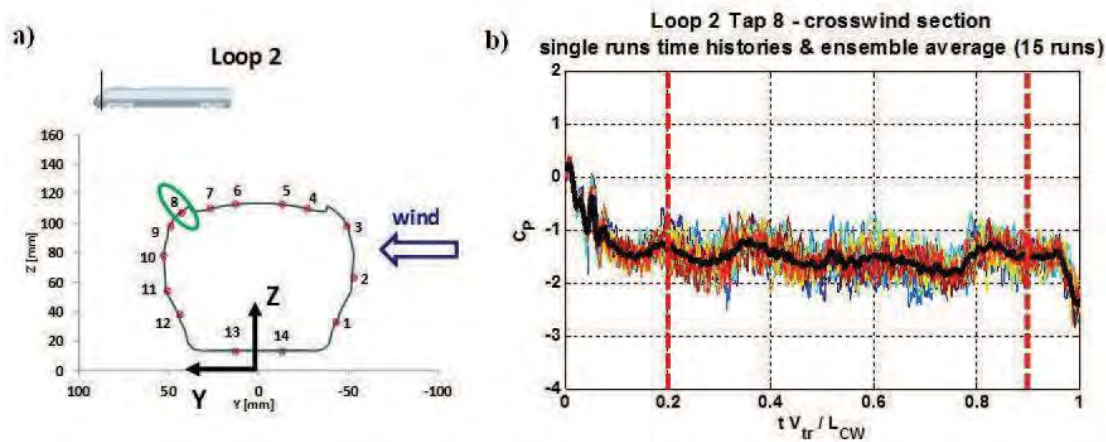

Figure 3. a) Loop 2: cross-section and taps' distribution. b) Single runs time histories (thin lines in grey colors) and ensemble average time history (thick line in black) trimmed within the crosswind section: C_P with respect to non-dimensional time (the vertical dotted lines denote the portion of time history considered for calculating the mean pressure coefficient).

3 RESULTS AND DISCUSSION

3.1 Stationary pressure distribution

In this section the data concerning the pressure distribution on the train are presented in terms of non-dimensional pressure coefficients. Considering each tapping point i on the train surface, the

instantaneous value of the pressure coefficient at a generic time t is indicated as C_{Pi} and defined as:

$$C_{Pi}(t) = \frac{P_i(t) - P_0}{0.5 \rho U V_{rel}^2} \qquad (1)$$

where $P_i(t)$ is the instantaneous value of the actual pressure, measured at the tapping point i, P_0 is the reference pressure, ρ is the crosswind air density and V_{rel} is the reference wind velocity relative to the train.

The reference pressure (P_0) adopted in this study, either in static or moving conditions, consists in the estimated double average static pressure: during any single run, the wind static pressure at a number of measuring positions were recorded over a 60s time interval. Selecting one of these positions as a reference, and averaging the data over the entire time interval, a local mean value for the static pressure during each run was calculated. The reference pressure P_0, as defined in the above, corresponds to the spanwise average extrapolated from such local mean value. It was obtained using a spanwise average-to-local ratio based on data obtained during the full flow characterization. For static tests only, an additional correction was applied to the reference static pressure calculated as explained in the above. Considering that different loops of tappings were at considerably different distances from the inlet, such correction was adopted to take into account the along-wind static pressure gradient (see Section 2.3). For the moving model experiments, the Cobra probe used for monitoring the reference wind conditions was positioned 0.2m upstream the track centreline, at 3m full scale equivalent height. During the static tests, although still at the same height, the probe was set close to the channel inlet and on the side with respect to the model.

For static tests, the relative wind corresponds to the absolute crosswind. Hence, the reference relative wind velocity (V_{rel}) coincided with the reference crosswind streamwise velocity, indicated as U. Both the definition and the process according to which U was calculated were consistent with those for the reference pressure. A local mean was calculated time averaging the 60s velocity time history recorded by the reference Cobra probe (the same that provided the data for the crosswind static reference pressure). The reference crosswind streamwise velocity (U) is the spanwise average extrapolated from such local mean velocity. Once again it was based on a spanwise average-to-local ratio obtained from the flow characterization data. An along-wind velocity gradient correction was applied when processing the data from static tests.

The results reported in what follows are relative to a stationary aerodynamic condition. Hence, they are expressed in terms of a mean pressure coefficient, $\overline{C}_{Pi}$, where i corresponds to a particular tapping point. For the static tests, the average was calculated over the entire 60s time interval, which corresponded to the full length of time histories recorded for the surface pressure. For the moving model tests, it was obtained considering only the central portion of the ensemble average time history relative to the crosswind section (noted by vertical dotted lines on Figure 3b). The transitions experienced by a running train at the entry and exit of the crosswind section determined a series of unsteady fluctuations respectively in the initial part and in the tail of the ensemble average time history. As not representative of a stationary aerodynamic condition, such effects were not taken into account in the analysis reported here.

Figures 4 and 5 present the mean pressure coefficient distribution in correspondence of two loops of pressure taps, loop 2 on the train nose and loop 6 approximately in the centre of the leading car. A comparison between static and moving tests results is outlined. Error bars are included in the figures to represent the experimental error that has been estimated through an uncertainty analysis (not discussed in the current paper). As specified above, experimental data for the surface pressure were collected for all the eight loops of tappings shown in Figure 1a. For

purposes of discussions, however, two cross-sections were selected to provide a significant example of different surface pressure conditions experienced along the vehicle.

On the nose of the train (Fig. 4) positive values of $\bar{c}_P$, which indicate a stagnation region, are
shown on the windward side and also on the roof windward corner. Negative values of $\bar{c}_P$,
which instead indicate suction, characterize the leeward side, the underbody region and also the roof leeward corner, with an evident suction peak arising in correspondence of the latter. Significantly reduced magnitudes of $\bar{c}_P$, for both positive and negative values, and also a partially dif- ferent trend are outlined at the centre of the train leading car (Fig. 5). Similarly to what observed
for loop 2, the results relative to loop 6 show areas of suction that embrace both the leeward side and the underbody region. A stagnation region is still present on the windward side, within which a uniform surface pressure is indicated by the very similar $\bar{c}_P$ values in correspondence of
taps 1 and 2. The pressure distribution on the roof presents the main variations with respect to what found on the train nose: in the centre of the leading car the roof is entirely characterized by an area of suction, which shows a peak in correspondence of the windward corner.
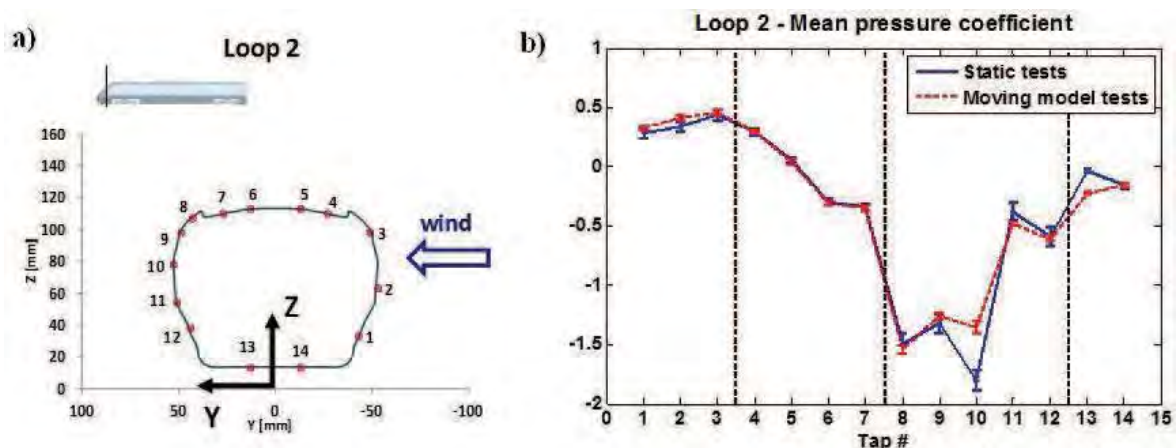

Figure 4. Mean pressure distribution over loop 2 on the nose of the train: Static vs Moving model tests comparison (Class 390 Pendolino, 1:25 scale, 30° yaw angle, FG scenario)
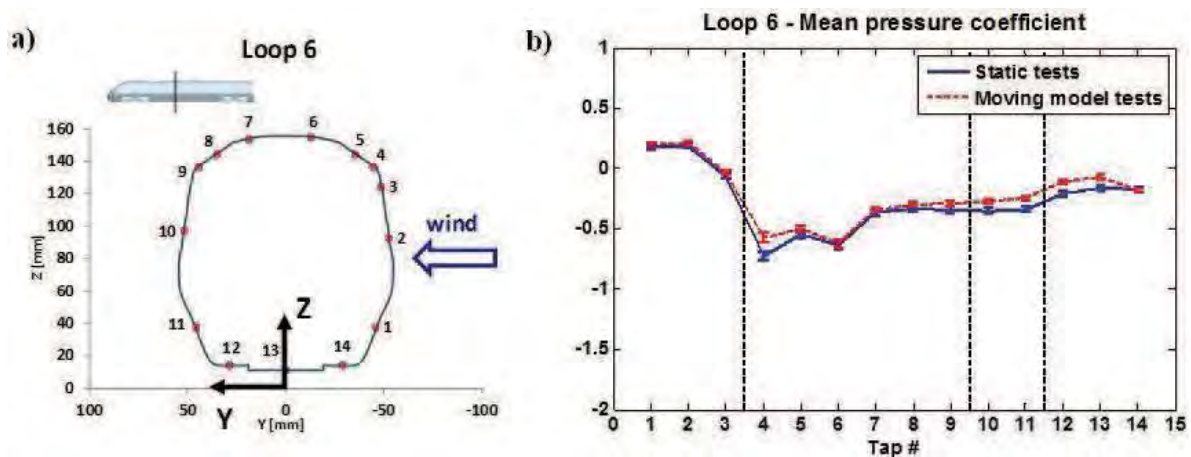

Figure 5. Mean pressure distribution over loop 6 in centre of the leading car: Static vs Moving model tests compari-son (Class 390 Pendolino, 1:25 scale, 30° yaw angle, FG scenario)

These results appear consistent with those reported by previous studies on trains which presented similar streamlined designs and were investigated at a 30° yaw angle [11, 15]. The stagnation on the windward side, which on the nose extends also to part of the roof, is determined by the relative crosswind directly impinging the train surface. The suction peak on the nose leeward side is compatible with the presence in that area of one (or more) vortex attached to the train surface. This being supported not only by the magnitude of the suction highlighted in Figure 4 on tap 8, 9 and 10, but also by the fluctuations observed in the time histories of the surface pressure and reflected by high values of standard deviation (not shown here). Moving towards the rear of the train, the data for the adjacent loops of tappings (not shown here) denotes a progressive attenuation in the intensity of this low pressure peak. Such a trend supporting the hypothesis of the vortices mentioned in the above progressively rolling up and moving away from the train surface. A smooth pressure distribution on the leeward side, still associated to a suction region but showing no peak, is reached already in correspondence of loop 4 (Fig. 1a) by where, hence, a complete detachment of the vortical structures seems to have occurred. A region of uniform low pressure is maintained on the leeward side from that section up the rear of the leading vehicle, as reflected by the results relative to the centre of the first car (Fig. 5). The suction peak observed on loop 6, in correspondence of the roof windward corner, suggests in that area the presence of a further vortex. The data from adjacent measuring sections seems to indicate that this vortex is rolling up on the roof. While moving towards the rear, it is drifting progressively from the windward edge to the centerline of the roof, and then it detaches from the train.

The comparison between static and moving model tests indicate good correspondence between the two cases. If the estimated measurement accuracy is taken into account, the majority of the data show a level of agreement that appears somehow remarkable. There are local differences that do not fall within the margin of experimental error. They tend to occur in correspondence of the suction peaks. Nevertheless, it is worth noting that they can be found only for a limited number of tapping points. The trend of the pressure distribution shows a good agreement between static and moving model test results. In correspondence of all the examined loops of pressure taps, the position and extension of the stagnation regions and of the suction peaks are very similar, and also the magnitude of such peaks is comparable. No major differences, hence, can be inferred with regard to the characteristics of the flowfield surrounding the train.

3.2 Mean aerodynamic load coefficients

The mean aerodynamic load coefficients for the side and lift forces, and for the rolling moment are presented in this section. Such coefficients are indicated in what follows as $\bar{C}_Y$, $\bar{C}_Z$ and $\bar{C}_{Mx}$, respectively. They were calculated by discrete integration of the pressure distribution over the entire leading car, according to the following equations:

$$\bar{C}_Y = \frac{1}{A_{ref}} \sum_i \bar{C}_{Pi} A_i \, n_i \cdot xy \; ; \quad \bar{C}_Z = \frac{1}{A_{ref}} \sum_i \bar{C}_{Pi} A_i \, n_i \cdot xz \; ; \quad \bar{C}_{Mx} = \frac{1}{A_{ref} H_{ref}} \sum_i \bar{C}_{Pi} A_i \left| d_i \wedge n_i \right| \quad (3)$$

In Equation 3, $\bar{C}_{Pi}$ is the mean pressure coefficient as defined in the previous section. A_i and n_i represent, respectively, the area and the normal unit vector associated to each flat surface into which the train geometry has been discretized. The discretized geometry adopted for the integra- tion was the same for both the static and moving model tests pressure data. d is the vector di- rected from the longitudinal axis X to the center of such flat surfaces i, while y and z are the unit vectors associated to the Y and Z axes, respectively (Fig. 1b). A_{ref} is the reference area, assumed as the nominal side area of the leading car and equivalent to 77m^2 at full scale, while H_{ref} is the reference height and corresponds to a full scale equivalent of 3.1m. The convention for positive

directions defined in accordance to the reference system specified in Figure 1a (for the rolling ꝒꝒꝗꝗꝑ ꝼꝆꝆꝆꝡꝛꝛꝗꝙꝓ ꝡꝛꝛ µꝪꝛꝓꝛꝬ-Ꝋꝗꝙꝓ Ꝯꝼꝛꝶꝡ ꝪꝶꝆꝒꝶ¶).

A comparison between the results obtained from static and moving model tests is illustrated in Figure 6. The differences appear to be very limited. In particular, whereas the experimental accuracy is taken into consideration (i.e. by specifying error bars on the figure), it can be appreciated how the discrepancies fall well within the estimated margin of error.
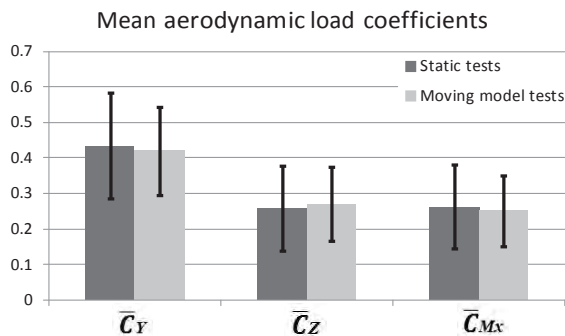

Figure 6. Mean aerodynamic load coefficients for the side force, lift force and rolling moment: Static vs Moving model tests comparison (Class 390 Pendolino, 1/25th scale, 30° yaw angle, FG scenario)

4 CONCLUSIONS

This paper has presented the results from an experimental campaign aimed to assess the effect of the vehicle movement simulation on the train aerodynamics in crosswinds. The existing TRAIN rig moving model test facility was updated by installing a new crosswind generator. A novel test methodology based on the use of an onboard pressure measuring system was developed. The combination of such factors enabled a rather extensive set of data to be collected through both static and moving model experiments. A Class 390 Pendolino scale model was tested on flat ground scenario at a 30° yaw angle. A first comparison, concerned with the mean pressure coefficient on the train leading car, shows limited differences between static and moving model tests. A second analysis, focused on the mean aerodynamic load coefficients, indicates non-significant impact of the vehicle movement on such parameters. Additional studies are ongoing. A further data analysis is investigating the unsteady aerodynamic effects. Also, the experimental results are being shared and used within the AeroTRAIN consortium for CFD benchmarking.

5 ACKNOWLEDGEMENTS

6 REFERENCES

1   Baker, C.J., Cheli, F., Orellano, A., Paradot, N., Proppe, C., Rocchi, D., 2009. Cross-wind effects on road and rail vehicles. Vehicle System Dynamics: International Journal of Vehicle Mechanics and Mobility 47, 983 - 1022.

2   Cheli, F., Corradi, R., Diana, G., Ripamonti, F., Rocchi, D., Tomasini, G., 2007. Methodologies for assessing trains CWC trhough time-domain multibody simulations, in: Proceedings of the 12th International Conference on Wind Engineering.

3   Baker, C.J., 2010. The simulation of unsteady aerodynamic cross wind forces on trains. Journal of Wind Engineering and Industrial Aerodynamics 98, 88-99.

4   CEN, 2010. Railway Applications - Aerodynamics - Part 6: Requirements and test procedure for cross wind assessment, EN 14067-6, Brussels.

5   EC, TSI - Technical Specification for Interaoperability of the trans-European high-speed rail system, in µ5R0ling ⅧRFN¶ 6XE-System. 2008, Official Journal of the European Union. p. 193-195.

6   Baker, C.J., Humphreys, N.D., 1996. Assessment of the adequacy of various wind tunnel techniques to obtain aerodynamic data for ground vehicles in cross winds. Journal of Wind Engineering and Industrial Aerodynamics 60, 49-68.

7   Baker, C.J., 1986. Train aerodynamic forces and moments from moving model experiments. Journal of Wind Engineering and Industrial Aerodynamics 24, 227-251.

8   Humphreys, N.D., 1995. High Cross Wind Gust Loads on Ground Vehicles from Moving Model Experiments. University of Nottingham, Nottingham, UK.

9   Bocciolone, M., Cheli, F., Corradi, R., Muggiasca, S., Tomasini, G., 2008. Crosswind action on rail vehicles: Wind tunnel experimental analyses. Journal of Wind Engineering and Industrial Aerodynamics 96, 584-610.

10 Li, Y., Hu, P., Zhang, M., Liao, H., 2009. Wind tunnel tests with moving vehicle model for aerodynamic forces of vehicle-bridge systems under crosswind, in: Proceedings of the The Seventh Asia-Pacific Conference on Wind Engineering, APCWE-VII.

11 Cheli, F., Rocchi, D., Schito, P., Tomasini, G., 2011. Steady and moving high-speed train crosswind simulations. Comparison with wind-tunnel tests, in: Proceedings of the 9th World Congress on Railway Research, WCRR 2011.

12 Quinn, A.D. The TRAIN (Transient Railway Aerodynamics INvestigation) Rig. 2009-2011 19/02/2012]; Available from: http://www.windresearch.org/mmr.html.

13 Pope, C.W. The simulation of flows in railway tunnels using a 1/25th scale moving model facility. in Aerodynamics and Ventilation of Vehicle Tunnels, p 709-737, edited by Alex Haerter, published by Elsevier, 1991.

14 Baker, C.J., et al., The slipstream and wake of a high-speed train. Proceedings of the Institution of Mechanical Engineers, Part F: Journal of Rail and Rapid Transit, 2001. 215(2): p. 83-99.

15 Hemida, H., Krajnovic, S., 2009. Exploring flow structure around a simplified ICE2 train subjected to a 30 degrees side wind using LES. Engineering Applications of Computational Fluid Mechanics 3, 28-41.